Sadao Adachi

Properties of Group-IV, III-V and II-VI Semiconductors

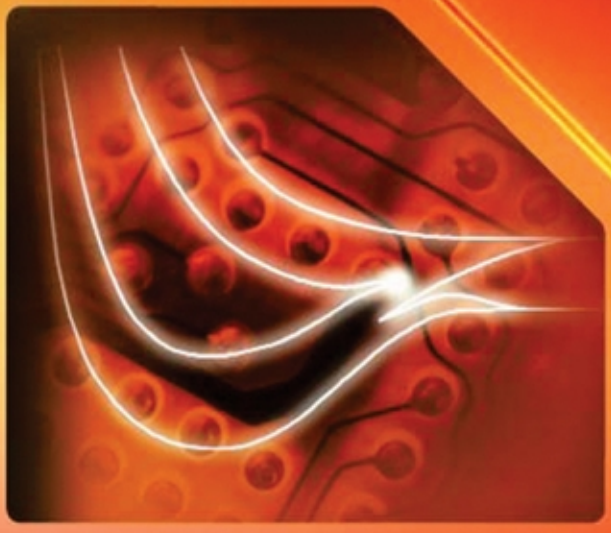

WILEY

Wiley Series in Materials for Electronic & Optoelectronic Applications

VISIT…

Properties of Group-IV, III–V and II–VI Semiconductors

Sadao Adachi
Department of Electronic Engineering
Gunma University
Japan

John Wiley & Sons, Ltd

Properties of Group-IV, III–V and II–VI Semiconductors

Wiley Series in Materials for Electronic and Optoelectronic Applications

Series Editors

Dr Peter Capper, *BAE Systems Infrared Ltd, Southampton, UK*
Professor Safa Kasap, *University of Saskatchewan, Canada*
Professor Arthur Willoughby, *University of Southampton, Southampton, UK*

Published Titles

Bulk Crystal Growth of Electronic, Optical and Optoelectronic Materials, Edited by P. Capper
Properties of Group-IV, III–V and II–VI Semiconductors, S. Adachi

Forthcoming Titles

Liquid Phase Epitaxy, Edited by P. Capper and M. Mauk
Thin Film Solar Cells: Fabrication, Characterization and Applications, Edited by J. Poortmans and A. Arkhipov
Optical Properties of Condensed Matter and Applications, Edited by J. Singh
Charge Transport in Disordered Solids with Applications in Electronics, Edited by S. Baranovski
Dielectric Films for Advanced Microelectronics, Edited by K. Maex, M. R. Baklanov and M. Green

Properties of Group-IV, III–V and II–VI Semiconductors

Sadao Adachi
Department of Electronic Engineering
Gunma University
Japan

John Wiley & Sons, Ltd

Copyright © 2005

John Wiley & Sons Ltd, The Atrium, Southern Gate, Chichester,
West Sussex PO19 8SQ, England

Telephone (+44) 1243 779777

Email (for orders and customer service enquiries): cs-books@wiley.co.uk
Visit our Home Page on www.wiley.com

All Rights Reserved. No part of this publication may be reproduced, stored in a retrieval system or transmitted in any form or by any means, electronic, mechanical, photocopying, recording, scanning or otherwise, except under the terms of the Copyright, Designs and Patents Act 1988 or under the terms of a licence issued by the Copyright Licensing Agency Ltd, 90 Tottenham Court Road, London W1T 4LP, UK, without the permission in writing of the Publisher. Requests to the Publisher should be addressed to the Permissions Department, John Wiley & Sons Ltd, The Atrium, Southern Gate, Chichester, West Sussex PO19 8SQ, England, or emailed to permreq@wiley.co.uk, or faxed to (+44) 1243 770620.

Designations used by companies to distinguish their products are often claimed as trademarks. All brand names and product names used in this book are trade names, service marks, trademarks or registered trademarks of their respective owners. The Publisher is not associated with any product or vendor mentioned in this book.

This publication is designed to provide accurate and authoritative information in regard to the subject matter covered. It is sold on the understanding that the Publisher is not engaged in rendering professional services. If professional advice or other expert assistance is required, the services of a competent professional should be sought.

Other Wiley Editorial Offices

John Wiley & Sons Inc., 111 River Street, Hoboken, NJ 07030, USA

Jossey-Bass, 989 Market Street, San Francisco, CA 94103-1741, USA

Wiley-VCH Verlag GmbH, Boschstr. 12, D-69469 Weinheim, Germany

John Wiley & Sons Australia Ltd, 33 Park Road, Milton, Queensland 4064, Australia

John Wiley & Sons (Asia) Pte Ltd, 2 Clementi Loop #02-01, Jin Xing Distripark, Singapore 129809

John Wiley & Sons Canada Ltd, 22 Worcester Road, Etobicoke, Ontario, Canada M9W 1L1

Wiley also publishes its books in a variety of electronic formats. Some content that appears in print may not be available in electronic books.

Library of Congress Cataloging-in-Publication Data

Properties of group-IV, III–V and II–VI semiconductors / Sadao Adachi.
p. cm.—(Wiley series in materials for electronic and optoelectronic applications)
Includes bibliographical references and index.
ISBN 0-470-09032-4 (cased)
1. Semiconductors—Materials. 2. Semiconductors—Analysis. I. Adachi, Sadao, 1950- II. Series.
TK7871.85.P765 2005
621.3815′2—dc22

2004021913

British Library Cataloguing in Publication Data

A catalogue record for this book is available from the British Library

ISBN 0-470-09032-4 (HB)

Typeset in 10/12pt Times by Laserwords Private Limited, Chennai, India
Printed and bound in Great Britain by Antony Rowe Ltd, Chippenham, Wiltshire
This book is printed on acid-free paper responsibly manufactured from sustainable forestry in which at least two trees are planted for each one used for paper production.

Contents

Series Preface **xiii**

Preface **xv**

Acknowledgments/Dedication **xvii**

1 Structural Properties **1**
1.1 Ionicity 1
1.1.1 Definition 1
(a) Phillips ionicity 2
(b) Pauling ionicity 2
(c) Harrison ionicity 2
1.1.2 Ionicity Value 3
1.2 Elemental Isotopic Abundance and Molecular Weight 3
1.2.1 Elemental Isotopic Abundance 3
1.2.2 Molecular Weight 4
1.3 Crystal Structure and Space Group 4
1.3.1 Crystal Structure 4
(a) Diamond, zinc-blende and wurtzite structures 4
(b) Hexagonal and rhombohedral structures 7
(c) Rocksalt structure 9
1.3.2 Space Group 10
1.4 Lattice Constant and Related Parameters 12
1.4.1 Lattice Constant 12
(a) Room-temperature value 12
(b) Near-neighbor distance 12
(c) External perturbation effect 13
1.4.2 Molecular and Crystal Densities 13
1.5 Structural Phase Transitions 14
1.6 Cleavage 15
1.6.1 Cleavage Plane 15
1.6.2 Surface Energy 18
(a) Theoretical value 18
(b) Experimental value 20
References 20

2 Thermal Properties **23**
2.1 Melting Point and Related Parameters 23
2.1.1 Phase Diagram 23
2.1.2 Melting Point 23
2.2 Specific Heat 26
2.3 Debye Temperature 28
2.4 Thermal Expansion Coefficient 30
2.5 Thermal Conductivity and Diffusivity 33
2.5.1 Thermal Conductivity 33
2.5.2 Thermal Diffusivity 39
References 39

3 Elastic Properties **41**
3.1 Elastic Constant 41
3.1.1 General Remarks 41
3.1.2 Room-temperature Value 42
3.1.3 External Perturbation Effect 48
(a) Temperature effect 48
(b) Pressure effect 50
3.2 Third-order Elastic Constant 51
3.3 Young's Modulus, Poisson's Ratio and Similar Properties 53
3.3.1 Young's Modulus and Poisson's Ratio: Cubic Lattice 53
3.3.2 Bulk Modulus, Shear Modulus and Similar Properties: Cubic Lattice 56
3.3.3 Young's Modulus and Poisson's Ratio: Hexagonal Lattice 60
3.3.4 Bulk Modulus, Shear Modulus and Similar Properties: Hexagonal Lattice 61
3.4 Microhardness 62
3.5 Sound Velocity 68
References 72

4 Lattice Dynamic Properties **73**
4.1 Phonon Dispersion Relation 73
4.1.1 Brillouin Zone 73
(a) Face-centered cubic lattice 74
(b) Hexagonal lattice 74
(c) Rhombohedral lattice 75
4.1.2 Phonon Dispersion Curve 75
(a) Cubic lattice 75
(b) Hexagonal lattice 77
4.1.3 Phonon Density of States 79
4.2 Phonon Frequency 80
4.2.1 Room-temperature Value 80
4.2.2 External Perturbation Effect 84
(a) Temperature effect 84
(b) Pressure effect 86
4.3 Mode Grüneisen Parameter 87

4.4 Phonon Deformation Potential 88
4.4.1 Cubic Lattice 88
4.4.2 Hexagonal Lattice 91
References 92

5 Collective Effects and Some Response Characteristics 95
5.1 Piezoelectric and Electromechanical Constants 95
5.1.1 Piezoelectric Constant 95
(a) Piezoelectric stress constant 95
(b) Piezoelectric strain constant 98
5.1.2 Electromechanical Coupling Constant 99
5.2 Fröhlich Coupling Constant 99
References 101

6 Energy-band Structure: Energy-band Gaps 103
6.1 Basic Properties 103
6.1.1 Energy-band Structure 103
(a) Diamond-type semiconductor 104
(b) Zinc-blende-type semiconductor 106
(c) Wurtzite-type semiconductor 108
6.1.2 Electronic Density of States 111
6.2 E_0-gap Region 114
6.2.1 Effective Γ-point Hamiltonian 114
6.2.2 Room-temperature Value 115
6.2.3 External Perturbation Effect 120
(a) Temperature effect 120
(b) Pressure effect 124
(c) Temperature and pressure coefficients 124
6.2.4 Doping Effect 126
6.3 Higher-lying Direct Gap 130
6.3.1 Cubic Semiconductor 130
(a) Room-temperature value 130
(b) External perturbation effect 133
6.3.2 Hexagonal and Rhombohedral Semiconductors 137
6.4 Lowest Indirect Gap 137
6.4.1 Room-temperature Value 137
6.4.2 External Perturbation Effect 138
(a) Temperature effect 138
(b) Pressure effect 139
(c) Temperature and pressure coefficients 142
6.5 Conduction-valley Energy Separation 142
6.6 Direct–Indirect-gap Transition Pressure 142
References 143

7 Energy-band Structure: Effective Masses 147
7.1 Electron Effective Mass: Γ Valley 147
7.1.1 General Remarks 147

7.1.2 Numerical Value 149
7.1.3 Polaron Effect 151
7.1.4 External Perturbation and Doping Effects 152
(a) Temperature effect 152
(b) Pressure effect 153
(c) Doping effect 155
7.2 Electron Effective Mass: Satellite Valley 158
7.2.1 Camel's Back Structure 158
7.2.2 Numerical Value 159
7.3 Hole Effective Mass 159
7.3.1 Effective Γ-valence-band Hamiltonian and Luttinger Parameter 159
7.3.2 Numerical Value 164
(a) Cubic semiconductor 164
(b) Hexagonal and rhombohedral semiconductors 167
7.3.3 Polaron Effect 168
7.3.4 External Perturbation and Doping Effects 170
(a) Temperature effect 170
(b) Pressure effect 170
(c) Doping effect 170
References 171

8 Deformation Potentials 173

8.1 Intravalley Deformation Potential: Γ Point 173
8.1.1 Conduction Band 173
8.1.2 Valence Band 175
8.1.3 E_0 Gap 179
8.1.4 Optical Phonon Deformation Potential 181
8.2 Intravalley Deformation Potential: High-symmetry Points 183
8.2.1 L Point 183
(a) Hydrostatic and shear deformation potentials: conduction band 183
(b) Optical phonon deformation potential 185
(c) Valence-band deformation potential 186
(d) Hydrostatic and interband deformation potentials: E_1 and $E_1 + \Delta_1$ gaps 186
8.2.2 X Point 188
(a) Hydrostatic and shear deformation potentials: conduction band 188
(b) Hydrostatic and interband deformation potentials: E_2 gap 189
8.3 Intervalley Deformation Potential 189
8.3.1 General Remarks 189
8.3.2 Numerical Value 192
References 192

9 Electron Affinity and Schottky Barrier Height 195

9.1 Electron Affinity 195
9.1.1 An Overview 195
9.1.2 Numerical Value 196

9.2 Schottky Barrier Height 198
9.2.1 An Ideal Schottky–Mott Contact 198
9.2.2 Case Study: Au/Semiconductor Contact 202
9.2.3 Surface Reconstruction and External Perturbation Effect 204
(a) Surface reconstruction 204
(b) Temperature effect 205
(c) Pressure effect 205
9.2.4 Breakdown Voltage 206
References 208

10 Optical Properties 211
10.1 Summary of Optical Dispersion Relations 211
10.1.1 Dielectric Permittivity 211
10.1.2 Optical Dispersion Relation 213
10.1.3 Optical Sum Rule 214
10.1.4 Optical Spectra 216
10.2 The Reststrahlen Region 217
10.2.1 Static and High-frequency Dielectric Constants 217
(a) Room-temperature value 217
(b) External perturbation effect 219
10.2.2 Reststrahlen Spectra 222
(a) Zinc-blende-type and rocksalt-type semiconductors 222
(b) Hexagonal semiconductor 226
(c) External perturbation effect 227
10.2.3 Multiphonon Optical Absorption Spectra 228
10.3 At or Near the Fundamental Absorption Edge 230
10.3.1 Free-exciton Binding Energy and Related Parameters 230
(a) Exciton states: direct exciton 230
(b) Exciton states: indirect exciton 232
(c) Exciton binding energy and related parameters 233
(d) Spin-exchange interaction constant 236
10.3.2 Refractive Index 236
(a) Theoretical dispersion model 236
(b) Long-wavelength n value: empirical formula 240
(c) External perturbation effect 241
10.3.3 Optical Absorption at the Fundamental Absorption Edge 244
(a) Critical point: definition 244
(b) Free electron–hole pair transition 245
(c) Excitonic transition 251
(d) Experimental 253
10.3.4 Urbach Tail 256
10.4 The Interband Transition Region 258
10.4.1 Model Dielectric Function 258
(a) Fundamental absorption edge 259
(b) E_1 and $E_1 + \Delta_1$ transitions 259
(c) E_0', E_2 and E_1' transitions 260
(d) Plasma and d-band effects 262

10.4.2 Fundamental Optical Spectra 263
(a) Si 263
(b) GaAs 265
(c) w-CdS 265
10.4.3 External Perturbation and Doping Effects 268
(a) Temperature effect 268
(b) Pressure effect 268
(c) Doping effect 269
10.5 Free-carrier Absorption and Related Phenomena 270
10.5.1 Free-carrier Absorption 270
10.5.2 Interconduction-band and Intervalence-band Absorption 274
(a) Interconduction-band absorption 274
(b) Intervalence-band absorption 275
10.5.3 Free-carrier-induced Change in Refractive Index 278
References 278

11 Elasto-optic, Electro-optic and Nonlinear Optical Properties 283
11.1 Elasto-optic Effect 283
11.1.1 Theoretical Expression 283
11.1.2 Experimental Value 285
11.2 Linear Electro-optic Constant 291
11.2.1 Theoretical Expression 291
11.2.2 Experimental Value 294
11.3 Quadratic Electro-optic Constant 295
11.3.1 Theoretical Expression 295
11.3.2 Experimental Value 298
11.4 Franz–Keldysh Effect 300
11.4.1 Theoretical Expression 300
11.4.2 Experimental Value 301
11.5 Nonlinear Optical Constant 302
11.5.1 Second-order Nonlinear Optical Susceptibility 302
11.5.2 Third-order Nonlinear Optical Susceptibility 308
11.5.3 Two-photon Absorption 309
References 311

12 Carrier Transport Properties 315
12.1 Low-field Mobility: Electrons 315
12.1.1 Electron Scattering Mechanism 315
(a) Intervalley scattering 317
(b) Polar optical scattering 317
(c) Nonpolar optical scattering 318
(d) Piezoelectric scattering 318
(e) Deformation potential scattering 318
(f) Ionized impurity scattering 319
(g) Neutral impurity scattering 319
(h) Space-charge scattering 319

(i) Alloy scattering 320
(j) Carrier–carrier scattering 320
12.1.2 Three-valley Model 320
12.1.3 Room-temperature Value 321
12.1.4 External Perturbation and Doping Effects 324
(a) Temperature effect 324
(b) Pressure effect 325
(c) Doping effect 326
12.1.5 Hall Factor 328
12.2 Low-field Mobility: Holes 331
12.2.1 Hole Scattering Mechanism 331
12.2.2 Room-temperature Value 333
12.2.3 External Perturbation and Doping Effects 333
(a) Temperature effect 333
(b) Pressure effect 337
(c) Doping effect 337
12.3 High-field Transport: Electrons 339
12.3.1 Electron Drift Velocity–Field Characteristic 339
12.3.2 Electron Saturation Drift Velocity 347
(a) Temperature dependence 347
(b) LO phonon scattering-limited electron saturation drift velocity 348
12.4 High-field Transport: Holes 349
12.4.1 Hole Drift Velocity–Field Characteristic 349
12.4.2 Hole Saturation Drift Velocity 352
12.5 Minority-carrier Transport: Electrons in p-type Materials 353
12.5.1 Minority-electron Mobility 353
12.5.2 Minority-electron Drift Velocity 356
12.5.3 Minority-electron Lifetime and Diffusion Length 356
12.6 Minority-carrier Transport: Holes in n-type Materials 359
12.6.1 Minority-hole Mobility 359
12.6.2 Minority-hole Lifetime and Diffusion Length 360
12.7 Impact Ionization Coefficient 362
12.7.1 Theoretical Consideration 362
12.7.2 Experimental Value 365
(a) Electric-field dependence 365
(b) Temperature dependence 366
(c) Crystallographic direction dependence 368
References 369

Index **373**

Series Preface

WILEY SERIES IN MATERIALS FOR ELECTRONIC AND OPTOELECTRONIC APPLICATIONS

This book series is devoted to the rapidly developing class of materials used for electronic and optoelectronic applications. It is designed to provide much-needed information on the fundamental scientific principles of these materials, together with how these are employed in technological applications. The books are aimed at postgraduate students, researchers and technologists, engaged in research, development and the study of materials in electronics and photonics, and industrial scientists developing new materials, devices and circuits for the electronic, optoelectronic and communications industries.

The development of new electronic and optoelectronic materials depends not only on materials engineering at a practical level, but also on a clear understanding of the properties of materials, and the fundamental science behind these properties. It is the properties of a material that eventually determine its usefulness in an application. The series therefore also includes such topics as electrical conduction in solids, optical properties, thermal properties, etc., all with applications and examples of materials in electronics and optoelectronics. The characterization of materials is also covered within the series in as much as it is impossible to develop new materials without the proper characterization of their structure and properties. Structure–property relationships have always been fundamentally and intrinsically important to materials science and engineering.

Materials science is well known for being one of the most interdisciplinary sciences. It is the interdisciplinary aspect of materials science that has led to many exciting discoveries, new materials and new applications. It is not unusual to find scientists with a chemical engineering background working on materials projects with applications in electronics. In selecting titles for the series, we have tried to maintain the interdisciplinary aspect of the field, and hence its excitement to researchers in this field.

Peter Capper
Safa Kasap
Arthur Willoughby

Preface

Almost all the semiconductors of practical interest are the group-IV, III–V and II–VI semiconductors and the range of technical applications of such semiconductors is extremely wide. All such semiconductor devices can be characterized to a greater or lesser degree. Many scientific papers, review papers, book chapters and specialized books exist that discuss the various semiconductor properties, but no one has integrated such topics on the group-IV, III–V and II–VI semiconductors into one volume.

The purpose of this book is twofold: (i) to discuss key properties of the group-IV, III–V and II–VI semiconductors; and (ii) to systemize these properties from a solid-state physics aspect. The bulk of the text is devoted to the comprehensive description of the lattice structural, thermal, elastic, lattice dynamic, electronic energy-band structural, optical and carrier transport properties of these semiconductors. Some corrective effects and related properties, such as piezoelectric, elasto-optic and electro-optic properties, have also been discussed.

The book contains convenient tables summarizing the various material parameters and the definitions of important semiconductor properties. The book also contains graphs in order to make the information more quantitative and intuitive. I felt that these have not been adequately covered in existing books.

The book is intended not only for semiconductor device engineers, but also physicists and physical chemists, and particularly students specializing in the fields of semiconductor synthesis, crystal growth, semiconductor device physics and technology.

SADAO ADACHI
Gunma, Japan

Acknowledgements/Dedication

The author wishes to thank the editors and authors of the following journals and symposium papers for permission to reproduce previously published figures: *Appl. Phys. Lett.* for Figs. 6.19, 10.37, 12.10, 12.13, 12.14 and 12.24; *IEEE Proc.-J* for Fig. 11.7; *IEEE Proc. Int. Electron. Dev. Meeting* for Figs. 6.18 and 6.20; *J. Appl. Phys.* for Figs. 4.4, 7.7, 10.25 and 12.26; *J. Cryst. Growth* for Fig. 10.36; *J. Phys. Chem. Solids* for Figs. 10.40 and 12.5; *Jpn. J. Appl. Phys.* for Figs. 6.14 and 12.32; *Kluwer Academic Publishers* for Figs. 2.7, 2.10, 2.11, 3.5, 4.9, 6.12, 6.25, 6.27, 9.4–9.8, 10.4, 10.15, 12.6–12.8, 12.15–12.17, 12.30, 12.33–12.38, 12.41–12.43; *Phys. Rev.* for Figs. 1.3, 2.1, 4.10, 6.1, 6.3, 6.5, 6.7, 8.6, 10.5(a), 10.11, 10.17, 10.21, 10.23, 10.24, 10.34, 10.38, 11.4, 11.9, 12.9, 12.19, 12.21, 12.22, 12.27–12.29; *Proc. Phys. Soc.* for Fig. 4.6; *Semicond. Sci. Technol.* for Fig. 10.5(b); *Solid State Commun.* for Figs. 4.5, 10.22 and 11.10; and *Solid-State Electron.* for Fig. 9.10.

1 Structural Properties

1.1 Ionicity 1
1.1.1 Definition 1
1.1.2 Ionicity value 3
1.2 Elemental isotopic abundance and molecular weight 3
1.2.1 Elemental isotopic abundance 3
1.2.2 Molecular weight 4
1.3 Crystal structure and space group 4
1.3.1 Crystal structure 4
1.3.2 Space group 10
1.4 Lattice constant and related parameters 12
1.4.1 Lattice constant 12
1.4.2 Molecular and crystal densities 13
1.5 Structural phase transitions 14
1.6 Cleavage 15
1.6.1 Cleavage plane 15
1.6.2 Surface energy 18
References 20

1.1 IONICITY

1.1.1 Definition

All tetrahedrally coordinated $A^N B^{8-N}$ semiconductors can be treated within the framework of a simple model. The success of this approach requires a careful choice of parameters entering in the model. The most important of these is the ionicity of the bond [1.1].

The ionicity of a bond can be defined as the fraction f_i^α of ionic or heteropolar character in the bond compared with the fraction f_h^α of covalent or homopolar character. By definition, these fractions satisfy the relation

$$f_i^\alpha + f_h^\alpha = 1 \tag{1.1}$$

In an elemental semiconductor such as Si, we must have $f_h^\alpha = 1$ and $f_i^\alpha = 0$. In contrast, we shall find that some alkali halides (NaCl, KCl, etc.) are more than 90% ionic.

Properties of Group-IV, III–V and II–VI Semiconductors Sadao Adachi

© 2005 John Wiley & Sons, Ltd

ISBN: 0-470-09032-4

(a) Phillips ionicity

Phillips studied the connection between the chemical bonding properties of the $A^N B^{8-N}$ family of crystals and their electronic energy-band structures [1.1]. His concept evolves from a molecular picture in terms of bonding and antibonding states separated by an energy gap E_g. His ionicity scale f_i is defined in terms of average quantities such as the homopolar E_h and heteropolar parts C of the complex energy gap E_g associated with the A–B bond in the crystal

$$E_g = E_h + iC \tag{1.2}$$

Ionicity is then introduced via the relation

$$f_i = \frac{C^2}{E_g^2} = \frac{C^2}{E_h^2 + C^2} \tag{1.3}$$

Some numerical examples of E_g (f_i) are: $E_g = 4.70 + i0$ ($f_i = 0$) for Si; $E_g = 4.32 + i2.90$ ($f_i = 0.310$) for GaAs; $E_g = 4.29 + i5.60$ ($f_i = 0.630$) for ZnSe, where E_g are in eV.

(b) Pauling ionicity

Pauling based his definition of ionicity scale f_i^P not on the total energy of the bond, but on empirical heats of formation [1.2]. Denote the power of an atom A to attract electrons to itself by a dimensionless number called its electronegativity X_A. The Coulomb interaction between the ionic charge left behind and the valence charge transferred is proportional to $(X_A - X_B)^2$, and this is the origin of the extra ionic energy (i.e., f_i^P). By definition f_i^P never exceeds one, and as $X_A - X_B$ becomes large f_i^P tends to one. Moreover, the ionicity of an A–B bond should be the same as ionicity of a B–A bond. Pauling then defined ionicity of a single bond

$$f_i^P = 1 - \exp\left(-\frac{(X_A - X_B)^2}{4}\right) \tag{1.4}$$

(c) Harrison ionicity

In Harrison's model [1.3], the ionicity parameter f_i^H can be given in terms of two of the parameters of the electronic structure, by

$$f_i^H = \frac{V_3}{\sqrt{V_2^2 + V_3^2}} \tag{1.5}$$

Here, V_2 is half the splitting between bonding and antibonding states; V_3 is half the energy change in transferring an electron from anion to cation. This parameter f_i^H can be defined as the excess number of electrons placed on the anion from each bond, called the polarity. Thus, each anion in a tetrahedral structure contains a charge of $Z^* = 4f_i^H - \Delta Z$,

Table 1.1 Phillips (f_i), Pauling (f_i^P) and Harrison ionicities (f_i^H) for a number of group-IV, III–V and II–VI semiconductors

System	Material	f_i	f_i^P	f_i^H	System	Material	f_i	f_i^P	f_i^H
IV	Diamond	0	0	0	II–VI	MgO	0.841	0.88	
	Si	0	0	0		MgS	0.786		
	Ge	0	0	0		MgSe	0.790		
	Sn	0	0	0		MgTe	0.554		
	SiC	0.177	0.11	0.35		ZnO	0.616	0.80	0.69
						ZnS	0.623	0.59	0.69
III–V	BN	0.221	0.42	0.43		ZnSe	0.630	0.57	0.70
	BP	0.032				ZnTe	0.609	0.53	0.68
	BAs	0.044				CdS	0.685	0.59	0.74
	AlN	0.449	0.56	0.57		CdSe	0.699	0.58	0.74
	AlP	0.307	0.25	0.47		CdTe	0.717	0.52	0.76
	AlAs	0.274	0.27	0.44		HgS	0.790		
	AlSb	0.250	0.26	0.56		HgSe	0.680		
	GaN	0.500	0.55	0.61		HgTe	0.650		0.78
	GaP	0.327	0.27	0.48					
	GaAs	0.310	0.26	0.47					
	GaSb	0.261	0.26	0.43					
	InN	0.578							
	InP	0.421	0.26	0.55					
	InAs	0.357	0.26	0.51					
	InSb	0.321	0.25	0.48					

where ΔZ is the difference in valence from 4 ($\Delta Z = 1$ for nitrogen, 2 for oxygen, etc.). Similarly, then, each bond provides an electronic dipole moment of $\boldsymbol{P} = \gamma f_i^H$ $(-e\boldsymbol{d})$, where $\boldsymbol{d}$ is vector distance from cation to anion and γ is a scale parameter to take into account local fields and charge symmetries; a value of $\sqrt{2}$ gave a good fit to experiment.

1.1.2 Ionicity value

Table 1.1 summarizes the values of Phillips (f_i) [1.1], Pauling (f_i^P) [1.2] and Harrison ionicities (f_i^H) [1.3] for a number of group-IV, III–V and II–VI semiconductors. We also show in Figure 1.1 Phillips ionicity f_i versus (a) Pauling (f_i^P) and (b) Harrison ionicities (f_i^H) for these semiconductors.

1.2 ELEMENTAL ISOTOPIC ABUNDANCE AND MOLECULAR WEIGHT

1.2.1 Elemental isotopic abundance

There are a great many semiconductor materials. We list in Table 1.2 the elements which form at least one tetrahedrally coordinated $A^N B^{8-N}$ semiconductor, together with their

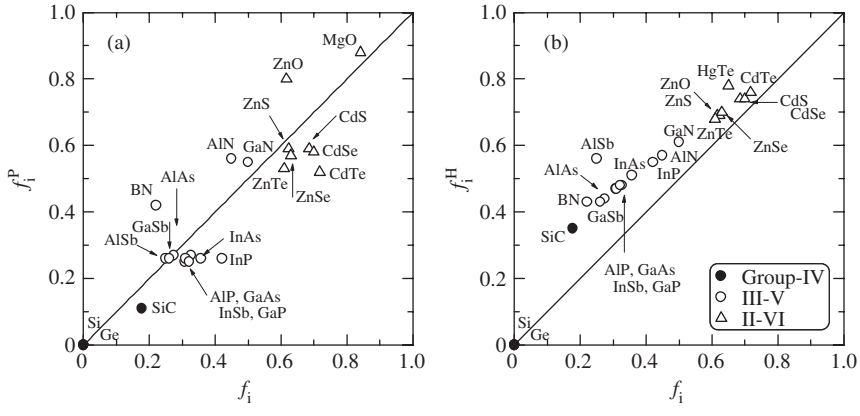

Figure 1.1 Phillips ionicity f_i versus (a) Pauling (f_i^P) and (b) Harrison ionicities (f_i^H) for some group-IV, III–V and II–VI semiconductors. The solid lines in (a) and (b) indicate the relations of $f_i = f_i^P$ and $f_i = f_i^H$, respectively

natural isotopic abundance in percent [1.4]. Table 1.3 also lists the standard atomic weight for some group IV, III, V, II and VI elements [1.4].

1.2.2 Molecular weight

The molecular weight M for an $A^N B^{8-N}$ semiconductor ($N \neq 4$) can be simply given by the sum of the atomic weights of atoms A and B. For an elemental semiconductor ($N = 4$), it is given by the atomic weight of the element atom A = B. Tables 1.4 and 1.5 list the values of M for a number of group-IV, III–V and II–VI semiconductors with cubic and hexagonal (rhombohedral) structures, respectively.

1.3 CRYSTAL STRUCTURE AND SPACE GROUP

1.3.1 Crystal structure

(a) Diamond, zinc-blende and wurtzite structures

The atoms of certain elements are held together in the solid by strongly covalent bonds at tetrahedral angles of 109.5°. Each atom has four nearest neighbors and twelve next nearest neighbors, which is a consequence of each atom sharing one of its outer electrons with each of four neighbors. The typical structure so formed is that of *diamond*, as shown in Figure 1.2(a). The space lattice is face-centered cubic with pairs of atoms at (0, 0, 0) and (1/4, 1/4, 1/4) forming a pattern unit.

The atomic orbitals that are used to form hybridized bonding orbitals are usually not the same ones that are occupied in the ground state of the atom. For example, in silicon the ground valence configuration of the atom is $3s^2 3p^2$, whereas the hybridized configuration appropriate for the diamond-type crystal structure is $3s^1 3p^3$ (tetrahedral coordination).

Table 1.2 Natural isotopic abundance in percent for some group IV, III, V, II and VI elements

Group	Isotope	Natural abundance (%)	Group	Isotope	Natural abundance (%)
IV	^{12}C	98.90	IV	^{112}Sn	0.97
	^{13}C	1.10		^{114}Sn	0.65
	^{28}Si	92.23		^{115}Sn	0.34
	^{29}Si	4.67		^{116}Sn	14.53
	^{30}Si	3.10		^{117}Sn	7.68
	^{70}Ge	21.23		^{118}Sn	24.23
	^{72}Ge	27.66		^{119}Sn	8.59
	^{73}Ge	7.73		^{120}Sn	32.59
	^{74}Ge	35.94		^{122}Sn	4.63
	^{76}Ge	7.44		^{124}Sn	5.79
III	^{10}B	19.9	V	^{14}N	99.634
	^{11}B	80.1		^{15}N	0.366
	^{27}Al	100		^{31}P	100
	^{69}Ga	60.108		^{75}As	100
	^{71}Ga	39.892		^{121}Sb	57.36
	^{113}In	4.3		^{123}Sb	42.64
	^{115}In	95.7			
II	^{24}Mg	78.99	VI	^{16}O	99.762
	^{25}Mg	10.00		^{17}O	0.038
	^{26}Mg	11.01		^{32}S	95.02
	^{64}Zn	48.6		^{33}S	0.75
	^{66}Zn	27.9		^{34}S	4.21
	^{67}Zn	4.1		^{36}S	0.02
	^{68}Zn	18.8		^{74}Se	0.89
	^{70}Zn	0.6		^{76}Se	9.36
	^{106}Cd	1.25		^{77}Se	7.63
	^{108}Cd	0.89		^{78}Se	23.78
	^{110}Cd	12.49		^{80}Se	49.61
	^{111}Cd	12.80		^{82}Se	8.73
	^{112}Cd	24.13		^{120}Te	0.096
	^{113}Cd	12.22		^{122}Te	2.603
	^{114}Cd	28.73		^{123}Te	0.908
	^{116}Cd	7.49		^{124}Te	4.816
	^{196}Hg	0.15		^{125}Te	7.139
	^{198}Hg	9.97		^{126}Te	18.95
	^{199}Hg	16.87		^{128}Te	31.69
	^{200}Hg	23.10		^{130}Te	33.80
	^{201}Hg	13.18			
	^{202}Hg	29.86			
	^{204}Hg	6.87			

Table 1.3 Standard atomic weight for some group IV, III, V, II and VI elements. Numbers in parentheses give the uncertainty in the last digit of the stated values

Group	Symbol	Atomic weight	Group	Symbol	Atomic weight
IV	C	12.0107(8)			
	Si	28.0855(3)			
	Ge	72.61(2)			
	Sn	118.710(7)			
III	B	10.811(7)	V	N	14.00674(7)
	Al	26.981538(2)		P	30.973761(2)
	Ga	69.723(1)		As	74.921560(2)
	In	114.818(3)		Sb	121.760(1)
II	Mg	24.3050(6)	VI	O	15.9994(3)
	Zn	65.39(2)		S	32.066(6)
	Cd	112.411(8)		Se	78.96(3)
	Hg	200.59(2)		Te	127.60(3)

The diamond cubic lattice is a consequence of the carbon valency of four. We can expect to find the same structure in compounds where one atom has more than four electrons and the other the same number less than four, so that a total of four valency electrons to each atom is maintained. If the compound is of the form of AB, this structure can be produced in two ways. The first is the cubic, *zinc-blende* structure as shown in Figure 1.2(b), with four A (Ga) and four B (As) atoms per conventional unit cell.

The second method by which a structure is formed where each atom of one kind is surrounded by four of another is shown in Figure 1.2(c). This is the hexagonal CdS (w-CdS or β-CdS) or *wurtzite* lattice, which differs only from the zinc-blende structure in the stacking sequence of the sulfur layers. Ideally, the wurtzite structure has the axial ratio $c/a = (8/3)^{1/2} = 1.633$ (hexagonal close-packed structure). Most III–V semiconductors crystallize in the zinc-blende structure, however, many II–VI and some III–V semiconductors crystallize in the wurtzite structure.

In III–V compounds, group III atoms have three electrons with an s^2p^1-configuration outside a core of closed shells and group V atoms five electrons in a s^2p^3-configuration. The III and V atoms have, therefore, an average of four valence electrons per atom available for bonding. We might then expect that the covalent bonds are formed between tetrahedral s^1p^3-hybrid orbitals, e.g., for GaAs:

$$\mathrm{Ga}(4s^24p^1) + \mathrm{As}(4s^24p^3) \rightarrow \mathrm{Ga}(4s^14p^3)^- + \mathrm{As}(4s^14p^3)^+ \tag{1.6}$$

For such a covalent bonding each V atom donates an electron to a III atom, so that V^+ and III^- ions are formed, each with four valence electrons.

An ionic bond is due to Coulomb attraction between the excess positive and negative charges on ions formed by transfer of electrons from the metallic to the nonmetallic atom in the scheme:

$$\mathrm{Ga}(4s^24p^1) + \mathrm{As}(4s^24p^3) \rightarrow \mathrm{Ga}(4s^04p^0)^{+3} + \mathrm{As}(4s^24p^6)^{-3} \tag{1.7}$$

Table 1.4 Molecular weight M, lattice constant a and crystal density g for a number of cubic group-IV, III–V and II–VI semiconductors at 300 K

System	Material	M (amu)	a (Å)	g (g/cm^3)
IV	Diamond	12.0107	3.5670	3.5156
	Si	28.0855	5.4310	2.3291
	Ge	72.61	5.6579	5.3256
	α-Sn	118.710	6.4892	5.7710
	3C-SiC	40.0962	4.3596	3.2142
III–V	c-BN	24.818	3.6155	3.4880
	BP	41.785	4.5383	2.9693
	BAs	85.733	4.777	5.224
	c-AlN	40.98828	4.38	3.24
	AlP	57.955299	5.4635	2.3604
	AlAs	101.903098	5.66139	3.73016
	AlSb	148.742	6.1355	4.2775
	β-GaN	83.730	4.52	6.02
	GaP	100.696	5.4508	4.1299
	GaAs	144.645	5.65330	5.31749
	GaSb	191.483	6.09593	5.61461
	InP	145.792	5.8690	4.7902
	InAs	189.740	6.0583	5.6678
	InSb	236.578	6.47937	5.77677
II–VI	MgO	40.3044	4.203	3.606
	β-MgS	56.371	5.62	2.11
	β-MgSe	103.27	5.91	3.32
	β-MgTe	151.91	6.42	3.81
	β-ZnS	97.46	5.4102	4.0879
	ZnSe	144.35	5.6692	5.2621
	ZnTe	192.99	6.009	5.908
	c-CdS	144.477	5.825	4.855
	c-CdSe	191.37	6.077	5.664
	CdTe	240.01	6.481	5.856
	β-HgS	232.66	5.8514	7.7135
	HgSe	279.55	6.084	8.245
	HgTe	328.19	6.4603	8.0849

The bonds in most III–V or II–VI semiconductors are not adequately described by any of these extreme types, but have characteristics intermediate to those usually associated with the terms covalent (Equation (1.6)) and ionic (Equation (1.7)).

(b) Hexagonal and rhombohedral structures

It is well known that silicon carbide (SiC) is a semiconductor crystallizing in a large number of polytypes [1.5]. The various types of SiC differ one from another only by the

Table 1.5 Molecular weight M, lattice constants a and c and crystal density g for a number of hexagonal and rhombohedral group-IV, III–V and II–VI semiconductors at 300 K

System	Material	M (amu)	Lattice constant (Å)		g (g/cm^3)
			a	c	
IV	6H-SiC	40.0962	3.0806	15.1173	3.2153
	15R-SiC	40.0962	3.079 ($\alpha = 13°54.5'$)	37.78	
III–V	h-BN	24.818	2.5040	6.6612	2.2787
	w-AlN	40.98828	3.112	4.982	3.258
	α-GaN	83.730	3.1896	5.1855	6.0865
	InN	128.825	3.548	5.760	6.813
II–VI	ZnO	81.39	3.2495	5.2069	5.6768
	α-ZnS	97.46	3.8226	6.2605	4.0855
	w-CdS	144.477	4.1367	6.7161	4.8208
	w-CdSe	191.37	4.2999	7.0109	5.6615

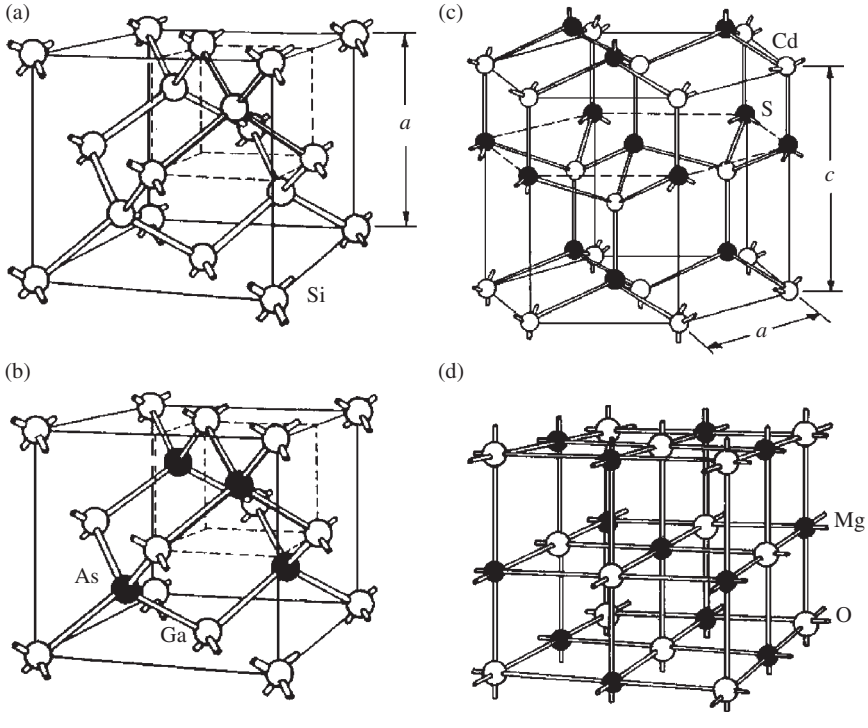

Figure 1.2 Some important crystal lattice structures. (a) diamond lattice (Si); (b) zinc-blende lattice (GaAs); (c) wurtzite lattice (w-CdS); and (d) rocksalt lattice (MgO)

order in which successive planes of Si (or C) atoms are stacked along the *c* axis; one polytype is cubic (3C-SiC) while the remainder, including two of the more frequently occurring forms, 6H and 15R, possess uniaxial symmetry. Note that in the polytype name, the integer refers to the number of Si (C) layers in the unit cell, and C, H and R indicate cubic, hexagonal and rhombohedral (trigonal) symmetry, respectively. Of all the polytypes, 6H is by far the most commonly occurring modification in commercial SiC. The next most common types are 15R and 4H, respectively. Silicon carbide can also crystallize in the wurtzite structure (2H-SiC).

Figure 1.3 shows the stacking sequences in 3C-SiC, 2H-SiC and 6H-SiC [1.6]. In the zinc-blende (3C) structure, the sequence involves three layers which are repeated periodically (ABC ABC . . .). All the Si–C bond lengths are the same, and the angles are exactly tetrahedral (109.5°). In the wurtzite (2H) structure, only two layers are repeated (AB AB . . .). The Si–C bond length along the stacking direction is not equal to that which is approximately perpendicular to it, and the angles are not exactly tetrahedral. In the 6H polytype, the basic sequence involves six layers (ABCACB ABCACB . . .). Similarly, in the 15R polytype the basic sequence involves fifteen layers (ABCACBCABACABCB . . .). The II–VI semiconductor, α-HgS, can also crystallize in the rhombohedral (red cinnabar) structure.

(c) Rocksalt structure

The II–VI compound MgO crystallizes in the rocksalt (NaCl) structure. The rocksalt structure shown in Figure 1.2(d) is typical of ionic bonding. The Bravais lattice is face-centered

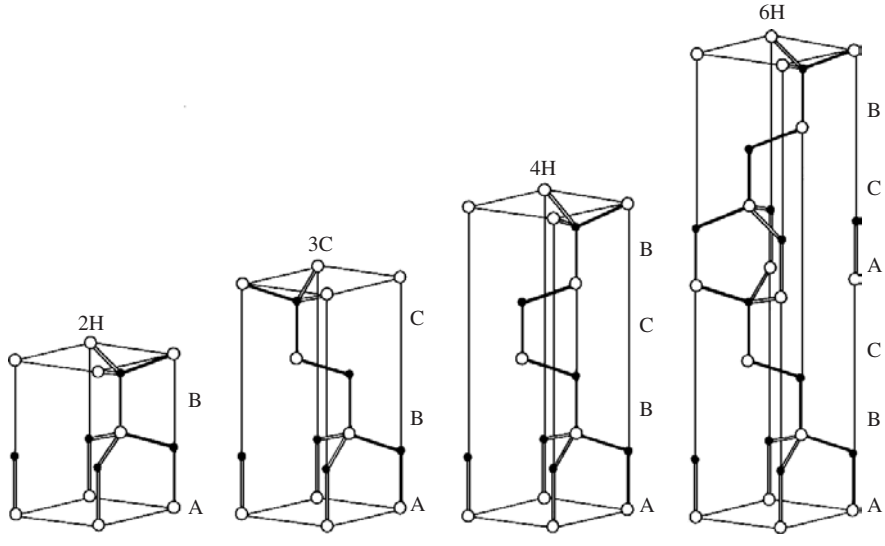

Figure 1.3 Three-dimensional perspective view of the 2H-SiC, 3C-SiC, 4H-SiC and 6H-SiC polytypes. The characteristic chain structures are represented by the heavy solid lines in the $(11\bar{2}0)$ plane. The stacking sequences AB (2H), ABC (3C), ABCB (4H) and ABCACB (6H) are also indicated. [From P. Käckell, B. Wenzien, and F. Bechstedt, *Phys. Rev. B* **50**, 17037 (1994), reproduced by permission from the American Physical Society]

cubic with the unit cell of atomic pattern consisting of one Mg and one O ion separated by one-half the body diagonal of the cube. Since each ion has six nearest neighbors of the opposite kind, the coordination number is six.

We summarize in Table 1.6 the crystal classes for easily or normally grown: (a) group-IV, (b) III–V and (c) II–VI binaries. Table 1.7 also lists the crystal structure for a number of group-IV, III–V and II–VI semiconductors.

1.3.2 Space group

A self-consistent arrangement of symmetry elements in a crystal lattice is known as a space group. The operation of any element of the group must have the pattern of symmetry elements unaltered. By inspection of the 230 space groups, or from first principles, there are just 32 different point groups. Crystals are, therefore, divided into 32 crystal classes according to the point-group symmetry they possess. In Table 1.7, we list the space (point) group for a number of group-IV, III–V and II–VI semiconductors.

Table 1.6 Summary of easily or normally grown crystal structure for: (a) group-IV; (b) III–V and; (c) II–VI semiconductors. d = diamond; zb = zinc-blende; h = hexagonal (wurtzite); rh = rhombohedral (trigonal); rs = rocksalt; or = orthorhombic

(a)

IV/IV	Si	C
Si	d	zb, h, rh
C	zb, h, rh	d

(b)

III/V	N	P	As	Sb
B	zb, h	zb	zb	
Al	h	zb	zb	zb
Ga	h	zb	zb	zb
In	h	zb	zb	zb

(c)

II/VI	O	S	Se	Te
Mg	rs	rs	zb	h
Zn	h	zb, h	zb	zb
Cd	rs	h	h	zb
Hg	rh, or	rh, zb	zb	zb

Table 1.7 Crystal structure, space group (point group) and lattice constants a and c ($T = 300$ K) for a number of group-IV, III–V and II–VI semiconductors. d = diamond; zb = zinc-blende; h = hexagonal; rh = rhombohedral; w = wurtzite; rs = rocksalt

System	Material	Crystal structure	Space group	a (Å)	c (Å)
IV	Diamond	d	$Fd3m$ (O_h)	3.5670	
	Si	d	$Fd3m$ (O_h)	5.4310	
	Ge	d	$Fd3m$ (O_h)	5.6579	
	α-Sn	d	$Fd3m$ (O_h)	6.4892	
	3C-SiC	zb	$F\bar{4}3m(T_d)$	4.3596	
	6H-SiC	h	$P6_3mc$ (C_{6v})	3.0806	15.1173
	15R-SiC	rh	$R3m$ (C_{3v})	3.079 ($\alpha = 13^\circ 54.5'$)	37.78
III–V	c-BN	zb	$F\bar{4}3m(T_d)$	3.6155	
	h-BN	h	$P6_3/mmc$ (D_{6h})	2.5040	6.6612
	BP	zb	$F\bar{4}3m(T_d)$	4.5383	
	BAs	zb	$F\bar{4}3m(T_d)$	4.777	
	w-AlN	w	$P6_3mc$ (C_{6v})	3.112	4.982
	c-AlN	zb	$F\bar{4}3m(T_d)$	4.38	
	AlP	zb	$F\bar{4}3m(T_d)$	5.4635	
	AlAs	zb	$F\bar{4}3m(T_d)$	5.66139	
	AlSb	zb	$F\bar{4}3m(T_d)$	6.1355	
	α-GaN	w	$P6_3mc$ (C_{6v})	3.1896	5.1855
	β-GaN	zb	$F\bar{4}3m(T_d)$	4.52	
	GaP	zb	$F\bar{4}3m(T_d)$	5.4508	
	GaAs	zb	$F\bar{4}3m(T_d)$	5.65330	
	GaSb	zb	$F\bar{4}3m(T_d)$	6.09593	
	InN	w	$P6_3mc$ (C_{6v})	3.548	5.760
	InP	zb	$F\bar{4}3m(T_d)$	5.8690	
	InAs	zb	$F\bar{4}3m(T_d)$	6.0583	
	InSb	zb	$F\bar{4}3m(T_d)$	6.47937	
II–VI	MgO	rs	$Fm3m(O_h)$	4.203	
	β-MgS	zb	$F\bar{4}3m(T_d)$	5.62	
	β-MgSe	zb	$F\bar{4}3m(T_d)$	5.91	
	β-MgTe	zb	$F\bar{4}3m(T_d)$	6.42	
	ZnO	w	$P6_3mc$ (C_{6v})	3.2495	5.2069
	α-ZnS	w	$P6_3mc$ (C_{6v})	3.8226	6.2605
	β-ZnS	zb	$F\bar{4}3m(T_d)$	5.4102	
	ZnSe	zb	$F\bar{4}3m(T_d)$	5.6692	
	ZnTe	zb	$F\bar{4}3m(T_d)$	6.009	
	c-CdS	zb	$F\bar{4}3m(T_d)$	5.825	
	w-CdS	w	$P6_3mc$ (C_{6v})	4.1367	6.7161
	c-CdSe	zb	$F\bar{4}3m(T_d)$	6.077	
	w-CdSe	w	$P6_3mc$ (C_{6v})	4.2999	7.0109
	CdTe	zb	$F\bar{4}3m(T_d)$	6.481	
	β-HgS	zb	$F\bar{4}3m(T_d)$	5.8514	
	HgSe	zb	$F\bar{4}3m(T_d)$	6.084	
	HgTe	zb	$F\bar{4}3m(T_d)$	6.4603	

1.4 LATTICE CONSTANT AND RELATED PARAMETERS

1.4.1 Lattice constant

(a) Room-temperature value

The lattice in the zinc-blende and rocksalt crystals can be defined by the one length parameter a. In hexagonal crystals, the lattice can be defined by the two length parameters, a and c. In rhombohedral crystals, the lattice can also be defined by the two length parameters, a and c, plus one angle parameter α. We have listed in Tables 1.4, 1.5 and 1.7 the lattice constants for a number of group-IV, III–V and II–VI semiconductors at $T = 300$ K. Figure 1.4 also plots the lattice constant a versus molecular weight $M = M_A + M_B$ for $A^N B^{8-N}$ semiconductors. From this plot, we can obtain the relation between a and M (a in Å; M in amu)

$$a = 0.579 + 1.04 \ln M \tag{1.8}$$

(b) Near-neighbor distance

There is a significant structural difference between the bond distance in the zinc-blende and wurtzite structures of binary compounds $A^N B^{8-N}$. The zinc-blende structure has only one type of first-neighbor distance

$$d(A - B) = \frac{\sqrt{3}}{4} a \text{ (four bonds)} \tag{1.9}$$

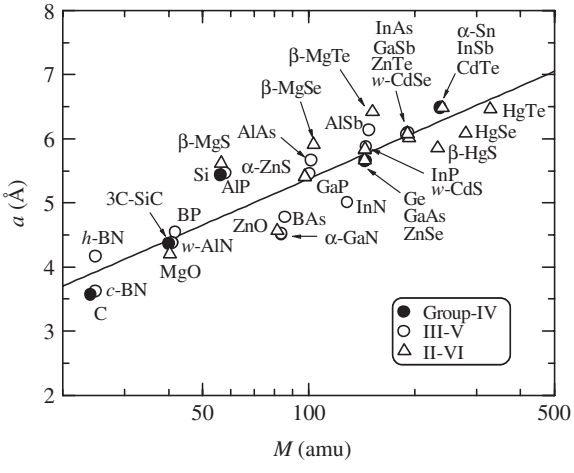

Figure 1.4 Lattice constant a versus molecular weight M for a number of group-IV, III–V and II–VI semiconductors. For hexagonal semiconductors, an effective lattice constant $a_{\text{eff}} = (\sqrt{3}a^2c)^{1/3}$ is plotted instead of a. The solid line represents the least-squares fit with $a = 0.579 + 1.04 \ln M$ (a in Å; M in amu)

Yet, the wurtzite structure has two types of first-neighbor anion–cation bond distances

$$d(\mathrm{A}-\mathrm{B}_1) = ua \text{ (one bond)} \tag{1.10a}$$

$$d(\mathrm{A}-\mathrm{B}_2) = \sqrt{\frac{1}{3} + \left(\frac{1}{2} - u\right)^2 \left(\frac{c}{a}\right)^2}\, a \text{ (three bonds)} \tag{1.10b}$$

where u denotes the cell internal structural parameter. In the case of an ideal tetragonal ratio $c/a = (8/3)^{1/2} = 1.633$ and an ideal cell internal parameter $u = 3/8$, it follows from Equation (1.10) that $d(\mathrm{A}-\mathrm{B}_1) = d(\mathrm{A}-\mathrm{B}_2)$.

In the case of the rocksalt structure, there is only one type of first-neighbor anion–cation bond distance

$$d(\mathrm{A}-\mathrm{B}) = \frac{a}{2} \quad \text{(six bonds)} \tag{1.11}$$

(c) External perturbation effect

The lattice constant is dependent to a great extent on both temperature and pressure. The temperature dependence of the lattice constant is explained by the thermal expansion coefficient. The lattice constant is related to the pressure by Murnaghan equation of state. It is also noted that the lattice constant is influenced by the crystalline perfection (i.e., stoichiometry, impurities, dislocations and surface damage). A well-known example is the dilation, or expansion, of the GaAs lattice induced by Te doping. Increase in the GaAs lattice constant of $\sim$0.01% has been reported at Te concentrations of $\sim 10^{19}$ cm^{-3} (see [1.7]).

1.4.2 Molecular and crystal densities

Molecular density d_{M} is given by

$$d_{\mathrm{M}} = \frac{8}{a^3} \tag{1.12}$$

for the diamond-type semiconductors,

$$d_{\mathrm{M}} = \frac{4}{a^3} \tag{1.13}$$

for the zinc-blende-type and rocksalt-type semiconductors and

$$d_{\mathrm{M}} = \frac{4}{a_{\mathrm{eff}}^3} \tag{1.14}$$

for the hexagonal (wurtzite) semiconductors, where a_{eff} is an effective cubic lattice constant defined by

$$a_{\mathrm{eff}} = (\sqrt{3}a^2 c)^{1/3} \tag{1.15}$$

The X-ray crystal density g can be simply written, in terms of d_M, as

$$g = \frac{M d_M}{N_A} \tag{1.16}$$

where M is the molecular weight and $N_A = 6.022 \times 10^{23}$ mol^{-1} is the Avogadro constant. We have listed in Tables 1.4 and 1.5 the values of g for a number of group-IV, III–V and II–VI semiconductors with cubic and hexagonal structures, respectively.

1.5 STRUCTURAL PHASE TRANSITIONS

It is known that at high pressure the group-IV elemental semiconductors show metallic transitions in a sequence from cubic (diamond)→tetragonal (β-Sn)→simple hexagonal→ hexagonal close packed. Similarly, the III–V and II–VI semiconductors exhibit a variety of the crystal structures at high pressures. In Table 1.6, we have summarized the crystal classes for easily or normally grown group-IV, III–V and II–VI binary semiconductors.

The electrical resistivity of semiconductors is known to drop discontinuously by several orders of magnitude at the transition pressures; therefore the phase transitions have been studied chiefly by electrical measurements. There have also been some attempts to determine the crystalline structures of the high-pressure polymorphs of semiconductors by various techniques, such as X-ray diffraction, optical microscopy and Raman scattering [1.8].

It is interesting to note the correlations between the ambient properties and high-pressure behavior. Chelikowsky [1.9] discussed empirical scales for transition pressures as a function of ionicity and bond length. By fixing his scaling parameters by experiment and theory, it becomes possible to determine the transition pressures for the zinc-blende to β-Sn structure and for the zinc-blende to rocksalt transition.

Table 1.8 Transition pressure to the first phase P_T for some group-IV, III–V and II–VI semiconductors

System	Material	P_T (GPa)	System	Material	P_T (GPa)
IV	Si	12	II–VI	ZnO	8.0–10
	Ge	12		α-ZnS	10.7–11.4
				β-ZnS	14.7–17.4
III–V	w-AlN	14–22.9		ZnSe	11.8–14.6
	AlP	9.5–17.0		ZnTe	7 –9.5
	AlAs	7–14.2		w-CdS	1.75–3
	AlSb	5.3–12.5		w-CdSe	2.13–2.9
	α-GaN	37–53.6		CdTe	3.53
	GaP	21.5		HgSe	0.7–0.75
	GaAs	16.6–17.3		HgTe	1.4
	GaSb	6.2–7.0			
	InN	12.1–23.0			
	InP	10.8			
	InAs	7			
	InSb	2.2			

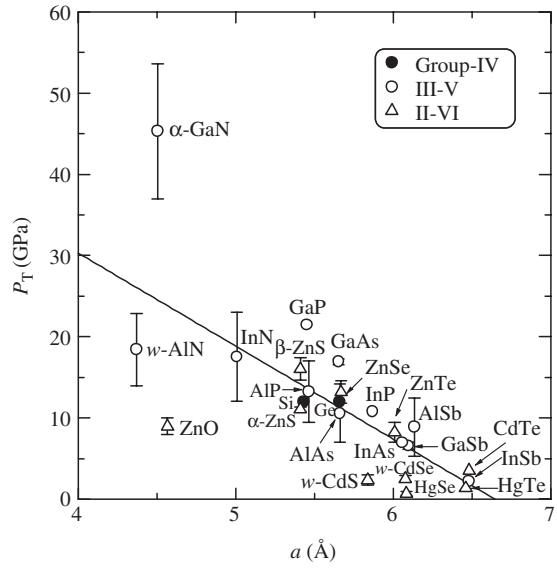

Figure 1.5 Transition pressure to the first phase P_T versus lattice constant a for some group-IV, III–V and II–VI semiconductors. For hexagonal semiconductors, an effective lattice constant $a_{eff} = (\sqrt{3}a^2c)^{1/3}$ is plotted instead of a. The solid line represents the least-squares fit with $P_T = 76.2 - 11.5a$ (a in Å; P_T in GPa)

We list in Table 1.8 the transition pressure to the first phase P_T observed for some group-IV, III–V and II–VI semiconductors. Figure 1.5 also plots P_T versus lattice constant a for these semiconductors. The solid line represents the least-squares fit with the relation (a in Å; P_T in GPa)

$$P_T = 76.2 - 11.5a \tag{1.17}$$

We summarize in Table 1.9 the sequence of the structural phase transitions for a number of group-IV, III–V and II–VI semiconductors observed at high pressures.

1.6 CLEAVAGE

1.6.1 Cleavage plane

The cleavage properties of a crystal are strongly related to the atomic arrangement and corresponding electron density map. The principles that determine a plane of cleavage are as follows:

1. The number of 'bonds' (nearest neighbors) to be separated per unit area of the plane is a minimum, as compared with all other crystal planes.
2. The plane is electrically neutral, with alternate arrays of positive and negative structure elements which permit the two separating surface layers to assume repelling positions when shifted with respect to each other.

Table 1.9 Sequence of the structural phase transitions observed for a number of group-IV, III–V and II–VI semiconductors at high pressures. bcc = body-centered cubic; bct = body-centered tetragonal; cin = cinnabar; d = diamond; dCsCl = distorted CsCl; dhc = double hexagonal close-packed; fcc = face-centered cubic; h = hexagonal; hcp = hexagonal close-packed; or = orthorhombic; rh = rhombohedral; rs = rocksalt (NaCl); sh = simple (primitive) hexagonal; w = wurtzite; zb = zinc-blende

System	Material	Crystal structure (normal pressure→high pressure)
IV	Diamond	d→no phase transition up to experimentally available pressure
	Si	d→ β-Sn→or (*Imma*)→sh→or (*Cmca*)→hcp→fcc
	Ge	d→ β-Sn→or (*Imma*)→sh→dhc (d→ β-Sn→or (*Imma*)→sh→or (*Cmca*)→hcp)
	α-Sn	d→(β-Sn)→bcc
	3C-SiC	zb→rs
	6H-SiC	h→rs
	15R-SiC	rh→no phase transition up to 150 GPa
III–V	*c*-BN	zb→no phase transition up to 115 GPa
	h-BN	h→?
	BP	zb→no phase transition up to 68 GPa
	BAs	zb→?
	w-AlN	w→rs
	c-AlN	zb→?
	AlP	zb→ β-Sn/h (NiAs)
	AlAs	zb→h (NiAs)
	AlSb	zb→ β-Sn/rs/or→unknown
	α-GaN	w→rs
	β-GaN	zb→?
	GaP	zb→ β-Sn
	GaAs	zb→or (*Pmm*2)/or (*Cmcm*)→or (*Imm*2)→sh
	GaSb	zb→ β-Sn/or (*Imma*)→sh→unknown
	InN	w→rs
	InP	zb→rs→ β-Sn/or (*Cmcm*)
	InAs	zb→rs→ β-Sn/or (*Cmcm*)
	InSb	zb→ β-Sn (?)→or (*Immm*)→or (*super-Cmcm*)→(?)→bcc (?)
II–VI	MgO	rs→no phase transition up to 227 GPa
	β-MgS	zb→?
	β-MgSe	zb→?
	β-MgTe	zb→?
	ZnO	wz→rs
	α-ZnS	wz→zb→rs
	β-ZnS	zb→rs→or (*Cmcm*)
	ZnSe	zb→rs→sh
	ZnTe	zb→cin→or (*Cmcm*)
	c-CdS	zb→wz (high temperature)
	w-CdS	wz→rs→or (*Pmmn*)
	c-CdSe	zb→wz (high temperature)
	w-CdSe	wz→rs
	CdTe	zb→cin→rs→or (*Cmcm*)
	β-HgS	zb→cin
	HgSe	zb→cin→rs→bct
	HgTe	zb→cin→rs→or (*Cmcm*)→dCsCl

Figure 1.6 represents schematic views of the atomic rearrangement in the direction along the (110), (111) and (100) planes of the zinc-blende lattice (GaAs). This arrangement is the same as for the diamond lattice, except that the two different kinds of atom occupy alternate positions in the lattice. Table 1.10 summarizes the crystallographic plane most readily cleaved for the diamond, zinc-blende, wurtzite and rocksalt structures.

In diamond-type crystals, such as diamond and Si, cleavage occurs along (111) surface planes. This is because the (111) surface atoms are only singly bonded to the opposite surface, but the (100) surface atoms are doubly bonded to the opposite surface (see Figure 1.6). The (110) surface atoms are also singly bonded to the opposite surface, but the plane spacing is shorter than that of the (111) planes. It is more difficult to separate the planes of shorter spacing.

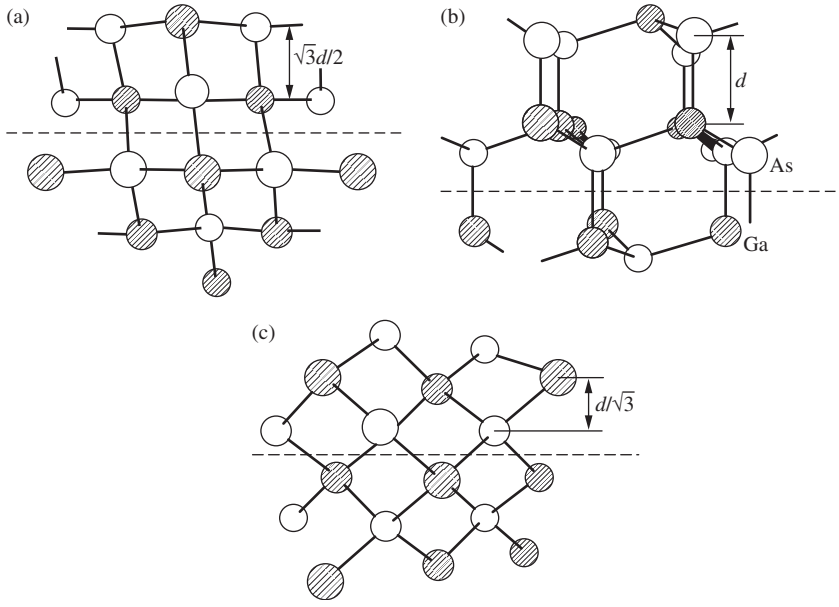

Figure 1.6 Schematic views of the atomic arrangement in the direction along the (110) (a), (111) (b) and (100) planes (c) of GaAs. Note that this arrangement is the same as the diamond lattice, except that the two different kinds of atom (Ga, As) occupy alternate positions in the lattice. The principal cleavage in the zinc-blende crystals is in a plane parallel to (110) (a), and that in the diamond-type crystals is in a plane parallel to (111) (b)

Table 1.10 Crystallographic plane most readily cleaved for various crystal structures

Crystal structure	Cleavage plane
Diamond	(111)
Zinc-blende	(110)
Wurtzite	$(11\bar{2}0)$, $(10\bar{1}0)$
Rocksalt	(100)

In the case of zinc-blende-type lattice, we must take into account the effects of surface polarity and electron density distribution. The zinc-blende-type lattice has two types of (111) surface polarities, (111)A and (111)B, and hence there will be an electrostatic attraction between these different planes. Such an attractive force will make it difficult to separate along the (111) planes. However, the (110) surfaces are composed of equal numbers of A and B atoms, so there will be no overall electrostatic force between the planes. Wolff and Broder [1.10] have investigated the bonding character and microcleavage in materials with tetrahedral coordination. They found that the (110) plane is the principal cleavage plane in III–V compounds. They also found microcleavages in GaAs in (*hhk*) planes ($h \geqslant k$). The microcleavage is revealed by the observation of light figure patterns from cleavage pits produced by grinding or abrading the surface.

The surface energy $E\gamma$ is defined by energy per unit surface area necessary to separate a crystal along a given plane. Berding *et al.* [1.11] have calculated the cleavage energies $E\gamma$ for Si, GaAs, CdTe and HgTe. Their results give an ordering of $E\gamma$(Si)> $E\gamma$(GaAs)> $E\gamma$(CdTe)> $E\gamma$(HgTe) for the experimentally observed cleavage planes; i.e., for the cleavage on (111) in Si and (110) in GaAs, CdTe and HgTe. This ordering is what one would expect based on simple bond-length and bond-density arguments. A simple estimate of the cleavage energy can be made by multiplying the number of bonds broken per unit area on the cleavage surfaces by the energy per bond. Thus, although for a given bond-length, the bond-density on the (110) surface (on which GaAs cleaves) is higher than on the (111) surface (on which Si cleaves), the shorter bond-length and the larger bond-strength of Si compared with GaAs combine to produce a larger cleavage energy in Si. In turn, both the shorter bond-length and the larger bond-strength of GaAs compared with HgTe and CdTe result in a larger cleavage energy in GaAs. Finally, the weaker HgTe bond, compared with CdTe, and their nearly equal bond lengths predict a smaller cleavage energy in HgTe.

It has been shown experimentally [1.12] that the (112) cleavage planes can be obtained, as the secondary cleavage plane, in the twinned regions between the (110) cleavage surfaces of the matrix grains in CdTe. Like the (111) surfaces, the (112) surfaces in the zinc-blende crystals have surface polarity. The electrostatic attraction in highly ionic II–VI compounds should contribute considerably to the cleavage energy for the (112) surfaces. This consideration predicts that the (112) surfaces may be more easily cleaved in III–V compounds than in II–VI compounds.

On the basis of the above-mentioned principle, it is possible to verify the $(11\bar{2}0)$ (and/or $(10\bar{1}0)$) and (100) planes as the most readily cleaved planes for the wurtzite (hexagonal) and rocksalt structures, respectively.

1.6.2 Surface energy

(a) Theoretical value

In an attempt to explain the 'easy' cleavage of solids, various methods have been employed to calculate the energies required to cleavage a crystal parallel to a particular plane. The cleavage energy was assumed equal to twice the surface energy of that plane. In this approximate method, the surface energy is calculated as the number of bonds cut per unit area multiplied by the thermodynamic energy of each bond, irrespective of whether

Table 1.11 Theoretical surface (cleavage) energy for some planes of cubic group-IV, III–V and II–VI semiconductors (J/m^2)

System	Material	(100)	(110)	(111)	$(\bar{1}\bar{1}\bar{1})$
IV	Diamond	9.2	6.5	5.3	
	Si	1.99	1.41	1.15	
	Ge			0.88–1.00	
	α-Sn			0.662	
	3C-SiC	1.908–4.65	2.330	1.767	0.7184
III–V	*c*-BN		4.53	4.02	3.07
	BP		2.38	1.64	1.93
	BAs		2.06	1.39	1.88
	c-AlN		2.12	2.30	1.12
	AlP		1.37	1.19	0.956
	AlAs		1.21	1.01	0.935
	AlSb		1.050	0.814	0.945
	GaP		1.38	1.24	0.95
	GaAs	1.06	1.00	1.05	
	GaSb		0.995	0.803	0.900
	InP		1.08	1.09	0.80
	InAs		1.015	0.980	0.728
	InSb		0.814	0.738	0.690
II–VI	β-ZnS		1.225	1.15	0.85
	ZnSe		0.98	0.885	0.75
	ZnTe		0.96	0.808	0.84
	c-CdS		1.06	1.07	0.69
	c-CdSe		0.94	0.91	0.88
	CdTe	0.85	0.18	0.58	
	β-HgS		1.13	1.00	0.73
	HgTe	0.05	0.12	0.09	

Table 1.12 Theoretical surface (cleavage) energy for some planes of hexagonal group-IV and II–VI semiconductors (J/m^2)

System	Material	(0001)	$(000\bar{1})$
IV	6H-SiC	1.80[a]	0.75[a]
II–VI	ZnO	1.95	0.96
	α-ZnS	1.30	0.96

[a] 4H-SiC value

Table 1.13 Cleavage plane and experimental surface energy for some group-IV, III–V and II–VI semiconductors. The experimental data are taken from various sources

System	Material	Crystal structure	Cleavage plane	Surface energy (J/m^2)
IV	Si	Diamond	(111)	1.14–1.240
	Ge	Diamond	(111)	1.060
III–V	GaP	Zinc-blende	(110)	1.96
	GaAs	Zinc-blende	(110)	0.86
II–VI	MgO	Rocksalt	(100)	1.2

the 'cut' is at an angle to the bonding direction. We summarize in Tables 1.11 and 1.12 the theoretical surface energies for some cubic and hexagonal semiconductors, respectively [1.11, 1.13–1.17].

Berding *et al*. [1.11] have presented a method for the calculation of the surface energy $E\gamma$ for Si based on a tight-binding Green's function approach, and obtained that $E\gamma$ for the (111) surface is considerably smaller than those for the (100) and (110) surfaces. The same conclusion has also been obtained by Hesketh *et al*. [1.14]

(b) Experimental value

There is a dearth of experimental measurements of surface energy. This is because many difficulties are associated with measuring it; especially when indirect methods are used. Since the surface energy can be defined as the work that is required to separate a crystal into two parts along a plane, cleavage is a particularly direct way of measuring it [1.18]. We list in Table 1.13 the experimentally determined surface energies for some group-IV, III–V and II–VI semiconductors.

REFERENCES

[1.1] J. C. Phillips, *Bonds and Bands in Semiconductors* (Academic, New York, 1973).
[1.2] See, J. C. Phillips, *Rev. Mod. Phys.* **42**, 317 (1970).
[1.3] W. A. Harrison, *Phys. Rev. B* **8**, 4487 (1973).
[1.4] D. R. Lide, *CRC Handbook of Chemistry and Physics*, 78th Edition (CRC Press, Boca Raton, 1997).
[1.5] A. R. Verma and P. Krishna, *Polymorphism and Polytypism in Crystals* (Wiley, New York, 1966).
[1.6] P. Käckell, B. Wenzien, and F. Bechstedt, *Phys. Rev. B* **50**, 17037 (1994).
[1.7] S. Adachi, *GaAs and Related Materials: Bulk Semiconducting and Superlattice Properties* (World Scientific, Singapore, 1994).
[1.8] U. D. Venkateswaran, L. J. Cui, B. A. Weinstein, and F. A. Chambers, *Phys. Rev. B* **45**, 9237 (1992), and references cited therein.
[1.9] J. R. Chelikowsky, *Phys. Rev. B* **35**, 1174 (1987).
[1.10] G. A. Wolff and J. D. Broder, *Acta Cryst.* **12**, 313 (1959).
[1.11] M. A. Berding, S. Krishnamurthy, A. Sher, and A.-B. Chen, *J. Appl. Phys.* **67**, 6175 (1990).

[1.12] H. Iwanaga, A. Tomizuka, and T. Shoji, *J. Mater. Sci. Lett.* **10**, 975 (1991).
[1.13] J. E. Field, in *Properties and Growth of Diamond*, EMIS Datareviews Series No. 9, edited by G. Davies (INSPEC, London, 1994), p. 36.
[1.14] P. J. Hesketh, C. Ju, S. Gowda, E. Zanoria, and S. Danyluk, *J. Electrochem. Soc.* **140**, 1080 (1993).
[1.15] B. N. Oshcherin, *Phys. Status Solidi A* **34**, K181 (1976).
[1.16] T. Takai, T. Halicioğlu, and W. A. Tiller, *Surf. Sci.* **164**, 341 (1985).
[1.17] R. Yakimova, M. Syväjärvi, and E. Janzén, *Mater. Sci. For.* **264–268**, 159 (1998).
[1.18] J. J. Cilman, *J. Appl. Phys.* **31**, 2208 (1960).

2 Thermal Properties

2.1 Melting point and related parameters 23
2.1.1 Phase diagram 23
2.1.2 Melting point 23
2.2 Specific heat 26
2.3 Debye temperature 28
2.4 Thermal expansion coefficient 30
2.5 Thermal conductivity and diffusivity 33
2.5.1 Thermal conductivity 33
2.5.2 Thermal diffusivity 39
References 39

2.1 MELTING POINT AND RELATED PARAMETERS

2.1.1 Phase diagram

Phase diagrams in semiconducting compound growth serve primarily as a guide to the solution compositions which will yield the desired solid layer, although they are also necessary for the interpretation of growth kinetic data. Many important differences between the properties of compounds prepared by different methods, such as vapor phase epitaxy, melt-grown or liquid phase epitaxy, are due to stoichiometric differences.

Figure 2.1 shows the theoretical and experimental pressure (p)–temperature (T) phase diagrams for Si, Ge and GaSb [2.1]. It is seen that these semiconductors show a β-Sn phase at high pressures and a metallic liquid phase at high temperatures. It is well established that the slope of the liquid–β-Sn solid-phase boundary is positive for the $A^N B^{8-N}$ semiconductors, so that the liquid is less dense than the high-pressure solid at the same pressure. It is also well established that the slope of the liquid–diamond (or zinc-blende) phase boundary is negative for these semiconductors, so that the liquid is denser than the semiconductor at the same pressure.

2.1.2 Melting point

The melting point is one of the most essential thermophysical parameters. We list in Table 2.1 the melting point T_m measured for some group-IV, III–V and II–VI semiconductors at normal pressure. The accurate measurement of temperature is not easy above 1000°C. This may lead to a large error in measuring T_m. Figure 2.2 also plots the melting

Properties of Group-IV, III–V and II–VI Semiconductors Sadao Adachi

© 2005 John Wiley & Sons, Ltd

ISBN: 0-470-09032-4

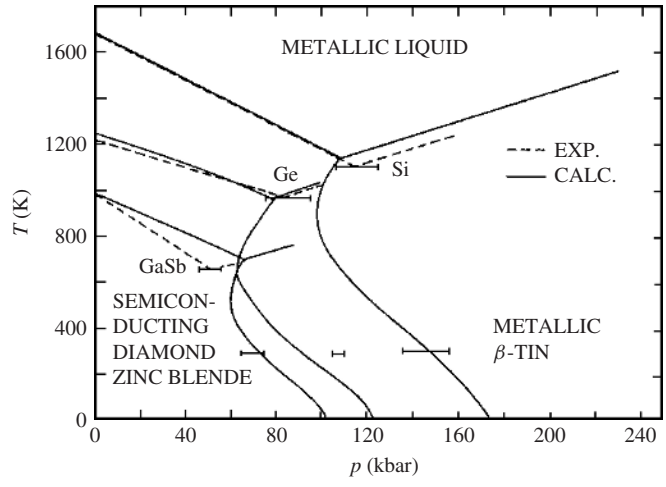

Figure 2.1 Theoretical and experimental pressure (p)–temperature (T) phase diagram for Si, Ge and GaSb. [From J. A. Van Vechten, *Phys. Rev. B* **7**, 1479 (1973), reproduced by permission from the American Physical Society]

point T_m versus lattice constant a for some group-IV, III–V and II–VI semiconductors. For hexagonal semiconductors, an effective lattice constant $a_{eff} = (\sqrt{3}a^2c)^{1/3}$ is plotted instead of a. The solid line represents the least-squares fit with the relation (a in Å; T_m in K)

$$T_m = 7159 - 957a \tag{2.1}$$

We can see from Figure 2.2 that the high melting point reflects low atomic mass and thus short interatomic bond-length.

A Lindemann relation [2.2]

$$\frac{d \ln T_m}{d \ln g} = 2\left(\gamma - \frac{1}{3}\right) \tag{2.2}$$

can be used to obtain the pressure dependence of the melting point T_m, where g is the density and γ is the thermal Grüneisen parameter. The effect of pressure on the melting point T_m can also be easily calculated from the Clausius–Clapeyron equation, which shows that [2.3]

$$\frac{dT_m}{dp} = T_m \frac{V_l - V_s}{H} \tag{2.3}$$

where $V_{l,s} = A/d_{l,s}$ (A = atomic weight; $d_{l,s}$ = density of liquid or solid at T_m; H = latent heat of fusion). We summarize in Table 2.2 the pressure coefficient of the melting point dT_m/dp determined experimentally for some group-IV, III–V and II–VI semiconductors. It is found that only MgO gives positive value in dT_m/dp [2.2].

Table 2.1 Melting point T_m, specific heat C_p and Debye temperature θ_D for some group-IV, III–V and II–VI semiconductors. C_p and θ_D are at 300 K

System	Material	T_m (K)	C_p (J/g K)	θ_D (K)
IV	Diamond	4100[a]	0.5148	1870
	Si	1687	0.713	643
	Ge	1210.4	0.3295[b]	348[b]
	α-Sn		0.278[c]	238[c]
	3C-SiC	2810	0.677[d]	1122
	6H-SiC	2810	0.58	1126
	15R-SiC	2810		
III–V	c-BN	>3246	0.643	1613
	h-BN		0.805	323
	BP	>3300	0.75	1025[e]
	BAs	2300	0.408	800
	w-AlN	3487	0.728	988
	AlP	2823	0.727	687
	AlAs	1740	0.424	450
	AlSb	1338	0.326[b]	370[b]
	α-GaN	2791	0.42	821
	GaP	1730	0.313	493[f]
	GaAs	1513	0.327	370
	GaSb	991	0.344[b]	240[b]
	InN	2146	2.274	674
	InP	1335	0.322	420[b]
	InAs	1210	0.352	280[b]
	InSb	797	0.350[b]	161[b]
II–VI	MgO	3250	0.928	745
	β-MgS	2783[g]		
	β-MgSe	~1560		
	β-MgTe	>1300		
	ZnO	1975	0.497	416
	α-ZnS	2196		351
	β-ZnS	2196	0.486	440
	ZnSe	1793	0.360	340
	ZnTe	1568	0.258	260
	c-CdS	1748		
	w-CdS	1748	0.3280	310
	c-CdSe	1531		
	w-CdSe	1531	0.281	135
	CdTe	1365	0.211	44[h]
	β-HgS	1723		
	HgSe	1072	0.355	242
	HgTe	943	0.162	

[a] At $p = 12.5$ GPa
[b] At $T = 273$ K
[c] At $T = 100$ K
[d] C_v value
[e] At $T = 320$ K
[f] t $T = 150$ K
[g] Theoretical
[h] At $T = 290$ K

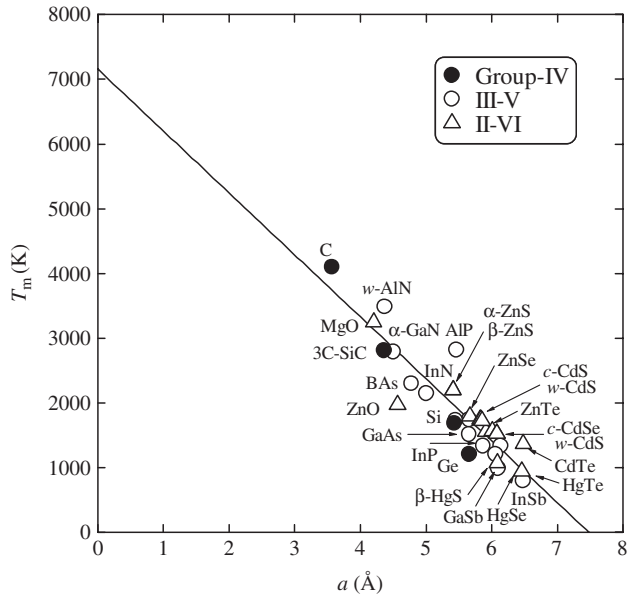

Figure 2.2 Melting point T_m versus lattice constant a for some group-IV, III–V and II–VI semiconductors. For hexagonal semiconductors, an effective lattice constant $a_{eff} = (\sqrt{3}a^2c)^{1/3}$ is plotted instead of a. The solid line represents the least-squares fit with $T_m = 7159 - 957a$ (a in Å; T_m in K)

Table 2.2 Pressure coefficient dT_m/dp determined experimentally for some group-IV, III–V and II–VI semiconductors

System	Material	dT_m/dp (°C/kbar)	System	Material	dT_m/dp (°C/kbar)
IV	Si	−5.8	II–VI	MgO	+3.6
	Ge	−3.8			
III–V	AlSb	−6.9			
	GaAs	−3.4			
	GaSb	−5.8			
	InP	−3.4			
	InAs	−4.3			
	InSb	−10			

2.2 SPECIFIC HEAT

Many practical uses of semiconductors demand knowledge of their thermal properties over a wide range of temperatures. A major step forward in our knowledge concerns the thermal energy content of a solid. This leads us to one of the most essential thermal properties, the specific heat or heat capacity of a solid [2.4]. Note that the specific heat or heat capacity is a scalar quantity (i.e., zero-rank tensor).

The specific heat at constant pressure, C_p is given by [2.4]

$$C_p = \left(\frac{\Delta Q}{\Delta T}\right)_p \tag{2.4}$$

where ΔQ is the heat input and ΔT is the corresponding change in temperature. In order to obtain the specific heat at constant volume C_v, which is the quantity usually resulting from theoretical calculations, one can use the following equation:

$$C_p - C_v \sim \frac{9\alpha_{th}^2 V T}{C_o} \tag{2.5}$$

where α_{th} is the linear thermal expansion coefficient, V is the volume of the crystal and C_o is the isothermal compressibility.

There have been many experimental data on the specific heat of crystalline semiconductors over a wide range of temperatures. We have listed in Table 2.1 the specific heat C_p measured at $T = 300$ K for a number of group-IV, III–V and II–VI semiconductors. Figure 2.3 also shows the experimental specific heat C_p as a function of temperature T for synthetic diamond [2.5, 2.6], GaAs [2.7] and CdTe [2.8–2.10]. It is easily understood from Figure 2.3 that C_p is strongly dependent on temperature T. At very low T, C_p (C_v) is proportional to T^3 which is known as Debye's T^3 law (see Section 2.3). In the limit $T \to \infty$, C_p (C_v) approaches $3R$ (where R is the gas constant); this is Dulong and Petit's law.

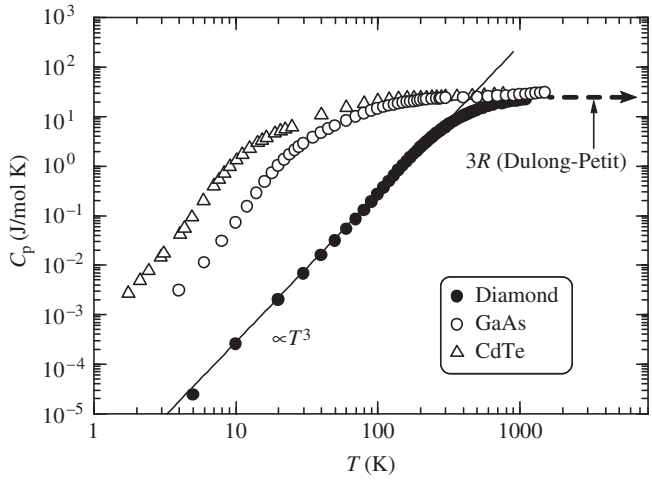

Figure 2.3 Specific heat C_p (at constant pressure) versus temperature T for synthetic diamond, GaAs and CdTe. The experimental data are taken for synthetic diamond from Atake *et al.* [2.5] and Victor [2.6], for GaAs from Blakemore [2.7] and for CdTe from Birch [2.8], Malkova *et al.* [2.9] and Gambino *et al.* [2.10]. The solid line shows the validity of Debye's T^3 law ($C_p \propto T^3$) for diamond

2.3 DEBYE TEMPERATURE

The Debye temperature θ_D is a useful parameter in solid-state problems because of its inherent relationship to lattice vibration. The temperature θ_D can be used in characterizing the excitation of phonons and to describe various lattice thermal phenomena [2.4]. The θ_D values of many materials are known very precisely from low-temperature measurements of the specific heat. Some materials have, however, not been investigated as yet in detail, especially those where it has not been possible to prepare large pure crystals.

The Debye model for lattice vibrational energy results in the relation [2.4]

$$C_p \sim C_v = 3RF(\theta_D/T) \tag{2.6}$$

where $F(\theta_D/T)$ is the Debye function defined by

$$F(\theta_D/T) = (T/\theta_D)^3 \int_0^{\theta_D/T} \frac{3x^4 e^x}{(e^x - 1)^2} dx \tag{2.7}$$

In the low-temperature limit ($T \ll \theta_D$, $\theta_D/T \to \infty$), $F(\theta_D/T)$ is approximated as $(4/5)\pi^4(T/\theta_D)^3$; then $C_p \sim (12/5)\pi^4 R(T/\theta_D)^3$ (i.e., Debye's T^3 law; see Figure 2.3). In the high-temperature limit ($T \gg \theta_D$, $\theta_D/T \ll 1$), on the other hand, $F(\theta_D/T)$ approaches unity; then $C_p \sim 3R$ (Dulong and Petit's law).

We have listed in Table 2.1 the Debye temperature θ_D at $T = 300$ K for a number of group-IV, III–V and II–VI semiconductors. Figure 2.4 also plots the Debye temperature

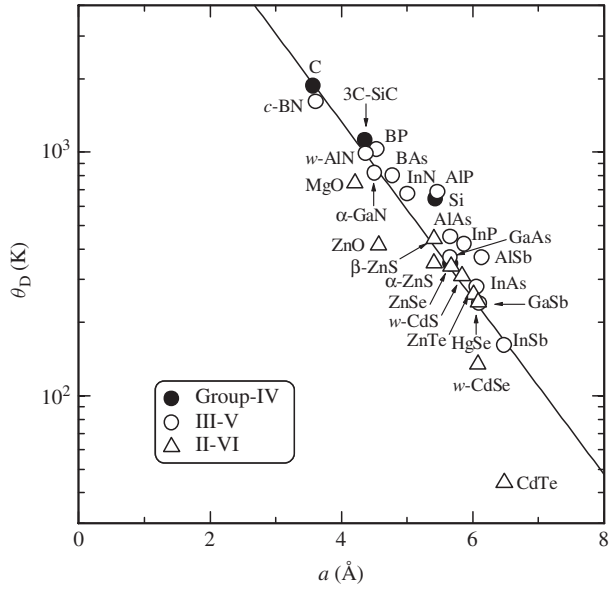

Figure 2.4 Debye temperature θ_D ($T = 300$ K) versus lattice constant a for some group-IV, III–V and II–VI semiconductors. For hexagonal semiconductors, an effective lattice constant $a_{eff} = (\sqrt{3}a^2c)^{1/3}$ is plotted instead of a. The solid line represents the least-squares fit with ln $\theta_D = 10.53 - 0.834a$ (a in Å; θ_D in K)

θ_D versus lattice constant a for some group-IV, III–V and II–VI semiconductors. The solid line in Figure 2.4 represents the least-squares fit with the relation (a in Å; θ_D in K)

$$\ln \theta_D = 10.53 - 0.834a \tag{2.8}$$

It is understood from Figure 2.4 that the high Debye temperature reflects low atomic mass and thus short interatomic bond-length in $A^N B^{8-N}$ semiconductors.

We plot in Figure 2.5 the Debye temperature θ_D as a function of temperature for Ge [2.11], InP [2.11] and CdTe [2.12, 2.13]. The θ_D value is found to be strongly dependent on temperature T.

Marcus and Kennedy [2.14] investigated the relation between the elastic constant and Debye temperature θ_D at $T = 0$ K in the Debye approximation. Steigmeier [2.15] has shown, using the Marcus–Kennedy formula, that it would be possible to estimate unknown Debye temperatures from simple material parameters such as the atomic mass and lattice constant. This consideration is based on the observation of Keyes [2.16] that the elastic constants of group-IV, III–V and II–VI semiconductors depend only on functions of their corresponding lattice constants. The formula derived by Steigmeier is given by

$$\theta_D(0) = \frac{4.19 \times 10^{-8}}{\sqrt{a^3 M}} \sqrt{\frac{C_{11}}{C_0}} f(r_1, r_2) \tag{2.9}$$

where a is the lattice constant, M is the mean mass, $r_1 = (C_{11} - C_{12})/C_{11}$, $r_2 = C_{44}/C_{11}$, C_0 is the reduced elastic constant of Keyes and $f(r_1, r_2)$ is an angular average over the reciprocal sound velocities in $\boldsymbol{k}$ space. Based on this formula and from numerical parameters of a and C_{ij}, we can estimate the Debye temperature θ_D at $T = 0$ K for AlAs to be 413 K [2.17]. Table 2.3 lists the Debye temperature in the low-temperature

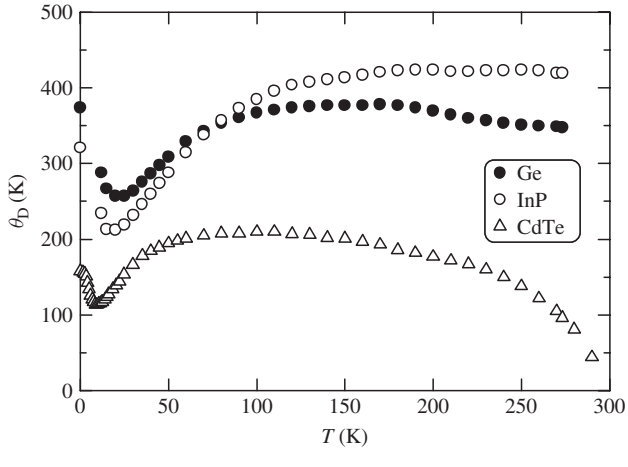

Figure 2.5 Debye temperature θ_D versus temperature T for Ge, InP and CdTe. The experimental data are taken for Ge and InP from Piesbergen [2.11] and for CdTe from Bagot *et al.* ($T \leqslant 50$ K) [2.12] and Demidenko ($T > 50$ K) [2.13]

Table 2.3 Debye temperature in the low-temperature limit $\theta_D(0)$ for some group-IV, III–V and II–VI semiconductors

System	Material	$\theta_D(0)$ (K)	System	Material	$\theta_D(0)$ (K)
IV	Diamond	2220	II–VI	MgO	946
	Si	652		β-ZnS	340
	Ge	374		ZnSe	275
	α-Sn	233		ZnTe	228
	3C-SiC	1080		w-CdS	265
				CdTe	158
III–V	c-BN	1987		β-HgS	178
	BP	985		HgSe	157
	AlP	588		HgTe	145
	AlAs	417			
	AlSb	292			
	GaP	457			
	GaAs	344			
	GaSb	266			
	InP	321			
	InAs	255			
	InSb	205			

limit $\theta_D(0)$ for some group-IV, III–V and II–VI semiconductors reported by Siethoff and Ahlborn [2.18].

2.4 THERMAL EXPANSION COEFFICIENT

If the temperature of a crystal is changed, the resulting deformation may be specified by the strain tensor $[e]$. The thermal expansion coefficient is a second-rank symmetric tensor relating the temperature T (scalar quantity) and the second-rank strain tensor $[e]$ by [2.19]

$$[e] = [\alpha]T \tag{2.10}$$

We have then, instead of Equation (2.10)

$$e_{ij} = \alpha_{ij}T \tag{2.11}$$

The thermal expansion phenomena of a crystal can thus be characterized by the magnitudes and directions of the three principal expansion coefficients. These magnitudes and directions must always conform to any restrictions imposed by crystal symmetry. The thermal deformation ellipsoid is a sphere in the cubic system and a spheroid of revolution in the hexagonal and rhombohedral systems. Table 2.4 summarizes the non-vanishing tensor components for these crystal systems.

The linear expansion coefficient α_{th} is known to be proportional to the specific heat C_v (Grüneisen's rule) [2.20]

$$\alpha_{th} = \frac{1}{a}\left(\frac{\partial a}{\partial T}\right)_p = \frac{\gamma C_v C_o}{3\ V} \tag{2.12}$$

Table 2.4 Form of the thermal expansion coefficient tensor for semiconductors of certain symmetry classes

Symmetry class	Material	Tensor form
Cubic	Si, 3C-SiC, GaAs, MgO, ZnSe, etc.	$\begin{bmatrix} \alpha_{xx} & 0 & 0 \\ 0 & \alpha_{xx} & 0 \\ 0 & 0 & \alpha_{xx} \end{bmatrix}$
Hexagonal Rhombohedral	4H-SiC, h-BN, α-GaN, w-CdS, etc. 15R-SiC	$\begin{bmatrix} \alpha_{xx} & 0 & 0 \\ 0 & \alpha_{xx} & 0 \\ 0 & 0 & \alpha_{zz} \end{bmatrix}$

Table 2.5 Thermal expansion coefficient α_{th} and thermal conductivity K for some cubic group-IV, III–V and II–VI semiconductors at 300 K

System	Material	α_{th} (10^{-6} K^{-1})	K (W/cm K)
IV	Diamond	1.05	22
	Si	2.616	1.56
	Ge	5.75	0.6
	α-Sn	5.25[a]	
	3C-SiC	2.77	3.4[b]
III–V	c-BN	1.15	~13[c]
	BP	2.94	3.5
	AlP		0.9
	AlAs	4.28	0.91
	AlSb	4.2[d]	0.57
	GaP	4.89	0.77
	GaAs	6.03	0.45
	GaSb	6.35	0.36
	InP	4.56	0.68
	InAs	~5.0	0.3
	InSb	5.04	0.165 – 0.185
II–VI	MgO	10.5	0.52
	β-ZnS	6.71	0.27
	ZnSe	7.8	0.19
	ZnTe	8.33	0.18
	CdTe	4.67[c]	0.075
	β-HgS	4.3 ($T = 484 - 621$ K)	
	HgSe	1.41	0.001 – 0.035
	HgTe	4.70	0.0238

[a] At $T = 220$ K
[b] At $T = 290$ K
[c] Estimated
[d] At $T = 280$ K

where γ is the averaged Grüneisen parameter, C_o is the isothermal compressibility and V is the volume of the crystal. The thermal expansion coefficient depends markedly on the temperature and is positive for most crystals. It is usually determined by measuring the temperature dependence of the lattice constant. We list in Tables 2.5 and 2.6 the thermal expansion coefficient α_{th} at $T = 300$ K for some cubic and hexagonal semiconductors, respectively.

It is known that $A^N B^{8-N}$ semiconductors show an 'unusual' negative thermal expansion below about $T = 100$ K. Figure 2.6 shows, as an example, the negative thermal expansion observed at low temperatures in ZnTe and HgTe [2.21, 2.22]. Figure 2.7 also shows the thermal expansion coefficient α_{th} versus temperature for ZnO both in the $\perp c$ and $\| c$ directions [2.23, 2.24]. It is seen from Figures 2.6 and 2.7 that α_{th} decreases from its positive value on cooling, passing through zero for T $\leqslant$ 120 K. Biernacki and Scheffler [2.25] performed density-functional-theory calculations of thermodynamic potentials to study the temperature dependence of α_{th}. Their result showed excellent agreement with published experimental data of Si. They concluded that the origin of the negative expansion effect is traced back to the entropy contribution of the Gibbs free energy.

The α_{th} values shown in Figures 2.6 and 2.7 are strongly dependent on temperature. The temperature variation of α_{th} can be expressed by a semi-empirical quasi-harmonic model. We present in Table 2.7 the resulting functional form and parameter values for GaP [2.26].

Table 2.6 Thermal expansion coefficient α_{th} and thermal conductivity K for some hexagonal group-IV, III–V and II–VI semiconductors at 300 K

System	Material	α_{th} (10^{-6} K^{-1})		K (W/cm K)
		α_a	α_c	
IV	6H-SiC	4.2[a]	4.7[a]	4.9[b], 3.30[c]
III–V	h-BN	−2.75	38.0	3.9[b]
	w-AlN	3.042	2.227	3.19[b]
	α-GaN	5.0	4.5	1.95[b]
	InN	3.830	2.751	0.45[d]
II–VI	ZnO	4.31	2.49	0.54[c]
	α-ZnS	6.54	4.59	0.17[c,e]
	w-CdS	4.30	2.77	0.20[c,f]
	w-CdSe	4.13	2.76	∼0.09

[a] At $T = 700$ K
[b] Heat flow parallel to the basal plane
[c] Heat flow perpendicular to the basal plane
[d] Ceramics
[e] Note that the α-ZnS crystal used in the experiment may be faulted; therefore, the value for α-ZnS is much smaller than that for β-ZnS (Table 2.5)
[f] At $T = 283$ K

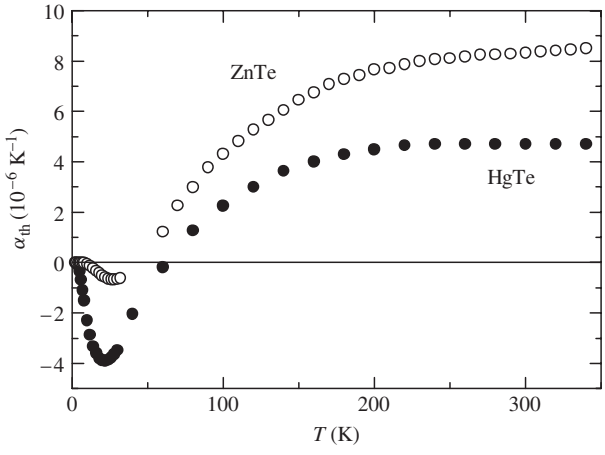

Figure 2.6 Thermal expansion coefficient α_{th} versus temperature T for ZnTe and HgTe. The experimental data are taken from Collins *et al*. [2.21] and Novikova and Abrikosov [2.22]

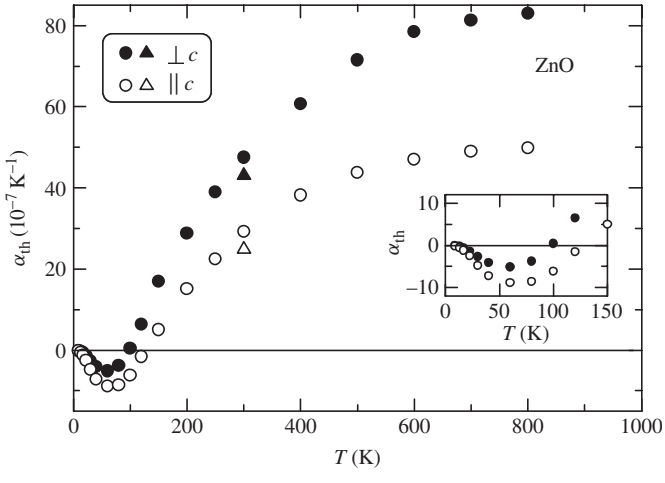

Figure 2.7 Thermal expansion coefficient α_{th} versus temperature T for ZnO. The experimental data are taken from Ibach (solid and open circles) [2.23] and Iwanaga *et al*. (solid and open triangles) [2.24]. [From S. Adachi, *Handbook on Physical Properties of Semiconductors Volume 3: II–VI Compound Semiconductors* (Kluwer Academic, Boston, 2004), reproduced by permission from Kluwer Academic Publishers]

2.5 THERMAL CONDUCTIVITY AND DIFFUSIVITY

2.5.1 Thermal conductivity

Thermal conductivity K, or thermal resistivity K^{-1}, is a quantity given by a second-rank symmetric tensor. Table 2.8 shows the non-vanishing tensor components for the cubic, hexagonal and rhombohedral systems. The thermal conductivity results essentially from

Table 2.7 Temperature variation of the linear thermal expansion coefficient α_{th} for GaP expressed using a semi-empirical quasi-harmonic model

$$\alpha_{\text{th}}(T) = \sum_{i=1}^{n} X_i \frac{(\theta_i/T)^2 \exp(\theta_i/T)}{[\exp(\theta_i/T) - 1]^2}$$

i	X_i (10^{-7} K^{-1})	θ_i (K)
1	−3.272	30
2	11.12	200
3	51.82	600
4	−1.125	1552.5

interactions between phonons and from the scattering of phonons by crystalline imperfections. Knowledge of the thermal conductivity of semiconductors forms an important part in the design of power-dissipating devices, such as diodes, transistors and optoelectronic devices. Numerical K values are also necessary in calculating the figure of merit for thermoelectronic devices (e.g., Peltier devices). A useful description of the theoretical and practical aspects of the thermal conductivity in semiconductors is given by Steigmeier and Kudman [2.27], Holland [2.28], Maycock [2.29], Bhandari and Rowe [2.30] and Srivastava [2.31], who review some of the works done on semiconductors, including some of the III–V binaries and their alloys.

An exact calculation of lattice thermal conductivity for semiconductors is possible in principle, but the lack of knowledge of various parameters and the difficulty of obtaining exact solutions of phonon–phonon interactions are formidable barriers to progress. Experimental evaluation of K for undoped (or low-doped) semiconductors has been carried out by many authors. We have summarized in Tables 2.5 and 2.6 the experimental K values at $T = 300$ K for some cubic and hexagonal semiconductors, respectively. Note that the α-ZnS crystal used in the experiment may be faulted; therefore, the value for α-ZnS listed in Table 2.6 is much smaller than that for β-ZnS in Table 2.5 (see [2.32]).

Table 2.8 Form of the thermal conductivity tensor for semiconductors of certain symmetry classes

Symmetry class	Material	Tensor form
Cubic	Si, 3C-SiC, GaAs, MgO, ZnSe, etc.	$\begin{bmatrix} K_{xx} & 0 & 0 \\ 0 & K_{xx} & 0 \\ 0 & 0 & K_{xx} \end{bmatrix}$
Hexagonal Rhombohedral	4H-SiC, h-BN, α-GaN, w-CdS, etc. 15R-SiC	$\begin{bmatrix} K_{xx} & 0 & 0 \\ 0 & K_{xx} & 0 \\ 0 & 0 & K_{zz} \end{bmatrix}$

Figure 2.8 plots the K value at $T = 300$ K versus scaling parameter $\overline{M}a\theta_D^3$ for some group-IV, III–V and II–VI semiconductors, where $\overline{M}$ is the average mass of an atom in the crystal, a is the lattice constant and θ_D is the Debye temperature. The solid line represents the least-squares fit with the relation ($\overline{M}a\theta_D^3$ in amu cm K^3; K in W/cm K)

$$K = 1.17 \times 10^{-3}(\overline{M}a\theta_D^3)^{1.15} \tag{2.13}$$

Figure 2.9 shows the thermal conductivity K at $T = 300$ K plotted versus Phillips ionicity f_i for some cubic group-IV, III–V and II–VI semiconductors. The Debye–Waller factors of atoms in compounds of $A^N B^{8-N}$ family in order of Phillips ionicity have been studied by Yoshiasa *et al.* [2.33] using extended X-ray absorption fine structure (EXAFS) and diffraction methods. They observed a divergent curve toward $f_i = 0.785$ in the mean-square displacement of the tetrahedrally coordinated covalent materials, which indicates the behavior of lattice instability. The elastic properties and lattice distortion parameters in the covalently bonded tetrahedral compounds are reported to show a systematic tendency toward lattice instability as the ionicity increases. The lattice thermal conductivity should be correlated to Phillips ionicity instability via the lattice instability or anharmonicity in the mean-square displacement. The solid line in Figure 2.9 represents the least-squares fit with the relation (K in W/cm K)

$$\ln K = 1.08 - 4.42 f_i \tag{2.14}$$

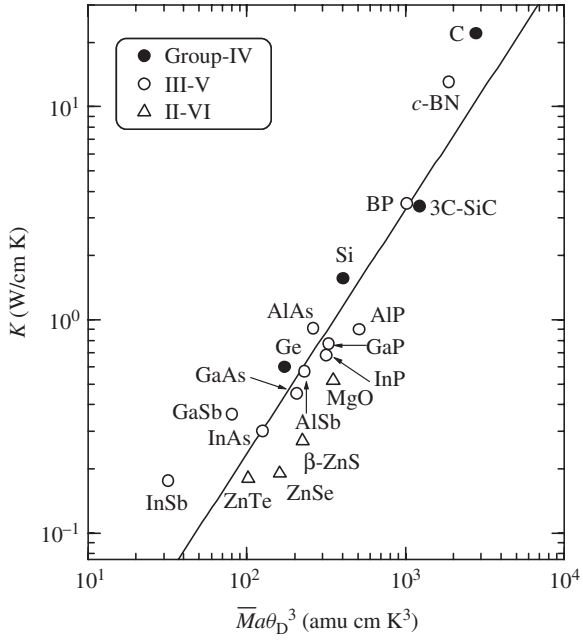

Figure 2.8 Thermal conductivity K at 300 K versus scaling parameter $\overline{M}a\theta_D^3$ for some cubic group-IV, III–V and II–VI semiconductors. The solid line represents the least-squares fit with $K = 1.17 \times 10^{-3}(\overline{M}a\theta_D^3)^{1.15}$ ($\overline{M}a\theta_D^3$ in amu cm K^3; K in W/cm K)

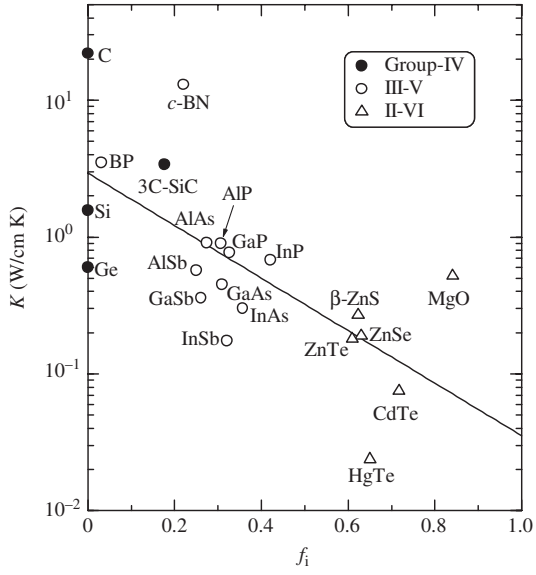

Figure 2.9 Thermal conductivity K at 300 K versus Phillips ionicity f_i for some cubic group-IV, III–V and II–VI semiconductors. The solid line represents the least-squares fit with $\ln K = 1.08 - 4.42 f_i$ (K in W/cm K)

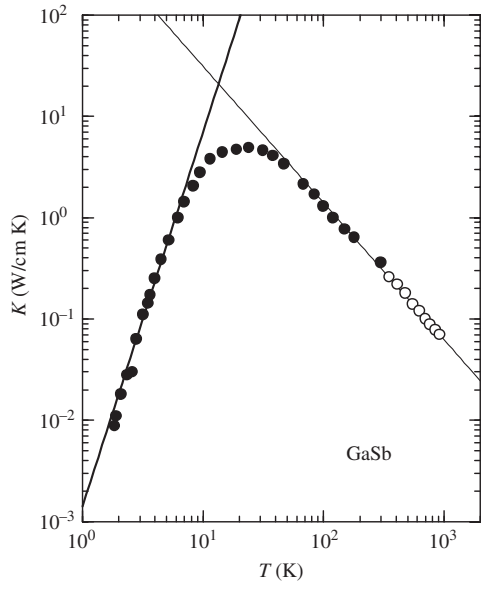

Figure 2.10 Thermal conductivity K versus temperature T for GaSb. The open and solid circles are taken from Steigmeier and Kudman [2.27] and Holland [2.34], respectively. The heavy and light solid lines represent the calculated results of $K = AT^n$ with $A = 0.0014$ W/cm K$^{4.7}$ and $n = 3.7$ and $A = 700$ W/cmK$^{-0.35}$ and $n = -1.35$, respectively. [From S. Adachi, *Handbook on Physical Properties of Semiconductors Volume 2: III–V Compound Semiconductors* (Kluwer Academic, Boston, 2004), reproduced by permission from Kluwer Academic Publishers]

In most semiconductors, we experimentally observe that the thermal conductivity of a pure single crystal is zero at $T = 0$ K and rises approximately exponentially to a maximum near 10 K, falls somewhat faster than T^{-1}, and then varies approximately as T^{-1} to the melting temperature. Figure 2.10 shows the experimental K value as a function of temperature T for GaSb [2.27, 2.34]. The theoretical lines in Figure 2.10 are obtained from the power law

$$K(T) = AT^n \tag{2.15}$$

The heavy and light solid lines are calculated with $A = 0.0014$ W/cm K$^{4.7}$ and $n = 3.7$ and $A = 700$ W/cm K$^{0.35}$ and $n = -1.35$, respectively. It can be seen that Equation (2.15) successfully explains the experimental K values in the low-temperature ($T \leqslant 5$ K) and high-temperature ranges ($T \geqslant 50$ K) (see also for GaAs in Figure 2.11, below). We

Table 2.9 Empirical equation for the lattice thermal conductivity K as a function of temperature T for some group-IV, III–V and II–VI semiconductors (K in W/cm K; T in K)

$$K(T) = AT^n$$

System	Material	A	n	T (K)
IV	Diamond	43500	−1.30	$100 \leqslant T \leqslant 1000$
	Si	8300	−1.50	$30 \leqslant T \leqslant 800$
	Ge	780	−1.26	$30 \leqslant T \leqslant 1000$
	3C-SiC	5300	−1.30	$120 \leqslant T \leqslant 300$
	4H-SiC	10500	−1.40	$150 \leqslant T \leqslant 300$ ($\perp c$)
	6H-SiC	22000	−1.48	$70 \leqslant T \leqslant 1700$ ($\perp c$)
III–V	h-BN	280	−0.75	$200 \leqslant T \leqslant 300$
	BP	32000	−1.60	$130 \leqslant T \leqslant 300$
	w-AlN	25000	−1.56	$100 \leqslant T \leqslant 1800$ ($\|c$)
	AlSb	1950	−1.42	$300 \leqslant T \leqslant 945$
	α-GaN	80000	−1.90	$120 \leqslant T \leqslant 320$ ($\|c$)
	GaP	1650	−1.35	$60 \leqslant T \leqslant 535$
	GaAs	750	−1.28	$150 \leqslant T \leqslant 1500$
	GaSb	700	−1.35	$50 \leqslant T \leqslant 920$
	InP	2200	−1.42	$20 \leqslant T \leqslant 800$
	InAs	4500	−1.73	$20 \leqslant T \leqslant 300$
	InSb	1450	−1.60	$20 \leqslant T \leqslant 300$
II–VI	MgO	250	−1.08	$100 \leqslant T \leqslant 1000$
	ZnO	260	−1.08	$25 \leqslant T \leqslant 240$ ($\perp c$)
	ZnO	420	−1.08	$30 \leqslant T \leqslant 190$ ($\|c$)
	β-ZnS	470	−1.31	$50 \leqslant T \leqslant 300$
	ZnSe	500	−1.40	$40 \leqslant T \leqslant 575$
	ZnTe	320	−1.31	$40 \leqslant T \leqslant 300$
	w-CdS	300	−1.30	$70 \leqslant T \leqslant 280$ ($\perp c$, $\|c$)
	CdTe	230	−1.43	$25 \leqslant T \leqslant 300$
	HgTe	550	−1.82	$20 \leqslant T \leqslant 220$

summarize in Table 2.9 the A and n values determined for some group-IV, III–V and II–VI semiconductors in the high-temperature ($T \geqslant 20$ K) range.

In doped semiconductors, the total thermal conductivity can be generally given by the sum of the lattice (K_l) and electronic contributions (K_e). In a metal, the electronic thermal conductivity K_e and electrical conductivity σ are related by the Wiedemann–Frantz–Lorenz law

$$K_e = L\sigma T \tag{2.16}$$

where L is the Lorentz number. In a semiconductor, a more complicated relationship exists between K_e and σ [2.28].

It has been found [2.28] that the n-type impurities (Te) in GaAs do not cause as large a decrease in low-temperature ($T < 100$ K) thermal conductivity as do comparable amounts of the p-type impurities (Zn, Cd and Mn). At high temperatures ($T \geqslant 300$ K) an increase in the free-electron concentration caused a decrease in thermal conductivity. This was attributed to scattering of phonons by electrons.

It is also important to point out that when large numbers of foreign atoms are added to the host lattice, as in alloying, the thermal conductivity decreases significantly. For example, a factor of eight reduction in thermal conductivity of $In_xGa_{1-x}As$ for $x \sim 0.5$, as compared to GaAs, has been reported [2.35].

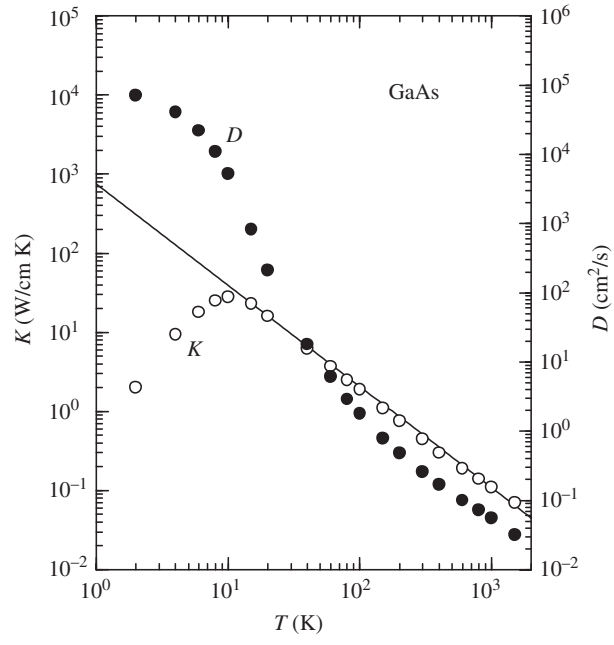

Figure 2.11 Thermal conductivity K and diffusivity D versus temperature T for GaAs. The experimental data are taken from Adachi [2.36]. The solid line represents the calculated result of $K = AT^n$ with $A = 750$ W/cm K$^{-0.28}$ and $n = -1.28$. [From S. Adachi, *Handbook on Physical Properties of Semiconductors Volume 2: III–V Compound Semiconductors* (Kluwer Academic, Boston, 2004), reproduced by permission from Kluwer Academic Publishers]

2.5.2 Thermal diffusivity

The thermal diffusivity D can be evaluated from the thermal conductivity K by means of the definition

$$D = \frac{K}{C_p g} \tag{2.17}$$

where C_p and g represent the specific heat at constant pressure and crystal density, respectively.

Figure 2.11 plots the temperature dependence of K and D for GaAs [2.36]. The K value for GaAs shows a maximum at $T \sim 10$ K, while the thermal diffusivity D gradually decreases with increasing temperature. The D value at the melting point of GaAs ($T \sim 1500$ K) is estimated to be about 0.03 cm^2/s.

REFERENCES

[2.1] J. A. Van Vechten, *Phys. Rev. B* **7**, 1479 (1973).
[2.2] A. Zerr and R. Boehler, *Nature* **371**, 506 (1994).
[2.3] J. C Brice, in *Properties of Crystalline Silicon*, EMIS Datareviews Series No. 20, edited by R. Hull (INSPEC, London, 1999), p. 155.
[2.4] U. Piesbergen, in *Semiconductors and Semimetals*, edited by R. K. Willardson and A. C. Beer (Academic, New York, 1966), Vol. 2, p. 49.
[2.5] T. Atake, S. Takai, A. Honda, Y. Saito, and K. Saito, *Rep. Res. Lab. Eng. Mater. Tokyo Inst. Technol.* **16**, 15 (1991).
[2.6] A. C. Victor, *J. Chem. Phys.* **36**, 1903 (1962).
[2.7] J. S. Blakemore, *J. Appl. Phys.* **53**, R123 (1982).
[2.8] J. A. Birch, *J. Phys. C: Solid State Phys.* **8**, 2043 (1975).
[2.9] A. S. Malkova, V. V. Zharov, G. I. Shmoilova, and A. S. Pashinkin, *Russ. J. Phys. Chem.* **63**, 2 (1989).
[2.10] M. Gambino, V. Vassiliev, and J. P. Bros, *J. Alloys Compounds* **176**, 13 (1991).
[2.11] U. Piesbergen, *Z. Naturf.* **18a**, 141 (1963).
[2.12] D. Bagot, R. Granger, and S. Rolland, *Phys. Status Solidi B* **177**, 295 (1993).
[2.13] A. F. Demidenko, *Inorg. Mater.* **5**, 210 (1969).
[2.14] P. M. Marcus and A. J. Kennedy, *Phys. Rev.* **114**, 459 (1959).
[2.15] E. F. Steigmeier, *Appl. Phys. Lett.* **3**, 6 (1963).
[2.16] R. W. Keyes, *J. Appl. Phys.* **33**, 3371 (1962).
[2.17] S. Adachi, *J. Appl. Phys.* **58**, R1 (1985).
[2.18] H. Siethoff and K. Ahlborn, *Phys. Status Solidi B* **190**, 179 (1995)
[2.19] J. F. Nye, *Physical Properties of Crystals* (Clarendon, Oxford, 1972).
[2.20] S. I. Novikova, in *Semiconductors and Semimetals*, edited by R. K. Willardson and A. C. Beer (Academic, New York, 1966), Vol. 2, p. 33.
[2.21] J. G. Collins, G. K. White, J. A. Birch, and T. F. Smith, *J. Phys. C: Solid State Phys.* **13**, 1649 (1980).
[2.22] S. N. Novikova and N. Kh. Abrikosov, *Sov. Phys. Solid State* **5**, 1558 (1964).
[2.23] H. Ibach, *Phys. Status Solidi* **33**, 257 (1969).
[2.24] H. Iwanaga, A. Kunishige, and S. Takeuchi, *J. Mater. Sci.* **35**, 2451 (2000).
[2.25] S. Biernacki and M. Scheffler, *Phys. Rev. Lett.* **63**, 290 (1989).
[2.26] D. C. Yin and Y. Inatomi, *Cryst. Res. Technol.* **35**, 221 (2000).
[2.27] E. F. Steigmeier and I. Kudman, *Phys. Rev.* **141**, 767 (1966).

[2.28] M. G. Holland, in *Semiconductors and Semimetals*, edited by R. K. Willardson and A. C. Beer (Academic, New York, 1966), Vol. 2, p. 3.
[2.29] P. D. Maycock, *Solid-State Electron.* **10**, 161 (1967).
[2.30] C. M. Bhandari and D. M. Rowe, *Thermal Conduction in Semiconductors* (Wiley, New York, 1988).
[2.31] G. P. Srivastava, *The Physics of Phonons* (Adam Hilger, Bristol, 1990).
[2.32] G. A. Slack, *Phys. Rev. B* **6**, 3791 (1972).
[2.33] A. Yoshiasa, K. Koto, H. Maeda, and T. Ishii, *Jpn. J. Appl. Phys.* **36**, 781 (1997).
[2.34] M. G. Holland, *Phys. Rev.* **134**, A471 (1964).
[2.35] S. Adachi, *J. Appl. Phys.* **54**, 1844 (1983).
[2.36] S. Adachi, in *Properties of Gallium Arsenide*, 3rd Edition, EMIS Datareviews Series No. 16, edited by M. R. Brozel and G. E. Stillman (INSPEC, London, 1996), p. 32.

3 Elastic Properties

3.1 Elastic constant 41
3.1.1 General remarks 41
3.1.2 Room-temperature value 42
3.1.3 External perturbation effect 48
3.2 Third-order elastic constant 51
3.3 Young's modulus, Poisson's ratio and similar properties 53
3.3.1 Young's modulus and Poisson's ratio: cubic lattice 53
3.3.2 Bulk modulus, shear modulus and similar properties: cubic lattice 56
3.3.3 Young's modulus and Poisson's ratio: hexagonal lattice 60
3.3.4 Bulk modulus, shear modulus and similar properties: hexagonal lattice 61
3.4 Microhardness 62
3.5 Sound velocity 68
References 72

3.1 ELASTIC CONSTANT

3.1.1 General remarks

The macroscopic theory of the elastic properties of solids has been described in detail in tensor notation by Nye [3.1]. The elastic stiffness $[C]$ and compliance tensors $[S]$ are defined by the generalized Hooke's law

$$[X] = [C][e] \tag{3.1a}$$

$$[e] = [S][X] \tag{3.1b}$$

where $[X]$ and $[e]$ are, respectively, the elastic stress and strain tensors having the six components. The stiffness and compliance tensors $[C]$ and $[S]$ are second-order fourth-rank ones having symmetric 6×6 components. We show in Table 3.1 the tensor forms of $[C]$ and $[S]$ for the cubic, hexagonal and rhombohedral systems.

It is evident from Equation (3.1) that the stiffness tensor $[C]$ can be connected reciprocally with the compliance tensor $[S]$

$$[C] = [S]^{-1} \tag{3.2}$$

Properties of Group-IV, III–V and II–VI Semiconductors Sadao Adachi

© 2005 John Wiley & Sons, Ltd

ISBN: 0-470-09032-4

Table 3.1 Form of the second-order elastic stiffness (compliance) tensor $[C]$ ($[S]$) for semiconductors of certain symmetry classes

Symmetry class	Material	Tensor form
Cubic	Si, 3C-SiC, GaAs, MgO, ZnSe, etc.	$\begin{bmatrix} C_{11} & C_{12} & C_{12} & 0 & 0 & 0 \\ C_{12} & C_{11} & C_{12} & 0 & 0 & 0 \\ C_{12} & C_{12} & C_{11} & 0 & 0 & 0 \\ 0 & 0 & 0 & C_{44} & 0 & 0 \\ 0 & 0 & 0 & 0 & C_{44} & 0 \\ 0 & 0 & 0 & 0 & 0 & C_{44} \end{bmatrix}$
Hexagonal	4H-SiC, h-BN, α-GaN, w-CdS, etc.	$\begin{bmatrix} C_{11} & C_{12} & C_{13} & 0 & 0 & 0 \\ C_{12} & C_{11} & C_{13} & 0 & 0 & 0 \\ C_{13} & C_{13} & C_{33} & 0 & 0 & 0 \\ 0 & 0 & 0 & C_{44} & 0 & 0 \\ 0 & 0 & 0 & 0 & C_{44} & 0 \\ 0 & 0 & 0 & 0 & 0 & C_{66} \end{bmatrix}$ $C_{66} = 1/2(C_{11} - C_{12})$
Rhombohedral	15R-SiC	$\begin{bmatrix} C_{11} & C_{12} & C_{13} & C_{14} & 0 & 0 \\ C_{12} & C_{11} & C_{13} & -C_{14} & 0 & 0 \\ C_{13} & C_{13} & C_{33} & 0 & 0 & 0 \\ C_{14} & -C_{14} & 0 & C_{44} & 0 & 0 \\ 0 & 0 & 0 & 0 & C_{44} & C_{14} \\ 0 & 0 & 0 & 0 & C_{14} & C_{66} \end{bmatrix}$ $C_{66} = 1/2(C_{11} - C_{12})$

Explicit equations for the stiffness constant C_{ij} in terms of S_{ij} are listed in Table 3.2 and vice versa in Table 3.3, where m and n in C_{mn} (S_{mn}) represent ij and kl, respectively, according to the rules $xx \rightarrow 1$, $yy \rightarrow 2$, $zz \rightarrow 3$, $yz \rightarrow 4$, $zx \rightarrow 5$ and $xy \rightarrow 6$.

3.1.2 Room-temperature value

Adiabatic elastic constants can be determined most accurately from ultrasound velocity measurements. The difference between the adiabatic and isothermal elastic compliance constants can be given by [3.1]

$$S_{ijkl}^{S} - S_{ijkl}^{T} = -\alpha_{ij}\alpha_{kl}\left(\frac{T}{C_{\mathrm{p}}}\right) \tag{3.3}$$

where α_{mn} represents the thermal expansion coefficient and C_{p} is the heat capacity at constant pressure. Since crystals usually have positive coefficients of thermal expansion and since C_{p} is positive, the right-hand side of Equation (3.3) is usually negative. The adiabatic compliances are, thus, smaller than the isothermal ones. However, the differences are small in most semiconductors. Therefore, no special attention has been given in the present work.

Table 3.2 Relations between the elastic stiffness C_{ij} and compliance constants S_{ij} for semiconductors of certain symmetry classes

Cubic (Si, GaAs, MgO, ZnSe, etc.)
$C_{11} = \dfrac{S_{11} + S_{12}}{(S_{11} - S_{12})(S_{11} + 2S_{12})}$
$C_{12} = \dfrac{-S_{12}}{(S_{11} - S_{12})(S_{11} + 2S_{12})}$
$C_{44} = \dfrac{1}{S_{44}}$
Hexagonal (4H-SiC, h-BN, α-GaN, w-CdS, etc.)
$C_{11} = \dfrac{S_{11}S_{33} - S_{13}^2}{S(S_{11} - S_{12})}$
$C_{12} = \dfrac{S_{13}^2 - S_{12}S_{33}}{S(S_{11} - S_{12})}$
$C_{13} = \dfrac{-S_{13}}{S}$
$C_{33} = \dfrac{S_{11} + S_{12}}{S}$
$C_{44} = \dfrac{1}{S_{44}}$, where $S = S_{33}(S_{11} + S_{12}) - 2S_{13}^2$
Rhombohedral (15R-SiC)
$C_{11} + C_{12} = \dfrac{S_{33}}{S}$
$C_{11} - C_{12} = \dfrac{S_{44}}{S'}$
$C_{13} = \dfrac{-S_{13}}{S}$
$C_{14} = \dfrac{-S_{14}}{S'}$
$C_{33} = \dfrac{S_{11} + S_{12}}{S}$
$C_{44} = \dfrac{S_{11} - S_{12}}{S'}$, where $S = S_{33}(S_{11} + S_{12}) - 2S_{13}^2$ and $S' = S_{44}(S_{11} - S_{12}) - 2S_{14}^2$

The elastic constants can be determined from measurements of ultrasound velocities, Brillouin scattering, neutron scattering, diffuse X-ray reflection, etc. We summarize in Table 3.4 the experimental C_{ij} and S_{ij} values for a number of cubic group-IV, III–V and II–VI semiconductors at $T = 300$ K. The C_{ij} and S_{ij} values for a

Table 3.3 Relations between the elastic compliance S_{ij} and stiffness constants C_{ij} for semiconductors of certain symmetry classes

Cubic (Si, GaAs, MgO, ZnSe, etc.)
$S_{11} = \dfrac{C_{11} + C_{12}}{(C_{11} - C_{12})(C_{11} + 2C_{12})}$
$S_{12} = \dfrac{-C_{12}}{(C_{11} - C_{12})(C_{11} + 2C_{12})}$
$S_{44} = \dfrac{1}{C_{44}}$
Hexagonal (4H-SiC, h-BN, α-GaN, w-CdS, etc.)
$S_{11} = \dfrac{C_{11}C_{33} - C_{13}^2}{C(C_{11} - C_{12})}$
$S_{12} = \dfrac{C_{13}^2 - C_{12}C_{33}}{C(C_{11} - C_{12})}$
$S_{13} = \dfrac{-C_{13}}{C}$
$S_{33} = \dfrac{C_{11} + C_{12}}{C}$
$S_{44} = \dfrac{1}{C_{44}}$, where $C = C_{33}(C_{11} + C_{12}) - 2C_{13}^2$
Rhombohedral (15R-SiC)
$S_{11} = \dfrac{1}{2}\dfrac{C'C_{33} + CC_{44}}{C'C}$
$S_{12} = \dfrac{1}{2}\dfrac{C'C_{33} - CC_{44}}{C'C}$
$S_{13} = \dfrac{-C_{13}}{C}$
$S_{14} = \dfrac{-C_{14}}{C'}$
$S_{33} = \dfrac{C_{11} + C_{12}}{C}$
$S_{44} = \dfrac{C_{11} - C_{12}}{C'}$, where $C = C_{33}(C_{11} + C_{12}) - 2C_{13}^2$ and $C' = C_{44}(C_{11} - C_{12}) - 2C_{14}^2$

number of hexagonal group-IV, III–V and II–VI semiconductors are summarized in Tables 3.5 and 3.6, respectively.

Based on a bond-orbital model, it is possible to write the quantities C_{11}, C_{12} and C_{12}/C_{11} by [3.2]

$$C_{11} = B_{\mathrm{u}}(1 + \alpha_{\mathrm{c}}^2) \tag{3.4}$$

Table 3.4 Elastic stiffness C_{ij} and compliance constants S_{ij} for a number of cubic group-IV, III–V and II–VI semiconductors at 300 K

System	Material	C_{ij} (10^{11} dyn/cm^2)			S_{ij} (10^{-12} cm^2/dyn)		
		C_{11}	C_{12}	C_{44}	S_{11}	S_{12}	S_{44}
IV	Diamond	107.9	12.4	57.8	0.0949	−0.00978	0.1730
	Si	16.564	6.394	7.951	0.7691	−0.2142	1.2577
	Ge	12.870	4.770	6.670	0.9718	−0.2628	1.499
	α-Sn	6.90[a]	2.93[a]	3.62[a]	1.94[a]	−0.578[a]	2.76[a]
	3C-SiC	39.0	14.2	25.6	0.318	−0.085	0.391
III–V	c-BN	82.0	19.0	48.0	0.134	−0.025	0.208
	BP	31.5	10	16	0.37	−0.09	1.00
	BAs	27.9[b]	12.0[b]	11.3[b]	0.484[b]	−0.145[b]	0.885[b]
	c-AlN	31.5[b]	15.0[b]	18.5[b]	0.458[b]	−0.148[b]	0.541[b]
	AlP	15.0[b]	6.42[b]	6.11[b]	0.897[b]	−0.269[b]	1.64[b]
	AlAs	11.93	5.72	5.72	1.216	−0.394	1.748
	AlSb	8.769	4.341	4.076	1.697	−0.5618	2.453
	β-GaN	29.1[b]	14.8[b]	15.8[b]	0.523[b]	−0.176[b]	0.633[b]
	GaP	14.050	6.203	7.033	0.9756	−0.2988	1.422
	GaAs	11.88	5.38	5.94	1.173	−0.366	1.684
	GaSb	8.838	4.027	4.320	1.583	−0.4955	2.315
	InP	10.22	5.73	4.42	1.639	−0.589	2.26
	InAs	8.329	4.526	3.959	1.945	−0.6847	2.526
	InSb	6.608	3.531	3.027	2.410	−0.8395	3.304
II–VI	MgO	29.4	9.3	15.5	0.401	−0.096	0.647
	β-MgS	8.88[b]	5.53[b]	3.87[b]	2.16[b]	−0.83[b]	2.58[b]
	β-MgSe	7.58[b]	4.86[b]	3.17[b]	2.64[b]	−1.03[b]	3.15[b]
	β-MgTe	5.28[b]	3.66[b]	1.93[b]	4.38[b]	−1.79[b]	5.18[b]
	β-ZnS	10.2	6.46	4.46	1.95	−0.76	2.25
	ZnSe	8.57	5.07	4.05	2.09	−0.78	2.47
	ZnTe	7.15	4.08	3.11	2.39	−0.85	3.25
	c-CdS	7.70	5.39	2.36	3.07	−1.26	4.24
	c-CdSe	6.67	4.63	2.23	3.48	−1.42	4.48
	CdTe	5.35	3.69	2.02	4.27	−1.74	4.95
	β-HgS	8.13	6.22	2.64	3.65	−1.58	3.79
	HgSe	6.08	4.46	2.23	4.34	−1.84	4.49
	HgTe	5.32	3.68	2.08	4.33	−1.77	4.80

[a] Obtained from an analysis of the phonon dispersion curves at 90 K
[b] Calculated or estimated

$$C_{12} = B_{\mathrm{u}}\left(\frac{2-\alpha_{\mathrm{c}}^2}{2}\right) \tag{3.5}$$

$$\frac{C_{12}}{C_{11}} = \frac{2-\alpha_{\mathrm{c}}^2}{2+2\alpha_{\mathrm{c}}^2} \tag{3.6}$$

where B_{u} is the bulk modulus and α_{c} is the covalency defined, using Phillips ionicity f_{i}, by $f_{\mathrm{i}} = 1 - \alpha_{\mathrm{c}}^2$.

Table 3.5 Elastic stiffness constant C_{ij} for a number of hexagonal group-IV, III–V and II–VI semiconductors at 300 K (in 10^{11} dyn/cm^2)

System	Material	C_{11}	C_{12}	C_{13}	C_{33}	C_{44}	C_{66}[a]
IV	6H-SiC	50.1	11.1	5.2	55.3	16.3	19.5
III–V	*h*-BN	52.0	43.1	37.0	42.4	6.5	4.5
	w-AlN	41.0	14.0	10.0	39.0	12.0	13.5
	α-GaN	37.3	14.1	8.0	38.7	9.4	11.6
	InN	19.0	10.4	12.1	18.2	0.99	4.3
II–VI	ZnO	20.9	12.0	10.4	21.8	4.41	4.45
	α-ZnS	12.2	5.8	4.2	13.8	2.87	3.2
	w-CdS	8.65	5.40	4.73	9.44	1.50	1.63
	w-CdSe	7.41	4.52	3.9	8.43	1.34	1.45

[a] $C_{66} = 1/2(C_{11} - C_{12})$

Table 3.6 Elastic compliance constant S_{ij} for a number of hexagonal group-IV, III–V and II–VI semiconductors at 300 K (in 10^{-12} cm^2/dyn)

System	Material	S_{11}	S_{12}	S_{13}	S_{33}	S_{44}	S_{66}[a]
IV	6H-SiC	0.211	−0.045	−0.016	0.184	0.614	0.512
III–V	*h*-BN	0.726	−0.398	−0.286	0.735	1.54	2.25
	w-AlN	0.285	−0.085	−0.051	0.283	0.833	0.740
	α-GaN	0.320	−0.112	−0.043	0.276	1.06	0.864
	InN	0.957	−0.206	−0.499	1.21	10.1	2.33
II–VI	ZnO	0.782	−0.345	−0.210	0.664	2.24	2.254
	α-ZnS	1.10	−0.45	−0.20	0.86	3.48	3.10
	w-CdS	2.08	−1.00	−0.54	1.60	6.66	6.16
	w-CdSe	2.32	−1.12	−0.55	1.69	7.47	6.88

[a] $S_{66} = 2(S_{11} - S_{12})$

We plot in Figure 3.1 the ratio of the elastic stiffness constants C_{12}/C_{11} versus (a) Phillips ionicity f_i and (b) covalency α_c for some cubic group-IV, III–V and II–VI semiconductors. The solid line in Figure 3.1(a) shows the least-squares fit with the relation

$$\frac{C_{12}}{C_{11}} = 0.469 f_i + 0.313 \tag{3.7}$$

while that in Figure 3.1(b) represents the ratio given by Equation (3.6). We can see that the plots for diamond (C), *c*-BN and MgO deviate markedly from the curves in Figure 3.1.

Keyes [3.3] found that the elastic constants of some group-IV, III–V and II–VI semiconductors are functions of their lattice constants only. He defined from a dimensional analysis an elastic constant $C_0 = e^2/d^4$, where e is the electronic charge and d is the distance between nearest-neighbor atoms in the unit cell. The elastic constants, reduced

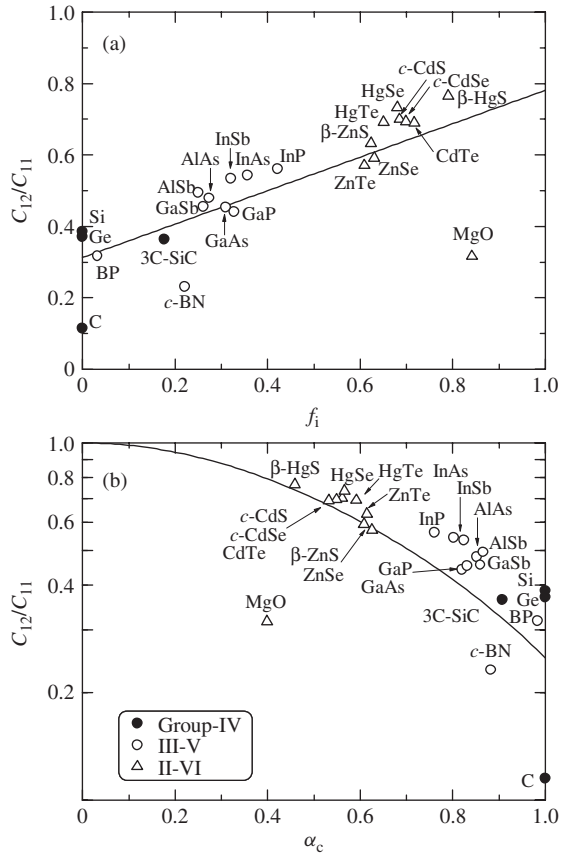

Figure 3.1 Ratio of the elastic stiffness constants C_{12}/C_{11} versus: (a) Phillips ionicity f_i; and (b) covalency α_c for some cubic group-IV, III–V and II–VI semiconductors. The solid line in (a) shows the least-squares fit with $C_{12}/C_{11} = 0.469 f_i + 0.313$ and that in (b) represents the theoretical curve of Equation (3.6)

by the quantity C_0, have nearly the same values among the III–V compounds. This fact can be used to obtain the elastic constants of other materials [3.4].

In a similar vein, Adachi [3.5] has used a relation between the elastic constants of various III–V compounds and their lattice constants to predict values for AlAs. We plot in Figure 3.2 the elastic stiffness constants, C_{11}, C_{12} and C_{44}, versus lattice constant a for some cubic group-IV, III–V and II–VI semiconductors. The solid lines in Figure 3.2 represent the least-squares fit from the relation

$$\ln C_{ij} = A_{ij} \ln a + B_{ij} \tag{3.8}$$

The A_{ij} and B_{ij} values determined from the fits in Figure 3.2 are summarized in Table 3.7.

Figure 3.3 shows the plots of C_{ij} versus a for some cubic II–VI semiconductors. The solid lines represent the least-squares fit with the relation

$$C_{ij} = D_{ij} a + E_{ij} \tag{3.9}$$

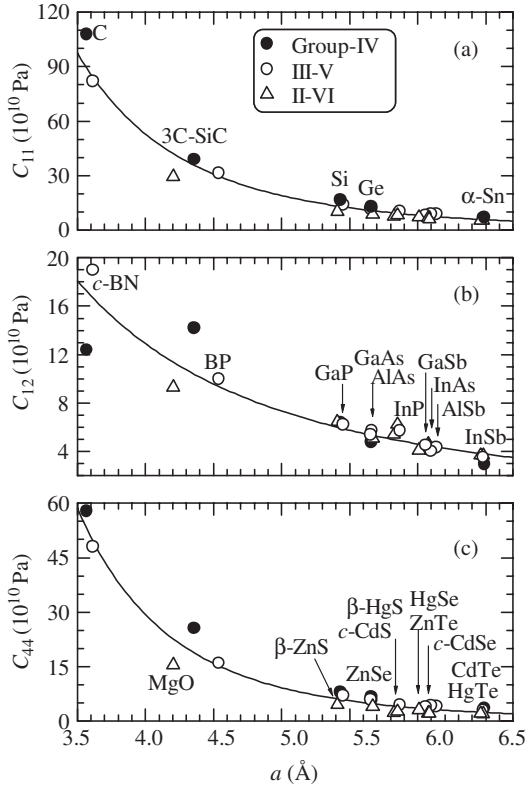

Figure 3.2 Elastic stiffness constant C_{ij} versus lattice constant a for some cubic group-IV, III–V and II–VI semiconductors. The solid lines represent the least-squares fits with: (a) $\ln C_{11} = -4.59 \ln a + 10.33$; (b) $\ln C_{12} = -2.54 \ln a + 6.07$; and (c) $\ln C_{44} = -5.20 \ln a + 10.59$ (a in Å; C_{ij} in 10^{10} Pa), respectively

The fitted D_{ij} and E_{ij} values are listed in Table 3.7. It is understood from Figure 3.3 that Equation (3.9) accurately represents the relation between C_{ij} and a. The C_{ij} values for β-MgS, β-MgSe and β-MgTe listed in Table 3.4 are obtained from Equation (3.9). The same plots, but for a number of hexagonal group-IV, III–V and II–VI semiconductors, are shown in Figure 3.4.

3.1.3 External perturbation effect

(a) Temperature effect

We plot in Figure 3.5 the elastic stiffness constant C_{ij} as a function of temperature T for GaSb. The experimental data are taken from Lin and Wong [3.6]. It is seen that the elastic constant C_{ij} for GaSb shows a small temperature variation for T up to ~50 K and gradually decreases with further increase of T. At $T \geqslant 150$ K, the temperature variation is found to be almost linear.

Table 3.7 Parameter values describing the relationship between C_{ij} and a

$\ln C_{ij} = A_{ij} \ln a + B_{ij}$ (a in Å; C_{ij} in 10^{10} Pa)[a]		
C_{ij}	A_{ij}	B_{ij}
C_{11}	−4.59	10.33
C_{12}	−2.54	6.07
C_{44}	−5.20	10.59
$C_{ij} = D_{ij}a + E_{ij}$ (a in Å; C_{ij} in 10^{10} Pa)[b]		
C_{ij}	D_{ij}	E_{ij}
C_{11}	−45.0	341.5
C_{12}	−23.4	186.8
C_{44}	−24.3	175.1

[a] Fitted from some cubic group-IV, III–V and II–VI semiconductors
[b] Fitted from some cubic II–VI semiconductors only

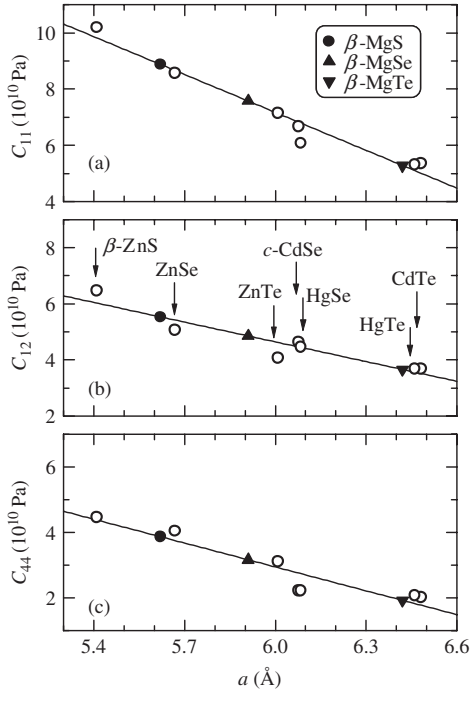

Figure 3.3 Elastic stiffness constant C_{ij} versus lattice constant a for some cubic II–VI semiconductors. The solid lines represent the least-squares fits with: (a) $C_{11} = -45.0a + 341.5$; (b) $C_{12} = -23.4a + 186.8$; and (c) $C_{44} = -24.3a + 175.1$ (a in Å; C_{ij} in 10^{10} Pa), respectively. The elastic stiffness constants for β-MgS, β-MgSe and β-MgTe can be determined from these simple relations

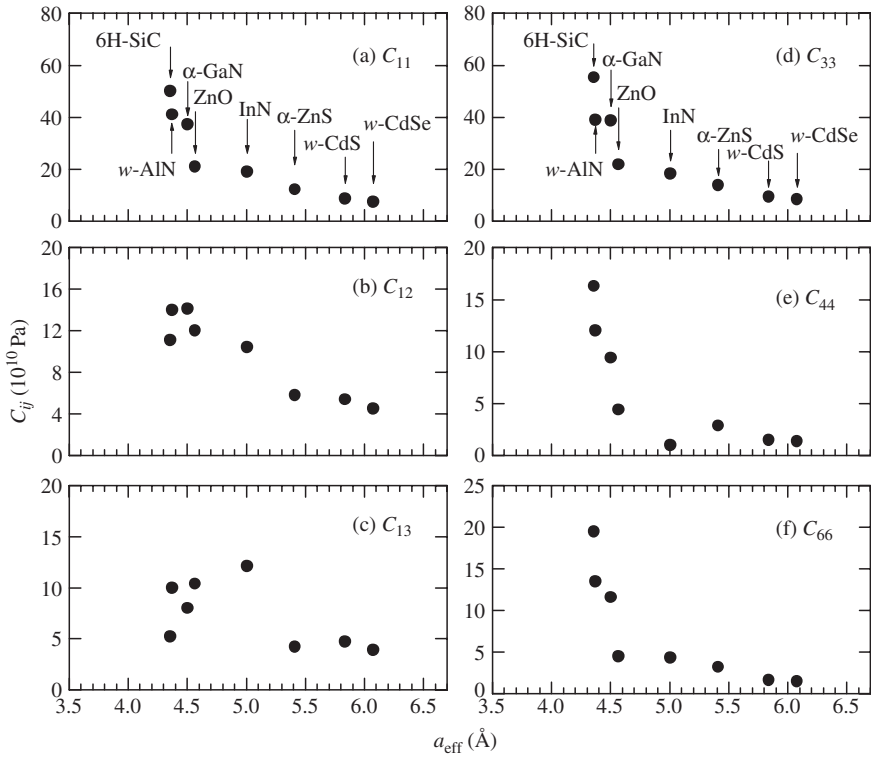

Figure 3.4 Elastic stiffness constant C_{ij} versus an effective lattice constant $a_{\text{eff}} = (\sqrt{3}a^2c)^{1/3}$ for a number of hexagonal group-IV, III–V and II–VI semiconductors

The solid lines in Figure 3.5 represent the fit using an expression

$$C_{ij}(T) = C_{ij}(0) - \frac{\alpha T^2}{T + \beta} \tag{3.10}$$

where $C_{ij}(0)$ is the $T = 0$ K value, α is in dyn/cm^2 per Kelvin and β is a quantity proportional to the Debye temperature (in Kelvin). Note that Equation (3.10) is widely known as the Varshni equation, used for explaining the temperature dependence of the band-gap energy [3.7].

Table 3.8 summarizes the temperature coefficient of the elastic stiffness constants $\mathrm{d}C_{ij}/\mathrm{d}T$ for some cubic group-IV, III–V and II–VI semiconductors at $T = 300$ K. The coefficients for some hexagonal semiconductors are shown in Table 3.9. We can see in Tables 3.8 and 3.9 that the temperature coefficient $\mathrm{d}C_{ij}/\mathrm{d}T$ is negative for many semiconductors.

(b) Pressure effect

The pressure coefficient $\mathrm{d}C_{ij}/\mathrm{d}p$ as normally measured from ultrasound velocities is mixed quantity, and refers to the variation of the adiabatic stiffness with pressure at

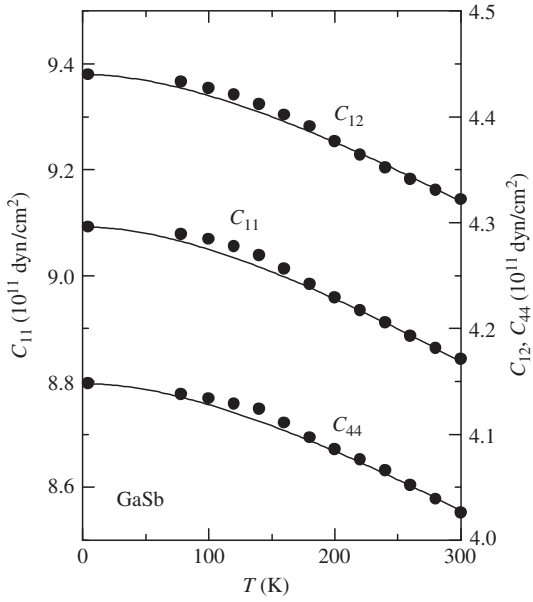

Figure 3.5 Temperature dependence of the elastic stiffness constants C_{ij} for GaSb. The experimental data are taken from Lin and Wong [3.6]. The solid lines represent the fitted results using $C_{ij}(T) = C_{ij}(0) - [\alpha T^2/(T+\beta)]$ with $C_{11}(0) = 9.09 \times 10^{11}$ dyn/cm^2, $\alpha = 1.7 \times 10^{-3}$ dyn/cm^2 K and $\beta = 300$ K for C_{11}; $C_{12}(0) = 4.44 \times 10^{11}$ dyn/cm^2, $\alpha = 8.0 \times 10^{-4}$ dyn/cm^2 K and $\beta = 300$ K for C_{12}; $C_{44}(0) = 4.15 \times 10^{11}$ dyn/cm^2, $\alpha = 8.0 \times 10^{-4}$ dyn/cm^2 K and $\beta = 300$ K for C_{44}. [From S. Adachi, *Handbook on Physical Properties of Semiconductors Volume 2: III–V Compound Semiconductors* (Kluwer Academic, Boston, 2004), reproduced by permission from Kluwer Academic Publishers]

constant temperature, i.e., $(\partial C_{ij}^S/\partial p)_T$, where S denotes constant entropy. The adiabatic and isothermal pressure coefficients can also be given by $(\partial C_{ij}^S/\partial p)_S$ and $(\partial C_{ij}^T/\partial p)_T$, respectively. Note that the pressure coefficient is a dimensionless quantity.

If the third-order elastic constants are known, the pressure coefficients can be calculated from unidirectional as well as hydrostatic stress data. In the great majority of cases, the $C_{ij}-p$ relationship is effectively linear, but some experiments show a nonlinear relationship [3.8].

We list in Table 3.8 the pressure coefficient of the elastic stiffness constants $\mathrm{d}C_{ij}/\mathrm{d}p$ for some cubic group-IV, III–V and II–VI semiconductors at $T = 300$ K. The coefficients for some hexagonal semiconductors are also listed in Table 3.10. We can see that $\mathrm{d}C_{ij}/\mathrm{d}p$ is positive for all cubic semiconductors except for $\mathrm{d}C_{44}/\mathrm{d}p$ of HgSe and HgTe, but for hexagonal semiconductors all $\mathrm{d}C_{44}/\mathrm{d}p$ values listed in Table 3.10 are negative.

3.2 THIRD-ORDER ELASTIC CONSTANT

Elastic constant–applied stress data allow the determination of the third-order elastic stiffness constants. For the cubic point groups, O, O_h and T_d, the third-order elastic tensor has six independent components, C_{111}, C_{112}, C_{123}, C_{144}, C_{166} and C_{456} [3.9]. For the hexagonal

Table 3.8 Temperature and pressure coefficients of the elastic stiffness constant C_{ij} for some cubic group-IV, III–V and II–VI semiconductors at 300 K

System	Material	dC_{ij}/dT (10^7 dyn/cm^2 K)			dC_{ij}/dp		
		C_{11}	C_{12}	C_{44}	C_{11}	C_{12}	C_{44}
IV	Diamond	−14.8	−7.07	−7.23	5.98	3.06	2.98
	Si	−15.6	−6.3	−6.6	4.33	4.19	0.80
	Ge	−13.0	−3.3	−9.0	5.03	4.31	1.41
III–V	GaP	−11.8	−5.25	−6.08	4.77	4.79	0.92
	GaAs	−13.9	−5.76	−7.01	4.63	4.42	1.10
	GaSb	−11.5	−6.3	−5.3	4.93	4.66	1.00
	InP	−14.0	−8.3	−4.0	4.17	4.80	0.36
	InAs	−18.6	−10.4	−9.9	4.52	4.92	0.41
	InSb	−14.8	−9.0	−3.7	4.748	4.974	0.533
II–VI	MgO	−58.5	+7.5	−12.6	9.38	1.94	1.15
	β-ZnS	−11.2	−7.8	−3.6			
	ZnSe	−14.2	−9.58	−4.33	4.5	4.9	0.45
	ZnTe	−13.4	−8.28	−4.39	4.9	5.1	0.44
	CdTe	−10.7	−8.5	−1.9			
	HgSe	−30	−27	−4.5	1.8	2.9	−0.56
	HgTe	−22	−16	−5.6	3.3	4.1	−0.12

Table 3.9 Temperature coefficient of the elastic stiffness constant C_{ij} for some hexagonal semiconductors at 300 K

System	Material	dC_{ij}/dT (10^7 dyn/cm^2 K)					
		C_{11}	C_{12}	C_{13}	C_{33}	C_{44}	C_{66}
II–VI	ZnO				−26	−3.1	
	α-ZnS	−13.9	−7.7	−6.2	−15	−2.8	
	CdS	−15	−11	−9.9	−16	−0.9	
	CdSe	−16.4	−12.6		−17.7	−1.5	−1.9

Table 3.10 Pressure coefficient of the elastic stiffness constant C_{ij} for some hexagonal semiconductors at 300 K

System	Material	dC_{ij}/dp					
		C_{11}	C_{12}	C_{13}	C_{33}	C_{44}	C_{66}
II–VI	ZnO	3.8	5.2	4.7	3.7	−0.53	
	α-ZnS	4.2	4.5	3.8	5.1	−0.083	
	CdS	3.08	5.24	4.73	3.25	−0.63	

Table 3.11 Third-order elastic constant C_{ijk} for some cubic group-IV, III–V and II–VI semiconductors (in 10^{12} dyn/cm^2)

System	Material	C_{111}	C_{112}	C_{123}	C_{144}	C_{166}	C_{456}
IV	Diamond	−62.6	−22.6	1.12	−6.74	−28.6	−8.23
	Si	−8.34	−5.31	−0.02	−0.95	−2.96	−0.074
	Ge	−7.2	−3.8	−0.3	−0.1	−3.05	−0.45
III–V	GaP	−7.37	−4.74	−1.31	−1.07	−2.34	−0.62
	GaAs	−6.22	−3.87	−0.57	0.02	−2.69	0.39
	GaSb	−4.75	−3.08	−0.44	0.50	−2.16	−0.25
	InP	−8.6	−1.85	−5.1	−6.5	1.6	−0.042
	InAs	−5.18	−2.25	−2.39	−1.90	−0.18	−0.068
	InSb	−3.56	−2.66	−1.00	0.16	−1.39	−0.004
II–VI	MgO	−49.0	−0.95	−0.69	1.13	−6.59	1.47
	ZnSe	−8.27	−1.36	−5.11	2.22	−2.65	−2.78
	ZnTe	−7.07	−1.21	−4.12	1.83	−2.17	−2.29
	c-CdS	−2.5	−2.8	−1.9	0.3	−0.6	0.4
	HgSe	−2.12	−1.27	−0.91	−0.071	−0.43	0.006
	HgTe	−2.60	−1.70	−0.77	−0.17	−0.57	−0.01

Table 3.12 Third-order elastic constant C_{ijk} of w-CdS

Modulus	Value (10^{12} dyn/cm^2)	Modulus	Value (10^{12} dyn/cm^2)
C_{111}	−4.59	C_{144}	−0.27
C_{112}	−2.07	C_{155}	+0.09
C_{113}	−1.82	C_{222}	−3.55
C_{123}	−2.35	C_{333}	−3.27
C_{133}	−3.06	C_{344}	−0.69

point groups, C_{6v} and D_{6h}, the third-order elastic tensor has ten independent components, C_{111}, C_{112}, C_{113}, C_{123}, C_{133}, C_{144}, C_{155}, C_{222}, C_{333} and C_{344}. We list in Table 3.11 the experimentally determined third-order elastic constant C_{ijk} for some cubic semiconductors. For hexagonal semiconductors, only the data for w-CdS are available [3.9]. These data are listed in Table 3.12.

3.3 YOUNG'S MODULUS, POISSON'S RATIO AND SIMILAR PROPERTIES

3.3.1 Young's modulus and Poisson's ratio: cubic lattice

There is a considerable interest in the effect of mechanical stresses resulting from crystal growth and device processing on the behavior and reliability of semiconductor devices.

Precise computation of such stresses requires knowledge of Young's modulus and Poisson's ratio, in particular, for specific orientations within the crystallographic plane defining the surface of the semiconductors.

Young's modulus is defined as the ratio of elastic stress to strain. It is not isotropic, even in cubic, zinc-blende-type crystals [3.10]. The modulus Y for an arbitrary crystallographic direction m can be written as

$$Y^{-1} = S_{11} - 2\left(S_{11} - S_{12} - \frac{1}{2}S_{44}\right)(m_1^2 m_2^2 + m_2^2 m_3^2 + m_1^2 m_3^2) \tag{3.11}$$

where S_{ij} are the elastic compliance constants and m_i are the direction cosines for m.

Poisson's ratio P is the ratio of the transverse contraction per unit dimension of a bar of uniform cross-section to its elongation per unit length, when subjected a tensile stress. The ratio P also varies with orientation. If a longitudinal stress in the direction m and the transverse strain along orthogonal direction n is under consideration, then P is given by

$$P = -\frac{S_{12} + \left(S_{11} - S_{12} - \frac{1}{2}S_{44}\right)(m_1^2 n_1^2 + m_2^2 n_2^2 + m_3^2 n_3^2)}{S_{11} - 2\left(S_{11} - S_{12} - \frac{1}{2}S_{44}\right)(m_1^2 m_2^2 + m_2^2 m_3^2 + m_1^2 m_3^2)} \tag{3.12}$$

The modulus Y for the direction of the cube axes $\langle 100\rangle$ is readily given by $Y = 1/S_{11}$. The ratio P, in this case, is written as $P = -S_{12}/S_{11}$. In Table 3.13, we list

Table 3.13 Functional expressions for Young's modulus Y and Poisson's ratio P within the crystallographic planes (100), (110) and (111) in cubic lattice. $S = S_{11} - S_{12} - (S_{44}/2)$, m is the direction for a longitudinal stress and n is the direction for a transverse strain (orthogonal to the direction m)

Parameter	Crystallographic plane	Expression
Young's modulus Y	(100) plane	
	[001] direction	$1/S_{11}$
	[011] direction	$1/(S_{11} - S/2)$
	(110) plane	
	[001] direction	$1/S_{11}$
	[111] direction	$1/(S_{11} - 2S/3)$
	(111) plane	$1/(S_{11} - S/2)$
Poisson's ratio P	(100) plane	
	$m = [010]$, $n = [001]$	$-S_{12}/S_{11}$
	$m = [011]$, $n = [0\bar{1}1]$	$-(S_{12} + S/2)/(S_{11} - S/2)$
	(110) plane	
	$m = [001]$, $n = [1\bar{1}0]$	$-S_{12}/S_{11}$
	$m = [1\bar{1}1]$, $n = [1\bar{1}2]$	$-(S_{12} + S/3)/(S_{11} - 2S/3)$
	(111) plane	$-(S_{12} + S/6)/(S_{11} - S/2)$

the functional expressions for Y and P for directions within the three important (100), (110) and (111) planes in cubic lattice. It should be noted that the Y and P are invariant within the {111} plane. In Tables 3.14 and 3.15, we also list the numerical values of Y and P for directions within the (100), (110) and (111) planes in a number of cubic group-IV, III–V and II–VI semiconductors at $T = 300$ K.

Table 3.14 Young's modulus Y within the crystallographic planes (100), (110) and (111) in a number of cubic group-IV, III–V and II–VI semiconductors at 300 K (in 10^{12} dyn/cm^2)

System	Material	(100)		(110)		(111)
		[001]	[011]	[001]	[111]	
IV	Diamond	10.53	11.65	10.53	12.08	11.65
	Si	1.300	1.690	1.300	1.877	1.690
	Ge	1.029	1.371	1.029	1.542	1.371
	α-Sn	0.515	0.729	0.515	0.846	0.729
	3C-SiC	3.14	4.63	3.14	5.50	4.63
III–V	c-BN	7.46	9.39	7.46	10.3	9.39
	BP	2.7	2.6	2.7	2.5	2.6
	BAs	2.07	2.56	2.07	2.78	2.56
	c-AlN	2.18	3.45	2.18	4.27	3.45
	AlP	1.11	1.38	1.11	1.50	1.38
	AlAs	0.822	1.179	0.822	1.379	1.179
	AlSb	0.589	0.847	0.589	0.991	0.847
	β-GaN	1.91	3.01	1.91	3.73	3.01
	GaP	1.03	1.44	1.03	1.67	1.44
	GaAs	0.853	1.213	0.853	1.412	1.213
	GaSb	0.632	0.891	0.632	1.03	0.891
	InP	0.610	0.917	0.610	1.10	0.917
	InAs	0.514	0.793	0.514	0.967	0.793
	InSb	0.415	0.621	0.415	0.744	0.621
II–VI	MgO	2.49	3.18	2.49	3.51	3.18
	β-MgS	0.463	0.763	0.463	0.973	0.763
	β-MgSe	0.379	0.628	0.379	0.804	0.628
	β-MgTe	0.228	0.386	0.228	0.502	0.386
	β-ZnS	0.513	0.864	0.513	1.12	0.864
	ZnSe	0.478	0.786	0.478	1.00	0.786
	ZnTe	0.418	0.632	0.418	0.761	0.632
	c-CdS	0.326	0.509	0.326	0.626	0.509
	c-CdSe	0.287	0.465	0.287	0.586	0.465
	CdTe	0.234	0.400	0.234	0.523	0.400
	β-HgS	0.274	0.504	0.274	0.701	0.504
	HgSe	0.230	0.422	0.230	0.583	0.422
	HgTe	0.231	0.403	0.231	0.537	0.403

Table 3.15 Poisson's ratio P within the crystallographic planes (100), (110) and (111) in a number of cubic group-IV, III–V and II–VI semiconductors at 300 K

System	Material	(100)		(110)		(111)
		$m = [010]$ $n = [001]$	$m = [011]$ $n = [0\bar{1}1]$	$m = [001]$ $n = [1\bar{1}0]$	$m = [1\bar{1}1]$ $n = [1\bar{1}\,\bar{2}]$	
IV	Diamond	0.103	0.0079	0.103	0.045	0.079
	Si	0.279	0.062	0.279	0.180	0.262
	Ge	0.270	0.028	0.270	0.156	0.250
	α-Sn	0.298	0.007	0.298	0.169	0.283
	3C-SiC	0.267	−0.081	0.267	0.092	0.235
III–V	c-BN	0.187	−0.024	0.187	0.069	0.149
	BP	0.24	0.28	0.24	0.26	0.25
	BAs	0.300	0.132	0.300	0.230	0.292
	c-AlN	0.323	−0.068	0.323	0.154	0.317
	AlP	0.300	0.133	0.300	0.231	0.292
	AlAs	0.324	0.031	0.324	0.205	0.320
	AlSb	0.331	0.039	0.331	0.216	0.330
	β-GaN	0.337	−0.046	0.337	0.181	0.338
	GaP	0.306	0.025	0.306	0.185	0.295
	GaAs	0.312	0.021	0.312	0.189	0.303
	GaSb	0.313	0.031	0.313	0.195	0.305
	InP	0.359	0.037	0.359	0.246	0.373
	InAs	0.352	0.001	0.352	0.222	0.362
	InSb	0.348	0.025	0.348	0.228	0.356
II–VI	MgO	0.239	0.029	0.239	0.134	0.213
	β-MgS	0.383	−0.016	0.383	0.255	0.416
	β-MgSe	0.390	−0.011	0.390	0.267	0.428
	β-MgTe	0.409	−0.000	0.409	0.299	0.461
	β-ZnS	0.390	−0.028	0.390	0.259	0.428
	ZnSe	0.373	−0.030	0.373	0.235	0.399
	ZnTe	0.356	0.027	0.356	0.237	0.367
	c-CdS	0.410	0.079	0.410	0.328	0.454
	c-CdSe	0.408	0.042	0.408	0.313	0.454
	CdTe	0.407	−0.011	0.407	0.294	0.460
	β-HgS	0.433	−0.044	0.433	0.328	0.517
	HgSe	0.424	−0.054	0.424	0.308	0.499
	HgTe	0.409	−0.032	0.409	0.288	0.465

3.3.2 Bulk modulus, shear modulus and similar properties: cubic lattice

Bulk moduli of semiconductors are of physical interest and also of practical importance in the interpretation of high-pressure experimental data. In semiconductor heterostructures, different bulk moduli in the different layers give rise in hydrostatic pressure experiments to large axial strains that can have a considerable effect on the result of experiments.

Conversely, observation of such effects can provide an accurate method of measuring the relative bulk moduli of the layers [3.11].

We summarize in Table 3.16 the functional expressions for the bulk modulus B_u, shear modulus C_s, isotropy factor A, linear compressibility C_o, Cauchy ratio C_a and Born ratio B_o in cubic lattice. The numerical values for a number of cubic group-IV, III–V and II–VI semiconductors at $T = 300$ K are also listed in Table 3.17.

Figure 3.6 shows a log–log plot of the bulk modulus B_u versus near-neighbor distance d(A–B) for some group-IV, III–V and II–VI semiconductors with (a) cubic and (b) hexagonal and rhombohedral structures. The solid lines represent the least-squares fit

Table 3.16 Functional expressions for bulk modulus B_u, shear modulus C_s, isotropy factor A, linear compressibility C_o, Cauchy ratio C_a and Born ratio B_o in a cubic lattice

Parameter	Expression
Bulk modulus B_u	$(C_{11} + 2C_{12})/3$
Shear modulus C_s	$(C_{11} - C_{12})/2$
Isotropy factor A	$(C_{11} - C_{12})/(2C_{44})$
Linear compressibility C_o	$1/(C_{11} + 2C_{12})$
Cauchy ratio C_a	C_{12}/C_{44}
Born ratio B_o	$\dfrac{(C_{11} + C_{12})^2}{4C_{44}(C_{11} - C_{44})}$

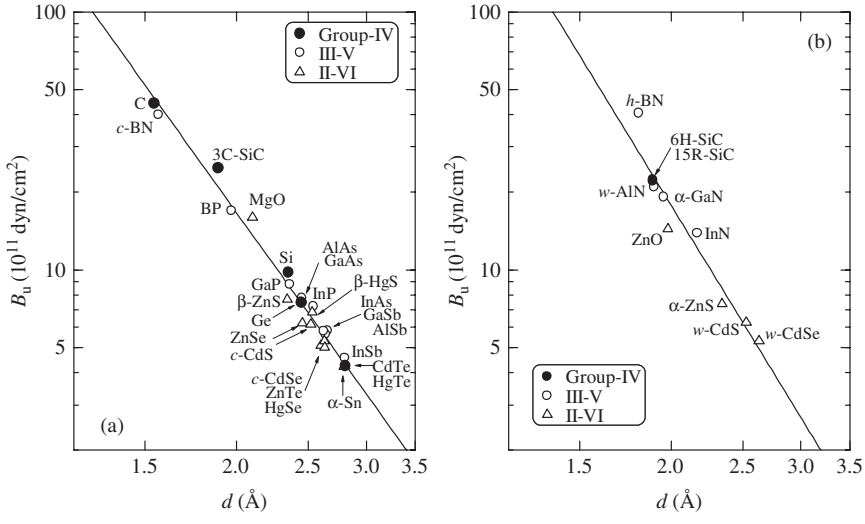

Figure 3.6 Bulk modulus B_u versus near-neighbor distance d(A–B) for some group-IV, III–V and II–VI semiconductors with (a) cubic; and (b) hexagonal and rhombohedral structures. The solid lines represent the least-squares fits with: (a) $B_u = (4.05/d)^{3.98}$; and (b) $B_u = (3.71/d)^{4.66}$ (d in Å; B_u in 10^{11} dyn/cm^2)

Table 3.17 Bulk modulus B_u (10^{11} dyn/cm^2), shear modulus C_s (10^{11} dyn/cm^2), isotropy factor A, linear compressibility C_o (10^{-13} cm^2/dyn), Cauchy ratio C_a and Born ratio B_o for a number of cubic group-IV, III–V and II–VI semiconductors at 300 K

System	Material	B_u	C_s	A	C_o	C_a	B_o
IV	Diamond	44.2	47.8	0.826	0.754	0.215	0.669
	Si	9.784	5.085	0.640	3.407	0.804	0.924
	Ge	7.47	4.05	0.607	4.46	0.715	0.975
	α-Sn	4.25	1.99	0.548	7.84	0.809	1.07
	3C-SiC	22.5	12.4	0.484	1.48	0.555	1.35
III–V	c-BN	40.0	31.5	0.656	0.833	0.396	0.915
	BP	17	11	0.67	1.9	0.63	0.88
	Bas	17.3	7.95	0.704	1.93	1.06	0.859
	c-AlN	20.5	8.25	0.446	1.63	0.811	1.32
	AlP	9.28	4.29	0.702	3.59	1.05	0.860
	AlAs	7.79	3.11	0.543	4.28	1.00	1.05
	AlSb	5.82	2.21	0.543	5.73	1.07	1.04
	β-GaN	19.6	7.15	0.453	1.70	0.937	1.25
	GaP	8.82	3.92	0.558	3.78	0.882	1.04
	GaAs	7.55	3.25	0.547	4.42	0.906	1.06
	GaSb	5.63	2.41	0.557	5.92	0.932	1.04
	InP	7.23	2.25	0.508	4.61	1.30	1.07
	InAs	5.79	1.90	0.480	5.75	1.14	1.14
	InSb	4.56	1.54	0.508	7.32	1.17	1.09
II–VI	MgO	16.0	10.1	0.648	2.08	0.600	0.916
	β-MgS	6.65	1.68	0.433	5.02	1.43	1.17
	β-MgSe	5.77	1.36	0.429	5.78	1.53	1.16
	β-MgTe	4.20	0.810	0.420	7.94	1.90	1.13
	β-ZnS	7.71	1.87	0.419	4.33	1.45	1.19
	ZnSe	6.24	1.75	0.432	5.34	1.25	1.20
	ZnTe	5.10	1.54	0.494	6.53	1.31	1.09
	c-CdS	6.16	1.16	0.489	5.41	2.28	1.04
	c-CdSe	5.31	1.02	0.457	6.28	2.08	1.08
	CdTe	4.24	0.830	0.411	7.86	1.83	1.15
	β-HgS	6.86	0.955	0.362	4.86	2.36	1.15
	HgSe	5.00	0.810	0.363	6.67	2.00	1.19
	HgTe	4.23	0.820	0.394	7.89	1.77	1.18

with the relation (d in Å; B_u in 10^{11} dyn/cm^2)

$$B_u = \left(\frac{a}{d}\right)^b \tag{3.13}$$

where (a) $a = 4.05$ and $b = 3.98$ and (b) $a = 3.71$ and $b = 4.66$. It should be noted that Gilman [3.12] related the slope of -4 to the relationship of electrostatic forces between atomic particles and bond-distance, which should reflect in the same way for the elastic moduli and bond-distance.

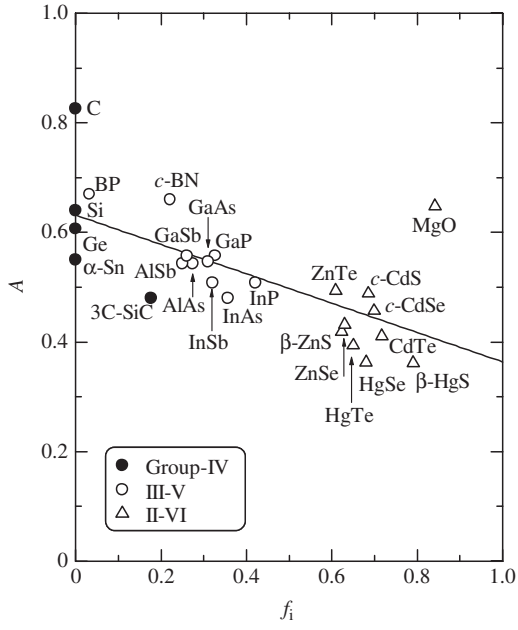

Figure 3.7 Isotropy factor A versus Philips ionicity f_i for some cubic group-IV, III–V and II–VI semiconductors. The solid line represents the least-squares fit with $A = 0.632 - 0.268 f_i$

The plots of the isotropy factor A versus Phillips ionicity f_i for some cubic group-IV, III–V and II–VI semiconductors are shown in Figure 3.7. The solid line represents the least-squares fit with

$$A = 0.632 - 0.268 f_i \tag{3.14}$$

The $A - f_i$ relationship is found to be linear, although only the data for diamond (C) and MgO deviate largely from the solid line. Note that $A = 1.0$ corresponds to a perfect isotropic material.

The bulk modulus B_u can be defined, from a phenomenological aspect, by

$$B_u = -V \frac{dp}{dV} \tag{3.15}$$

where V is the crystal volume. The lattice parameter a is dependent relatively largely on the pressure p. The lattice compression in a cubic crystal is related to p with the following Murnaghan equation of state

$$p = \frac{B_u}{B_u'} \left[\left(\frac{a(0)}{a(p)} \right)^{3B_u'} - 1 \right] \tag{3.16}$$

where B_u' is the pressure derivative of the bulk modulus, given by

$$B_u' = \frac{dB_u}{dp} = \frac{1}{3} \left(\frac{dC_{11}}{dp} \right) + \frac{2}{3} \left(\frac{dC_{12}}{dp} \right) \tag{3.17}$$

and $a(0)$ and $a(p)$ are the lattice parameters at pressures $p = 0$ and $p \neq 0$, respectively. The pressure derivative of the bulk modulus B'_{u} can also be expressed, in terms of the third-order elastic constants, as

$$B'_{\mathrm{u}} = \frac{\mathrm{d}B_{\mathrm{u}}}{\mathrm{d}p} = -\frac{C_{111} + 6C_{112} + 2C_{123}}{9B_{\mathrm{u}}} \tag{3.18}$$

We list in Table 3.18 the B'_{u} values for some cubic group-IV, III–V and II–VI semiconductors at $T = 300$ K. It is found that almost all semiconductors listed in Table 3.18 have a value of $B'_{\mathrm{u}} \sim 4$.

Figure 3.8 shows the pressure dependence of the lattice parameter a for Si, GaAs and ZnTe as calculated from Equation (3.16). The pressure-induced change in a for GaAs is about -3.5% at 10 GPa.

3.3.3 Young's modulus and Poisson's ratio: hexagonal lattice

We summarize in Table 3.19 the functional expressions for Young's modulus Y and Poisson's ratio P in the two major directions $\perp c$ and $\| c$ of a hexagonal lattice. The corresponding numerical data at $T = 300$ K are listed in Table 3.20.

Table 3.18 Pressure derivative of the bulk modulus $B'_{\mathrm{u}} = \mathrm{d}B_{\mathrm{u}}/\mathrm{d}p$ for some cubic group-IV, III–V and II–VI semiconductors at 300 K

System	Material	B'_{u}	System	Material	B'_{u}
IV	Diamond	4.03	II–VI	MgO	4.0
	Si	4.24		β-ZnS	4
	Ge	4.55		ZnSe	4
	α-Sn	4.6[a]		ZnTe	4.7
	3C-SiC	4.0		c-CdS	4.8[a]
				c-CdSe	4.8[a]
III–V	c-BN	4.0		CdTe	6.4
	BP	3.51[a]		β-HgS	5.0[a]
	BAs	3.49[a]		HgSe	2.53
	c-AlN	3.3[a]		HgTe	3.8
	AlP	3.99[a]			
	AlSb	4.55			
	β-GaN	3.9[a]			
	GaP	4.5			
	GaAs	4.49			
	GaSb	4.78			
	InP	4.59			
	InAs	4.79			
	InSb	4.899			

[a] Calculated or estimated

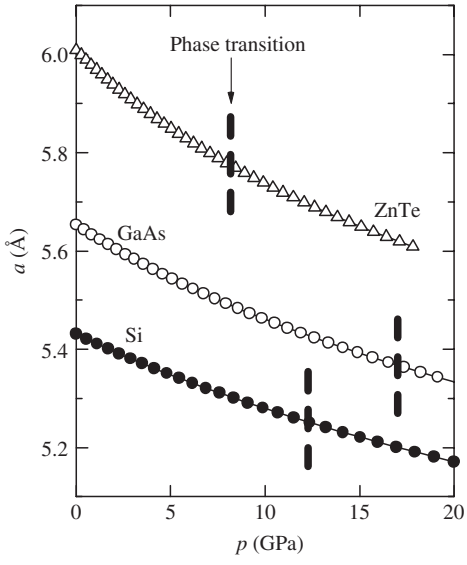

Figure 3.8 Pressure dependence of the lattice parameter a for Si, GaAs and ZnTe as calculated from the Murnaghan equation of state

Table 3.19 Functional expressions for Young's modulus Y and Poisson's ratio P in a hexagonal lattice. $\boldsymbol{l}$: directional vector; B_u: bulk modulus

Parameter	Direction	Expression
Y	$c \perp \boldsymbol{l}$	$1/S_{11}$
	$c \parallel \boldsymbol{l}$	$1/S_{33}$
P	$c \perp \boldsymbol{l}, c \parallel \boldsymbol{l}$	$\frac{1}{2}\left(1 - \frac{Y}{3B_u}\right)$

3.3.4 Bulk modulus, shear modulus and similar properties: hexagonal lattice

We summarize in Table 3.21 the functional expressions for the bulk modulus B_u and linear compressibility C_o in a hexagonal lattice. The corresponding B_u and C_o values at $T = 300$ K are listed in Table 3.22, together with those for dB_u/dp.

It is possible to define the isothermal bulk modulus by

$$B_u = -V\left(\frac{\partial p}{\partial V}\right) = \frac{2}{9}\left(C_{11} + C_{12} + 2C_{13} + \frac{C_{33}}{2}\right) \tag{3.19}$$

where V is the crystal volume.

Table 3.20 Young's modulus Y and Poisson's ratio P for a number of hexagonal group-IV, III–V and II–VI semiconductors at 300 K. $\boldsymbol{l}$: directional vector

System	Material	Y (10^{12} dyn/cm^2)		P	
		$c \perp \boldsymbol{l}$	$c \parallel \boldsymbol{l}$	$c \perp \boldsymbol{l}$	$c \parallel \boldsymbol{l}$
IV	6H-SiC	4.73	5.44	0.143	0.090
III–V	h-BN	1.38	1.36	0.44	0.44
	w-AlN	3.50	3.54	0.22	0.21
	α-GaN	3.13	3.62	0.23	0.19
	InN	1.04	0.83	0.38	0.40
II–VI	ZnO	1.28	1.51	0.35	−1.25
	α-ZnS	0.91	1.16	0.30	0.24
	w-CdS	0.481	0.625	0.37	0.33
	w-CdSe	0.431	0.592	0.37	0.31

Table 3.21 Functional expressions for bulk modulus B_u and linear compressibility C_o in a hexagonal lattice. $\boldsymbol{l}$: directional vector

Parameter	Expression
B_u	$\dfrac{(C_{11}+C_{12})C_{33}-2C_{13}^2}{C_{11}+C_{12}+2C_{33}-4C_{13}}$
C_o	$S_{11}+S_{12}+S_{13}(c \perp \boldsymbol{l})$ $2S_{13}+S_{33}(c \parallel \boldsymbol{l})$

The linear compressibility C_o of a crystal is the relative decrease in length of a line when the crystal is subjected to unit hydrostatic pressure. In general, it varies with direction. The expression for C_o for the hexagonal and rhombohedral systems can be written in matrix notation as

$$C_o = (S_{11}+S_{12}+S_{13}) - (S_{11}+S_{12}-S_{13}-S_{33})\boldsymbol{l}^2 \tag{3.20}$$

where $\boldsymbol{l}$ is the unit directional vector ($\boldsymbol{l}^2 = 0$ for $\perp c$; for $\boldsymbol{l}^2 = 1$ for $\parallel c$). Thus, the linear compressibility in the uniaxial materials is rotationally symmetrical about the unique axis c. Note that the linear compressibility in the cubic system is isotropic: a sphere of a cubic crystal under hydrostatic pressure thus remains a sphere.

3.4 MICROHARDNESS

The hardness test has been used for a long time as a simple means of characterizing the mechanical behavior of solids [3.13]. The interest in the hardness of semiconductors

Table 3.22 Bulk modulus B_u, its pressure derivative $B_u' = dB_u/dp$ and linear compressibility C_o for a number of hexagonal group-IV, III–V and II–VI semiconductors at 300 K. $\boldsymbol{l}$: directional vector

System	Material	B_u (10^{11} dyn/cm^2)	B_u'	C_o (10^{-13} cm^2/dyn)	
				$c \perp \boldsymbol{l}$	$c \parallel \boldsymbol{l}$
IV	6H-SiC	22.1	2.9	1.50	1.53
III–V	h-BN	40.6	5.6	0.42	1.63
	w-AlN	21.0	5.7–6.3	1.49	1.80
	α-GaN	19.2	3.2–4.5	1.65	1.90
	InN	13.9	12.7	2.52	2.12
II–VI	ZnO	14.4	3.6–9.4	2.27	2.44
	α-ZnS	7.40	4	4.50	4.60
	w-CdS	6.27		5.40	5.20
	w-CdSe	5.31		6.50	5.90

stems principally from their use in many device applications. There are many indications that dislocations induced during the fabrication of these devices subsequently have a very damaging effect on their operational performance and degradation behavior [3.14].

The microhardness can be measured by several methods, among which Knoop and Vickers indentations are most commonly used. In both methods, a diamond stylus is pressed into the surface of the body by a given load and at a given loading rate. Upon unloading, the size of the residual indentation mark in the surface is measured and related to a characteristic hardness parameter denoted by H. In the Knoop method, the diamond stylus has the shape of a rhombic pyramid with the major base diagonal 7.1 times longer than the minor diagonal, whereas the Vickers stylus has a low-profile, square pyramid [3.15].

We list in Table 3.23 Knoop microhardness H and bulk modulus B_u for a number of cubic group-IV, III–V and II–VI semiconductors. The numerical H and B_u values for a number of hexagonal semiconductors are listed in Table 3.24. Note that diamond is the least compressible and hardest material known.

If the materials are isoelectronic, isostructural and have the same packing density (or bond distance), we can expect certain correlations to exist between their cell volumes, melting points, bulk moduli, microhardness, etc. We have already shown the existence of such correlations about the structural phase transition (P_T, Section 1.5), melting point (T_m, Section 2.1), Debye temperature (θ_D, Section 2.3), elastic constant (C_{ij}, Section 3.1) and bulk modulus (B_u, Section 3.3) for $A^N B^{8-N}$ semiconductors.

Let us plot in Figure 3.9 Knoop microhardness H versus inverse unit-cell volume $V^{-1} = a^{-3}$ for some group-IV, III–V and II–VI semiconductors. The solid line represents the least-squares fit with the relation (V in Å^3; H in GPa)

$$H = \frac{3220}{V} - 14.6 \tag{3.21}$$

Table 3.23 Knoop microhardness H and bulk modulus B_u for a number of cubic group-IV, III–V and II–VI semiconductors

System	Material	H (GPa)	B_u (GPa)
IV	Diamond	56–115	442
	Si	2–16	97.84
	Ge	9.92	74.70
	α-Sn	2.6[a]	42.5
	3C-SiC	26.70–28.15	248
III–V	c-BN	34.3–73.0	400
	BP	3.2	170
	BAs	19.0	173[a]
	c-AlN		205[a]
	AlP	5.5	92.8[a]
	AlAs	5.0	77.9
	AlSb	4.0	58.2
	β-GaN		196[a]
	GaP	9.45	88.19
	GaAs	7–7.5	75.5
	GaSb	4.48–4.68	56.31
	InP	3.93	72.3
	InAs	3.74–3.8	57.94
	InSb	2.25–2.93	45.57
II–VI	MgO	4.0–9.3	160
	β-MgS		66.5[a]
	β-MgSe		57.7[a]
	β-MgTe		42.0[a]
	β-ZnS	1.78	77.1
	ZnSe	1.37–1.83	62.4
	ZnTe	0.6–0.9	51.0
	c-CdS		61.6
	c-CdSe		53.1
	CdTe	0.45–0.60	42.4
	β-HgS		68.6
	HgSe	0.23	50.0
	HgTe	0.23–0.37	42.3

[a] Calculated or estimated

We can recognize in Figure 3.9 the linear relationship between H and V^{-1}. A linear relationship between H and V (not V^{-1}) has also been found for ABC_2 ternary pnictides [3.16].

It has been shown by Plendl *et al.* [3.17] that the microhardness H is directly proportional to bulk modulus B_u. It has also been shown by Kumar *et al.* [3.18] that H and B_u have the relation

$$H = aB_u + b \tag{3.22}$$

Table 3.24 Knoop microhardness H and bulk modulus B_u for a number of hexagonal group-IV, III–V and II–VI semiconductors

System	Material	H (GPa)	B_u (GPa)
IV	6H-SiC	21.30–27.55	221
III–V	h-BN	14.6	406
	w-AlN	12	210
	α-GaN	10.2	192
	InN	10	139
II–VI	ZnO	4.0	144
	α-ZnS	1.78	74.0
	w-CdS	1.21–2.3	62.7
	w-CdSe	0.90	53.1

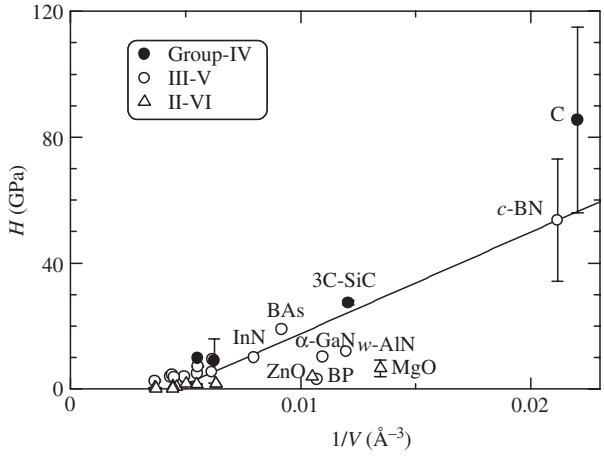

Figure 3.9 Knoop microhardness H versus inverse unit-cell volume $1/V = a^{-3}$ for some group-IV, III–V and II–VI semiconductors. For hexagonal semiconductors, an effective lattice constant $a_{\text{eff}} = (\sqrt{3}a^2c)^{1/3}$ is used in the calculation of $1/V$. The solid line represents the least-squares fit with $H = 3220/V - 14.6$ (V in Å^3; H in GPa)

where a and b are constants. The a and b values are determined to be 0.16 and -5.74 GPa for III–V semiconductors and 0.034 and -0.78 GPa for II–VI semiconductors, respectively (B_u in GPa). The solid and dashed lines in Figure 3.10(a) represent the calculated results of Equation (3.22) with these a and b values. A semilogarithmic plot of Knoop hardness H versus B_u for some cubic semiconductors is also shown in Figure 3.10(b). The solid line represents the least-squares fit with the relation (B_u and H in GPa)

$$H = aB_u^b \tag{3.23}$$

where a and b are constants given by 0.0013 and 1.80, respectively.

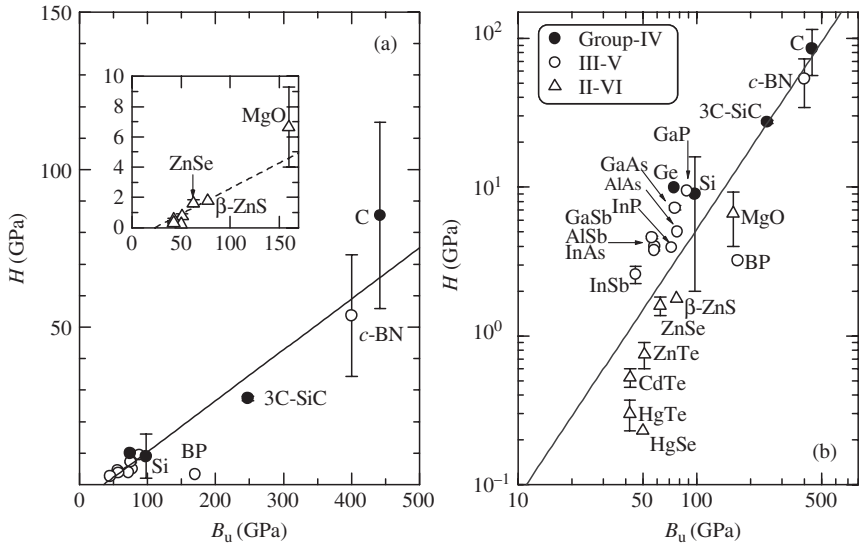

Figure 3.10 Knoop microhardness H versus bulk modulus B_u plotted: (a) linearly; and (b) logarithmically for some cubic group-IV, III–V and II–VI semiconductors. In (a) the solid and dashed lines are calculated from the relations of $H = 0.16B_u - 5.74$ and $H = 0.034B_u - 0.78$ (B_u and H in GPa), respectively. In (b) the solid line represents the least-squares fit with $H = 0.0013B_u^{1.80}$ (B_u and H in GPa)

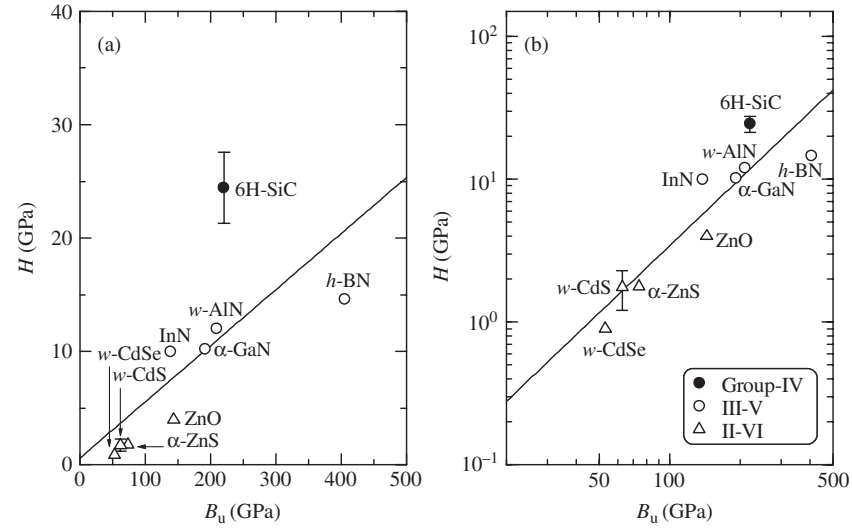

Figure 3.11 Knoop microhardness H versus bulk modulus B_u plotted: (a) linearly; and (b) logarithmically for some hexagonal group-IV, III–V and II–VI semiconductors. The solid lines represent the least-squares fits with: (a) $H = 0.049B_u + 0.59$; and (b) $H = 0.0026B_u^{1.56}$, respectively (B_u and H in GPa)

Figure 3.11 presents Knoop microhardness H versus B_u data plotted (a) linearly and (b) logarithmically for some hexagonal semiconductors. The solid lines in Figures 3.11(a) and 3.11(b) show the calculated results of Equation (3.22) with $a = 0.049$ and $b = 0.59$ GPa and of Equation (3.23) with $a = 0.0026$ and $b = 1.56$ (B_u and H in GPa), respectively. There is a general trend toward greater hardness H with increasing B_u for both cubic (Figure 3.10) and hexagonal semiconductors (Figure 3.11).

We plot in Figure 3.12 Knoop microhardness as a function of Voigt averaged shear modulus G for some cubic semiconductors. Here, G is defined by

$$G = \frac{3C_{44} + C_{11} - C_{12}}{5} \tag{3.24}$$

The solid line in Figure 3.12 represents the least-squares fit with the relation (G and H in GPa)

$$H = 0.139G \tag{3.25}$$

In general, the shear modulus G is slightly smaller than the value of C_{44} for cubic semiconductors. It has been reported [3.19] that G is a better indicator of hardness than B_u. We note, however, that H values of BP and MgO are much lower than what might be expected from the general trend in Figure 3.12.

The $B_u - d$ (bond-distance), P_T (transition pressure to the first phase; see Section 1.5)$-d$ and $H - B_u$ plots show that there is a simple relation between these quantities. We can

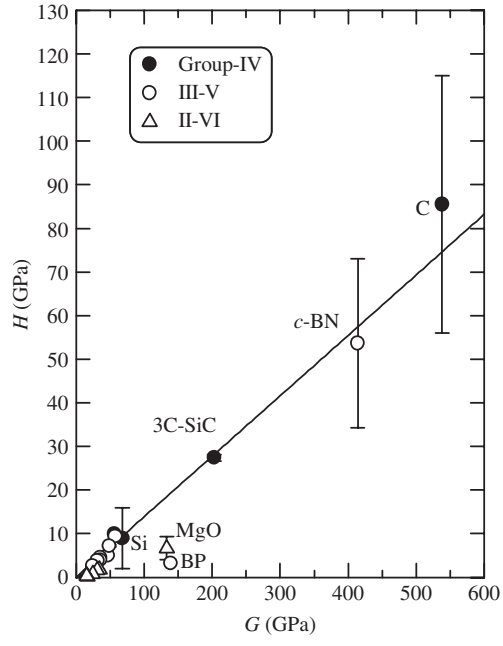

Figure 3.12 Knoop microhardness H versus Voigt averaged shear modulus G for some cubic group-IV, III–V and II–VI semiconductors. The Voigt parameter G can be defined by $G = (3C_{44} + C_{11} - C_{12})/5$. The solid line represents the least-squares fit with $H = 0.139G$ (G and H in GPa)

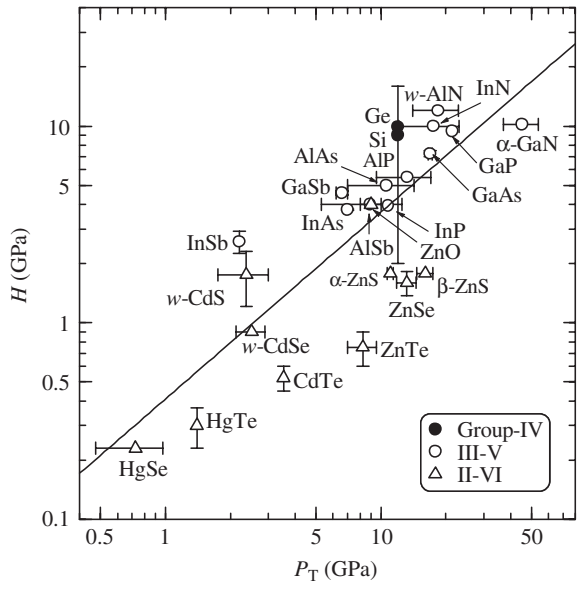

Figure 3.13 Knoop microhardness H versus transition pressure to the first phase P_T for some cubic and hexagonal group-IV, III–V and II–VI semiconductors. The solid line represents the least-squares fit with $H = 0.41 P_T^{0.95}$ (P_T and H in GPa)

thus, expect a simple relation between H and P_T. It is found that the variation of H with P_T follows a relation of the form

$$H = a P_T^b \tag{3.26}$$

This is shown in Figure 3.13 in the form of a log–log plot of H against P_T. The values of a and b obtained by a least-squares fit to the data are 0.41 and 0.95 (P_T and H in GPa), respectively.

The Knoop hardness anisotropy is a well-known phenomenon [3.20] and has been measured for many semiconductors [3.21]. The Knoop hardness number not only varies both with the plane and direction of indentation, but also depends on the type of dopant. For InP, S-doped crystals are the hardest among S-doped, Se-doped and Zn-doped crystals [3.21, 3.22]. These crystals are all harder than undoped InP. On the other hand, the addition of Sn apparently softens the InP lattice.

3.5 SOUND VELOCITY

If the crystal density g and elastic stiffness C_{ij} of a solid is known, one can calculate sound velocity v from the simple relation

$$v = \sqrt{\frac{C_{ij}}{g}} \tag{3.27}$$

If we neglect nonlinear terms in the equation of motion of cubic lattice, pure longitudinal sound waves may propagate in the [100], [110] and [111] directions. Pure transverse waves may propagate not only in these three major directions, but also in the crystallographic directions $[hkl]$ ($h = k; l$ arbitrary) and $[hk0]$ (h and k arbitrary).

We list in Table 3.25 the functional forms for the sound velocity propagating along the three major directions [100], [110] and [111] in cubic lattice. Table 3.26 also lists the numerical values for the longitudinal (LA) and transverse (TA1 and TA2) sound velocities propagating along the [100], [110] and [111] directions in a number of cubic semiconductors at $T = 300$ K. The corresponding expressions and numerical values for the case of hexagonal semiconductors are listed in Tables 3.27 and 3.28, respectively.

If we take into consideration the nonlinear term in cubic lattice, we find that pure transverse modes do not exist. The transverse waves are always accompanied by a longitudinal wave. Pure longitudinal modes, on the other hand, continue to exist for all three principal directions [100], [110] and [111]. For these directions, the nonlinear wave equation can be reduced to the form [3.23]

$$\frac{\partial^2 u}{\partial t^2} = \frac{1}{g}\frac{\partial^2 u}{\partial t^2}\left(M_2 + M_3\frac{\partial u}{\partial x} + \text{higher-order terms}\right) \tag{3.28}$$

where u is the atomic displacement velocity. The constants M_2 and M_3 can be written in terms of the second-order and third-order elastic coefficients K_2 and K_3

$$M_2 = K_2, \quad M_3 = K_3 + 2K_2 \tag{3.29}$$

Table 3.25 Propagation direction, direction or plane of polarization, velocity and mode of sounds in a cubic lattice. g = crystal density; LA = longitudinal acoustic; TA1, TA2 = transverse acoustic

Propagation direction	Direction or plane of polarization	Velocity	Mode
[100]	[100]	$\sqrt{\frac{C_{11}}{g}}$	LA
	(100)	$\sqrt{\frac{C_{44}}{g}}$	TA1, TA2
[110]	[110]	$\sqrt{\frac{C_{11}+C_{12}+2C_{44}}{2g}}$	LA
	(110)	$\sqrt{\frac{C_{11}-C_{12}}{2g}}$	TA1
	(001)	$\sqrt{\frac{C_{44}}{g}}$	TA2
[111]	[111]	$\sqrt{\frac{C_{11}+2C_{12}+4C_{44}}{3g}}$	LA
	(111)	$\sqrt{\frac{C_{11}-C_{12}+C_{44}}{3g}}$	TA1, TA2

Table 3.26 Sound velocity propagating along the three major directions [100], [110] and [111] in a number of cubic group-IV, III–V and II–VI semiconductors at 300 K (in 10^5 cm/s)

System	Material	[100]		[110]			[111]	
		LA	TA1, TA2	LA	TA1	TA2	LA	TA1, TA2
IV	Diamond	17.5	12.8	18.3	11.7	12.8	18.6	12.1
	Si	8.43	5.84	9.13	4.67	5.84	9.36	5.09
	Ge	4.92	3.54	5.39	2.76	3.54	5.54	3.04
	α-Sn	3.46	2.51	3.85	1.86	2.51	3.97	2.09
	3C-SiC	11.0	8.92	12.7	6.21	8.92	13.3	7.23
III–V	c-BN	15.3	11.7	16.8	9.50	11.7	17.3	10.3
	BP	10	7.3	11	6.0	7.3	11	6.5
	BAs	7.31	4.65	7.73	3.90	4.65	7.87	4.17
	c-AlN	9.86	7.56	11.4	5.05	7.56	11.8	6.00
	AlP	7.97	5.09	8.44	4.26	5.09	8.59	4.56
	AlAs	5.66	3.92	6.24	2.89	3.92	6.43	3.27
	AlSb	4.53	3.09	4.99	2.28	3.09	5.13	2.57
	β-GaN	6.95	5.12	7.92	3.45	5.12	8.22	4.08
	GaP	5.83	4.13	6.45	3.08	4.13	6.64	3.47
	GaAs	4.73	3.34	5.24	2.47	3.34	5.39	2.79
	GaSb	3.97	2.77	4.38	2.07	2.77	4.50	2.33
	InP	4.62	3.04	5.09	2.17	3.04	5.23	2.49
	InAs	3.83	2.64	4.28	1.83	2.64	4.42	2.14
	InSb	3.38	2.29	3.74	1.63	2.29	3.86	1.88
II–VI	β-MgS	6.49	4.28	7.24	2.82	4.28	7.48	3.38
	β-MgSe	4.78	3.09	5.32	2.02	3.09	5.49	2.43
	β-MgTe	3.72	2.25	4.10	1.46	2.25	4.22	1.76
	β-ZnS	5.00	3.30	5.59	2.14	3.30	5.78	2.59
	ZnSe	4.04	2.77	4.55	1.82	2.77	4.70	2.19
	ZnTe	3.48	2.29	3.84	1.61	2.29	3.96	1.87
	c-CdS	3.98	2.20	4.28	1.54	2.20	4.38	1.79
	c-CdSe	3.43	1.98	3.73	1.34	1.98	3.82	1.59
	CdTe	3.02	1.86	3.34	1.19	1.86	3.44	1.45
	β-HgS	3.25	1.85	3.57	1.11	1.85	3.67	1.40
	HgSe	2.72	1.64	3.02	0.99	1.64	3.11	1.25
	HgTe	2.57	1.60	2.85	1.01	1.60	2.94	1.24

The coefficients K_2 and K_3 are in turn related to the more familiar C_{ij} and C_{ijk}, and are given by

$$K_2 = C_{11}, \quad K_3 = C_{111} \tag{3.30}$$

for the [100] direction,

$$K_2 = \frac{C_{11} + C_{12} + 2C_{44}}{2} \tag{3.31a}$$

$$K_3 = \frac{C_{111} + 3C_{112} + 12C_{166}}{4} \tag{3.31b}$$

Table 3.27 Functional expression for sound velocity propagating parallel ($\boldsymbol{a} \| c$) and perpendicular to the c axis ($\boldsymbol{a} \perp c$) in a hexagonal lattice

$\boldsymbol{a} \| c$		$\boldsymbol{a} \perp c$		
LA	TA1, TA2	LA	TA1	TA2
$\sqrt{\frac{C_{33}}{g}}$	$\sqrt{\frac{C_{44}}{g}}$	$\sqrt{\frac{C_{11}}{g}}$	$\sqrt{\frac{C_{11}-C_{12}}{g}}$	$\sqrt{\frac{C_{44}}{g}}$

Table 3.28 Sound velocity propagating parallel ($\boldsymbol{a} \| c$) and perpendicular to the c axis ($\boldsymbol{a} \perp c$) in a number of hexagonal group-IV, III–V and II–VI semiconductors at 300 K (10^5 cm/s)

System	Material	$\boldsymbol{a} \| c$		$\boldsymbol{a} \perp c$		
		LA	TA1, TA2	LA	TA1	TA2
IV	6H-SiC	13.1	7.12	12.5	7.79	7.12
III–V	h-BN	13.6	5.34	15.1	4.42	5.34
	w-AlN	10.9	6.07	11.2	7.80	6.07
	α-GaN	7.97	3.93	7.83	4.37	3.93
	InN	5.17	1.21	5.28	2.51	1.21
II–VI	ZnO	6.20	2.79	6.07	2.80	2.79
	α-ZnS	5.81	2.65	5.47	2.80	2.65
	w-CdS	4.43	1.76	4.24	1.84	1.76
	w-CdSe	3.86	1.54	3.62	1.60	1.54

for the [110] direction and

$$K_2 = \frac{C_{11} + 2C_{12} + 4C_{44}}{3} \tag{3.32a}$$

$$K_3 = \frac{C_{111} + 6C_{112} + 12C_{144} + 24C_{166} + 2C_{123} + 16C_{456}}{9} \tag{3.32b}$$

for the [111] direction.

The nonlinearity parameter β is defined by

$$\beta = -\frac{3K_2 + K_3}{K_2} \tag{3.33}$$

The amplitude of the generated acoustic second harmonic is proportional to this parameter [3.23].

REFERENCES

[3.1] J. F. Nye, *Physical Properties of Crystals* (Clarendon, Oxford, 1972).
[3.2] M. Kitamura, S. Muramatsu, and W. A. Harrison, *Phys. Rev. B* **46**, 1351 (1992).
[3.3] R. W. Keyes, *J. Appl. Phys.* **33**, 3371 (1962).
[3.4] J. D. Wiley, in *Semiconductors and Semimetals*, edited by R. K. Willardson and A. C. Beer (Academic, New York, 1975), Vol. 10, p. 91.
[3.5] S. Adachi, *J. Appl. Phys.* **58**, R1 (1985).
[3.6] J. T. Lin and C. Wong, *J. Phys. Chem. Solids* **33**, 241 (1972).
[3.7] Y. P. Varshni, *Physica* **34**, 149 (1967).
[3.8] S. V. Sinogeikin and J. D. Bass, *Phys. Rev. B* **59**, R14141 (1999).
[3.9] *Numerical Data and Functional Relationships in Science and Technology*, edited by K.-H. Hellwege and A. M. Hellwege, Landolt–Börnstein, New Series, Group III, Vol. 11 (Springer, Berlin, 1979).
[3.10] W. A. Brantley, *J. Appl. Phys.* **44**, 534 (1973).
[3.11] A. D. Prins and D. J. Dunstan, *Semicond. Sci. Technol.* **4**, 239 (1989).
[3.12] See, C. F. Cline, H. L. Dunegan, and G. W. Henderson, *J. Appl. Phys.* **38**, 1944 (1967).
[3.13] N. A. Goryunova, A. S. Borschevskii, and D. N. Tretiakov, in *Semiconductors and Semimetals*, Vol. 4, edited by R. K. Willardson and A. C. Beer (Academic, New York, 1968), p. 3.
[3.14] See, for example, S. N. G. Chu and S. Nakahara, *Appl. Phys. Lett.* **56**, 434 (1990).
[3.15] K. Hjort, F. Ericson, J.-Å. Schweitz, C. Hallin, and E. Janzén, *Thin Solid Films* **250**, 157 (1994).
[3.16] R. Asokamani and R. Rita, *Phys. Status Solidi B* **226**, 375 (2001).
[3.17] J. N. Plendl, S. S. Mitra, and P. J. Gielisse, *Phys. Status Solidi* **12**, 367 (1965).
[3.18] V. Kumar, G. M. Prasad, A. R. Chetal, and D. Chandra, *J. Phys. Chem. Solids* **57**, 503 (1996).
[3.19] J. M. Léger, P. Djemia, F. Ganot, J. Haines, A. S. Pereira, and J. A. H. da Jornada, *Appl. Phys. Lett.* **79**, 2169 (2001).
[3.20] C. A. Brookes, J. B. O'Neill, and B. A. W. Redfern, *Proc. Roy. Soc. London A* **322**, 73 (1971).
[3.21] D. Y. Watts and A. F. W. Willoughby, *J. Appl. Phys.* **56**, 1869 (1984).
[3.22] S. Mahajan and A. K. Chin, *J. Cryst. Growth* **54**, 138 (1981).
[3.23] D. N. Joharapurkar and M. A. Breazeale, *J. Appl. Phys.* **67**, 76 (1990).

4 Lattice Dynamic Properties

4.1 Phonon dispersion relation 73
4.1.1 Brillouin zone 73
4.1.2 Phonon dispersion curve 75
4.1.3 Phonon density of states 79
4.2 Phonon frequency 80
4.2.1 Room-temperature value 80
4.2.2 External perturbation effect 84
4.3 Mode Grüneisen parameter 87
4.4 Phonon deformation potential 88
4.4.1 Cubic lattice 88
4.4.2 Hexagonal lattice 91
References 92

4.1 PHONON DISPERSION RELATION

4.1.1 Brillouin zone

An electron in a crystal, under the influence of an external force, such as that due to the electric field, acquires energy during its acceleration, but changes its energy and/or momentum by various scattering mechanisms that come about because of lattice vibrations or other carriers in its surrounding, as well as defects of the crystal lattice. The lattice vibrations in crystals can be described in a framework that is analogous to the description of electrons. The lattice vibronic and electronic states are best described in reciprocal space or $\boldsymbol{k}$ space. The smallest unit cell in reciprocal space is called the first Brillouin zone.

Both the energy (E)–momentum ($\boldsymbol{k}$) dispersion relations and the wavefunctions of the electrons (and phonons) in the crystal are largely determined from the symmetry of the periodic crystal potential in which the electrons move, and thus by the symmetry of the crystal. The classification of electron states in a real crystal must, therefore, commence with a symmetry analysis of the crystal.

Let us consider the values of $k = |\boldsymbol{k}|$ at which the discontinuities in energy E occur. They occur whenever cos ka reaches its maximum value, that is, when cos $ka = \pm 1$ or $k = n\pi/a$ where a is the lattice period and $n = 1, 2, 3 \ldots$. At these values of k a small increase in electron momentum, that is, in k, will make the energy of the electron jump discontinuously from the top of one allowed band to the bottom of the next. The region between the values of k where the first energy discontinuity takes place is called the first Brillouin zone. The region between the first and second values of k for which discontinuities occur is called the second Brillouin zone, and so on.

Properties of Group-IV, III–V and II–VI Semiconductors Sadao Adachi

© 2005 John Wiley & Sons, Ltd

ISBN: 0-470-09032-4

The symmetry of a crystal can be expressed by its space group, consisting of all transformations which leave the crystal invariant. The unit cell of the reciprocal lattice is the Brillouin zone. The reciprocal lattice is invariant under the same point group as the corresponding real lattice. The groups of a wavevector $\boldsymbol{k}$ in the reciprocal lattice then consist of all transformations which leave $\boldsymbol{k}$ invariant or transform it into an equivalent wavevector $\boldsymbol{k} + \boldsymbol{K}_j$. The Hamiltonian for an electron in the periodic crystal potential is also invariant for all transformations of the point group. In this way the symmetry is transferred on to the Hamiltonian so that the irreducible representations of the point group characterize the eigenvalues of the operator and give the degeneracy and symmetry of the associated wavefunctions [4.1]. The character tables of all 32 point groups have been given by Koster *et al*. [4.2].

(a) Face-centered cubic lattice

Figure 4.1 shows the first two Brillouin zones for the face-centered cubic lattice. As shown in Figure 4.1(a), the first Brillouin zone for cubic semiconductors is a truncated octahedron. It has fourteen plane faces; six square faces along the ⟨100⟩ directions and eight hexagonal faces along the ⟨111⟩ directions. The coordinate axes of the Brillouin zone are the wavevectors of the plane waves corresponding to the Bloch states (electrons) or vibration modes (phonons). The points and directions of symmetry are usually referred to by letters, as shown in Figure 4.1(a) [4.3]. The zone center is called the Γ point, the directions ⟨100⟩, ⟨110⟩ and ⟨111⟩ are called, respectively, Δ, Σ and Λ directions and their intersections with the zone boundaries are called, respectively, X, K and L points. Since the real lattice in the diamond-type, zinc-blende-type and rocksalt-type crystals is the face-centered cubic lattice, the Brillouin zone for materials with any of these crystal structures is the same as that shown in Figure 4.1.

(b) Hexagonal lattice

The real lattice for the wurtzite structure is hexagonal. The spaces of the first two Brillouin zones are shown in Figure 4.2. As seen in Figure 4.2, the first Brillouin zone for the

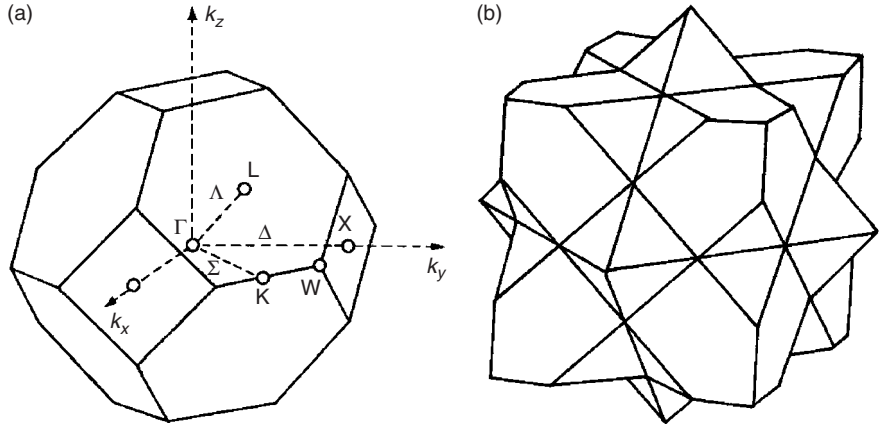

Figure 4.1 The first two Brillouin zones for the face-centered cubic lattice

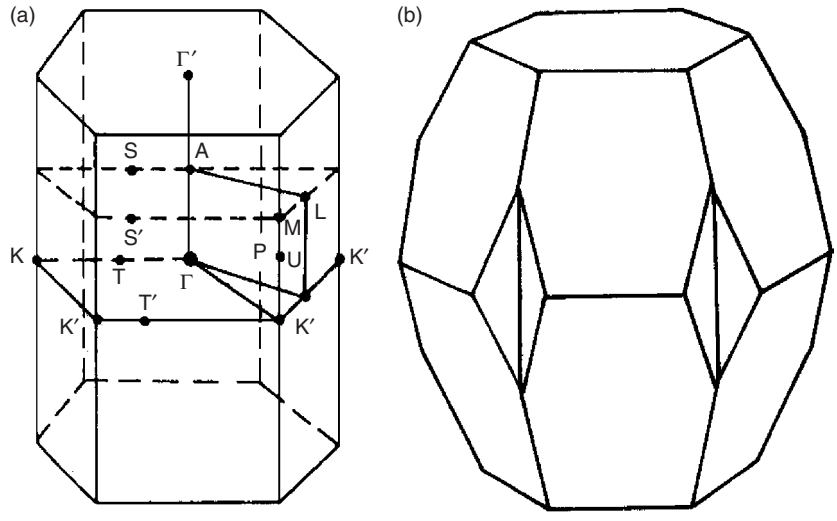

Figure 4.2 The first two Brillouin zones for the wurtzite lattice

wurtzite lattice is a hexagonal prism. The wurtzite unit cell contains twice the number of the atoms of the zinc-blende cell, and hence the Brillouin zone has about half the volume of that of the zinc-blende cell. To make the picture consistent with that for the face-centered cubic lattice, it is usual to take a double Brillouin zone, obtained by putting two wurtzite zones together in the ⟨001⟩ direction [4.1]. There is then a correspondence between the vector ΓL in zinc-blende and the vector ΓAΓ′ in wurtzite. In the reduced wurtzite zone Γ′ coincides with Γ and hence the L point in zinc-blende is equivalent to Γ in wurtzite, i.e., the distance AΓ′ is folded into AΓ. The number of Γ states is thus double that of zinc-blende. Half of the Γ states correspond directly to Γ states of zinc-blende; the other half of the states corresponds to L states of zinc-blende.

(c) Rhombohedral lattice

The structure of 15R-SiC is described in terms of a rhombohedral lattice with fifteen molecules in a unit cell; the space-group symbol being $R3m - C_{3v}^5$. Figure 4.3 shows the first Brillouin zone for the rhombohedral lattice. It should be noted that the Brillouin zone for 15R-SiC is highly compressed parallel to the three-fold axis.

4.1.2 Phonon dispersion curve

(a) Cubic lattice

As shown in Figure 4.1, the first Brillouin zone in cubic semiconductors is a truncated octahedron. Phonons, representing lattice vibrations occurring at a frequency ω_q, have an energy $\hbar\omega_q$, where $\hbar$ is the reduced Planck's constant, and have a momentum $\hbar\boldsymbol{q}$. In the primitive cell, if there are N different types of atoms either of differing mass or ordering

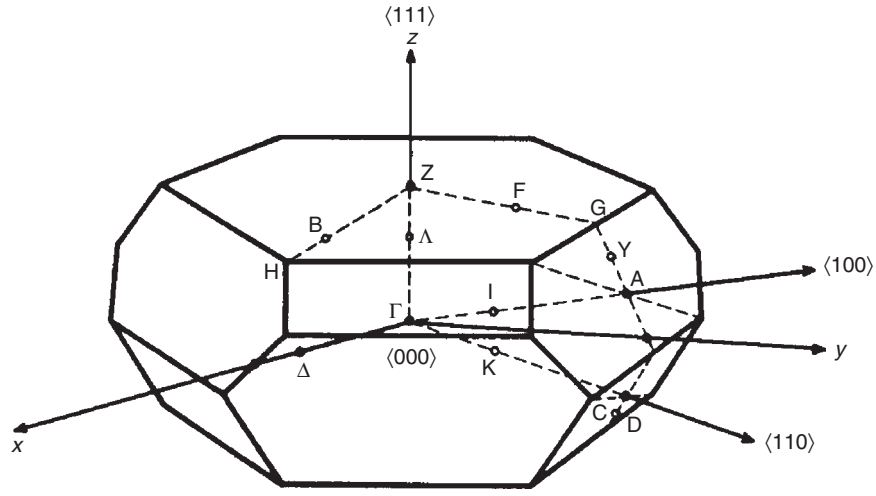

Figure 4.3 The first Brillouin zone for the rhombohedral lattice (15R-SiC)

in space, $3N$ vibration modes will result. In general, three of these branches, namely the acoustic branches, will disappear at the zone center Γ. The remaining $3N - 3$ branches will be optical branches. For cubic crystals, such as Si or GaAs, $N = 2$, and hence there are three acoustic and three optical branches, each three comprising one longitudinal and two transverse modes.

Research on the crystal dynamics of perfect lattices has aroused considerable interest in many semiconductors. This development is the outcome of many experimental results, particularly inelastic neutron scattering data for phonon dispersion curves. For example, Waugh and Dolling [4.4] have made neutron scattering measurements on pure GaAs at $T = 296$ K. We reproduce in Figure 4.4 the phonon frequency (ν)–reduced wavevector ($\boldsymbol{q}$) results for $\boldsymbol{q}$ along the principal symmetry directions [100] (Δ), [110] (Σ) and [111] (Λ) of GaAs [4.5]. The various curves in Figure 4.4, some with solid lines and others dotted, for $\nu(\boldsymbol{q})$ of the acoustic and optical phonon branches, represent the attempts by Waugh and Dolling [4.4] to fit their data with two different versions of a dipole-approximation force-constant model. The application of a four-parameter valence-force model has also been used by Kane [4.6] to describe this experimental result correctly. The dashed lines in Figure 4.4 in the region near $\boldsymbol{q} \to 0$, $\nu \to 0$ represent the initial slopes of the acoustic modes as calculated from the sound velocities v_i in Section 3.5 from the relation

$$\omega_{\mathrm{q},i}(q) = v_i|\boldsymbol{q}| \tag{4.1}$$

In contrast to the acoustic phonons, which have a large speed at small values of $\boldsymbol{q}$, the group velocity of optical phonons vanishes near the zone center so that they hardly move. The same happens at the zone boundary for the acoustic as well as for the optical phonons (see Figure 4.4).

Strauch and Dorner [4.7] have determined the phonon dispersion curves in GaAs at low temperature ($T = 12$ K) for wavevectors along the six directions Γ–(Δ)–X–(Σ)–(Λ)–L–X–(Z)–W–(Q)–L by high-precision inelastic neutron scattering. Their studied propagation directions are, thus, twice as many as had been studied by Waugh and Dolling [4.4].

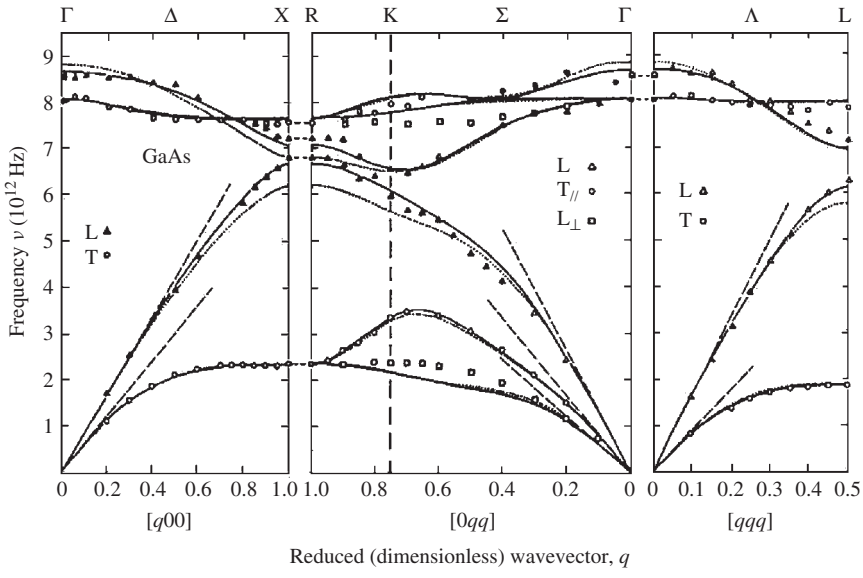

Figure 4.4 Dispersion curves for the acoustic and optical branch phonons in GaAs at 300 K. The dashed lines have slopes for the various speeds of sound wave, as described in Section 3.5. [From J. S. Blakemore, *J. Appl. Phys.* **53**, R123 (1982), reproduced by permission from the American Institute of Physics]

They also used various existing lattice dynamic models to reproduce the experimental data and discussed the relative merits and drawbacks of these models.

When comparing the phonon dispersion curve of GaAs with that of Si, it becomes apparent that, while the general shapes in the dispersion curves are similar between these materials, there is one important difference. At $\boldsymbol{q} = 0(\Gamma)$ the transverse and longitudinal optical branches are degenerate in Si, while $\omega(\text{LO}) > \omega(\text{TO})$ in GaAs (see Section 4.2). It is found that the splitting of the LO (longitudinal optical) and TO (transverse optical) branches for long wavelengths occurs in almost all crystals which are heteropolar or ionic. The origin of this splitting is the electrostatic field created by the long-wavelength modes of vibrations in such heteropolar crystals [4.8].

(b) Hexagonal lattice

We reproduce in Figure 4.5 the phonon frequency—reduced wavevector results for $\boldsymbol{q}$ along the principal symmetry directions (T, Σ, Δ) of ZnO, predicted by a shell model based on elastic constants and Raman spectrum by Hewat [4.9]. The dashed lines in the region near $\boldsymbol{q} \rightarrow 0$, $\nu \rightarrow 0(\Sigma)$ represent the initial slopes of the acoustic modes estimated from the elastic constants (sound velocities).

The zinc-blende crystal lattice is cubic with two atoms per unit cell, whereas the wurtzite lattice has a hexagonal structure with four atoms per unit cell. The Brillouin zone in the zinc-blende lattice along the [111] direction is, therefore, twice as large as that of the wurtzite lattice along the [0001] direction. Hence, we can derive the phonon dispersion curves for the wurtzite structure by simply folding the curves for the zinc-blende

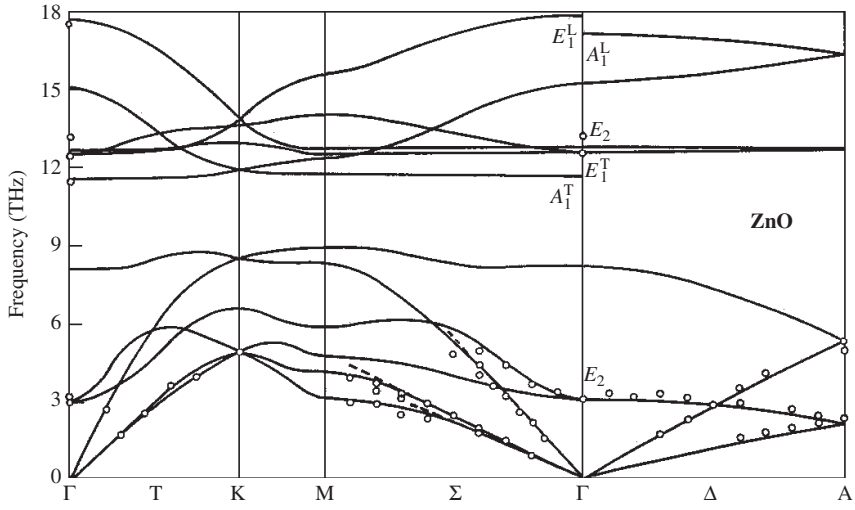

Figure 4.5 Phonon dispersion curves along the principal symmetry directions of ZnO, predicted by a shell model based on elastic constants and Raman spectrum. The dashed lines at region near $\boldsymbol{q} \to 0, \nu \to 0$ (Σ) represent the initial slopes of the acoustic modes estimated from the elastic constants. [From A. W. Hewat, *Solid State Commun.* **8**, 187 (1970), reproduced by permission from Elsevier]

structure [4.10], as can be understood from Figure 4.5. As a result, the two nonpolar modes E_2 in the wurtzite structure correspond to the TO(L) and TA(L) modes in the zinc-blende structure and the two nonpolar B_1 modes in the wurtzite structure correspond to the LO (L) and LA (L) modes in the zinc-blende structure. We summarize in Table 4.1 such corresponding relations in phonon modes between the zinc-blende (diamond) and wurtzite (hexagonal) structures.

As mentioned before, the wurtzite lattice has four atoms (two molecular units) in the primitive cell which gives rise to twelve phonon branches ($N = 4$). At the center of the Brillouin zone, the acoustic modes comprise the representations

$$1A_1 + 1E_1 \tag{4.2}$$

Table 4.1 Corresponding relation in phonon modes between the zinc-blende and wurtzite structures

Zinc-blende (diamond)	Wurtzite (hexagonal)
TO (Γ)	$\frac{1}{3}[A_1(\mathrm{TO}) + 2E_1(\mathrm{TO})]$
LO (Γ)	$\frac{1}{3}[A_1(\mathrm{LO}) + 2E_1(\mathrm{LO})]$
TA (L)	E_2 low
TO (L)	E_2 high

and the remaining nine optical modes the representations

$$1A_1 + 2B_1 + 1E_1 + 2E_2 \tag{4.3}$$

Except the silent B_1 modes all the other optical modes are Raman active, and the A_1 and E_1 modes are IR active for incident radiation with the polarizations $\boldsymbol{E} \parallel c$ and $\boldsymbol{E} \perp c$, respectively, c being the hexagonal axis of the crystal.

4.1.3 Phonon density of states

The properties of critical points and their consequences for the phonon dispersion curves in crystals were first discussed by Van Hove [4.11] by making use of topological considerations. The phonon density of states $g(\nu)$ increases greatly when $\nabla_{\mathrm{q}}(\nu) \to 0$ (critical points) for one of the various branches, and this happens predominantly when $\boldsymbol{q}$ for that branch reaches a zone boundary.

The phonon density of states can be calculated in the same way as that for electrons [4.12]. An expression for the phonon density of states $g(\omega)$ can be given by

$$g(\omega) = \sum_{i=1}^{3N} \frac{1}{\hbar} \frac{\mathrm{d}}{\mathrm{d}\omega} \int \frac{\mathrm{d}^3 q}{(2\pi)^3} \delta[\hbar\omega - \hbar\omega_{\mathrm{q},i}(q)] \tag{4.4}$$

where $\hbar\omega = h\nu$ and the number $3N$ in the summation corresponds to the total vibration modes ($3N = 6$ for Si and GaAs). The dispersion relations for acoustic phonons near $\boldsymbol{q} = 0$ can be given by Equation (4.1). The dispersion relations for optical phonons are written as

$$\omega_{\mathrm{q},i}(q) = \omega_{0,i} - \frac{\omega_i}{2} q^2 \tag{4.5}$$

where $\omega_{0,i} = \omega_i(q = 0)$. Inserting Equation (4.1) into Equation (4.4), we obtain near $\boldsymbol{q} = 0$

$$g_{\mathrm{ac}}(\omega) = \sum_{i=1}^{3} \frac{1}{2\pi^2 \hbar} \frac{\omega^2}{v_i^3} \tag{4.6}$$

For the optical branch, the result is given by

$$g_{\mathrm{op}}(\omega) = \sum_{i=1}^{3N-3} \frac{1}{4\pi^2} \left(\frac{2}{\hbar\omega_i} \right)^{3/2} \sqrt{\hbar\omega_{0,i} - \hbar\omega} \tag{4.7}$$

Thus, we can see that the energy dependence of the density of states of optical phonons is similar to that of electrons at the top of the Γ valence band ($\boldsymbol{k} = 0$).

Calculation of the phonon density of states $g(\nu)$ for GaAs has been made by Dolling and Cowley [4.13] on the basis of detailed lattice dynamic models. Their model construction was based on the inelastic neutron scattering data measured by Waugh and Dolling [4.4], as provided in Figure 4.4. We reproduce in Figure 4.6 the phonon density of states $g(\nu)$ reported by Dolling and Cowley [4.13]. The $g(\nu)$ curve shows a first maximum near 2 THz, associated with TA (transverse acoustic) modes. Shorter-wavelength

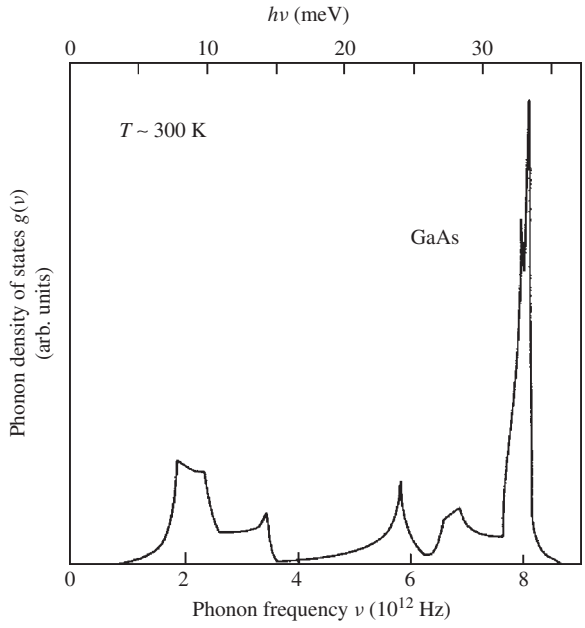

Figure 4.6 Room-temperature phonon density of states for GaAs. [From G. Dolling and R. A. Cowley, *Proc. Phys. Soc.* **88**, 463 (1966), reproduced by permission from Institute of Physics Publishing]

LA (longitudinal acoustic) modes give rise to a relatively smaller peak near 5.7 THz, and the massive concentration of optical phonons near 8 THz produces the largest peak.

4.2 PHONON FREQUENCY

4.2.1 Room-temperature value

The phonon frequencies can be determined by using various measurement techniques, such as neutron scattering, Raman scattering and infrared reflectivity. The first-order Raman scattering measurements give information only about phonon states with $\boldsymbol{q} = 0$ (i.e., long-wavelength phonons). This severe limitation can be overcome by using second-order Raman spectra; two phonons with $\boldsymbol{q}_1 + \boldsymbol{q}_2 \sim 0$ are then produced, and the complete phonon spectrum may become accessible. In fact, the second-order GaAs Raman line observed at 300 K [4.14] gives the 2TA(X) phonon frequency of 160.3 cm^{-1} which agrees well with the neutron scattering TA(X) phonon data of 79 cm^{-1} [4.4]. Infrared reflectivity measurements can also give information about phonon states both with $\boldsymbol{q} = 0$ and $\boldsymbol{q} \neq 0$.

Measurements of phonon-assisted optical transitions at the fundamental absorption edge of indirect-gap semiconductors can also give us information on the zone-boundary phonon frequencies. Monemar [4.15] measured the photoluminescence excitation spectra of AlAs and obtained the momentum-conserving phonon frequencies (X-point phonons) to be TA(X) = 167 cm^{-1} (13.5 meV), LA(X) = 341 cm^{-1} (27.5 meV), TO(X) = 515 cm^{-1} (41.5 meV) and LO(X) = 620 cm^{-1} (50.0 meV). Onton and Chicotka [4.16] have

also measured optical absorption spectra of AlAs at 6 K using the wavelength-modulation technique. The data showed fine structure at the free-exciton energy. The X-point phonon frequencies determined in this experiment are: TA(X) = 161 cm^{-1} (13.0 meV); LA(X) = 329 cm^{-1} (26.5 meV); TO(X) = 513 cm^{-1} (41.4 meV); and LO(X) = 609 cm^{-1} (49.1 meV).

We summarize in Table 4.2 the long-wavelength optical phonon frequencies, $\hbar\omega_{LO}$ and $\hbar\omega_{TO}$, for some cubic group-IV, III–V and II–VI semiconductors at $T = 300$ K. Table 4.3 compiles those for some hexagonal III–V and II–VI semiconductors at $T = 300$ K. These data are gathered from various sources.

Table 4.2 Long-wavelength optical phonon frequencies, $\hbar\omega_{LO}$ and $\hbar\omega_{TO}$, for some cubic group-IV, III–V and II–VI semiconductors at 300 K

System	Material	$\hbar\omega_{LO}$			$\hbar\omega_{TO}$		
		THz	meV	cm^{-1}	THz	meV	cm^{-1}
IV	Diamond	39.93	165.2	1332	39.93	165.2	1332
	Si	15.57	64.38	519.2	15.57	64.38	519.2
	Ge	9.02	37.3	301	9.02	37.3	301
	α-Sn	6.00	24.8	200	6.00	24.8	200
	3C-SiC	29.1	121	972	23.9	98.7	796
III–V	*c*-BN	39.12	161.8	1305	31.619	130.78	1054.7
	BP	24.85	102.8	828.9	24.0	99.1	799
	c-AlN	19.5[a]	80.8[a]	652[a]	27.3	113[a]	909[a]
	AlP	15.02	62.12	501.0	13.17	54.48	439.4
	AlAs	12.1	49.8	402	10.8	44.6	360
	AlSb	10.19	42.16	340.0	9.555	39.52	318.7
	β-GaN	22.2	91.6	739	16.6	68.6	553
	GaP	12.07	49.91	402.5	10.95	45.30	365.3
	GaAs	8.54	35.3	285	8.00	33.1	267
	GaSb	6.99	28.9	233	6.72	27.8	224
	InP	10.38	42.95	346.4	9.129	37.76	304.5
	InAs	7.237	29.93	241.4	6.584	27.23	219.6
	InSb	5.717	23.65	190.7	5.387	22.28	179.7
II–VI	MgO	21.7	89.9	725	12.0	49.7	401
	β-MgS	12.7	52.7	425	9.80	40.5	327
	β-MgSe	10.2	42.2	340	7.11	29.4	237
	β-MgTe	8.75	36.2	292	7.05	29.1	235
	β-ZnS	10.51	43.46	350.5	8.154	33.73	272.0
	ZnSe	7.55	31.2	252	6.15	25.4	205
	ZnTe	6.30	26.0	210	5.43	22.4	181
	c-CdS	9.08[a]	37.6[a]	303[a]	7.11[a]	29.4[a]	237[a]
	c-CdSe	6.33[a]	26.2[a]	211[a]	5.07[a]	21.0[a]	169[a]
	CdTe	5.01	20.7	167	4.17	17.2	139
	β-HgS	6.72	27.8	224	5.31	21.9	177
	HgSe	5.22	21.6	174	3.96	16.4	132
	HgTe	4.05	16.7	135	3.48	14.4	116

[a] Calculated or estimated

Table 4.3 Long-wavelength optical phonon frequencies for some hexagonal III–V and II–VI semiconductors at 300 K

System	Material	Phonon frequency (cm^{-1})					
		E_2 low	A_1 (TO)	E_1 (TO)	E_2 high	A_1 (LO)	E_1 (LO)
III–V	*h*-BN	49	770	1383	1367	778	1610
	w-AlN	248	610	670	657	890	915
	α-GaN	144	533	560	569	736	743
	InN	87	457	490	475	588	582
II–VI	ZnO	100	380	410	439	576	587
	α-ZnS	65	270	273	281	350	350
	w-CdS	41	233	239	255	301	304
	w-CdSe	34	166	170		210	211

A simple linear chain model with a two-point basis, which would correspond to a one-dimensional analogue of a cubic semiconductor in the form of $A^N B^{8-N}$, provides the zone-center ($\boldsymbol{q} = 0$) optical phonon frequency ω_q [4.10]

$$\omega_q = \sqrt{\frac{\kappa_A + \kappa_B}{M}} \tag{4.8}$$

where M is the reduced mass of atoms A and B given by

$$M = \frac{M_A M_B}{M_A + M_B} \tag{4.9}$$

and κ_i is the spring constant of the lattice.

Table 4.4 lists the long-wavelength optical phonon frequency $\hbar\omega_{LO}$, optical phonon frequency difference $\Delta\omega_{op} = \hbar\omega_{LO} - \hbar\omega_{TO}$, Phillips ionicity f_i and reduced atomic mass M for some group-IV, III–V and II–VI semiconductors. We can expect from Equation (4.8) a relation between the optical phonon frequency ω_q and an inverse atomic mass M^{-1}. In Figure 4.7, we plot the values of ω_{LO} versus M^{-1} for some group-IV, III–V and II–VI semiconductors. The solid line represents the least-squares fit with the relation (M in amu; ω_{LO} in cm^{-1})

$$\omega_{LO} = \frac{a}{M} \tag{4.10}$$

where $a = 7.85 \times 10^3$ cm^{-1} amu. The general trend of a larger ω_{LO} with decreasing M is clearly seen in Figure 4.7. It is thus possible to suppose that $(\kappa_A + \kappa_B)$ in Equation (4.8) is proportional to M^{-1}. As a result, ω_q is proportional to M^{-1}.

As can be understood from Table 4.4, the long-wavelength optical phonon frequency difference $\Delta\omega_{op} = \omega_{LO} - \omega_{TO}$ is zero for covalent semiconductors (Si, Ge, etc.), but is not zero for ionic semiconductors. We can, therefore, expect to find a relationship between $\Delta\omega_{op}$ and material ionicity f_i. However, no clear relationship can be found between these quantities, as demonstrated in Figure 4.8.

Table 4.4 Long-wavelength optical phonon frequency $\hbar\omega_{LO}$, optical phonon frequency difference $\Delta\omega_{op} = \omega_{LO} - \omega_{TO}$, Phillips ionicity f_i and reduced atomic mass $M = M_A M_B/(M_A + M_B)$ for a number of group-IV, III–V and II–VI semiconductors

System	Material	ω_{LO} (cm^{-1})	$\Delta\omega_{op}$ (cm^{-1})	f_i	M (amu)
IV	Diamond	1332	0	0	6.01
	Si	519.2	0	0	14.04
	Ge	301	0	0	36.31
	α-Sn	200	0	0	59.36
	3C-SiC	972	176	0.177	8.41
	6H-SiC	965	167	0.177	8.41
III–V	c-BN	1305	250	0.221	6.10
	h-BN	1333[a]	154[a]	0.221	6.10
	BP	828.9	30	0.032	8.01
	BAs			0.044	9.45
	w-AlN	907[a]	257[a]	0.449	9.22
	c-AlN	907	257	0.449	9.22
	AlP	501.0	61.6	0.307	14.42
	AlAs	402	42	0.274	19.84
	AlSb	340.0	21.3	0.250	22.09
	α-GaN	741[a]	190[a]	0.500	11.66
	β-GaN	739	186	0.500	11.66
	GaP	402.5	37.2	0.327	21.45
	GaAs	285	18	0.310	36.11
	GaSb	233	9	0.261	44.34
	InN	584	105	0.578	12.48
	InP	346.4	41.9	0.421	24.39
	InAs	241.4	21.8	0.357	45.34
	InSb	190.7	11.0	0.321	59.09
II–VI	MgO	725	324	0.841	9.65
	β-MgS	425	98	0.786	13.83
	β-MgSe	340	103	0.790	18.58
	β-MgTe	292	57	0.554	20.42
	ZnO	582[a]	182[a]	0.616	12.85
	α-ZnS	350[a]	78[a]	0.623	21.52
	β-ZnS	350.5	78.5	0.623	21.52
	ZnSe	252	47	0.630	35.77
	ZnTe	210	29	0.609	43.23
	c-CdS	303	66	0.685	24.95
	w-CdS	303[a]	66[a]	0.685	24.95
	c-CdSe	211	42	0.699	46.38
	w-CdSe	211[a]	42[a]	0.699	46.38
	CdTe	167	28	0.717	59.76
	β-HgS	224	47	0.790	27.65
	HgSe	174	42	0.680	56.66
	HgTe	135	19	0.650	77.99

[a] Values correspond to those for cubic approximation: LO(Γ)$\leftrightarrow$(1/3)[A_1(LO)+2E_1(LO)]; TO(Γ) $\leftrightarrow$(1/3)[A_1(TO)+2E_1(TO)]

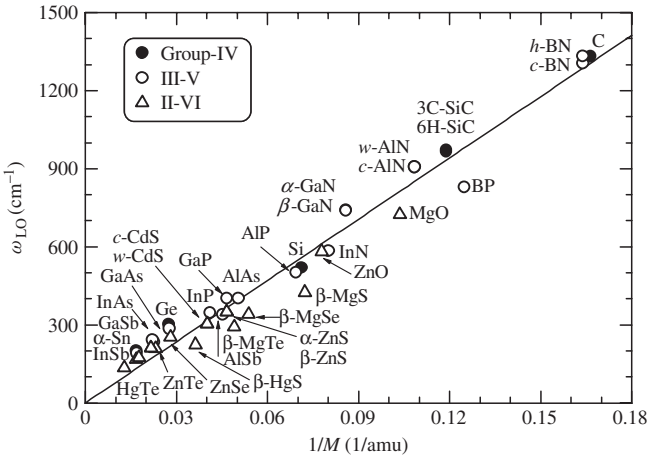

Figure 4.7 Long-wavelength optical phonon frequency ω_{LO} versus inverse atomic mass $1/M = (M_A + M_B)/(M_A M_B)$ for some group-IV, III–V and II–VI semiconductors. The solid line represents the least-squares fit with $\omega_{LO} = 7.85 \times 10^{-3}/M$ (M in amu; ω_{LO} in cm^{-1})

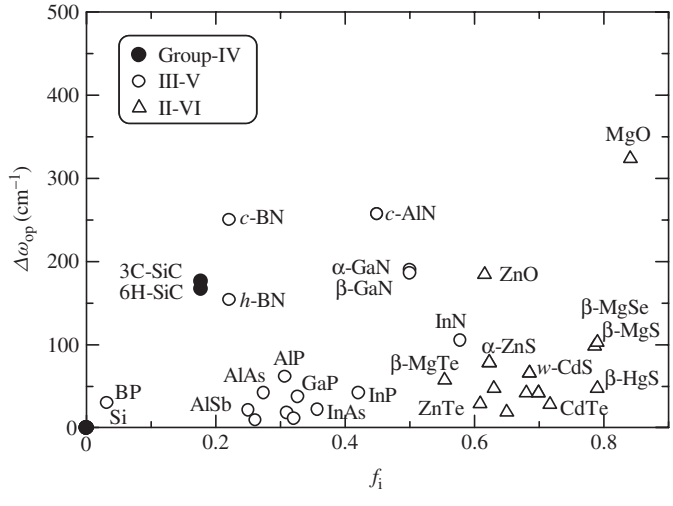

Figure 4.8 Long-wavelength optical phonon frequency difference $\Delta\omega_{op} = \omega_{LO} - \omega_{TO}$ versus Phillips ionicity f_i for some group-IV, III–V and II–VI semiconductors

4.2.2 External perturbation effect

(a) Temperature effect

The phonon frequency is dependent both on temperature T and pressure p. The effect of temperature on the phonon frequency measured by Raman scattering is due primarily to the thermal expansion of the crystal lattice. The dependence of phonon frequency $\nu(\boldsymbol{q},T)$

with temperature T, in this case, can be written as

$$\nu(\boldsymbol{q}, T) = \nu_0(\boldsymbol{q}) \left(1 - \frac{\alpha_{\text{th}}^2 a T}{\kappa_{\text{L}} k}\right) \tag{4.11}$$

where $\nu_0(\boldsymbol{q})$ is the phonon dispersion of the harmonic linear chain, a is the lattice constant, α_{th} is the linear thermal expansion coefficient, κ_{L} is the compressibility of the linear chain, k is the Boltzmann constant and $\boldsymbol{q}$ is the phonon wavevector. This expression simply predicts a linear decrease in the phonon frequency with increasing T.

We plot in Figure 4.9 the long-wavelength optical phonon frequencies, ω_{LO} and ω_{TO}, versus temperature T for InP. The experimental data were measured by near-infrared Raman spectroscopy at $T = 80$–290 K by Irmer *et al.* [4.17]. These authors also obtained the phonon damping energies and found that they are mainly affected by decay processes into acoustic phonons.

The optical phonon frequencies in Figure 4.9 show a small variation with T for $T <$ 100 K and gradually decrease with increase of T. At $T \geqslant 200$ K, the temperature variation is seen to be almost linear. The solid lines in Figure 4.9 represent the best-fit results for an expression

$$\omega_{ij}(T) = \omega_{ij}(0) - \frac{\alpha T^2}{T + \beta} \tag{4.12}$$

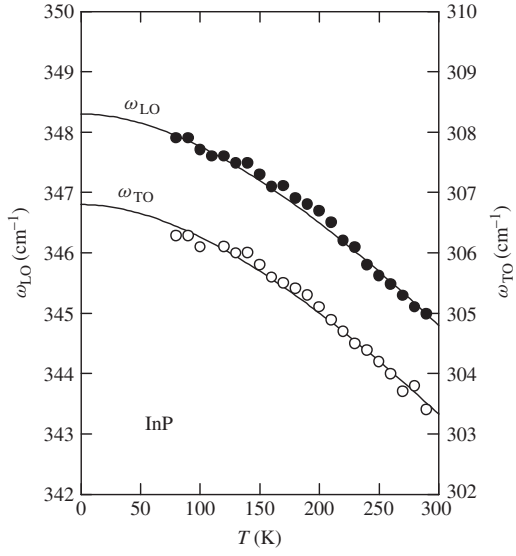

Figure 4.9 Temperature dependence of the long-wavelength optical phonon frequencies, ω_{LO} and ω_{TO}, for InP. The experimental data are taken from Irmer *et al.* [4.17]. The solid lines represent the fitted results using $\omega_{\text{LO}}(T) = \omega_{\text{LO}}(0) - [\alpha T^2/(T + \beta)]$ with $\omega_{\text{LO}}(0) = 348.3$ cm^{-1}, $\alpha = 2.8 \times 10^{-2}$ cm^{-1}/K and $\beta = 420$ K and $\omega_{\text{TO}}(T) = \omega_{\text{TO}}(0) - [\alpha T^2/(T + \beta)]$ with $\omega_{\text{TO}}(0) =$ 306.8 cm^{-1}, $\alpha = 2.7 \times 10^{-2}$ cm^{-1}/K and $\beta = 400$ K. [From S. Adachi, *Handbook on Physical Properties of Semiconductors Volume 2: III–V Compound Semiconductors* (Kluwer Academic, Boston, 2004), reproduced by permission from Kluwer Academic Publishers]

where $\omega_{ij}(0)$ is the $T = 0$ K value, α is in cm^{-1} per Kelvin and β is a quantity proportional to the Debye temperature (in Kelvin). Note that Equation (4.12) is widely known as the Varshni equation used for explaining the temperature dependence of the band-gap energy [4.18].

(b) Pressure effect

The pressure dependence of the phonon frequency can be represented by the mode Grüneisen parameter (see Section 4.3). Venkateswaran *et al.* [4.14] have measured the hydrostatic pressure dependence of the acoustic [2TA(X) and 2A(K)] and optical phonons [TO(Γ) and LO(Γ)] in GaAs and TO(Γ) and LO(Γ) phonons in AlAs at $T = 300$ K. We reproduce in Figure 4.10 their experimental data [4.14]. We can see that the optical phonon frequencies increase with increasing pressure p (i.e., showing positive Grüneisen parameters) while the zone-boundary acoustic phonons 2TA(X) and 2A(K) soften under compression. The softening of the TA(L) phonons has also been observed by Trommer *et al.* [4.19].

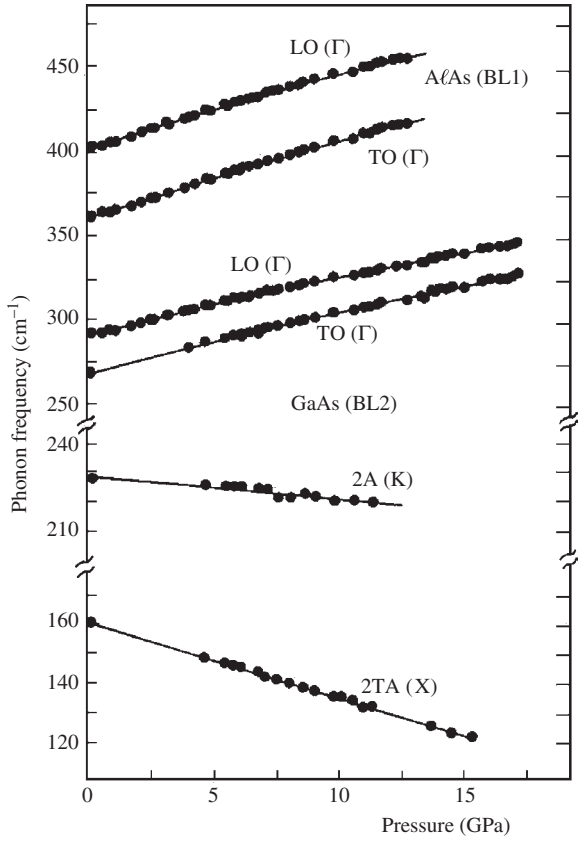

Figure 4.10 Hydrostatic pressure dependence of the acoustic (2TA(X) and 2A(K)) and optical phonons (TO(Γ) and LO(Γ)) in GaAs and TO(Γ) and LO(Γ) in AlAs at 300 K. [From U. D. Venkateswaran, L. J. Cui, B. A. Weinstein, and F. A. Chambers, *Phys. Rev. B* **45**, 9237 (1992), reproduced by permission from the American Physical Society]

The hydrostatic pressure dependence of the phonon frequencies can be usually expressed as a quadratic equation

$$\omega_{\mathrm{q}}(p) = \omega_{\mathrm{q}}(0) + ap + bp^2 \tag{4.13}$$

where $\omega_{\mathrm{q}}(0)$ is the $p = 0$ value. The solid lines in Figure 4.10 represent the calculated results of Equation (4.13). Note that the phonon frequencies also vary with the application of uniaxial or biaxial stress, as we will see in Section 4.4.

4.3 MODE GRÜNEISEN PARAMETER

Anharmonic properties of solids are customarily described in terms of the Grüneisen parameter γ. As a measure of the volume dependence of the phonon frequency $\nu_i(\boldsymbol{q})$ of the ith mode, the mode Grüneisen parameter $\gamma_i(\boldsymbol{q})$ is defined by

$$\gamma_i(\boldsymbol{q}) = -\frac{\mathrm{d}[\ln \nu_i(\boldsymbol{q})]}{\mathrm{d}[\ln V]} = -\frac{V}{\nu_i(\boldsymbol{q})}\frac{\mathrm{d}\nu_i(\boldsymbol{q})}{\mathrm{d}V} \tag{4.14}$$

The mode Grüneisen parameters can thus be calculated from knowledge of the phonon frequencies as a function of the crystal volume V. We summarize in Tables 4.5 and 4.6 the mode Grüneisen parameters for the long-wavelength ($\boldsymbol{q} = 0$) phonons in some cubic and hexagonal semiconductors, respectively.

Table 4.5 Mode Grüneisen parameter for the long-wavelength optical phonons in some cubic group-IV, III–V and II–VI semiconductors

System	Material	TO	LO	System	Material	TO	LO
IV	Diamond	0.95	0.95	II–VI	MgO	3.90	1.42
	Si	0.96	0.96		β-ZnS	1.84	1.02
	Ge	1.00	1.00		ZnSe	1.52	0.85
	3C-SiC	1.084	1.019		ZnTe	1.58	1.10
III–V	c-BN	1.5	1.2		CdTe	1.61	1.01
	BP	1.3	1.12				
	c-AlN	1.14[a]	0.89[a]				
	AlP	1.49[a]					
	AlAs	1.05	0.93				
	AlSb	1.21	1.15				
	β-GaN	1.4	1.2				
	GaP	1.09	0.95				
	GaAs	1.11	0.97				
	GaSb	1.33	1.21				
	InP	1.52	1.19				
	InAs	1.21	1.06				
	InSb	1.41	1.17				

[a] Calculated

Table 4.6 Mode Grüneisen parameter for the long-wavelength phonons in some hexagonal III–V and II–VI semiconductors

System	Material	E_2 low	A_1 (TO)	E_1 (TO)	E_2 high	A_1 (LO)	E_1 (LO)
III–V	w-AlN	0.10	1.51	1.41	1.58	0.93	1.06
	α-GaN	−0.4	1.47	1.41	1.50	1.20	
II–VI	ZnO	−1.6	2.1	1.8	2.0		1.4
	w-CdS					0.87	0.87

In principle, the specific heat at constant volume C_v is given by [4.8]

$$C_v = \sum_{i,\boldsymbol{q}} C_i(\boldsymbol{q}) \tag{4.15}$$

where $C_i(\boldsymbol{q})$ is the heat capacity due to mode i at constant volume and temperature. The volume thermal expansion coefficient β is also written as

$$\beta = \frac{C_o}{V} \sum_{i,\boldsymbol{q}} \gamma_i(\boldsymbol{q}) C_i(\boldsymbol{q}) \tag{4.16}$$

where $\gamma_i(\boldsymbol{q})$ is the mode Grüneisen parameter and C_o is the compressibility, assumed to be independent of temperature T. The averaged Grüneisen parameter γ can, then, be defined by

$$\gamma = \frac{\sum_{i,\boldsymbol{q}} \gamma_i(\boldsymbol{q}) C_i(\boldsymbol{q})}{\sum_{i,\boldsymbol{q}} C_i(\boldsymbol{q})} \tag{4.17}$$

Introducing Equations (4.15) and (4.17) into Equation (4.16), we obtain

$$\beta = \frac{C_o}{V} \gamma C_v \tag{4.18}$$

This expression is the original Grüneisen relation. Grüneisen considered C_o and γ to be independent of temperature and concluded that the thermal expansion coefficient has the same temperature dependence as the specific heat. Note that we defined β as the volume thermal expansion coefficient. It is common to define the linear thermal expansion coefficient α_{th} by

$$\alpha_{th} = \frac{1}{L}\left(\frac{\partial L}{\partial T}\right)_p = \frac{1}{3V}\left(\frac{\partial V}{\partial T}\right)_p = \frac{\beta}{3} \tag{4.19}$$

Introducing Equation (4.19) into Equation (4.18), we obtain the expression of Grüneisen's rule presented in Section 2.4, (Equation (2.12)).

4.4 PHONON DEFORMATION POTENTIAL

4.4.1 Cubic lattice

As described in Section 4.2, the phonon frequency is strongly influenced by hydrostatic pressure. The phonon frequency is also strongly influenced by uniaxial stress. Such a

stress-induced frequency shift of phonons is essentially explained by the phonon deformation potential (PDP). The PDP is an important anharmonicity parameter, useful in a number of physical and technological applications. Detailed expressions for PDP and its consequences for the first-order Raman shifts in semiconductors were first presented by Cerdeira *et al.* [4.20].

The PDP is a component of a fourth-rank tensor K_{ij} in suppressed notation. For a zinc-blende-type crystal, there are only three independent components of the PDP tensor

$$K_{11} = K_{22} = K_{33} = Mp \tag{4.20a}$$

$$K_{12} = K_{23} = K_{13} = Mq \tag{4.20b}$$

$$K_{44} = K_{55} = K_{66} = Mr \tag{4.20c}$$

where M is the reduced mass of the two atoms. According to Cerdeira *et al.* [4.20], the long-wavelength optical phonon frequencies in the presence of strain e_{ij} obey the following secular equation

$$\begin{vmatrix} pe_{xx} + q(e_{yy} + e_{zz}) - \lambda & 2re_{xy} & 2re_{xz} \\ 2re_{xy} & pe_{yy} + q(e_{xx} + e_{zz}) - \lambda & 2re_{yz} \\ 2re_{xz} & 2re_{yz} & pe_{zz} + q(e_{xx} + e_{zz}) - \lambda \end{vmatrix} = 0 \tag{4.21}$$

where $\lambda = \Omega^2 - \omega_i^2$ and $\Omega \sim \omega_i + (\lambda/2\omega_i)$ is the strain-dependent phonon frequency (ω_i = phonon frequency without strain).

The strain e_{ij} and stress X_{kl} relation is now given by

$$e_{ij} = \sum_{kl} S_{ijkl} X_{kl} \tag{4.22}$$

where S_{ijkl} is the elastic compliance component. This relation yields the nonzero strain components

$$e_{xx} = e_{yy} = e_{zz} = (S_{11} + 2S_{12})\frac{X}{3} \tag{4.23}$$

for the hydrostatic pressure,

$$e_{xx} = S_{11}X \tag{4.24a}$$

$$e_{yy} = e_{zz} = S_{12}X \tag{4.24b}$$

for the [100] uniaxial stress and

$$e_{xx} = e_{yy} = e_{zz} = \frac{S_{11} + 2S_{12}}{3}X \tag{4.25a}$$

$$e_{xy} = e_{yz} = e_{zx} = \frac{S_{44}}{6}X \tag{4.25b}$$

for the [111] uniaxial stress.

Introducing Equations (4.23)–(4.25) into Equation (4.21), one obtains a shift of the phonon frequency. For the hydrostatic stress, the shift of the phonon frequency is written as

$$\Delta\Omega_{\mathrm{H}} = \frac{X}{6\omega_i}(p + 2q)(S_{11} + 2S_{12}) \tag{4.26}$$

For the [100] and [111] uniaxial stresses, the three-fold degeneracy of the $\boldsymbol{q} = 0$ phonons is split into a singlet Ω_{s} with an eigenvector parallel to the stress and a doublet Ω_{d} with eigenvectors perpendicular to the stress, where Ω_{s} and Ω_{d} are given by

$$\Omega_{\mathrm{s}} = \omega_i + \Delta\Omega_{\mathrm{H}} + \frac{2}{3}\Delta\Omega \tag{4.27a}$$

$$\Omega_{\mathrm{d}} = \omega_i + \Delta\Omega_{\mathrm{H}} - \frac{1}{3}\Delta\Omega \tag{4.27b}$$

The splitting energy $\Delta\Omega$ is also written as

$$\Delta\Omega = \Omega_{\mathrm{s}} - \Omega_{\mathrm{d}} = \begin{cases} \dfrac{X}{2\omega_i}(p - q)(S_{11} - S_{12}) & \text{for [100] stress} \quad (4.28a) \\ \dfrac{X}{2\omega_i} r S_{44} & \text{for [111] stress} \quad (4.28b) \end{cases}$$

The PDP could then be determined experimentally by measuring either a shift of the phonon frequency for each mode ($\Delta\Omega_{\mathrm{s}} = \omega_i - \Omega_{\mathrm{s}}$ or $\Delta\Omega_{\mathrm{d}} = \omega_i - \Omega_{\mathrm{d}}$) or the splitting energy $\Delta\Omega$. It is noted that the hydrostatic pressure component corresponds to the mode Grüneisen parameter γ_i in the manner

$$\gamma_i = -\frac{p + 2q}{6\omega_i} \tag{4.29}$$

Under (100) coplanar stress X (i.e., the biaxial stress along the [010] and [001] directions is applied), the nonzero strain components in the layer are given by

$$e_{xx} = 2S_{12}X, \qquad e_{yy} = e_{zz} = (S_{11} + S_{12})X \tag{4.30}$$

The energy shift $\Delta\omega_{\mathrm{LO}}$ for the allowed LO phonons is then given by

$$\Delta\omega_{\mathrm{LO}} = \omega_{\mathrm{LO}}(X = 0) - \omega_{\mathrm{LO}}(X \neq 0) = 2\Delta\Omega_{\mathrm{H}} - \frac{2}{3}\Delta\Omega \tag{4.31}$$

where $\Delta\Omega_{\mathrm{H}}$ and $\Delta\Omega$ are given by Equations (4.26) and (4.28a), respectively. Typically, for light scattering from a (100) surface (zinc-blende-type crystals), only the LO mode is allowed and the TO mode is forbidden in the backscattering configuration. This coplanar strain configuration is just the case where a large residual strain is usually induced in lattice-mismatched superlattices and heterostructures grown on (100) substrates.

The dimensionless PDP K_{ij} can be defined, using p, q and r, as

$$K_{11} = \frac{p}{\omega_i^2}, \qquad K_{12} = \frac{q}{\omega_i^2}, \qquad K_{44} = \frac{r}{\omega_i^2} \tag{4.32}$$

Table 4.7 Long-wavelength PDP for some cubic group-IV, III–V and II–VI semiconductors

System	Material	TO phonon			LO phonon		
		K_{11}	K_{12}	K_{44}	K_{11}	K_{12}	K_{44}
IV	Diamond	−2.81	−1.77	−1.9	−2.81	−1.77	−1.9
	Si	−1.51	−1.99	−0.61	−1.51	−1.99	−0.61
	Ge	−1.93	−2.39	−0.87	−1.93	−2.39	−0.87
	3C-SiC	−2.01	−2.31		−2.52	−1.95	
III–V	AlSb	−2.1	−2.6	−0.7	−1.6	−2.6	−0.3
	GaP	−1.50	−2.10	−0.58	−1.48	−2.51	−0.50
	GaAs	−1.9	−2.2	−0.80	−1.4	−1.9	−0.54
	GaSb	−2.52	−2.74	−1.08	−2.29	−2.51	−1.08
	InP	−2.5	−3.2	−0.47	−1.6	−2.8	−0.18
	InAs	−2.05	−2.62	−0.76	−1.75	−2.32	−0.76
	InSb	−2.45	−3.04	−0.54	−1.72	−2.65	−0.22
II–VI	β-ZnS	−2.81	−4.11	−0.61	−1.23	−2.45	−0.30
	ZnSe	−1.97	−3.21	−0.43	−0.97	−2.21	−0.43
	ZnTe	−3.0	−3.6	−0.5	−1.8	−2.7	−0.2
	CdTe	−3.25	−3.20	−2.1	−1.08	−2.49	−4.54

We compile in Table 4.7 the dimensionless PDPs for the long-wavelength ($\boldsymbol{q} = 0$) optical phonons in some cubic group-IV, III–V and II–VI semiconductors.

4.4.2 Hexagonal lattice

The effect of stress on $\boldsymbol{q} = 0$ phonons in wurtzite crystal has been studied by piezo-Raman spectroscopy by Briggs and Ramdas [4.21]. The perturbation potential V can be given, in the linear deformation potential theory, by

$$V = \sum_{ij} V_{ij} e_{ij} \tag{4.33}$$

where e_{ij} is the component of the strain tensor and V_{ij} is the deformation potential. For the wurtzite crystal, the representation generated by V_{ij} is $\Gamma(V) = 2A_1 + E_1 + E_2$. Hence, the perturbation potential V can be grouped as follows

$$\begin{aligned} V = {} & \frac{1}{2}(V_{xx} + V_{yy})(e_{xx} + e_{yy}) + V_{zz} e_{zz} + 2[(V_{yz} e_{yz}) + (-V_{zx})(-e_{zx})] \\ & + \frac{1}{2}[(V_{xx} - V_{yy})(e_{xx} - e_{yy}) + (-2V_{xy})(-2e_{xy})] \end{aligned} \tag{4.34}$$

In Equation (4.34), $(V_{xx} + V_{yy})$ and V_{zz} belong to A_1, V_{yz} and $-V_{zx}$ belong to E_1 and $(V_{xx} - V_{yy})$ and $-2V_{xy}$ belong to E_2 as understood from the basis functions appropriate

Table 4.8 Long-wavelength PDP for some hexagonal III–V and II–VI semiconductors

System	Material		PDP (cm^{-1})					
			E_2 low	A_1 (TO)	E_1 (TO)	E_2 high	A_1 (LO)	E_1 (LO)
III–V	w-AlN	a		−930	−982	−1092	−643	
		b		−904	−901	−965	−1157	
	α-GaN	a	115	−630	−820	−850	−685	−776
		b	−80	−1290	−680	−920	−997	−704
	InN	a			−735	−610		
		b			−699	−857		
II–VI	w-CdS	a	∼96	−526	−235	−404	−526	−235
		b	∼104	−328	−330	−483	−328	−330
		c	16		57	107		57

for the representations A_1, E_1 and E_2 of point group C_{6v}. Thus, under stress the energy of a state belonging to A_1 will shift by

$$\frac{1}{2}\langle A_1|V_{xx}+V_{yy}|A_1\rangle(e_{xx}+e_{yy})+\langle A_1|V_{zz}|A_1\rangle e_{zz}$$

since the remaining terms vanish from the orthogonality theorem. The energy shift of the A_1 state can, then, be given by

$$\Delta\Omega_{A_1}=a_{A_1}(e_{xx}+e_{yy})+b_{A_1}e_{zz} \tag{4.35}$$

where $a_{A_1}=(1/2)\langle A_1|V_{xx}+V_{yy}|A_1\rangle$ and $b_{A_1}=\langle A_1|V_{zz}|A_1\rangle$ represent the phonon deformation potentials.

For the calculation of V for the doubly degenerate E_1 and E_2 modes, we need the decomposition of the products of the basis functions of C_{6v}. The resultant energy shifts are given by

$$\Delta\Omega_{E_1}=a_{E_1}(e_{xx}+e_{yy})+b_{E_1}e_{zz}\pm c_{E_1}\sqrt{(e_{xx}-e_{yy})^2+4e_{xy}^2} \tag{4.36}$$

for the E_1 mode, and similarly

$$\Delta\Omega_{E_2}=a_{E_2}(e_{xx}+e_{yy})+b_{E_2}e_{zz}\pm c_{E_2}\sqrt{(e_{xx}-e_{yy})^2+4e_{xy}^2} \tag{4.37}$$

for the E_2 mode. We summarize in Table 4.8 the PDPs a, b and c for the long-wavelength ($\boldsymbol{q}=0$) optical phonons experimentally determined for some hexagonal III–V and II–VI semiconductors.

REFERENCES

[4.1] D. L. Greenaway and G. Harbeke, *Optical Properties and Band Structure of Semiconductors* (Pergamon, Oxford, 1968).

[4.2] F. Koster, J. O. Dimmock, R. G. Wheeler, and H. Statz, *Properties of the Thirty-Two Point Groups* (MIT Press, Cambridge, 1963).
[4.3] H. Jones, *The Theory of Brillouin Zones and Electronic States in Crystals* (North-Holland, Amsterdam, 1975).
[4.4] J. L. T. Waugh and G. Dolling, *Phys. Rev.* **132**, 2410 (1963).
[4.5] J. S. Blakemore, *J. Appl. Phys.* **53**, R123 (1982).
[4.6] E. O. Kane, *Phys. Rev. B* **31**, 7865 (1985).
[4.7] D. Strauch and B. Dorner, *J. Phys.: Condens. Matter* **2**, 1457 (1990).
[4.8] G. P. Srivastava, *The Physics of Phonons* (Adam Hilger, Bristol, 1990).
[4.9] A. W. Hewat, *Solid State Commun.* **8**, 187 (1970).
[4.10] J. L. Birman, *Phys. Rev.* **115**, 1493 (1959).
[4.11] L. Van Hove, *Phys. Rev.* **89**, 1189 (1953).
[4.12] H. G. Grahn, *Introduction to Semiconductor Physics* (World Scientific, Singapore, 1999).
[4.13] G. Dolling and R. A. Cowley, *Proc. Phys. Soc.* **88**, 463 (1966).
[4.14] U. D. Venkateswaran, L. J. Cui, B. A. Weinstein, and F. A. Chambers, *Phys. Rev. B* **45**, 9237 (1992).
[4.15] B. Monemar, *Phys. Rev. B* **8**, 5711 (1973).
[4.16] A. Onton and R. J. Chicotka, *Phys. Rev. B* **10**, 591 (1974).
[4.17] G. Irmer, M. Wenzel, and J. Monecke, *Phys. Status Solidi B* **195**, 85 (1996).
[4.18] Y. P. Varshni, *Physica* **34**, 149 (1967).
[4.19] R. Trommer, H. Müller, M. Cardona, and P. Vogl, *Phys. Rev. B* **21**, 4869 (1980).
[4.20] F. Cerdeira, C. J. Buchenauer, F. H. Pollak, and M. Cardona, *Phys. Rev. B* **5**, 580 (1972).
[4.21] R. J. Briggs and A. K. Ramdas, *Phys. Rev. B* **13**, 5518 (1976).

5 Collective Effects and Some Response Characteristics

5.1 Piezoelectric and electromechanical constants 95
5.1.1 Piezoelectric constant 95
5.1.2 Electromechanical coupling constant 99
5.2 Fröhlich coupling constant 99
References 101

5.1 PIEZOELECTRIC AND ELECTROMECHANICAL CONSTANTS

5.1.1 Piezoelectric constant

(a) Piezoelectric stress constant

If a stress is applied to certain crystals, they develop an electric moment whose magnitude is proportional to the applied stress. This is known as the direct piezoelectric effect [5.1]. A crystal with a center of symmetry cannot be piezoelectric. Thus, the diamond-type crystals (Si, Ge, etc.) cannot be piezoelectric. The III–V compounds crystallizing in the zinc-blende structure are the simplest crystals lacking a center of symmetry and, hence, capable of exhibiting piezoelectric and related effects. The piezoelectric constants form a third-rank tensor. We summarize in Table 5.1 the form of the piezoelectric stress tensor $[e]$ for the cubic, hexagonal and rhombohedral systems, where m and n in e_{mn} represent m and ij, respectively, according to the rules $x \rightarrow 1$, $y \rightarrow 2$ and $z \rightarrow 3$ (m); and $xx \rightarrow 1$, $yy \rightarrow 2$, $zz \rightarrow 3$, $yz \rightarrow 4$, $zx \rightarrow 5$ and $xy \rightarrow 6$ (n) [5.1].

We list in Tables 5.2 and 5.3 the piezoelectric stress constant e_{ij} for some cubic and hexagonal group-IV, III–V and II–VI semiconductors, respectively. If the III–V semiconductors were expanded in the $\langle 111 \rangle$ direction, the A-faces (metal-atom faces) became negatively charged, in contrast to II–VI compounds, in which the equivalent faces became positively charged. Arlt and Quadflieg [5.2] have proposed macroscopic origins of piezoelectricity as being due to factors such as ionic polarization, strain-dependent ionicity and electronic polarization.

Figure 5.1 shows a plot of the piezoelectric stress constant e_{14} versus Phillips ionicity f_i for some cubic III–V and II–VI semiconductors. This plot suggests that e_{14} passes through zero at $f_i \sim 0.5$ while undergoing a reversal in sign (i.e., smaller f_i values of III–V compounds possess negative e_{14} values and larger f_i values of II–VI compounds

Properties of Group-IV, III–V and II–VI Semiconductors Sadao Adachi

© 2005 John Wiley & Sons, Ltd

ISBN: 0-470-09032-4

Table 5.1 Form of the piezoelectric stress tensor for semiconductors of certain symmetry classes

Symmetry class	Material	Tensor form
Cubic (Class O_h)	Si, Ge, MgO, etc.	$\begin{bmatrix} 0 & 0 & 0 & 0 & 0 & 0 \\ 0 & 0 & 0 & 0 & 0 & 0 \\ 0 & 0 & 0 & 0 & 0 & 0 \end{bmatrix}$ Showing no piezoelectric effect
Cubic (Class T_d)	3C-SiC, GaAs, ZnSe, etc.	$\begin{bmatrix} 0 & 0 & 0 & e_{14} & 0 & 0 \\ 0 & 0 & 0 & 0 & e_{14} & 0 \\ 0 & 0 & 0 & 0 & 0 & e_{14} \end{bmatrix}$
Hexagonal (Class C_{6v})	2H-SiC, α-GaN, w-CdS, etc.	$\begin{bmatrix} 0 & 0 & 0 & 0 & e_{15} & 0 \\ 0 & 0 & 0 & e_{15} & 0 & 0 \\ e_{31} & e_{31} & e_{33} & 0 & 0 & 0 \end{bmatrix}$
Hexagonal (Class D_{6h})	h-BN	$\begin{bmatrix} 0 & 0 & 0 & 0 & 0 & 0 \\ 0 & 0 & 0 & 0 & 0 & 0 \\ 0 & 0 & 0 & 0 & 0 & 0 \end{bmatrix}$ Showing no piezoelectric effect
Rhombohedral (Class C_{3v})	15R-SiC	$\begin{bmatrix} 0 & 0 & 0 & 0 & e_{15} & -2e_{22} \\ -e_{22} & e_{22} & 0 & e_{15} & 0 & 0 \\ e_{31} & e_{31} & e_{33} & 0 & 0 & 0 \end{bmatrix}$

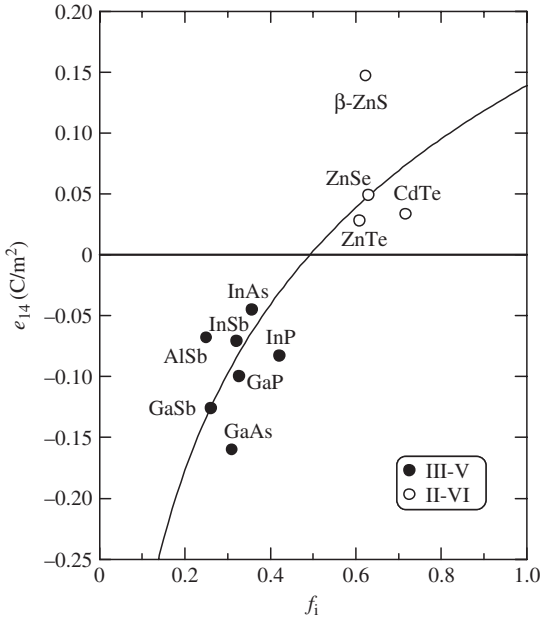

Figure 5.1 Plots of e_{14} versus Phillips ionicity f_i for some cubic III–V and II–VI semiconductors. The solid line represents the least-squares fit with $e_{14} = 0.20 \ln f_i + 0.14$ (e_{14} in C/m^2)

Table 5.2 Piezoelectric stress and strain constants, e_{14} and d_{14}, for some cubic group-IV, III–V and II–VI semiconductors

System	Material	e_{14} (C/m^2)	d_{14} (10^{-12} m/V)
IV	Diamond[a]		
	Si[a]		
	Ge[a]		
	α-Sn[a]		
	3C-SiC	−0.345[b]	−1.35[b]
III–V	*c*-BN	−1.04[b]	
	BP	−0.36[b]	
	c-AlN	1.13[b]	9.7[b]
	AlP	−0.06[b]	
	AlAs	−0.23[b]	−3.9[b]
	AlSb	0.068	1.7
	β-GaN	0.61[b]	6.4[b]
	GaP	0.10	1.42
	GaAs	−0.16	−2.7
	GaSb	0.126	2.92
	InP	−0.083	−1.80
	InAs	0.045	1.14
	InSb	0.071	2.4
II–VI	MgO[a]		
	β-ZnS	0.147	3.18
	ZnSe	0.049	1.10
	ZnTe	0.028	0.91
	CdTe	0.0335	1.68
	β-HgS	0.14[b]	5.3[b]
	HgSe	0.058[b]	2.6[b]
	HgTe	0.029[b]	1.4[b]

[a] Principally showing no piezoelectricity
[b] Estimated or calculated

possess positive ones). Theoretical calculations [5.3–5.5] of e_{14} for GaAs yielded considerably different values ranging from −0.11 to −0.18. Phillips and Van Vechten [5.6] showed the reversal in sign of e_{14} on going from $N = 1$, 2 to $N = 3$ in tetrahedrally coordinated $A^N B^{8-N}$ crystals based on the lattice dynamic treatment with the addition of the concept of their ionicity scale. Hübner [5.3] predicted e_{14} values for a number of III–V, II–VI and I–VII compounds and found them to be in good numerical agreement with experimental data including sign.

More recently, Gironcoli *et al.* [5.5] have presented an *ab initio* approach to piezoelectricity in semiconductors. The piezoelectric tensor was given in their model by the stress induced by a homogeneous electric field, and the perturbation was treated self-consistently by linear response, thus avoiding both supercells and numerical differentiation. They calculated nine III–V binary semiconductors (Al,Ga,In)(P,As,Sb) and found that, contrary to

Table 5.3 Piezoelectric stress and strain constants e_{ij} and d_{ij} for some hexagonal group-IV, III–V and II–VI semiconductors

System	Material	e_{ij} (C/m^2)			d_{ij} (10^{-12} m/V)		
		e_{15}	e_{31}	e_{33}	d_{15}	d_{31}	d_{33}
IV	6H-SiC	−0.08		0.2			
III–V	h-BN[a]						
	w-AlN	−0.48	−0.58	1.55	−4.07	−2.65	5.53
	α-GaN	−0.33[b]	−0.55	1.12	3.1	−1.9	3.7
	InN		−0.41[c]	0.81[c]			
II–VI	ZnO	−0.37	−0.62	0.96	−8.3	−5.12	12.3
	α-ZnS	−0.118	−0.238	0.265	−4.37	−2.14	3.66
	w-CdS	−0.183	−0.262	0.385	−11.91	−5.09	9.71
	w-CdSe	−0.138	−0.160	0.347	−10.51	−3.92	7.84

[a] Principally showing no piezoelectricity
[b] Estimated from cubic phase data
[c] Calculated

common belief, two III–V compounds AlP and InP have positive e_{14} values. This result is in direct contrast to those obtained by Hübner [5.3] and Miura *et al.* [5.4].

The e_{ij} for the wurtzite crystals may be estimated from that of the zinc-blende-type crystals (e_{14}) [5.7]

$$\begin{aligned} e_{15} = e_{31} &= -\frac{1}{\sqrt{3}} e_{14} \\ e_{33} &= \frac{2}{\sqrt{3}} e_{14} \end{aligned} \tag{5.1}$$

(b) Piezoelectric strain constant

The piezoelectric strain constant d_{ij} has the same tensor form as in Table 5.1. The constant d_{ij} is connected reciprocally with the piezoelectric stress constant e_{ik} through

$$d_{ij} = \sum_k e_{ik} S_{kj} \tag{5.2}$$

or, vice versa

$$e_{ij} = \sum_k d_{ik} C_{kj} \tag{5.3}$$

where S_{kj} (C_{kj}) is the elastic compliance (stiffness) constant as discussed in Section 3.1. In the case of zinc-blende crystals, the piezoelectric tensor $[d]$ can be expressed by the component d_{14} only

$$d_{14} = e_{14} S_{44} \tag{5.4}$$

We have listed in Tables 5.2 and 5.3 the piezoelectric strain constant d_{ij} reported for some cubic and hexagonal semiconductors, respectively.

5.1.2 Electromechanical coupling constant

It is known [5.8] that injected ultrasonic waves can be amplified in piezoelectric semiconductors by the application of a sufficiently high electric field because of the strong interaction of ultrasonic waves with mobile electrons. Domains of intense acoustic flux, showing a broad band of frequencies in the low-GHz range, can be generated in piezoelectric semiconductors by acoustoelectric amplification of phonons from the thermal equilibrium spectrum [5.9, 5.10]. The gain of such acoustoelectric interactions is explained in terms of the material parameter K, called the electromechanical coupling constant [5.1, 5.11, 5.12]. Carrier mobilities in semiconductors are strongly affected by this coupling constant. The parameter value is also necessary in calculating figures of merit for piezoelectric transducer devices [5.13].

The electromechanical coupling constant K is a crystal-direction-dependent dimensionless quantity. The maximum coupling of transverse acoustic waves occurs along the [110] direction in the zinc-blende crystals [5.11]. This is the reason why the majority of experiments have been carried out with crystals cut in this direction [5.9, 5.10]. The maximum coupling constant $K_{[110]}$ in this case is given by

$$K_{[110]} = \frac{e_{14}}{\sqrt{\varepsilon_0 \varepsilon_s^S C_{44}^D}} \tag{5.5}$$

where e_{14} is the piezoelectric stress constant, ε_0 is the dielectric permittivity of free space (8.8542×10^{-12} F/m), ε_s^S is the static dielectric constant at constant strain and C_{44}^D is the elastic stiffness constant at constant electric displacement. In Table 5.4, we present the functional expressions for the electromechanical coupling constant K giving maximum coupling in the zinc-blende (class T_d) and hexagonal lattices (class C_{6v}) [5.13].

5.2 FRÖHLICH COUPLING CONSTANT

It is known that the coupling between the electrons and LO phonons cannot be neglected in the study of transport and optical properties in polar semiconductors. A measure of the interaction between the electrons and LO phonons can be represented by the well-known Fröhlich coupling constant [5.14]

$$\alpha_F = \frac{1}{2} \frac{e^2/\sqrt{\hbar/2m_c^\alpha \omega_{LO}}}{\hbar\omega_{LO}} \left(\frac{1}{\varepsilon_\infty} - \frac{1}{\varepsilon_s} \right) \tag{5.6}$$

where e is the electron charge, m_c^α is the electron effective mass (conductivity mass), ω_{LO} is the longitudinal optical (LO) phonon frequency and ε_∞ and ε_s are, respectively, the high-frequency and static dielectric constants. Using the effective mass values $m_c^\Gamma = 0.067m_0$ (GaAs) and $0.150m_0$ (AlAs), we obtain the values of α_F for GaAs and AlAs to be 0.068 and 0.126, respectively [5.15].

Table 5.4 Functional expression for the electromechanical coupling constant K giving a maximum coupling in the zinc-blende and hexagonal lattices. Superscripts S and T mean at constant strain and stress, respectively, and D and E at constant electric displacement and field, respectively

Zinc-blende lattice (Class T_d; GaAs, ZnSe, etc.)
$K_{[110]} = \dfrac{e_{14}}{\sqrt{\varepsilon_0 \varepsilon_s^S C_{44}^D}}$
Hexagonal lattice (Class C_{6v}; 4H-SiC, α-GaN, w-CdS, etc.)
$K_{15} = \dfrac{e_{15}}{\sqrt{\varepsilon_0 \varepsilon_{33}^S C_{44}^D}}$
$K_{31} = \dfrac{d_{31}}{\sqrt{\varepsilon_0 \varepsilon_{33}^T S_{11}^E}}$
$K_{33} = \dfrac{d_{33}}{\sqrt{\varepsilon_0 \varepsilon_{33}^T S_{33}^E}}$

Table 5.5 Fröhlich coupling constant α_F and Phillips ionicity f_i for some group-IV, III–V and II–VI semiconductors

System	Material	α_F	f_i	System	Material	α_F	f_i
IV	Diamond	*a*	0	II–VI	ZnO	1.19	0.616
	Si	*a*	0		β-ZnS	0.63	0.623
	Ge	*a*	0		ZnSe	0.432	0.630
	α-Sn	*a*	0		ZnTe	0.332	0.609
	3C-SiC	0.256	0.177		w-CdS	0.514	0.685
					w-CdSe	0.46	0.699
III–V	w-AlN	0.65	0.449		CdTe	0.35	0.717
	AlAs	0.126	0.274				
	AlSb	0.023	0.250				
	α-GaN	0.48	0.500				
	GaP	0.201	0.327				
	GaAs	0.068	0.310				
	GaSb	0.025	0.261				
	InN	0.24	0.578				
	InP	0.15	0.421				
	InAs	0.0454	0.357				
	InSb	0.022	0.321				

[a] Principally showing no Fröhlich coupling interaction

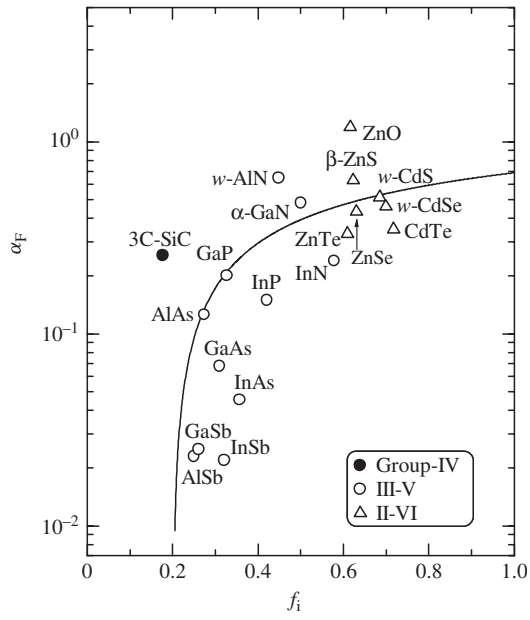

Figure 5.2 Fröhlich coupling constant α_F versus Philips ionicity f_i for some group-IV, III–V and II–VI semiconductors. The solid line represents the least-squares fit with $\alpha_F = 0.43 \ln f_i + 0.69$

The Fröhlich coupling constant α_F is strongly dependent on the ionic polarization of the crystal, which is related to the static and high-frequency dielectric constants ε_s and ε_∞. We summarize in Table 5.5 the Fröhlich coupling constant α_F and Phillips ionicity f_i for some group-IV, III–V and II–VI semiconductors. Figure 5.2 also shows the plots of α_F versus Phillips ionicity f_i for $A^N B^{8-N}$ semiconductors ($N = 2$–4). As clearly seen in Figure 5.2, the Fröhlich coupling constant α_F increases gradually with increasing f_i. This is the general trend of α_F. The solid line in Figure 5.2 represents the least-squares fit with the relation

$$\alpha_F = 0.43 \ln f_i + 0.69 \tag{5.7}$$

REFERENCES

[5.1] J. F. Nye, *Physical Properties of Crystals* (Clarendon, Oxford, 1972).
[5.2] G. Arlt and P. Quadflieg, *Phys. Status Solidi* **25**, 323 (1968).
[5.3] K Hübner, *Phys. Status Solidi B* **57**, 627 (1973).
[5.4] M. Miura, H. Murata, Y. Shiro, and K. Iishi, *J. Phys. Chem. Solids* **42**, 931 (1981).
[5.5] S. de Gironcoli, S. Baroni, and R. Resta, *Phys. Rev. Lett.* **62**, 2853 (1989).
[5.6] J. C. Phillips and J. A. Van Vechten, *Phys. Rev. Lett.* **23**, 1115 (1969).
[5.7] A. Bykhovski, B. Gelmont, M. Shur, and A. Khan, *J. Appl. Phys.* **77**, 1616 (1995); A. Bykhovski, V. V. Kaminski, M. S. Shur, Q. C. Chen, and M. A. Khan, *Appl. Phys. Lett.* **68**, 818 (1996).
[5.8] N. I. Meyer and M. H. Jørgensen, in *Advances in Solid State Physics*, edited by O. Madelung (Pergamon, Vieweg, 1970), p. 21.
[5.9] D. L. Spears, *Phys. Rev. B* **2**, 1931 (1970).

[5.10] E. D. Palik and R. Bray, *Phys. Rev. B* **3**, 3302 (1971).
[5.11] R. Klein, *Solid State Commun.* **7**, 917 (1969).
[5.12] V. M. Bright and W. D. Hunt, *J. Appl. Phys.* **68**, 1985 (1990).
[5.13] H. Jaffe and D. A. Berlincourt, *Proc. IEEE* **53**, 1372 (1965).
[5.14] J. T. Devreese, *Polarons in Ionic Crystals and Polar Semiconductors* (North-Holland, Amsterdam, 1972).
[5.15] S. Adachi, *J. Appl. Phys.* **58**, R1 (1985).

6 Energy-band Structure: Energy-band Gaps

6.1 Basic properties 103
6.1.1 Energy-band structure 103
6.1.2 Electronic density of states 111
6.2 E_0-gap region 114
6.2.1 Effective Γ-point hamiltonian 114
6.2.2 Room-temperature value 115
6.2.3 External perturbation effect 120
6.2.4 Doping effect 126
6.3 Higher-lying direct gap 130
6.3.1 Cubic semiconductor 130
6.3.2 Hexagonal and rhombohedral semiconductors 137
6.4 Lowest indirect gap 137
6.4.1 Room-temperature value 137
6.4.2 External perturbation effect 138
6.5 Conduction-valley energy separation 142
6.6 Direct–indirect-gap transition pressure 142
References 143

6.1 BASIC PROPERTIES

6.1.1 Energy-band structure

The wavefunction $\Psi(\boldsymbol{r})$ of the electrons in a crystal lattice is expressed by the well-known Bloch theorem

$$\Psi(\boldsymbol{r}) = \exp(i\boldsymbol{k} \cdot \boldsymbol{r}) U_k(\boldsymbol{r}) \tag{6.1}$$

where the function $U_k(\boldsymbol{r})$ has a period of the crystal lattice such that $U_k(\boldsymbol{r}) = U_k(\boldsymbol{r} + \boldsymbol{T})$ (here $\boldsymbol{T}$ is any vector of the Bravais lattice). The nearly free-electron approximation is a good starting point for discussing the energy-band theory. It explains the origins of the band gap and of the effective mass m^* which is defined as the reciprocal of the curvature of E (energy) versus $\boldsymbol{k}$ (wavevector) diagram. The functional dependence of E on $\boldsymbol{k}$ for the various bands, $E_n(\boldsymbol{k})$, is defined by the Schrödinger equation

$$H\Psi(\boldsymbol{r}) = \frac{p^2}{2m^*} + V(\boldsymbol{r}) = E\Psi(\boldsymbol{r}) \tag{6.2}$$

Properties of Group-IV, III–V and II–VI Semiconductors Sadao Adachi

© 2005 John Wiley & Sons, Ltd

ISBN: 0-470-09032-4

where $p^2/2m^*$ is the kinetic energy ($\boldsymbol{p} = -i\hbar\nabla$), $V(\boldsymbol{r})$ is the potential energy and E is the energy eigenvalue. Since the electrons in the crystal are influenced by the periodic potential, the electron mass m^* used in Equation (6.2) differs significantly from the free-electron mass m_0.

The reciprocal space, also called phase space, $\boldsymbol{k}$ space and momentum space, is a convenient tool to describe the behavior of both vibrational states and electronic states. The coordinate axes of the reciprocal lattice are the wavevectors of the plane waves corresponding to the vibrational modes or the Bloch states. The Wigner–Seitz unit cell in the reciprocal space is the first Brillouin zone that has already been illustrated in Figures 4.1–4.3.

The characteristics of the electronic energy bands are usually indicated by plotting the energy eigenvalues of the electrons for different values of $\boldsymbol{k}$ in the Brillouin zone. The crystal potential is different in different directions because of the difference in the atomic spacing; as a result, the value of E depends both on the magnitude and on the direction of $\boldsymbol{k}$. In the following, we review the characteristic features of the E–$\boldsymbol{k}$ diagrams for crystals with three different crystal structures: Si (diamond), InP (zinc-blende) and w-CdSe (wurtzite).

(a) Diamond-type semiconductor

In Figure 6.1, we show the relativistic energy-band structure of Si as calculated by Schmid *et al*. [6.1] in the local-density approximation, but with the adjusting potentials included

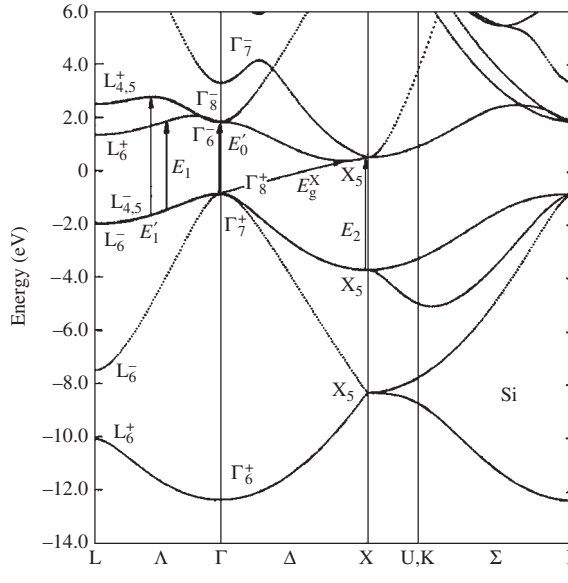

Figure 6.1 Electronic energy-band structure of Si along high-symmetry lines as calculated in the local-density approximation, but with the adjusting potentials included self-consistently. The electronic states are labeled using the notation for the representations of the double-group of the diamond structure. The main interband transitions are indicated by vertical arrows. [From U. Schmid, N. E. Christensen, and M. Cardona, *Phys. Rev. B* **41**, 5919 (1990), reproduced by permission from the American Physical Society]

Table 6.1 Energies of the indirect band gap (E_g^X) and critical point (CP) in Si at 300 K. E_g^X: $\Gamma_8^+ \rightarrow X_5$ transitions

E_g^X, CP	Energy (eV)
E_g^X	1.12
E_0'	3.281–3.5
E_1	3.38
E_0	4.06
$E_0 + \Delta_0$	4.13
E_2	4.27
E_1'	5.32

self-consistently. The electronic states are labeled with the notation for the representations of the double group of the diamond structure. The locations of several interband transitions are indicated in Figure 6.1 by the vertical arrows. These are transitions, which may play an important role in the analysis of optical spectra [6.2]. We also summarize in Table 6.1 the indirect band-gap (E_g^X) and critical-point energies observed in the optical spectra of Si at $T = 300$ K [6.2].

The fundamental absorption edge of Si corresponds to indirect transitions from the highest valence band at the Γ point to the lowest conduction band near X, i.e., $\Gamma_{25'}(\Gamma_8^+) \rightarrow X_1(X_5)$. There is a clear difference in ordering of the first two conduction bands between Si and Ge (α-Sn). In Si, the lowest-lying conduction band at Γ, Γ_{15}, is p-like; however, in Ge and α-Sn the s-like $\Gamma_{2'}$ band is the lowest conduction band. A related effect is the decrease in the optical gap of Si from $\sim$3.3 eV to identically zero is the semimetallic α-Sn.

As schematically shown in Figure 6.2(a), the spin–orbit interaction splits the $\Gamma_{25'}$ valence band into Γ_8^+ and Γ_7^+ (double-group notation, splitting energy Δ_0) and the Γ_{15} conduction band into Γ_6^- and Γ_8^- (splitting energy Δ_0'). The corresponding transitions at or near $\boldsymbol{k} = 0$ are, respectively, labeled E_0 ($\Gamma_8^+ \rightarrow \Gamma_7^-$), $E_0 + \Delta_0$ ($\Gamma_7^+ \rightarrow \Gamma_7^-$), E_0' ($\Gamma_8^+ \rightarrow \Gamma_6^-$), $E_0' + \Delta_0'$ ($\Gamma_8^+ \rightarrow \Gamma_8^-$), $E_0' + \Delta_0$ ($\Gamma_7^+ \rightarrow \Gamma_6^-$, dipole forbidden) and $E_0' + \Delta_0' + \Delta_0$ ($\Gamma_7^+ \rightarrow \Gamma_8^-$).

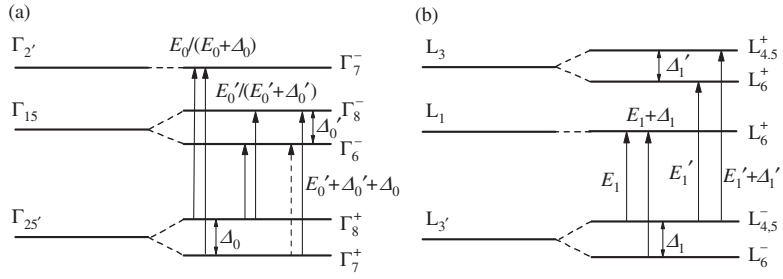

Figure 6.2 (a) Energy gaps at or near the Γ point in Si with and without considering the spin–orbit interaction. Note that the $E_0' + \Delta_0$ transitions are dipole forbidden; (b) energy gaps at or near the L point in Si with and without considering the spin–orbit interaction

As seen in Figure 6.2(b), the spin–orbit interaction splits the $L_{3'}$ valence band into $L_{4,5}^-$ and L_6^- and the L_3 conduction band into L_6^+ and $L_{4,5}^+$. The corresponding transitions at or near L (along the ⟨111⟩ direction (Λ) of the Brillouin zone) are, respectively, labeled E_1 ($L_{4,5}^- \rightarrow L_6^+$), $E_1 + \Delta_1$ ($L_6^- \rightarrow L_6^+$), E_1' ($L_{4,5}^- \rightarrow L_6^+$) and $E_1' + \Delta_1'$ ($L_{4,5}^- \rightarrow L_{4,5}^+$). The E_2 transitions are also expected to occur along the ⟨110⟩ (Σ) or near X, i.e., X_5 (X_4) → X_5 (X_1).

The spin–orbit splitting energies Δ_0 and Δ_0' of Si are very small and have not been taken into consideration in the analysis of optical spectrum [6.2]. Similarly, the spin–orbit splitting energies Δ_1 and Δ_1' of Si are extremely small and, thus, no clear observations relating to them have been reported so far. It is also not easy to observe the $E_0/(E_0 + \Delta_0)$ edges of Si because of their exceedingly weak nature in this material [6.3].

The lowest direct band gap of Si is the E_0' edge. The E_1 transitions in Si are nearly degenerate with the E_0' transitions and, therefore, most attention had been given to these complicated E_1-edge structures (3.1–3.4 eV region). The edge labeled E_1' is well separated in energy from other critical points.

(b) Zinc-blende-type semiconductor

InP crystallizes in the zinc-blende structure. The electronic energy-band structure of InP as calculated by an empirical nonlocal pseudopotential method by Chelikowsky and Cohen [6.4] is reproduced in Figure 6.3. The electronic states are labeled with the notation for the representations of the double-group of the zinc-blende structure. Several interband

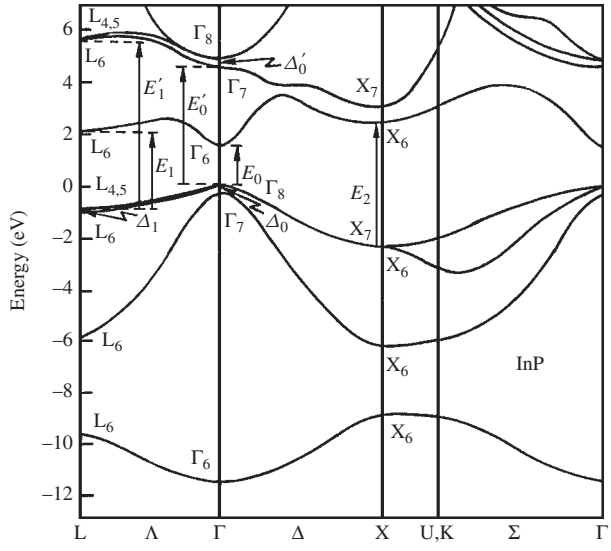

Figure 6.3 Electronic energy-band structure of InP as calculated by an empirical nonlocal pseudopotential method. The electronic states are labeled using the notation for the representations of the double-group of the zinc-blende structure. The main interband transitions are indicated by vertical arrows. [From J. R. Chelikowsky and M. L. Cohen, *Phys. Rev. B* **14**, 556 (1976), reproduced by permission from the American Physical Society]

Table 6.2 Energies of the critical point (CP) and indirect band gap (E_g^{ID}) in InP at 300 K. E_g^L: $\Gamma_8 \rightarrow L_6$ transitions; E_g^X: $\Gamma_8 \rightarrow X_6$ transitions

CP, E_g^{ID}	Energy (eV)
E_0	1.35
$E_0 + \Delta_0$	1.45
E_g^L	2.05
E_g^X	2.21
E_1	3.17
$E_1 + \Delta_1$	3.29
E_0'	4.70
$E_0' + \Delta_0'$	4.79
E_2	5.10
$E_2 + \delta$	5.69
E_1'	~6.5

transitions are included in Figure 6.3. Table 6.2 summarizes the critical-point and indirect band-gap energies for InP at $T = 300$ K [6.5, 6.6].

The fundamental absorption edge of InP corresponds to direct transitions from the highest valence band at the Γ point to the lowest conduction band at the Γ point (E_0, $\Gamma_8 \rightarrow \Gamma_6$). Transitions at this edge are sometimes dominated by free excitons, a fact which is particularly evident at low temperatures [6.7]. The excitonic transition energy is ~5 meV less than the E_0 edge. The second lowest interband critical point, $E_0 + \Delta_0$, corresponds to transitions from the larger component of the spin–orbit split-off valence band to the lowest conduction band at the Γ point ($\Gamma_7 \rightarrow \Gamma_6$). In Figure 6.4(a), we show the energy diagram indicating the spin–orbit splitting at or near the Γ point of the zinc-blende-type semiconductors.

The E_1 and $E_1 + \Delta_1$ transitions in InP occur along the Λ lines ($\langle 111 \rangle$ directions) or at the L point of the Brillouin zone (Figure 6.4(b)). In the energy region from 4.7 to 5.7 eV

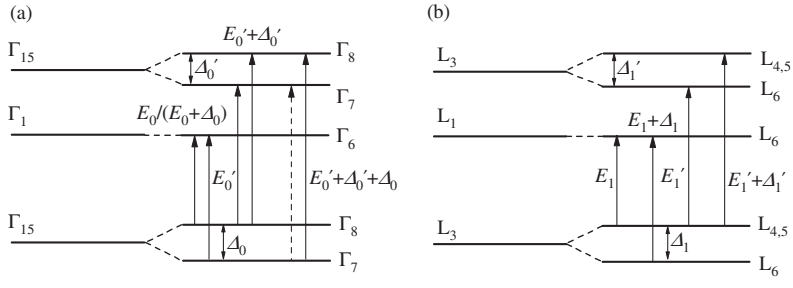

Figure 6.4 (a) Energy gaps at or near the Γ point in InP with and without considering the spin–orbit interaction. Note that the $E_0' + \Delta_0$ transitions are dipole forbidden; (b) energy gaps at or near the L point in InP with and without considering the spin–orbit interaction

in InP, several critical points have been resolved [6.5, 6.6, 6.8]. The most prominent ones have been assigned to transitions near the Γ point (E_0' triplet). In the 5.1–5.7 eV region, the E_2 and $E_2 + \delta$ transitions are expected to occur along the ⟨110⟩ (Σ) or near X ($X_7 \rightarrow X_6$ (E_2), $X_7 \rightarrow X_7$ ($E_2 + \delta$)). Note that the splitting energy δ at the X point is zero in covalent, diamond-type semiconductors (Si, Ge, etc.).

(c) Wurtzite-type semiconductor

CdSe normally crystallizes in the wurtzite structure (w-CdSe). Figure 6.5 shows the electronic energy-band structure of w-CdSe as calculated in terms of a nearest-neighbor empirical tight-binding theory by Kobayashi *et al.* [6.9]. The dashed lines show the results derived from the semi-empirical pseudopotential method [6.10]. It should be noted that in the calculations no account had been taken of spin–orbit interaction effects. Table 6.3 lists the critical-point energies of w-CdS at $T = 300$ K [6.11, 6.12].

Birman [6.13] discussed the relationship between the $\boldsymbol{k} = 0$ conduction-band and valence-band states of the wurtzite structure and the corresponding states of the zinc-blende structure. As noted by him, the essential difference between the potential that an electron experiences in an ideal wurtzite lattice and that in a zinc-blende lattice is the relatively small difference in 'crystal field' due to sites beyond the next nearest neighbors. The detailed differences in the energy bands then arise from the difference in the crystal field and from the difference in the Brillouin zones. The conduction-band and valence-band structures proposed for wurtzite at $\boldsymbol{k} = 0$ (Γ) are illustrated in Figure 6.6. As seen in Figure 6.6, the triplet states of zinc-blende (Γ_{15}) correspond to a doublet (Γ_5) and a singlet (Γ_1) of wurtzite. The Γ_5 and Γ_1 states are separated by Δ_{cr}, the crystal-field splitting. In the actual valence-band structure of a wurtzite crystal, the three valence bands illustrated in Figures 6.6(d) and 6.6(e) can be thought of as arising from Figure 6.6(a) by the combined effect of both spin–orbit and crystal-field perturbations, while the wavefunction for each band may be written as a linear combination of p_x, p_y and p_z and spin functions, provided the interaction of the Γ_7 levels with the conduction band is neglected. This result is known as the quasi-cubic model [6.14].

Under the spin–orbit interaction, represented by the matrix element Δ_{so} and that of the crystal field represented by Δ_{cr}, the differences in energy of the split-off valence bands are given by [6.14]

$$E_{BA} = E_{0B} - E_{0A} = \frac{\Delta_{so} + \Delta_{cr}}{2} - \sqrt{\left(\frac{\Delta_{so} + \Delta_{cr}}{2}\right) - \frac{2}{3}\Delta_{so}\Delta_{cr}} \tag{6.3a}$$

$$E_{CA} = E_{0C} - E_{0A} = \frac{\Delta_{so} + \Delta_{cr}}{2} + \sqrt{\left(\frac{\Delta_{so} + \Delta_{cr}}{2}\right) - \frac{2}{3}\Delta_{so}\Delta_{cr}} \tag{6.3b}$$

The corresponding wavefunctions of the three valence bands are given by

$$|A\rangle : S_+ \uparrow \tag{6.4a}$$

$$|B\rangle : \alpha_B S_- \uparrow + \alpha_C S_0 \downarrow \tag{6.4b}$$

$$|C\rangle : \alpha_C S_- \uparrow + \alpha_B S_0 \downarrow \tag{6.4c}$$

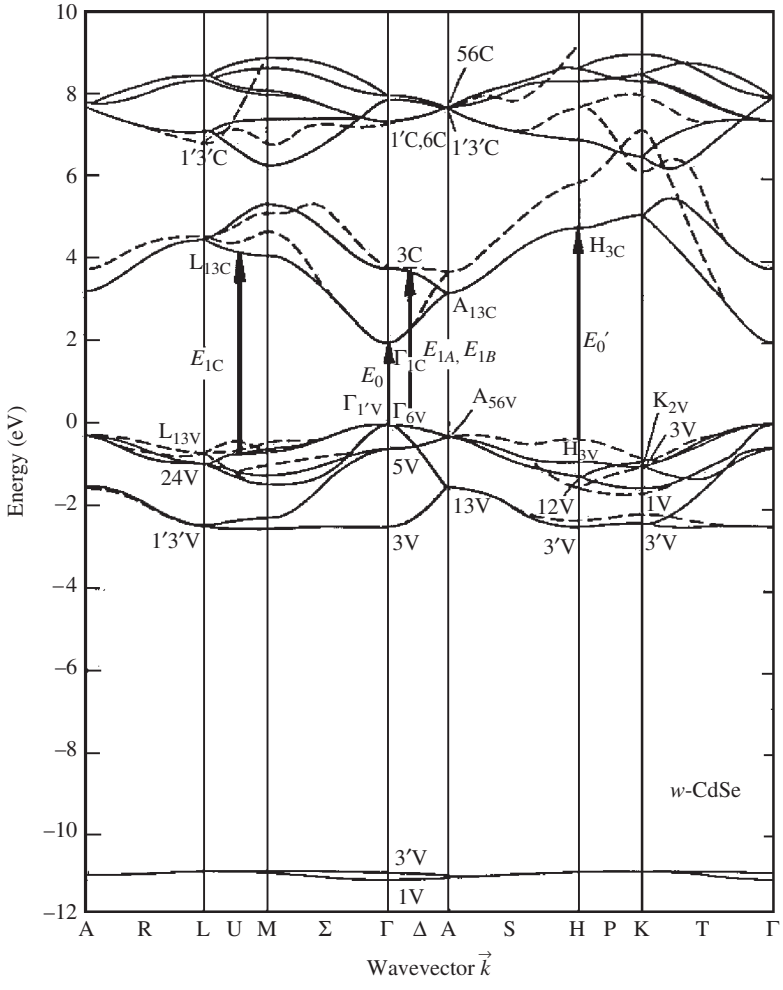

Figure 6.5 Electronic energy-band structure of *w*-CdSe as calculated with an empirical tight-binding theory. In the calculation, no account had been taken of the spin–orbit interaction effects. The dashed lines show the results derived from the semiempirical pseudopotential method by Bergstresser and Cohen [6.10]. The locations of several interband transitions are also indicated by the vertical arrows. These are transitions, which may play an important part in the analysis of optical spectra. [From A. Kobayashi, O. F. Sankey, S. M. Volz, and J. D. Dow, *Phys. Rev. B* **28**, 935 (1983), reproduced by permission from the American Physical Society]

where $\uparrow$ and $\downarrow$ represent spin-up and spin-down, respectively, and S_+, S_- and S_0 are functions defined by the p-like basis functions. The admixture coefficients α_B and α_C can now be given by

$$\alpha_B = \left[1 + \frac{1}{2}\left(2 - \frac{3}{\Delta_{so}} E_{BA}\right)^2\right]^{-1/2} \tag{6.5a}$$

Table 6.3 Energies of the critical point (CP) in w-CdSe at 300 K

CP	Energy (eV)	
	$\boldsymbol{E} \perp c$	$\boldsymbol{E} \parallel c$
E_{0A}	1.732	
E_{0B}	1.761	1.761
E_{0C}	2.161	2.161
E_{1A}	4.10	
E_{1B}	4.55	
E_{1C}	4.85	4.78
E_0'	5.6	6.0
E_2'	7.6, 8.7[a]	
E_1'	9.5[a]	

[a]For unpolarized light

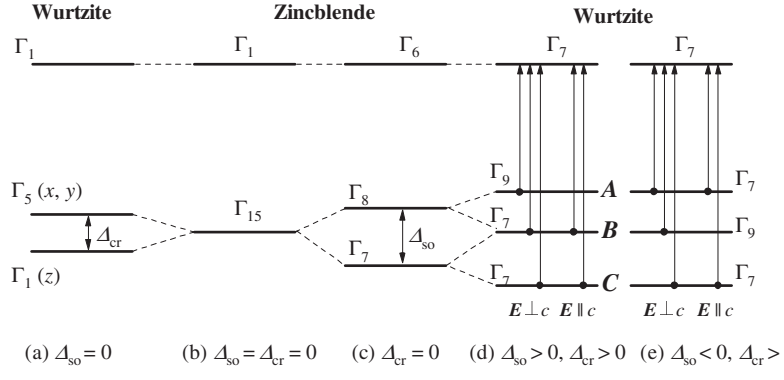

Figure 6.6 Relationships between the valence-band splitting in the zinc-blende and wurtzite lattices and between the irreducible representations of the bands at the Γ point ($\boldsymbol{k} = 0$). (c) shows the actual splitting found in the zinc-blende crystals, while (d) and (e) give that found in the wurtzite crystals. (a)–(c) show the relationship of these splitting to simpler cases where spin–orbit and/or crystal-field interaction vanish

$$\alpha_C = \left[1 + \frac{1}{2}\left(2 - \frac{3}{\Delta_{so}} E_{CA}\right)^2\right]^{-1/2} \tag{6.5b}$$

with

$$\alpha_B^2 + \alpha_C^2 = 1 \tag{6.6}$$

For w-CdSe, we obtain $\Delta_{so} = 412.8$ meV, $\Delta_{cr} = 45.2$ meV, $\alpha_B = 0.620$ and $\alpha_C = 0.785$ (Figure 6.6(d)), while those for ZnO are $\Delta_{so} = -19$ meV, $\Delta_{cr} = 49$ meV, $\alpha_B = 0.988$ and $\alpha_C = 0.155$ (Figure 6.6(e)).

The corresponding momentum matrix (p-matrix) elements $|\langle c|\boldsymbol{p}|v\rangle|^2$ between the p-like valence and s-like conduction bands are given by

$$P_{0A}(\perp)^2 = P^2/2, \quad P_{0B}(\perp)^2 = \alpha_B^2 P^2/2, \quad P_{0C}(\perp)^2 = \alpha_C^2 P^2/2 \tag{6.7a}$$

for the light polarization $\boldsymbol{E} \perp c$ (ordinary ray), and

$$P_{0A}(\parallel)^2 = 0, \quad P_{0B}(\parallel)^2 = \alpha_C^2 P^2, \quad P_{0C}(\parallel)^2 = \alpha_B^2 P^2 \tag{6.7b}$$

for the light polarization $\boldsymbol{E} \parallel c$ (extraordinary ray).

The wurtzite-type crystals have a C_{6v} point-group symmetry. At the center of the Brillouin zone, the conduction band has Γ_7 (s-like) symmetry and the A, B and C valence bands have, respectively, Γ_9, Γ_7 and Γ_7 (p-like) symmetries. The polarization vectors $\boldsymbol{E} \perp c$ and $\boldsymbol{E} \parallel c$ of the point group C_{6v} belong to Γ_5 and Γ_1 symmetries, respectively. The direct products can now be given by

$$\Gamma_9 \rightarrow \Gamma_7(\mathrm{A}) : \Gamma_9 \times \Gamma_7 = \Gamma_5 + \Gamma_6 \tag{6.8a}$$

$$\Gamma_7 \rightarrow \Gamma_7(\mathrm{B, C}) : \Gamma_7 \times \Gamma_7 = \Gamma_1 + \Gamma_2 + \Gamma_5 \tag{6.8b}$$

The direct product $\Gamma_7 \times \Gamma_7$ then contains the representations for both $\boldsymbol{E} \perp c$ and $\boldsymbol{E} \parallel c$, but $\Gamma_9 \times \Gamma_7$ contains only the representation for $\boldsymbol{E} \perp c$. This means that for $\boldsymbol{E} \parallel c$ the optical transition between the A valence and conduction bands is forbidden, while for $\boldsymbol{E} \perp c$ all the optical transitions are possible, in agreement with those given by Equation (6.7).

The structures seen in w-CdSe in the energy region higher than $E_{0\alpha}$ (α = A, B and C; ~1.7 eV) are labeled $E_{1\alpha}$ (α = A, B and C; ~4.1–4.9 eV). The original assignment of these structures was made by Cardona [6.12]; they correspond to the E_1 and $E_1 + \Delta_1$ transitions of the zinc-blende-type materials, except for the existence of a strong polarization effect related to the optical anisotropy of wurtzite. The E_{1A} and E_{1B} peaks may be related to transitions along the Δ axis ($\Delta_5 \rightarrow \Delta_3$) in the Brillouin zone which are split by the spin–orbit interaction. These peaks are forbidden for $\boldsymbol{E} \parallel c$ (i.e., only the E_{1C} peak appears for $\boldsymbol{E} \parallel c$ polarization). The E_{1C} structure may originate from transitions at the U point in the Brillouin zone.

The E_0' structure (~6 eV) may originate from transitions at the M point in the Brillouin zone [6.15]. Spectroscopic ellipsometry measurements revealed several additional peaks, such as F_1, E_2, E_1', C' and D', at energies higher than 7 eV [6.16]. These transitions correspond to higher critical points and core excitons.

6.1.2 Electronic density of states

The electronic density of states can be calculated in the same way as that for phonons (Section 4.1). An expression for the electron density of states $g(E)$ per unit volume ($n = 3$), area ($n = 2$) or length ($n = 1$) can be given by

$$g(E) = 2\frac{\mathrm{d}}{\mathrm{d}E}\int \frac{\mathrm{d}^n k}{(2\pi)^n}\delta[E - E_C(\boldsymbol{k})] \tag{6.9}$$

where $n = 3, 2$ or 1 depending on the dimension of the system. A factor two in Equation (6.9) accounts for spin-up and spin-down. Assuming a parabolic band with an isotropic effective mass m^*, the energy of the conduction-band electrons is given by

$$E_C(\boldsymbol{k}) = E_{C0} + \frac{(\hbar \boldsymbol{k})^2}{2m^*} \tag{6.10}$$

where E_{C0} is the energy at the conduction-band minimum. The volume elements of $\boldsymbol{k}$ space in Equation (6.9) can be replaced by $\mathrm{d}^3k = 4\pi k^2 \mathrm{d}k$ for $n = 3$, $\mathrm{d}^2k = 2\pi k\,\mathrm{d}k$ for $n = 2$ and $\mathrm{d}k = \mathrm{d}k$ for $n = 1$. The density of states can, then, be written as

$$g(E) = \frac{(2m^*)^{3/2}}{2\pi^2\hbar^3}\sqrt{E - E_{C0}}H(E - E_{C0}) \tag{6.11}$$

for $n = 3$,

$$g(E) = \frac{m^*}{\pi\hbar^2}H(E - E_{C0}) \tag{6.12}$$

for $n = 2$ and

$$g(E) = \frac{1}{\pi\hbar}\sqrt{\frac{2m^*}{E - E_{C0}}}H(E - E_{C0}) \tag{6.13}$$

for $n = 1$, where $H(x)$ is the Heaviside function, defined by

$$H(x) = \begin{cases} 0 & \text{for } x < 0 \\ 1 & \text{for } x > 0 \end{cases} \tag{6.14}$$

Since the longitudinal effective masses at the L-conduction and X-conduction bands in the zinc-blende-type semiconductors are much larger than their counterparts, these electrons can be treated as those in the two dimensional state ($n = 2$). The two-dimensional density of states has also been directly observed in field-effect transistors and quantum wells. A one-dimensional system can be realized by a semiconductor quantum wire and by a bulk semiconductor experiencing a magnetic field. The results given in Equations (6.11)–(6.13) are valid for electrons near the conduction-band minimum. In order to use these results for holes near the valence-band maximum, one has to replace $E - E_{C0}$ by $E_{V0} - E$, where E_{V0} is the energy at the valence-band maximum.

In Figure 6.7, we show the calculated band structure and Gaussian-broadened density of states for Ge compared to experimental X-ray photoelectron spectroscopy (XPS) and bremsstrahlung isochromat spectroscopy (BIS) results recorded with $E = 1486.6$ eV [6.17]. The theoretical band structure and density of states were obtained with the empirical pseudopotential method. The XPS usually supplies direct information about the absolute energies of the valence-band states and less direct information about the empty states. The development of $\boldsymbol{k}$-resolved inverse-photoemission spectroscopy and the application of BIS can give a broad overview of both occupied and empty states. As seen in Figure 6.7, the conduction-band structure in the 2–5 eV region is reproduced by band theory quite accurately. Chelikowsky *et al.* [6.17] investigated the density of states not only for Ge, but also for GaAs and ZnSe. These materials have the same lattice parameters and the same electronic configuration within the ion core. Hence, differences in the electronic structure can be attributed to bonding changes. They found the great

similarity in the conduction-band density of states for the series Ge to GaAs to ZnSe. The main features of the conduction-band density of states are not changed by increasing ionicity of the crystals. This is not true for the valence-band density of states, and there is no real analog in the conduction bands for the antisymmetric gap in the valence bands. The largest effect of increasing ionicity is to increase the band gaps from Ge to GaAs to ZnSe, but not to change significantly the band dispersion.

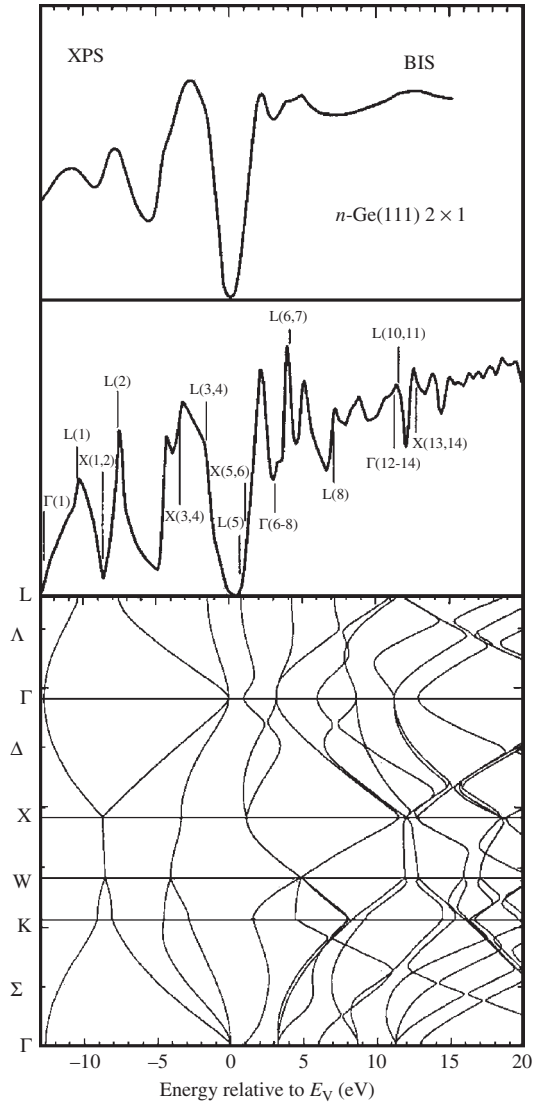

Figure 6.7 Calculated energy bands and Gaussian-broadened density of states for Ge compared to experimental XPS and BIS results taken with $E = 1486.6$ eV. The XPS and BIS results are normalized for visual clarity. [From J. R. Chelikowsky, T. J. Wagener, J. H. Weaver, and A. Jin, *Phys. Rev. B* **40**, 9644 (1989), reproduced by permission from the American Physical Society]

6.2 E_0-GAP REGION

6.2.1 Effective Γ-point hamiltonian

As mentioned in Section 6.1, the six valence bands (p-like Γ_{15}) in a scalar-relativistic representation of a zinc-blende semiconductor are all degenerate at point Γ ($\boldsymbol{k} = 0$). Each band has, in general, a different curvature so that they split near Γ ($\boldsymbol{k} \neq 0$). The scalar bands retain two-fold spin degeneracy, and they are symmetric in $\pm\boldsymbol{k}$ due to time-reversal symmetry. When spin–orbit effects are included, the two spin–orbit split-off hole states (Γ_7) drop in energy, opening a gap (Δ_0) to the Γ_8 light-hole and heavy-hole bands. The $\pm\boldsymbol{k}$ symmetry is lost when the spin–orbit interaction is included. The four-fold-degenerate Γ_8 states are split by small amounts and intermixed away from the Γ point, depending on the direction of $\boldsymbol{k}$ for the states in question [6.18–6.20]. This splitting is linear to lowest order in the distance $|\boldsymbol{k}|$ from the center of the Brillouin zone so that the extrema of the valence bands are displaced. The spin–orbit split-off hole band (Γ_7) is two-fold spin degenerate at point Γ, and it splits as $|\boldsymbol{k}|^3$ to lowest order in all but the [111] and [100] directions where it remains degenerate. The s-like Γ_6 conduction band also splits as $|\boldsymbol{k}|^3$ for $\boldsymbol{k}$ in the [110] direction. The spin–orbit splitting in zinc-blende-type semiconductors has been investigated theoretically by several authors using various calculation techniques [6.20]. They have, however, not been usually observed experimentally because of the small size of $|\boldsymbol{k}|$ and their small energies.

The effective Hamiltonians for the lowest two conduction bands and the highest six valence bands at the Γ point in the zinc-blende-type semiconductors are, respectively, written as [6.21]

$$H_{\mathrm{c}}^{\mathrm{ZB}} = \frac{\hbar^2 k^2}{2m_{\mathrm{e}}^{\Gamma}} + a_{\mathrm{c}}^{\Gamma}(e_{xx} + e_{yy} + e_{zz}) \tag{6.15}$$

and

$$H_{\mathrm{v}}^{\mathrm{ZB}} = \frac{1}{3}\Delta_{\mathrm{so}}(\boldsymbol{L}\cdot\boldsymbol{\sigma}) - (\gamma_1 + 4\gamma_2)k^2 + 6\gamma_2(\boldsymbol{L}\cdot\boldsymbol{k})^2 - 6(\gamma_2 - \gamma_3)\sum_{i,j}[L_i, L_j]k_i k_j$$
$$+ (a + 2b)(e_{xx} + e_{yy} + e_{zz}) - 3b\sum_i L_i^2 e_{ii} - \sqrt{3}d\sum_{i,j}[L_i, L_j]e_{ij} \tag{6.16}$$

where m_{e}^{Γ} is the electron effective mass, a_{c}^{Γ}, a, b and d are Bir–Pikus deformation potentials, e_{ij} is the strain-tensor component (i, $j = x, y$ or z), $\Delta_{\mathrm{so}} = \Delta_0$ is the spin–orbit split-off energy, $\boldsymbol{L}$ and $\boldsymbol{\sigma}$ are the orbital and spin angular momentum operators, respectively, $[L_i, L_j]$ is defined by $[L_i, L_j] = (L_i L_j + L_j L_i)/2$ and γ_i ($i = 1 - 3$) are Luttinger valence-band parameters.

The effective Hamiltonians for the lowest two conduction bands and the highest six valence bands at the Γ point in the wurtzite-type semiconductors are, respectively, given by [6.21]

$$H_{\mathrm{c}}^{\mathrm{W}} = \frac{\hbar^2 k_z^2}{2m_{\mathrm{e}}^{\parallel}} + \frac{\hbar^2(k_x^2 + k_y^2)}{2m_{\mathrm{e}}^{\perp}} + D_1 e_{zz} + D_2(e_{xx} + e_{yy}) \tag{6.17}$$

and

$$H_{\mathrm{v}}^{\mathrm{W}} = \Delta_1 L_z^2 + \Delta_2 L_z \sigma_z + \sqrt{2}\Delta_3 (L_+ \sigma_- + L_- \sigma_+) + (A_1 + A_3 L_z^2) k_z^2 + (A_2 + A_4 L_z^2) k_\perp^2 - A_5 (L_+^2 k_-^2 + L_-^2 k_+^2) - 2A_6 k_z ([L_z, L_+] k_- + [L_z, L_-] k_+) + i A_7 (L_+ k_- - L_- k_+) + (C_1 + C_3 L_z^2) e_{zz} + (C_2 + C_4 L_z^2) e_\perp - C_5 (L_+^2 e_- + L_-^2 e_+) - 2C_6 ([L_z, L_+] e_{-z} + [L_z, L_-] e_{+z}) \tag{6.18}$$

where $m_{\mathrm{e}}^{\parallel}$ and $m_{\mathrm{e}}^{\perp}$ are $\boldsymbol{k}$-dependent electron effective masses, D_i ($i = 1, 2$) and C_i ($i = 1$–6) are Bir–Pikus deformation potentials, A_i ($i = 1$–6) are Luttinger valence-band parameters and Δ_1 and $\Delta_{2,3}$ correspond to the crystal-field and spin–orbit splitting parameters in eV, respectively. $L_\pm = (L_x \pm i L_y)/\sqrt{2}$, $\sigma_\pm = (\sigma_x \pm i\sigma_y)/2$, $k_\perp^2 = k_x^2 + k_y^2$, $k_\pm = k_x \pm i k_y$, $e_\perp = e_{xx} + e_{yy}$, $e_\pm = e_{xx} - e_{yy} \pm 2i e_{xy}$ and $e_{\pm z} = e_{xz} \pm i e_{yz}$. Note that in the quasi-cubic approximation, the energy parameters Δ_1–Δ_3 in the wurtzite structure are related to the zinc-blende parameters Δ_{cr} and Δ_{so} in the manner

$$\begin{aligned} \Delta_1 &= \Delta_{\mathrm{cr}} \\ 3\Delta_2 &= 3\Delta_3 = \Delta_{\mathrm{so}} \end{aligned} \tag{6.19}$$

6.2.2 Room-temperature value

There have been many experimental measurements of E_0-gap and $E_0 + \Delta_0$-gap energies of semiconductors over a wide range of temperatures. We list in Table 6.4 the room-temperature E_0 and $E_0 + \Delta_0$ values for some cubic group-IV, III–V and II–VI semiconductors. Table 6.5 also lists the lowest direct band-gap values $E_{0\alpha}$ (α = A, B or C) for some hexagonal semiconductors at $T = 300$ K. The InN value is reported to be $E_0 = 1.89$ eV [6.22]. Note, however, that very recent studies suggest evidence of the narrow band-gap energy of ~0.7–1.1 eV for this material [6.23–6.28].

We plot in Figure 6.8 the E_0-gap energy versus lattice constant a for some group-IV, III–V and II–VI semiconductors. The solid line represents the least-squares fit with the relation (a in Å; E_0 in eV)

$$E_0 = 18.55 - 2.84a \tag{6.20}$$

An increase in E_0 with decreasing a can be understood from Figure 6.9 in which the energy banding of allowed levels in tetrahedrally bonded group-IV semiconductors as a result of the sp^3 hybridization of electron orbitals is schematically shown, together with their E_0 versus a plots.

Figure 6.10 shows the lowest direct band-gap energy E_0 plotted versus molecular weight M for some group-IV, III–V and II–VI semiconductors. The solid line represents the least-squares fit with the relation (M in amu; E_0 in eV)

$$E_0 = 20.51 - 3.72 \ln M \tag{6.21}$$

It has already been shown in Section 1.4 that the relation between the lattice constant a and molecular weight M can be simply given by $a = 0.579 + 1.04 \ln M$ (M in amu; a in

Table 6.4 E_0-gap and $E_0 + \Delta_0$-gap energies for some cubic group-IV, III–V and II–VI semiconductors at 300 K

System	Material	E_0 (eV)	$E_0 + \Delta_0$ (eV)
IV	Diamond	15.3	
	Si	4.06	4.13
	Ge	0.795	1.08
	α-Sn	$-0.413^{a,b}$	~ 0.4 ($\lvert\Gamma_7^{-c} - \Gamma_7^{+v}\rvert$)^a
	3C-SiC	7.4	
III–V	c-BN	$7.9-11.40^c$	
	BP	5	
	BAs	1.45^d	
	c-AlN	5.2	
	AlP	3.91^e	
	AlAs	3.01	3.22
	AlSb	2.27	2.94
	β-GaN	3.231^f	3.248^f
	GaP	2.76	2.84
	GaAs	1.43	1.76
	GaSb	0.72	1.50
	InP	1.35	1.46
	InAs	0.359	0.726
	InSb	0.17	1.04
II–VI	MgO	7.8	
	β-MgS	4.45	4.52
	β-MgSe	4.0	4.4
	β-MgTe	3.4	4.35
	β-ZnS	3.726	3.796
	ZnSe	2.721	3.145
	ZnTe	2.27	3.22
	c-CdS	2.46	2.53
	c-CdSe	1.675	2.07
	CdTe	1.51	2.41
	β-HgS	$-0.04^{c,g}$	~ 0.03 ($\lvert\Gamma_6^c - \Gamma_7^v\rvert$)^c
	HgSe	-0.08^g	~ 0.3 ($\lvert\Gamma_6^c - \Gamma_7^v\rvert$)
	HgTe	-0.15^g	~ 0.8 ($\lvert\Gamma_6^c - \Gamma_7^v\rvert$)

[a] At $T = 1.5$ K
[b] The sign is chosen positive for a normal band structure like that of Ge
[c] Calculated or estimated
[d] Tentative assignment
[e] Estimated from $Al_xGa_{1-x}P$ data
[f] Grown on MgO(100) substrate
[g] The sign is chosen positive for a normal band structure like that of CdTe

Table 6.5 $E_{0\alpha}$ (α = A, B or C)-gap or its excitonic gap energy for some hexagonal group-IV, III–V and II–VI semiconductors at 300 K

System	Material	E_{0A} (eV)	E_{0B} (eV)	E_{0C} (eV)
IV	6H-SiC	5.14[a]		
III–V	w-AlN	6.2		
	α-GaN	3.420	3.428	
	InN	1.89 (0.7–1.1[b])		
II–VI	ZnO	3.40	3.45	3.55
	α-ZnS	3.75	3.78	3.87
	w-CdS	2.501	2.516	2.579
	w-CdSe	1.751	1.771	2.176

[a] Calculated

[b] Note that very recent studies for InN suggest an evidence of the narrow band-gap energy of $E_0 \sim 0.7$–1.1 eV

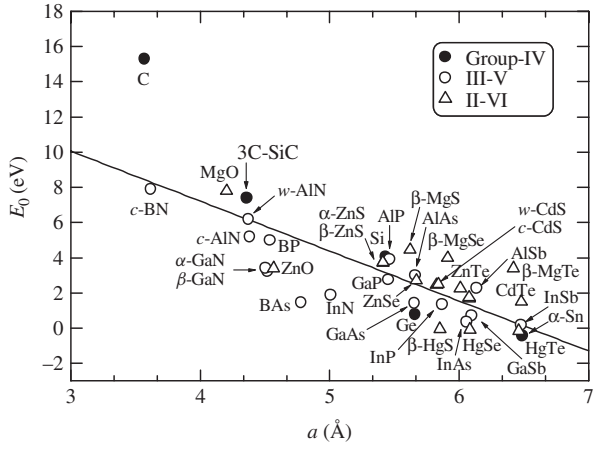

Figure 6.8 E_0-gap energy versus lattice constant a for some group-IV, III–V and II–VI semiconductors at 300 K. For hexagonal semiconductors, an effective lattice constant $a_{\text{eff}} = (\sqrt{3}a^2c)^{1/3}$ is plotted instead of a. The solid line represents the least-squares fit with $E_0 = 18.55 - 2.84a$ (a in Å; E_0 in eV)

Å). Introducing this equation into Equation (6.20), we obtain (M in amu; E_0 in eV)

$$E_0 = 16.91 - 2.95 \ln M \tag{6.22}$$

The dashed line in Figure 6.10 shows the calculated result of Equation (6.22).

We summarize in Table 6.6 the spin–orbit split-off Δ_{so} and crystal-field splitting energies Δ_{cr} for some group-IV, III–V and II–VI semiconductors. Note that these energies may not vary so largely with temperature if one supposes the valence-band rigidity of such semiconductors. In Figure 6.11, we plot the variation of Δ_0 for some group-IV, III–V

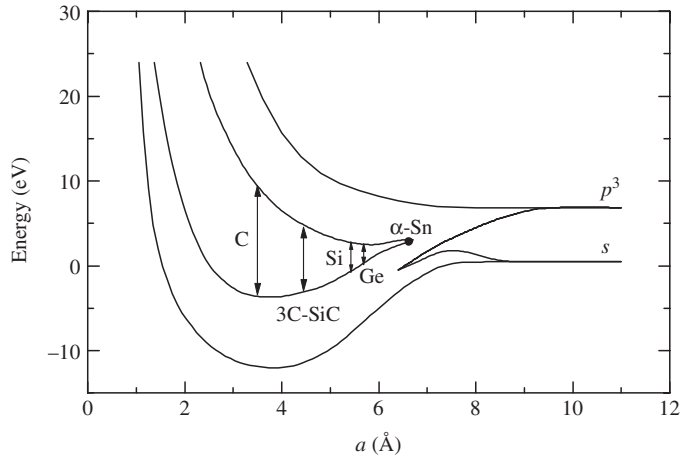

Figure 6.9 Energy banding of allowed levels in tetrahedrally bonded group-IV semiconductors versus lattice constant a

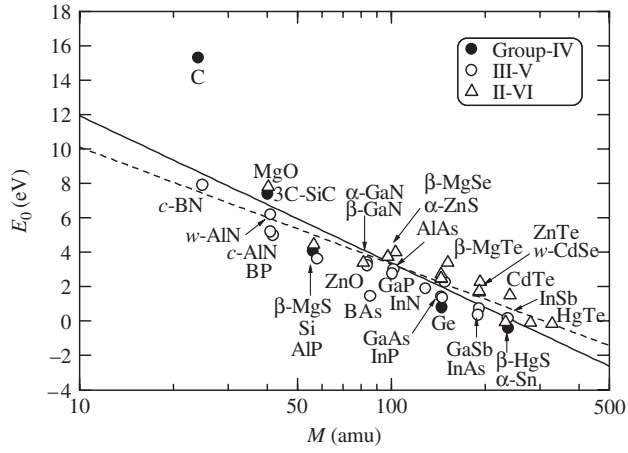

Figure 6.10 E_0-gap energy at 300 K versus molecular weight M for some group-IV, III–V and II–VI semiconductors. The solid line represents the least-squares fit with $E_0 = 20.51 - 3.72 \ln M$, while the dashed line represents the relation with $E_0 = 16.91 - 2.95 \ln M$ (M in amu; E_0 in eV)

and II–VI semiconductors with respect to the group IV, V and VI anions. The valence and conduction bands of the III–V (II–VI) semiconductors can be well characterized by electron orbital of the group V (VI) anions and group III (II) cations, respectively. It is evident from Figure 6.11 that there is an increase in Δ_0 with increase in the atomic number of the anion atoms. It is also clear from Figure 6.11 that the common anion group has nearly the same Δ_0 value. It is noted that GaAs, AlAs and their alloy are the common anion group. We can, therefore, expect that if the bowing parameter is small, Δ_0 in $Al_xGa_{1-x}As$ alloy is nearly constant over the entire cation concentration ($0 \leqslant x \leqslant 1.0$).

Table 6.6 Spin–orbit split-off and crystal-field splitting energies, Δ_{so} (Δ_0) and Δ_{cr}, for some group-IV, III–V and II–VI semiconductors. Note that for wurtzite semiconductors the quasi-cubic approximation ($\Delta_{cr} = \Delta_1$; $\Delta_{so} = 3\Delta_2 = 3\Delta_3$) is assumed

System	Material	Δ_{so} (meV)	Δ_{cr} (meV)	System	Material	Δ_{so} (meV)	Δ_{cr} (meV)
IV	Diamond	6		II–VI	MgO	22	
	Si	42.62			β-MgS	70[a]	
	Ge	295			β-MgSe	420[a]	
	α-Sn	800			β-MgTe	950[a]	
	3C-SiC	10			ZnO	−3.5 (16[b])	39.4 (43[b])
	6H-SiC	7.8	48.7		α-ZnS	92	55
	15R-SiC	7.15	51		β-ZnS	70	
					ZnSe	424	
III–V	c-BN	21[a]			ZnTe	950	
	w-AlN	16[a]	−161[a]		c-CdS	∼70	
	c-AlN	11–33[a]			w-CdS	65	28
	AlP	40[a]			c-CdSe	410	
	AlAs	325			w-CdSe	420	40
	AlSb	673			CdTe	900	
	α-GaN	15.5	15.2		β-HgS	70[a]	
	β-GaN	15			HgSe	400	
	GaP	85			HgTe	1000	
	GaAs	341					
	GaSb	780					
	InN	1[a]	41[a]				
	InP	114					
	InAs	367					
	InSb	870					

[a] Calculated or estimated

[b] These values promise an ordering of the three valence bands $\Gamma_9^v - \Gamma_7^v - \Gamma_7^v$, which is the same as that for w-CdS

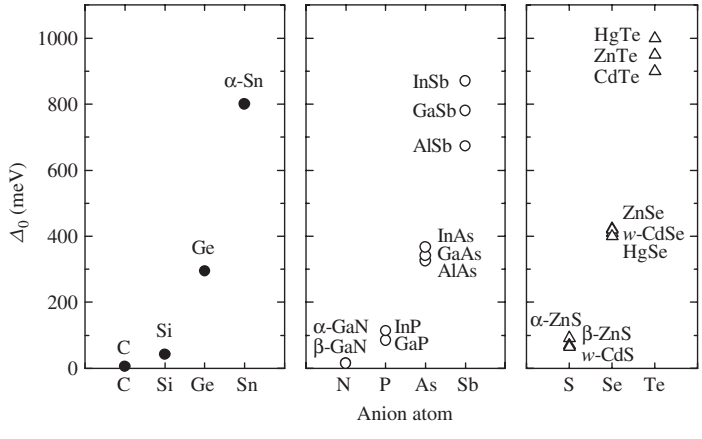

Figure 6.11 Δ_0-gap energy plotted against anion atoms for some group-IV, III–V and II–VI semiconductors

6.2.3 External perturbation effect

(a) Temperature effect

Traditionally, temperature variation of the band-gap energy E_g is expressed in terms of the Varshni formula [6.29]

$$E_g(T) = E_g(0) - \frac{\alpha T^2}{T + \beta} \tag{6.23}$$

where $E_g(0)$ is the band-gap energy at $T = 0$ K, α is in electron volts per Kelvin and β is closely related to the Debye temperature of the material (in Kelvin). The fitted results using Equation (6.23) for the E_0- and $E_0 + \Delta_0$-gaps in GaAs are shown in Figure 6.12. The experimental data are taken from Adachi [6.30].

Table 6.7 summarizes the Varshni parameters, $E_0(0), \alpha$ and β, for the E_0-gap energy variation in some group-IV, III–V and II–VI semiconductors. Figure 6.13 also plots the Varshni parameter β against Debye temperature θ_D for some of these semiconductors. No clear correlation can be recognized in Figure 6.13 between β and θ_D.

Differentiating Equation (6.23) with respect to T, we obtain

$$\frac{\partial E_g(T)}{\partial T} = -\alpha \left[\frac{2T}{T + \beta} - \frac{T^2}{(T + \beta)^2} \right] \tag{6.24}$$

If $T \gg \beta$, then Equation (6.24) becomes

$$\frac{\partial E_g(T)}{\partial T} \sim -\alpha \tag{6.25}$$

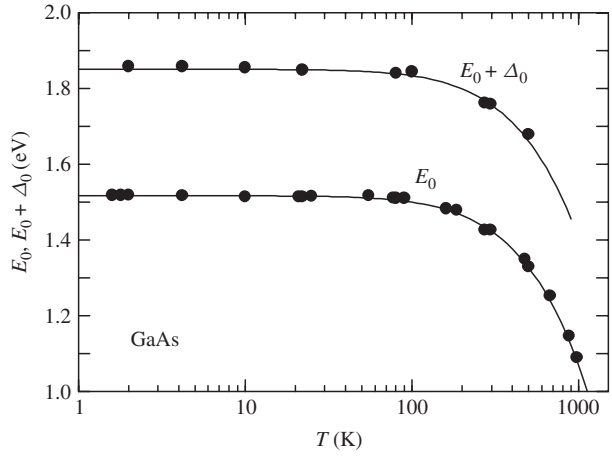

Figure 6.12 E_0-gap and $E_0 + \Delta_0$-gap energies versus temperature T for GaAs. The experimental data are taken from Adachi [6.30]. The solid lines show the calculated results of $E_g(T) = E_g(0) - [\alpha T^2/(T + \beta)]$ with $E_g(0) = 1.517$ eV, $\alpha = 5.5 \times 10^{-4}$ eV/K and $\beta = 225$ K (E_0); $E_g(0) = 1.851$ eV, $\alpha = 5.5 \times 10^{-4}$ eV/K and $\beta = 225$ K ($E_0 + \Delta_0$). [From S. Adachi, *Handbook on Physical Properties of Semiconductors Volume 2: III–V Compound Semiconductors* (Kluwer Academic, Boston, 2004), reproduced by permission from Kluwer Academic Publishers]

Table 6.7 Empirical equation for the E_0-gap energy variation with temperature T for some group-IV, III–V and II–VI semiconductors

$$E_0(T) = E_0(0) - \frac{\alpha T^2}{T + \beta}$$

System	Material	$E_0(0)$ (eV)	α (10^{-4} eV/K)	β (K)
IV	Ge	0.8893	6.842	398
III–V	w-AlN	6.242[a]	7.2	500
	α-GaN	3.484 (A)[a]	12.8	1190
	α-GaN	3.490 (B)[a]	12.9	1280
	α-GaN	3.512 (C)[a]	6.6	840
	β-GaN	3.22[a]	5.61	700
	GaP	2.864	6.20	190
	GaAs	1.517	5.5	225
	GaSb	0.809	5.3	234
	InN	1.915	2.45	624
	InP	1.422	4.5	335
	InAs	0.417	3.07	191
	InSb	0.235	2.7	106
II–VI	ZnO	3.3772 (A)[a]	7.2	1077
	α-ZnS	3.8652 (A)[a]	10	600
	α-ZnS	3.8927 (B)[a]	10	600
	β-ZnS	3.810	6.32	254
	ZnSe	2.8071[a]	5.58	187
	ZnTe	2.3832[a]	5.49	159
	c-CdS	2.445[a]	3.451	208
	w-CdS	2.579 (A)	4.7	230
	w-CdS	2.599 (B)	4.8	230
	w-CdS	2.659 (C)	5.1	230
	c-CdSe	1.766	6.96	281
	w-CdSe	1.8265 (A)[a]	17	1150
	w-CdSe	1.8503 (B)[a]	17	1050
	CdTe	1.600	5.0	180
	HgSe	−0.23	−6.0	16
	HgTe	−0.30	−6.0	10

[a] Excitonic gap

Viña *et al.* [6.31] proposed a new expression for the temperature dependence of the band-gap energy by taking into account the Bose–Einstein occupation factor

$$E_g(T) = E_B - \alpha_B \left(1 + \frac{2}{e^{\Theta_B/T} - 1}\right) \tag{6.26}$$

where the parameter Θ_B describes the mean frequency of the phonons involved and α_B is the strength of the electron–phonon interaction. This expression is more palatable than Equation (6.23) from the theoretical point of view [6.31].

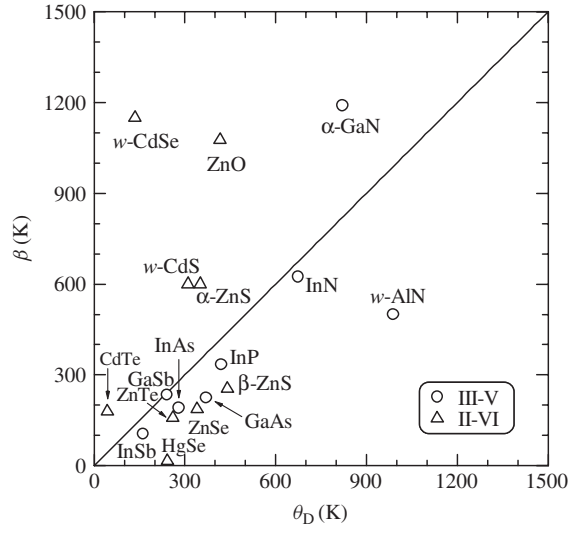

Figure 6.13 β in Varshni expression for the E_0-gap energy variation with temperature plotted against Debye temperature θ_D ($T = 300$ K) for some III–V and II–VI direct band-gap semiconductors

Differentiating Equation (6.26) with respect to T, we obtain

$$\frac{\partial E_g(T)}{\partial T} = -2\alpha_B \frac{\Theta_B}{T^2} \frac{e^{\Theta_B/T}}{(e^{\Theta_B/T} - 1)^2} \tag{6.27}$$

Equation (6.27) can yield the linear temperature coefficient of the band-gap energy at optional temperature T.

More recently, Pässler [6.32, 6.33] proposed an analytical expression which takes into account the band-gap shrinkage effect in accordance with general equations and parameter relationships governing the electron–phonon interaction mechanism

$$E_g(T) = E_g(0) - \frac{\alpha_p \Theta_p}{2} \left[\sqrt[p]{1 + \left(\frac{2T}{\Theta_p}\right)^p} - 1 \right] \tag{6.28}$$

where α_p plays the role of a $T \to \infty$ limiting value of the band-gap shrinkage coefficient $-\partial E_g(T)/\partial T$, Θ_p is approximately equal to the average phonon temperature and the exponent p is closely related to the overall shape of the electron–phonon spectral function in the given material.

Figure 6.14 shows the temperature dependence of the three-dimensional critical-point $E_{0\alpha}$ and excitonic-gap energies $E_{0\alpha}(ex)$ for ZnO determined by photoreflectance measurements [6.34]. The dashed and solid lines represent the calculated results of Equations (6.23) and (6.28), respectively. It is understood from Figure 6.14 that Equations (6.23) and (6.28) show equally good agreement with the experimental data in the measured temperature range $T = 15$–300 K.

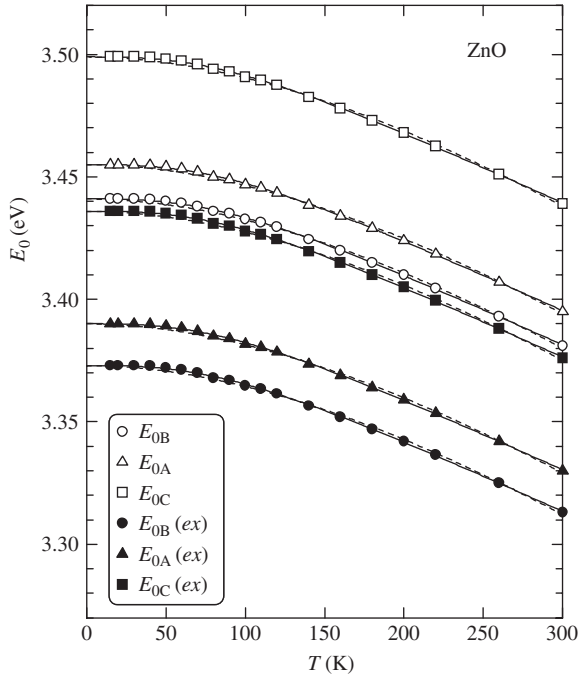

Figure 6.14 Temperature variation of the three-dimensional critical-point $E_{0\alpha}$ and excitonic-gap energies $E_{0\alpha}$ (ex) for ZnO determined by photoreflectance measurements. The dashed and solid lines represent the calculated results of Equations (6.23) and (6.28), respectively. [From S. Ozaki, T. Mishima, and S. Adachi, *Jpn. J. Appl. Phys.* **42**, 5465 (2003), reproduced by permission from the Institute of Pure and Applied Physics]

Differentiating Equation (6.28) with respect to T, one obtains

$$\frac{\partial E_g(T)}{\partial T} = -\alpha_p \left(\frac{2T}{\Theta_p}\right)^{p-1} \left[1 + \left(\frac{2T}{\Theta_p}\right)^{p}\right]^{(1-p)/p} \tag{6.29}$$

It is well known that the temperature shift of the energy gap $\Delta E_g(T)$ is arising from the effects of thermal expansion (ΔE_{th}) and electron–phonon interaction (ΔE_{ph})

$$\Delta E_g(T) = E_g(T) - E_g(0) = -\Delta E_{th}(T) - \Delta E_{ph}(T) \tag{6.30}$$

Practically, it is very difficult to separate these two components experimentally. However, it is possible to calculate the thermal expansion effect if the interband hydrostatic deformation potential a_H and the linear thermal expansion coefficient α are known [6.35, 6.36]

$$\Delta E_{th}(T) = -3a_H \int_0^T \alpha(T')\mathrm{d}T' \tag{6.31}$$

The electron–phonon interaction term $\Delta E_{\rm ph}$ can be given by the same form as the second term of Equation (6.23) or (6.28)

$$\Delta E_{\rm ph}(T) = \begin{cases} \dfrac{\alpha T^2}{T+\beta} & \text{(6.32a)} \\ \dfrac{\alpha_p \Theta_p}{2}\left[\sqrt[p]{1+\left(\dfrac{2T}{\Theta_p}\right)^p}-1\right] & \text{(6.32b)} \end{cases}$$

Figure 6.15 shows the least-squares fit of the experimental $\Delta E_{0\rm B}(T)$ values to Equation (6.30) for ZnO. The dashed and solid lines are calculated from Equations (6.32a) and (6.32b), respectively. The corresponding numerically calculated $\Delta E_{\rm th}(T)$ values are also plotted in Figure 6.15. It is understood from Figure 6.15 that the thermal expansion effect accounts for only 7% of the observed temperature shift at $T = 300$ K.

(b) Pressure effect

The band-structure parameters, such as the band gaps and band masses, are dependent both on temperature and pressure. Increasing hydrostatic pressure p usually increases the band-gap energy $E_{\rm g}$ in the following manner

$$E_{\rm g}(p) = E_{\rm g}(0) + ap + bp^2 \tag{6.33}$$

Table 6.8 summarizes the hydrostatic pressure parameters, a and b, for the E_0-gap energy in some group-IV, III–V and II–VI semiconductors obtained at $T = 300$ K.

(c) Temperature and pressure coefficients

We summarize in Table 6.9 the experimentally determined temperature and pressure coefficients of the E_0-gap energy for some group-IV, III–V and II–VI semiconductors at

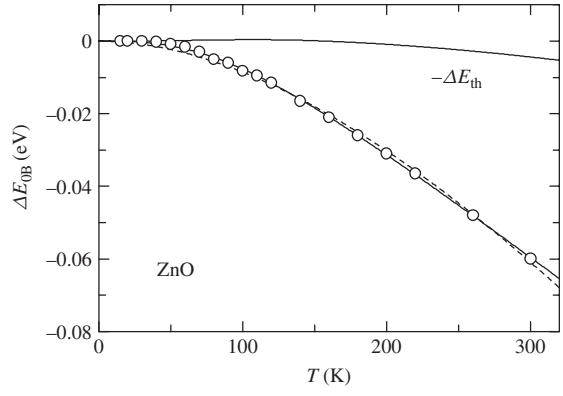

Figure 6.15 Least-squares fit of the experimental $\Delta E_{0\rm B}(T)$ values to Equation (6.30) for ZnO. The dashed and solid lines are calculated from Equations (6.32a) and (6.32b), respectively. The corresponding $\Delta E_{\rm th}(T)$ values are also calculated. The numerical parameters used in the calculation are taken from Ozaki *et al*. [6.34]

Table 6.8 Empirical equation for the E_0-gap energy variation with pressure p for some group-IV, III–V and II–VI semiconductors at 300 K

$$E_0(p) = E_0(0) + ap + bp^2$$

System	Material	$E_0(0)$ (eV)	a (10^{-2} eV/GPa)	b (10^{-4} eV/GPa^2)
IV	Si	3.273[a]	10.08[a]	0.5[a]
	Ge	0.795	12.1	−2
	3C-SiC	6.27[a]	5.50[a]	−29.7[a]
III–V	w-AlN	6.05[a]	4.0[a]	−3.2[a]
	c-AlN	4.53[a]	4.2[a]	−3.4[a]
	AlSb	2.215[a]	10.6[a]	−54[a]
	α-GaN	3.4762 (A)[b]	4.27	−3.9
	α-GaN	3.4813 (B)[b]	4.29	−3.9
	α-GaN	3.498 (C)[b]	4.30	−4
	β-GaN	3.302[b]	4.6	−6.7
	GaP	2.76	9.7	−35
	GaAs	1.427	11.5	−24.5
	GaSb	0.72	13.8	
	InN	1.89	2.0	
	InP	1.35	8.2	
	InAs	0.359	11.4	
	InSb	0.17	16.0	
II–VI	ZnO	3.4410 (A)[c]	2.47	−2.8
	ZnO	3.4434 (B)[c]	2.53	−2.8
	ZnO	3.4817 (C)[c]	2.68	−2.8
	α-ZnS	3.75	6.3	
	β-ZnS	3.666	6.35	−13.1
	ZnSe	2.688	7.2	−15
	ZnTe	2.29	10.3	−24
	c-CdS	2.46	−0.7[d]	
	w-CdS	2.501	4.4	
	c-CdSe	1.675	−1.5[e]	
	w-CdSe	1.713	4.81	−19
	CdTe	1.529	8.40	−39.6
	HgSe	−0.08	∼0[f]	
	HgTe	−0.15	−15.3	

[a] Calculated
[b] At $T = 10$ K
[c] At $T = 6$ K
[d] At $p > 6$ GPa
[e] At $p > 3$ GPa
[f] At $p < 7.5$ GPa

$T = 300$ K. Figure 6.16 also suggests a trend in $\mathrm{d}E_0/\mathrm{d}p$ versus Phillips ionicity f_i for some of these semiconductors. The solid line in Figure 6.16 represents the least-squares fit with the relation ($\mathrm{d}E_0/\mathrm{d}p$ in 10^{-2} eV/GPa)

$$\frac{\mathrm{d}E_0}{\mathrm{d}p} = 20.6 - 27.3 f_\mathrm{i} \tag{6.34}$$

Table 6.9 E_0-gap energy and its temperature and pressure coefficients determined experimentally at 300 K for some group-IV, III–V and II–VI semiconductors

System	Material	E_0 (eV)	dE_0/dT (10^{-4} eV/K)	dE_0/dp (10^{-2} eV/GPa)
IV	Ge	0.795	−4.0	12.1
	α-Sn	−0.413[a]	∼0[b]	
III–V	w-AlN	6.2	−5.5	4.9
	AlAs	3.01	−5.1	10.5
	AlSb	2.27	−3.5	
	α-GaN	3.420	−4.4	4.3
	β-GaN	3.231	−2.8	3.0
	GaP	2.76	−5.3	10.7
	GaAs	1.43	−4.4	11.6
	GaSb	0.72	−3.7	13.8
	InN	1.89	−1.3	3.0
	InP	1.35	−3.3	8.2
	InAs	0.359	−4.2	11.4
	InSb	0.17	−2.7	16.0
II–VI	ZnO	3.40	−3.65	2.7
	α-ZnS	3.75	−7.4	6.3
	β-ZnS	3.726	−5.05	6.5
	ZnSe	2.721	−4.7	7.5
	ZnTe	2.27	−4.53	10.2
	c-CdS	2.46		−0.7[c]
	w-CdS	2.501	−4.45	4.4
	c-CdSe	1.675	−5.3	−1.5[d]
	w-CdSe	1.751	−3.63	5.0
	CdTe	1.51	−3.5	7.9
	HgSe	−0.08	+7.4	∼0[e]
	HgTe	−0.15	−1.15 ∼ +6.0	−15.3

[a] At $T = 1.5$ K. The sign is chosen positive for a normal band structure like that of Ge
[b] At $T = 1.5$–85 K
[c] At $p > 6$ GPa
[d] At $p > 3$ GPa
[e] At $p < 7.5$ GPa

6.2.4 Doping effect

It is well known that the electronic energy bands in heavily doped semiconductors are shifted in energy, owing to the presence of the ionized dopant ions and related charge carriers. Heavy doping of semiconductors causes a reduction of the fundamental band gap and, for degenerate p-type material, a partial filling of the valence band at all temperatures. Accurate knowledge of the shifts in the conduction-band and valence-band edges due to heavy doping effects is crucial in modeling semiconductor devices that utilize heavily doped layers.

Many-body effects, such as the electron–electron and electron–impurity interactions, contribute most dominantly to the electronic energy-band changes. Besides a shift of

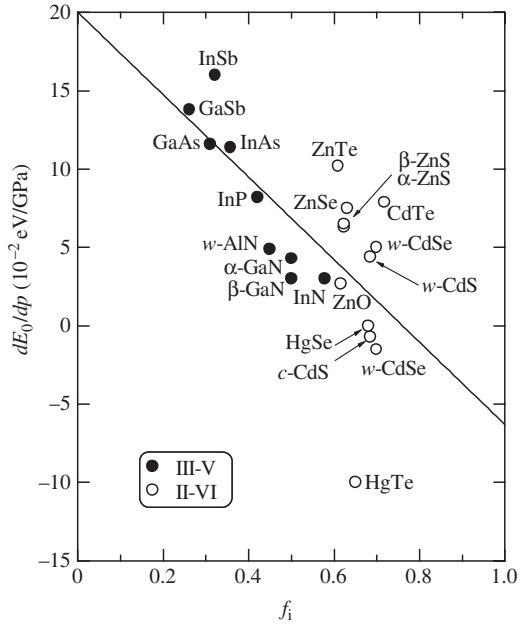

Figure 6.16 Trend in dE_0/dp versus Phillips ionicity f_i for some III–V and II–VI direct band-gap semiconductors. The solid line represents the least-squares fit with $dE_0/dp = 20.0 - 26.3 f_i$ (dE_0/dp in 10^{-2} eV/GPa)

the energy levels leading to band-gap narrowing, the electron–electron interactions also weakly deform the density of states from its unperturbed distribution [6.37]. Apart from a slight shrinking of the band gap, the electron–impurity scattering modifies the density of states more significantly and causes states that tail into the forbidden gap [6.38]. Along with these many-body effects, the random distribution of impurities merely distorts the density of states by creating significant band tails.

We show schematically in Figure 6.17 the band structures for heavily doped (a) *n*-type and (b) *p*-type semiconductors along with those for the undoped ones. Owing to the Burstein–Moss effect [6.39], the 'absorption' band gap in heavily doped semiconductors is larger than the band gap of the undoped material. As a result of the doping-induced band gap narrowing, however, the band gap of the doped semiconductors is smaller than that of the undoped material.

In *n*-Si and *p*-Si, the band-gap narrowing is negligible at low doping densities. However, in *n*-GaAs the narrowing becomes large, even at low doping densities. This is because the electron effective mass in *n*-GaAs is much smaller than the electron and hole effective masses in *n*-Si and *p*-Si. In fact, we show in Figures 6.18 and 6.19 the band-gap shrinkage as a function of electron concentration in *n*-Si [6.40] and *n*-GaAs [6.41], respectively. The solid line in Figure 6.19 represents the calculated result by Bennett and Lowney [6.42]. We find that the shrinkage in *n*-Si is ~5 meV at $n \sim 1 \times 10^{18}$ cm^{-3}, which is much smaller than the value of ~60 meV in *n*-GaAs at the same doping level. It is noted, however, that the results for *p*-Si should be directly applicable to *p*-GaAs because of the nearly equal hole effective masses. For example, we show in Figure 6.20

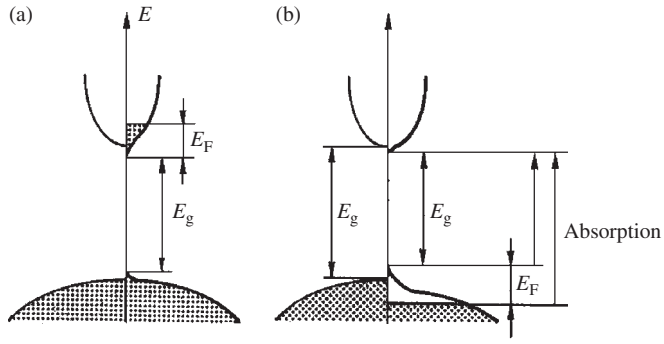

Figure 6.17 Schematic drawing of the band structures for heavily doped (a) *n*-type; and (b) *p*-type semiconductors, together with those for the undoped ones (left-hand sides)

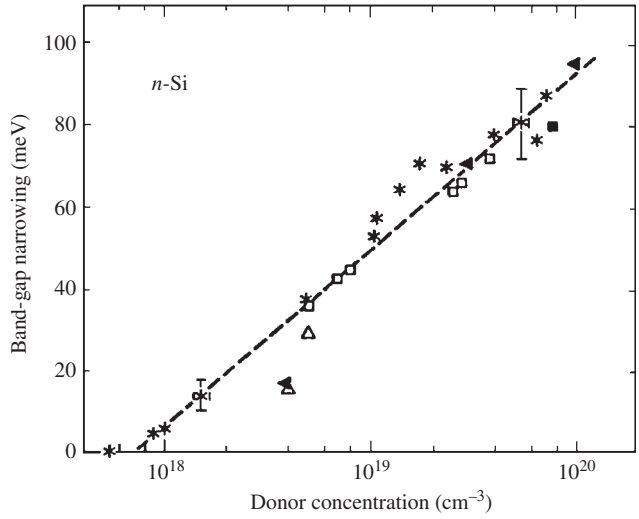

Figure 6.18 Apparent band-gap narrowing versus donor concentration in *n*-Si. The experimental data plotted are taken from various sources. [From J. del Alamo, S. Swirhun, and R. M. Swanson, in *Proc. Int. Electron Dev. Meeting* (IEEE, USA, 1985), p. 290; © 1985 IEEE]

the band-gap narrowing as a function of acceptor doping in *p*-Si as reported by Swirhun *et al*. [6.43]. The solid line represents the fit by Slotboom and de Graaf [6.44]. The band-gap shrinkage in *p*-Si is ~40 meV at $p \sim 1 \times 10^{18}$ cm^{-3}, which is comparable to that observed in *p*-GaAs at the same acceptor level [6.45].

The location of the Fermi level with respect to doping density has been reported for many heavily doped semiconductors. For example, Jain *et al*. [6.46] presented experimental values of the Fermi level in *n*-GaAs obtained by analyzing luminescence data of several workers. Silberman *et al*. [6.47] used X-ray photoemission spectroscopy to deduce the shift in the valence-band edge induced by carbon doping to a carrier density of 1×10^{20} cm^{-3} based on a determination of the bulk binding energy of the Ga and As core levels in GaAs. The penetration depth of the Fermi level into the valence band

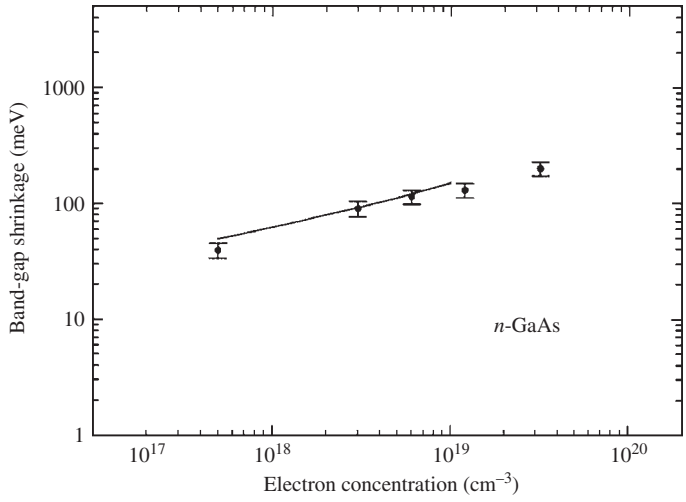

Figure 6.19 Band-gap shrinkage as a function of electron concentration N_a for n-GaAs at 80 K compared with calculation by Bennett and Lowney (solid line) [6.42]. [From H. Yao and A. Compaan, *Appl. Phys. Lett.* **57**, 147 (1990), reproduced by permission from the American Institute of Physics]

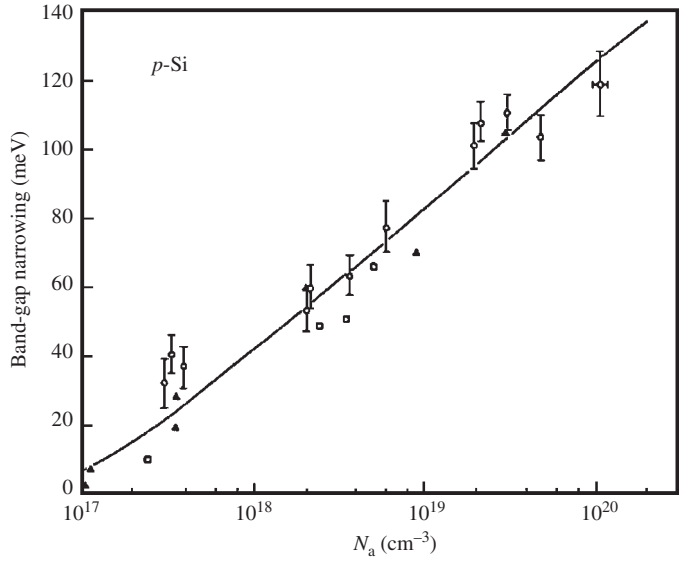

Figure 6.20 Apparent band-gap narrowing versus acceptor doping in p-Si. The experimental data plotted are taken from various sources. The solid line represents the fit by Slotboom and de Graaf [6.44]. [From S. E. Swirhun, Y.-H. Kwark, and R.M. Swanson, in *Proc. Int. Electron Dev. Meeting* (IEEE, USA, 1986), p. 24; © 1986 IEEE]

was found to be 0.12 ± 0.05 eV at this degenerate carrier density. Wang *et al.* [6.48] used photoluminescence excitation spectroscopy to study the optical absorption in heavily carbon-doped GaAs. Since the Fermi level penetrates into the valence band in heavily doped p-GaAs, only states with $\boldsymbol{k} \neq 0$ are occupied by electrons. In the process of band-to-band absorption, electrons could be excited either directly into states with $\boldsymbol{k} \neq 0$ in the conduction band or indirectly into states with $\boldsymbol{k} \sim 0$ at the bottom of the conduction band, depending upon whether the $\boldsymbol{k}$ selection rule is required. If indirect absorption is significant, then the onset energy in the photoluminescence excitation spectra should be equal to $E_g + E_F$ (see Figure 6.17). In heavily doped GaAs, conservation of the crystal momentum $\boldsymbol{k}$ is known to be no longer required in optical transitions because the scattering of carriers by impurity ions and other free carriers can efficiently relax the extra momentum. The locations of the Fermi level determined by this method were 0.08, 0.22 and 0.24 eV below the top of the valence band in the samples doped to 6.2×10^{19}, 1.6×10^{20} and 4.1×10^{20} cm^{-3}, respectively [6.48]

6.3 HIGHER-LYING DIRECT GAP

6.3.1 Cubic semiconductor

(a) Room-temperature value

The E_1 and $E_1 + \Delta_1$ transitions in many cubic semiconductors take place along the Λ direction or at the L point in the Brillouin zone. There is also an accumulation of the direct band gaps in energies higher than E_1 and $E_1 + \Delta_1$. These correspond to E_0', E_2, E_1', etc. Table 6.10 lists the higher-lying direct band-gap energies, E_1, $E_1 + \Delta_1$, E_0', E_2 and E_1', for some cubic group-IV, III–V and II–VI semiconductors. Figure 6.21 plots the E_1-gap

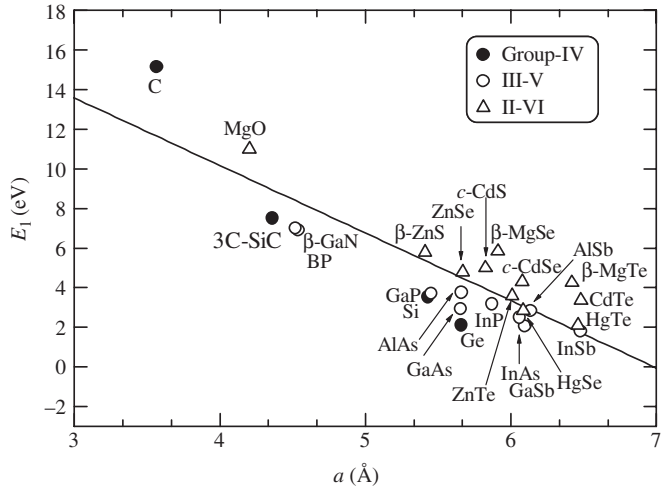

Figure 6.21 E_1-gap energy versus lattice constant a for some group-IV, III–V and II–VI semiconductors at 300 K. The solid line represents the least-squares fit with $E_1 = 23.8 - 3.41a$ (a in Å; E_1 in eV)

Table 6.10 Higher-lying direct band-gap energy for some cubic group-IV, III–V and II–VI semiconductors at 300 K (in eV)

System	Material	E_1	$E_1 + \Delta_1$	E_0'	E_2	E_1'
IV	Diamond	14.0, 16.3		6.0–7.4	12.6	
	Si	3.360–3.7		3.281–3.5	4.270–4.5	5.32
	Ge	2.11	2.31	2.99	4.39	5.80
	α-Sn	1.25[a]	1.65[a]	2.25[a]	3.02[a]	
	3C-SiC	7.5		9.0	5.8	
III–V	BP	6.9			8.0	
	AlP	4.30[b]		5.14[b]	4.63[b]	
	AlAs	3.62–3.90	3.83–4.10	4.54–4.69	4.853, 4.89	
	AlSb	2.78–2.890	3.209–3.316	3.72–3.76	4.20–4.25	5.30
	β-GaN	7.0			7.6	
	GaP	3.71	3.82	4.74	5.28	~6.7
	GaAs	2.89–2.97	3.1–3.212	4.44–4.64	4.960–5.45	6.62–6.63
	GaSb	2.05	2.50	3.27–3.85	4.08–4.20	~5.4
	InP	3.17	3.29	4.70	5.10	~6.5
	InAs	2.50	2.78	4.44	4.70	~6.4
	InSb	1.80	2.30		3.90	~5.3
II–VI	MgO	11.0			13.45	17.6
	β-MgSe	5.84	6.21			
	β-MgTe	4.255	4.673	5.327	5.156	
	β-ZnS	5.8			7.0	9.2
	ZnSe	4.79	5.08	8.1	6.6	8.9
	ZnTe	3.59	4.17	4.92	5.30	~6.8
	c-CdS	5.0		7.4	6.4, 6.9	8.3
	c-CdSe	4.314	4.568	$\geqslant$6.5	~6.0	
	CdTe	3.36	3.95	4.80–5.34	4.96–5.56	6.4–6.76
	β-HgS	3.54–5.76			6.43	8.95
	HgSe	2.84	3.14	5.00–5.08	5.50–5.83	8.20–8.36
	HgTe	2.11	2.75	4.1, 4.19	4.96, 5.0	7.50

[a] At $T = 278$ K

[b] Estimated from $Al_xGa_{1-x}P$ ($0 \leqslant x \leqslant 0.52$) data

energy versus lattice constant a for some group-IV, III–V and II–VI semiconductors. The solid line represents the least-squares fit with the relation (a in Å; E_1 in eV)

$$E_1 = 23.8 - 3.41a \tag{6.35}$$

Figure 6.22 shows the lowest direct band-gap energy E_1 plotted versus molecular weight M for some cubic group-IV, III–V and II–VI semiconductors. The solid line represents the least-squares fit with the relation (M in amu; E_1 in eV)

$$E_1 = 22.8 - 3.79 \ln M \tag{6.36}$$

It has been shown in Section 1.4 that the relation between the lattice constant a and molecular weight M can be simply given by $a = 0.579 + 1.04 \ln M$ (M in amu; a in Å).

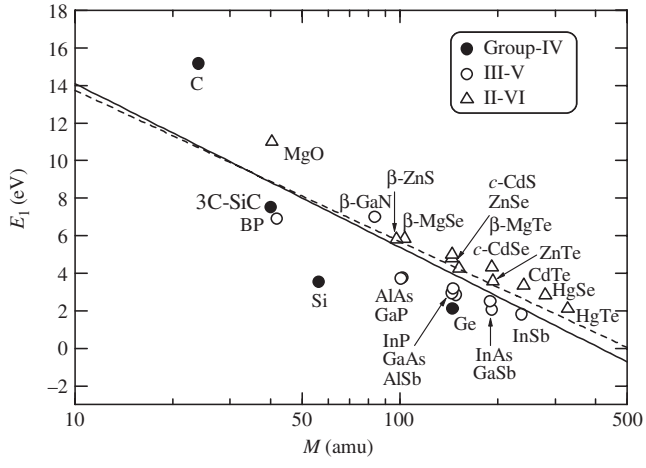

Figure 6.22 E_1-gap energy at 300 K versus molecular weight M for some cubic group-IV, III–V and II–VI semiconductors. The solid line represents the least-squares fit with $E_1 = 22.8 - 3.79 \ln M$, while the dashed line represents the relation with $E_1 = 21.8 - 3.55 \ln M$ (M in amu; E_1 in eV)

Introducing this equation into Equation (6.35), one obtains (M in amu; E_1 in eV)

$$E_1 = 21.8 - 3.55 \ln M \tag{6.37}$$

The dashed line in Figure 6.22 shows the calculated result of Equation (6.37).

We summarize in Table 6.11 the spin–orbit split-off energies, Δ_0 and Δ_1, at the $E_0/(E_0 + \Delta_0)$ and $E_1/(E_1 + \Delta_1)$ edges, respectively, and their ratio Δ_0/Δ_1 for some

Table 6.11 Experimental spin–orbit split-off energies, Δ_0 and Δ_1, and their ratio Δ_0/Δ_1 for some cubic group-IV, III–V and II–VI semiconductors (Δ_0 and Δ_1 in meV)

System	Material	Δ_0	Δ_1	Δ_0/Δ_1	System	Material	Δ_0	Δ_1	Δ_0/Δ_1
IV	Diamond	6			II–VI	β-ZnS	70	50[a]	1.40
	Si	42.62				c-CdS	70		
	Ge	295	200	1.48		ZnSe	424	290	1.46
	α-Sn	800	482	1.66		c-CdSe	410	254	1.61
						HgSe	400	300	1.33
III–V	β-GaN	15				ZnTe	950	580	1.64
	GaP	85	55	1.55		CdTe	900	590	1.53
	InP	114	140	0.81		HgTe	1000	640	1.56
	AlAs	325	190	1.71					
	GaAs	341	222	1.54					
	InAs	367	267	1.37					
	AlSb	673	386	1.74					
	GaSb	780	460	1.70					
	InSb	870	500	1.74					

[a] Theoretical

cubic semiconductors. Note that the Δ_0-gap and Δ_1-gap energies may not vary so greatly with temperature if one assumes the valence-band rigidity of the semiconductors. Figure 6.23 also plots the variation of Δ_1 for some cubic group-IV, III–V and II–VI semiconductors with respect to the group IV, V and VI anions. The valence and conduction bands of the III–V (II–VI) semiconductors can be well characterized by electron orbital of the group V (VI) anion and group III (II) cation atoms, respectively. As clearly seen in Figure 6.23, there is an increase in Δ_1 with increasing atomic number of the anion atoms. It is also evident that the common anion semiconductors have nearly the same Δ_1 values, as similar to the case for Δ_0 (Figure 6.11).

In the framework of the $\boldsymbol{k} \cdot \boldsymbol{p}$ method, the spin–orbit splitting Δ_0 at the Γ point is approximately 3/2 of the spin–orbit splitting Δ_1 along the $\langle 111 \rangle$ direction [6.49]

$$\frac{\Delta_0}{\Delta_1} \sim \frac{3}{2} \tag{6.38}$$

In Figure 6.24, we plot the ratio of Δ_0/Δ_1 against Δ_0 for some cubic group-IV, III–V and II–VI semiconductors. This figure suggests that all the semiconductors, except InP ($\Delta_0/\Delta_1 \sim 0.81$), obey the relation of Equation (6.38) well. An anomaly in InP can be attributed to changes in weight coefficient when going from the Γ to the L point ($\langle 111 \rangle$ direction) [6.50].

(b) External perturbation effect

As mentioned in Section 6.2, the temperature-induced change in the band-gap energy can be commonly given in terms of the α and β coefficients of the Varshni formula. Table 6.12 summarizes the Varshni parameters, $E_g(0)$, α and β, for the E_1-gap and $E_1 + \Delta_1$-gap energies in some cubic group-IV, III–V and II–VI semiconductors. Figure 6.25 also shows, as an example, the fitted results of the E_1-gap and $E_1 + \Delta_1$-gap energies

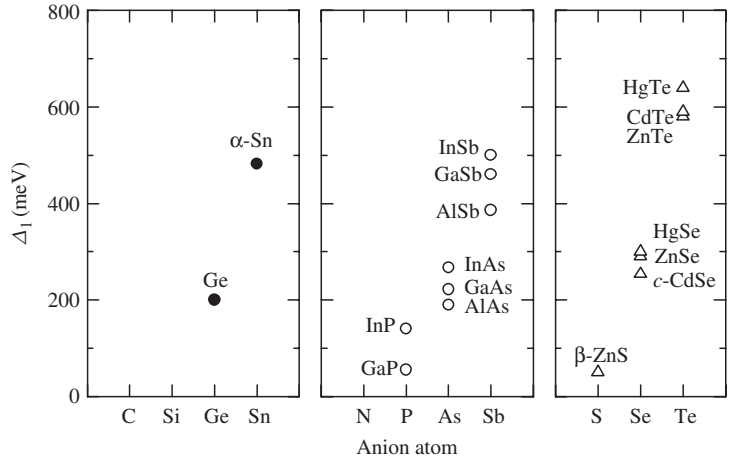

Figure 6.23 Δ_1-gap energy plotted against anion atoms for some cubic group-IV, III–V and II–VI semiconductors

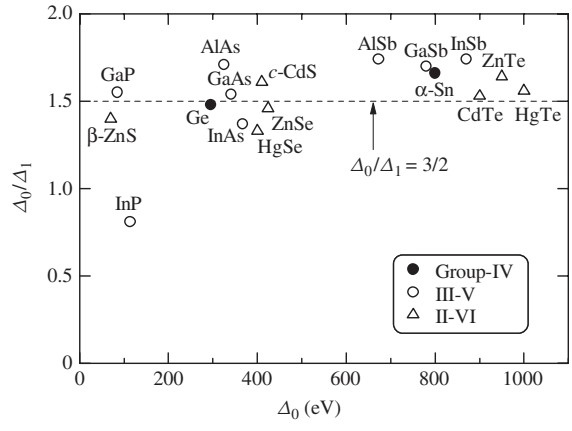

Figure 6.24 Δ_0/Δ_1 plotted against Δ_0 for some cubic group-IV, III–V and II–VI semiconductors

Table 6.12 Empirical equation for the E_1-gap and $E_1 + \Delta_1$-gap energy variation with temperature T for some group-IV, III–V and II–VI semiconductors

$$E_g(T) = E_g(0) - \frac{\alpha T^2}{T + \beta}$$

System	Material	E_g	$E_g(0)$ (eV)	α (10^{-4} eV/K)	β (K)
IV	Si	E_1	3.482	8.00	645
	Ge	E_1	2.22	6.8	240
	α-Sn	E_1	1.38	6	230
		$E_1 + \Delta_1$	1.853	7	270
III–V	β-GaN	E_1	7.03	9.5	553
	GaP	E_1	3.785	6.1	240
	GaAs	E_1	3.044	6.7	188
	GaSb	E_1	2.186	6.8	147
		$E_1 + \Delta_1$	2.621	6.7	176
	InSb	E_1	2.00	6.84	132
		$E_1 + \Delta_1$	2.49	6.46	170
II–VI	ZnTe	E_1	3.772	9.50	260
		$E_1 + \Delta_1$	4.345	8.80	260
	CdTe	E_1	3.55	8.0	90
		$E_1 + \Delta_1$	4.08	6.0	120
	HgSe	E_1	2.949	5.8	60
		$E_1 + \Delta_1$	3.219	5.8	60

versus temperature in CdTe using the Varshni formula. The experimental data are gathered from various sources [6.51]. Figure 6.26 plots the Varshni parameter β against Debye temperature θ_D for some group-IV, III–V and II–VI semiconductors. A weak correlation can be seen in Figure 6.26 between β and θ_D.

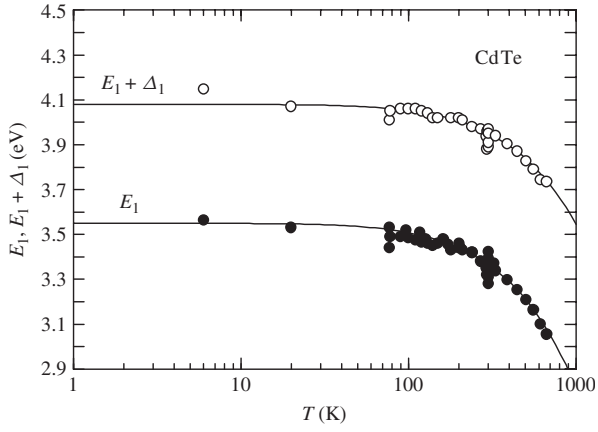

Figure 6.25 E_1-gap and $E_1 + \Delta_1$-gap energies versus temperature T for CdTe. The experimental data are gathered from various sources [6.51]. The solid lines show the calculated results of $E_g(T) = E_g(0) - [\alpha T^2/(T + \beta)]$ with $E_g(0) = 3.55$ eV, $\alpha = 8.0 \times 10^{-4}$ eV/K and $\beta = 90$ K (E_1); $E_g(0) = 4.08$ eV, $\alpha = 6.0 \times 10^{-4}$ eV/K and $\beta = 120$ K ($E_1 + \Delta_1$). [From S. Adachi, *Handbook on Physical Properties of Semiconductors Volume 3: II–VI Compound Semiconductors* (Kluwer Academic, Boston, 2004), reproduced by permission from Kluwer Academic Publishers]

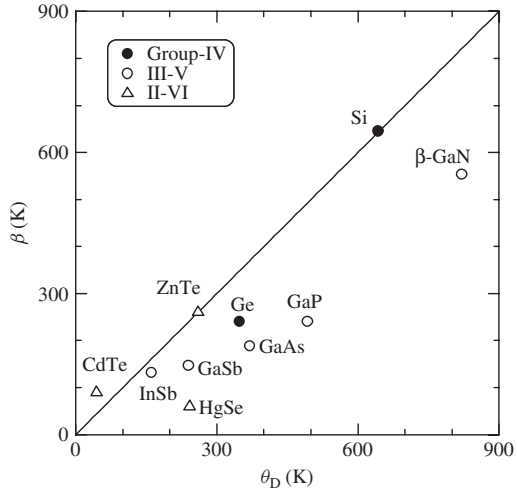

Figure 6.26 β in Varshni expression for the E_1-gap energy variation with temperature plotted against Debye temperature θ_D ($T = 300$ K) for some group-IV, III–V and II–VI semiconductors. Note that θ_D values plotted for β-GaN and GaP correspond to those for α-GaN and at $T = 150$ K, respectively

Table 6.13 summarizes the experimental temperature and hydrostatic pressure coefficients of the higher-lying direct band-gap energies, E_1, E_0' and E_2, for some cubic group-IV, III–V and II–VI semiconductors determined at $T = 300$ K. We can see in Table 6.13 that all the semiconductors listed here have negative temperature and positive pressure coefficients of the higher-lying direct band gaps.

Table 6.13 Temperature and pressure coefficients of the higher-lying direct band-gap energy for some cubic group-IV, III–V and II–VI semiconductors at 300 K

System	Material	E_g	dE_g/dT (10^{-4} eV/K)	dE_g/dp (10^{-2} eV/GPa)
IV	Diamond	E_0'	−6.3	
	Si	E_1	−3.0	5.2
		E_0'	−1.7	1
		E_2	−2.5	2.9
	Ge	E_1	−4.3	7.5
		E_0'	−1.4	1.4
		E_2	−2.8	5.6
	α-Sn	E_1	−4.6	
		E_0'	−4.5	
		E_2	−5.1	
III–V	AlSb	E_1	−4.7	
	β-GaN	E_1	−4.5	
		E_2	−1.9	
	GaP	E_1	−3.4	5.8
		E_0'	−3.2	
		E_2	−3.4	
	GaAs	E_1	−5.4	7.2
		E_0'	−3.0	
		E_2	−3.6	
	GaSb	E_1	−5.7	7.35
		E_2	−5.5	6.08
	InP	E_1	−5.6	
		E_0'	−1.9	
	InAs	E_1	−5.0	7.4
		E_2	−5.6	
	InSb	E_1	−5.0	8.5
		E_0'	−4.6	
		E_2	−5.5	5.8
II–VI	β-ZnS	E_1	−5.1	
		E_2	−3.0	
	ZnSe	E_1	−6.2	
		E_2	−4.7	
	ZnTe	E_1	−4.2	8.3
		E_2	−6.1	
	c-CdSe	E_1	−5.9	
		E_2	−3.6	
	CdTe	E_1	−7.2	6.0
		E_2	−3.6	
	HgSe	E_1	−4.6	
	HgTe	E_1	−5.5	
		E_0'	−6.66	
		E_2	−6.97	

Table 6.14 Higher-lying direct band-gap energy for some hexagonal and rhombohedral group-IV, III–V and II–VI semiconductors at 300 K (in eV)

System	Material	E_1	E_2	E_3	E_4	E_5	E_6	E_7
IV	6H-SiC	4.07[a]	4.71[a]	5.54[a]				
	6H-SiC	3.85[b]	4.68[b]					
	15R-SiC	4.6[c]	5.5[c]	6.7[c]	7.1[c]	7.8[c]	8.3[c]	9.6[c]
III–V	*h*-BN							
	w-AlN	7.76	8.79					
	α-GaN	6.9	8.0	9.3	10.5–11.5	12.2–13.4	13.9	
	InN	5.0	7.6	8.6				
II–VI	ZnO							
	α-ZnS	5.5[a]	5.74–5.80[a]	7.00–7.52[a]	9.43–9.61[a]			
	α-ZnS	5.6[b]	5.76–5.86[b]	6.98–7.56[b]	9.56–9.73[b]			
	w-CdS	4.98[a,d]	5.50[a,e]	6.1[a,f]	7.8[a,g]			
	w-CdS		5.48[b,e]	6.2[b,f]	7.8[b,g]			
	w-CdSe	4.10[a,d]	4.55[a,e]	4.85[a,h]	5.6[a,f]	7.6, 8.7[g]	9.5[i]	
	w-CdSe			4.78[b,h]	6.0[b,f]			

[a] $\boldsymbol{E} \perp c$
[b] $\boldsymbol{E} \parallel c$
[c] $\boldsymbol{E} \perp c$ (one of these gaps may occur at the Γ point, i.e., E_0 gap)
[d] E_1(A)
[e] E_1(B)
[f] E_0'
[g] E_2
[h] E_1(C)
[i] E_1'

6.3.2 Hexagonal and rhombohedral semiconductors

Table 6.14 summarizes the higher-lying direct band-gap energies, E_1, E_2, E_3, etc., for some hexagonal and rhombohedral semiconductors at $T = 300$ K. It should be noted that only the limited data are available on the external perturbation effects of the higher-lying direct band-gap energies in such anisotropic semiconductors [6.15, 6.52].

6.4 LOWEST INDIRECT GAP

6.4.1 Room-temperature value

The electronic energy-band structure of semiconductors can be classified into two types: direct band gap semiconductors (such as GaAs and ZnSe) in which the lowest conduction-band minimum and the highest valence-band maximum are at the same wavevector in the Brillouin zone; indirect band gap semiconductors (such as Si and GaP) in which the extrema are at different wavevectors.

It is well known that not only the direct transitions at the direct band gap, but also the indirect transitions at the indirect band gap influence the optical dispersion relations

of semiconductors. The indirect transitions in indirect band-gap semiconductors take part at energies below the onset of the direct transitions, and vice versa above the onset of the direct transitions in direct band-gap semiconductors. Because the indirect transitions are higher order in perturbation than the direct ones, their strength is very weak and one can expect to observe them only in spectra below the direct threshold as a tail of the direct absorption edge in indirect band-gap materials. Table 6.15 summarizes the lowest and second lowest indirect band-gap energies in some group-IV, III–V and II–VI semiconductors at $T = 300$ K.

6.4.2 External perturbation effect

(a) Temperature effect

We summarize in Table 6.16 the Varshni parameters, $E_g^{ID}(0)$, α and β, for the lowest indirect band-gap energy in some group-IV and III–V indirect band-gap semiconductors.

Table 6.15 Energies of the lowest and second-lowest indirect band gaps in some group-IV, III–V and II–VI semiconductors at 300 K. LCBV = lowest conduction-band valley; ID = indirect band-gap semiconductor; D = direct band-gap semiconductor

System	Material	Type (LCBV)	Lowest indirect-gap energy (eV)	2nd lowest indirect-gap energy (eV)
IV	Diamond	ID (X or Δ)	5.50	
	Si	ID (X)	1.12	2.0 ($\Gamma \rightarrow$ L)
	Ge	ID (L)	0.6657	0.852 ($\Gamma \rightarrow$ X)
	α-Sn	D (Γ)	0.092 ($\Gamma \rightarrow$ L)[a]	
	3C-SiC	ID (X)	2.39	4.20 ($\Gamma \rightarrow$ L)
	6H-SiC	ID (L–M)	3.0	
	15R-SiC	ID	2.9863[b]	
III–V	*c*-BN	ID (X)	6.27	
	BP	ID (X or L)	2.0	
	c-AlN	D (Γ) or ID (X)	5.34 ($\Gamma \rightarrow$ X)	
	AlP	ID (X)	2.48	
	AlAs	ID (X)	2.15	2.37 ($\Gamma \rightarrow$ L)
	AlSb	ID (X or Δ)	1.615	2.211 ($\Gamma \rightarrow$ L)
	GaP	ID (X or Δ)	2.261	2.63 ($\Gamma \rightarrow$ L)
	GaAs	D (Γ)	1.72 ($\Gamma \rightarrow$ L)	1.91 ($\Gamma \rightarrow$ X)
	GaSb	D (Γ)	0.76 ($\Gamma \rightarrow$ L)	1.05 ($\Gamma \rightarrow$ X)
	InP	D (Γ)	2.05 ($\Gamma \rightarrow$ L)	2.21 ($\Gamma \rightarrow$ X)
	InAs	D (Γ)	1.07 ($\Gamma \rightarrow$ L)	1.37 ($\Gamma \rightarrow$ X)
	InSb	D (Γ)	0.93 ($\Gamma \rightarrow$ L)	1.63 ($\Gamma \rightarrow$ X)
II–VI	ZnSe	D (Γ)	3.4 ($\Gamma \rightarrow$ X)	3.8 ($\Gamma \rightarrow$ L)
	ZnTe	D (Γ)	3.05 ($\Gamma \rightarrow$ X)	

[a] At $T = 4.2$ K
[b] At $T = 2$ K

Table 6.16 Empirical equation for the lowest indirect band-gap energy variation with temperature T determined experimentally for some group-IV and III–V indirect band-gap semiconductors

$$E_g^{ID}(T) = E_g^{ID}(0) - \frac{\alpha T^2}{T + \beta}$$

System	Material	Band gap	$E_g^{ID}(0)$ (eV)	α (10^{-4} eV/K)	β (K)
IV	Diamond	E_g^X (or E_g^Δ)	5.4125	−1.979	−1437
	Si	E_g^X	1.1692	4.9	655
	Ge	E_g^L	0.7437	4.774	235
	6H-SiC	E_g^{L-M}	3.024	−0.3055	−311
III–V	AlAs	E_g^X	2.25	3.6	204
	AlSb	E_g^X (or E_g^Δ)	1.687	4.97	213
	GaP	E_g^X (or E_g^Δ)	2.3254	5.8	387

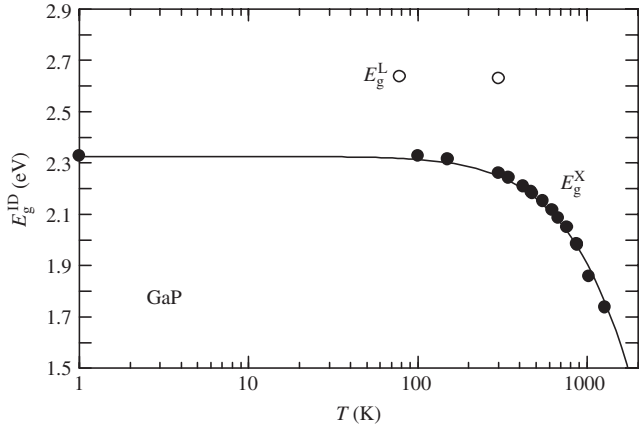

Figure 6.27 Indirect band-gap energies, E_g^X and E_g^L, versus temperature T for GaP. The experimental data are taken from various sources. The solid line shows the calculated result of $E_g^X(T) = E_g^X(0) - [\alpha T^2/(T + \beta)]$ with $E_g^X(0) = 2.3254$ eV, $\alpha = 5.8 \times 10^{-4}$ eV/K and $\beta = 387$ K. [From S. Adachi, *Handbook on Physical Properties of Semiconductors Volume 2: III–V Compound Semiconductors* (Kluwer Academic, Boston, 2004), reproduced by permission from Kluwer Academic Publishers]

Figure 6.27 also shows the fitted result of E_g^X in GaP using the Varshni formula, together with several experimental data of E_g^L.

(b) Pressure effect

In Table 6.17, we list the hydrostatic pressure parameters, a and b, for the lowest indirect band-gap energy in some group-IV and III–V indirect band-gap semiconductors at $T =$ 300 K. It is noted that in many semiconductors the pressure coefficients of the E_0-gap

Table 6.17 Empirical equation for the lowest indirect band-gap energy variation with pressure p for some group-IV and III–V semiconductors at 300 K

$$E_g^{ID}(p) = E_g^{ID}(0) + ap + bp^2$$

System	Material	Band gap	$E_g^{ID}(0)$ (eV)	a (10^{-2} eV/GPa)	b (10^{-4} eV/GPa^2)
IV	Diamond	E_g^X (or E_g^Δ)	5.50	0.597	
	Si	E_g^X	1.110	−1.43	
	Ge	E_g^L	0.6657	4.8	
	3C-SiC	E_g^X	2.39	−0.34	10.6
	6H-SiC	E_g^{L-M}	3.0	0.20	
III–V	c-BN	E_g^X	6.27	0.60	
	AlP	E_g^X	2.48	−1.6[a]	
	AlAs	E_g^X	2.15	−1.53	
	AlSb	E_g^X (or E_g^Δ)	1.610	−4.2	−1
	GaP	E_g^X (or E_g^Δ)	2.25	−1.3	

[a] Calculated

Table 6.18 Indirect band-gap energy and its temperature and pressure coefficients for some group-IV and III–V indirect band-gap semiconductors at 300 K

System	Material	Band gap	E_g^{ID} (eV)	dE_g^{ID}/dT (10^{-4} eV/K)	dE_g^{ID}/dp (10^{-2} eV/GPa)
IV	Diamond	E_g^X (or E_g^Δ)	5.50	−5.4	0.597
	Si	E_g^X	1.12	−2.59	−1.43
	Ge	E_g^L	0.6657	−4.0	4.8
	3C-SiC	E_g^X	2.39	−5.8	−0.34
	6H-SiC	E_g^{L-M}	3.0	−3.3	0.20
III–V	c-BN	E_g^X	6.27		0.60
	BP	E_g^X (or E_g^L)	2	−4.5	
	AlP	E_g^X	2.48	−5.8	
	AlAs	E_g^X	2.15	−4.0	−1.53
	AlSb	E_g^X (or E_g^Δ)	1.615	−3.1	−1.6
	GaP	E_g^X (or E_g^Δ)	2.261	−4.0	−1.3

and E_g^L-gap energies are positive while that of the E_g^X-gap energy is negative. As a result, the Γ_6 and L_6 conduction minima will shift to high energies while the X_6 minimum shifts to low energy with increasing pressure. Since the Γ_6 and X_6 conduction minima in a direct band-gap semiconductor will cross at any pressure, it becomes an indirect band-gap semiconductor (see Section 6.6, below).

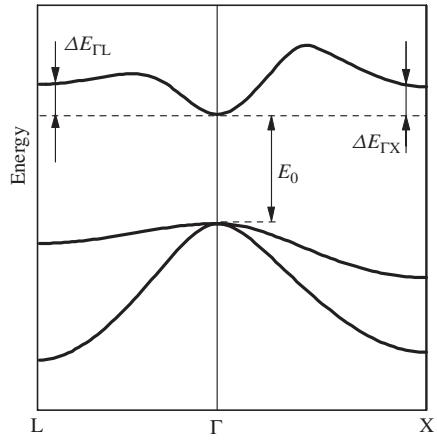

Figure 6.28 Schematic diagram showing the Γ–X and Γ–L conduction-valley energy separations $\Delta E_{\Gamma X} = \Delta E_g(\Gamma - X)$ and $\Delta E_{\Gamma L} = \Delta E_g(\Gamma - L)$, respectively

Table 6.19 Conduction-valley energy separation ΔE_g for some cubic group-IV, III–V and II–VI semiconductors. LCBV = lowest conduction-band valley; ID = indirect band-gap semiconductor; D = direct band-gap semiconductor

System	Material	Type (LCBV)	ΔE_g (eV)		
			$\lvert\Gamma - X(\Delta)\rvert$	$\lvert\Gamma - L\rvert$	$\lvert X(\Delta) - L\rvert$
IV	Diamond	ID (X or Δ)	1.52		
	Si	ID (X)	2.22	1.3	0.9
	Ge	ID (L)	0.057	0.129	0.186
	3C-SiC	ID (X)	5.01	3.20	1.81
III–V	*c*-BN	ID	4.51[a]	1.40[a]	5.91[a]
	BP	ID (X or L)	3[b]	3[b]	
	AlP	ID (X)	1.15		
	AlAs	ID (X)	0.79	0.59	0.20
	AlSb	ID (X or Δ)	0.69	0.09	0.60
	β-GaN	D (Γ)	1.3[a]	2.7[a]	1.4[a]
	GaP	ID (X or Δ)	0.50	0.13	0.37
	GaAs	D (Γ)	0.47	0.28	0.19
	GaSb	D (Γ)	0.33	0.04	0.29
	InP	D (Γ)	0.96	0.86	0.10
	InAs	D (Γ)	1.82	1.10	0.72
	InSb	D (Γ)	1.45	0.75	0.70
II–VI	MgO	D (Γ)[c]	3.8[a]	2.9[a]	
	ZnSe	D (Γ)	∼0.7	∼1.1	∼0.4
	ZnTe	D (Γ)	∼0.7		

[a] Calculated
[b] Estimated
[c] Tentative assignment

(c) Temperature and pressure coefficients

Table 6.18 summarizes the experimental temperature and hydrostatic pressure coefficients of the lowest indirect band-gap energy E_g^{ID} for some group-IV and III–V indirect band-gap semiconductors at $T = 300$ K.

6.5 CONDUCTION-VALLEY ENERGY SEPARATION

The band structure of a semiconductor is schematically drawn in Figure 6.28 in which the top of the valence band and the direct (Γ) and indirect minima (X and L) of the conduction band are shown. It is known that major influences on carrier effective mass, mobility and lifetime are the positions and shape of the conduction-band second minima most often found at the L point in the Brillouin zone [6.53]. The effect of the conduction-band satellite valleys is also illustrated by the Gunn effect [6.54]. Here, we list in Table 6.19 the conduction-valley energy separation ΔE_g for some cubic group-IV, III–V and II–VI semiconductors.

6.6 DIRECT–INDIRECT-GAP TRANSITION PRESSURE

Since the sign of the pressure coefficients of E_0 and E_g^X is opposite in many semiconductors, a direct band-gap semiconductor sometimes changes to an indirect band-gap one at any pressure. As an example, we show in Figure 6.29 the hydrostatic pressure dependence

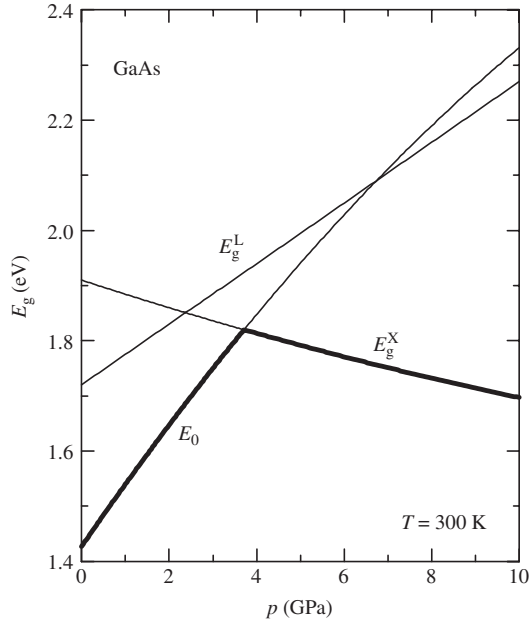

Figure 6.29 E_0, E_g^X and E_g^L versus hydrostatic pressure p for GaAs at $T = 300$ K

Table 6.20 Direct–indirect-gap transition pressure for some III–V and II–VI semiconductors

System	Material	Transition pressure (GPa)
III–V	GaAs	4.2 ($\Gamma_6 - X_6$)
	GaSb	1.05 ($\Gamma_6 - L_6$)
	InP	10.4 ($\Gamma_6 - X_6$)
II–VI	β-ZnS	*a*
	ZnSe	*a*
	ZnTe	~6.5 ($\Gamma_6 - X_6$)
	CdTe	*a*

[a] No direct–indirect-gap crossing occurs for pressures up to the first structural phase transition

of the E_0-gap, E_g^X-gap and E_g^L-gap energies for GaAs at $T = 300$ K. The solid lines are calculated from the following expressions [6.30]

$$E_0(p) = 1.427 + 1.15 \times 10^{-1} p - 2.45 \times 10^{-3} p^2 \tag{6.39a}$$

$$E_g^X(p) = 1.91 - 2.6 \times 10^{-2} p + 4.7 \times 10^{-4} p^2 \tag{6.39b}$$

$$E_g^L(p) = 1.72 + 5.5 \times 10^{-2} p \tag{6.39c}$$

It is understood from Figure 6.29 that GaAs becomes an indirect band-gap semiconductor at $p \sim 4$ GPa. Note that this value is well below ~17 GPa to the first structural phase transition (see Section 1.5). It is also expected that an indirect–indirect (L_6–X_6) crossing occurs at ~2.5 GPa.

The direct–indirect (Γ_6–X_6) crossing in GaAs has been studied experimentally by many authors [6.30]. These authors, except Yu and Welber [6.55], indicate that the Γ_6–X_6 crossing occurs at ~4 GPa. The value reported by Yu and Welber (~3 GPa) is considerably smaller than this. Kangarlu *et al*. [6.56] observed the L_6–X_6 indirect–indirect crossing at $p = 2.5$–3.0 GPa from photoluminescence measurements under hydrostatic pressure. Our estimated L_6–X_6 crossing pressure (~2.5 GPa) is in reasonable agreement with this value.

Table 6.20 summarizes the direct–indirect (Γ_6–X_6) crossing pressures observed for some III–V and II–VI semiconductors.

REFERENCES

[6.1] U. Schmid, N. E. Christensen, and M. Cardona, *Phys. Rev. B* **41**, 5919 (1990).

[6.2] S. Adachi, *Phys. Rev. B* **38**, 12966 (1988); *J. Appl. Phys.* **66**, 3224 (1989).

[6.3] D. E. Aspnes and A. A. Studna, *Solid State Commun.* **11**, 1375 (1972).

[6.4] J. R. Chelikowsky and M. L. Cohen, *Phys. Rev. B* **14**, 556 (1976).

[6.5] S. Adachi, *Physical Properties of III–V Semiconductor Compounds: InP, InAs, GaAs, GaP, InGaAs, and InGaAsP* (Wiley-Interscience, New York, 1992).

[6.6] H. Yoshikawa and S. Adachi, *Jpn. J. Appl. Phys.* **35**, 5946 (1996).

[6.7] W. J. Turner, W. E. Reese, and G. D. Pettit, *Phys. Rev.* **136**, A1467 (1964).
[6.8] P. Lautenschlager, M. Garriga, and M. Cardona, *Phys. Rev. B* **36**, 4813 (1987).
[6.9] A. Kobayashi, O. F. Sankey, S. M. Volz, and J. D. Dow, *Phys. Rev. B* **28**, 935 (1983).
[6.10] T. K. Bergstresser and M. L. Cohen, *Phys. Rev.* **164**, 1069 (1967).
[6.11] S. Ninomiya and S. Adachi, *J. Appl. Phys.* **78**, 4681 (1995).
[6.12] M. Cardona, *Phys. Rev.* **129**, 1068 (1963).
[6.13] J. L. Birman, *Phys. Rev.* **115**, 1493 (1959).
[6.14] D. G. Thomas and J. J. Hopfield, *Phys. Rev.* **116**, 573 (1959); J. J. Hopfield, *J. Phys. Chem. Solids* **15**, 97 (1960).
[6.15] S. Logothetidis, M. Cardona, P. Lautenschlager, and M. Garriga, *Phys. Rev. B* **34**, 2458 (1986).
[6.16] C. Janowitz, O. Günther, G. Jungk, R. L. Johnson, P. V. Santos, M. Cardona, W. Faschinger, and H. Sitter, *Phys. Rev. B* **50**, 2181 (1994).
[6.17] J. R. Chelikowsky, T. J. Wagener, J. H. Weaver, and A. Jin, *Phys. Rev. B* **40**, 9644 (1989).
[6.18] R. H. Paramenter, *Phys. Rev.* **100**, 573 (1955).
[6.19] G. Dresselhaus, *Phys. Rev.* **100**, 580 (1955).
[6.20] M. P. Surh, M.-F. Li, and S. G. Louie, *Phys. Rev. B* **43**, 4286 (1991).
[6.21] M. Suzuki and T. Uenoyama, in *Properties, Processing and Applications of Gallium Nitride and Related Semiconductors*, EMIS Datareviews Series No. 23, edited by J. H. Edgar, S. Strite, I. Akasaki, H. Amano, and C. Wetzel (INSPEC, London, 1999), p. 155.
[6.22] T. L. Tansley and C. P. Foley, *J. Appl. Phys.* **59**, 3241 (1986).
[6.23] T. Inushima, V. V. Mamutin, V. A. Vekshin, S. V. Ivanov, T. Sakon, M. Motokawa, and S. Ohoya, *J. Cryst. Growth* **227–228**, 481 (2001).
[6.24] V. Yu. Davydov, A. A. Klochikhin, R. P. Seisyan, V. V. Emtsev, S. V. Ivanov, F. Bechstedt, J. Furthmüller, H. Harima, A. V. Mudryi, J. Aderhold, O. Semchinova, and J. Graul, *Phys. Status Solidi B* **229**, R1 (2002).
[6.25] V. Yu. Davydov, A. A. Klochikhin, V. V. Emtsev, S. V. Ivanov, V. V. Vekshin, F. Bechstedt, J. Furthmüller, H. Harima, A. V. Mudryi, A. Hashimoto, A. Yamamoto, J. Aderhold, J. Graul, and E. E. Haller, *Phys. Status Solidi B* **230**, R4 (2002).
[6.26] J. Wu, W. Walukiewicz, K. M. Yu, J. W. Ager III, E. E. Haller, H. Lu, W. J. Schaff, Y. Saito, and Y. Nanishi, *Appl. Phys. Lett.* **80**, 3967 (2002).
[6.27] J. Wu, W. Walukiewicz, W. Shan, K. M. Yu, J. W. Ager III, E. E. Haller, H. Lu, and W. J. Schaff, *Phys. Rev. B* **66**, 201403 (2002).
[6.28] T. Matsuoka, H. Okamoto, M. Nakao, H. Harima, and E. Kurimoto, *Appl. Phys. Lett.* **81**, 1246 (2002).
[6.29] Y. P. Varshni, *Physica* **34**, 149 (1967).
[6.30] S. Adachi, *GaAs and Related Materials: Bulk Semiconducting and Superlattice Properties* (World Scientific, Singapore, 1994).
[6.31] L. Viña, S. Logothetidis, and M. Cardona, *Phys. Rev. B* **30**, 1979 (1984).
[6.32] R. Pässler, *Phys. Status Solidi B* **200**, 155 (1997).
[6.33] R. Pässler, *Phys. Status Solid B* **216**, 975 (1999).
[6.34] S. Ozaki, T. Mishima, and S. Adachi, *Jpn. J. Appl. Phys.* **42**, 5465 (2003).
[6.35] P. Lautenschlager, P. B. Allen, and M. Cardona, *Phys. Rev. B* **31**, 2163 (1985).
[6.36] L. Malikova, W. Krystek, F. H. Pollak, N. Dai, A. Cavus, and M. C. Tamargo, *Phys. Rev. B* **54**, 1819 (1996).
[6.37] K.-F. Berggren and B. E. Sernelius, *Phys. Rev. B* **24**, 1971 (1981).
[6.38] J. Serre and A. Ghazali, *Phys. Rev. B* **28**, 4704 (1983).
[6.39] E. Burstein, *Phys. Rev.* **93**, 632 (1954).
[6.40] J. del Alamo, S. Swirhun, and R. M. Swanson, in *Proc. Int. Electron Dev. Meeting* (IEEE, USA, 1985), p. 290.
[6.41] H. Yao and A. Compaan, *Appl. Phys. Lett.* **57**, 147 (1990).
[6.42] H. S. Bennett and J. R. Lowney, *J. Appl. Phys.* **62**, 521 (1987).

[6.43] S. E. Swirhun, Y.-H. Kwark, and R. M. Swanson, in *Proc. Int. Electron Dev. Meeting* (IEEE, USA, 1986), p. 24.
[6.44] J. W. Slotboom and H. C. de Graaf, *Solid-State Electron.* **19**, 857 (1976).
[6.45] R. Benzaquen, T. Erland, C. Lacelle, E. Fortin, and A. P. Roth, *Can. J. Phys.* **69**, 339 (1991).
[6.46] S. C. Jain, J. M. McGregor, D. J. Roulston, and P. Balk, *Solid-State Electron.* **35**, 639 (1992).
[6.47] J. A. Silberman, T. J. de Lyon, and J. M. Woodall, *Appl. Phys. Lett.* **58**, 2126 (1991).
[6.48] L. Wang, B. J. Aitchison, and N. M. Haegel, *Appl. Phys. Lett.* **60**, 1111 (1992).
[6.49] M. Cardona, K. L. Shaklee, and F. H. Pollak, *Phys. Rev.* **154**, 696 (1967).
[6.50] M. Cardona and N. E. Christensen, *Solid State Commun.* **116**, 421 (2000).
[6.51] A. Kaneta and S. Adachi, *J. Appl. Phys.* **87**, 7360 (2000).
[6.52] S. Logothetidis, J. Petalas, M. Cardona, and T. D. Moustakas, *Phys. Rev. B* **50**, 18017 (1994).
[6.53] C. B. Geller, W. Wolf, S. Picozzi, A. Continenza, R. Asahi, W. Mannstadt, A. J. Freeman, and E. Wimmer, *J. Appl. Phys.* **79**, 368 (2001).
[6.54] J. B. Gunn, *Solid State Commun.* **1**, 88 (1963).
[6.55] P. Y. Yu and B. Welber, *Solid State Commun.* **25**, 209 (1978).
[6.56] A. Kangarlu, H. Guarriello, R. Berney, and P. W. Yu, *Appl. Phys. Lett.* **59**, 2290 (1991).

7 Energy-band Structure: Effective Masses

7.1 Electron effective mass: Γ valley 147
7.1.1 General remarks 147
7.1.2 Numerical value 149
7.1.3 Polaron effect 151
7.1.4 External perturbation and doping effects 152
7.2 Electron effective mass: satellite valley 158
7.2.1 Camel's back structure 158
7.2.2 Numerical value 159
7.3 Hole effective mass 159
7.3.1 Effective Γ-valence-band Hamiltonian and Luttinger parameter 159
7.3.2 Numerical value 164
7.3.3 Polaron effect 168
7.3.4 External perturbation and doping effects 170
References 171

7.1 ELECTRON EFFECTIVE MASS: Γ VALLEY

7.1.1 General remarks

Since the carrier effective mass is strongly connected with carrier mobility, it is known to be one of the most important device parameters. A way of displaying useful information about the effective mass is to show the constant-energy surface near the band edge in $\boldsymbol{k}$ space. We show in Figure 7.1 the constant-energy surfaces for electrons near the (a) Γ, (b) X and (c) L valleys of diamond-type and zinc-blende-type semiconductors. The constant-energy surface can now be defined by

$$E = \frac{\hbar^2 \boldsymbol{k}_x^2}{2m_x} + \frac{\hbar^2 \boldsymbol{k}_y^2}{2m_y} + \frac{\hbar^2 \boldsymbol{k}_z^2}{2m_z} \tag{7.1}$$

As seen in Figure 7.1(a), the Γ-valley electron has a spherical constant-energy surface at the zone center, i.e., $m_x = m_y = m_z$.

There are six constant-energy ellipsoids along the principal diagonal [100] and equivalent directions (Figure 7.1(b)) and eight ellipsoids along the ⟨111⟩ directions

Properties of Group-IV, III–V and II–VI Semiconductors Sadao Adachi

© 2005 John Wiley & Sons, Ltd

ISBN: 0-470-09032-4

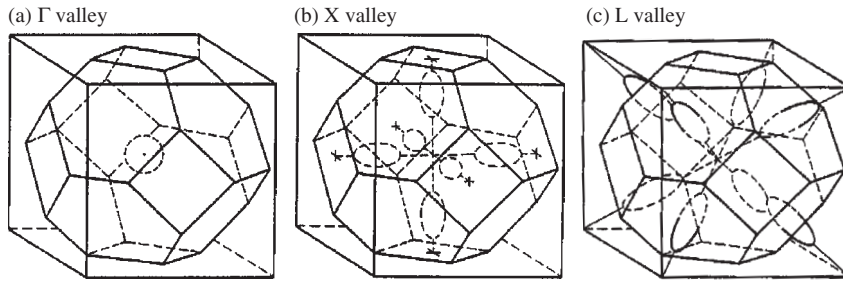

Figure 7.1 Constant-energy surfaces for electrons near the: (a) Γ; (b) X; and (c) L valleys of the diamond-type and zinc-blende-type semiconductors

(Figure 7.1(c)). In such ellipsoidal constant-energy surfaces, Equation (7.1) can be written as

$$E = \frac{\hbar^2 \boldsymbol{k}_{\mathrm{t}}^2}{m_{\mathrm{t}}} + \frac{\hbar^2 \boldsymbol{k}_{\mathrm{l}}^2}{2m_{\mathrm{l}}} \tag{7.2}$$

The two masses m_{l} and m_{t} in Equation (7.2) are called the longitudinal mass and transverse mass, respectively, because m_{l} (m_z) is defined along the ⟨111⟩ axis (X valley) and along the ⟨100⟩ axis (L valley), whereas m_{t} ($m_x = m_y$) is defined in a plane transverse to the said axis. (The x and y axes have now been taken as the minor or transverse axes of the ellipsoids.) The longitudinal effective mass m_{l} is usually much larger than its counterparts m_{t}. The energy, thus, varies relatively slowly with respect to k_{l}, but varies relatively rapidly with k_{t}.

The density-of-states mass m_{e}^{α} for electrons in the conduction-band minima $\alpha = \Gamma$, X or L is given by

$$m_{\mathrm{e}}^{\alpha} = N^{2/3} m_{\mathrm{t}\alpha}^{2/3} m_{\mathrm{l}\alpha}^{1/3} \tag{7.3}$$

where N is the number of equivalent α minima ($N = 1$ for the Γ minimum, $N = 3$ for the X minima and $N = 4$ for the L minima). The density-of-states effective mass can be used for density-of-states calculations.

The conductivity effective mass m_{c}^{α}, which can be used for conductivity (mobility) calculations, is obtained from the equation

$$m_{\mathrm{c}}^{\alpha} = \frac{3m_{\mathrm{t}\alpha} m_{\mathrm{l}\alpha}}{m_{\mathrm{t}\alpha} + 2m_{\mathrm{l}\alpha}} \tag{7.4}$$

Since $m_{\mathrm{t}\Gamma} = m_{\mathrm{l}\Gamma}$ at the $\alpha = \Gamma$ minimum (Γ_6) of cubic semiconductors, we have the relation $m_{\mathrm{e}}^{\Gamma} = m_{\mathrm{c}}^{\Gamma}$. The electron effective mass can be measured by a variety of techniques, such as the Shubnikov–de Haas effect, magnetophonon resonance, cyclotron resonance and interband magnetooptical measurements [7.1].

In hexagonal semiconductors, the conduction-band electron has an ellipsoidal constant-energy surface, not spherical, even at the zone center (Γ)

$$m_{\mathrm{e}}^{\perp} \equiv m_x = m_y \neq m_z \equiv m_{\mathrm{e}}^{\parallel} \tag{7.5}$$

Thus, $m_{\mathrm{e}}^{\Gamma} \neq m_{\mathrm{c}}^{\Gamma}$ holds in such anisotropic semiconductors, but its difference is very small.

7.1.2 Numerical value

We list in Table 7.1 the zone-center electron effective mass m_e^Γ for a number of cubic group-IV, III–V and II–VI semiconductors, together with the corresponding lowest direct band-gap energy E_0. Figure 7.2 also plots m_e^Γ versus E_0 values for some of these semiconductors.

The $k \cdot p$ perturbation method is a powerful procedure for evaluating the conduction-band effective mass parameters in the vicinity of certain important points in $\boldsymbol{k}$ space. The simple five-level $\boldsymbol{k} \cdot \boldsymbol{p}$ theory of Hermann and Weisbuch [7.2] at $\boldsymbol{k} = 0$ (Γ) in diamond-type and zinc-blende-type semiconductors can be shown to lead to the electron effective-mass ratio

$$\frac{m_0}{m_e^\Gamma} = 1 + \frac{P^2}{3}\left(\frac{2}{E_0} + \frac{1}{E_0 + \Delta_0}\right) - \frac{P'^2}{3}\left(\frac{2}{E(\Gamma_8^c) - E_0} + \frac{1}{E(\Gamma_7^c) - E_0}\right) + C \qquad (7.6)$$

where m_0 is the free-electron mass, P is the momentum matrix element concerning the p-like valence band with the s-like conduction band, P' is the momentum matrix element connecting the s-like conduction band with next-higher-lying p-like conduction band and C is a small correction for all higher-lying bands.

For all III–V compounds, P'^2 is considerably smaller than P^2. The energy denominators in Equation (7.6) for the P'^2 term are also much larger than those for P^2. The effective mass is thus strongly connected with the lowest direct gaps E_0 and $E_0 + \Delta_0$. Assuming that $E_0 \gg \Delta_0$ and $m_0/m_e^\Gamma \gg 1$, Equation (7.6) can be simply rewritten as

$$\frac{m_0}{m_e^\Gamma} \sim \frac{P^2}{E_0} \qquad (7.7)$$

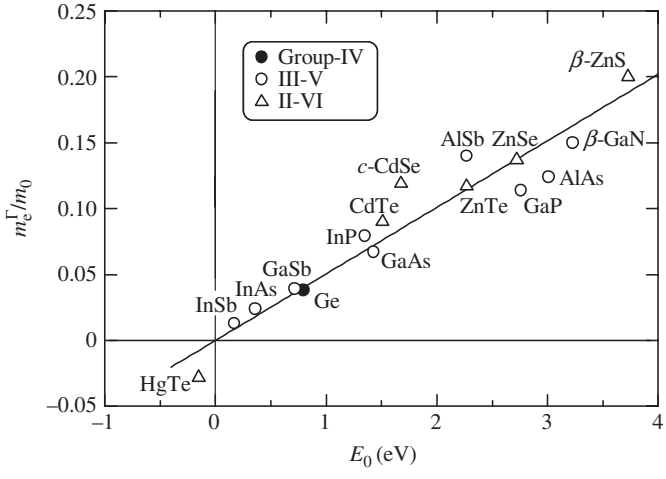

Figure 7.2 Electron effective mass m_e^Γ/m_0 versus E_0 for some cubic group-IV, III–V and II–VI semiconductors. The solid line represents the least-squares fit with $m_e^\Gamma/m_0 = 0.0505E_0$ (E_0 in eV)

Table 7.1 Electron effective mass m_e^Γ and lowest direct band-gap energy E_0 ($T = 300$ K) for some cubic group-IV, III–V and II–VI semiconductors

System	Material	m_e^Γ/m_0	E_0 (eV)
IV	Diamond	0.36–2.030[a]	15.3
	Si	0.188[a]	4.06
	Ge	0.038	0.795
	α-Sn	−0.058[b]	−0.413 ($T = 1.5$ K)[b]
	3C-SiC	0.449[a]	7.4
III–V	c-BN	0.752[a]	7.9–11.40[a]
	BP	0.150[a]	
	BAs	0.0499[a]	1.45
	c-AlN	0.26[a]	5.2
	AlP	0.220[a]	3.91[c]
	AlAs	0.124	3.01
	AlSb	0.14	2.27
	β-GaN	0.15	3.231
	GaP	0.114	2.76
	GaAs	0.067	1.43
	GaSb	0.039	0.72
	InP	0.07927	1.35
	InAs	0.024	0.359
	InSb	0.013	0.17
II–VI	MgO	0.35[a]	7.8
	β-MgS	0.225[a]	4.45
	β-MgSe	0.20[a]	4.0
	β-MgTe	0.17[a]	3.4
	β-ZnS	0.20	3.726
	ZnSe	0.137	2.721
	ZnTe	0.117	2.27
	c-CdS	0.14[a]	2.46
	c-CdSe	0.119	1.675
	CdTe	0.090	1.51
	β-HgS	−0.006[a,d]	−0.04[a,d]
	HgSe	−0.042[a,d]	−0.08[d]
	HgTe	−0.028[d]	−0.15[d]

[a] Calculated or estimated
[b] The sign is chosen positive for a normal band structure like that of Ge.
[c] Estimated from $Al_xGa_{1-x}P$ data
[d] The sign is chosen positive for a normal band structure like that of CdTe.

If one also assumes that P^2 is independent of material, m_e^Γ is directly related to the lowest direct band-gap energy E_0. The relationship between m_e^Γ and E_0 given in Figure 7.2

$$\frac{m_e^\Gamma}{m_0} = 0.0505 E_0 \tag{7.8}$$

shows an excellent agreement with the theoretical prediction of Equation (7.7).

Table 7.2 Γ-valley electron effective masses, $m_e^{\perp}$, $m_e^{\parallel}$ and m_e^{Γ}, and lowest direct band-gap energy $E_0(T = 300\ \text{K})$ for some wurtzite III–V and II–VI semiconductors. $m_e^{\Gamma} = (m_e^{\perp 2} m_e^{\parallel})^{1/3}$: density-of-states effective mass

System	Material	$m_e^{\perp}/m_0$	$m_e^{\parallel}/m_0$	m_e^{Γ}/m_0	E_0 (eV)
III–V	w-AlN	0.29[a]	0.30[a]	0.29–0.45 (0.29[a])	6.2
	α-GaN	0.21	0.22	0.21	3.420
	InN			0.11 (0.07[b])	1.89 (0.7–1.1[b])
II–VI	ZnO			0.234	3.40
	α-ZnS	0.28	0.28	0.28	3.75
	w-CdS	0.150	0.152	0.151	2.501
	w-CdSe	0.127	0.122	0.125	1.751

[a] Calculated

[b] Note that very recent studies for InN suggest an evidence of the narrow band-gap energy E_0 and of the small m_e^{Γ} value

Table 7.2 lists the zone-center electron effective masses $m_e^{\perp}, m_e^{\parallel}$ and m_e^{Γ} for some wurtzite III–V and II–VI semiconductors, together with their corresponding lowest direct band-gap energy E_0. Figure 7.3 also plots m_e^{Γ} versus E_0 values for these semiconductors. The solid line represents the least-squares fit with the relation (E_0 in eV)

$$\frac{m_e^{\Gamma}}{m_0} = 0.0675 E_0 \tag{7.9}$$

Note that the InN value is reported to be $m_e^{\Gamma} = 0.11 m_0$ [7.3]; however, recent studies suggest evidence of the narrow band-gap energy E_0 (~0.7–1.1 eV) and of the small m_e^{Γ} value of $0.07 m_0$ for this material [7.4].

7.1.3 Polaron effect

Electron–LO-phonon coupling is known to modify the electron effective mass [7.5]. One way to get information about the electron effective mass is a cyclotron resonance experiment. It is noted that the cyclotron resonance experiment gives the polaron mass rather than the 'bare' band mass. In order to deduce the true band mass from cyclotron measurements, it is therefore necessary to correct for such a polaron enhancement. This correction can be written, by means of Langreth formula, as [7.6]

$$m_e^{\Gamma} = \left(\frac{1 - 0.0008\alpha_F^2}{1 - \left(\frac{\alpha_F}{6}\right) + 0.0034\alpha_F^2} \right) m_{ep}^* \tag{7.10}$$

where α_F is the Fröhlich coupling constant (see Section 5.2) and m_{ep}^* is the cyclotron (polaron) mass known from experiment. Typical value for this correction is a few percent

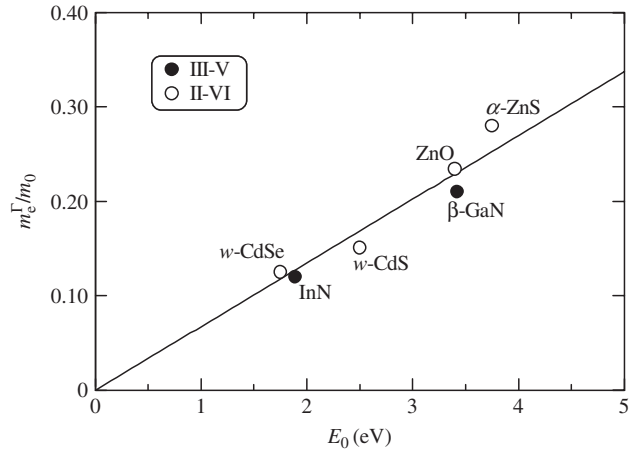

Figure 7.3 Electron effective mass m_e^Γ/m_0 versus E_0 for some wurtzite III–V and II–VI semiconductors. The solid line represents the least-squares fit with $m_e^\Gamma/m_0 = 0.0675E_0$ (E_0 in eV)

for the III–V semiconductors. The correction is, thus, less than the other experimental uncertainties.

7.1.4 External perturbation and doping effects

(a) Temperature effect

The effect of temperature on the electron effective mass in semiconductors has been studied by several authors (see, e.g., GaAs [7.1]). Figure 7.4 plots, as an example, the electron mass m_e^Γ as a function of temperature T for GaAs. The experimental data are taken from Stradling and Wood [7.7]. These data were deduced from magnetophonon resonance measurements on a high-purity n-GaAs sample. Small corrections were performed for the polaron effect. It is understood from Figure 7.4 that m_e^Γ decreases with increasing T.

The temperature variation of m_e^Γ can be simply assumed to be given by

$$m_e^\Gamma(T) = m_e^\Gamma(0)\frac{E_0(T)}{E_0(0)} \tag{7.11}$$

where m_e^Γ (0) and $E_0(0)$ represent the mass and E_0 values at $T = 0$ K, respectively. The change in the effective mass with temperature can also be estimated by substituting the change in the energy gap with temperature into the three-level $\boldsymbol{k}\cdot\boldsymbol{p}$ formula

$$\frac{m_0}{m_e^\Gamma(T)} = 1 + \frac{P^2}{3}\left(\frac{2}{E_0(T)} + \frac{1}{[E_0 + \Delta_0(T)]}\right) \tag{7.12}$$

The $E_0(T)$ and $E_0 + \Delta_0(T)$ in Equations (7.11) and (7.12) can be given by the Varshni equation (see Section 6.2).

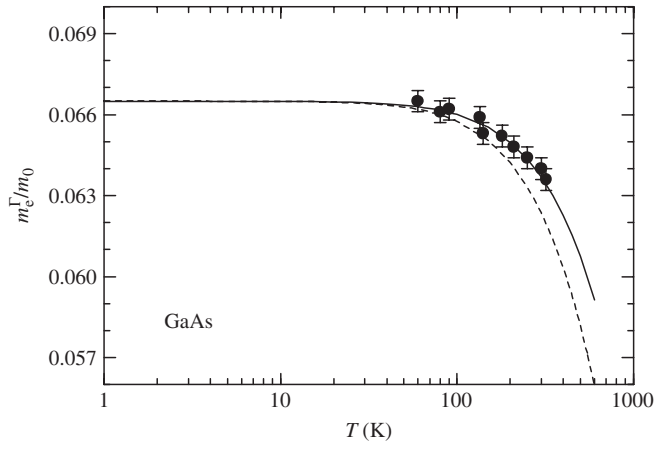

Figure 7.4 Electron effective mass m_e^Γ as a function of temperature T for GaAs. The experimental data (solid circles) are taken from Stradling and Wood [7.7]. The dashed and solid lines are obtained from Equations (7.11) and (7.12), respectively

The dashed and solid lines in Figure 7.4 are calculated from Equations (7.11) and (7.12), respectively. Here, we used the following numerical values: $m_e^\Gamma(0) = 0.0665m_0$; $P^2 = 22.66$ eV; and the Varshni parameters from Lautenschlager *et al.* [7.8]. It is seen that the expression (7.12) yields better agreement with the experimental data than Equation (7.11).

(b) Pressure effect

The effect of hydrostatic pressure p on the electron effective mass in semiconductors has been studied both theoretically and experimentally (see, e.g., GaAs [7.1]). We summarize in Table 7.3 the change in the electron effective mass $\mathrm{d}\ln m_e^\Gamma/\mathrm{d}p = (m_e^\Gamma)^{-1}(\mathrm{d}m_e^\Gamma/\mathrm{d}p)$ observed for some III–V and II–VI semiconductors. Figure 7.5 also shows the plots of $\mathrm{d}\ln m_e^\Gamma/\mathrm{d}p$ versus E_0 for some of these semiconductors.

Table 7.3 Hydrostatic pressure coefficient $\mathrm{d}\ln m_e^\Gamma/\mathrm{d}p$ experimentally obtained for some III–V and II–VI semiconductors

System	Material	$\dfrac{\mathrm{d}\ln m_e^\Gamma}{\mathrm{d}p}$ (%/kbar)
III–V	GaAs	0.72
	InP	0.53
	InAs	2.0
	InSb	6.3
II–VI	ZnSe	0.00

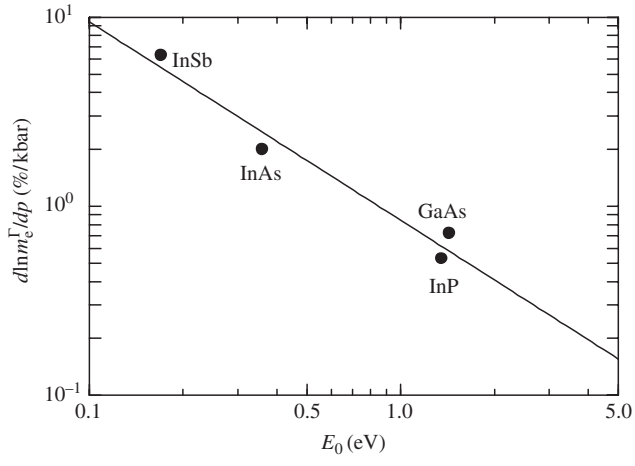

Figure 7.5 Hydrostatic pressure change in the electron effective mass $\mathrm{d}\ln m_\mathrm{e}^\Gamma/\mathrm{d}p$ versus E_0 for some III–V semiconductors. The solid line represents the fit with $\mathrm{d}\ln m_\mathrm{e}^\Gamma/\mathrm{d}p = (0.85/E_0)^{1.05}$ with E_0 in eV and $\mathrm{d}\ln m_\mathrm{e}^\Gamma/\mathrm{d}p$ in %/kbar

Increasing p increases not only the band-gap energy, but also the band effective mass through the relation (three-level $\boldsymbol{k}\cdot\boldsymbol{p}$ formula)

$$\frac{m_0}{m_\mathrm{e}^\Gamma(p)} = 1 + \frac{P^2}{3}\left(\frac{2}{E_0(p)} + \frac{1}{[E_0 + \Delta_0(p)]}\right) \tag{7.13}$$

The solid line in Figure 7.6 represents the calculated result of Equation (7.13) for GaAs with $P^2 = 22.66$ eV and $E_0(p)$ taken from Besson *et al.* [7.9] ($\Delta_0 = 0.341$ eV). The dashed line provides the experimental linear pressure coefficient of 0.72%/kbar.

When uniaxial strain is applied to a cubic semiconductor, its conduction-band mass m_e^Γ becomes anisotropic [7.10, 7.11]. This anisotropy can be described in terms of the ratio $\mathrm{d}m_{\mathrm{e}\|}^\Gamma/\mathrm{d}m_{\mathrm{e}\perp}^\Gamma$, where $m_{\mathrm{e}\|}^\Gamma$ is the mass corresponding to the conduction-band dispersion for $\boldsymbol{k}$ in the direction of the shear axis, whereas $m_{\mathrm{e}\perp}^\Gamma$ is the mass for $\boldsymbol{k}$ perpendicular to the shear axis. Christensen [7.10] obtained the trigonal strain coefficient of the mass ratio for GaAs to be

$$\frac{\mathrm{d}}{\mathrm{d}\gamma}\left[\frac{m_{\mathrm{e}\|}^\Gamma}{m_{\mathrm{e}\perp}^\Gamma}\right]_{\langle 111\rangle} \sim -8.0 \tag{7.14}$$

where γ is a strain coefficient describing a change in the Bravais lattice point under strain. The corresponding trigonal strain coefficient for the parallel mass $m_{\mathrm{e}\|}^\Gamma$ is given by

$$\left[\frac{1}{m_{\mathrm{e}\|}^\Gamma}\frac{\mathrm{d}}{\mathrm{d}\gamma}(m_{\mathrm{e}\|}^\Gamma)\right]_{\langle 111\rangle} \sim -9 \pm 3 \tag{7.15}$$

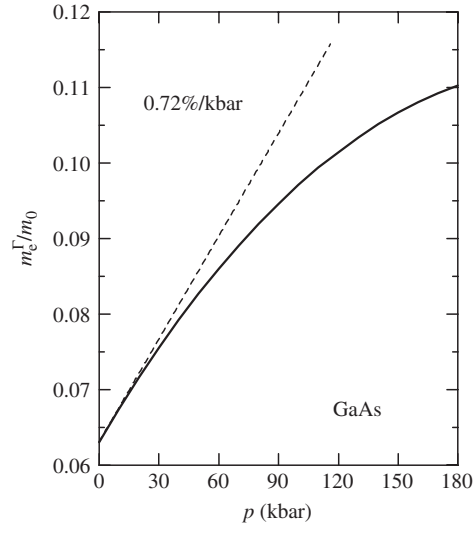

Figure 7.6 Variation of the electron effective mass m_e^Γ as a function of hydrostatic pressure p for GaAs obtained from Equation (7.13). The dashed line corresponds to liner pressure coefficient of 0.72%/kbar determined experimentally

The tetragonal-strain coefficients obtained by Christensen [7.10] are also given by

$$\frac{\mathrm{d}}{\mathrm{d}\gamma}\left[\frac{m_{e\parallel}^\Gamma}{m_{e\perp}^\Gamma}\right]_{\langle 100\rangle} \sim -0.9 \tag{7.16}$$

and

$$\left[\frac{1}{m_{e\parallel}^\Gamma}\frac{\mathrm{d}}{\mathrm{d}\gamma}(m_{e\parallel}^\Gamma)\right]_{\langle 100\rangle} \sim -3.5 \tag{7.17}$$

(c) Doping effect

In the case of an isotropic parabolic band, the mass at the Γ-conduction minimum can be defined by

$$E = \frac{\hbar^2 k^2}{2m_e^\Gamma} \tag{7.18}$$

However, for a nonparabolic band the band mass m_e^* is not identical to m_e^Γ. This is due to band nonparabolicity. The band nonparabolicity can be expressed in the form [7.12]

$$E = \frac{\hbar^2 k^2}{2m_e^\Gamma} - \frac{\alpha}{E_0}\left(\frac{\hbar^2 k^2}{2m_e^\Gamma}\right)^2 \tag{7.19}$$

where E_0 is the lowest direct band-gap energy. We neglected in the expression higher-order terms in the wavenumber $\boldsymbol{k}$. The conduction-band mass can now be defined by

$$m_e^* = \hbar \left(\frac{d^2 E}{dk^2} \right)^{-1} \sim m_e^{\Gamma}(n) \left(1 + 6 \frac{\alpha}{E_0} E \right) \tag{7.20}$$

where the approximation is obtained from Equation (7.19). For degenerate material, the electron scattering occurs at the Fermi surface E_F and m_e^* at E_F enters into the carrier transport equations.

Measurement techniques, such as Faraday rotation, Shubnikov–de Haas oscillation and magnetophonon resonance, can provide information on an optical effective mass m_{opt}^*, but not on the band mass m_e^*. The optical effective mass is now defined by

$$m_{opt}^* = \hbar^2 k \left(\frac{dE}{dk} \right)^{-1} \sim m_e^{\Gamma}(n) \left(1 + 2 \frac{\alpha}{E_0} E \right) \tag{7.21}$$

Since the nonparabolicity of the band becomes significant as the Fermi level moves up in the band, the electron effective mass in GaAs increases with doping level for carrier concentrations larger than 10^{18} cm^{-3}. The dependence of the electron mass on electron concentration in GaAs has been reported by several authors. We show in Figure 7.7, as an example, the optical mass m_{opt}^* at the Fermi energy E_F as a function of electron concentration n for GaAs as reported by Szmyd *et al.* [7.13]. The effective mass at the bottom of the conduction band m_e^{Γ} is also plotted by the solid circles. It is clear from Figure 7.7 that both m_e^{Γ} and m_{opt}^* increase with increasing electron concentration n.

The increase in m_e^{Γ} with electron concentration n at 300 K is found empirically to be [7.13]

$$\frac{m_e^{\Gamma}(n)}{m_0} = 0.0635 + 2.06 \times 10^{-22} n + 1.16 \times 10^{-40} n^2 \tag{7.22}$$

where n is in cm^{-3}. This increase in m_e^{Γ} is considered to be due to the perturbation by the donor atoms (but not by the free electrons). Szmyd *et al.* [7.13] also found that the increase in m_e^* at 300 K, due to the band nonparabolicity and the increase in m_e^{Γ} with doping, can be fitted by (n in cm^{-3})

$$m_e^*(n)\Big|_{E=E_F} = (0.0640 + 1.26 \times 10^{-20} n - 4.37 \times 10^{-40} n^2) m_0 \tag{7.23}$$

Result of Equation (7.22) is shown in Figure 7.7 by the dashed line. The solid line also indicates the calculated result of Equation (7.21) with $\alpha = 1.25$.

The expression for a carrier concentration correction on the band mass at the Fermi energy of GaAs has been proposed by Maude *et al.* [7.14]. Using their result and the pressure coefficient of ~0.7%/kbar, we obtain the variation of the band mass with electron concentration n and pressure p at the Fermi energy E_F as

$$m_e^*(n, p)\Big|_{E=E_F} = 0.0665 m_0 \frac{1 + 7 \times 10^{-3} p \text{ kbar}}{1 - 3.9 \times 10^{-15} n^{2/3} \text{ cm}^2} \tag{7.24}$$

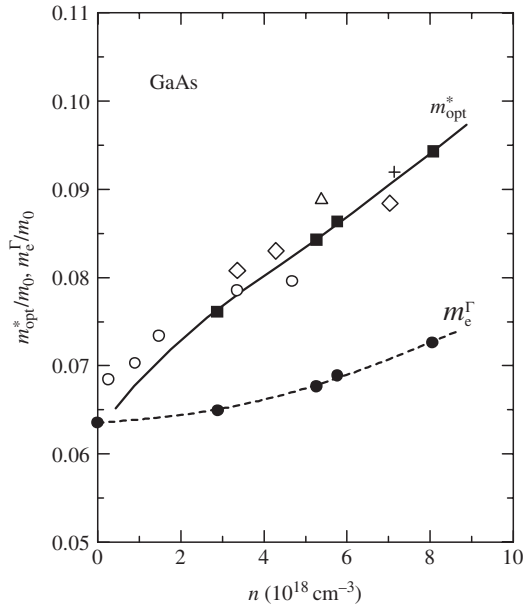

Figure 7.7 Electron optical mass m^*_{opt} at the Fermi energy E_F as a function of electron concentration n for GaAs. The effective mass m^Γ_e at the bottom of the conduction band is also shown by the solid circles. The solid line is calculated from Equation (7.21) with $\alpha = 1.25$. The dashed line is also calculated from Equation (7.22). [From D. M. Szmyd, P. Porro, A. Majerfeld, and S. Lagomarsino, *J. Appl. Phys.* **68**, 2367(1990), reproduced by permission from the American Institute of Physics]

The expression for the energy-dependent effective mass in GaAs has also been proposed by Chaudhuri and Bajaj [7.15]. It can be written as

$$\frac{m^*_e(E)}{m_0} = 0.0665 + 0.0436E + 0.236E^2 - 0.147E^3 \tag{7.25}$$

where E is expressed in electron volts.

A value of nonparabolicity factor $\alpha = 0.83$ was calculated by Vrehen [7.12] from the three-level $\boldsymbol{k} \cdot \boldsymbol{p}$ analysis of GaAs. Recent calculations, which include higher bands [7.13], yield values of α between 1.21 and 1.30.

Johnson *et al.* [7.16] have pointed out that the conduction-band structure of the common III–V semiconductors exhibits a nonparabolicity which is universal, to a good approximation, when the dispersion is plotted in the natural units of effective Rydberg energies and Bohr radii. This universality is a consequence of the scaling theory of the simple effective-mass equation for the envelope function, as in the theory of shallow donors. They also showed [7.17] that the nonparabolicity of the conduction band is approximately universal in direct band-gap GaAs under varying pressure and in direct band-gap $Al_xGa_{1-x}As$ for various alloy compositions x. The predicted universality was found to be a better approximation than the Kane's three-level $\boldsymbol{k} \cdot \boldsymbol{p}$ approximation.

The conduction-band nonparabolicity and anisotropy in GaAs have been studied by Hopkins *et al.* [7.18] by cyclotron resonance over a wide range of energies using the

photoconductive detection technique. The band-edge mass found in their experiment ($0.0660m_0$) was lower than the often quoted value of $0.0665m_0$, but agreed with the result of Sigg *et al.* [7.19].

7.2 ELECTRON EFFECTIVE MASS: SATELLITE VALLEY

7.2.1 Camel's back structure

Figures 7.8(a) and 7.8(b) show the conduction-band structures near the zone boundary, $\boldsymbol{k} = (2\pi/a)(1, 0, 0)$, for diamond-type and zinc-blende-type semiconductors, respectively. For a diamond-type semiconductor, the two conduction bands intersect at the X point. This degeneracy at the X point may be lifted by exposing the semiconductor to a large uniaxial stress along appropriate crystallographic directions. This has been well investigated in Si, where a shift of cyclotron resonance line versus stress [7.20] and a nonlinear stress dependence of the indirect band-gap energy [7.21] have been found.

For a zinc-blende-type semiconductor, the X conduction-band degeneracy is crystal-field split. The result is twofold: (i) the longitudinal effective mass increases while the transverse effective masses are hardly modified; (ii) the shift of the conduction minimum toward the Brillouin-zone boundary gives the so-called camel's back structure [7.22].

The effective Hamiltonian for the conduction-band electrons in the zinc-blende-type semiconductors can be given by [7.23]

$$H = \begin{array}{c} \begin{array}{cc} X_1 & X_3 \end{array} \\ \begin{pmatrix} Ak_\perp^2 + Bk_\parallel^2 - \dfrac{\Delta}{2} & Pk_\parallel \\ Pk_\parallel & Ak_\perp^2 + Bk_\parallel^2 + \dfrac{\Delta}{2} \end{pmatrix} \end{array} \tag{7.26}$$

where $k_\parallel$ and $k_\perp$ are, respectively, the wavevectors along and perpendicular to the $\langle 100 \rangle$ direction, Δ is the energy splitting, $A = (\hbar^2/m_t)$, $B = (\hbar^2/2m_l)$ and P is the band parameter representing the magnitude of k-linear term. Here, m_t and m_l should be distinguished from those obtained on the basis of the ellipsoidal model of Equation (7.2).

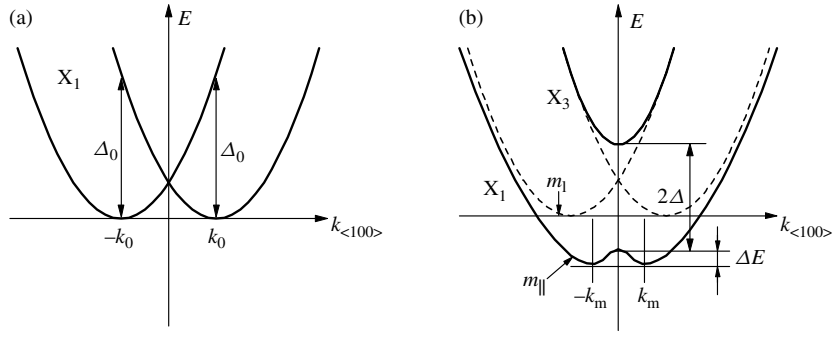

Figure 7.8 Conduction-band structure near the Brillouin-zone boundary $\boldsymbol{k} = (2\pi/a)(1, 0, 0)$ for: (a) diamond-type; and (b) zinc-blende-type semiconductors. The solid lines in (b) show the crystal-field splitting and the resulting camel's back structure

A straightforward calculation of Equation (7.26) gives an energy of the X_1 band [7.23]

$$E(k) = Ak_{\perp}^2 + Bk_{\parallel}^2 - \sqrt{\left(\frac{\Delta}{2}\right)^2 + P^2k_{\parallel}^2} \tag{7.27}$$

so that the k position of the conduction-band minimum on the $\langle 100 \rangle$ axis is given by

$$k_{\mathrm{m}} = \begin{cases} \dfrac{P}{2B}\sqrt{1 - \left(\dfrac{\Delta}{\Delta_0}\right)^2} & (\Delta \leqslant \Delta_0) \\ 0 & (\Delta \geqslant \Delta_0) \end{cases} \tag{7.28}$$

where

$$\Delta_0 = \frac{P^2}{B} \tag{7.29}$$

For $\Delta \leqslant \Delta_0$, the conduction-band minima have a camel's back structure with a camel's back height

$$\Delta E = \frac{\Delta_0}{4}\left(1 - \frac{\Delta}{\Delta_0}\right)^2 \tag{7.30}$$

The apparent effective mass $m_{\parallel}$ at the minimum is then given by

$$\frac{m_0}{m_{\parallel}} = \frac{m_0}{m_1}\left[1 - \left(\frac{\Delta}{\Delta_0}\right)^2\right] \tag{7.31}$$

It should be noted that the apparent effective mass $m_{\parallel}$ at the minimum $k_{\parallel} = k_{\mathrm{m}}$ may become much larger than m_1 for the camel's back structure.

7.2.2 Numerical value

We list in Table 7.4 the electron effective masses in the X (Δ) and L minima reported for some cubic group-IV and III–V semiconductors. The X-valley and L-valley electron density-of-states and conductivity masses for these semiconductors are listed in Table 7.5 (see definitions in Section 7.1).

7.3 HOLE EFFECTIVE MASS

7.3.1 Effective Γ-valence-band Hamiltonian and Luttinger parameter

In general, the effective Hamiltonian is derived from a $\boldsymbol{k} \cdot \boldsymbol{p}$ theory or from the theory of invariants developed by Bir and Pikus. We have already presented in Section 6.2 the effective Hamiltonians for the conduction and valence bands in the zinc-blende and

Table 7.4 Electron effective mass in the X (Δ) and L minima for some cubic group-IV and III–V semiconductors

System	Material	X		L	
		m_{tX}/m_0	m_{lX}/m_0	m_{tL}/m_0	m_{lL}/m_0
IV	Diamond	0.36	1.4		
	Si	0.1905	0.9163	0.130[a]	1.418[a]
	Ge	0.29	1.35	0.081	1.61
	α-Sn	0.086[a]	0.89[a]	0.075[a]	1.478[a]
	3C-SiC	0.25	0.67		
III–V	c-BN	0.23[a]	0.94[a]		
	BP	0.204[a]	1.125[a]		
	c-AlN	0.32[a]	0.52[a]		
	AlP	0.212[a]	3.67[a]		
	AlAs	0.19	1.1	0.15[a]	1.32[a]
	AlSb	0.21	1.50	0.20[a]	1.82[a]
	β-GaN	0.30[a]	0.58[a]		
	GaP	0.252	6.9	0.150[a]	1.184[a]
	GaAs	0.23	1.3	0.0754	1.9
	GaSb	0.33[a]	1.30[a]	0.085	1.4
	InP	0.34[a]	1.26[a]	0.13[a]	1.64[a]
	InAs	0.28[a]	1.32[a]	0.12[a]	3.57[a]

[a] Theoretical

wurtzite semiconductors. Let us rewrite those for the valence bands in the zinc-blende and wurtzite semiconductors as follows

$$H_{\mathrm{v}}^{\mathrm{ZB}} = \frac{1}{3}\Delta_{\mathrm{so}}(\boldsymbol{L}\cdot\boldsymbol{\sigma}) - (\gamma_1 + 4\gamma_2)k^2 + 6\gamma_2(\boldsymbol{L}\cdot\boldsymbol{k})^2 - 6(\gamma_2 - \gamma_3)\sum_{i,j}[L_i, L_j]k_i k_j + (a + 2b)(e_{xx} + e_{yy} + e_{zz}) - 3b\sum_i L_i^2 e_{ii} - \sqrt{3}d\sum_{i,j}[L_i, L_j]e_{ij} \tag{7.32}$$

and

$$\begin{aligned} H_{\mathrm{v}}^{\mathrm{W}} = {} & \Delta_1 L_z^2 + \Delta_2 L_z\sigma_z + \sqrt{2}\Delta_3(L_+\sigma_- + L_-\sigma_+) + (A_1 + A_3L_z^2)k_z^2 \\ & + (A_2 + A_4L_z^2)k_\perp^2 - A_5(L_+^2k_-^2 + L_-^2k_+^2) - 2A_6k_z([L_z, L_+]k_- + [L_z, L_-]k_+) \\ & + iA_7(L_+k_- - L_-k_+) + (C_1 + C_3L_z^2)e_{zz} + (C_2 + C_4L_z^2)e_\perp - C_5(L_+^2e_- + L_-^2e_+) \\ & - 2C_6([L_z, L_+]e_{-z} + [L_z, L_-]e_{+z}) \end{aligned} \tag{7.33}$$

In Equation (7.32), $\Delta_{\mathrm{so}} = \Delta_0$ is the spin–orbit split-off energy, $\boldsymbol{L}$ and $\boldsymbol{\sigma}$ are the orbital and spin angular momentum operators, respectively, $[L_i, L_j]$ is defined by $[L_i, L_j] = (L_iL_j + L_jL_i)/2$, a, b and d are Bir–Pikus deformation potentials and e_{ij} is the strain tensor component ($i, j = x, y$ or z). γ_i ($i = 1 - 3$) are Luttinger valence-band parameters. In Equation (7.33), Δ_1 and $\Delta_{2,3}$ correspond to the crystal-field and spin–orbit

Table 7.5 Electron density-of-states mass $m_e^{X,L}$ and electron conductivity mass $m_c^{X,L}$ in the X and L minima for some cubic group-IV and III–V semiconductors

System	Material	Density-of-states mass		Conductivity mass	
		m_e^X/m_0	m_e^L/m_0	m_c^X/m_0	m_c^L/m_0
IV	Diamond	1.18		0.48	
	Si	0.669	0.73	0.259	0.19
	Ge	1.01	0.553	0.39	0.119
	α-Sn	0.39[a]	0.51[a]	0.12[a]	0.11[a]
	3C-SiC	0.72		0.32	
III–V	c-BN	0.76[a]		0.31[a]	
	BP	0.75[a]		0.28[a]	
	c-AlN	0.78[a]		0.37[a]	
	AlP	1.14[a]		0.31[a]	
	AlAs	0.71	0.78	0.26[a]	0.21[a]
	AlSb	0.84	1.05[a]	0.29	0.28[a]
	β-GaN	0.78[a]		0.36[a]	
	GaP	1.58	0.75[a]	0.37	0.21[a]
	GaAs	0.85	0.56	0.32	0.11
	GaSb	1.08[a]	0.54	0.44[a]	0.12
	InP	1.09[a]	0.76[a]	0.45[a]	0.19[a]
	InAs	0.98[a]	0.94[a]	0.38[a]	0.18[a]

[a] Theoretical

splitting parameters in eV, respectively, $L_\pm = (L_x \pm iL_y)/\sqrt{2}$, $\sigma_\pm = (\sigma_x \pm i\sigma_y)/2$, $k_\perp^2 = k_x^2 + k_y^2$, $k_\pm = k_x \pm ik_y$, C_i $(i = 1 - 6)$ are Bir–Pikus deformation potentials, $e_\perp = e_{xx} + e_{yy}$, $e_\pm = e_{xx} - e_{yy} \pm 2ie_{xy}$ and $e_{\pm z} = e_{xz} \pm ie_{yz}$. A_i $(i = 1–6)$ are Luttinger valence-band parameters. Note that in the quasi-cubic approximation, the Luttinger parameters in Equations (7.32) and (7.33) have the relationships

$$\begin{aligned} A_1 &= -(\gamma_1 + 4\gamma_3) \\ A_2 &= -(\gamma_1 - 2\gamma_3) \\ A_3 &= 6\gamma_3 \\ A_4 &= -3\gamma_3 \\ A_5 &= -(\gamma_2 + 2\gamma_3) \\ A_6 &= -\sqrt{2}(2\gamma_2 + \gamma_3) \end{aligned} \tag{7.34}$$

and

$$\begin{aligned} &A_1 - A_2 = -A_3 = 2A_4 = 4A_5 - \sqrt{2}A_6 \\ &A_7 = 0 \end{aligned} \tag{7.35}$$

Table 7.6 presents the relations between the Luttinger parameters γ_i and other common sets of the valence-band reciprocal mass parameters [7.24–7.27] (see also [7.28]). For

Table 7.6 Comparison of notations used for representing the band curvatures in the valence band of cubic semiconductors

Luttinger[a]	LK–DKK[b]	Kane[c]
γ_1	$-A$	$-r_1/\sqrt{3}$
γ_2	$-B/2$	$-r_3/2\sqrt{3}$
γ_3	$\sqrt{3B^2+C^2}/2\sqrt{3}$	$-r_5/2\sqrt{6}$

[a] J. M. Luttinger, *Phys. Rev.* **102**, 1030 (1956)
[b] J. M. Luttinger and W. Kohn, *Phys. Rev.* **97**, 869 (1955); G. Dresselhaus, A. F. Kip, and C. Kittel, *Phys. Rev.* **98**, 368 (1955)
[c] E. O. Kane, *Phys. Rev.* **178**, 1368 (1969)

simplicity, we set $\hbar^2/2m_0 \rightarrow 1$. Note that the parameter C in the LK–DKK notation is related to parameters in Table 7.6 by $C^2 = D^2 - 3B^2$.

The heavy-hole and light-hole valence bands are anisotropic even in the diamond-type and zinc-blende-type semiconductors. Figure 7.9 schematically shows the two-dimensional and three-dimensional constant-energy surfaces for holes in the heavy-hole and light-hole bands of diamond-type and zinc-blende-type semiconductors. As easily understood from Figure 7.9, the anisotropy effect is most pronounced for the heavy-hole band, which has a strongly directionally dependent effective mass, with a larger mass along the [111] direction than along the [100] direction [7.29].

Hamiltonians for various directions can be readily derived by expressing $J_{x,y,z}$ and $k_{x,y,z}$ in terms of their projections in the new coordinate systems, chosen so that one axis is along the chosen direction and the other two perpendicular to it. We summarize in Table 7.7 the functional forms for the heavy-hole and light-hole masses, m_{HH} and m_{LH}, expressed in terms of γ_i, along the [001], [110] and [111] directions in diamond-type and zinc-blende-type semiconductors [7.30]. Table 7.8 also shows the functional expressions for the density-of-states heavy-hole mass (m^*_{HH}), averaged light-hole mass (m^*_{LH}) and spherically averaged heavy-hole ($m^{\mathrm{s}}_{\mathrm{HH}}$) and light-hole masses ($m^{\mathrm{s}}_{\mathrm{LH}}$).

The Γ_7 spin–orbit split-off valence band has nearly the spherical constant-energy surface at the center of the Brillouin zone ($\boldsymbol{k} = 0$). The three-level $\boldsymbol{k} \cdot \boldsymbol{p}$ formula can provide the spin–orbit split-off hole mass m_{SO}

$$\frac{m_0}{m_{\mathrm{SO}}} = \gamma_1 - \frac{P^2}{3}\left(\frac{1}{E_0} - \frac{1}{E_0 - \Delta_0}\right) \tag{7.36}$$

where γ_1 is the Luttinger parameter and P^2 is the squared momentum matrix element. Introducing $\gamma_1 = 7.10$, $P^2 = 22.66$ eV, $E_0 = 1.43$ eV and $E_0 + \Delta_0 = 1.76$ eV for GaAs, we obtain $m_{\mathrm{SO}}/m_0 = 0.164$, in excellent agreement with the experimental data ($m_{\mathrm{SO}}/m_0 = 0.165$, see below).

The wurtzite-type semiconductor has C_{6v} point-group symmetry. At the center of the Brillouin zone, the conduction band has Γ_7 (s-like) symmetry and the A, B and C valence

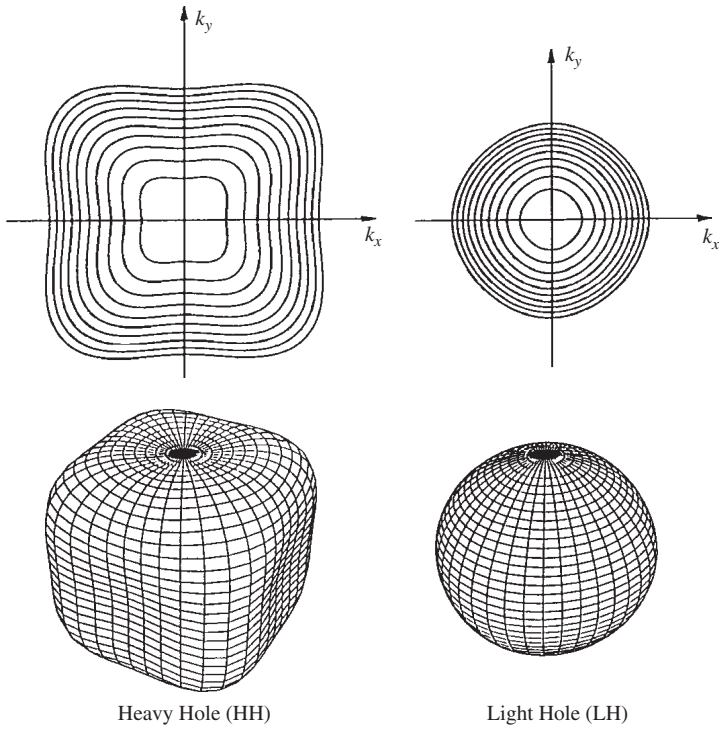

Figure 7.9 Two-dimensional (upper parts) and three-dimensional constant-energy surfaces (lower parts) for holes in the heavy-hole and light-hole bands of the diamond-type and zinc-blende-type semiconductors

Table 7.7 Functional expression for the heavy-hole and light-hole effective band masses, m_{HH} and m_{LH}, along the [001], [110] and [111] directions represented by Luttinger valence-band parameters γ_i

Direction	m_{HH}/m_0	m_{LH}/m_0
[001]	$\dfrac{1}{\gamma_1 - 2\gamma_2}$	$\dfrac{1}{\gamma_1 + 2\gamma_2}$
[110]	$\dfrac{2}{2\gamma_1 - \gamma_2 - 3\gamma_3}$	$\dfrac{2}{2\gamma_1 + \gamma_2 + 3\gamma_3}$
[111]	$\dfrac{1}{\gamma_1 - 2\gamma_3}$	$\dfrac{1}{\gamma_1 + 2\gamma_3}$

bands have, respectively, Γ_9, Γ_7 and Γ_7 symmetries (p-like). We summarize in Table 7.9 functional forms for the hole effective masses in the A, B and C valence bands along ($\| c$) and perpendicular to the c axis ($\perp c$) expressed in terms of A_i (Luttinger valence-band parameters) in wurtzite-type semiconductors.

Table 7.8 Functional expression for the density-of-states heavy-hole mass ($m^*_{\rm HH}$), averaged light-hole mass ($m^*_{\rm LH}$) and spherically averaged heavy-hole ($m^{\rm s}_{\rm HH}$) and light-hole masses ($m^{\rm s}_{\rm LH}$)

Mass	Expression
$m^*_{\rm HH}/m_0$	$\dfrac{(1+0.05\gamma_{\rm h}+0.0164\gamma_{\rm h}^2)^{2/3}}{\gamma_1-\overline{\gamma}}$
$m^*_{\rm LH}/m_0$	$\dfrac{1}{\gamma_1+\overline{\gamma}}$
$m^{\rm s}_{\rm HH}/m_0$	$\dfrac{1}{\gamma_1(1-\mu)}$
$m^{\rm s}_{\rm LH}/m_0$	$\dfrac{1}{\gamma_1(1+\mu)}$
$\overline{\gamma}=(2\gamma_2^2+2\gamma_3^2)^{1/2},\ \gamma_{\rm h}=\dfrac{6(\gamma_3^2-\gamma_2^2)}{\overline{\gamma}(\gamma_1-\overline{\gamma})},\ \mu=\dfrac{6\gamma_3+4\gamma_2}{5\gamma_1}$	

Table 7.9 Functional expression for the hole effective masses in the A, B and C valence bands along ($\| c$) and perpendicular to the c axis ($\perp c$) in the wurtzite-type semiconductors

Expression	
k_z direction ($\| c$)	k_x-k_y plane ($\perp c$)
$\dfrac{m_{\rm A\|}}{m_0}=\dfrac{-1}{A_1+A_3}$	$\dfrac{m_{\rm A\perp}}{m_0}=\dfrac{-1}{A_2+A_4}$
$\dfrac{m_{\rm B\|}}{m_0}=\dfrac{-1}{A_1+\dfrac{A_3E^0_{7+}}{E^0_{7+}-E^0_{7-}}}$	$\dfrac{m_{\rm B\perp}}{m_0}=\dfrac{-1}{A_2+\dfrac{A_4E^0_{7+}}{E^0_{7+}-E^0_{7-}}}$
$\dfrac{m_{\rm C\|}}{m_0}=\dfrac{-1}{A_1-\dfrac{A_3E^0_{7-}}{E^0_{7+}-E^0_{7-}}}$	$\dfrac{m_{\rm C\perp}}{m_0}=\dfrac{-1}{A_2-\dfrac{A_4E^0_{7-}}{E^0_{7+}-E^0_{7-}}}$
$E^0_{7\pm}=\dfrac{\Delta_1-\Delta_2}{2}\pm\sqrt{\left(\dfrac{\Delta_1-\Delta_2}{2}\right)^2+2\Delta_3^2}$	

7.3.2 Numerical value

(a) Cubic semiconductor

An accurate determination of the hole effective mass is important not only for the interpretation of the optical and transport measurements in bulk semiconductors, but

also for the prediction of the electronic properties of low-dimensional semiconductor structures. In Table 7.10, we summarize the reported γ values for some cubic semiconductors. Figure 7.10 also plots γ_i versus lowest direct band-gap energy E_0 for some cubic group-IV, III–V and II–VI semiconductors. The solid lines in Figure 7.10 represent the least-squares fit using the relation

$$\ln \gamma_i = A_i \ln E_0 + B_i \tag{7.37}$$

The A_i and B_i values determined here are summarized in Table 7.11. The values of γ_i for β-MgS, β-MgSe, β-MgTe, c-CdS and c-CdSe in Table 7.10 have been estimated from Equation (7.37).

Table 7.10 Luttinger valence-band parameter γ_i for some cubic group-IV, III–V and II–VI semiconductors (in $\hbar^2/2m_0$)

System	Material	γ_1	γ_2	γ_3
IV	Diamond	4.24	0.82	1.71
	Si	4.285	0.339	1.446
	Ge	13.38	4.24	5.69
	α-Sn	−15.0	−11.5	−8.6
	3C-SiC	2.817	0.508	0.860
III–V	c-BN	1.92[a]	0.02[a]	0.56[a]
	c-AlN	1.73[a]	0.43[a]	0.65[a]
	AlP	3.47[a]	0.06[a]	1.15[a]
	AlAs	3.76[a]	0.90[a]	1.42[a]
	AlSb	4.15[a]	1.01[a]	1.75[a]
	β-GaN	2.84[a]	0.82[a]	1.12[a]
	GaP	4.04	0.53	1.26
	GaAs	7.10	2.02	2.91
	GaSb	13.3	4.4	5.7
	InP	5.33	1.57	2.11
	InAs	20.4	8.3	9.1
	InSb	36.3	16.1	17.2
II–VI	β-MgS	2.62[a]	0.38[a]	0.91[a]
	β-MgSe	2.84[a]	0.43[a]	1.00[a]
	β-MgTe	3.21[a]	0.52[a]	1.15[a]
	β-ZnS	1.77[a]	0.30[a]	0.62[a]
	ZnSe	3.94	1.00	1.52
	ZnTe	3.96	0.86	1.39
	c-CdS	4.11[a]	0.77[a]	1.53[a]
	c-CdSe	5.51[a]	1.24[a]	2.14[a]
	CdTe	4.14	1.09	1.62
	β-HgS	−41.28[a]	−21.00[a]	−20.73[a]
	HgSe	−25.96[a]	−13.69[a]	−13.20[a]
	HgTe	−15.6	−9.6	−8.6

[a] Calculated or estimated

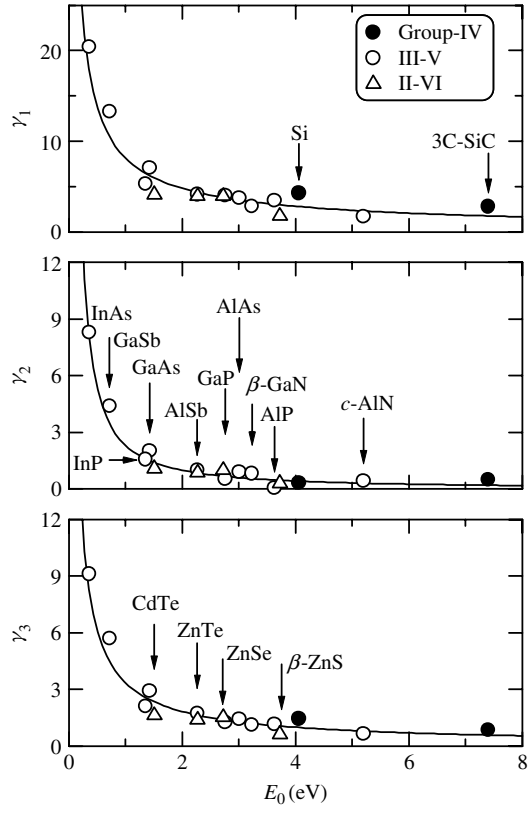

Figure 7.10 Luttinger valence-band parameter γ_i (in $\hbar^2/2m_0$) versus E_0 for some cubic group-IV, III–V and II–VI semiconductors. The solid lines represent the least-squares fit of Equation (7.37). The A_i and B_i values determined here are listed in Table 7.11

Table 7.11 Parameter value describing the relationship between γ_i and E_0

$\ln\gamma_i = A_i + B_i \ln E_0$ (E_0 in eV; γ_i in $\hbar^2/2m_0$)		
γ_i	A_i	B_i
γ_1	2.10	0.76
γ_2	0.84	1.22
γ_3	1.21	0.88

Table 7.12 lists the heavy-hole and light-hole effective band masses, m_{HH} and m_{LH}, along the [001] and [111] directions for some cubic group-IV, III–V and II–VI semiconductors. Table 7.13 also lists the density-of-states heavy-hole (m^*_{HH}), averaged light-hole (m^*_{LH}) and spin–orbit split-off effective hole masses (m_{SO}) in these semiconductors. Figure 7.11 plots the Γ-valley electron effective mass m_e^Γ versus averaged light-hole mass

Table 7.12 Heavy-hole and light-hole effective band masses, m_{HH} and m_{LH}, along the [001] and [111] directions for some cubic group-IV, III–V and II–VI semiconductors

System	Material	m_{HH}/m_0		m_{LH}/m_0	
		[001]	[111]	[001]	[111]
IV	Diamond	0.38	1.22	0.17	0.13
	Si	0.277	0.718	0.202	0.139
	Ge	0.204	0.500	0.0457	0.0404
	α-Sn	0.125	0.46	-0.026^a	-0.031^a
	3C-SiC	0.56	0.91	0.26	0.22
III–V	c-BN	0.53^b	1.25^b	0.51^b	0.33^b
	BP	0.375^b	0.926^b	0.150^b	0.108^b
	c-AlN	1.15^b	2.33^b	0.39^b	0.33^b
	AlP	0.30^b	0.85^b	0.28^b	0.17^b
	AlAs	0.51^b	1.09^b	0.18^b	0.15^b
	AlSb	0.47^b	1.54^b	0.16^b	0.13^b
	β-GaN	0.83^b	1.67^b	0.22^b	0.20^b
	GaP	0.34	0.66	0.20	0.15
	GaAs	0.33	0.78	0.090	0.077
	GaSb	0.22	0.53	0.045	0.040
	InP	0.46	0.90	0.12	0.11
	InAs	0.26	0.45	0.027	0.026
	InSb	0.24	0.53	0.015	0.014
II–VI	MgO	1.60^b	2.77^b	0.35^b	0.31^b
	β-MgS	0.54^b	1.25^b	0.30^b	0.23^b
	β-MgSe	0.51^b	1.19^b	0.27^b	0.21^b
	β-MgTe	0.46^b	1.10^b	0.24^b	0.18^b
	β-ZnS	0.85^b	1.9^b	0.42^b	0.33^b
	ZnSe	0.52	1.11	0.168	0.143
	ZnTe	0.45	0.85	0.176	0.148
	c-CdS	0.39^b	0.95^b	0.18^b	0.14^b
	c-CdSe	0.33^b	0.81^b	0.13^b	0.10^b
	CdTe	0.51	1.11	0.158	0.136
	β-HgS	1.39^b	5.56^b	$-0.012^{b,c}$	$-0.012^{b,c}$
	HgSe	0.70^b	2.27^b	$-0.019^{b,c}$	$-0.019^{b,c}$
	HgTe	0.28	0.63	-0.029^c	-0.030^c

[a] The sign is chosen positive for a normal band structure like that of Ge
[b] Calculated or estimated
[c] The sign is chosen positive for a normal band structure like that of CdTe

m^*_{LH} for some cubic group-IV, III–V and II–VI semiconductors. It is easily understood from Figure 7.11 that the simple relation $m_e^\Gamma \sim m^*_{LH}$ holds for these semiconductors.

(b) Hexagonal and rhombohedral semiconductors

No detailed experimental data are available on the Luttinger parameters A_i of anisotropic semiconductors. We list in Table 7.14 the theoretical Luttinger valence-band parameters for some hexagonal and rhombohedral semiconductors.

Table 7.13 Density-of-states heavy-hole (m^*_{HH}), averaged light-hole (m^*_{LH}) and spin–orbit split-off effective hole masses (m_{SO}) in some cubic group-IV, III–V and II–VI semiconductors

System	Material	m^*_{HH}/m_0	m^*_{LH}/m_0	m_{SO}/m_0
IV	Diamond	0.78	0.14	0.394[a]
	Si	0.528	0.157	0.29
	Ge	0.345	0.0427	0.095
	α-Sn	−0.029[b]	0.19	0.041
	3C-SiC	0.76	0.24	0.51
III–V	*c*-BN	0.99[a]	0.37[a]	0.52[a]
	BAs		0.0800[a]	0.2220[a]
	c-AlN	1.77[a]	0.35[a]	0.58[a]
	AlP	0.63[a]	0.20[a]	0.29[a]
	AlAs	0.81[a]	0.16[a]	0.30[a]
	AlSb	0.9	0.13	0.317[a]
	β-GaN	1.27[a]	0.21[a]	0.35[a]
	GaP	0.52	0.17	0.34
	GaAs	0.55	0.083	0.165
	GaSb	0.37	0.043	0.12
	InP	0.69	0.11	0.21
	InAs	0.36	0.026	0.14
	InSb	0.38	0.014	0.10
II–VI	β-MgS	0.93[a]	0.25[a]	0.38[a]
	β-MgSe	0.88[a]	0.23[a]	0.35[a]
	β-MgTe	0.80[a]	0.20[a]	0.31[a]
	β-ZnS	1.42[a]	0.36[a]	0.56[a]
	ZnSe	0.82	0.154	0.24
	ZnTe	0.67	0.159	0.25
	c-CdS	0.68[a]	0.15[a]	0.24[a]
	c-CdSe	0.57[a]	0.11[a]	0.18[a]
	CdTe	0.82	0.145	0.24
	β-HgS	−0.012[a,c]	2.22[a]	−0.013[a,c]
	HgSe	−0.019[a,c]	1.07[a]	0.031[a]
	HgTe	−0.030[c]	0.38	0.102[a]

[a] Calculated or estimated
[b] The sign is chosen positive for a normal band structure like that of Ge
[c] The sign is chosen positive for a normal band structure like that of CdTe

7.3.3 Polaron effect

The mass measured in cyclotron resonance experiments in polar semiconductors is the polaron mass rather than the 'bare' band-edge mass given by theoretical calculations of the band parameters γ_i. For $\alpha_F \ll 1$, Equation (7.10) can be successfully approximated by

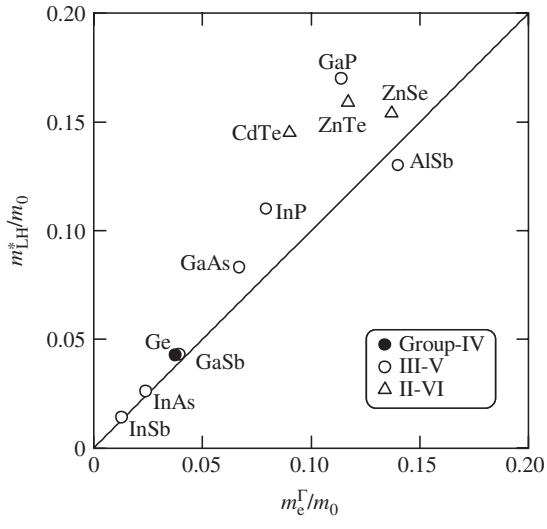

Figure 7.11 Electron effective mass m_e^Γ at the Γ-conduction band plotted versus averaged light-hole mass m^*_{LH} for some cubic group-IV, III–V and II–VI semiconductors. The solid line provides an approximate relation of $m_e^\Gamma = m^*_{LH}$

Table 7.14 Theoretically obtained Luttinger valence-band parameter A_i for some hexagonal and rhombohedral group-IV, III–V and II–VI semiconductors

System	Material	A_1	A_2	A_3	A_4	A_5	A_6	$\lvert A_7\rvert$
IV	6H-SiC	−4.76	−0.590	4.14	−1.15	−1.50	−1.34	0.0119
	15R-SiC	−4.70	−0.55	4.07	−1.12	1.35	−0.94	0.012
III–V	*w*-AlN	−4.15	−0.39	3.76	−1.61	−1.76	−2.07	0.10
	α-GaN	−6.87	−0.68	6.27	−2.98	−3.05	−4.25	0.23
	InN	−9.15	−0.66	8.50	−4.52	−4.47	−5.74	0.33
II–VI	ZnO	−3.78	−0.44	3.45	−1.63	1.68	−2.23	0.025
	α-ZnS	−4.58	−0.53	4.14	−2.34	−2.34	−3.69	
	w-CdS	−5.92	−0.70	5.37	−1.82	−1.82	−1.36	
	w-CdSe	−10.2	−0.76	9.53	−3.2	−3.2	−2.31	

$$m_h^* \sim \frac{m_{hp}^*}{1 - \left(\frac{\alpha_F}{6}\right)} \tag{7.38}$$

where m_h^* and m_{hp}^* are the bare and polaron masses, respectively. For the Γ-valley electrons in GaAs, $\alpha_F = 0.068$ (see Section 5.2). Since α_F is proportional to the square root of the carrier effective mass, $\alpha_F \sim 0.2$ (heavy holes) and ~ 0.1 (light holes) for GaAs. Hence, the bare hole mass in GaAs will be $\leqslant 5\%$ larger than the polaron mass.

7.3.4 External perturbation and doping effects

(a) Temperature effect

Although the effect of temperature on the hole effective mass has been studied theoretically by several authors, no experimental data have been reported up to now. As mentioned in Section 7.1, the simplest way for correction of temperature dependence is to assume that the hole mass varies in accord with the temperature shift of the lowest direct band-gap energy E_0. The hole effective mass variation with temperature T can, then, be written as

$$m_{\mathrm{h}}^{*}(T) = m_{\mathrm{h}}^{*}(0)\frac{E_0(T)}{E_0(0)} \tag{7.39}$$

where $m_{\mathrm{h}}^{*}(0)$ and $E_0(0)$ are the mass and E_0 values at $T = 0$ K, respectively.

(b) Pressure effect

The effect of hydrostatic pressure on the hole effective mass in semiconductors has been studied both theoretically and experimentally (see, e.g., GaAs [7.1]). No direct determination has, however, yet been made on the pressure dependence of the hole masses in semiconductors. From a study of the pressure dependence of tunnel diode characteristics, Alekseeva *et al.* [7.31] deduced $\mathrm{d}\ln m_{\mathrm{HH}}/\mathrm{d}p$ and $\mathrm{d}\ln m_{\mathrm{LH}}/\mathrm{d}p$ values to be $-(0.9 \pm 0.1)$ and 0.74 ± 0.18 %/kbar, respectively. They also calculated values of $\mathrm{d}\ln m_{\mathrm{HH}}/\mathrm{d}p$ and $\mathrm{d}\ln m_{\mathrm{LH}}/\mathrm{d}p$ from the valence-band parameters of the pseudopotential calculation. The agreement of the calculated $\mathrm{d}\ln m_{\mathrm{LH}}/\mathrm{d}p$ value with experiment was found to be good; but, the calculated $\mathrm{d}\ln m_{\mathrm{HH}}/\mathrm{d}p$ value was not so good.

Adams and Shantharama [7.32, 7.33] have measured the pressure dependence of the hole mobility in GaAs from which they concluded that

$$\frac{\mathrm{d}\ln m_{\mathrm{HH}}}{\mathrm{d}p} = -(0.01 - 0.015)\ \%/\mathrm{kbar} \tag{7.40}$$

Adams [7.33] concluded that the pressure dependence of the heavy-hole effective mass is considerably less than that for the Γ-valley electrons expected from the $\boldsymbol{k} \cdot \boldsymbol{p}$ theory.

Based on $\boldsymbol{k} \cdot \boldsymbol{p}$ theory, we can expect the light-hole mass to vary with pressure by nearly the same percentage as the electron effective mass. In fact, calculations by Unlu [7.34] give $\mathrm{d}\ln m_{\mathrm{LH}}/\mathrm{d}p \sim 0.8$ %/kbar, which is almost equal to the Γ-valley electron value ($\sim$0.7 %/kbar). Note that the sign of the pressure coefficient of m_{HH} is negative, meaning that the effective mass m_{HH} decreases with increasing hydrostatic pressure.

(c) Doping effect

As in the case of the electron effective mass (Section 7.1), the hole effective mass may be influenced by the doping concentration of acceptor impurities or, in other words, by

the free-hole concentration. A full $\boldsymbol{k} \cdot \boldsymbol{p}$ theory has been used to calculate the density-of-states effective masses as a function of energy for holes in the heavy-hole (m^*_{HH}), light-hole (m^*_{LH}) and spin–orbit split-off bands (m_{SO}) in GaAs [7.35]. These results indicate important nonparabolicities which should be taken into account in modeling the valence band of GaAs. There has, however, been reported no detailed experimental data on the carrier-concentration dependence of the hole effective mass in semiconductors.

REFERENCES

[7.1] S. Adachi, *GaAs and Related Materials: Bulk Semiconducting and Superlattice Properties* (World Scientific, Singapore, 1994).
[7.2] C. Hermann and C. Weisbuch, *Phys. Rev. B* **15**, 823 (1977).
[7.3] V. A. Tyagi, A. M. Evstigneev, A. N. Krasiko, A. F. Andreeva, and V. Ya. Malakhov, *Sov. Phys. Semicond.* **11**, 1257 (1977).
[7.4] J. Wu, W. Walukiewicz, W. Shan, K. M. Yu, J. W. Ager III, E. E. Haller, H. Lu, and W. J. Schaff, *Phys. Rev. B* **66**, 201403 (2002).
[7.5] J. T. Devreese, *Polarons in Ionic Crystals and Polar Semiconductors* (North-Holland, Amsterdam, 1972).
[7.6] D. C. Langreth, *Phys. Rev.* **159**, 717 (1967).
[7.7] R. A. Stradling and R. A. Wood, *J. Phys. C: Solid State Phys.* **3**, L94 (1970).
[7.8] P. Lautenschlager, M. Garriga, S. Logothetidis, and M. Cardona, *Phys. Rev. B* **35**, 9174 (1987).
[7.9] J. M. Besson, J. P. Itié, A. Polian, G. Weill, J. L. Mansot, and J. Gonzalez, *Phys. Rev. B* **44**, 4214 (1991).
[7.10] N. E. Christensen, *Phys. Rev. B* **30**, 5753 (1984).
[7.11] D. E. Aspnes and M. Cardona, *Phys. Rev. B* **17**, 726 (1978); **17**, 741 (1978).
[7.12] Q. H. F. Vrehen, *J. Phys. Chem. Solids* **29**, 129 (1968).
[7.13] D. M. Szmyd, P. Porro, A. Majerfeld, and S. Lagomarsino, *J. Appl. Phys.* **68**, 2367 (1990).
[7.14] D. K. Maude, L. Eaves, T. J. Foster, and J. C. Portal, *Phys. Rev. Lett.* **62**, 1922 (1989).
[7.15] S. Chaudhuri and K. K. Bajaj, *Phys. Rev. B* **29**, 1803 (1984).
[7.16] E. A. Johnson, A. MacKinnon, E. P. O'Reilly, and M. Silver, *Phys. Rev. Lett.* **65**, 752 (1990).
[7.17] E. A. Johnson, A. MacKinnon, E. P. O'Reilly, and M. Silver, *Semicond. Sci. Technol.* **7**, 165 (1992).
[7.18] M. A. Hopkins, R. J. Nicholas, P. Pfeffer, W. Zawadzki, D. Gauthier, J. C. Portal, and M. A. DiForte–Poisson, *Semicond. Sci. Technol.* **2**, 568 (1987).
[7.19] H. Sigg, P. Wyder, and J. A. A. J. Perenboom, *Phys. Rev. B* **31**, 5253 (1985).
[7.20] J. C. Hensel, H. Hasegawa, and M. Nakayama, *Phys. Rev.* **138**, A225 (1965).
[7.21] L. D. Laude, F. H. Pollak, and M. Cardona, *Phys. Rev. B* **3**, 2623 (1971).
[7.22] P. Lawaetz, *Solid State Commun.* **16**, 65 (1975).
[7.23] N. Miura, G. Kido, M. Suekane, and S. Chikazumi, *J. Phys. Soc. Jpn* **52**, 2838 (1983).
[7.24] J. M. Luttinger, *Phys. Rev.* **102**, 1030 (1956).
[7.25] J. M. Luttinger and W. Kohn, *Phys. Rev.* **97**, 869 (1955).
[7.26] G. Dresselhaus, A. F. Kip, and C. Kittel, *Phys. Rev.* **98**, 368 (1955).
[7.27] E. O. Kane, *Phys. Rev.* **178**, 1368 (1969).
[7.28] Yu. M. Sirenko, J. B. Jeon, B. C. Lee, K. W. Kim, M. A. Littlejohn, M. A. Stroscio, and G. J. Iafrate, *Phys. Rev. B* **55**, 4360 (1997).
[7.29] C. Y.-P. Chao and S. L. Chuang, *Phys. Rev. B* **46**, 4110 (1992).
[7.30] J. C. Hensel and K. Suzuki, *Phys. Rev. B* **9**, 4219 (1974).

[7.31] Z. M. Alekseeva, A. P. Vyatkin, G. F. Karavaev, and N. P. Krivorotov, *Phys. Status Solidi B* **88**, 321 (1978).
[7.32] A. R. Adams and L. G. Shantharama, *Physica B* **139&140**, 419 (1986).
[7.33] A. R. Adams, in *Properties of Gallium Arsenide*, 2nd Edition, EMIS Datareviews Series No. 2 (INSPEC, London, 1990), p. 143.
[7.34] H. Unlu, *Solid-State Electron.* **35**, 1343 (1992).
[7.35] J. R. Lowney and A. H. Kahn, *J. Appl. Phys.* **64**, 447 (1988).

8 Deformation Potentials

8.1 Intravalley deformation potential: Γ point 173
8.1.1 Conduction band 173
8.1.2 Valence band 175
8.1.3 E_0 gap 179
8.1.4 Optical phonon deformation potential 181
8.2 Intravalley deformation potential: high-symmetry points 183
8.2.1 L point 183
8.2.2 X point 188
8.3 Intervalley deformation potential 189
8.3.1 General remarks 189
8.3.2 Numerical value 192
References 192

8.1 INTRAVALLEY DEFORMATION POTENTIAL: Γ POINT

8.1.1 Conduction band

A deformation potential (DP) is a quantity proportional to a matrix element of an operator belonging to a crystal deformation between a final and initial electron (or hole) state. It usually has the units of eV or eV/Å. The DP is called an intravalley DP if the wavevectors of the final and initial states are within the same valley; otherwise it is called an intervalley DP. Also, it is called an intraband DP if the band indices of the final and initial states are the same; otherwise it is called an interband DP.

We have already presented in Section 6.2 the effective Hamiltonians for the conduction and valence bands in the zinc-blende-type and wurtzite-type semiconductors. Let us rewrite those for the lowest conduction bands as follows

$$H_{\mathrm{c}}^{\mathrm{ZB}} = \frac{\hbar^2 k^2}{2m_{\mathrm{e}}^{\Gamma}} + a_{\mathrm{c}}^{\Gamma}(e_{xx} + e_{yy} + e_{zz}) \tag{8.1}$$

and

$$H_{\mathrm{c}}^{\mathrm{W}} = \frac{\hbar^2 k_z^2}{2m_{\mathrm{e}}^{\parallel}} + \frac{\hbar^2 (k_x^2 + k_y^2)}{2m_{\mathrm{e}}^{\perp}} + D_1 e_{zz} + D_2(e_{xx} + e_{yy}) \tag{8.2}$$

where m_{e}^{Γ}, $m_{\mathrm{e}}^{\parallel}$ and $m_{\mathrm{e}}^{\perp}$ are the electron effective masses, a_{c}^{Γ}, D_1 and D_2 are Bir–Pikus deformation potentials, and e_{ij} is the strain tensor component (i, $j = x$, y or z). Note that

Properties of Group-IV, III–V and II–VI Semiconductors Sadao Adachi

© 2005 John Wiley & Sons, Ltd

ISBN: 0-470-09032-4

in the quasi-cubic approximation, we have the relation

$$a_c^{\Gamma} = D_1 = D_2 \tag{8.3}$$

In Figure 8.1, we schematically show the uniaxial stress (strain) effects on the electronic energy-band structure near the Γ point in the zinc-blende-type semiconductors. Let us consider the case of the scattering of electrons due to the strain caused by acoustic waves, that is, the intravalley (acoustic) deformation potential scattering. If the strains involved are small as in the usual case, the electronic energy shifts caused by them may be described adequately with linear terms in the strain. By symmetry, for spherical constant-energy surfaces and acoustic-mode scattering, one may write the shift of the Γ_6 conduction-band minimum ΔE_c^{Γ} as

$$\Delta E_c^{\Gamma} = E_1^{\Gamma}(e_{xx} + e_{yy} + e_{zz}) \tag{8.4}$$

where E_1^{Γ} is the so-called acoustic (intravalley) deformation potential. Equation (8.4) is based on the fact that the matrix element of Equation (8.1) is practically equal to that obtained by replacing H_c^{ZB} by ΔE_c^{Γ} [8.1]. The deformation potential $E_1^{\Gamma} = a_c^{\Gamma}$ can now

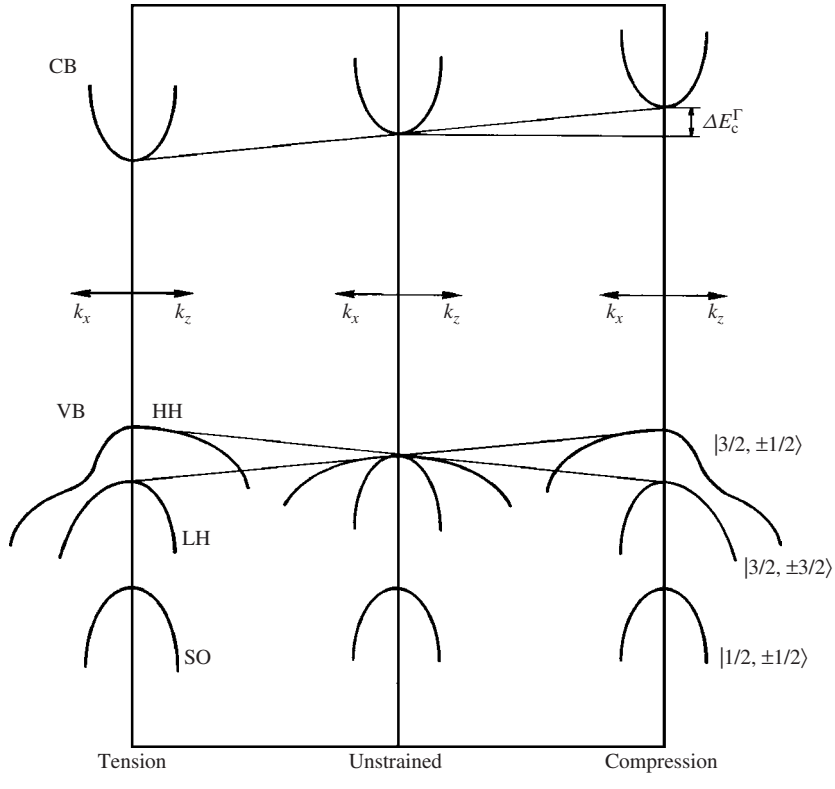

Figure 8.1 A uniaxial stress ($X \parallel [100]$) effect on the electronic energy-band structure near the Γ point in zinc-blende-type semiconductors

be written, in a phenomenological form, as [8.2]

$$E_1^{\Gamma} = -B_u \frac{dE_c^{\Gamma}}{dp} \tag{8.5}$$

or, equivalently [8.3]

$$E_1^{\Gamma} = \frac{dE_c^{\Gamma}}{d \ln V} \tag{8.6}$$

where B_u is the bulk modulus (see Section 3.3), dE_c^{Γ}/dp is the hydrostatic pressure coefficient of the Γ_6 conduction-band minimum and $d \ln V = dV/V$ is the fractional volume change of the semiconductor.

We summarize in Table 8.1 the $a_c^{\Gamma} = E_1^{\Gamma}$ values for some cubic group-IV, III–V and II–VI semiconductors. We also summarize in Table 8.2 the reported D_1 and D_2 values for some wurtzite semiconductors. We can see that the signs of a_c^{Γ}, D_1 and D_2 are all negative for such semiconductors.

8.1.2 Valence band

The DPs for holes at the center of the Brillouin zone ($\boldsymbol{k} = 0$) play an important role in many physical phenomena. The lattice mobility of holes in III–V compounds, for

Table 8.1 Γ-conduction-band intravalley deformation potential, $a_c^{\Gamma} = E_1^{\Gamma}$, for some cubic group-IV, III–V and II–VI semiconductors

System	Material	a_c^{Γ} (eV)	System	Material	a_c^{Γ} (eV)
IV	Diamond	$-30.7^{a,b}$	II–VI	β-ZnS	-4.09^{b}
	Si	$-15.3^{a,b}$		ZnSe	-4.17^{b}
	Ge	$-8.24^{a,b}$		ZnTe	-5.83^{b}
	α-Sn	$-13.7^{a,b}$		c-CdS	-27.1^{b}
	3C-SiC	-7.50^{b}		c-CdSe	-11.0^{b}
				CdTe	-3.96^{b}
III–V	c-BN	-36.5^{b}		HgTe	-4.60^{b}
	BP	-13.3^{b}			
	c-AlN	-11.7^{b}			
	AlP	-5.54^{b}			
	AlAs	-5.64^{b}			
	AlSb	-6.97^{b}			
	β-GaN	-21.3^{b}			
	GaP	-7.14^{b}			
	GaAs	-11.0			
	GaSb	-9			
	InP	-11.4			
	InAs	-10.2			
	InSb	-15			

[a] $\Gamma_{2'}$-conduction band
[b] Calculated

Table 8.2 Γ-conduction-band deformation potentials, D_1 and D_2, for some wurtzite III–V semiconductors

System	Material	D_1 (eV)	D_2 (eV)
III–V	w-AlN	-10.23^a	-9.65^a
	α-GaN	-9.47^a	-7.17^a

[a] Calculated

example, is limited primarily by acoustic and nonpolar optical phonon scattering. The strengths of these scattering mechanisms are determined by the valence-band DPs, a, b and d (Bir–Pikus notation).

We have already seen in Section 6.2 the effective Hamiltonians for the conduction and valence bands in the zinc-blende-type and wurtzite-type semiconductors. Let us rewrite those for the highest valence bands as follows

$$H_{\rm v}^{\rm ZB} = \frac{1}{3}\Delta_{\rm so}(\boldsymbol{L}\cdot\boldsymbol{\sigma}) - (\gamma_1+4\gamma_2)k^2 + 6\gamma_2(\boldsymbol{L}\cdot\boldsymbol{k})^2 - 6(\gamma_2-\gamma_3)\sum_{i,j}[L_i, L_j]k_ik_j + (a+2b)(e_{xx}+e_{yy}+e_{zz}) - 3b\sum_i L_i^2 e_{ii} - \sqrt{3}d\sum_{i,j}[L_i, L_j]e_{ij} \qquad (8.7)$$

and

$$\begin{aligned} H_{\rm v}^{\rm W} = {} & \Delta_1 L_z^2 + \Delta_2 L_z\sigma_z + \sqrt{2}\Delta_3(L_+\sigma_- + L_-\sigma_+) + (A_1+A_3L_z^2)k_z^2 \\ & + (A_2+A_4L_z^2)k_\perp^2 - A_5(L_+^2k_-^2 + L_-^2k_+^2) - 2A_6k_z([L_z, L_+]k_- + [L_z, L_-]k_+) \\ & + iA_7(L_+k_- - L_-k_+) + (C_1+C_3L_z^2)e_{zz} + (C_2+C_4L_z^2)e_\perp - C_5(L_+^2e_- + L_-^2e_+) \\ & - 2C_6([L_z, L_+]e_{-z} + [L_z, L_-]e_{+z}) \end{aligned} \qquad (8.8)$$

In Equation (8.7), $\Delta_{\rm so} = \Delta_0$ is the spin–orbit split-off energy, $\boldsymbol{L}$ and $\boldsymbol{\sigma}$ are the orbital and spin angular momentum operators, respectively, $[L_i, L_j]$ is defined by $[L_i, L_j] = (L_iL_j + L_jL_i)/2$, γ_i ($i = 1$–3) are Luttinger valence-band parameters and e_{ij} is the strain tensor component (i, $j = x$, y or z); a, b and d are Bir–Pikus deformation potentials. We summarize in Table 8.3 the relations between a, b, d and other common sets of the DP parameters used in cubic semiconductors [8.4–8.6] (see also [8.7]). In Equation (8.8), Δ_1 and $\Delta_{2,3}$ correspond to the crystal-field and spin–orbit split-off parameters in units of eV, respectively, $L_\pm = (L_x \pm iL_y)/\sqrt{2}$, $\sigma_\pm = (\sigma_x \pm i\sigma_y)/2$, $k_\perp^2 = k_x^2 + k_y^2$, $k_\pm = k_x \pm ik_y$, $e_\perp = e_{xx} + e_{yy}$, $e_\pm = e_{xx} - e_{yy} \pm 2ie_{xy}$, $e_{\pm z} = e_{xz} \pm ie_{yz}$ and A_i ($i = 1$–6) are Luttinger valence-band parameters. C_i ($i = 1$–6) are Bir–Pikus deformation potentials. Note that in the quasi-cubic approximation, the DPs in Equations (8.7) and (8.8) have the relationships

$$C_1 = a + \frac{2}{\sqrt{3}}d$$

$$C_2 = a - \frac{1}{\sqrt{3}}d$$

Table 8.3 Comparison of notations popularly used for representing the valence-band deformation potentials in cubic semiconductors

Kleiner–Roth[a]	Bir–Pikus[b]	Kane[c]
$-D_d^{\mathrm{v}}$	$-a_{\mathrm{v}}$	$-d_1/\sqrt{3}$
$D_{\mathrm{u}}/3$	$-b/2$	$-d_3/2\sqrt{3}$
$D'_{\mathrm{u}}/3$	$-d/2\sqrt{3}$	$-d_5/2\sqrt{6}$

[a] W. H. Kleiner and L. Roth, *Phys. Rev. Lett.* **2**, 234 (1959)
[b] G. L. Bir and G. E. Pikus, *Symmetry and Strain-Induced Effects in Semiconductors* (Wiley, New York, 1974)
[c] E. O. Kane, *Phys. Rev.* **178**, 1368 (1969)

$$\begin{aligned} C_3 &= -\sqrt{3}d \\ C_4 &= \frac{\sqrt{3}}{2}d \\ C_5 &= \frac{1}{2}b + \frac{1}{\sqrt{3}}d \\ C_6 &= \sqrt{2}b + \frac{1}{\sqrt{6}}d \end{aligned} \tag{8.9}$$

and

$$C_1 - C_2 = -C_3 = 2C_4 = 4C_5 - \sqrt{2}C_6 \tag{8.10}$$

The application of a uniaxial stress X to a semiconductor produces a strain that reduces the symmetry of the material and results in significant change in the energy bands, as schematically shown in Figure 8.1. The remarkable effect of the compressive or tensile uniaxial stress on the electronic energy-band structure is to split the heavy-hole ($J = 3/2$, $m_j = \pm 3/2$ in spherical notation) and light-hole ($J = 3/2$, $m_j = \pm 1/2$) degeneracy at the Γ point. If we introduce the following strain components

$$e_{xx} = S_{11}X, \quad e_{yy} = e_{zz} = S_{12}X \tag{8.11}$$

for the [100] uniaxial stress, or

$$e_{xx} = e_{yy} = e_{zz} = \frac{S_{11} + 2S_{12}}{3}X, \quad e_{yz} = e_{zx} = e_{xy} = \frac{S_{44}}{6}X \tag{8.12}$$

for the [111] uniaxial stress, into Equation (8.7), we obtain the changes in the band-gap energies to first order in stress as [8.8]

$$\begin{cases} \Delta(E_{\mathrm{v}1} - E_{\mathrm{v}2}) = \delta E \\ \Delta(E_{\mathrm{v}2} - E_{\mathrm{v}3}) = \Delta_0 - \dfrac{\delta E}{2} \end{cases} \tag{8.13}$$

Table 8.4 Γ-valence-band deformation potentials, a, b and d, for some cubic group-IV, III–V and II–VI semiconductors

System	Material	a (eV)	b (eV)	d (eV)
IV	Diamond	−36.1[a]	−11.1[a]	
	Si	−5	−2.3	−5.3
	Ge	−5.2	−2.4	−4.8
	α-Sn	−3.3[a]	−2.3	−4.1
	3C-SiC	4.30[a]	−2.20[a]	−6.26[a]
III–V	c-BN	−7.3[a]	−3.41[a]	−3.75[a]
	BP	4.2[a]	−4.9[a]	
	BAs		−4.5[a]	
	c-AlN	−5.9[a]	−1.7[a]	−4.4[a]
	AlP	3.15[a]	−1.5[a]	
	AlAs	−2.6[a]	−2.3[a]	
	AlSb	1.38[a]	−1.35	−4.3
	β-GaN	−13.33[a]	−2.09[a]	−1.75[a]
	GaP	1.70[a]	−1.7	−4.4
	GaAs	−0.85	−1.85	−5.1
	GaSb	0.79[a]	−2.4	−5.4
	InP	−0.6	−1.7	−4.3
	InAs	1.00[a]	−1.8	−3.6
	InSb	0.36[a]	−2.0	−5.4
II–VI	β-MgSe	−1.0[a]	−1.27[a]	
	β-ZnS	2.31[a]	−1.1	−4.4
	ZnSe	1.65[a]	−1.8	−5.0
	ZnTe	0.79[a]	−1.4	−4.4
	c-CdS	0.92[a]	−4.7	
	c-CdSe	−8.9[a]	−0.8	
	CdTe	0.55[a]	−1.0	−4.4
	β-HgS		−1.24[a]	
	HgSe		−1.16[a]	
	HgTe	−0.13[a]	−1.5	−8.0

[a] Calculated

where $\delta E = 2b(S_{11} - S_{12})X$ for the [100] stress or $\delta E = (d/\sqrt{3})S_{44}X$ for the [111] stress; thus, the splitting energies are proportional to the shear DPs b or d.

The DPs a, b and d for some cubic, covalent and zinc-blende semiconductors are summarized in Table 8.4. Figure 8.2 plots the experimental b, d and $\eta = d/\sqrt{3}b$ values versus Phillips ionicity f_i for some of these semiconductors. Note that the quantity η is given by the ratio of the splitting for a shear strain along [111] to the splitting for a shear strain of the same magnitude along [100]. The solid lines in Figures 8.2(a), 8.2(b) and 8.2(c) represent the least-squares fit with $b = 1.73f_i - 2.36$, $d = 0.42f_i - 4.78$ and $\eta = 1.39f_i + 1.11$ (b and d in eV), respectively. It is evident from Figure 8.2 that the shear DPs b, d and η increase with increasing f_i. Such a trend may be interpreted by a point-ion model proposed by Gavini and Cardona [8.9].

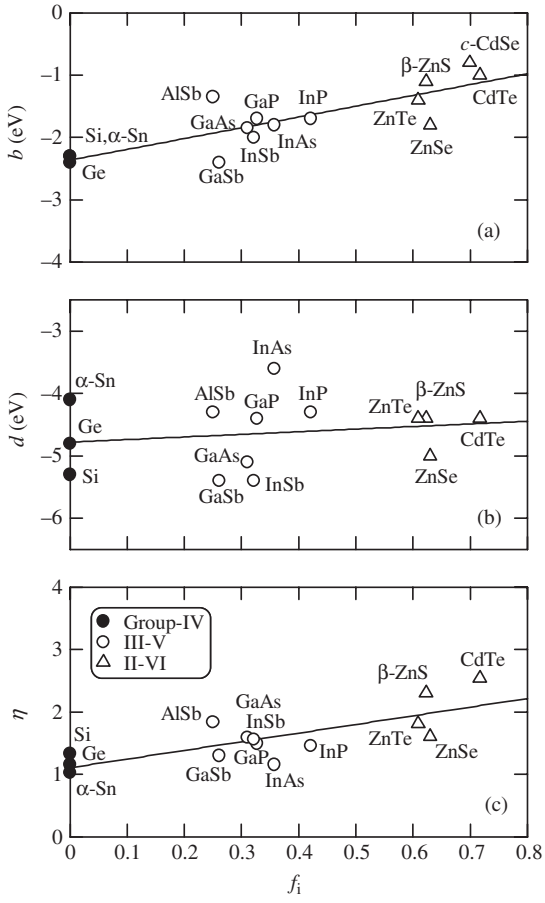

Figure 8.2 Plots of: (a) b; (b) d; (c) $\eta = d/\sqrt{3}b$ determined experimentally versus Phillips ionicity f_i for some cubic group-IV, III–V and II–VI semiconductors. The solid lines represent the least-squares fit with: (a) $b = 1.73 f_i - 2.36$; (b) $d = 0.42 f_i - 4.78$; (c) $\eta = 1.39 f_i + 1.11$ (b and d in eV), respectively

We show in Figure 8.3 the experimental or theoretical DP parameter b plotted against lattice constant a for some cubic semiconductors. The general trend we can obtain from this figure is that the semiconductor has larger negative b value as its lattice constant gets smaller [8.10]. It is thus suspected, although not reported previously, that the DP will get more negative as we apply hydrostatic pressure or the bath temperature is lowered since the average lattice constant gets smaller in such conditions.

Table 8.5 lists the valence-band DP parameters C_i for some hexagonal semiconductors. The conduction-band DP parameters D_i in this table are defined in Equation (8.2).

8.1.3 E_0 gap

The hydrostatic DP a for holes at the top of the valence band is smaller than that for the Γ-conduction-band electrons a_c^Γ. Hence, it is a good approximation to set the electron DP

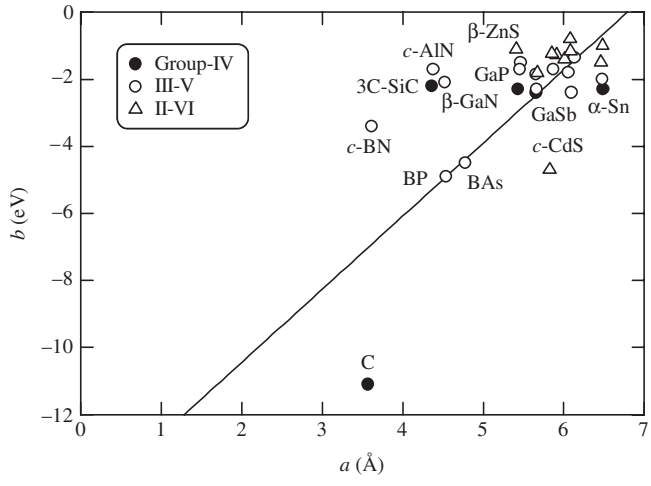

Figure 8.3 Experimental or theoretical DP parameter b plotted against lattic constant a for some cubic group-IV, III–V and II–VI semiconductors. The solid line is a guide to the eye showing the trend toward larger negative values of b with decreasing a

Table 8.5 Γ-valence-band deformation potential C_i for some hexagonal group-IV, III–V and II–VI semiconductors (in eV)

System	Material	C_1	$D_1 - C_1$	C_2	$D_2 - C_2$	C_3	C_4	C_5	C_6
IV	6H-SiC		−3.6		1.7	6.6	−3.0		|3.2|
III–V	w-AlN	−12.9[a]		−8.4[a]		4.5[a]	−2.2[a]	−2.6[a]	−4.1[a]
	α-GaN	−41.4	−3.1	−33.3	−11.2	8.2	−4.1	−4.7	
	InN		−4.05[a]		−6.67[a]	4.92[a]	−1.79[a]		
II–VI	ZnO		−3.90		−4.13	1.15	−1.22	−1.53	2.88
	w-CdS		−1.36		−2.28	1.54	−2.34	−1.20	
	w-CdSe		−0.76		−3.7	4.0	−2.2	1.2	3.0

[a]Calculated

a_c^Γ to the DP a_0^Γ of the corresponding gap, i.e., the E_0 gap. The DP parameter a_0^Γ can be determined relatively easily by measuring photoluminescence, reflectivity or absorption under pressure.

By analogy with Equation (8.5), we can write a_0^Γ to as

$$a_0^\Gamma = -B_u \frac{dE_0}{dp} \tag{8.14}$$

or, equivalently

$$a_0^\Gamma = \frac{dE_0}{d\ln V} \tag{8.15}$$

where dE_0/dp is the hydrostatic pressure coefficient of the E_0-gap energy.

Table 8.6 Hydrostatic deformation potential a_0^Γ for some cubic and hexagonal semiconductors

System	Material	a_0^Γ (eV)	System	Material	a_0^Γ (eV)
IV	Diamond	$-27^{a,b}$	II–VI	β-MgSe	-4.2^b
	Si	$-11.84^{a,b}$		ZnO	-3.51(A)
	Ge	-9.8^a		ZnO	-3.59(B)
	α-Sn	$-7.04^{a,b}$		ZnO	-3.81(C)
	3C-SiC	-11.5^b		α-ZnS	-4.7^b
III–V	BP	-17.5^b		β-ZnS	-5.2
	w-AlN	-10.3^b		ZnSe	-5.1
	c-AlN	-9.5^b		ZnTe	-5.3
	AlP	-9.52^b		c-CdS	0.43^b
	AlAs	-8.93^b		w-CdS	-2.9
	AlSb	-5.9		c-CdSe	0.80^b
	α-GaN	-8.8		w-CdSe	-2.3
	β-GaN	-9.0^b		CdTe	-2.9
	GaP	-9.3		β-HgS	-2.16^b
	GaAs	-8.8		HgSe	-2.15^b
	GaSb	-8.3		HgTe	-3.19^b
	InN	-4.2^b			
	InP	-7.6			
	InAs	-6.3			
	InSb	-7.0			

[a] $\Gamma^{\rm v}_{25'} - \Gamma^{\rm c}_{2'}$ gap
[b] Calculated or estimated from Equation (8.14)

We summarize in Table 8.6 the hydrostatic DP a_0^Γ for some group-IV, III–V and II–VI semiconductors. Since the signs of $B_{\rm u}$ and $\mathrm{d}E_0/\mathrm{d}p$ in Equation (8.14) are usually positive, a_0^Γ has negative value in many semiconductors.

8.1.4 Optical phonon deformation potential

The phonons that usually dominate in the scattering probability are the long-wavelength optical phonons. These phonons produce a short-range potential in the crystal that shifts the electronic band states. In polar semiconductors such as GaAs, the phonons are also accompanied by a long-range macroscopic electric field that produces additional scattering. The shifts of the electronic band states per unit ionic displacement associated with the long-wavelength optical phonons are called the optical phonon deformation potential d_0.

The DP parameter d_0 is defined by the splitting of the Γ_{15} valence-band state produced, in the absence of spin–orbit interaction, by a phonon along the [111] direction [8.11]

$$\delta E = d_0 \frac{u}{a} \tag{8.16}$$

where δE is the shift of the singlet component of Γ_{15} polarized along [111], a is the lattice constant and u is the change in the bond length in the [111] direction due to the

displacement of the two sublattices. The DPs d and d_0 are related linearly through the internal strain parameter ζ [8.11]

$$d = d' - \frac{1}{4}\zeta d_0 \tag{8.17}$$

A direct measurement of ζ is, however, rather difficult since it requires the measurement of the intensity of an X-ray reflection forbidden in the unstrained crystal.

The experimental deduction of d_0 from either low-field transport or Raman data is quite involved. Several theoretical calculations of d_0 have been carried out by using various methods [8.12]. We list in Table 8.7 the Γ-valence-band d_0 values for some cubic and hexagonal semiconductors. We also plot in Figure 8.4 the d_0 value versus lattice constant a for some group-IV, III–V and II–VI semiconductors. The solid line in Figure 8.4 represents the least-squares fit using the relation (a in Å; d_0 in eV).

$$d_0 = 123.2 - 15.2a \tag{8.18}$$

Brey *et al*. [8.13] discussed the deformation potential d_0 from an aspect of the sp^3 bond order ρ, where ρ was obtained by projecting out the sp^3 bonding and antibonding components and subsequently integrating over $\boldsymbol{k}$ space. Intuitively, one can expect the bond order ρ to be a measure of the covalent bond strength, and therefore that a large value of ρ should correspond to a small internal strain, and vice versa. Indeed, it was

Table 8.7 Optical phonon deformation potential d_0 at the Γ-valence band of some cubic and hexagonal semiconductors

System	Material	d_0 (eV)	System	Material	d_0 (eV)
IV	Diamond	80	II–VI	β-MgS	15.2[a]
	Si	33		β-ZnS	18
	Ge	36		ZnSe	20
	α-Sn	31.6[a]		ZnTe	29
	3C-SiC	58.1		c-CdS	6.9[a]
				c-CdSe	8.9[a]
III–V	c-BN	54.0[a]		w-CdSe	32
	BP	35.8[a]		CdTe	22
	BAs	41.5[a]			
	c-AlN	19.4[a]			
	AlP	23.7[a]			
	AlAs	27[a]			
	AlSb	37			
	β-GaN	14.6[a]			
	GaP	39			
	GaAs	40			
	GaSb	32			
	InP	35			
	InAs	42			
	InSb	39			

[a] Calculated

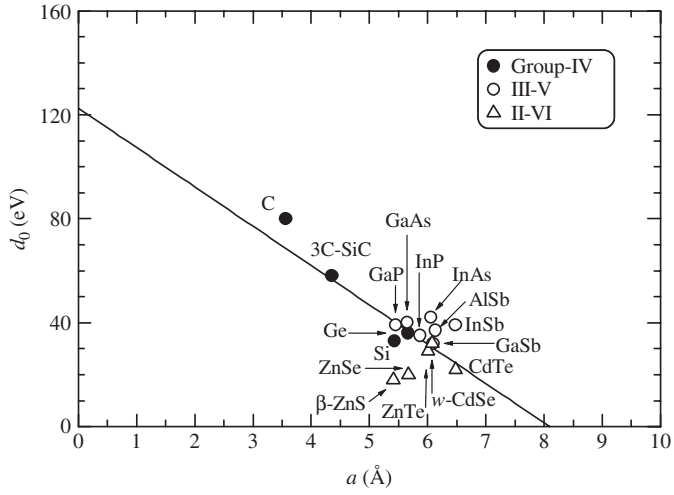

Figure 8.4 Optical phonon deformation potential d_0 versus lattice constant a for some group-IV, III–V and II–VI semiconductors. For w-CdSe, an effective lattice constant $a_{\text{eff}} = (\sqrt{3}a^2c)^{1/3}$ is plotted instead of a. The solid line represents the least-squares fit with $d_0 = 123.2 - 15.2a$ (a in Å; d_0 in eV)

found that the internal strain parameter ζ in Equation (8.17) decreases with increasing sp^3 bond order, resulting in increase in d_0.

8.2 INTRAVALLEY DEFORMATION POTENTIAL: HIGH-SYMMETRY POINTS

8.2.1 L point

(a) Hydrostatic and shear deformation potentials: conduction band

There are eight equivalent [111] directions (L valley) and six equivalent [100] directions (X valley). These conduction-band valleys all coincide at equilibrium, but can be split by the application of stress in appropriate directions. We show in Figure 8.5 the uniaxial stress effects on the conduction-band structure near the L point in the zinc-blende-type semiconductors. The $\langle 111 \rangle$ uniaxial stress removes the degeneracy of equivalent valleys which is not symmetrical to the direction of the applied stress, namely, it shifts the energy of the valley whose symmetry axis is parallel to the stress direction ($\langle 111 \rangle$; $L^{(1)}$ valley) with respect to the energy of the equivalent valleys which are not parallel to the direction of the applied stress ($\langle \bar{1}\,\bar{1}1 \rangle$, $\langle \bar{1}1\bar{1} \rangle$, and $\langle 1\bar{1}\,\bar{1} \rangle$; $L^{(3)}$ valleys). The $\langle 001 \rangle$ stress does not split the L valleys, but shifts the energy of all L valleys.

Following the notation of Herring and Vogt [8.14], the energy shift of valley α for a homogeneous deformation described by the strain tensor $\overline{\varepsilon}$ can be expressed as [8.15]

$$\Delta E_{\text{c}}^{\alpha} = (\Xi_{\text{d}}^{\alpha} \boldsymbol{1} + \Xi_{\text{u}}^{\alpha} \{\overline{\boldsymbol{a}}_i \overline{\boldsymbol{a}}_i\}) : \overline{\varepsilon} \tag{8.19}$$

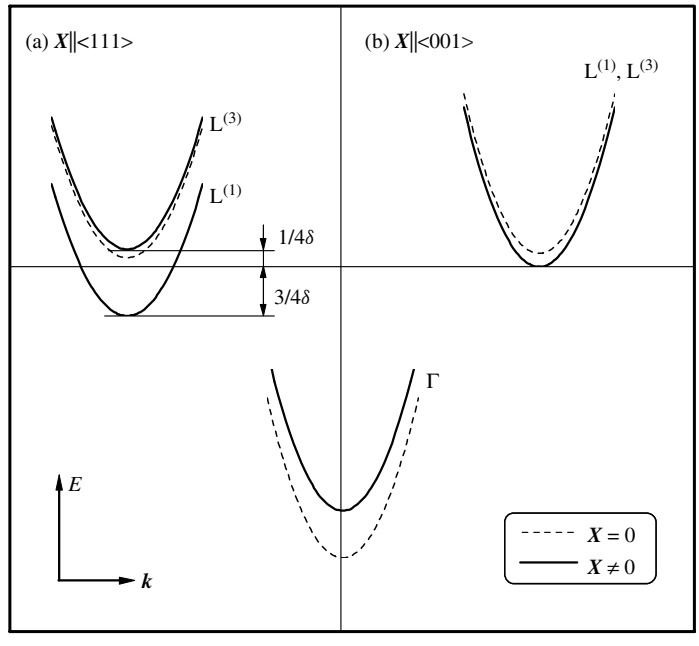

Figure 8.5 Stress effects on the conduction-band structure near the L point in the zinc-blende-type semiconductors for uniaxial stresses along (a) ⟨111⟩; (b) ⟨001⟩ directions

where $\boldsymbol{1}$ is the unit tensor, i is a unit vector parallel to the $\boldsymbol{k}$ vector of valley α and $\{\ \}$ denotes a dyadic product. The shift of the mean energy of the conduction-band extrema is

$$\Delta E_{\mathrm{c,av}}^{\alpha} = \left(\Xi_{\mathrm{d}}^{\alpha} + \frac{1}{3}\Xi_{\mathrm{u}}^{\alpha}\right)\boldsymbol{1} : \overline{\varepsilon} \tag{8.20}$$

The hydrostatic DP, $a_{\mathrm{c}}^{\alpha} = (\Xi_{\mathrm{d}}^{\alpha} + 1/3\Xi_{\mathrm{u}}^{\alpha})$, is sometimes denoted as E_1^{α}. The DP $\Xi_{\mathrm{u}}^{\alpha}$ is also denoted as E_2^{α}.

The change in the L-valley energies with ⟨111⟩ stress can now be written as [8.16]

$$\Delta E_{\mathrm{c}}^{\mathrm{L}} = (S_{11} + 2S_{12})X\left(\Xi_{\mathrm{d}}^{\mathrm{L}} + \frac{1}{3}\Xi_{\mathrm{u}}^{\mathrm{L}}\right) + \begin{cases} \dfrac{1}{9}S_{44}X\Xi_{\mathrm{u}}^{\mathrm{L}} & \text{for } \mathrm{L}^{(3)} \\ -\dfrac{1}{3}S_{44}X\Xi_{\mathrm{u}}^{\mathrm{L}} & \text{for } \mathrm{L}^{(1)} \end{cases} \tag{8.21}$$

where S_{ij} is the elastic compliance constant. The first term in Equation (8.21) describes the shift of the energy of all L valleys due to the dilatation of the crystal. The $\mathrm{L}^{(1)}$–$\mathrm{L}^{(3)}$ splitting is described by the second term in Equation (8.21).

As in the case of the Γ-conduction band, it is a reasonable approximation to set $a_{\mathrm{c}}^{\mathrm{L}}$ (E_1^{L}) equal to the DP for the indirect band-gap energy $E_{\mathrm{g}}^{\mathrm{L}}$ [8.17]. The DP $a_{\mathrm{c}}^{\mathrm{L}}$ can be obtained from band-structure calculations under hydrostatic pressure or by measuring the hydrostatic pressure dependence of the indirect band-gap energy $E_{\mathrm{g}}^{\mathrm{L}}$.

We summarize in Table 8.8 the L-conduction-band DPs, E_1 (E_1^{L}) and E_2 (E_2^{L}), for some cubic group-IV and III–V semiconductors.

Table 8.8 Hydrostatic E_1 and shear deformation potentials E_2 for electrons at the L-conduction band of some cubic group-IV and III–V semiconductors

System	Material	E_1 (eV)	E_2 (eV)	System	Material	E_1 (eV)	E_2 (eV)
IV	Si	-3.1^a	18.0^a	III–V	c-BN		27.9^a
	Ge	-3.8	15.9		c-AlN		25.5^a
					AlAs	-4.2^b	
					β-GaN		27.5^a
					GaAs	-2	14.5
					GaSb	-3.2	17.5

[a] Calculated
[b] Estimated

(b) Optical phonon deformation potential

The optical DP parameter d_0 is determined by the splitting of the Γ-valence-band states produced by the long-wavelength optical phonons (Γ_{15} phonons). Similarly, the optical DP $d_{1o}(c)$ can be determined by the shift of the L-conduction-band states produced by the Γ_{15}-phonon displacement, which is decomposed into the L_1 and L_3 representation of the $\boldsymbol{k}$-group C_{3v} at the L point [8.18]. The L_1 part of the phonon deformation causes a shift of the L-conduction band. In transport studies of n-Ge, it is common [8.19] to introduce a deformation potential D, which is related to $d_{1o}(c)$ by

$$D = \frac{d_{1o}(c)}{2a} \tag{8.22}$$

where a is the lattice parameter.

As in the case of the L-conduction band, the L_1 part of the Γ_{15}-phonon deformation causes a shift of the L-valence band by the optical DP $d_{1o}(v)$ ($d_{1o}(so)$). In the approximation that the strain dependence of the spin–orbit interaction is neglected, $d_{1o}(v) = d_{1o}(so)$ [8.18]. If the spin–orbit interaction is neglected altogether, the L_3 part of the phonon deformation splits the doubly degenerate valence-band edge. This splitting is caused by the optical DP d_{3o}. If the Γ point is approached from the [111] direction, the DPs behave as [8.20]

$$\begin{aligned} d_{1o}(c) &\to 0 \\ d_{1o}(v) &\to -d_0 \\ d_{3o} &\to \sqrt{2}d_0 \end{aligned} \tag{8.23}$$

We summarize in Table 8.9 the optical phonon deformation potential values, $d_{1o}(c)$, $d_{1o}(v)$ and d_{3o}, at the L point of some cubic group-IV, III–V and II–VI semiconductors. Some of these values were obtained experimentally (Ge, GaAs, GaSb, InSb and HgTe).

Table 8.9 Optical phonon deformation potentials, $d_{1o}(c)$, $d_{1o}(v)$ and d_{3o}, at the L point of some cubic group-IV, III–V and II–VI semiconductors (in eV)

System	Material	$d_{1o}(c)$	$d_{1o}(v)$	d_{3o}	System	Material	$d_{1o}(c)$	$d_{1o}(v)$	d_{3o}
IV	Si	-3.7^a	-20.8^a	49.0^a	II–VI	β-ZnS	-22.4^a	1.4^a	22.1^a
	Ge	-24.9^a	-13.6^a	45		ZnSe	-23.8^a	-2.1^a	24.9^a
	α-Sn	-22.4^a	-9.5^a	38.1^a		ZnTe	-21.5^a	-5.1^a	27.9^a
						CdTe	-27.5^a	-17.4^a	42.5^a
III–V	c-BN	-24.0^a	-14.6^a	56.3^a		HgTe	-19.9		14.7
	c-AlN	-12.1^a	-13.3^a	-16.7^a					
	AlP	-4.4^a	-18.2^a	33.9^a					
	AlAs	-18.2^a		35.0^a					
	AlSb	-15.5^a	-15.7^a	35.6^a					
	β-GaN	-11.0^a	0.4^a	-27.0^a					
	GaP	-20.8^a	-10.2^a	41.3^a					
	GaAs	|17|		45					
	GaSb	-24.7^a	-9.2^a	60					
	InP	-24.8^a	-14.1^a	43.3^a					
	InAs	-33.0^a	-11.1^a	40.3^a					
	InSb	-28.0^a	-10.2^a	33					

[a] Calculated

(c) Valence-band deformation potential

The valence bands at L are split in the absence of spin–orbit coupling by the ⟨111⟩ stress. The splitting is now given, in Kane's DP notation D [8.21], as [8.5]

$$\Delta E_{\mathrm{v}}^{\mathrm{L}} = 4\sqrt{\frac{2}{3}} D_3^5 e_{ij} \tag{8.24}$$

where e_{ij} is the off-diagonal component of the ⟨111⟩ strain. Similarly, the ⟨001⟩ strain splits the valence bands equally for all L valleys by [8.5]

$$\Delta E_{\mathrm{v}}^{\mathrm{L}} = 2\sqrt{\frac{2}{3}} D_3^3 \left[e_{zz} - \frac{1}{2}(e_{xx} + e_{yy}) \right] \tag{8.25}$$

Note that the ⟨001⟩ strain does not split the ⟨111⟩ conduction-band valleys among each other.

We list in Table 8.10 the valence-band DPs D_3^5 and D_3^3 determined experimentally for some cubic group-IV, III–V and II–VI semiconductors.

(d) Hydrostatic and interband deformation potentials: E_1 and $E_1 + \Delta_1$ gaps

It is interest to know the effects of uniaxial stress and also of optical phonons (Γ_{15} phonons) on the E_1 and $E_1 + \Delta_1$ transitions. We show in Figure 8.6 the stress dependence of the E_1-gap and $E_1 + \Delta_1$-gap energies in GaAs for stresses along (a) [001] and (b) [111]

Table 8.10 Valence-band deformation potentials, D_3^5 and D_3^3, at the L-valence bands of some cubic group-IV, III–V and II–VI semiconductors determined experimentally

System	Material	D_3^5 (eV)	D_3^3 (eV)	System	Material	D_3^5 (eV)	D_3^3 (eV)
IV	Si	4.3	4.6	II–VI	ZnSe	−27	−17
	Ge	3.7	−5.6 (E_1)		ZnTe	−15	−29
			−6.2 ($E_1 + \Delta_1$)				
III–V	GaAs	−6.4	−5.4				
	InP	−12.9	−4.1				

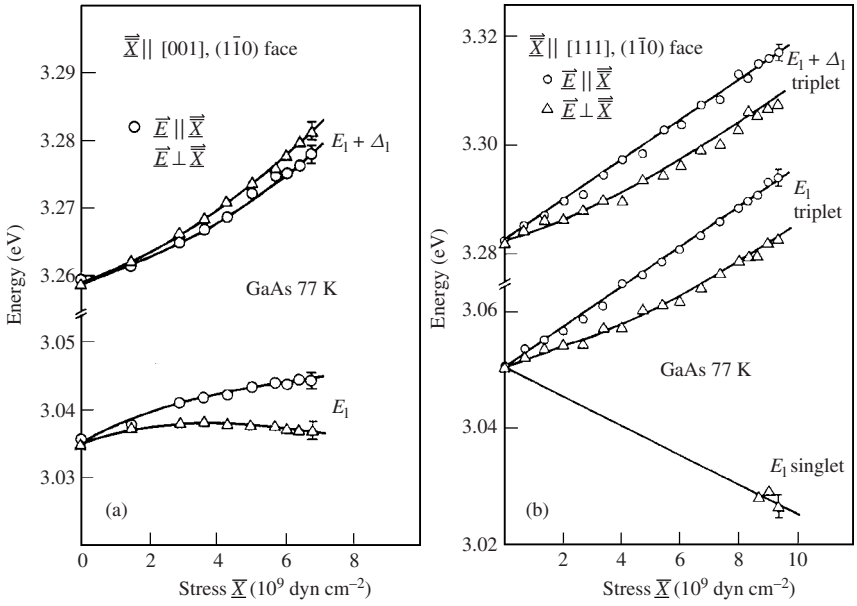

Figure 8.6 Stress dependence of the E_1-transition and $E_1 + \Delta_1$-transition energies in GaAs for uniaxial stresses along (a) [001]; (b) [111] directions with light polarized parallel and perpendicular to the stress axes. [From M. Chandrasekhar and F. H. Pollak, *Phys. Rev. B* **15**, 2127 (1977), reproduced by permission from the American Physical Society]

directions measured by the Schottky barrier electroreflectance with light polarized parallel and perpendicular to the stress axis at $T = 77$ K [8.22]. The data along [001] clearly show the linear stress dependence of the center of gravity, nonlinear intraband effect and polarization-dependent splitting of the E_1 and $E_1 + \Delta_1$ structures. These data enable us to obtain the DP values of D_1^1 and D_3^3.

A uniaxial stress along the [111] direction preferentially selects out the [$\bar{1}\bar{1}\bar{1}$] direction (singlet), while making equal angles with the other three[$\bar{1}\,\bar{1}\,1$], [$\bar{1}1\bar{1}$], and [$1\bar{1}\,\bar{1}$] directions (triplet) [8.5, 8.22]. This gives rise to an interband splitting between the singlet and triplet. The data shown in Figure 8.6(b) enable to determine the DPs of D_1^1, D_1^5 and D_3^5. The hydrostatic DP D_1^1 and interband DP D_1^5 can be calculated from the splitting between the singlet and $\boldsymbol{E} \parallel \boldsymbol{X}$ triplet. The existence of the interband splitting (D_1^5) confirms that the

Table 8.11 Hydrostatic D_1^1 $(= \sqrt{3}a_1^L)$ and interband deformation potentials D_1^5 for the E_1 and $E_1 + \Delta_1$ gaps of some cubic group-IV, III–V and II–VI semiconductors determined experimentally

System	Material	D_1^1 (eV)	D_1^5 (eV)
IV	Si	−9.0	9
	Ge	−8.7	12.2
III–V	GaAs	−8.3	12.0
	GaSb	−12.3 (E_1)	7.4 (E_1)
		−17.7 ($E_1 + \Delta_1$)	
	InP	−9.2	20.4
	InSb	−7.4 (E_1)	−7.4 (E_1)
		−8.5 ($E_1 + \Delta_1$)	−6.5 ($E_1 + \Delta_1$)
II–VI	ZnSe	−5.8	30
	ZnTe	−5.5	40

transitions are along the Λ directions. The DP parameters D_1^1 and D_1^5 are now connected with the DPs of Herring and Vogt [8.14] through

$$D_1^1 = \sqrt{3}\left(\Xi_d + \frac{1}{3}\Xi_u\right)$$

$$D_1^5 = \frac{1}{\sqrt{3}}\Xi_u \tag{8.26}$$

An overview of the different notations used has been given by Kane [8.5].

By analogy with Equations (8.5) and (8.14), it is possible to obtain the hydrostatic DP $a_1^L = D_1^1/\sqrt{3}$ of the E_1 and $E_1 + \Delta_1$ gaps from the corresponding hydrostatic pressure dependence data. We show in Table 8.11 the hydrostatic DP $D_1^1 = \sqrt{3}a_1^L$ and interband DP D_1^5 for the E_1 and $E_1 + \Delta_1$ gaps of some cubic group-IV, III–V and II–VI semiconductors determined experimentally.

8.2.2 X point

(a) Hydrostatic and shear deformation potentials: conduction band

The DPs $E_1 = a_c^X$, Ξ_d and $E_2 = \Xi_u$ at the three X-conduction valleys can be defined just as in the case of the L valleys. The conduction-band minima at X or along Δ are, however, not affected by uniaxial strain along the [111] direction. Under compressive uniaxial strain along [001], on the other hand, an X valley along [001] ($X^{(1)}$) splits off from the other two along [100] and [010] ($X^{(2)}$) with a ratio of 2 : 1 with respect to the average (i.e., the $X^{(1)}$ valley under compressive strain lies in energy lower than the $X^{(2)}$ valleys).

We list in Table 8.12 the L-conduction-band DPs, E_1 (E_1^X) and E_2 (E_2^X), for some cubic group-IV and III–V semiconductors.

Table 8.12 Hydrostatic E_1 and shear deformation potentials E_2 for electrons at the X point of some cubic group-IV and III–V semiconductors

System	Material	E_1 (eV)	E_2 (eV)	System	Material	E_1 (eV)	E_2 (eV)
IV	Si	2.9	8.6	III–V	c-BN		17.9[a]
	Ge	5.75[a]	9.75[a]		c-AlN	−5.5[a]	6.6[a]
					AlP	1.81[a]	6.75[a]
					AlAs	1.20	6.9
					AlSb		5.4
					β-GaN	−6.8[a]	7.1[a]
					GaP	2.7	6.3
					GaAs	1.05[b]	6.5
					GaSb	1.99[a]	6.46[a]
					InP	1.85[a]	3.3[a]
					InAs	1.59[a]	3.7[a]
					InSb	1.56[a]	4.53[a]

[a] Calculated
[b] Estimated

Table 8.13 Hydrostatic D_1^1 ($= \sqrt{3}a_2^{\mathrm{X}}$) and interband deformation potentials D_1^3 for the E_2 gap of some cubic semiconductors

System	Material	D_1^1 (eV)	D_1^3 (eV)
IV	Si	2.6	
III–V	GaAs	−5.9[a]	−10.4[a]

[a] Calculated

(b) Hydrostatic and interband deformation potentials: E_2 gap

We show in Table 8.13 the hydrostatic DPs at the E_2 gap of Si and GaAs. The $D_1^1 = \sqrt{3}a_2^{\mathrm{X}}$ value for Si has been determined from piezobirefringence measurements in the opaque region [8.23]. The E_2 ($\mathrm{X}_5 \rightarrow \mathrm{X}_1$) gap splits by a [001] strain in a manner somewhat similar to the case of the E_1 gap by [001] strain. The splitting of the [001] valley from [100] and [010] can be given by the DP parameter D_1^3 [8.5]. Values of D_1^1 and D_1^3 for GaAs have been obtained by the empirical pseudopotential calculation [8.17, 8.24].

8.3 INTERVALLEY DEFORMATION POTENTIAL

8.3.1 General remarks

It is believed that the Gunn effect arises from a negative conductance mechanism in which the electrons are transferred from a low-mass center valley (Γ) to a higher-lying large-mass

satellite valley (L and/or X) such as exist in the conduction band of GaAs. The strength of this type of electron-transfer mechanism can be represented by the coupling constant D_{ij} [8.19]. The coupling constant D_{ij} is the so-called intervalley deformation potential (in units of eV/cm), where $i = j$ corresponds to the equivalent intervalley scattering and $i \neq j$ to the nonequivalent one.

The matrix element for the intervalley scattering of a carrier $|\boldsymbol{k}\rangle$ by absorption or emission of a phonon $|\boldsymbol{q}, j\rangle$ is written as [8.19]

$$\left|\langle \boldsymbol{k} \pm \boldsymbol{q}| H_{ij}^{\mathrm{IV}} |\boldsymbol{k}\rangle\right| = \frac{D_{ij}^2 \boldsymbol{K}^2 \hbar}{2Vg\omega_{\mathrm{q}}} \left(N_{\mathrm{q}} + \frac{1}{2} + \frac{\delta N_{\mathrm{q}}}{2}\right) \tag{8.27}$$

where $\boldsymbol{K}$ is a reciprocal lattice vector, V is the volume of the unit cell, g is the crystal density and N_{q} is the phonon occupation number given by

$$N_{\mathrm{q}} = \frac{1}{e^{\hbar\omega_{\mathrm{q}}/kT} - 1} \tag{8.28}$$

The corresponding intervalley scattering time τ_{ij} of carriers initially in a state with energy E in the ith valley can be given by

$$\tau_{ij}^{-1} = \sum \frac{D_{ij}^2 (m_x^{(j)} m_y^{(j)} m_z^{(j)})^{1/2}}{\sqrt{2}\pi\hbar^3 g\omega_{\mathrm{q}}} \left[N_{\mathrm{q}}\sqrt{E - \Delta E^{(j)} + \hbar\omega_{\mathrm{q}}} + (N_{\mathrm{q}} + 1)\sqrt{E - \Delta E^{(j)} - \hbar\omega_{\mathrm{q}}}\right] \tag{8.29}$$

where $m_i^{(j)}$ is the effective mass in the i direction ($i = x$, y or z) and $\Delta E^{(j)}$ is the energy of the valley the electron scatters into (jth valley).

As the Hamiltonian H_{ij}^{IV} in Equation (8.27) has the symmetry of the phonon involved, the transition is forbidden unless the representation belonging to the state $|\boldsymbol{k} \pm \boldsymbol{q}\rangle$ is contained in the product of the representations belonging to $|\boldsymbol{q}, j\rangle$ and $|\boldsymbol{k}\rangle$ [8.25]. In a zinc-blende semiconductor, the symmetries for the two lowest conduction-band states at X are X_1 (X_6) and X_3 (X_7), with the anion at the origin. Usually X_1 is the lower state, with the exception of GaSb, where X_3 seems to have lower energy [8.26]. The transverse phonons, TA and TO, have X_5 symmetry and do not contribute to the intervalley scattering between Γ and X. The longitudinal acoustic (LA) and optical phonons (LO) have X_1 and X_3 symmetry. If the anion is heavier than the cation, as in the case of AlAs, AlSb and GaSb, then the X_1 state (with the anion at rest) has higher energy (LO) than the X_3 state (LA). In the reverse case (e.g., GaP, InP and InAs), the LA (LO) phonon has X_1 (X_3) symmetry. Note that for GaAs the Ga atom is lighter than the As atom (although these two masses are very similar). However, recent analysis of phonon dispersion in GaAs has suggested that the lighter Ga atom vibrates in the higher-frequency (LO) mode (X_3 representation); the As atom is at rest; then the other (LA) mode belongs to the X_1 representation [8.27].

The symmetry for the lowest conduction-band state at L is L_1 (L_6). Both the LA and LO phonons have L_1 symmetry [8.27] and contribute to scattering processes at L. The TA and TO phonons have L_3 symmetry and, therefore, do not contribute to the intervalley scattering between Γ and L. Similarly, since the transverse phonons have X_5 symmetry, they do not contribute to the scattering between Γ and X. The LA and LO phonons have X_1 and X_3 symmetries, respectively, and thus they will contribute. Scattering between

different equivalent L valleys (X valleys) is allowed for LO and LA phonons (X_1 phonon). All phonon modes are important for scattering from L_1 state to an X_1 state, whereas only the transverse phonons can scatter to X_3 [8.28, 8.29].

The selection rules for the intervalley scattering processes have been given by Birman, Lax and Loudon [8.25]. The conditions for these selection rules to be valid are usually not fulfilled, since energy conservation rules out scattering processes between electrons exactly at high-symmetry points [8.17]. Nevertheless, it is generally assumed that the matrix elements for the intervalley transitions are nearly independent of the phonon wavevector. Therefore, the matrix elements can be integrated over all possible final states in a spherical energy band, resulting in Conwell expression, Equation (8.29), for the intervalley scattering time.

Table 8.14 Intervalley deformation potential D_{ij} for electrons in some cubic group-IV, III–V and II–VI semiconductors (in eV/Å)

System	Material	$D_{\Gamma X}$[a]	$D_{\Gamma L}$	D_{LL}	D_{XX}	D_{LX}
IV	Diamond				8.0	
	Si			2.63	0.15–4.0	4.0
	Ge	10.0	2.0	0.2–3.0	0.79–9.5	4.1
III–V	AlP	5.0	5.0	0.3–1.0	8.1	
	AlAs	3.1	1.6–2.3	1.6	4.7	0.4–1.7
	AlSb	1.3–4.9	2.3–3.4	0.5–0.6	9.5	0.8–3.7
	GaP	0.8–1.1	0.7–1.1	0.6	3.0	0.4–1.6
	GaAs	5.2–15	1.5–9.5	5	10	2.75–3.1
	GaSb	2.5–4.5	2.7–2.8	0.6–1.2	6.0	1.0–2.2
	InP	1.6	1.3–2.7	0.3–0.9	3.6	0.7–3.3
	InAs	2.0–2.2	1.0–2.0	1.1	2.5	0.6–1.9
	InSb	3.3–4.9	1.1–4.3	0.3–0.6	6.8	0.2–2.9
II–VI	β-ZnS	1.10–1.89	2.18–4.13			
	ZnSe	0.72–1.37	2.17–2.71			
	ZnTe	1.17–1.43	3.19–3.31			
	CdTe	0.40–1.23	1.68–1.76			

[a] $D_{\Gamma X(1)}$ and $D_{\Gamma X(3)}$

Table 8.15 Intervalley deformation potential D_{ij} for electrons in some hexagonal group-IV and III–V semiconductors

System	Material	D_{ij} (eV/Å)	
		Equivalent valley	Nonequivalent valley
IV	6H-SiC	6–27	
III–V	w-AlN	10	10
	α-GaN	5–10	10
	InN	10	10

Herbert [8.30] has pointed out that the intervalley deformation potential is not independent of the phonon wavevector $\boldsymbol{q}$. This effect has been studied in detail by Zollner *et al*. [8.29, 8.31, 8.32]. They introduced the concept of effective intervalley deformation potentials to account for the $\boldsymbol{q}$-dependence under actual experimental conditions. This $\boldsymbol{q}$-dependence allows the TA phonons to contribute to the intervalley scattering processes and causes an apparent temperature dependence of the intervalley deformation potentials observed in the experiment.

8.3.2 Numerical value

There have been several theoretical calculations of the intervalley deformation potentials for semiconductors. They are based on parameterized lattice dynamic models for the phonon eigenvectors and empirical pseudopotential or tight-binding electron wavefunctions. Estimates of the intervalley deformation potentials have also been achieved from a number of different optical and electrical measurements. We summarize in Tables 8.14 and 8.15 the intervalley deformation potential for some cubic and hexagonal semiconductors, respectively. These data are obtained from various sources.

REFERENCES

[8.1] J. Bardeen and W. Shockley, *Phys. Rev.* **80**, 72 (1950).
[8.2] H. Ehrenreich, *Phys. Rev.* **120**, 1951 (1960).
[8.3] C. G. Van de Walle and R. M. Martin, *Phys. Rev. Lett.* **62**, 2028 (1989).
[8.4] W. H. Kleiner and L. Roth, *Phys. Rev. Lett.* **2**, 234 (1959).
[8.5] E. O. Kane, *Phys. Rev.* **178**, 1368 (1969).
[8.6] G. L. Bir and G. E. Pikus, *Symmetry and Strain-Induced Effects in Semiconductors* (Wiley, New York, 1974).
[8.7] Yu. M. Sirenko, J. B. Jeon, B. C. Lee, K. W. Kim, M. A. Littlejohn, M. A. Stroscio, and G. J. Iafrate, *Phys. Rev. B* **55**, 4360 (1997).
[8.8] F. H. Pollak and M. Cardona, *Phys. Rev.* **172**, 816 (1968).
[8.9] A. Gavini and M. Cardona, *Phys. Rev. B* **1**, 672 (1970).
[8.10] B. Rockwell, H. R. Chandrasekhar, M. Chandrasekhar, A. K. Ramdas, M. Kobayashi, and R. L. Gunshor, *Phys. Rev. B* **44**, 11307 (1991).
[8.11] A. Blacha, H. Presting, and M. Cardona, *Phys. Status Solidi B* **126**, 11 (1984).
[8.12] S. Adachi, *GaAs and Related Materials: Bulk Semiconducting and Superlattice Properties* (World Scientific, Singapore, 1994).
[8.13] L. Brey, N. E. Christensen, and M. Cardona, *Phys. Rev. B* **36**, 2638 (1987).
[8.14] C. Herring and E. Vogt, *Phys. Rev.* **101**, 944 (1956).
[8.15] C. G. Van de Walle, *Phys. Rev. B* **39**, 1871 (1989).
[8.16] D. N. Mirlin, V. F. Sapega, I. Y. Karlik, and R. Katilius, *Solid State Commun.* **61**, 799 (1987).
[8.17] M. Cardona and S. Zollner, in *Properties of Gallium Arsenide*, 2nd Edition, EMIS Datareviews Series No. 2 (INSPEC, London, 1990), p. 126.
[8.18] W. Pötz and P. Vogl, *Phys. Rev. B* **24**, 2025 (1981).
[8.19] E. M. Conwell, *High Field Transport in Semiconductors* (Academic, New York, 1967).
[8.20] M. A. Renucci, J. B. Renucci, R. Zeyher, and M. Cardona, *Phys. Rev. B* **10**, 4309 (1974).
[8.21] H. Qiang, F. H. Pollak, and G. Hickman, *Solid State Commun.* **76**, 1087 (1990).
[8.22] M. Chandrasekhar and F. H. Pollak, *Phys. Rev. B* **15**, 2127 (1977).

[8.23] P. Etchegoin, J. Kircher, and M. Cardona, *Phys. Rev. B* **47**, 10292 (1993).
[8.24] Y.-F. Tsay, S. S. Mitra, and B. Bendow, *Phys. Rev. B* **10**, 1476 (1974).
[8.25] J. L. Birman, M. Lax, and R. Loudon, *Phys. Rev.* **145**, 620 (1966); J. L. Birman, *Phys. Rev.* **150**, 771 (1966).
[8.26] R. M. Wentzcovitch, M. Cardona, M. L. Cohen, and N. E. Christensen, *Solid State Commun.* **67**, 927 (1988).
[8.27] D. Strauch and B. Dorner, *J. Phys.: Condens. Matter* **2**, 1457 (1990).
[8.28] S. Zollner, S. Gopalan, and M. Cardona, *Appl. Phys. Lett.* **54**, 614 (1989).
[8.29] S. Zollner, S. Gopalan, and M. Cardona, *J. Appl. Phys.* **68**, 1682 (1990).
[8.30] D. C. Herbert, *J. Phys. C: Solid State Phys.* **6**, 2788 (1973).
[8.31] S. Zollner, S. Gopalan, and M. Cardona, *Solid State Commun.* **76**, 877 (1990).
[8.32] S. Zollner, S. Gopalan, and M. Cardona, *Semicond. Sci. Technol.* **7**, B137 (1992).

9 Electron Affinity and Schottky Barrier Height

9.1 Electron affinity 195
9.1.1 An overview 195
9.1.2 Numerical value 196
9.2 Schottky barrier height 198
9.2.1 An ideal Schottky–Mott contact 198
9.2.2 Case study: Au/semiconductor contact 202
9.2.3 Surface reconstruction and external perturbation effect 204
9.2.4 Breakdown voltage 206
References 208

9.1 ELECTRON AFFINITY

9.1.1 An overview

The electron affinity χ_e in a semiconductor is defined as the work required to remove an electron from an energy level corresponding to the bottom of the conduction band to a point corresponding to the vacuum level and situated just outside the material, beyond the range of the image force. Because the definition of the electron affinity implies bulk and surface effects, the problem of χ_e is a very intricate one.

For most semiconductors, an electron at the bottom of the conduction band is bound to the material by a potential barrier of several volts. This barrier is the electron affinity and is defined as a positive electron affinity. If χ_e becomes negative, that is, the vacuum level lies below the conduction-band edge, any electron that is excited into the conduction band has enough energy to leave the crystal. It means that an electron at the conduction-band edge would not see a surface barrier and could be freely emitted into the vacuum. This no-barrier electron emission has potential for cold-cathode device applications, such as field emitters and flat-panel displays.

The effect of a negative electron affinity was recognized on hydrogen-terminated diamond surfaces [9.1, 9.2]. More recently, some III–V nitrides have been shown to exhibit a negative electron affinity [9.3]. This unusual character can be related in a general sense to the similar bonding of all materials of the diamond, zinc-blende or wurtzite structures. All of these structures exhibit sp^3 bonding with four-fold coordination. Given the similar origin of the electronic states, then as the band-gap energy is increased it is natural

Properties of Group-IV, III–V and II–VI Semiconductors Sadao Adachi

© 2005 John Wiley & Sons, Ltd

ISBN: 0-470-09032-4

to consider that the conduction-band edge will move closer to the vacuum level [9.4]. However, recent study on $Al_xGa_{1-x}N(0001)$ suggested a decrease in the electron affinity with increasing AlN composition x, but χ_e remained positive for all x [9.5]. In this study, surface cleanness and stoichiometry were monitored with X-ray photoelectron spectroscopy. Oxygen was believed to be located on the bulk and the surface contamination was estimated to be smaller than 3% of a monolayer.

9.1.2 Numerical value

We summarize in Table 9.1 the experimental electron affinity χ_e for some group-IV, III–V and II–VI semiconductors. It should be noted that the electron affinity for diamond can be controlled by desorption of hydrogen from an initially fully hydrogenated surface (i.e., negative χ_e surface) to positive values [9.6, 9.7]. The surface-orientation-dependent χ_e values have also been reported for ZnO [9.8].

The conduction and valence bands of compound semiconductors can be well characterized by electron orbitals of the cation and anion atoms, respectively. We have already seen in Section 6.2 that there is an increase in the valence-band spin–orbit split-off energy Δ_0 with increase in the atomic number of the anion atom. Let us plot in Figure 9.1 the variation of χ_e for some group-IV, III–V and II–VI semiconductors with respect to the group IV, III and II cations. It is understood from Figure 9.1 that there is an increase in χ_e with increase in the atomic number of the cation atom.

Figure 9.2 plots the electron affinity χ_e versus lattice constant a for some group-IV, III–V and II–VI semiconductors. The solid line in Figure 9.2 represents the least-squares

Table 9.1 Electron affinity χ_e for some group-IV, III–V and II–VI semiconductors

System	Material	χ_e (eV)	System	Material	χ_e (eV)
IV	Diamond	$-2.2 \sim 0.8^a$	II–VI	MgO	−2.5 (Negative value)
	Si	4.05		ZnO	$3.7 \sim 4.60^b$
	Ge	4.14		α-ZnS	3.9
	3C-SiC	3.83		ZnSe	4.06
	6H-SiC	3.34		ZnTe	3.68
				w-CdS	4.5
III–V	w-AlN	$-1.0 \sim 3.2$		w-CdSe	4.95
	AlAs	3.5		CdTe	4.28
	AlSb	3.65			
	α-GaN	3.3			
	GaP	3.75			
	GaAs	4.15			
	GaSb	4.21			
	InP	4.50			
	InAs	5.06			
	InSb	4.72			

[a] χ_e value depends on a surface coverage of hydrogen
[b] Depending on surface orientation

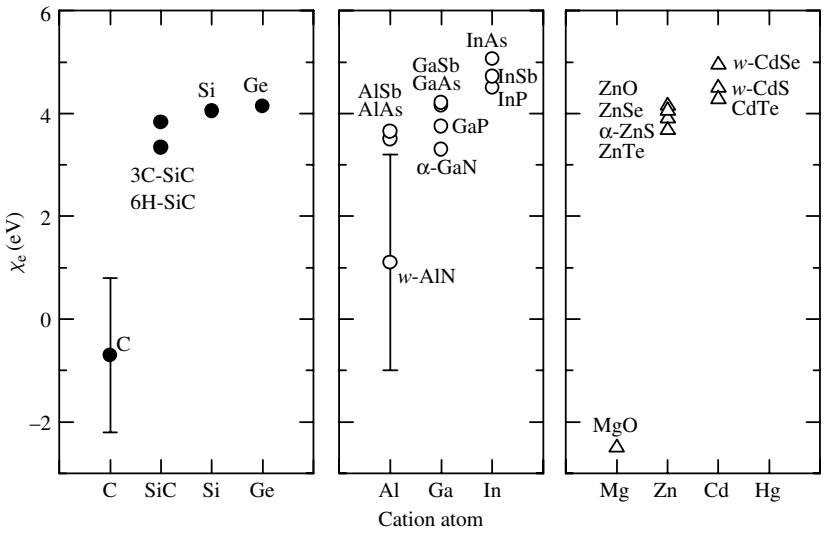

Figure 9.1 Electron affinity χ_e plotted against cation atoms for some group-IV, III–V and II–VI semiconductors

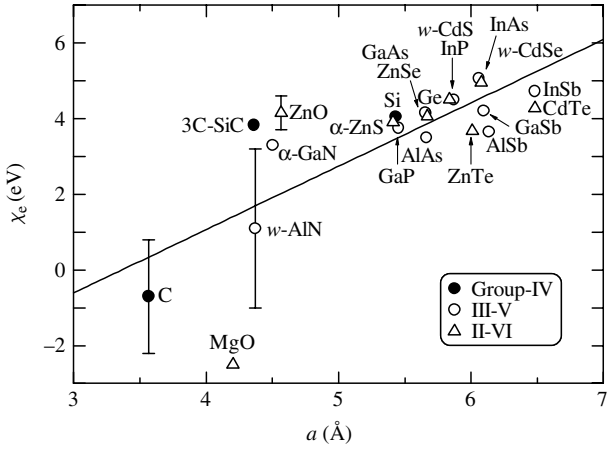

Figure 9.2 Electron affinity χ_e versus lattice constant a for some group-IV, III–V and II–VI semiconductors. For hexagonal semiconductors, an effective lattice constant $a_{\text{eff}} = (\sqrt{3}a^2c)^{1/3}$ is plotted instead of a. The solid line represents the least-squares fit with $\chi_e = 1.67a - 5.63$ (a in Å; χ_e in eV)

fit with the relation (a in Å; χ_e in eV)

$$\chi_e = 1.67a - 5.63 \tag{9.1}$$

The electron affinities χ_e plotted as a function of the lowest direct band-gap energy E_0 for some group-IV, III–V and II–VI semiconductors are shown in Figure 9.3. The solid

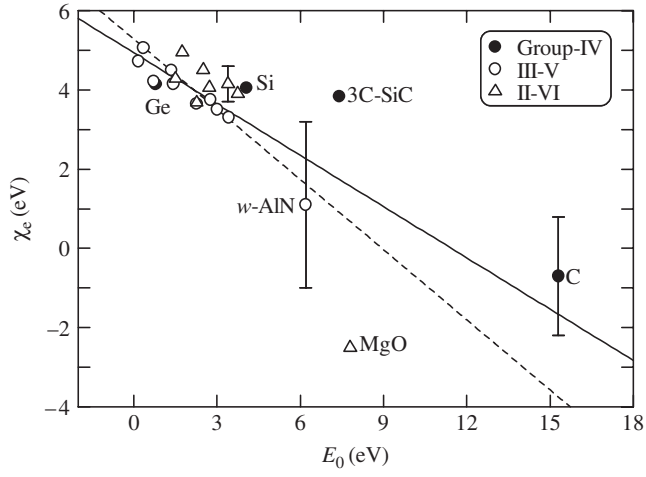

Figure 9.3 Electron affinity χ_e versus E_0-gap energy for some group-IV, III–V and II–VI semiconductors. For hexagonal semiconductors, an effective lattice constant $a_{eff} = (\sqrt{3}a^2c)^{1/3}$ is plotted instead of a. The solid line represents the least-squares fit with $\chi_e = 4.94 - 0.43E_0$, while the dashed line represents the relation with $\chi_e = 5.28 - 0.59E_0$ (E_0 and χ_e in eV)

line represents the least-squares fit with the relation (E_0 and χ_e in eV)

$$\chi_e = 4.94 - 0.43E_0 \tag{9.2}$$

It has already been shown in Section 6.2 that the relation between the lowest direct band-gap energy E_0 and a can be simply written as $E_0 = 18.55 - 2.84a$ (a in Å; E_0 in eV). Introducing this expression into Equation (9.1), we obtain (E_0 and χ_e in eV)

$$\chi_e = 5.28 - 0.59E_0 \tag{9.3}$$

The dashed line in Figure 9.3 shows the calculated result of Equation (9.3).

The variation of χ_e with temperature of some cubic semiconductors has been discussed theoretically by Soonckindt *et al.* [9.9]. They considered that

$$\frac{\partial \chi_e}{\partial T} = -\frac{\partial \Gamma_1^c}{\partial T} \tag{9.4}$$

where Γ_1^c is an energy of the Γ_1 conduction-band edge.

9.2 SCHOTTKY BARRIER HEIGHT

9.2.1 An ideal Schottky–Mott contact

Most semiconductor devices are based on the use of barriers to control the motion of electrons and/or holes in the semiconductor. The types of barrier predominantly used in semiconductors are insulating layers, semiconductor–semiconductor junctions and

metal–semiconductor junctions. One of the simplest and yet most basic questions which immediately arises is, how do the bulk band structures of the two materials line up relative to each other. For metals on semiconductors, the question is basic to the origin of Schottky barriers. For semiconductor–semiconductor heterojunctions, the band alignments determine the relative barriers for electrons and holes in quantum wells.

The choice of a metal for fabricating the Schottky barrier with a particular semiconductor is determined by its electronic work function ϕ_M. For an n-type semiconductor, ϕ_M should be greater, while for a p-type semiconductor, it should be less than the electron affinity χ_e of the semiconductor. The barrier heights in such cases are written, respectively, as

$$n\text{-type: } \phi_n = \phi_M - \chi_e \tag{9.5a}$$

$$p\text{-type: } \phi_p = E_g - \phi_M + \chi_e \tag{9.5b}$$

where E_g is the band-gap energy of the semiconductor. The maximum value of the barrier height for an ideal Schottky–Mott contact is, thus, about equal to the band-gap energy of the semiconductor: $\phi_n + \phi_p = E_g$.

We summarize in Table 9.2 the work function ϕ_M of some important metals used as the Schottky contact [9.10]. In the literature, there are numerous experimental data on ϕ_M, with a considerable variation among them. Michaelson [9.11] has analyzed these data and has attempted to correlate them theoretically with the atomic electron negativity. The metal ϕ_M values listed in Table 9.2 are taken from a tabulation by Frederikse [9.10].

In practice, it is difficult to have an ideal Schottky contact and to have simple relationships such as Equation (9.5). This is due to interface states originating from surface states [9.12] or from metal-induced gap states [9.13] and/or due to interface chemical reactions of metal and semiconductor atoms [9.14].

Figures 9.4–9.7 show the Schottky barrier height ϕ_n versus metal work function ϕ_M observed for metal/n-4H-SiC (6H-SiC), metal/n-GaN (α-GaN), metal/n-GaAs and metal/n-ZnO contacts, respectively. The solid lines indicate the least-squares fitts with

Table 9.2 Electronic work function ϕ_M for some important metals

Metal	ϕ_M (eV)	Metal	ϕ_M (eV)	Metal	ϕ_M (eV)
Ag	4.63	Ga	4.32	Pd	5.41
Al	4.17	Hf	3.9	Pt	5.55
Au	5.38	Hg	4.475	Re	4.72
Ba	2.52	In	4.09	Rh	4.98
Be	4.98	Ir	5.46	Ru	4.71
Bi	4.34	K	2.29	Sb	4.63
Ca	2.87	Mg	3.66	Sm	2.7
Cd	4.08	Mn	4.1	Sn	4.42
Co	5.0	Mo	4.57	Ta	4.30
Cr	4.5	Nb	4.33	Tb	3.0
Cs	1.95	Ni	5.20	Ti	4.33
Cu	4.76	Os	5.93	W	4.61
Fe	4.74	Pb	4.25	Zn	3.63

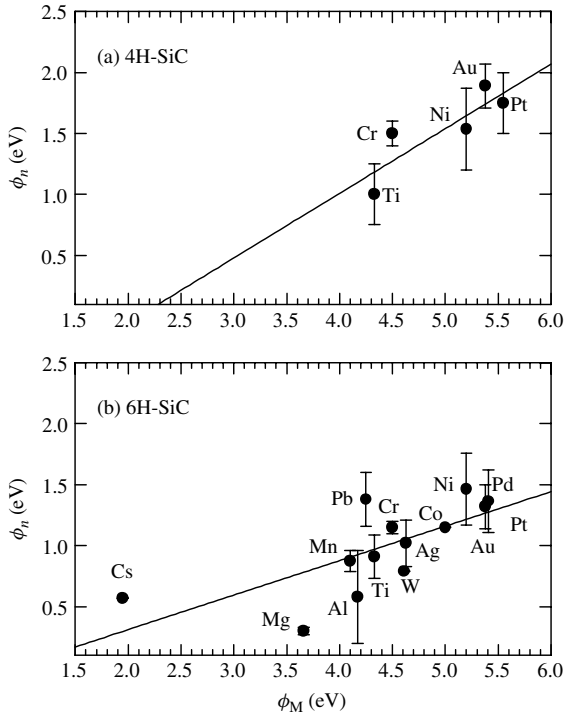

Figure 9.4 Schottky barrier height ϕ_n versus metal work function observed for: (a) metal/n-4H-SiC; (b) metal/n-6H-SiC contacts. The solid lines represent the least-squares fit with: (a) $\phi_n = 0.53\phi_M - 1.11$; (b) $\phi_n = 0.28\phi_M - 0.25$ (ϕ_M and ϕ_n in eV). [From S. Adachi, *Handbook on Physical Properties of Semiconductors Volume 1: Group-IV Semiconductors* (Kluwer Academic, Boston, 2004), reproduced by permission from Kluwer Academic Publishers]

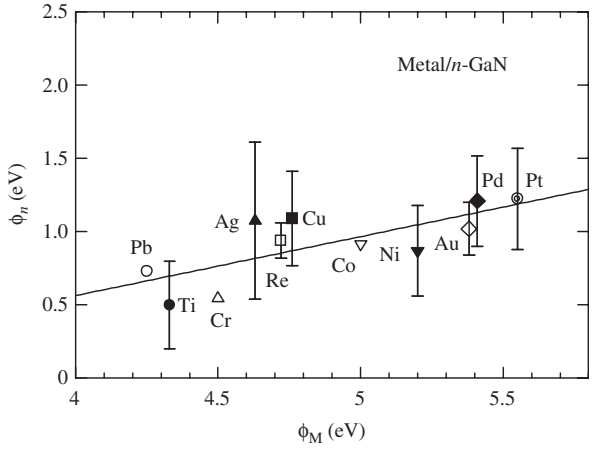

Figure 9.5 Schottky barrier height ϕ_n versus metal work function ϕ_M observed for metal/n-GaN (α-GaN) contacts. The solid line represents the least-squares fit with $\phi_n = 0.40\phi_M - 1.05$ (ϕ_M and ϕ_n in eV). [From S. Adachi, *Handbook on Physical Properties of Semiconductors Volume 2: III–V Compound Semiconductors* (Kluwer Academic, Boston, 2004), reproduced by permission from Kluwer Academic Publishers]

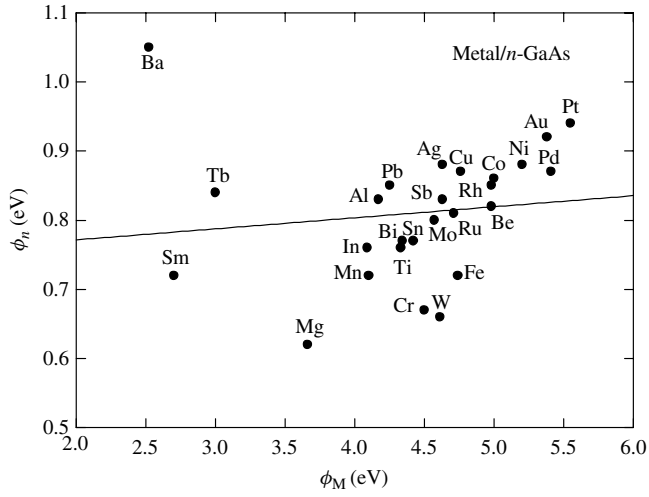

Figure 9.6 Schottky barrier height ϕ_n versus metal work function ϕ_M observed for metal/n-GaAs contacts. The solid line represents the least-squares fit with $\phi_n = 0.016\phi_M + 0.740$ (ϕ_M and ϕ_n in eV). [From S. Adachi, *Handbook on Physical Properties of Semiconductors Volume 2: III–V Compound Semiconductors* (Kluwer Academic, Boston, 2004), reproduced by permission from Kluwer Academic Publishers]

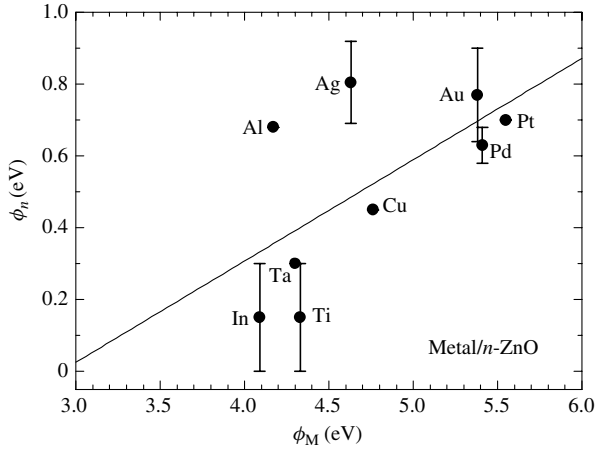

Figure 9.7 Schottky barrier height ϕ_n versus metal work function ϕ_M observed for metal/n-ZnO contacts. The solid line represents the least-squares fit with $\phi_n = 0.28\phi_M - 0.82$ (ϕ_M and ϕ_n in eV). [From S. Adachi, *Handbook on Physical Properties of Semiconductors Volume 3: II–VI Compound Semiconductors* (Kluwer Academic, Boston, 2004), reproduced by permission from Kluwer Academic Publishers]

the relation (ϕ_M and ϕ_n in eV)

$$\phi_n = a\phi_M + b \tag{9.6}$$

The fitted a and b values for some group-IV, III–V and II–VI semiconductors are summarized in Table 9.3. If we assume an ideal Schottky–Mott contact of Equation (9.5), we obtain $a = 1.0$ and $b = -\chi_e$ (n-type).

Table 9.3 Expression for the Schottky barrier heights $\phi_{n,p}$ as a function of metal work function ϕ_M determined from various contacts on some group-IV, III–V and II–VI semiconductors. Note that $a = 1.0$ (-1.0) suggests an ideal Schottky–Mott contact for an n-type (p-type) semiconductor

$$\phi_{n,p} = a\phi_M + b$$

System	Material	Type	a	b (eV)
IV	Si	n	0.088	0.238
	Si	p	−0.11	1.01
	Ge	n	0.410	0.006
	3C-SiC	n	0.31	−0.83
	4H-SiC	n	0.53	−1.11
	6H-SiC	n	0.28	−0.25
III–V	β-GaN	n	0.40	−1.05
	GaP	n	0.225	0.212
	GaAs	n	0.016	0.740
	InP	n	−0.037	0.636
II–VI	ZnO	n	0.28	−0.82
	α-ZnS[a]	n	0.62	−1.43
	ZnSe	n	0.38	−0.64
	ZnTe	p	−0.50	3.27
	w-CdS	n	0.24	−0.56
	w-CdSe	n	0.12	−0.14
	CdTe	n	0.084	0.278

[a] Type of crystal structure (α- or β-ZnS) was ignored in this work

The Schottky barrier height ϕ_p versus metal work function ϕ_M observed for metal/p-ZnTe contacts is plotted in Figure 9.8. In a p-type semiconductor, an ideal Schottky–Mott contact can be given, from Equation (9.5), by $a = -1.0$ and $b = E_g + \chi_e$.

We can easily understand from Figures 9.4–9.8 and Table 9.3 that the actual Schottky contacts deviate largely from ideal Schottky–Mott behavior. It has been demonstrated that for GaAs the barrier heights are almost independent of the surface orientation of the substrate and the preparation method of the surface [9.15–9.17]. The facts suggest that a large density of states, including vacancies, antisites and even more complex defects such as EL2, may exist at the metal/GaAs interface that are responsible for the Fermi level pinning in GaAs [9.18, 9.19].

9.2.2 Case study: Au/semiconductor contact

The Au/semiconductor interface is undoubtedly one of the most studied systems for all metal/semiconductor Schottky barriers. This interest stems largely from the importance of Au/semiconductor from a technological point of view. Gold is often used to

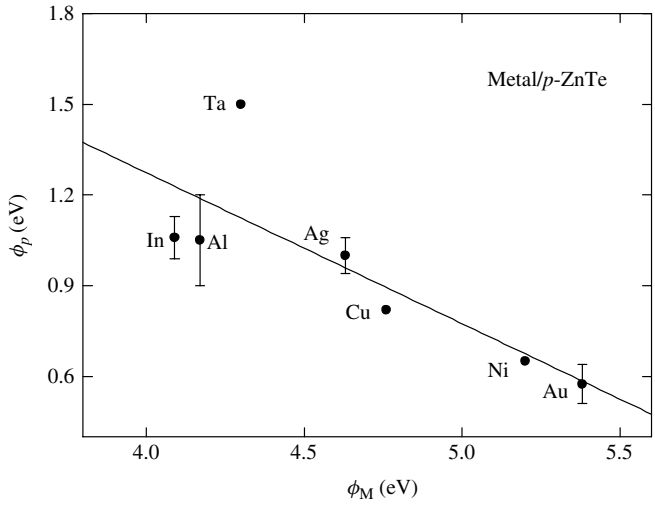

Figure 9.8 Schottky barrier height ϕ_p versus metal work function ϕ_M observed for metal/p-ZnTe contacts. The solid line represents the least-squares fit with $\phi_p = 3.27 - 0.50\phi_M$ (ϕ_M and ϕ_p in eV). [From S. Adachi, *Handbook on Physical Properties of Semiconductors Volume 3: II–VI Compound Semiconductors* (Kluwer Academic, Boston, 2004), reproduced by permission from Kluwer Academic Publishers]

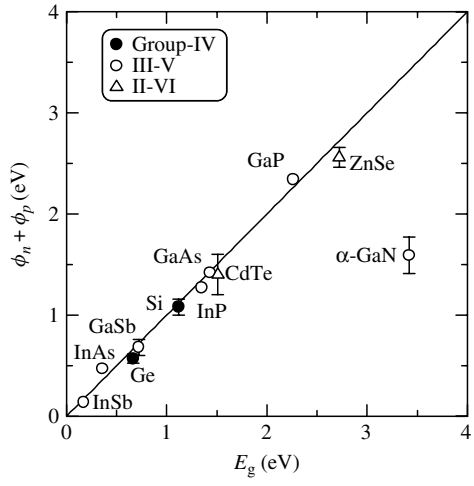

Figure 9.9 Schottky barrier height $\phi_n + \phi_p$ (Au metal) versus band-gap energy E_g for some group-IV, III–V and II–VI semiconductors. The solid line provides the relation of $\phi_n + \phi_p = E_g$

metallize semiconductor structures as it serves as the gate electrode in field-effect transistor (FET) devices and the rectifying contact in high-frequency Schottky diodes. Summarized in Table 9.4 are the results of Au/semiconductor Schottky barrier heights obtained for some n-type and p-type group-IV, III–V and II–VI semiconductors. Figure 9.9 plots the Au-contact Schottky barrier height $\phi_n + \phi_p$ versus band-gap energy E_g for various

Table 9.4 Schottky barrier heights ϕ_n and ϕ_p between Au/n-type and Au/p-type semiconductors, respectively, $\phi_n + \phi_p$ and semiconductor band-gap energy E_g at 300 K

System	Material	ϕ_n (eV)	ϕ_p (eV)	$\phi_n + \phi_p$ (eV)	E_g (eV)
IV	Diamond		1.13–2.0		5.50
	Si	0.75–0.81	0.25–0.35	1.00–1.16	1.12
	Ge	0.45–0.54	0.07	0.52–0.61	0.6657
	3C-SiC	0.78–1.2			2.39
	6H-SiC	1.14–1.50			3.0
III–V	c-BN		3.1		6.27
	h-BN		3.1		3.8–5.9
	BP	~1.4	1.8–1.9	~3.2–3.3	2
	AlAs	1.08–1.82			2.15
	AlSb		0.53–0.59		1.615
	α-GaN	0.84–1.2	0.57	1.41–1.77	3.420
	GaP	1.38	0.96	2.34	2.261
	GaAs	0.92	0.50	1.42	1.43
	GaSb	0.60–0.75	Ohmic	0.60–0.75	0.72
	InP	0.41	0.86	1.27	1.35
	InAs	Ohmic ($T = 77$, 300 K)	0.47 ($T = 77$ K)	0.47	0.359
	InSb	0.14	Ohmic ($T = 77$ K)	0.14	0.17
II–VI	ZnO	0.64–0.90			3.40
	α-ZnS	2.0–2.19[a]			3.75
	β-ZnS	2.0–2.19[a]			3.726
	ZnSe	1.36–1.55	1.2	2.56–2.75	2.721
	ZnTe		0.51–0.64		2.27
	w-CdS	0.68–0.84			2.501
	w-CdSe	0.49–0.7			1.751
	CdTe	0.59–1.0	0.6	1.19–1.6	1.51

[a] Type of crystal structure (α- or β-ZnS) was ignored in this work

semiconductors. The solid line in Figure 9.9 represents the relation of $\phi_n + \phi_p = E_g$ from Equation (9.5).

9.2.3 Surface reconstruction and external perturbation effect

(a) Surface reconstruction

The (001)GaAs surface has a number of reconstructions with widely varying structure and composition. Cho and Dernier [9.20] and Wang [9.21] reported that the Schottky barrier height depends on the particular reconstruction adopted by the GaAs surface prior to Al deposition. However, detailed studies by Svensson *et al.* [9.22] and Barret and Massies [9.23] and later work by Missous *et al.* [9.24] find no clear dependence of the barrier height on surface reconstruction.

In metal/n-Si contacts, the barrier heights of Na, Al, Ag and Pb on (7×7) reconstructed surfaces were found to be by 80 meV smaller than the values of the corresponding (1×1) unreconstructed interfaces [9.25]. This reduction was attributed to structure-induced interface dipoles.

(b) Temperature effect

The temperature dependence of the Schottky barrier heights for metal/semiconductor contacts has been studied by various authors. We show in Figure 9.10, as an example, the barrier height ϕ_p versus temperature plots for an Al/p-InP Schottky diode reported by Song *et al*. [9.26]. From this plot, we obtain $\mathrm{d}\phi_p/\mathrm{d}T \sim -3.3 \times 10^{-4}$ eV/K (solid line). This value is found to be of the same order as the E_0-gap value, $\mathrm{d}E_0/\mathrm{d}T$, for InP ($-3.3 \times 10^{-4}$ eV/K, see Section 6.2). A very similar dependence of $\mathrm{d}\phi_p/\mathrm{d}T \sim -3.9 \times 10^{-4}$ eV/K has also been reported on Yb/p-InP contact [9.27].

For metal/n-GaAs contacts, the values of $\mathrm{d}\phi_n/\mathrm{d}T$ ranging from -2.3×10^{-4} to -4.7×10^{-4} eV/K have been reported for Al, Au, Cu and Pt [9.28–9.30]. These values are of about the same order as the E_0-gap value of GaAs (-4.4×10^{-4} eV/K, Section 6.2); however, the barrier height ϕ_p for Al on p-GaAs [9.28] is found to be much less temperature dependent than for n-GaAs, giving $\mathrm{d}\phi_p/\mathrm{d}T \sim -1.6 \times 10^{-4}$ eV/K.

For metal (silicide)/Si contacts, the published $\mathrm{d}\phi_n/\mathrm{d}T$ and $\mathrm{d}\phi_p/\mathrm{d}T$ data scatter largely from nearly zero to -3.54×10^{-4} eV/K and from $+1.49 \times 10^{-4}$ to -1.26×10^{-4} eV/K, respectively [9.31–9.40]. Note that the temperature variation of the lowest indirect bandgap energy for Si is given by $\mathrm{d}E_\mathrm{g}^\mathrm{X}/\mathrm{d}T \sim +4.9 \times 10^{-4}$ eV/K (Section 6.4). We can thus conclude that in the case for Si there is no strong correlation between $\mathrm{d}\phi_n/\mathrm{d}T$ ($\mathrm{d}\phi_p/\mathrm{d}T$) and $\mathrm{d}E_\mathrm{g}^\mathrm{X}/\mathrm{d}T$.

(c) Pressure effect

The pressure coefficients of the Schottky barrier height for metal (silicide)/Si contacts are $\mathrm{d}\phi_n/\mathrm{d}p = -(0.8 - 2.2)$ meV/kbar for n-Si and $\mathrm{d}\phi_p/\mathrm{d}p = -0.1$ meV/kbar for p-Si

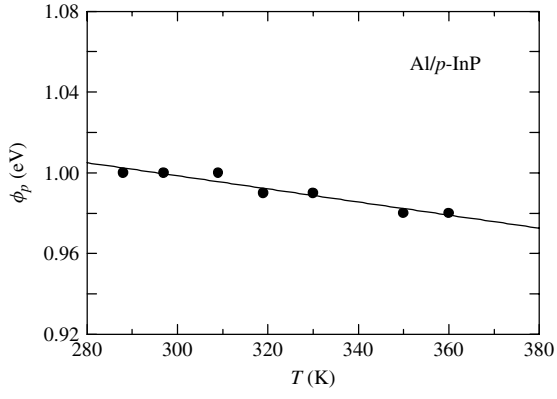

Figure 9.10 Schottky barrier height ϕ_p versus temperature T for an Al/p-InP Schottky diode. [From Y. P. Song, R. L. Van Meirhaeghe, W. H. Laflère, and F. Cardon, *Solid-State Electron.* **29**, 633 (1986), reproduced by permission from Elsevier]

[9.40], while the pressure coefficient of the lowest band-gap energy for Si is reported to be $dE_g^X/dp \sim -1.43$ meV/kbar (Section 6.4).

The pressure dependence of the barrier height for GaAs has been studied by several authors [9.41–9.44]. The linear pressure coefficients $d\phi_n/dp$ determined in these studies are in the range 9.5–11 meV/kbar. These values are the same as that of the E_0 gap of GaAs ($dE_0/dp \sim 11.6$ meV/kbar, Section 6.2).

Shan *et al*. [9.41] have studied the pressure dependence of the barrier height at the Pt/*n*-GaAs interface for hydrostatic pressures from 0 to 16.7 kbar. The pressure variation is found to follow an equation: $\phi_n(p) = 703 + 11p - 0.26p^2$ meV (p in kbar). The linear pressure coefficient, 11 meV/kbar, is found to be almost the same as $dE_0/dp \sim$ 11.6 meV/kbar for GaAs. This value is also very close to the pressure coefficients of the deep defect levels E3 and E4, which are located within the band gap and generated by electron irradiation in GaAs at room temperature regardless of the crystal growth method and sample doping. On the other hand, the EL2 defect energy level with p can be expressed as $\Delta\text{EL2}(p) = 4.4p - 0.11p^2$ meV. From these facts, they concluded that the amphoteric deep defects E2 and E3 play a major role in the Fermi level stabilization and formation of Schottky barriers in GaAs, but the native defect EL2 does not perceptibly do so [9.41].

The linear pressure coefficients $d\phi_n/dp$ determined for ZnO, *w*-CdS and *w*-CdSe are 11.6, ~10 and 7.0 meV/kbar [9.45], respectively, which are considerably larger than the corresponding dE_0/dp values 2.7, 4.4 and 5.0 meV/kbar.

9.2.4 Breakdown voltage

The breakdown voltage V_{BR} or breakdown field E_{BR} is often used in calculating Johnson [9.46] and Keyes figures of merit [9.47]. These figures of merit are used when

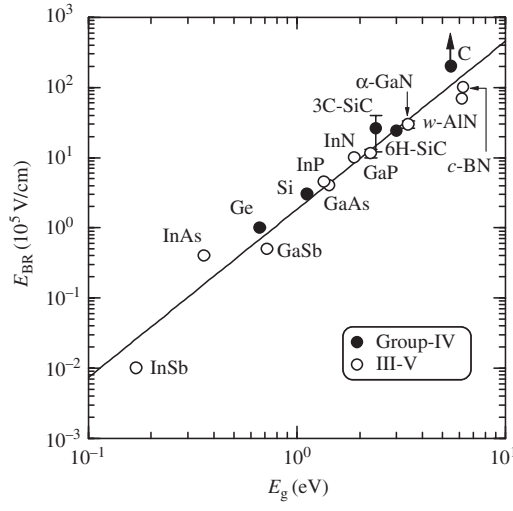

Figure 9.11 Breakdown field E_{BR} versus band-gap energy E_g for some group-IV and III–V semiconductors. The solid line represents the least-squares fit with $E_{BR} = 1.84E_g^{2.40}$ (E_g in eV; E_{BR} in 10^5 V/cm)

Table 9.5 Breakdown field E_{BR} in some group-IV, III–V and II–VI semiconductors

System	Material	E_{BR} (10^5 V/cm)	System	Material	E_{BR} (10^5 V/cm)
IV	Diamond	>200[a]	II–VI	ZnO	35[b]
	Si	3		α-ZnS	44[b]
	Ge	1		β-ZnS	43[b]
	3C-SiC	12–40		ZnSe	20[b]
	6H-SiC	24		ZnTe	13[b]
				c-CdS	16[b]
III–V	c-BN	100		w-CdS	17[b]
	h-BN	100		c-CdSe	6.3[b]
	BP	10[b]		w-CdSe	7.1[b]
	w-AlN	20–117		CdTe	4.9[b]
	c-AlN	99[b]			
	AlP	16[b]			
	AlAs	12[b]			
	AlSb	5.8[b]			
	α-GaN	26–33			
	β-GaN	31[b]			
	GaP	10–13			
	GaAs	4			
	GaSb	0.5			
	InN	10			
	InP	4.5			
	InAs	0.4			
	InSb	0.01			

[a] CVD-diamond
[b] Estimated from a linear relation between E_{BR} and E_g (i.e., $E_{BR} = 1.84{E_g}^{2.40}$)

comparisons are made among semiconductors to be used for electron-transport device applications [9.48].

The breakdown voltage V_{BR} in Schottky barriers and p–n junctions can be given by [9.49]

$$V_{BR} = 60\left(\frac{E_g}{1.1}\right)^{3/2}\left(\frac{N}{10^{16}}\right)^{-3/4} \tag{9.7}$$

where E_g is the band-gap energy in eV, N is the carrier density in cm^{-3} and V_{BR} is in V.

We summarize in Table 9.5 the breakdown field E_{BR} in some group-IV, III–V and II–VI semiconductors. Figure 9.11 also shows the E_{BR} value plotted versus E_g for some group-IV and III–V semiconductors. The solid line in Figure 9.11 represents the least-squares fit with the relation (E_g in eV; E_{BR} in 10^5 V/cm)

$$E_{BR} = 1.84E_g^{2.40} \tag{9.8}$$

Some E_{BR} values listed in Table 9.5 are estimated from Equation (9.8).

REFERENCES

[9.1] F. J. Himpsel, J. A. Knapp, J. A. Van Vechten, and D. E. Eastman, *Phys. Rev. B* **20**, 624 (1979).

[9.2] B. B. Pate, *Surf. Sci.* **165**, 83 (1986).

[9.3] M. C. Benjamin, C. Wang, R. F. Davis, and R. J. Nemanich, *Appl. Phys. Lett.* **64**, 3288 (1994); M. C. Benjamin, M. D. Bremser, T. W. Weeks, Jr., S. W. King, R. F. Davis, and R. J. Nemanich, *Appl. Surf. Sci.* **104/105**, 455 (1996).

[9.4] R. J. Nemanich, in *Properties, Processing and Applications of Gallium Nitride and Related Semiconductors*, EMIS Datareviews Series No. 23, edited by J. H. Edgar, S. Strite, I. Akasaki, H. Amano, and C. Wetzel (INSPEC, London, 1999), p. 98.

[9.5] S. P. Grabowski, M. Scnneider, H. Nienhaus, W. Mönch, R. Dimitrov, O. Ambacher, and M. Stutzmann, *Appl. Phys. Lett.* **78**, 2503 (2001).

[9.6] J. van der Weide, Z. Zhang, P. K. Baumann, M. G. Wensell, J. Bernholc, and R. J. Nemanich, *Phys. Rev. B* **50**, 5803 (1994).

[9.7] J. B. Cui, J. Ristein, and L. Ley, *Phys. Rev. B* **60**, 16135 (1999).

[9.8] K. Jacobi, G. Zwicker, and A. Gutmann, *Surf. Sci.* **141**, 109 (1984).

[9.9] L. Soonckindt, J. Bonnet, P. Masri, and L. Lassabatère, *Surf. Sci.* **130**, L337 (1983).

[9.10] H. P. R. Frederikse, in *CRC Handbook of Chemistry and Physics*, 78th Edition, edited by D. R. Lide (CRC Press, Boca Raton, 1997), p. 12–115.

[9.11] H. B. Michaelson, *IBM J. Res. Develop.* **22**, 72 (1978).

[9.12] A. M. Cowley and S. M. Sze, *J. Appl. Phys.* **36**, 3212 (1965).

[9.13] S. G. Louie, J. R. Chelikowsky, and M. L. Cohen, *Phys. Rev. B* **15**, 2154 (1977).

[9.14] M. Schluter, *Phys. Rev. B* **17**, 5044 (1978).

[9.15] J. van Laar and A. Huijser, *J. Vac. Sci. Technol.* **13**, 769 (1976).

[9.16] W. E. Spicer, I. Lindau, P. E. Gregory, C. M. Garner, P. Pianetta, and P. W. Chye, *J. Vac. Sci. Technol.* **13**, 780 (1976).

[9.17] N. Newman, M. van Schilfgaarde, T. Kendelwicz, M. D. Williams, and W. E. Spicer, *Phys. Rev. B* **33**, 1146 (1986).

[9.18] W. E. Spicer, I. Lindau, P. Skeath, C. Y. Su, and P. Chye, *Phys. Rev. Lett.* **44**, 420 (1980); W. E. Spicer, I. Lindau, P. Skeath, and C. Y. Su, *J. Vac. Sci. Technol.* **17**, 1019 (1980).

[9.19] M. S. Daw and D. L. Smith, *Solid State Commun.* **37**, 205 (1981).

[9.20] A. Y. Cho and P. D. Dernier, *J. Appl. Phys.* **49**, 3328 (1978).

[9.21] W. I. Wang, *J. Vac. Sci. Technol. B* **1**, 574 (1983).

[9.22] S. P. Svensson, G. Landgren, and T. G. Andersson, *J. Appl. Phys.* **54**, 4474 (1983).

[9.23] C. Barret and J. Massies, *J. Vac. Sci. Technol. B* **1**, 819 (1983).

[9.24] M. Missous, E. H. Rhoderick, and K. E. Singer, *J. Appl. Phys.* **60**, 2439 (1986).

[9.25] W. Mönch, *J. Vac. Sci. Technol. B* **17**, 1867 (1999).

[9.26] Y. P. Song, R. L. Van Meirhaeghe, W. H. Laflère, and F. Cardon, *Solid-State Electron.* **29**, 633 (1986).

[9.27] A. Singh, K. C. Reinhardt, and W. A. Anderson, *J. Appl. Phys.* **68**, 3475 (1990).

[9.28] M. Missous and E. H. Rhoderick, *J. Appl. Phys.* **69**, 7142 (1991).

[9.29] S. J. Pilkington, M. Missous, and D. A. Woolf, *J. Appl. Phys.* **74**, 6256 (1993).

[9.30] H.-W. Hübers and H. P. Röser, *J. Appl. Phys.* **84**, 5326 (1998).

[9.31] M. O. Aboelfotoh, *J. Appl. Phys.* **64**, 4046 (1988).

[9.32] S. Zhu, R. L. Van Meirhaeghe, C. Detavernier, F. Cardon, G.-P. Ru, X.-P. Qu, and B.-Z. Li, *Solid-State Electron.* **44**, 663 (2000).

[9.33] S. Zhu, C. Detavernier, R. L. Van Meirhaeghe, F. Cardon, G.-P. Ru, X.-P. Qu, and B.-Z. Li, *Solid-State Electron.* **44**, 1807 (2000).

[9.34] S. Chand and J. Kumar, *Semicond. Sci. Technol.* **10**, 1680 (1995).

[9.35] V. W. L. Chin, J. W. V. Storey, and M. A. Green, *J. Appl. Phys.* **68**, 4127 (1990).

[9.36] J. H. Werner and H. H. Güttler, *J. Appl. Phys.* **69**, 1522 (1991).
[9.37] M. Wittmer, *Phys. Rev. B* **43**, 4385 (1991).
[9.38] P. G. McCafferty, A. Sellai, P. Dawson, and H. Elabd, *Solid-State Electron.* **39**, 583 (1996).
[9.39] S. Zhu, R. L. Van Meirhaeghe, C. Detavernier, G.-P. Ru, B.-Z. Li, and F. Cardon, *Solid State Commun.* **112**, 611 (1999).
[9.40] J. H. Werner and H. H. Güttler, *J. Appl. Phys.* **73**, 1315 (1993).
[9.41] W. Shan, M. F. Li, P. Y. Yu, W. L. Hansen, and W. Walukiewicz, *Appl. Phys. Lett.* **53**, 974 (1988).
[9.42] P. Phatak, N. Newman, P. Dreszer, and E. R. Weber, *Phys. Rev. B* **51**, 18003 (1995).
[9.43] G. Çankaya, N. Uçar, E. Ayyildiz, H. Efeoğlu, A. Türüt, S. Tüzemen, and Y. K. Yoğurtçu, *Phys. Rev. B* **60**, 15944 (1999).
[9.44] C. S. Gworek, P. Phatak, B. T. Jonker, E. R. Weber, and N. Newman, *Phys. Rev. B* **64**, 45322 (2001).
[9.45] M. J. Peanasky and H. G. Drickamer, *J. Appl. Phys.* **56**, 3471 (1984).
[9.46] E. O. Johnson, *RCA Rev.* **26**, 163 (1965).
[9.47] R. W. Keyes, *Proc. IEEE* **60**, 225 (1972).
[9.48] See, for example, R. F. Davis, *Mater. Sci. Eng. B* **1**, 77 (1988).
[9.49] Yu. A. Goldberg, *Semicond. Sci. Technol.* **14**, R41 (1999).

10 Optical Properties

10.1 Summary of optical dispersion relations 211
10.1.1 Dielectric permittivity 211
10.1.2 Optical dispersion relation 213
10.1.3 Optical sum rule 214
10.1.4 Optical spectra 216
10.2 The reststrahlen region 217
10.2.1 Static and high-frequency dielectric constants 217
10.2.2 Reststrahlen spectra 222
10.2.3 Multiphonon optical absorption spectra 228
10.3 At or near the fundamental absorption edge 230
10.3.1 Free-exciton binding energy and related parameters 230
10.3.2 Refractive index 236
10.3.3 Optical absorption at the fundamental absorption edge 244
10.3.4 Urbach tail 256
10.4 The interband transition region 258
10.4.1 Model dielectric function 258
10.4.2 Fundamental optical spectra 263
10.4.3 External perturbation and doping effects 268
10.5 Free-carrier absorption and related phenomena 270
10.5.1 Free-carrier absorption 270
10.5.2 Interconduction-band and intervalence-band absorption 274
10.5.3 Free-carrier-induced change in refractive index 278
References 278

10.1 SUMMARY OF OPTICAL DISPERSION RELATIONS

10.1.1 Dielectric permittivity

First, we consider the polarization, that is, the electric moment per unit volume or the polarization charge per unit area taken perpendicular to the direction of polarization. The relationship of the ith spatial component of the polarization is expressed in terms of the dielectric field components by a power series of the form

$$P_i = \sum_j \chi_{ij} E_j + \sum_{j,k} \gamma_{ijk} E_j E_k + \cdots \tag{10.1}$$

Properties of Group-IV, III–V and II–VI Semiconductors Sadao Adachi

© 2005 John Wiley & Sons, Ltd

ISBN: 0-470-09032-4

With the advent of lasers, it is now quite common to observe nonlinear optical effects. However, the concern here is only with linear optics, and only linear terms will be retained in expressions such as Equation (10.1). The nonlinear optical properties of semiconductors will be discussed in Section 11.5.

The vectors are now connected by the relation

$$\boldsymbol{D} = \varepsilon_0 \boldsymbol{E} + \boldsymbol{P} \tag{10.2}$$

where $\boldsymbol{D}$ and $\boldsymbol{E}$ are the electric displacement and field strength, respectively, and ε_0 is a scalar constant, the permittivity of a vacuum, with the numerical value 8.854×10^{-12} F/m. In many substances, the polarization is directly proportional to the field strength $\boldsymbol{E}$, and thus we write

$$\boldsymbol{P} = \varepsilon_0 \chi \boldsymbol{E} \tag{10.3}$$

Hence

$$\boldsymbol{D} = \varepsilon_0 (1 + \chi) \boldsymbol{E} \tag{10.4}$$

where χ is known as the dielectric susceptibility.

The dielectric susceptibility χ is a symmetric second-rank tensor. We have then, instead of Equation (10.4)

$$\boldsymbol{D}_i = \sum_j \varepsilon_0 (\delta_{ij} + \chi_{ij}) = \sum_j \varepsilon_0 \varepsilon_{ij} \boldsymbol{E}_j \tag{10.5}$$

where $\varepsilon_{ij} \equiv (\delta_{ij} + \chi_{ij})$ is the relative dielectric constant and δ is the Kronecker delta. The dielectric or optical properties of a crystal may thus be characterized by the magnitudes and directions of the three principal dielectric constants, dielectric permittivities or dielectric susceptibilities. These magnitudes and directions will, in principle, depend on the frequency of the electric field, but they must always, of course, conform to any restrictions imposed by crystal symmetry [10.1]. Table 10.1 summarizes the effect of crystal symmetry on dielectric properties represented by a symmetric second-rank tensor.

Table 10.1 Effect of crystal symmetry on the dielectric and optical properties represented by a second-order tensor

Symmetry class	Material	Tensor form
Cubic	Si, 3C-SiC, GaAs, MgO, ZnSe, etc.	$\begin{bmatrix} \varepsilon_{11} & 0 & 0 \\ 0 & \varepsilon_{11} & 0 \\ 0 & 0 & \varepsilon_{11} \end{bmatrix}$
Hexagonal Rhombohedral	4H-SiC, *h*-BN, α-GaN, *w*-CdS, etc. 15R-SiC	$\begin{bmatrix} \varepsilon_{11} & 0 & 0 \\ 0 & \varepsilon_{11} & 0 \\ 0 & 0 & \varepsilon_{33} \end{bmatrix}$

10.1.2 Optical dispersion relation

A number of useful relations can be derived which link the real and imaginary parts of the dielectric function and optical constants. These so-called optical dispersion relations and sum rules have been extremely valuable in the analyzing and testing optical constant data.

The complex dielectric function

$$\varepsilon(E) = \varepsilon_1(E) + i\varepsilon_2(E) \tag{10.6}$$

can describe the optical properties of the medium at all photon energies, $E = \hbar\omega = h\nu$. From the causality principle and the principle of superposition as applied to a linear medium, the Kramers–Kronig relations linking ε_1 and ε_2 can be derived. These are [10.2]

$$\varepsilon_1(E) = 1 + \frac{2}{\pi}\int_0^\infty \frac{E'\varepsilon_2(E')}{E'^2 - E^2}\mathrm{d}E' \tag{10.7a}$$

$$\varepsilon_2(E) = -\frac{2E}{\pi}\int_0^\infty \frac{\varepsilon_1(E')}{E'^2 - E^2}\mathrm{d}E' \tag{10.7b}$$

The Kramers–Kronig relations are of fundamental importance.

The complex refractive index $n^*(E)$ can now be given by

$$n^*(E) = n(E) + ik(E) = \varepsilon(E)^{1/2} = [\varepsilon_1(E) + i\varepsilon_2(E)]^{1/2} \tag{10.8}$$

where $n(E)$ is the ordinary (real) refractive index and $k(E)$ is the extinction coefficient, also called the attenuation index. The optical constants, $n(E)$ and $k(E)$, are real and positive numbers, and can be determined from optical measurements. From Equation (10.8), it follows that

$$\varepsilon_1 = n^2 - k^2 \tag{10.9a}$$

$$\varepsilon_2 = 2nk \tag{10.9b}$$

and

$$n(E) = \sqrt{\frac{\sqrt{\varepsilon_1(E)^2 + \varepsilon_2(E)^2} + \varepsilon_1(E)}{2}} \tag{10.10a}$$

$$k(E) = \sqrt{\frac{\sqrt{\varepsilon_1(E)^2 + \varepsilon_2(E)^2} - \varepsilon_1(E)}{2}} \tag{10.10b}$$

The Kramers–Kronig relations can also link $n(E)$ and $k(E)$ in the manner

$$n(E) = 1 + \frac{2}{\pi}\int_0^\infty \frac{E'k(E')}{E'^2 - E^2}\mathrm{d}E' \tag{10.11a}$$

$$k(E) = -\frac{2E}{\pi}\int_0^\infty \frac{n(E') - 1}{E'^2 - E^2}\mathrm{d}E' \tag{10.11b}$$

The absorption coefficient $\alpha(E)$ depends not only on $\varepsilon_2(E)$, but also on both parts of the dielectric function through $k(E)$ as

$$\alpha(E) = \frac{4\pi}{\lambda} k(E) \tag{10.12}$$

where λ is the wavelength of light in vacuum.

The normal-incidence reflectivity $R(E)$ can also be given by

$$R(E) = \frac{(n(E) - 1)^2 + k(E)^2}{(n(E) + 1)^2 + k(E)^2} \tag{10.13}$$

10.1.3 Optical sum rule

From the asymptotic behavior of $\varepsilon(\omega)$ at high frequencies

$$\varepsilon(\omega \to \infty) = 1 - \frac{\omega_\mathrm{p}^2}{\omega^2} \tag{10.14}$$

together with the analyticity of $\varepsilon(E)$ and $\varepsilon(E)^{-1}$, one can obtain the following relations [10.3]

$$\int_0^\infty \omega \varepsilon_2(\omega) \mathrm{d}\omega = \frac{1}{2}\pi\omega_\mathrm{p}^2 \tag{10.15}$$

and

$$\int_0^\infty \omega \,\mathrm{Im}\, \varepsilon(\omega)^{-1} \mathrm{d}\omega = -\frac{1}{2}\pi\omega_\mathrm{p}^2 \tag{10.16}$$

where ω_p is the free-electron plasma frequency corresponding to the total electron density of the system.

Equation (10.15) is closely related to the Thomas–Reiche–Kuhn sum rule for an atom in an initial state i

$$\sum_j f_{ij} = Z \tag{10.17}$$

where the number of electrons in the atomic system is Z and the sum over j includes continuum states. Here, a dimensionless quantity f_{ij} is known as the oscillator strength and is defined by

$$f_{ij} = \frac{2m_\mathrm{e}}{\hbar}\omega_{ij}(M_{ij})^2 \tag{10.18}$$

For a condensed rather than isolated atomic system, a sum rule analogous to Equation (10.17) takes the form

$$\int_0^\infty f(\omega) \mathrm{d}\omega = N \tag{10.19}$$

where N is the electron density in the condensed matter.

Philipp and Ehrenreich [10.4] have shown that how these rules can be applied to the valence electrons of a semiconductor such as Si in the absence of d bands. Since the results given by Equation (10.16) for an infinite range of integration would involve a plasma frequency characteristic simply of four electrons per atom each having the free-electron mass, it is simplest to express the results of the integration over a finite range to E_m in terms of n_{eff}, an effective number of free electrons contributing to the optical properties in this range [10.4]

$$n_{eff} = \frac{8\pi m_e \varepsilon_0}{Ne^2h^2} \int_0^{E_m} E\varepsilon_2(E)\mathrm{d}E = 7.66 \times 10^{-1} \frac{A}{g} \int_0^{E_m} E\varepsilon_2(E)\mathrm{d}E \tag{10.20}$$

where A is the atomic weight, g is the crystal density in kg/m^3 and E is in eV.

Similarly, the effective dielectric constant, $\varepsilon_1(0)_{eff}$, produced by interband transitions in this range may be written as

$$\varepsilon_1(0)_{eff} = 1 + \frac{2}{\pi} \int_0^{E_m} \frac{\varepsilon_2(E)}{E}\mathrm{d}E \tag{10.21}$$

where $\varepsilon_1(0)_{eff}$ is an expression for the static or optical dielectric constant. The static dielectric constant results if the infrared lattice absorption is taken into account in the integration, and the optical dielectric constant is obtained otherwise.

We plot in Figure 10.1 the values of n_{eff} and $\varepsilon_1(0)_{eff}$ versus E_m for Si and GaAs. The numerical $\varepsilon_2(E)$ data used in the calculation were taken from [10.5]. It should be noted

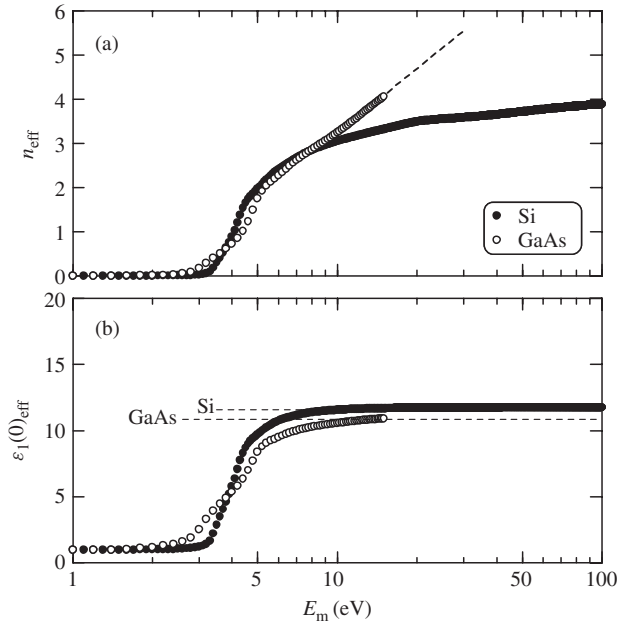

Figure 10.1 (a) n_{eff} versus E_m; (b) $\varepsilon_1(0)_{eff}$ versus E_m for Si and GaAs. The long-wavelength dielectric constants are indicated by the dashed-line segments; $\varepsilon_\infty = \varepsilon_s = 11.6$ for Si and $\varepsilon_\infty = 10.86$ for GaAs

that the n_{eff} curve for Si appears to saturate very nearly at a value of four electrons per atom. By contrast, the curve for GaAs extends appreciably above four. The increase above four is due to the *d*-band excitations (i.e., transitions between the filled *d* bands, lying below the valence band, and empty conduction-band states). The *d* bands are absent in Si, but not in GaAs.

From the tendency toward saturation for $\varepsilon_1(0)_{\text{eff}}$ at photon energies below ~5 eV (Figure 10.1(b)), it is clear that strong interband transitions at critical points below this energy are mainly responsible for the value of the long-wavelength dielectric constant. The curves are also seen to saturate at values corresponding to the independently measured long-wavelength dielectric constants, as indicated by the dashed-line segments.

10.1.4 Optical spectra

It is convenient to classify the optical spectrum of a crystalline semiconductor into several photon energy regions based on their own optical transition mechanisms. Figure 10.2 represents a rough sketch of how the components ε_1 and ε_2 of $\varepsilon(E)$ for a semiconductor (GaAs) vary through the spectral range from 15 meV to a few tens of eV. Three spectral regions are distinguished.

The first region is the so-called reststrahlen region. The reststrahlen region is the region where the radiation field interacts with the fundamental lattice vibrations. Two effects result: (1) absorption or emission of the electromagnetic wave due to the creation or annihilation of lattice vibrations; and (2) scattering of the electromagnetic wave by the lattice vibrational modes. Below the reststrahlen range in optical spectra, the real part of the dielectric constant asymptotically approaches the static or low-frequency dielectric constant ε_s. The optical constant connecting the reststrahlen–near-infrared range is called the high-frequency or optical dielectric constant ε_∞. The strong dispersion properties of GaAs in this region are indicated crudely in Figure 10.2, where the S shape of dispersion

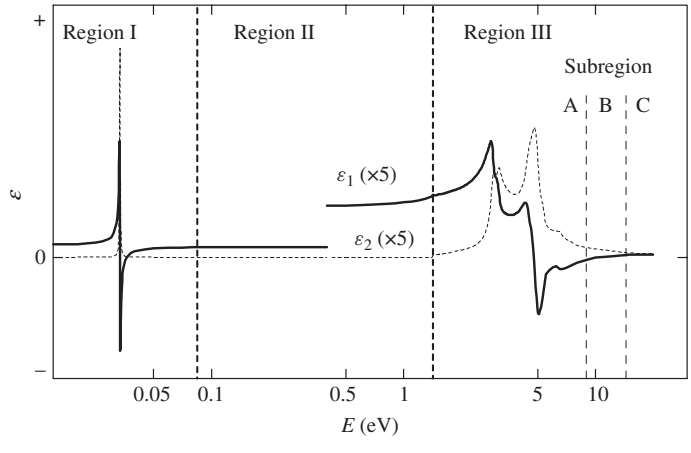

Figure 10.2 Symbolic representation of the real (ε_1) and imaginary parts (ε_2) of the complex dielectric constant for a semiconductor (GaAs), from the 'low-frequency' regime well below the reststrahlen region of the infrared, through to the highly absorbing visible and ultraviolet regions of interband transitions

of ε_1 and the inverted V shape of absorption of ε_2 have been popularly observed. It is noted that in diamond-type semiconductors, such as Si and Ge, the fundamental vibration has no dipole moment and is therefore infrared inactive.

The second region is the region where the material is considered to be primarily transmitting (i.e., near or below the fundamental absorption edge). Appropriately doped samples can show free-carrier, interconduction-band and intervalence-band absorptions in this spectral region. Knowledge of the refractive indices and absorption coefficients in this region is especially important in the design and analysis of various optical and optoelectronic devices.

The third region is the strongly absorbing or opaque region. Various opportunities for direct electron–hole pair creation ensure that dispersion and absorption are strong in this region. According to Philipp and Ehrenreich [10.4], this region can be classified into three subregions. The first subregion A is characterized by sharp structures associated with valence-to-conduction band transitions at the critical points. The second subregion B is marked by a rapid decrease in the reflectance which is reminiscent of the behavior of certain metals in the ultraviolet region [10.6]. The function $-\mathrm{Im}\varepsilon^{-1}$ describing the energy loss of fast electrons traversing the material shows sharp peak in this subregion. Sharp maxima in $-\mathrm{Im}\varepsilon^{-1}$ have been frequently associated with the existence of plasma oscillations [10.7]. In the third subregion C, the reflectance again rises, indicating the onset of additional optical absorption. As mentioned before, this absorption is associated with transitions between the filled d bands and empty conduction states. Because of the absence of the d bands in Si, we cannot recognize subregion C in this material [10.4].

10.2 THE RESTSTRAHLEN REGION

10.2.1 Static and high-frequency dielectric constants

(a) Room-temperature value

Below the reststrahlen range in optical spectra, the real part of the dielectric constant asymptotically approaches the static or low-frequency dielectric constant ε_s. The optical constant connecting the reststrahlen–near-infrared range is called the high-frequency or optical dielectric constant ε_∞. The high-frequency dielectric constant is, thus, measured for frequencies well above the long-wavelength longitudinal optical (LO) phonon frequency, but below the fundamental absorption edge. The concept of the dielectric behavior of solids is an old topic that is very important both from technological and scientific points of view.

The dielectric constant ε_s can, in principle, be written as

$$\varepsilon_s = \varepsilon_\infty + \frac{4\pi N e_T^{*2}}{\omega_{TO}^2 M} \tag{10.22}$$

where M is the reduced mass of the solid, N is the number of unit cells per unit volume, e_T^* is the transverse dynamic effective charge and ω_{TO} is the long-wavelength transverse optical (TO) phonon frequency. The second term in Equation (10.22) is the lattice contribution which arises because the LO mode in heteropolar semiconductors produces a

macroscopic electric moment separating it in energy from the TO mode. The dielectric constants ε_s and ε_∞ are related to the long-wavelength TO and LO phonon frequencies ω_{TO} and ω_{LO} by the Lyddane–Sachs–Teller relationship

$$\frac{\varepsilon_s}{\varepsilon_\infty} = \left(\frac{\omega_{LO}}{\omega_{TO}}\right)^2 \tag{10.23}$$

We summarize in Table 10.2 the static and high-frequency dielectric constants, ε_s and ε_∞, for some cubic semiconductors at $T = 300$ K. Table 10.3 also lists those for hexagonal and rhombohedral semiconductors.

Table 10.2 Static and high-frequency dielectric constants, ε_s and ε_∞, for some cubic group-IV, III–V and II–VI semiconductors at 300 K and their temperature and pressure derivatives

System	Material	ε_s	ε_∞	$d\varepsilon_s/dT$ (10^{-3} K^{-1})	$d\varepsilon_\infty/dT$ (10^{-3} K^{-1})	$d\varepsilon_s/dp$ (10^{-2} GPa^{-1})	$d\varepsilon_\infty/dp$ (10^{-2} GPa^{-1})
IV	Diamond	5.70000	—	0.0461	—	−0.41	—
	Si	11.6	—	0.93	—	−3.4	—
	Ge	16.00	—	2.2	—	−36	—
	α-Sn	23	—				
	3C-SiC	9.69	6.48			−2.02[a]	−1.45[a]
III–V	c-BN	6.80	4.46			−0.87[a]	−0.48[a]
	BP	11	10.2				
	c-AlN	8.16[a]	4.20			−6.51[a]	0.14[a]
	AlP	9.6	7.4				
	AlAs	10.06	8.16				
	AlSb	11.21	9.88				
	β-GaN	9.40[a]	5.35[a]			−6.9[a]	0.26[a]
	GaP	11.0	8.8	1.27	0.67	−5.5	−12.0
	GaAs	12.90	10.86	1.58	0.98	−23	−9
	GaSb	15.5	14.2				
	InP	12.9	9.9	2.66			
	InAs	14.3	11.6				
	InSb	17.2	15.3				
II–VI	MgO	9.8	3.1	0.98		−17.9	
	β-MgSe	7.8	3.8				
	β-MgTe	7.0	4.5				
	β-ZnS	8.3	5.1	0.91	0.34	−9.0	−1.4
	ZnSe	8.9	5.9	1.50		−13.6	
	ZnTe	9.4	6.9				
	c-CdS	9.8[a]	5.4[a]				
	c-CdSe	9.6[a]	6.2[a]				
	CdTe	10.4	7.1	2.34			
	β-HgS	18.2	11.36				
	HgSe	26	7.5				
	HgTe	21	7				

[a] Calculated or estimated

Table 10.3 Static and high-frequency dielectric constants, ε_s and ε_∞, for some hexagonal and rhombohedral group-IV, III–V and II–VI semiconductors at 300 K

System	Material	$\boldsymbol{E} \perp c$		$\boldsymbol{E} \parallel c$	
		ε_s	ε_∞	ε_s	ε_∞
IV	6H-SiC	9.66	10.09	6.520	6.742
	15R-SiC	9.66	10.09	6.520	6.742
III–V	*h*-BN	7.04	4.95	5.09	4.10
	w-AlN	8.3	4.4	8.9	4.8
	α-GaN	9.6	5.4	10.6	5.4
	InN	13.1[a]	8.4[a]	14.4[a]	8.4[a]
II–VI	ZnO	7.8	3.7	8.75	3.75
	α-ZnS	8.1	5.4	8.1	5.4
	w-CdS	10.2	5.4	9.0	5.3
	w-CdSe	9.29	6.20	10.16	6.30

[a] Estimated

Let us sketch the dielectric constants of a specific family of $A^N B^{8-N}$ semiconductors from a simplified point of view. Figures 10.3(a) and 10.3(b) plot the dielectric constants, ε_s and ε_∞, as a function of the lowest direct band-gap energy E_0 for some cubic III–V and II–VI semiconductors. It is seen that both ε_s and ε_∞ decrease with increasing E_0. The solid lines in Figure 10.3 represent the least-squares fit with (a) $\varepsilon_s = 18.52 - 3.08E_0$ and (b) $\varepsilon_\infty = 11.26 - 1.42E_0$, respectively.

Note that $\varepsilon_\infty^{1/2}$ corresponds to the long-wavelength refractive index of the material. We can, therefore, conclude that the smaller E_0-gap material has a larger value of the refractive index. If the refractive index in the active region of an injection laser is larger than the index of the cladding layer on both sides, the effect is like that of a waveguiding configuration, which confines radiation to the active region. This simple rule is known to be very useful for the design of various optical waveguiding devices.

(b) External perturbation effect

We have summarized in Table 10.2 the temperature and pressure coefficients of the static and high-frequency dielectric constants, ε_s and ε_∞, for some cubic group-IV, III–V and II–VI semiconductors. Most of those data are from Samara [10.8] who studied the temperature and hydrostatic pressure effects of ε_s and ε_∞ for some semiconductors, such as Si, GaP, GaAs, β-ZnS and *w*-CdS.

Figure 10.4 shows, as an example, the temperature dependence of ε_s measured for GaAs by Samara [10.8] using a radiofrequency capacitance technique at $f = 100$ kHz at atmospheric pressure. Below $T \sim 150$ K there was no clear frequency dependence, but relatively strong frequency dependence was observed at higher temperatures. Samara considered that this is associated with dipolar contributions becoming activated at higher temperatures. The dielectric loss tanδ was also found to become frequency independent at 100 kHz up to $T \sim 300$ K.

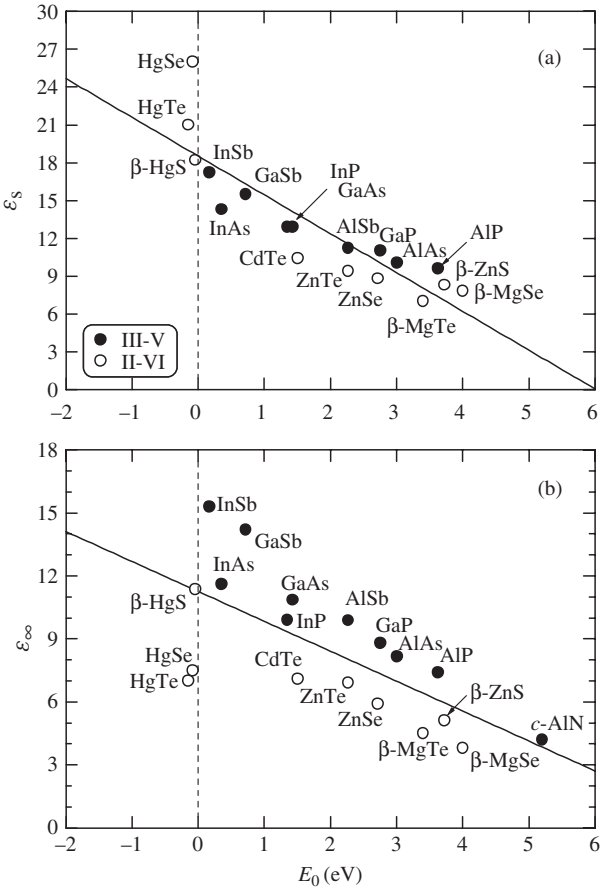

Figure 10.3 (a) Static ε_s; (b) high-frequency dielectric constants ε_∞ versus lowest direct band-gap energy E_0 for some cubic III–V and II–VI semiconductors. The solid lines represent the least-squares fit with (a) $\varepsilon_s = 18.52 - 3.08E_0$ and (b) $\varepsilon_\infty = 11.26 - 1.42E_0$, respectively

As suggested by Samara [10.8], it is not likely that the quantities ε_s and ε_∞ are truly linearly dependent on temperature over any very wide T range. We shall, therefore, fit the temperature dependence of such quantities by

$$\varepsilon_{s,\infty}(T) = \varepsilon_{s,\infty}(0) + \frac{\alpha T^2}{\beta + T} \tag{10.24}$$

where $\varepsilon_{s,\infty}(0)$ is the $T = 0$ K value, α is constant in inverse Kelvin and β is a quantity proportional to the Debye temperature (in Kelvin). Note that this expression is popularly known as the Varshni equation used for explaining the temperature dependence of the band-gap energy [10.9]. The solid line in Figure 10.4 represents the calculated result of Equation (10.24) with $\varepsilon_s(0) = 12.69$, $\alpha = 4.8 \times 10^{-3}$ K^{-1} and $\beta = 550$ K.

We reproduce in Figures 10.5(a) and 10.5(b) the pressure effect on ε_s and ε_∞ for GaAs as measured by Samara [10.8] and Goñi *et al.* [10.10], respectively. It is understood that

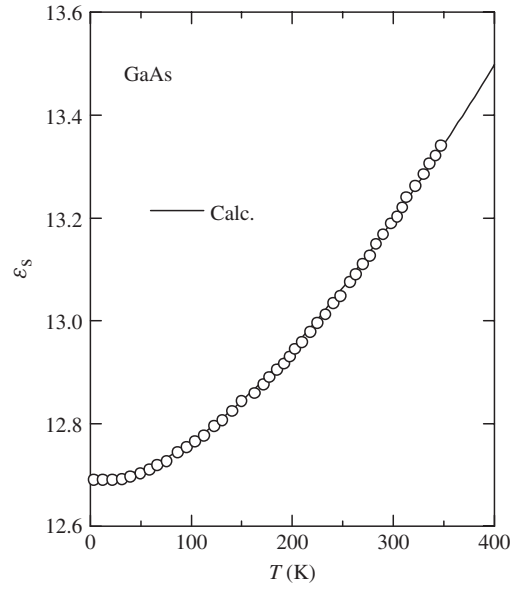

Figure 10.4 Temperature dependence of the static dielectric constant ε_s for GaAs at $f = 100$ kHz and atmospheric pressure. The experimental data are taken from Samara [10.8]. The solid line represents the calculated result of $\varepsilon_s(T) = \varepsilon_s(0) - [\alpha T^2/(\beta + T)]$ with $\varepsilon_s(0) = 12.69$, $\alpha = 4.8 \times 10^{-3}$ K^{-1} and $\beta = 550$ K. [From S. Adachi, *Handbook on Physical Properties of Semiconductors Volume 2: III–V Compound Semiconductors* (Kluwer Academic, Boston, 2004), reproduced by permission from Kluwer Academic Publishers]

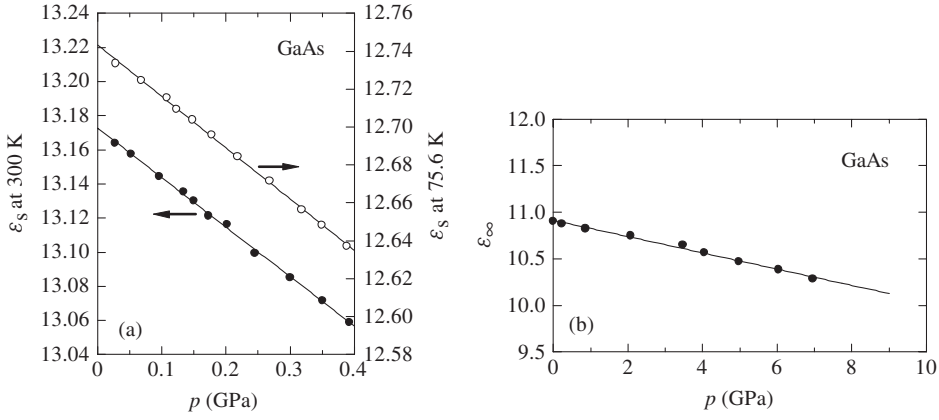

Figure 10.5 (a) Hydrostatic pressure dependence of the static dielectric constant ε_s for GaAs at $T = 300$ and 75.6 K. [From G. A. Samara, *Phys. Rev. B* **27**, 3494 (1983), reproduced by permission from the American Physical Society]; (b) hydrostatic pressure dependence of the high-frequency dielectric constant ε_∞ for GaAs at room temperature. [From A. R. Goñi, K. Syassen, K. Strössner, and M. Cardona, *Semicond. Sci. Technol.* **4**, 246 (1989), reproduced by permission from Institute of Physics Publishing]

both ε_s and ε_∞ decrease almost linearly with increasing pressure p. Samara reported logarithmic pressure derivatives for GaAs to be $d(\ln \varepsilon_s)/dp = -16.7 \pm 0.3$ ($T = 75.6$ K), $d(\ln \varepsilon_s)/dp = -17.3 \pm 0.3$ ($T = 300$ K) and $d(\ln \varepsilon_\infty)/dp = -14.0$ ($T = 300$ K) (all in units of 10^{-3} GPa^{-1}).

It has been found experimentally [10.11] that the pressure coefficient of the dielectric constant ε_s (ε_∞) for Ge can be expressed as

$$\varepsilon_{s,\infty}(p) = \varepsilon_{s,\infty}(0) + ap + bp^2 \tag{10.25}$$

with $\varepsilon_s(0) = 15.94$, $a = -0.36$ GPa^{-1} and $b = 0.014$ GPa^{-2}. Theoretically, Theodorou and Tsegas [10.12] reported the values of $\varepsilon_s(0) = 10.57$, $a = -0.058$ GPa^{-1} and $b = 0$ GPa^{-2} for Si, $\varepsilon_s(0) = 13.92$, $a = -0.26$ GPa^{-1} and $b = 0.006$ GPa^{-2} for Ge, $\varepsilon_\infty(0) = 11.47$, $a = -0.093$ GPa^{-1} and $b = 0.003$ GPa^{-2} for GaAs and $\varepsilon_\infty(0) = 10.52$, $a = -0.13$ GPa^{-1} and $b = 0.003$ GPa^{-2} for InP. Note that $\varepsilon_s = \varepsilon_\infty$ for Si and Ge.

Wagner and Bechstedt [10.13] calculated ε_s and ε_∞ values as a function of pressure p for α-GaN, β-GaN, w-AlN and c-AlN. Their data show significant nonlinear behavior, even for not too large pressures. According to Harrison's bond-orbital model, the volume dependence of ε_∞ may be described by [10.13]

$$\varepsilon_\infty(V) = 1 + (\varepsilon_\infty(V_0) - 1)\frac{\left(\frac{V_0}{V}\right)^{5/3}}{\left\{1 + C\left[\left(\frac{V_0}{V}\right)^{4/3} - 1\right]\right\}^{3/2}} \tag{10.26}$$

with constant C given by

$$C = \frac{1}{2}\left[\frac{B_u}{\varepsilon_\infty(V_0) - 1}\left(-\frac{\partial \varepsilon_\infty}{\partial p}\right)_{p=0} + \frac{5}{3}\right] \tag{10.27}$$

where B_u is the bulk modulus. The values of C are found to be 1.29 ($\perp c$, α-GaN), 1.30 ($\| c$, α-GaN), 1.39 (β-GaN), 1.08 ($\perp c$, w-AlN), 1.05 ($\| c$, w-AlN) and 1.07 (c-AlN).

10.2.2 Reststrahlen spectra

(a) Zinc-blende-type and rocksalt-type semiconductors

It should be noted that in homopolar semiconductors such as diamond, Si and Ge, the fundamental vibration has no dipole moment and is infrared inactive. In heteropolar crystals, as in GaAs, the first-order dipole moment gives rise to a very strong absorption band associated with optical modes having an of essentially zero $\boldsymbol{k}$ vector (i.e., long-wavelength optical phonons).

The complex dielectric permittivity $\varepsilon(\omega)$ in the long-wavelength limit can be generally explained by a single harmonic oscillator model

$$\varepsilon(\omega) = \varepsilon_\infty\left(1 + \frac{\omega_{LO}^2 - \omega_{TO}^2}{\omega_{TO}^2 - \omega^2 - i\omega\gamma}\right) \tag{10.28}$$

where γ is the phonon damping constant. This expression can be modified using the Lyddane–Sachs–Teller relationship of Equation (10.23) as

$$\varepsilon(\omega) = \varepsilon_\infty + \frac{\omega_{\mathrm{TO}}^2(\varepsilon_\mathrm{s} - \varepsilon_\infty)}{\omega_{\mathrm{TO}}^2 - \omega^2 - i\omega\gamma} \tag{10.29}$$

The so-called reststrahlen parameters, such as ε_s, ε_∞, ω_{TO}, ω_{LO} and γ, can be determined from measurements of absorption, refractive index dispersion and reflection at normal and oblique incidence.

We show in Figure 10.6(a) the spectral variation of $\varepsilon(\omega) = \varepsilon_1(\omega) + i\varepsilon_2(\omega)$ for InP obtained from numerical modeling of (Equation (10.29)) using the reststrahlen parameters reported by Bairamov *et al.* [10.14] at room temperature ($\varepsilon_\mathrm{s} = 12.50$, $\varepsilon_\infty = 9.71$, $\omega_{\mathrm{TO}} = 303.7$ cm^{-1}, $\omega_{\mathrm{LO}} = 344.5$ cm^{-1} and $\gamma = 1.9$ cm^{-1}).

The imaginary part of Equation (10.28) can be modified as

$$\varepsilon_2(\omega) = \frac{S\omega_{\mathrm{TO}}^2\omega\gamma}{(\omega_{\mathrm{TO}}^2 - \omega^2)^2 + \omega^2\gamma^2} \tag{10.30}$$

with

$$S \equiv \frac{\varepsilon_\infty(\omega_{\mathrm{LO}}^2 - \omega_{\mathrm{TO}}^2)}{\omega_{\mathrm{TO}}^2} \tag{10.31}$$

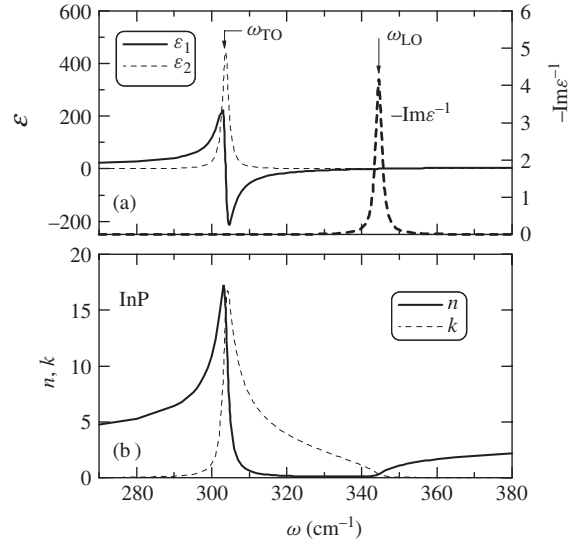

Figure 10.6 (a) Spectral variation of $\varepsilon_1(\omega)$ and $\varepsilon_2(\omega)$ for InP obtained from numerical modeling of Equation (10.28) (Equation (10.29)) with the room-temperature reststrahlen parameters ($\varepsilon_\mathrm{s} = 12.50$, $\varepsilon_\infty = 9.71$, $\omega_{\mathrm{TO}} = 303.7$ cm^{-1}, $\omega_{\mathrm{LO}} = 344.5$ cm^{-1} and $\gamma = 1.9$ cm^{-1}). The corresponding $-\mathrm{Im}\varepsilon(\omega)^{-1}$ spectrum is shown by the dashed line; (b) spectral variation of $n(\omega)$ and $k(\omega)$ for InP as obtained from Equations (10.10a) and (10.10b), respectively

Since the phonon frequency ω_{TO} is usually much larger than γ, $\varepsilon_2(\omega)$ has a significant value only when ω is close to ω_{TO}. For such values of ω, it is a good approximation to replace ω by ω_{TO} everywhere in Equation (10.30), except in the factor $\omega_{TO} - \omega$, which gives

$$\varepsilon_2(\omega) = \frac{S\omega_{TO}\gamma/4}{(\omega_{TO} - \omega)^2 + (\gamma/2)^2} \quad (\gamma \ll \omega_{TO}) \tag{10.32}$$

The $\varepsilon_2(\omega)$ then reaches a maximum value $S\omega_{TO}/\gamma$ for frequency $\omega = \omega_{TO}$ (resonance frequency) and drops to half that peak value for frequencies $\omega = \omega_{TO} \pm \gamma/2$. Equation (10.32) is known as the Lorentzian line shape. The frequency region just above ω_{TO} is one in which ε_1 is driven strongly negative, as shown in Figure 10.6(a). Note that in homopolar semiconductors (Si, Ge, etc.), $\omega_{TO} = \omega_{LO}$ then $S = 0$ ($\varepsilon_s = \varepsilon_\infty$).

From Equation (10.29), we obtain the relation

$$-\mathrm{Im}\varepsilon(\omega)^{-1} = \frac{\varepsilon_2(\omega)}{\varepsilon_1(\omega)^2 + \varepsilon_2(\omega)^2} = \frac{(\varepsilon_\infty^{-1} - \varepsilon_s^{-1})\omega_{LO}^2\omega\gamma}{(\omega_{LO}^2 - \omega^2)^2 + \omega^2\gamma^2} \tag{10.33}$$

which becomes for $\omega \sim \omega_{LO}$

$$-\mathrm{Im}\varepsilon(\omega)^{-1} = \frac{(\varepsilon_\infty^{-1} - \varepsilon_s^{-1})\omega_{LO}\gamma}{4(\omega_{LO} - \omega)^2 + \gamma^2} \tag{10.34}$$

Hence, the maximum in $-\mathrm{Im}\varepsilon(\omega)^{-1}$ determines the phonon frequency ω_{LO}, as demonstrated in Figure 10.6(a).

The $n(\omega)$ and $k(\omega)$ curves obtained from Equations (10.10a) and (10.10b) for InP are shown in Figure 10.6(b). The absorption coefficient $\alpha(\omega)$ and normal-incidence reflectivity $R(\omega)$ as calculated from Equations (10.12) and (10.13) are also shown in Figures 10.7(a) and 10.7(b), respectively. Both n and k dispersion curves show a strong peak at the resonance frequency $\omega = \omega_{TO}$. The reflectivity R at ω close to ω_{LO} is nearly zero and $R \sim 1$ at $\omega_{TO} \leqslant \omega \leqslant \omega_{LO}$, as shown in Figure 10.7(b).

The optical properties at the reststrahlen region of semi-insulating crystals can be adequately interpreted by the above-mentioned single harmonic oscillator model. If free carriers (electrons) are present in the medium, we must take into account plasma contribution to the dielectric permittivity. When the frequency of free-carrier plasma excitations (plasmons) is close to the frequency of the LO phonons ω_{LO}, the two excitations interact via their macroscopic electric fields. The dielectric permittivity $\varepsilon(\omega)$ in such case is given by (cf. Equation (10.28))

$$\varepsilon(\omega) = \varepsilon_\infty \left(1 + \frac{\omega_{LO}^2 - \omega_{TO}^2}{\omega_{TO}^2 - \omega^2 - i\omega\gamma} - \frac{\omega_p^2}{\omega(\omega + i\Gamma)}\right) \tag{10.35}$$

where

$$\omega_p = \sqrt{\frac{ne^2}{m_e\varepsilon_\infty\varepsilon_0}} \tag{10.36}$$

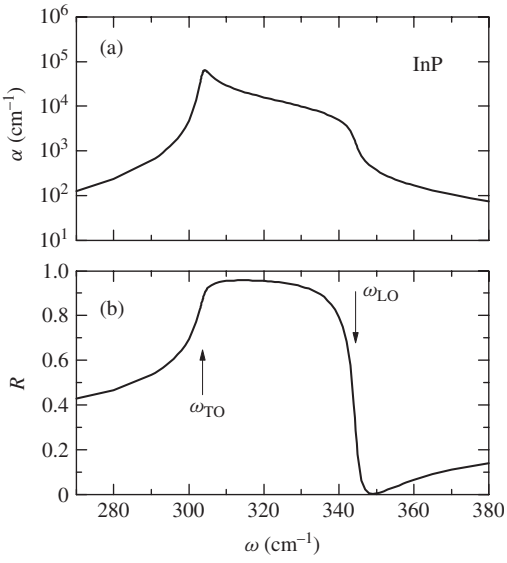

Figure 10.7 Numerically calculated spectral dependence of: (a) $\alpha(\omega)$; (b) $R(\omega)$ for InP using the same set of reststrahlen parameters as in Figure 10.6

is the plasma frequency, Γ is the plasmon damping constant and n and m_e are, respectively, the free-electron concentration and its effective mass ('optical mass'). The frequencies of the coupled plasmon–LO phonon modes are deduced in the limit of zero damping as the roots of the equation $\varepsilon(\omega) = 0$ and are written as

$$\omega_{\pm} = \frac{\omega_{LO}^2 + \omega_p^2}{2} \pm \sqrt{\left(\frac{\omega_{LO}^2 + \omega_p^2}{2}\right)^2 - \omega_p^2 \omega_{TO}^2} \tag{10.37}$$

As the damping values increase, however, this equation is no longer valid. The two sharp dips in the reflectivity minima get smeared out and the coupled-mode frequencies become complex.

In the case of multivalley semiconductors, we must take into account the effects of multivalley nature of the conduction-band structure. A three-valley model is used to account for the Γ, L and X valleys in the conduction band of such semiconductors. Considering the Γ minimum as the energy reference, the electron concentration in the Γ valley and those in the L (X) valley relative to the Γ valley are given by [10.15]

$$n_\Gamma = 2\left(\frac{2\pi m_e^\Gamma kT}{h^2}\right)^{3/2} \exp\left(-\frac{E_F}{kT}\right) \tag{10.38}$$

$$\frac{n_{L(X)}}{n_\Gamma} = \left(\frac{m_e^{L(X)}}{m_e^\Gamma}\right)^{3/2} \exp\left(-\frac{\Delta E_{\Gamma L(X)}}{kT}\right) \tag{10.39}$$

where E_F is the Fermi energy and $\Delta E_{\Gamma L}$ ($\Delta E_{\Gamma X}$) is the energy difference between the L-conduction (X-conduction) and Γ-conduction minima. The total free-electron density

can be given by $n = n_\Gamma + n_L + n_X$. Then, the plasmon term in Equation (10.35) can be modified as follows

$$\frac{\omega_p^2}{\omega(\omega + i\Gamma)} \rightarrow \frac{\omega_{p\Gamma}^2}{\omega(\omega + i\Gamma_\Gamma)} + \frac{\omega_{pL}^2}{\omega(\omega + i\Gamma_L)} + \frac{\omega_{pX}^2}{\omega(\omega + i\Gamma_X)} \tag{10.40}$$

with

$$\omega_{p\Gamma} = \sqrt{\frac{n_\Gamma e^2}{m_e^\Gamma \varepsilon_\infty \varepsilon_0}}, \quad \omega_{pL} = \sqrt{\frac{n_L e^2}{m_e^L \varepsilon_\infty \varepsilon_0}}, \quad \omega_{pX} = \sqrt{\frac{n_X e^2}{m_e^X \varepsilon_\infty \varepsilon_0}} \tag{10.41}$$

where m_e^Γ, m_e^L and m_e^X are the effective masses at the Γ-conduction, L-conduction and X-conduction bands, respectively.

In the case of p-type semiconductors, we must consider the contributions from the heavy-hole and light-hole subbands with the hole effective masses m_{HH}^* and m_{LH}^* and densities p_{HH} and p_{LH}, respectively. It should be noted, however, that the sum of these contributions has the form similar to Equation (10.40).

Equation (10.35) has been used as the basis for sorting out plasmon–LO phonon effects in a number of investigations [10.16–10.20]. Kukharskii [10.21], however, showed that this expression oversimplifies the coupling of plasmons and phonons and can lead, principally, to errors in deducing the damping constants γ and Γ. In Kukharskii's model (factorized form), $\varepsilon(\omega)$ is given by

$$\varepsilon(\omega) = \varepsilon_\infty \frac{(\omega^2 + i\omega\Gamma_- - \omega_-^2)(\omega^2 + i\omega\Gamma_+ - \omega_+^2)}{\omega(\omega + i\Gamma)(\omega^2 + i\omega\gamma - \omega_{TO}^2)} \tag{10.42}$$

In his model, two additional parameters are the damping constants $\Gamma_\pm$ of the coupled plasmon–phonon modes. The plasmon and single-oscillator models are related to each other through the equation

$$\omega_+ \omega_- = \omega_p \omega_{TO} \tag{10.43}$$

Note that in contrast to most other III–V semiconductors which have an appreciable ionic character, BP is very much covalent, as may be seen from its smaller Phillips ionicity $f_i = 0.032$ (Section 1.1). Wang *et al.* [10.22] tried to measure the reststrahlen spectrum of BP and contributed their failure to the almost completely covalent character of the material.

(b) Hexagonal semiconductor

At normal temperature and pressure GaN crystallizes in the wurtzite lattice with two molecular units in the primitive cell, which gives rise to twelve phonon branches ($N = 4$). At the center of the Brillouin zone (Γ), the acoustic modes comprise the representations

$$1A_1 + 1E_1 \tag{10.44}$$

and the remaining nine optical modes the representations

$$1A_1 + 2B_1 + 1E_1 + 2E_2 \tag{10.45}$$

Except the silent B_1 modes all the other optical modes are Raman active, and the A_1 and E_1 modes are IR active for incident radiation with the polarizations $\boldsymbol{E} \parallel c$ and $\boldsymbol{E} \perp c$, respectively, c being the hexagonal axis of the crystal.

In the uniaxial media, two different solutions of the wave equation exist, which describe the ordinary ($\boldsymbol{E} \perp c$) and extraordinary ($\boldsymbol{E} \parallel c$) rays [10.23]. Figure 10.8 shows the spectral variations of $\varepsilon_1(\omega)$ and $\varepsilon_2(\omega)$ for α-GaN obtained from numerical modeling of Equation (10.28) (Equation (10.29)). The parameter values used in the calculation are as follows [10.24]: $\varepsilon_s = 9.44$ (10.43), $\varepsilon_\infty = 5.35$ (5.35), $\omega_{TO} = 560\ \text{cm}^{-1}$ ($530\ \text{cm}^{-1}$), $\omega_{LO} = 744\ \text{cm}^{-1}$ ($740\ \text{cm}^{-1}$) and $\gamma = 6\ \text{cm}^{-1}$ ($7\ \text{cm}^{-1}$) for $\boldsymbol{E} \perp c$ ($\boldsymbol{E} \parallel c$). The peaks in the corresponding $-\text{Im}\varepsilon(\omega)^{-1}$ curves occur at $\omega_{LO} = 744\ \text{cm}^{-1}$ for $\boldsymbol{E} \perp c$ and at $740\ \text{cm}^{-1}$ for $\boldsymbol{E} \parallel c$.

The $n(\omega)$ and $k(\omega)$ curves obtained from Equations (10.10a) and (10.10b) for α-GaN are shown in Figure 10.9. The absorption coefficient $\alpha(\omega)$ and normal-incidence reflectivity $R(\omega)$ as calculated from Equations (10.12) and (10.13) are also shown in Figures 10.10(a) and 10.10(b), respectively. The variation of n and k is found to show a strong peak at $\omega = \omega_{TO}$. In the limit $\omega \to 0$ (∞), the refractive index n approaches a value of $\varepsilon_s^{1/2}$ ($\varepsilon_\infty^{1/2}$). It is also seen that $R \sim 0$ at $\omega \sim \omega_{LO}$ and $R \sim 1$ at $\omega_{TO} \leqslant \omega \leqslant \omega_{LO}$.

(c) External perturbation effect

It is noted that the phonon frequency usually decreases with increasing temperature (see Section 4.2). The static and high-frequency dielectric constants are functions of temperature T; they usually increase with increasing T (see Table 10.2). The damping constant

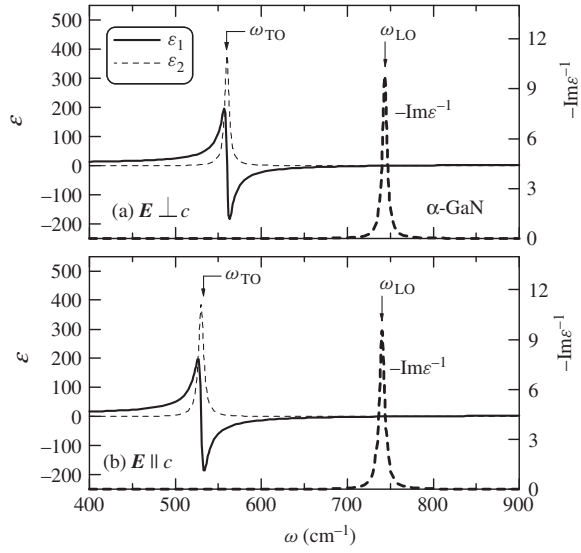

Figure 10.8 Spectral variation of $\varepsilon_1(\omega)$ and $\varepsilon_2(\omega)$ for α-GaN obtained from numerical modeling of Equation (10.28) (Equation (10.29)) with the room-temperature reststrahlen parameters $\varepsilon_s = 9.44$ (10.43), $\varepsilon_\infty = 5.35$ (5.35), $\omega_{TO} = 560\ \text{cm}^{-1}$ ($530\ \text{cm}^{-1}$), $\omega_{LO} = 744\ \text{cm}^{-1}$ ($740\ \text{cm}^{-1}$) and $\gamma = 6\ \text{cm}^{-1}$ ($7\ \text{cm}^{-1}$) for $\boldsymbol{E} \perp c$ ($\boldsymbol{E} \parallel c$). The corresponding $-\text{Im}\varepsilon(\omega)^{-1}$ spectra are shown by the dashed lines

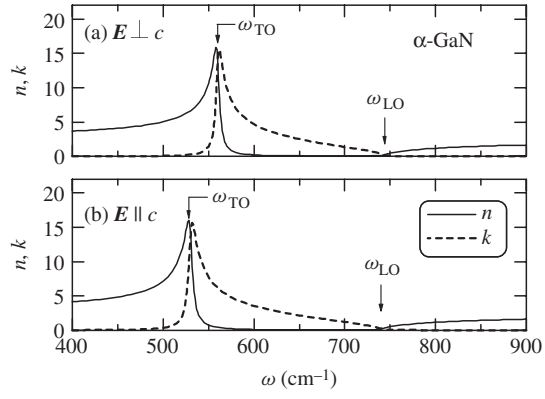

Figure 10.9 Numerically calculated spectral dependence of $n(\omega)$ and $k(\omega)$ for α-GaN for: (a) $\boldsymbol{E} \perp c$; (b) $\boldsymbol{E} \parallel c$ with the same sets of reststrahlen parameters as in Figure 10.8

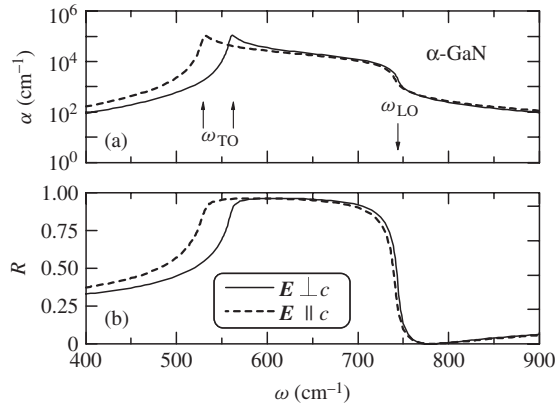

Figure 10.10 Numerically calculated spectral dependence of: (a) $\alpha(\omega)$; (b) $R(\omega)$ for α-GaN using the same sets of reststrahlen parameters as in Figure 10.8

γ may also be strongly dependent on T, and will increase with increasing T. Similarly, the zone-center optical phonon frequency usually increases with increasing hydrostatic pressure p. The static and high-frequency dielectric constants decrease with increasing p (Table 10.2). We can, therefore, easily expect that the optical spectra in the reststrahlen region of semiconductors are dependent both on temperature and hydrostatic pressure.

10.2.3 Multiphonon optical absorption spectra

The lattice absorption bands in semiconductors have been investigated by a number of investigators. In homopolar semiconductors such as diamond, Si and Ge, the fundamental lattice vibration has no dipole moment and is, therefore, infrared inactive. Consequently, the lattice absorption bands observed in such semiconductors are probably due to the multiple-phonon processes, not due to the one-phonon process.

For Si, the multiphonon processes occur predominantly in the spectral range between 500 and 1500 cm^{-1}. We show in Figure 10.11, as an example, the absorption coefficient plotted against wavenumber for Si measured at four different temperatures $T = 5, 77, 300$ and 412 K [10.25]. The most intense peak seen in Figure 10.11 is identified to as a summation band of TO and LO phonons (610 cm^{-1}) and the second one to as a combination of LO and TA (transverse acoustic) phonons (570 cm^{-1}) or that of LO and LA (longitudinal acoustic) phonons (740 cm^{-1}) [10.25]. More recently, these multiphonon bands have been identified to as TO(L) + TA(X) (610 cm^{-1}), TO(X) + TA(L) (566 cm^{-1}) and 2TA(X) + TO(X) (740 cm^{-1}), respectively [10.26]. The 1040–1200 cm^{-1} spectral region is largely obscured by the residual impurity (oxygen) band, but in the cases of the 5 and 77 K curves this band is observed to be fairly narrow. Pradhan *et al.* [10.26] identified the 1160 cm^{-1} peak band as a summation band of 2TO(Γ) + TA(L). Jichang *et al.* [10.27], on the other hand, suggested from Fourier transform infrared measurements that the 1160 cm^{-1} band is due to interstitial oxygen.

The absorption coefficient just at the 610 cm^{-1} peak is ~9 cm^{-1} ($T = 300$ K, Figure 10.11). From this α value, we obtain the following imaginary optical constants:

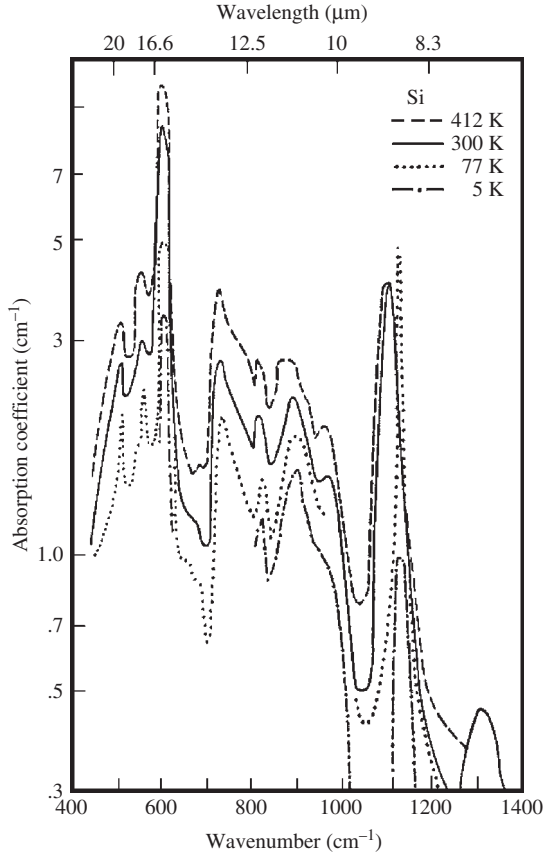

Figure 10.11 Lattice absorption in Si at four different temperatures. [From R. J. Collins and H. Y. Fan, *Phys. Rev.* **93**, 674 (1954), reproduced by permission from the American Physical Society]

$k \sim 1 \times 10^{-3}$ and $\varepsilon_2 \sim 8 \times 10^{-3}$. These values are too small to have a noticeable effect on the real optical constants, ε_1, n and R.

10.3 AT OR NEAR THE FUNDAMENTAL ABSORPTION EDGE

10.3.1 Free-exciton binding energy and related parameters

(a) Exciton states: direct exciton

Because the Coulomb interaction is always present between electrons and holes, excitonic transitions play an important role in the fundamental optical process of semiconductors [10.28–10.30]. The exciton state can be expanded in terms of the Bloch functions for a perfect periodic lattice. The Schrödinger equation for the exciton problem can be written, in terms of the electron and hole coordinates $\boldsymbol{r}_e$ and $\boldsymbol{r}_h$, respectively, as

$$\left[H_e\left(\boldsymbol{p} + \frac{1}{2}\boldsymbol{P} - \boldsymbol{p}_e\right) + H_h\left(-\boldsymbol{p} + \frac{1}{2}\boldsymbol{P} - \boldsymbol{p}_h\right) - \frac{e^2}{\varepsilon_0 \varepsilon_s |\boldsymbol{r}|}\right] \Phi = E\Phi \tag{10.46}$$

where $\boldsymbol{p}$, $\boldsymbol{P}$ are the momenta conjugate to $\boldsymbol{r}$, $\boldsymbol{R}$; $\boldsymbol{p}_e$, $\boldsymbol{p}_h$ are $\hbar$ multiplied by $\boldsymbol{k}_e$, $\boldsymbol{k}_h$; and ε_s is the static dielectric constant. $\boldsymbol{R}$ and $\boldsymbol{r}$ are the center-of-mass coordinate and relative position, respectively, being given by

$$\boldsymbol{R} = \frac{m_e \boldsymbol{r}_e + m_h \boldsymbol{r}_h}{m_e + m_h} \tag{10.47a}$$

$$\boldsymbol{r} = \boldsymbol{r}_e - \boldsymbol{r}_h \tag{10.47b}$$

The eigenvalue E and eigenfunction Φ can be found by solving Equation (10.46). The exciton energy E_{ex} of interest here is written as

$$E_{ex} = E_0 + E \tag{10.48}$$

where $E_0 = E_c(\boldsymbol{k} = 0) - E_v(\boldsymbol{k} = 0)$ is the lowest direct band-gap energy at $\boldsymbol{k} = 0$ (Γ).

The two-particle wave equation (Equation (10.46)) can be expressed as a sum of two separate terms if it is written in a coordinate system of the center-of-mass coordinate $\boldsymbol{R}$ (translational part) and the electron–hole separation part $\boldsymbol{r}$ (rotational part). The translational part is written as

$$-\frac{\hbar^2}{2M}\nabla_R^2 \Phi_R(\boldsymbol{R}) = E_K \Phi_R(\boldsymbol{R}) \tag{10.49}$$

which describes just the motion of a free particle with a mass

$$M = m_e + m_h \tag{10.50}$$

Equation (10.49) gives

$$E_K = \frac{\hbar^2 |\boldsymbol{K}|^2}{2M} \tag{10.51}$$

and

$$\Phi_R(\boldsymbol{R}) = e^{i\boldsymbol{K}\cdot\boldsymbol{R}} \tag{10.52}$$

where $\boldsymbol{K} = \boldsymbol{k}_e + \boldsymbol{k}_h$.

The rotational part, on the other hand, is written as

$$\left[-\frac{\hbar^2}{2\mu}\nabla_r^2 - \frac{e^2}{\varepsilon_0\varepsilon_s|\boldsymbol{r}|}\right]\phi_n(\boldsymbol{r}) = E_n\phi_n(\boldsymbol{r}) \tag{10.53}$$

This equation is similar to that for the hydrogenic problem, but with the electron charge replaced by $e/\sqrt{\varepsilon_s}$ and the free-electron mass m_0 replaced by the exciton reduced mass μ

$$\frac{1}{\mu} = \frac{1}{m_{o,e}} + \frac{1}{m_{o,h}} \tag{10.54}$$

where $m_{o,e}$ and $m_{o,h}$ are the optical electron and hole masses, respectively. The optical masses can now be defined in terms of the longitudinal mass m_l and the transverse mass, m_t, by

$$\frac{1}{m_o} = \frac{1}{3}\left(\frac{1}{m_l} + \frac{2}{m_t}\right) \tag{10.55}$$

For holes at $\boldsymbol{k} = 0$, one has to take the spherically averaged heavy-hole (HH) and light-hole (LH) masses (Section 7.3)

$$\frac{1}{m_{o,h}} = \frac{1}{2}\left(\frac{1}{m_{HH}^s} + \frac{1}{m_{LH}^s}\right) \tag{10.56}$$

The eigenvalue of Equation (10.53) can be given, by analogy with the hydrogenic problem, as

$$E_n = -\frac{G^{3D}}{n^2}, \quad n = 1, 2, 3, \ldots\ldots \tag{10.57}$$

where G^{3D} is the three-dimensional exciton binding (Rydberg) energy given by

$$G^{3D} = \frac{\mu e^4}{2\hbar^2(\varepsilon_0\varepsilon_s)^2} = 13.6\frac{\mu/m_0}{\varepsilon_s^2}\ \text{eV} \tag{10.58}$$

The corresponding exciton Bohr radius a_B^{3D} can be given by

$$a_B^{3D} = \frac{\hbar^2\varepsilon_0\varepsilon_s}{\mu e^2} = 0.53\frac{\varepsilon_s}{\mu/m_0}\ \text{Å} \tag{10.59}$$

In obtaining Equations (10.58) and (10.59), we assumed that the relative dielectric constant is equal to the static dielectric constant ε_s. This is because the exciton binding energy is usually smaller than the lattice vibrational (LO phonon) energy in many semiconductors. If not so, we must use ε_∞ instead of ε_s.

It is evident from Equation (10.53) that $\phi_n(\boldsymbol{r})$ is a hydrogenic wavefunction with substituted for $m_0 \to \mu$ and $\varepsilon_0 \to \varepsilon_0\varepsilon_s$. Since $\phi_n(\boldsymbol{r})$ is a smooth function extending over a

large region of the crystal, it is usually called the 'envelope function.' Because $\phi_n(\boldsymbol{r})$ describes the rotational motion of the exciton, it is characterized by the three quantum numbers n (principal), l (azimuthal) and m (magnetic). However, it is known that only the s-rotational state ($l = 0$) is important for the optically created excitons. It is, therefore, sufficient for our purpose to label the envelope function with only one quantum number n.

For the simple case of two spherical bands of masses m_e and m_h, the envelope function of the nth exciton state $\phi_n(0)$ can be given by

$$|\phi_n(0)|^2 = \frac{1}{n^3}\frac{V_0}{\pi(a_B^{3D})^3} \equiv \frac{1}{n^3}|\phi_1(0)|^2 \tag{10.60}$$

A series of the exciton lines can, then, be predicted at energies

$$E_{ex}^n = E_0 + \frac{\hbar^2 \boldsymbol{K}^2}{2M} - \frac{G^{3D}}{n^2} \tag{10.61}$$

with intensity falling as n^{-3} by Equation (10.60).

As the photon energy E approaches the absorption edge, the infinite number of lines will overlap so that it may be considered as a continuum. In the true continuum where $E - E_0 > 0$, we obtain for the envelope function of the continuum state

$$|\phi_k(0)|^2 = \frac{\pi\alpha_k e^{\pi\alpha_k}}{N\sinh(\pi\alpha_k)} = \frac{2\pi\alpha_k}{N(1 - e^{-2\pi\alpha_k})} \tag{10.62}$$

with

$$\alpha_k = \left|\frac{G^{3D}}{E - E_0}\right|^{1/2} = \left|\frac{G^{3D}}{(\hbar^2\boldsymbol{k}^2/2\mu)}\right|^{1/2} \tag{10.63}$$

The continuum exciton state corresponds to positive energy solutions of the hydrogen-like equation (10.53). The energy of this type of excitons may be written as

$$E_{ex}^k = E_0 + \frac{\hbar^2\boldsymbol{K}^2}{2M} + \frac{\hbar^2\boldsymbol{k}^2}{2\mu} \tag{10.64}$$

In the true continuum, the rotational energy is much larger than the Coulomb interaction energy, and therefore the excitons behave like free particles with an effective mass μ. Consequently, the three-dimensional exciton spectrum consists of a series of discrete parabolic bands below E_0 at $\boldsymbol{K} = 0$, which merges into a continuum at higher energies, as depicted in Figure 10.12.

(b) Exciton states: indirect exciton

Exact calculation of the exciton effect at the indirect band gap is quite complicated, and it is convenient at this stage to make approximations and consider a more specific model. Let us assume that the maximum in the valence band is at $\boldsymbol{k} = \boldsymbol{k}_1$ and is nondegenerate, the minimum in the conduction band at $\boldsymbol{k} = \boldsymbol{k}_2$ and nondegenerate (see Figure 10.20,

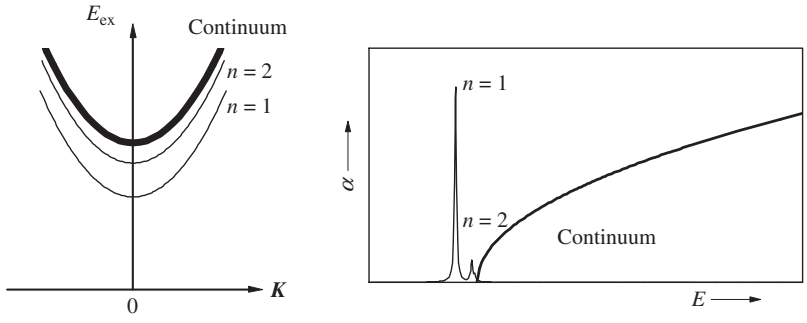

Figure 10.12 Schematic diagram showing the energy and absorption coefficient of Wannier–Mott excitons (discrete and continuum excitons)

below). The envelope function $\phi(0)$ is also assumed to be independent of $\boldsymbol{k}$. The resultant indirect exciton state can be given by

$$E_{ex}^{ID} = E_g^{ID} - G^{ID} \mp \hbar\omega_q \tag{10.65}$$

where E_g^{ID} is the indirect band-gap energy, G^{ID} is the indirect exciton binding energy and $\hbar\omega_q$ is the energy of phonons involved in the indirect optical transitions. It should be noted that the indirect exciton binding energy G^{ID} can be expressed by the same expression as Equation (10.58) and the indirect exciton Bohr radius as Equation (10.59).

(c) Exciton binding energy and related parameters

In Table 10.4, we list the exciton binding energy G (G^{3D}, G^{ID}), 1st-orbital ($n = 1$) Bohr radius a_B and exciton reduced mass μ determined experimentally or theoretically for some group-IV, III–V and II–VI semiconductors. Figures 10.13 and 10.14 also plot G^{3D} and a_B^{3D} versus E_0 (lowest direct band-gap energy) values for these semiconductors. From these plots, we obtain the relations (E_0 in eV; G^{3D} in meV)

$$G^{3D} = 4.36E_0^{1.60} \tag{10.66}$$

and (E_0 in eV; a_B^{3D} in Å)

$$a_B^{3D} = \left(\frac{66.9}{E_0}\right)^{1.18} \tag{10.67}$$

As we have already seen (Chapter 7), a larger band-gap energy E_0 is correlated with a larger effective mass. This promises that G^{3D} increases, but a_B^{3D} decreases, with increasing E_0, as clearly demonstrated in Figures 10.13 and 10.14.

As mentioned in Section 10.2, the values of ε_s in many semiconductors increase with increasing temperature T. The electron and hole effective masses are also expected to decrease with increasing T. We can, therefore, expect that the value of G decreases with increasing T. In fact, the experimental data on GaAs support this consideration [10.31, 10.32].

Table 10.4 Free-exciton parameters (G = binding energy; a_B = 1st-orbital Bohr radius; μ = reduced mass) at the fundamental absorption edge of some group-IV, III–V and II–VI semiconductors. D = direct exciton; ID = indirect exciton

System	Material	G (meV)	a_B (Å)	μ (m_0)	Remark
IV	Diamond	80	16	0.191	ID
	Si	14.7	42	0.145	ID
	Ge	4.15 ($\pm$3/2)	108	0.079	ID
		3.14 ($\pm$1/2)	143	0.059	ID
	3C-SiC	26.7[a]	28[a]	0.184[a]	ID
	6H-SiC	60	12	0.424	ID
III–V	AlAs	18	40	0.134	ID
		13[a]	55[a]	0.097[a]	D
	AlSb	10	64	0.092	ID
		1.44–1.45[a]	$\sim$ 445[a]	0.013[a]	D
	α-GaN	24.0 (A)	31	0.164	D
		22.8 (B)	33	0.156	
		24.5 (C)	31	0.168	
	β-GaN	24	32	0.156	D
	GaP	22	29	0.201	ID
		13	50	0.116	D
	GaAs	3.6	155	0.044	D
	GaSb	1.5	306	0.027	D
	InP	4.8	120	0.055	D
	InAs	1.0	494	0.016	D
	InSb	0.4	1017	0.009	D
II–VI	MgO	145	16	0.102	D
	β-MgSe	57.3	33	0.061	D
	ZnO	61 (A)	32	0.062	D
		56 (B)	35	0.057	
		53 (C)	37	0.054	
	α-ZnS	40 (A, B, C)	27	0.128	D
	β-ZnS	34	33	0.106	D
	ZnSe	18.7	41	0.119	D
	ZnTe	12.8	62	0.078	D
	w-CdS	28 (A)	26	0.197	D
		29 (B)	25	0.204	
		30 (C)	25	0.211	
	w-CdSe	15.7 (A)	48	0.106	D
		16.7 (B)	45	0.112	
	CdTe	10.5	65	0.085	D

[a] Calculated

Goñi *et al.* [10.32] studied the hydrostatic pressure dependence of the E_0-exciton binding energy in GaAs for pressures up to 9 GPa by analyzing the absorption curve in terms of the Elliott model [10.28] of the exciton line. The experimental data showed an essentially linear increase of G^{3D} with respect to hydrostatic pressure. Actually, the simple

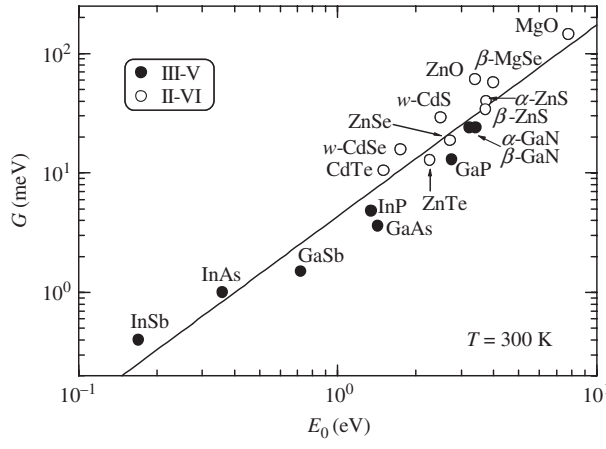

Figure 10.13 Direct-exciton Rydberg (binding) energy G^{3D} versus E_0 for some III–V and II–VI semiconductors. The solid line represents the least-squares fit with $G^{3D} = 4.36E_0^{1.60}$ (E_0 in eV; G^{3D} in meV)

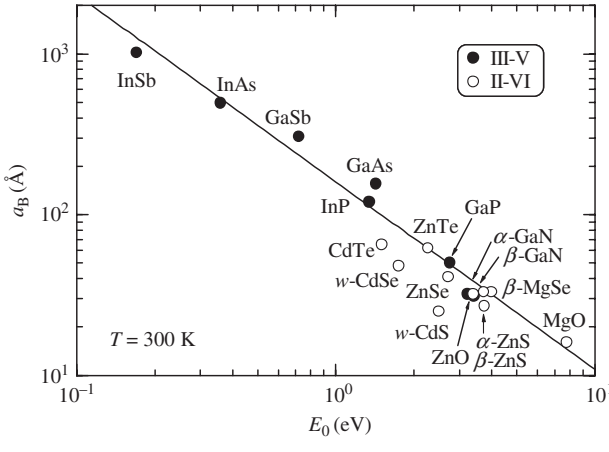

Figure 10.14 Direct-exciton Bohr radius a_B^{3D} versus E_0 for some III–V and II–VI semiconductors. The solid line represents the least-squares fit with $a_B^{3D} = (66.9/E_0)^{1.18}$ (E_0 in eV; a_B^{3D} in Å)

hydrogen model predicts, to a first approximation, a linear pressure dependence of G^{3D} in GaAs [10.32]. The static dielectric constant ε_s of GaAs does not change appreciably with pressure. Thus, the binding energy G^{3D} is proportional to the exciton reduced mass μ. Within the $\boldsymbol{k} \cdot \boldsymbol{p}$ theory, we have $\mu \propto E_0$ and then $G^{3D} \propto E_0$. Because E_0 increases almost linearly with p, we finally obtain the relation $G^{3D} \propto p$. Goñi *et al.* obtained the following linear pressure coefficients for GaAs: $\mathrm{d} \ln G^{3D}/\mathrm{d}p = 0.086 \pm 0.003$ GPa^{-1} at $T = 20$ K; 0.080 ± 0.003 GPa^{-1} at 100 K; and 0.083 ± 0.003 GPa^{-1} at 200 K [10.32]. The pressure coefficient of G^{3D} has also been reported for some II–VI semiconductors, such as ZnO [10.33], β-ZnS [10.34], ZnSe [10.35] and ZnTe [10.36].

(d) Spin-exchange interaction constant

The exciton Hamiltonian at the Γ point can be written as

$$H = H_{\mathrm{c}}^{\mathrm{ZB(W)}} - H_{\mathrm{v}}^{\mathrm{ZB(W)}} - G^{\mathrm{3D}} + H_{\mathrm{exch}} \tag{10.68}$$

where $H_{\mathrm{c}}^{\mathrm{ZB(W)}}$ and $H_{\mathrm{v}}^{\mathrm{ZB(W)}}$ are the effective Hamiltonians for the lowest two conduction bands and the highest six valence bands in the zinc-blende-type (wurtzite-type) semiconductors (see Section 6.2), respectively, G^{3D} is the exciton binding energy and H_{exch} now describes the electron–hole exchange interaction. The last term H_{exch} in Equation (10.68) is given by

$$H_{\mathrm{exch}} = \frac{1}{2} j \sigma_{\mathrm{h}} \sigma_{\mathrm{e}} \tag{10.69}$$

where j is the spin-exchange interaction constant between the hole and electron spins and σ_{h} and σ_{e} are the Pauli spin matrices of the holes and electrons, respectively. Note that the operator σ_{h} operates on valence-hole spin functions, not on valence-electron spin functions.

In Table 10.5, we list the spin-exchange interaction constant j reported for some III–V and II–VI semiconductors. The data are gathered form various sources [10.37–10.40]. We can see that ZnO has the largest j value among these semiconductors. The oscillator strength in ZnO is thus expected to be largely influenced by this effect. Gil [10.40] has examined how the electron–hole exchange interaction influences the strain-induced variation of the oscillator strengths in ZnO films. He has shown that the overall sets of optical properties of ZnO films are in general compatible with the natural valence-band ordering: Γ_9–Γ_7–Γ_7.

10.3.2 Refractive index

(a) Theoretical dispersion model

Knowledge of the refractive index n of semiconductors in the region below or near the fundamental absorption edge is of great importance in optoelectronic device design and performance analysis. In the following, we review several calculation models of

Table 10.5 Spin-exchange interaction constant j for some III–V and II–VI semiconductors

System	Material	j (meV)	System	Material	j (meV)
III–V	α-GaN	0.58	II–VI	ZnO	4.73
	GaP	0.6		β-ZnS	4.0
	GaAs	0.25		ZnSe	1.0
	GaSb	$\leqslant$0.03		ZnTe	0.21
	InP	0.04		w-CdS	2.5
				w-CdSe	0.4
				CdTe	0.045

the refractive index dispersion in semiconductors at the transparent region. Since the imaginary part of the dielectric function ε_2 may be taken as zero in a transparent region, we can successfully assume that

$$n(E) \sim \sqrt{\varepsilon_1(E)} \tag{10.70}$$

1. Sellmeier equation. The refractive-index dispersion can be simply given by the first-order Sellmeier equation [10.41]

$$n(\lambda)^2 = A + B\left(\frac{\lambda^2}{\lambda^2 - C^2}\right) \tag{10.71}$$

where λ is the light wavelength in vacuum. This expression is obtained based on an empirical relation and is valid only over a limited spectral range.

2. Ketteler–Helmholtz formula. Another common expression for the refractive index dispersion is the Ketteler–Helmholtz formula

$$n(E)^2 = A + \frac{BE^2}{1 - \left(\dfrac{E}{C}\right)^2} \tag{10.72}$$

where $E < C$. Not only Equation (10.71) but also Equation (10.72) has the appropriate physical basis to represent n dispersion in the simplest manner throughout the transparent region.

3. Single oscillator model. A semiempirical single effective oscillator model has been proposed by Wemple and DiDomenico [10.42] to analyze the n dispersion in more than 100 widely different solids and liquids. This model requires two parameters, E_p and E_d, where the imaginary part of the dielectric constant ε_2 of the material was assumed to be a delta function at energy E_p and the strength of an effective oscillator at energy E_p was defined to be $\pi E_\mathrm{d}/2$. Introducing these quantities into Equation (10.7a), we obtain

$$n(E)^2 - 1 = \frac{E_\mathrm{p}E_\mathrm{d}}{E_\mathrm{p}^2 - E^2} \tag{10.73}$$

By replacing $B \equiv E_\mathrm{d}/E_\mathrm{p}$ and $C \equiv ch/E_\mathrm{p}$ (c is the velocity of light and h is Planck's constant), we can find that Equations (10.71) and (10.73) agree with each other exactly. The single-oscillator model gives reasonable results for photon energies well below the lowest direct band-gap edge in semiconductors. We note, however, that this photon energy region is not of immediate interest for semiconductor lasers.

4. Modified single oscillator model. Afromowitz [10.43] has proposed an improved model for the variation of ε_2 with photon energy by taking into account the lowest direct band-gap (E_g) contribution

$$\varepsilon_2(E) = \begin{cases} \eta E^4 & E_\mathrm{g} \leqslant E \leqslant E_\mathrm{f} \\ 0 & \text{elsewhere} \end{cases} \tag{10.74}$$

where the new parameters E_f and η can be determined by requiring that the corresponding expression for n^2 agrees with Equation (10.73) for $E \ll E_g$. The resulting expression for n^2 is

$$n(E)^2 - 1 = \frac{E_d}{E_p} + \frac{E_d E^2}{E_p^3} + \frac{\eta E^4}{\pi} \ln\left(\frac{2E_p^2 - E_g^2 - E^2}{E_g^2 - E^2}\right) \tag{10.75}$$

where

$$\eta = \frac{\pi E_d}{2E_p^3(E_p^2 - E_g^2)} \tag{10.76}$$

The parameters E_d, E_p and E_g appearing in Equations (10.75) and (10.76) are known for many binary semiconductors and may be calculated for ternary and quaternary compounds by using an interpolation scheme [10.43].

5. Pikhtin–Yas'kov formula. The Pikhtin–Yas'kov formula [10.44] is nearly the same as a Drude form with the addition of another term representing a broadband electronic contribution to n^2

$$n(E)^2 - 1 = \frac{A}{\pi} \ln\frac{E_1^2 - E^2}{E_0^2 - E^2} + \sum_i \frac{G_i}{E_i^2 - E^2} \tag{10.77}$$

The unique term arises from assuming that $\varepsilon_2(E)$ is constant for $E_0 \leqslant E \leqslant E_1$ and that infinitely narrow resonances occur at E_i due to the lattice absorption bands. The formula in Equation (10.77) is obtained by performing the Kramers–Kronig transformation on this model.

6. Simplified interband transition model. The $E_0/(E_0 + \Delta_0)$-gap transitions contribute strongly to the n dispersion, but not to its values. On the contrary, the higher-lying band-gap contributions (E_1, $E_1 + \Delta_1$, E_2, etc.) do not contribute to the wavelength dispersions in the transparent region, but contribute to their absolute values. The n value in the transparent region can, then, be simply expressed, using Equations (10.99), (10.116) and (10.120) (see Section 10.3.3, below), as [10.45]

$$\begin{aligned} n(E)^2 = A^* &\left[f(\chi_0^*) + \frac{1}{2}\left(\frac{E_0}{E_0 + \Delta_0}\right)^{3/2} f(\chi_{so}^*) \right] \\ &+ \sum_{n=1}^{\infty} \frac{1}{n^3} \frac{F^D}{(E_{ex}^n)^2 - E^2} + \frac{F^C E_{ex}^{C1}}{G^{3D} E^2} \ln\frac{E_0^2}{E_0^2 - E^2} + B^* \end{aligned} \tag{10.78}$$

with

$$f(\chi_0^*) = \chi_0^{*-2}(2 - \sqrt{1 + \chi_0^*} - \sqrt{1 - \chi_0^*}) \tag{10.79a}$$

$$f(\chi_{so}^*) = \chi_{so}^{*-2}(2 - \sqrt{1 + \chi_{so}^*} - \sqrt{1 - \chi_{so}^*}) \tag{10.79b}$$

$$A^* = \frac{4}{3}\left(\frac{3}{2}\mu_0\right)^{3/2} E_0^{-3/2} P^2 \tag{10.80a}$$

$$\chi_0^* = \frac{E}{E_0} \tag{10.80b}$$

$$\chi_{so}^* = \frac{E}{E_0 + \Delta_0} \tag{10.80c}$$

where A^* and F^D (F^C) represent the strength parameters of the $E_0/(E_0 + \Delta_0)$-gap one-electron and excitonic transitions, respectively, and B^* corresponds to the nondispersive contribution arising from the higher-lying band gaps (E_1, $E_1 + \Delta_1$, E_2, etc.). μ_0 and P^2 in Equation (10.80a) are, respectively, the combined density-of-states mass and squared momentum matrix element at the $E_0/(E_0 + \Delta_0)$ edges.

The one-electron term in Equation (10.78) is obtained from a simplified model of the interband transitions proposed by Korovin [10.46] and Cardona [10.47]. The model has been applied to II–VI and III–V semiconductors, and the results exhibit quite good agreement with the published experimental data for some II–VI [10.48] and III–V binaries [10.45], $Al_xGa_{1-x}As$ ternary alloy [10.49] and $In_{1-x}Ga_xAs_yP_{1-y}$ quaternary alloy [10.45]. The model has also been adopted to estimate the n dispersion in $Al_xGa_{1-x}As_ySb_{1-y}$, $Ga_xIn_{1-x}As_ySb_{1-y}$ and $InP_xAs_ySb_{1-x-y}$ quaternary systems lattice-matched to GaSb and InAs [10.50].

Figure 10.15 shows, as an example, the experimental n dispersion for ZnTe fitted to the Sellmeier equation, Equation (10.71). The experimental data are taken from [10.5]. The fitted parameter values are: $A = 4.04$, $B = 3.22$ and $C^2 = 0.149$ μm^2. As we can see, the calculated n values are in good agreement with the experimental data.

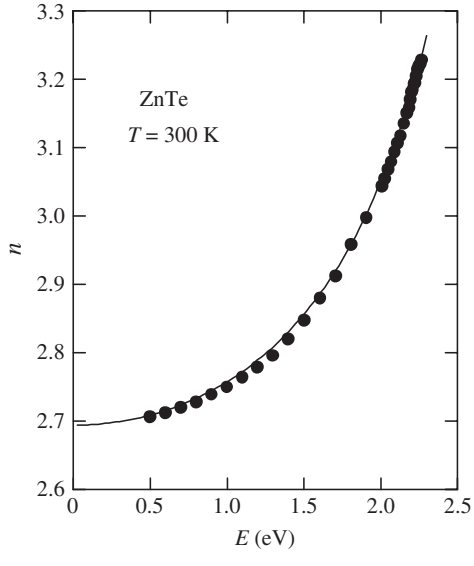

Figure 10.15 Refractive-index dispersion in ZnTe. The experimental data are taken from Adachi [10.5]. The solid line represents the calculated result of the Sellmeier equation, $n(\lambda)^2 = A + B\lambda^2/(\lambda^2 - C^2)$, with $A = 4.04$, $B = 3.22$ and $C^2 = 0.149$ μm^2 (λ in μm). [From S. Adachi, *Handbook on Physical Properties of Semiconductors Volume 3: II–VI Compound Semiconductors* (Kluwer Academic, Boston, 2004), reproduced by permission from Kluwer Academic Publishers]

(b) Long-wavelength n value: empirical formula

A relation between the refractive index and an accurately known physical parameter, if available, would be useful in finding an acceptable n value of the unknown material from this relation. The basic concept that higher band-gap material has a lower dielectric constant ε_1 can be derived from Moss's rule [10.51], which states that energy levels are inversely proportional to the square of the dielectric constant. Then, the band-gap energy E_g (or E_0) and refractive index n ($\sim \varepsilon_1^{1/2}$) satisfy the relation

$$n^4 E_g = \text{const.} \tag{10.81}$$

As shown in Figure 10.16, the plots of $n^4(\lambda \to \infty) = \varepsilon_1^2(\lambda \to \infty) = \varepsilon_\infty^2$ versus E_0 for some group-IV, III–V and II–VI semiconductors support the dependence of Equation (10.81) in a general way.

Double-heterojunction lasers are composed of a lower band-gap active layer sandwiched between higher band-gap cladding layers, and the refractive index of the active layer has to be higher than that of the cladding layer. This is certainly the case for GaAs/$Al_xGa_{1-x}As$ and $In_{1-x}Ga_xAs_yP_{1-y}$/InP lasers. A number of published papers are, therefore, based on the belief that higher band-gap materials necessarily have lower refractive indexes, so that the correct double-heterojunction structure automatically satisfies the requirement for the refractive index.

If the refractive index in the active region of an injection laser is smaller than the index of the cladding layer on both sides, the effect is like that of an antiwaveguide configuration which does not confine radiation to the neighborhood of the active region. This effect implies an optical loss in the waveguide, leading to an increase in the threshold current. Toda [10.52] pointed out the existence of a number of inappropriate double-heterostructures (i.e., antiwaveguiding material systems). Reference [10.50] also deals with inappropriate laser structures of $In_{1-x}Ga_xAs_ySb_{1-y}$/GaSb(InAs) and $InP_xAs_ySb_{1-x-y}$/GaSb(InAs).

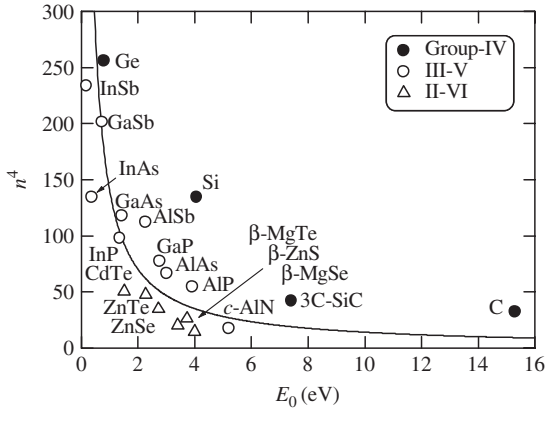

Figure 10.16 Relationship between $n^4(\lambda \to \infty)$ versus E_0 for some group-IV, III–V and II–VI semiconductors at 300 K. The solid line represents the relation of Equation (10.81) with a constant value of 140 eV

(c) External perturbation effect

1. Temperature effect. The refractive index of a material is usually measured relative to air (i.e., n/n_{air} is the measured quantity). In order to determine the temperature variation of n of the material, it is necessary to take into account the temperature variation of the refractive index of the ambient air n_{air}

$$\frac{d}{dT}\left(\frac{n}{n_{air}}\right) = \frac{dn}{dT} - n\frac{dn_{air}}{dT} \tag{10.82}$$

where dn_{air}/dT is about 1×10^{-6} K^{-1}. The second term in Equation (10.82) is, thus, usually masked by the experimental uncertainty.

We now start from a simple one-gap model of ε_1 given by the expression

$$\varepsilon_1(E) = n(E)^2 = 1 + \frac{A}{E_g^2 - E^2} \tag{10.83}$$

where E_g is the average gap in the Penn model [10.53] and A is proportional to $1/V$ (V is the atomic volume, here we shall assume the proportionality constant of this quantity to be unity, namely $A \sim V^{-1}$). By replacing $A \to E_p E_d$ and $E_g \to E_p$, we find that Equation (10.83) agrees exactly with Equation (10.73). Equation (10.83) for $E \to 0$ ($n^2 \sim \varepsilon_\infty$) leads to the following formula for the temperature derivative [10.54]

$$\frac{1}{n}\left(\frac{dn}{dT}\right)_p = \frac{1}{2}\left(1 - \frac{1}{\varepsilon_1}\right)\left[-\beta_{th} - \frac{2\beta_{th}V}{E_g}\left(\frac{\partial E_g}{\partial V}\right)_T - \frac{2}{E_g}\left(\frac{\partial E_g}{\partial T}\right)_V\right] \tag{10.84}$$

where $\beta_{th} = V^{-1}(\partial V/\partial T)_p$ is the volume coefficient of thermal expansion ($\beta_{th} = 3\alpha_{th}$ in cubic crystals, where α_{th} is the linear thermal expansion coefficient). Since $n^{-1}(dn/dT)$ is positive in many semiconductors (see Table 10.6), we can conclude that in Equation (10.84) the $\partial E_g/\partial T$ ($\partial E_g/\partial V$) term dominates the β_{th} term. This is because dE_g/dT ($\partial E_g/\partial V$) is negative while β_{th} or α_{th} is positive ($\varepsilon_1 > 1$) for many semiconductors. It is also recognized that the thermal expansion contribution is relatively small, because α_{th} is usually of the order of 10^{-6} K^{-1}.

In Moss's empirical relationship Equation (10.81), we assume that both a ($\equiv$ const.) and E_g (E_0) are temperature dependent. Then, we obtain

$$\frac{1}{n}\left(\frac{dn}{dT}\right) = \frac{1}{4}\left[\frac{1}{a}\left(\frac{da}{dT}\right) - \frac{1}{E_g}\left(\frac{dE_g}{dT}\right)\right] \tag{10.85}$$

If $da/dT = 0$, then Equation (10.85) follows

$$\frac{1}{n}\left(\frac{dn}{dT}\right) \sim -\frac{1}{4E_g}\left(\frac{dE_g}{dT}\right) \tag{10.86}$$

Data on $n^{-1}(dn/dT)$ are available for many semiconductors, as summarized in Table 10.6. Usually, when T increases, E_g or E_0 decreases, resulting in positive value of $n^{-1}(dn/dT)$. The temperature dependence of n for diamond is positive, but about

Table 10.6 Temperature coefficient of the refractive index, $n^{-1}(\mathrm{d}n/\mathrm{d}T)$, in the long-wavelength limit for some group-IV, III–V and II–VI semiconductors

System	Material	$\frac{1}{n}\frac{\mathrm{d}n}{\mathrm{d}T}$ $(10^{-5}\ \mathrm{K}^{-1})$	System	Material	$\frac{1}{n}\frac{\mathrm{d}n}{\mathrm{d}T}$ $(10^{-5}\ \mathrm{K}^{-1})$
IV	Diamond	0.32	II–VI	MgO	1.4
	Si	4.0		β-ZnS	1.9
	Ge	6.9		ZnSe	2.6
	6H-SiC	1.1		ZnTe	6
				w-CdS	4
III–V	AlP	3.6		w-CdSe	4
	AlAs	4.6		CdTe	4.4
	AlSb	1.19[a]			
	α-GaN	2.6			
	GaP	3.7			
	GaAs	4.5			
	GaSb	8.2			
	InP	2.7			
	InAs	12			
	InSb	6.9			

[a] Calculated

an order of magnitude smaller than those for other semiconductors. Note that the lead salts exhibit properties, which are unusual, and possibly unique, relative to other semiconductors. For example, they possess high dielectric constant, high mobility and a narrow fundamental gap whose temperature coefficient is positive (not negative) [10.55]. As expected from Equation (10.86), the lead salts have negative valves of $n^{-1}(\mathrm{d}n/\mathrm{d}T)$, e.g., $n^{-1}(\mathrm{d}n/\mathrm{d}T) = -2 \times 10^{-4}\ \mathrm{K}^{-1}$ for PbS [10.56]. Unfortunately, this equation gives only the correct sign of the coefficient, but does not yield quantitative agreement with experiment.

The temperature dependence of the refractive index dispersion near the fundamental absorption edge of InP has been studied by Gini and Melchior [10.57] by means of an integrated optical demultiplexer. The data suggested that the linear temperature coefficient $\mathrm{d}n/\mathrm{d}T$ increases as the photon energy approaches the lowest direct band-gap energy E_0. Similar photon energy dependence of the linear temperature coefficient $\mathrm{d}n/\mathrm{d}T$ has been found in various semiconductors, such as group-IV [10.58–10.61], III–V [10.59, 10.60, 10.62] and II–VI semiconductors [10.59, 10.63].

2. Pressure effect. Let us obtain theoretical expression for the pressure coefficient of the refractive index in terms of the Penn model. Equation (10.83) for $E \to 0$ and $A \equiv V^{-1}$ leads to

$$\begin{aligned}\frac{1}{n}\left(\frac{\mathrm{d}n}{\mathrm{d}p}\right)_T &= \frac{1}{2}\left(1-\frac{1}{\varepsilon_1}\right)\left[C_\mathrm{o} - \frac{2}{E_\mathrm{g}}\left(\frac{\partial E_\mathrm{g}}{\partial p}\right)_T\right] \\ &= \frac{1}{2}\left(1-\frac{1}{\varepsilon_1}\right)\left[-\beta_\mathrm{th} - \frac{2\beta_\mathrm{th}V}{E_\mathrm{g}}\left(\frac{\partial E_\mathrm{g}}{\partial V}\right)_T\right]\left(-\frac{C_\mathrm{o}}{\beta_\mathrm{th}}\right) \qquad (10.87)\end{aligned}$$

where $C_o = -V^{-1}(\partial V/\partial p)_T$ is the isothermal compressibility. If we assume for the moment that in Equation (10.84) the $(\partial E_g/\partial T)_V$ term is negligible compared with the other terms, then

$$\left(\frac{\partial n}{\partial p}\right)_T = -\frac{C_o}{\beta_{th}}\left(\frac{\partial n}{\partial T}\right)_p \tag{10.88}$$

It should be noted, however, that this assumption is not substantial.

The pressure coefficient of the long-wavelength refractive index can be estimated from the high-frequency dielectric constant data, $d\varepsilon_\infty/dp$, using the relation

$$\frac{1}{n}\left(\frac{dn}{dp}\right) = \frac{1}{2n^2}\left(\frac{d\varepsilon_\infty}{dp}\right) = \frac{1}{2\varepsilon_\infty}\left(\frac{d\varepsilon_\infty}{dp}\right) \tag{10.89}$$

We have already listed the ε_∞ and $d\varepsilon_\infty/dp$ values in Table 10.2. From this table, we obtain $n^{-1}(dn/dp) = -6.8 \times 10^{-3}$ GPa^{-1} (GaP), -4.1×10^{-3} GPa^{-1} (GaAs) and -1.4×10^{-3} GPa^{-1} (β-ZnS), respectively.

The pressure dependence of the refractive index near the lowest direct band-gap energy E_0 can be expressed as

$$\frac{dn}{dp} = \frac{dn}{dE_0}\frac{dE_0}{dp} \sim -\frac{dn}{dE}\frac{dE_0}{dp} \tag{10.90}$$

Since the signs of dn/dE and dE_0/dp are positive in most semiconductors, one can expect that n decreases with increasing pressure p.

The refractive index dispersion as a function of pressure p has been measured on some group-IV [10.11], III–V [10.11, 10.64] and II–VI semiconductors [10.65, 10.66]. As expected from Equation (10.90), these data showed a decrease in n with increasing p. We show in Figure 10.17, as an example, the refractive index dispersion for GaP measured at $T = 300$ K and at different pressures from $p = 0.53$ to 11.8 GPa [10.64]. The solid lines represent the theoretical dispersion curves.

3. Doping effect. The doping-induced change in the refractive index Δn may be explained by a sum of the three independent contributions

$$\Delta n = \Delta n_f + \Delta n_{0g} + \Delta n_{hg} \tag{10.91}$$

where Δn_f is arising from free-carrier absorption (see Section 10.5, below), Δn_{0g} is a contribution from the doping-induced change in the E_0-gap parameters (energy, strength and broadening), and Δn_{hg} is a contribution from the change in the higher-lying gap parameters. Note that Δn_f and Δn_{hg} can be considered to be nondispersive in the E_0 region. Therefore, the refractive index change Δn caused by doping near the E_0 region is mainly governed by Δn_{0g}. At longer wavelengths, the free-carrier absorption has a stronger effect on the infrared spectrum.

The doping-induced change in the refractive index has been studied experimentally for some group-IV (Si [10.67], 6H-SiC [10.68]) and III–V semiconductors (GaAs [10.69], GaSb [10.70], InP [10.71, 10.72], InAs [10.73], InSb [10.73]). All these data, except for 6H-SiC, showed an obvious decrease in n with increasing electron or hole concentration. The data for 6H-SiC suggested that the n value slightly increases as the electron concentration increases from 1.2 to 7.0×10^{18} cm^{-3} [10.68].

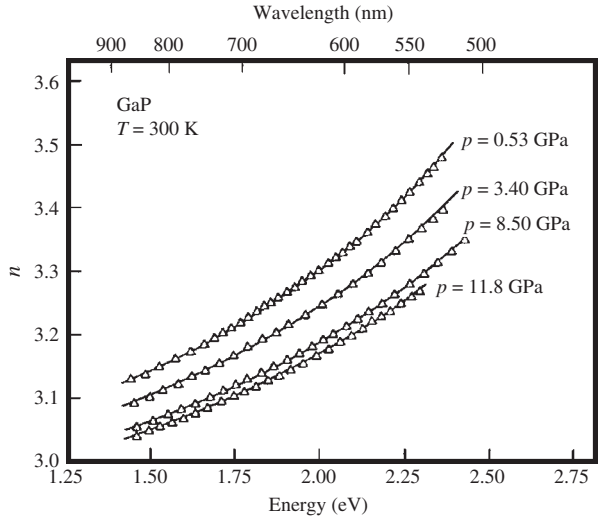

Figure 10.17 Refractive-index dispersion for GaP at 300 K and at different pressures. The solid lines represent the theoretical curves. [From K. Strössner, S. Ves, and M. Cardona, *Phys. Rev. B* **32**, 6614 (1985), reproduced by permission from the American Physical Society]

10.3.3 Optical absorption at the fundamental absorption edge

(a) Critical point: definition

The optical constants in the interband transition region of semiconductors depend fundamentally on the electronic energy-band structure of the semiconductors. The relation between the electronic energy-band structure and $\varepsilon_2(E)$ can now be given by [10.2]

$$\varepsilon_2(E) = \frac{4e^2\hbar^2}{\pi\mu^2E^2}\int \mathrm{d}\boldsymbol{k}\,|P_{\mathrm{cv}}(\boldsymbol{k})|^2\delta(E_{\mathrm{c}}(k) - E_{\mathrm{v}}(k) - E) \tag{10.92}$$

where μ is the combined density-of-states mass, the Dirac δ function represents the spectral joint density of states between the valence-band $E_{\mathrm{v}}(\boldsymbol{k})$ and conduction-band states $E_{\mathrm{c}}(\boldsymbol{k})$, differing by the energy $E = \hbar\omega$ of the incident light, $P_{\mathrm{cv}}(\boldsymbol{k})$ is the momentum matrix element between the valence-band and conduction-band states and the integration is performed over the first Brillouin zone.

Equation (10.92) can be transformed into a surface integral

$$\varepsilon_2(E) = \frac{4e^2\hbar^2}{\pi\mu^2E^2}\int_S \frac{\mathrm{d}S|P_{\mathrm{cv}}(\boldsymbol{k})|^2}{|\nabla_k(E_{\mathrm{c}} - E_{\mathrm{v}})|_{E_{\mathrm{c}}-E_{\mathrm{v}}=E}} \tag{10.93}$$

where the integration goes over the equal-energy-difference surface in $\boldsymbol{k}$ space defined by $E_{\mathrm{c}} - E_{\mathrm{v}} = E$. In most cases $|P_{\mathrm{cv}}(\boldsymbol{k})|^2$ can safely be assumed to be a slowly varying function such that we can define

$$J_{\mathrm{cv}}(E) = \int_S \frac{\mathrm{d}S}{|\nabla_k(E_{\mathrm{c}} - E_{\mathrm{v}})|_{E_{\mathrm{c}}-E_{\mathrm{v}}=E}} \tag{10.94}$$

the joint density-of-states function measuring the product density of full and empty states of equal energy difference. The $\varepsilon_2(E)$ can, then, be simply written as

$$\varepsilon_2(E) = \frac{4e^2\hbar^2}{\pi\mu^2 E^2}|P_{\mathrm{cv}}(\boldsymbol{k})|^2 J_{\mathrm{cv}}(E) \tag{10.95}$$

The $J_{\mathrm{cv}}(E)$ shows strong variations as a function of E for those frequencies at which

$$\nabla_k[E_{\mathrm{c}}(\boldsymbol{k}) - E_{\mathrm{v}}(\boldsymbol{k})] = \nabla_k E_{\mathrm{c}}(\boldsymbol{k}) - \nabla_k E_{\mathrm{v}}(\boldsymbol{k}) = 0 \tag{10.96}$$

for some value of $\boldsymbol{k}$. These critical points defined by Equation (10.96) are of paramount importance for the discussion of optical spectra.

The energy difference $E_{\mathrm{c}} - E_{\mathrm{v}}$ can be expanded about a critical point of energy $E_{\mathrm{c}}(\boldsymbol{k}_{\mathrm{c}})$ in a Taylor series [10.2]

$$E_{\mathrm{c}} - E_{\mathrm{v}} = E_{\mathrm{c}} + \sum_{j=1}^{3}\left[\frac{\mathrm{d}^2(E_{\mathrm{c}} - E_{\mathrm{v}})}{\mathrm{d}k_j^2}\right]_{\boldsymbol{k}=\boldsymbol{k}_{\mathrm{c}}}(k_j - k_{\mathrm{c}j})^2 \tag{10.97}$$

The linear term in the expansion is identically zero at a critical point because of Equation (10.96) and in the parabolic approximation we retain only the quadratic term. Inserting Equation (10.97) into Equation (10.94) and performing the integral, we obtain the analytical behavior of the joint density-of-states function J_{cv} at the three-dimensional critical points. According to different combinations of the sign of

$$a_j = \left[\frac{\mathrm{d}^2(E_{\mathrm{c}} - E_{\mathrm{v}})}{\mathrm{d}k_j^2}\right]_{\boldsymbol{k}=\boldsymbol{k}_{\mathrm{c}}} \tag{10.98}$$

one has to distinguish between four types of critical points, M_0–M_3. For example, an M_0-type critical point is realized by having all $a_j > 0$. We list in Table 10.7 the analytical behavior of $J_{\mathrm{cv}}(E)$ at the four types of critical points (three-dimensional critical points). The different constants depend on the values of a_j. We also list in Table 10.7 the energy dependence of J_{cv} in the cases of two-dimensional and one-dimensional $\boldsymbol{k}$ spaces.

Figure 10.18 schematically shows the form of $J_{\mathrm{cv}}(E)$ for all these nine cases. It should be noted that there is a characteristic line shape for each critical point. For example, one finds a step function for the two-dimensional M_0 ($a_j > 0$) or two-dimensional M_2-type ($a_j < 0$) and a logarithmic singularity for the two-dimensional M_1 saddle point ($a_1 > 0$, $a_2 < 0$) (see Figure 10.18(b)). Such a feature gives us a valuable tool for identifying the structure in optical spectra which are experimentally observed.

(b) Free electron–hole pair transition

1. At the direct absorption edge. The lowest direct transitions in $\mathrm{A}^N\mathrm{B}^{8-N}$ semiconductors occur at the center of the Brillouin zone. These transitions are of the three-dimensional M_0 type (E_0 and $E_0 + \Delta_0$, see Table 10.7). Introducing the three-dimensional $\mathrm{M}_0 J_{\mathrm{cv}}(E)$

Table 10.7 Joint density-of-states function $J_{cv}(E)$ for different critical points (CPs)

Three-dimensional (3D)

Type of CP	Notation	a_1	a_2	a_3	$J_{cv}(E)$	
					$E < E_c$	$E > E_c$
Minimum	M_0	+	+	+	0	$C_0(E - E_c)^{1/2}$
Saddle point	M_1	+	+	−	$C_1 - C_0'(E_c - E)^{1/2}$	C_1
Saddle point	M_2	+	−	−	C_2	$C_2 - C_2'(E - E_c)^{1/2}$
Maximum	M_3	−	−	−	$C_3(E_c - E)^{1/2}$	0

Two-dimensional (2D)

Type of CP	Notation	a_1	a_2	$J_{cv}(E)$	
				$E < E_c$	$E > E_c$
Minimum	M_0	+	+	0	B_1
Saddle point	M_1	+	−	$\frac{B_1}{\pi}(B_2 - \ln\lvert E_c - E\rvert)$	$\frac{B_1}{\pi}(B_2 - \ln\lvert E_c - E\rvert)$
Maximum	M_2	−	−	B_1	0

One-dimensional (1D)

Type of CP	Notation	a_1	$J_{cv}(E)$	
			$E < E_c$	$E > E_c$
Minimum	M_0	+	0	$A(E - E_c)^{-1/2}$
Maximum	M_1	−	$A(E_c - E)^{-1/2}$	0

into Equation (10.95) and performing the Kramers–Kronig transformation, we obtain the contribution of these transitions to $\varepsilon(E)$

$$\varepsilon(E) = AE_0^{-3/2}\left[f(\chi_0) + \frac{1}{2}\left(\frac{E_0}{E_0 + \Delta_0}\right)^{3/2} f(\chi_{so})\right] \tag{10.99}$$

with

$$A = \frac{4}{3}\left(\frac{3}{2}\mu_0\right)^{3/2} P^2 \tag{10.100a}$$

$$\chi_0 = \frac{E + i\Gamma}{E_0} \tag{10.100b}$$

$$\chi_{so} = \frac{E + i\Gamma}{E_0 + \Delta_0} \tag{10.100c}$$

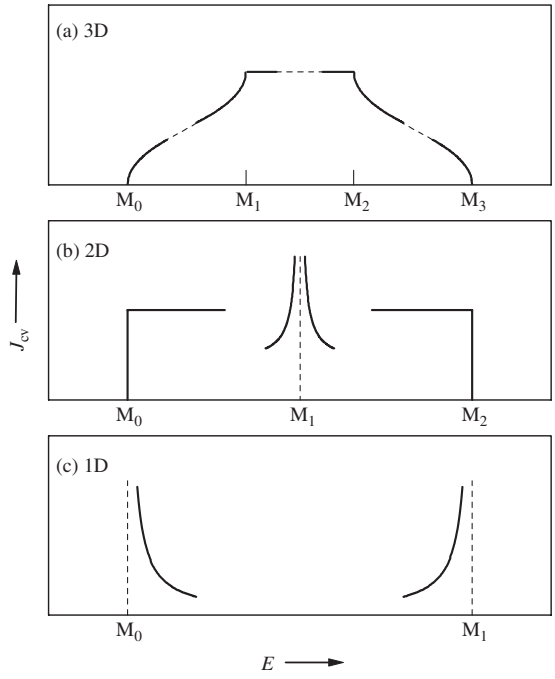

Figure 10.18 Joint density-of-states function $J_{cv}(E)$ plotted against E for: (a) three-dimensional critical points; (b) two-dimensional critical points; (c) one-dimensional critical points

where P^2 is the square of the momentum matrix element ($\propto |P_{cv}(\boldsymbol{k})|^2$), Γ is the broadening energy of the $E_0/(E_0 + \Delta_0)$ transitions and $f(\chi)$ is a function defined by Equation (10.79). For simplicity, we have assumed that the three (or six, accounting for the spin states) valence bands have the same reduced mass μ_0. It is noted that the calculated $\varepsilon_2(E)$ (Im$\varepsilon(E)$) spectrum of Equation (10.99) in the limit $\Gamma \to 0$ eV produces the well-known 1/2-power law

$$\varepsilon_2(E) = \frac{A}{E^2}\left[\sqrt{E - E_0}H(\chi_0 - 1) + \frac{1}{2}\sqrt{E - E_0 - \Delta_0}H(\chi_{so} - 1)\right] \tag{10.101}$$

where H is the Heaviside function defined by Equation (6.14).

In cases where transitions are forbidden in dipole approximation, one can make use of the $\boldsymbol{k}$ dependence of the matrix element and expand around the critical point at $\boldsymbol{k}_c$

$$P_{cv}(\boldsymbol{k}) = P_{cv}(\boldsymbol{k}_0) + \sum_{j=1}^{3}\left(\frac{\partial P_{cv}(\boldsymbol{k})}{\partial \boldsymbol{k}_j}\right)_{\boldsymbol{k}=\boldsymbol{k}_c}(\boldsymbol{k}_j - \boldsymbol{k}_{cj}) + \cdots \tag{10.102}$$

and keep only the linear term. We can, then, obtain for 'forbidden' direct transitions at the three-dimensional M_0 critical point [10.2]

$$\varepsilon_2(E) \propto \left|\frac{\partial P_{cv}(\boldsymbol{k})}{\partial |\boldsymbol{k}|}\right|^2\left[(E - E_0)^{3/2}H(\chi_0 - 1) + \frac{1}{2}(E - E_0 - \Delta_0)^{3/2}H(\chi_{so} - 1)\right] \tag{10.103}$$

This result is to be contrasted with the square-root energy dependence found in Equation (10.101) for the 'allowed' direct transitions. It is noted, however, that the strength of ε_2 is generally much lower for the 'forbidden' transitions since we have only the contribution from the matrix element in first order in $\boldsymbol{k}$.

Figure 10.19 schematically shows the line shapes of absorption coefficient $\alpha(E)$ for (a) dipole-allowed and (b) dipole-forbidden transitions at the direct band gap (three-dimensional M_0 critical point (E_0)), together with those for (c) dipole-allowed and (d) dipole-forbidden transitions at the indirect band gap (E_g^{ID}, see below) and (e) impurity-induced absorption band.

2. At the indirect absorption edge. Optical transitions between states which are not vertical in an energy-band diagram are called indirect transitions. We show in Figure 10.20 an example of the energy-band diagram for an indirect band-gap semiconductor, where the top of the valence band and the direct conduction-band and indirect conduction-band minima are shown.

The theory of indirect optical absorption can be developed by considering the perturbation Hamiltonian [10.74]

$$H = H_{eR} + H_{eL} \tag{10.104}$$

where H_{eR} represents the electron–radiation perturbation which is linear in both electron and photon creation–annihilation operators and H_{eL} is the electron–lattice perturbation which is linear in the phonon creation–annihilation operator, but bilinear in the electron creation-annihilation operator. The indirect optical transition can thus be expressed as a second-order perturbation process. Using the results of second-order time-dependent perturbation theory, we obtain transition probability per unit time for a process in which

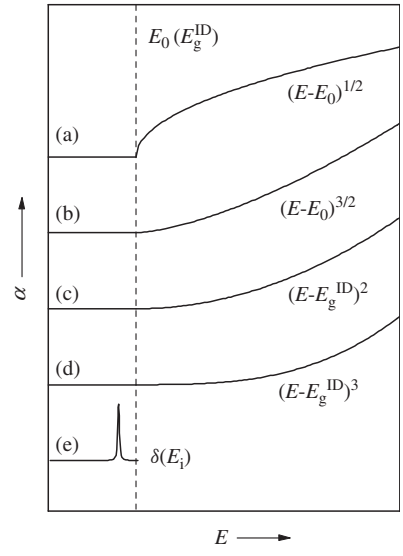

Figure 10.19 Line shapes of absorption coefficient $\alpha(E)$ for: (a) dipole-allowed; (b) dipole-forbidden transitions at the direct band gap (three-dimensional M_0 critical point (E_0)), together with those for (c) dipole-allowed; (d) dipole-forbidden transitions at the indirect band gap (E_g^{ID}) and (e) impurity-induced absorption band

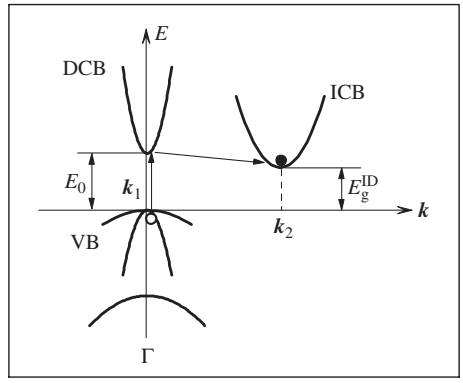

Figure 10.20 Schematic diagram showing the indirect optical absorption process. VB: valence band; DCB: direct conduction band; ICB: indirect conduction band

the valence electron is scattered to the conduction band (ICB) and a photon of energy E and a phonon of momentum $\hbar \boldsymbol{q} = \hbar(\boldsymbol{k}_2 - \boldsymbol{k}_1)$ (and energy $\hbar\omega_q$) are both absorbed as follows

$$W = \tau^{-1} \propto D_0 n_q \cdot \delta[E_c(\boldsymbol{k}_2) - E_v(\boldsymbol{k}_1) - E + \hbar\omega_q] \tag{10.105}$$

with

$$D_0 = \sum_\beta \left| \sum_\alpha \frac{\langle \beta | H_{eL} | \alpha \rangle \langle \alpha | H_{eR} | 0 \rangle}{E_\alpha(\boldsymbol{k}_1) - E_v(\boldsymbol{k}_1) - E} \right|^2 \tag{10.106}$$

where n_q is the Bose–Einstein phonon occupation number given by ($N_q \to n_q$ in Equation (8.28))

$$n_q = \frac{1}{e^{\hbar\omega_q/kT} - 1} \tag{10.107}$$

E_c and E_v represent the conduction-band and valence-band energies, respectively, $|0\rangle$ the electronic ground (initial) state, $|\alpha\rangle$ the intermediate state in the DCB with energy E_α, $|\beta\rangle$ the final state in the ICB, $\langle \alpha | H_{eR} | 0 \rangle$ the momentum matrix element between the VB and DCB extrema located near the Γ point and separated by $E_0(\boldsymbol{k}_1)$ and $\langle \beta | H_{eL} | \alpha \rangle$ is the matrix element of the phonon-assisted transition from the DCB to ICB. The energy denominator in Equation (10.106) is popularly assumed to be $(E_\alpha(\boldsymbol{k}_1) - E_v(\boldsymbol{k}_1) - E) \sim (E_0 - E) \sim E_0$. The quantity D_0 is also assumed to be independent of $\boldsymbol{k}$.

Considering the case of indirect optical transitions between spherical bands and summing over $\boldsymbol{k}_1$ and $\boldsymbol{k}_2$ of Equation (10.105) in the Brillouin zone, we obtain the following expression for the imaginary part of the complex dielectric function $\varepsilon_2(E)$ [10.74]

$$\varepsilon_2(E) = \begin{cases} \dfrac{D}{E^2} n_q (E - E_g^{ID} + \hbar\omega_q)^2 & \text{for } E > E_g^{ID} - \hbar\omega_q \\ 0 & \text{for } E < E_g^{ID} - \hbar\omega_q \end{cases} \tag{10.108}$$

where D is the indirect transition strength parameter. The absorption of light, thus, begins at $E = E_g^{ID} - \hbar\omega_q$. Another contribution to the indirect optical transitions is due to the

emission of a phonon and can be obtained by the same procedure, where the only differences from the previous case are the sign of the phonon energy $\hbar\omega_q$ and $n_q \to (n_q + 1)$. Combining all these contributions, we obtain

$$\varepsilon_2(E) = \frac{D}{E^2}\left(n_q + \frac{1}{2} \mp \frac{1}{2}\right)(E - E_g^{ID} \pm \hbar\omega_q)^2 H(1 - \chi_g) \tag{10.109}$$

with

$$\chi_g = \frac{E_g^{ID} \mp \hbar\omega_q}{E} \tag{10.110}$$

The parabolic bands extending to infinite energies implied by Equation (10.109) should be nonphysical. We, therefore, modify the model by taking into account a cutoff at energy E_c. This modification gives

$$\varepsilon_2(E) = \frac{D}{E^2}\left(n_q + \frac{1}{2} \mp \frac{1}{2}\right)(E - E_g^{ID} \pm \hbar\omega_q)^2 H(1 - \chi_g) H(1 - \chi_c) \tag{10.111}$$

with

$$\chi_c = \frac{E}{E_c} \tag{10.112}$$

Assuming $\hbar\omega_q \to 0$ eV and performing the Kramers–Kronig transformation, we finally obtain

$$\varepsilon(E) = \frac{2D}{\pi}(2n_q + 1)\left[-\frac{(E_g^{ID})^2}{(E + i\Gamma)^2}\ln\left(\frac{E_c}{E_g^{ID}}\right) + \frac{1}{2}\left(1 + \frac{E_g^{ID}}{E + i\Gamma}\right)^2 \ln\frac{E + i\Gamma + E_c}{E + i\Gamma + E_g^{ID}} + \frac{1}{2}\left(1 - \frac{E_g^{ID}}{E + i\Gamma}\right)^2 \ln\frac{E + i\Gamma - E_c}{E + i\Gamma - E_g^{ID}}\right] \tag{10.113}$$

Here, $\varepsilon_1(E) = \mathrm{Re}\varepsilon(E)$ and $\varepsilon_2(E) = \mathrm{Im}\varepsilon(E)$.

We see that the 'allowed' indirect transitions have the square energy dependence expressed by Equation (10.108). In case where the indirect transitions are forbidden we proceed as for direct transitions mentioned before. If the parameter D in Equation (10.111) is replaced by its first derivative, again a factor to the first power in E comes in and we obtain a cubic dependence on energy E

$$\varepsilon_2(E) \propto \left(n_q + \frac{1}{2} \mp \frac{1}{2}\right)(E - E_g^{ID} \pm \hbar\omega_q)^3 H(1 - \chi_g) H(1 - \chi_c) \tag{10.114}$$

Summarizing the four possible cases of transitions we have the energy exponents 1/2 for direct *allowed*, 3/2 for direct *forbidden*, 2 for indirect *allowed* and 3 for indirect *forbidden* transitions (see Figure 10.19). Such behavior is often used to distinguish experimentally between the different types.

(c) Excitonic transition

1. Direct exciton. The contribution of the discrete excitons to ε_2 can be given by [10.28]

$$\varepsilon_2(E) = \frac{f^{\mathrm{D}}}{E^2} \sum_{n=1}^{\infty} \frac{1}{n^3} |\phi_1(0)|^2 \delta(E_{\mathrm{ex}}^n - E) \tag{10.115}$$

where f^{D} is the strength parameter proportional to the square of the momentum matrix element. The Kramers–Kronig transformation of Equation (10.115) gives

$$\varepsilon_1(E) = \sum_{n=1}^{\infty} \frac{1}{n^3} \frac{F^{\mathrm{D}}}{(E_{\mathrm{ex}}^n)^2 - E^2} \tag{10.116}$$

where, for simplicity, we replaced $F^{\mathrm{D}} = 2E_{\mathrm{ex}}^n f^{\mathrm{D}} |\phi_1(0)|^2/\pi$. The contribution of the discrete exciton series to $\varepsilon(E)$ ($\varepsilon_1(E) = \mathrm{Re}\varepsilon(E)$, $\varepsilon_2(E) = \mathrm{Im}\varepsilon(E)$) can be finally written as

$$\varepsilon(E) = \sum_{n=1}^{\infty} \frac{1}{n^3} \frac{F^{\mathrm{D}}}{[E_0 - (G^{3\mathrm{D}}/n^2)]^2 - E^2 - i2E\Gamma} \tag{10.117}$$

where Γ is the exciton lifetime-broadening energy.

The contribution of the continuum excitons to ε_2 can be given by [10.28]

$$\varepsilon_2(E) = \frac{f^{\mathrm{C}}}{E^2} \sum_{k} |\phi_k(0)|^2 \delta(E_{\mathrm{ex}}^k - E) \tag{10.118}$$

where f^{C} is the continuum exciton strength parameter.

Equation (10.118) is known to give a continuous exciton spectrum at $E - E_0 \geqslant 0$ when $\alpha_k \to \infty$ [10.28]. For $E - E_0 \gg G^{3\mathrm{D}}$ where $\alpha_k \to 0$, $\varepsilon_2(E)$ will become proportional to $(E - E_0)^{1/2}$, in agreement with the case neglecting the electron–hole interaction. If we neglect the exponential in the denominator of Equation (10.62), i.e.,

$$\frac{\pi \alpha_k e^{\pi \alpha_k}}{N \sinh(\pi \alpha_k)} \sim 2\pi \alpha_k \tag{10.119}$$

the Kramers–Kronig transformation of Equation (10.118) gives

$$\varepsilon_1(E) = \frac{F^{\mathrm{C}} E_{\mathrm{ex}}^{\mathrm{C1}}}{G^{3\mathrm{D}} E^2} \ln \frac{E_0^2}{E_0^2 - E^2} \tag{10.120}$$

where $E_{\mathrm{ex}}^{\mathrm{C1}}$ is the ground-state exciton energy ($\sim E_0$) and F^{C} is the strength constant having a similar physical meaning as F^{D} in Equation (10.116). Finally, the contribution of the continuum excitons to $\varepsilon(E)$ ($\varepsilon_1(E) = \mathrm{Re}\varepsilon(E)$, $\varepsilon_2(E) = \mathrm{Im}\varepsilon(E)$) can be given by

$$\varepsilon(E) = \frac{F^{\mathrm{C}} E_{\mathrm{ex}}^{\mathrm{C1}}}{G^{3\mathrm{D}} (E + i\Gamma)^2} \ln \frac{E_0^2}{E_0^2 - (E + i\Gamma)^2} \tag{10.121}$$

In a case where transitions are forbidden in the sense of the dipole approximation, Equation (10.60) can be modified as [10.28]

$$\left|\frac{\partial\phi_n(0)}{\partial x}\right|^2 = \frac{n^2-1}{n^5}\frac{V_0}{3\pi(a_{\mathrm{B}}^{3\mathrm{D}})^5} \equiv \frac{n^2-1}{n^5}\left|\frac{\partial\phi_1(0)}{\partial x}\right|^2 \tag{10.122}$$

where x is a quantity which is roughly the atomic radius. The corresponding ε_2 can be written as

$$\varepsilon_2(E) = \frac{f^{\mathrm{D,F}}}{E^2}\sum_{n=1}^{\infty}\frac{n^2-1}{n^5}\left|\frac{\partial\phi_1(0)}{\partial x}\right|^2\delta(E_{\mathrm{ex}}^n - E) \tag{10.123}$$

A series of exciton lines, thus, occur at energies given by Equation (10.61), except that the $n = 1$ line is now missing.

Similarly, in the true continuum we have an expression

$$\left|\frac{\partial\phi_k(0)}{\partial x}\right|^2 = \frac{\pi\alpha_k(1+\alpha_k^2)e^{\pi\alpha_k}x^2}{3N\sinh(\pi\alpha_k)} \tag{10.124}$$

The contribution of the forbidden continuum-exciton transitions to ε_2 can, therefore, be written as [10.28]

$$\varepsilon_2(E) = \frac{f^{\mathrm{C,F}}}{E^2}\sum_{k}\left|\frac{\partial\phi_k(0)}{\partial x}\right|^2\delta(E_{\mathrm{ex}}^k - E) \tag{10.125}$$

Equation (10.125) gives continuous exciton absorption at $E - E_0 \geqslant 0$ when $\alpha_k \to \infty$ [10.28]. For $E - E_0 \gg G^{3\mathrm{D}}$ where $\alpha_k \to 0$, $\varepsilon_2(E)$ will become proportional to $(E - E_0)^{3/2}$, in agreement with that neglected the electron–hole interaction, i.e., Equation (10.103).

2. Indirect exciton. Exact calculation of the exciton effect at the indirect absorption edge is quite complicated, and it is convenient at this stage to make approximations and consider a more specific model. Let us assume that the maximum in the valence band is at $\boldsymbol{k} = \boldsymbol{k}_1$ and is nondegenerate, the minimum in the conduction band at $\boldsymbol{k} = \boldsymbol{k}_2$ and nondegenerate (see Figure 10.20). The envelope function $\phi(0)$ is also assumed to be independent of $\boldsymbol{k}$. The resultant $\varepsilon_2(E)$ formula can be given by [10.28]

$$\varepsilon_2(E) = \frac{F^{\mathrm{IDD}}}{E^2}\left(n_{\mathrm{q}} + \frac{1}{2} \mp \frac{1}{2}\right)\sqrt{E + G^{\mathrm{ID}} - E_{\mathrm{g}}^{\mathrm{ID}} \pm \hbar\omega_{\mathrm{q}}}\,H(1-\chi_{\mathrm{g}})H(1-\chi_{\mathrm{c}}) \tag{10.126}$$

where G^{ID} represents the binding energy of the indirect exciton (see Table 10.4). Note that the functional form of Equation (10.126) is almost the same as that of Equation (10.101). Then, the Kramers–Kronig transformation of Equation (10.126) may give

$$\varepsilon(E) = F^{\mathrm{IDD}}\left(n_{\mathrm{q}} + \frac{1}{2} \mp \frac{1}{2}\right)(E_{\mathrm{g}}^{\mathrm{ID}} - G^{\mathrm{ID}} \mp \hbar\omega_{\mathrm{q}})^{-3/2} f(\chi_{\mp}) \tag{10.127}$$

with

$$\chi_{\mp} = \frac{E + i\Gamma}{E_{\mathrm{g}}^{\mathrm{ID}} - \dfrac{G^{\mathrm{ID}}}{n^2} \mp \hbar\omega_{\mathrm{q}}} \tag{10.128}$$

and $f(\chi)$ is a function defined by Equation (10.79). Here, $\varepsilon_1(E) = \mathrm{Re}\varepsilon(E)$ and $\varepsilon_2(E) = \mathrm{Im}\varepsilon(E)$.

Beyond the series limit, i.e., $E > E_g^{ID} \pm \hbar\omega_q$, there is further absorption from the continuum. When $E - E_g^{ID} \pm \hbar\omega_q \gg G^{ID}$, we obtain [10.28]

$$\varepsilon_2(E) = \frac{F^{IDC}}{E^2}\left(n_q + \frac{1}{2} \mp \frac{1}{2}\right)(E - E_g^{ID} \pm \hbar\omega_q)^2 H(1-\chi_g)H(1-\chi_c) \qquad (10.129)$$

Note that this expression has the same power dependence as that obtained from the one-electron approximation, Equation (10.111). Thus, the Kramers–Kronig transformation of Equation (10.129) gives the same result as Equation (10.113).

In a case where transitions are dipole forbidden, we obtain

$$\varepsilon_2(E) = \frac{F^{IDD,F}}{E^2}\left(n_q + \frac{1}{2} \mp \frac{1}{2}\right)(E + G^{ID} - E_g^{ID} \pm \hbar\omega_q)^{3/2} H(1-\chi_g)H(1-\chi_c) \qquad (10.130)$$

for the lower-energy series and

$$\varepsilon_2(E) = \frac{F^{IDC,F}}{E^2}\left(n_q + \frac{1}{2} \mp \frac{1}{2}\right)(E - E_g^{ID} \pm \hbar\omega_q)^3 H(1-\chi_g)H(1-\chi_c) \qquad (10.131)$$

for the continuum.

(d) Experimental

1. Temperature effect. We show in Figure 10.21 the optical absorption spectra of high-quality GaAs measured by Sturge [10.31] over the photon energy range 0.6–2.75 eV at four different temperatures, $T = 21$, 90, 186 and 294 K. The sample used in this study was cut from a semi-insulating ingot of GaAs in which the carrier concentration was less than 10^{10} cm^{-3}. As can be seen in Figure 10.21, the saturated value of α at high energies (just above the band edge) does not depend so largely on temperature between $T = 21$ and 294 K ($\alpha \sim (8.5\text{–}9.5) \times 10^3$ cm^{-1}). At low temperatures, the main absorption edge shows a sharp peak due to the formation of the discrete excitons ($n = 1$). The step-like component seen in the true continuum region $E > E_0$ suggests the presence of continuum excitons in the optical transition processes. Sturge [10.31] also observed an exponential broadening at the low-energy side of the absorption edge that is known as the Urbach tail.

Figure 10.22 shows the low-temperature ($T = 2$, 77 and 145 K) absorption spectra of AlAs at the fundamental absorption edge measured by Lorenz *et al.* [10.75]. At the fundamental absorption edge, we can expect to see, at low absorption coefficients, a structure due to free-exciton absorption assisted by various phonons. This structure should be more clearly observed at low temperatures, as definitely seen in Figure 10.22. The absorption line marked A in the $T = 77$ K data is a bound-exciton line of unknown origin, but believed to be due to an isoelectronic impurity. This line has four relatively weak phonon replicas at approximately 13, 27, 42 and 50 meV higher energy. If we assume that line A is a zero-phonon process, then the five absorption thresholds correspond to

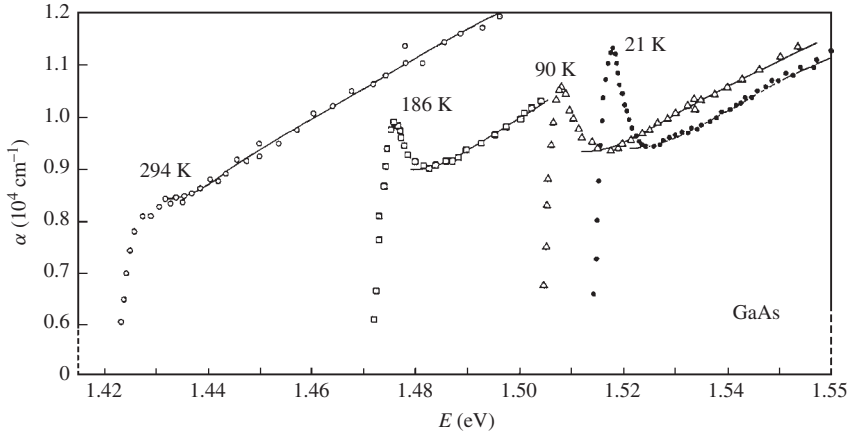

Figure 10.21 Excitonic absorption observed in GaAs at four different temperatures. [From M. D. Sturge, *Phys. Rev.* **127**, 768 (1962), reproduced by permission from the American Physical Society]

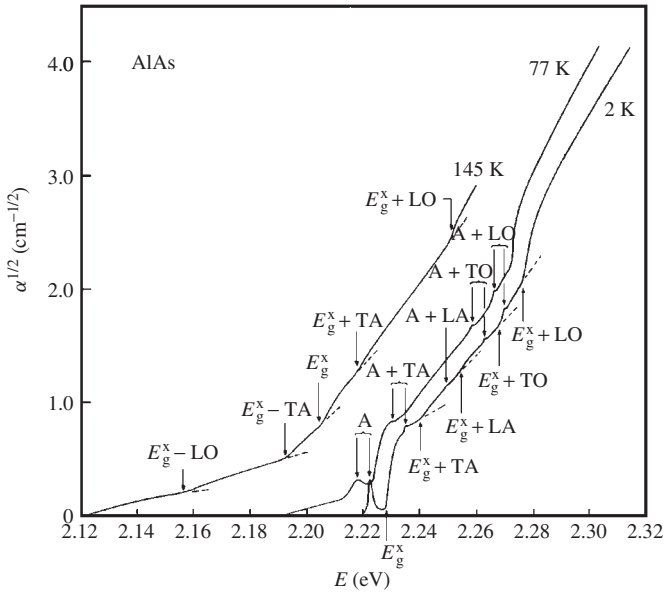

Figure 10.22 Optical absorption spectra at the indirect absorption edge of AlAs measured at 2, 77 and 145 K. The excitonic band-gap energy E_g^X, bound-exciton line A and their phonon replicas are indicated. [From M. R. Lorenz, R. Chicotka, G. D. Pettit, and P. J. Dean, *Solid State Commun.* **8**, 693 (1970), reproduced by permission from Elsevier]

E_g^X, $E_g^X + \text{TA}$, $E_g^X + \text{LA}$, $E_g^X + \text{TO}$ and $E_g^X + \text{LO}$, where E_g^X is the excitonic energy gap. The four phonon-assisted components are expected for an indirect-gap material according to the theory of Elliott [10.28].

2. Pressure effect. Figure 10.23 shows the hydrostatic pressure dependence of the absorption spectra of a 1.7-μm-thick GaAs sample measured at $T = 300$ K by Goñi

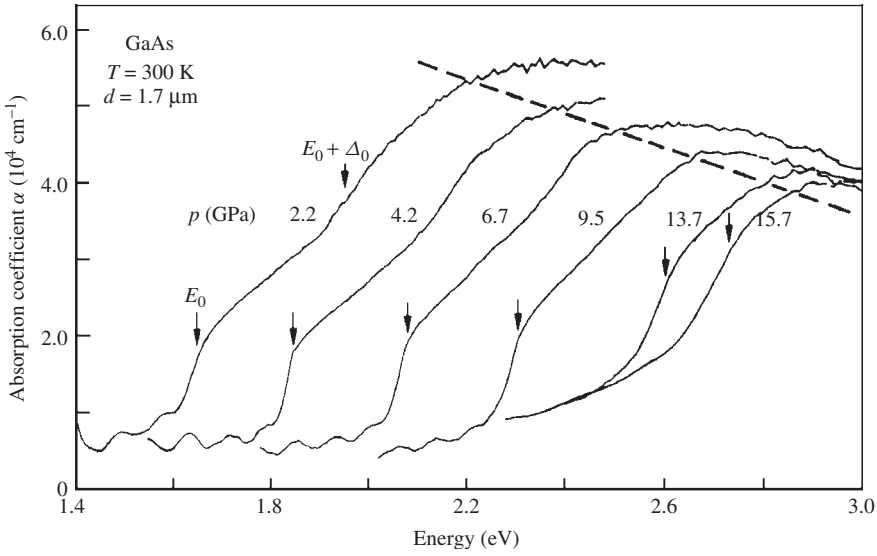

Figure 10.23 Optical absorption spectra of a 1.7-μm-thick sample of GaAs at 300 K at different hydrostatic pressures from 2.2 to 15.7 GPa. The arrows indicate the position of the direct absorption edge. [From A. R. Goñi, K. Strössner, K. Syassen, and M. Cardona, *Phys. Rev. B* **36**, 1581 (1987), reproduced by permission from the American Physical Society]

et al. [10.76]. The arrows correspond to the energies of the direct absorption edge as defined by the kink in the absorption spectra. The energy of the kink was determined from the corresponding edge in the first derivative with respect to the photon energy of the transmission spectra. These authors observed the direct absorption edge followed by a 'plateau' at higher energies up to the structural phase transition pressure, ~17 GPa. The gradual broadening with pressure of the direct band-gap kink was attributed to the fact that, with increasing pressure, the energy of the indirect gap E_g^{ID} ($\Gamma_{15} \rightarrow X_1$) becomes smaller than that of the direct gap E_0.

Goñi *et al*. [10.32] also measured low-temperature exciton absorption spectra at the lowest direct edge E_0 of GaAs as a function of hydrostatic pressure up to 9 GPa. The measured spectra were analyzed in terms of Elliott's model [10.28] by taking into account the broadening of the exciton line. The exciton binding energy in GaAs was found to increase linearly with pressure at a rate of $\mathrm{d}\ln G^{3D}/\mathrm{d}p = 0.08–0.09\ \mathrm{GPa}^{-1}$. The exciton lifetime became smaller for pressures above the $\Gamma-X$ conduction-band crossing ($\geqslant$4.2 GPa), a fact which was attributed to phonon-assisted intervalley scattering.

Figure 10.24 shows the absorption spectra in the region close to the indirect absorption edge of a 70-μm-thick AlSb sample measured at $T = 300$ K at hydrostatic pressures $p = 0.22–6.30$ GPa by Strössner *et al*. [10.77]. The absorption curves show an overall shift toward lower energies with increasing pressure p ($\mathrm{d}E_g^X/\mathrm{d}p < 0$). The pressure shift of α becomes smaller in the region well above the indirect band edge, no doubt a result of the positive pressure coefficient of the lowest direct band gap E_0 which modifies the energy of the Γ-intermediate state relevant for the indirect transitions.

3. Doping effect. Since optical absorption is determined by electron transition from a filled state in the valence band to an empty state in the conduction band, the band tail will

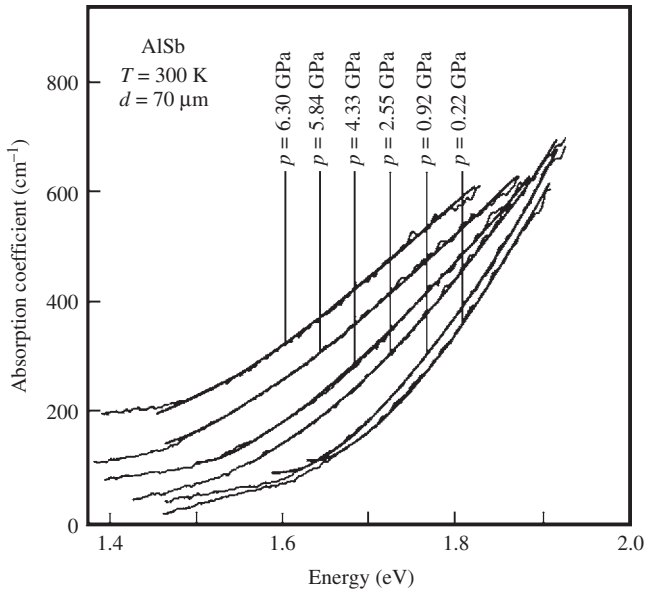

Figure 10.24 Absorption coefficient at the indirect band-gap edge of a 70-μm-thick AlSb at different hydrostatic pressures from 0.22 to 6.30 GPa at 300 K. The jagged lines represent the experimental data, while the smooth ones correspond to the theoretical fits. [From K. Strössner, S. Ves, C. K. Kim, and M. Cardona, *Phys. Rev. B* **33**, 4044 (1986), reproduced by permission from the American Physical Society]

influence absorption differently in n-type and p-type semiconductors. For heavily doped n-GaAs [10.78], for example, the lowest states in the conduction band are filled with free electrons so that absorption takes an electron from the top of the filled valence band to an empty state well up in the conduction band (see Figure 6.17). Hence, the absorption curve shifts to higher energy as shown in Figure 10.25(a), called the Burstein–Moss shift. For p-GaAs, the hole mass is large so that most of the holes are in the valence-band tails. Therefore, absorption raises an electron from a filled state that is near or above the parabolic valence-band edge to the conduction-band tail, and the absorption shifts to lower energy as the band tails increase (Figure 10.25(b)). Lush *et al.* [10.79] also measured the doping-dependent absorption coefficient in n-GaAs thin films ($n \sim 1.3 \times 10^{17}$–$3.8 \times 10^{18}$ cm^{-3}) and found that the results show good qualitative agreement with Casey *et al.* [10.78] and good quantitative agreement, except for the heavily doped samples. For $n \sim 3.8 \times 10^{18}$ cm^{-3}, α was approximately four times larger than that reported by Casey *et al.*

10.3.4 Urbach tail

The absorption coefficient $\alpha(E, T)$ near the fundamental absorption edge usually shows a simple exponential energy dependence

$$\alpha(E, T) = \alpha_0 \exp\left(\frac{E - E_g(T)}{E_u(T)}\right) \tag{10.132}$$

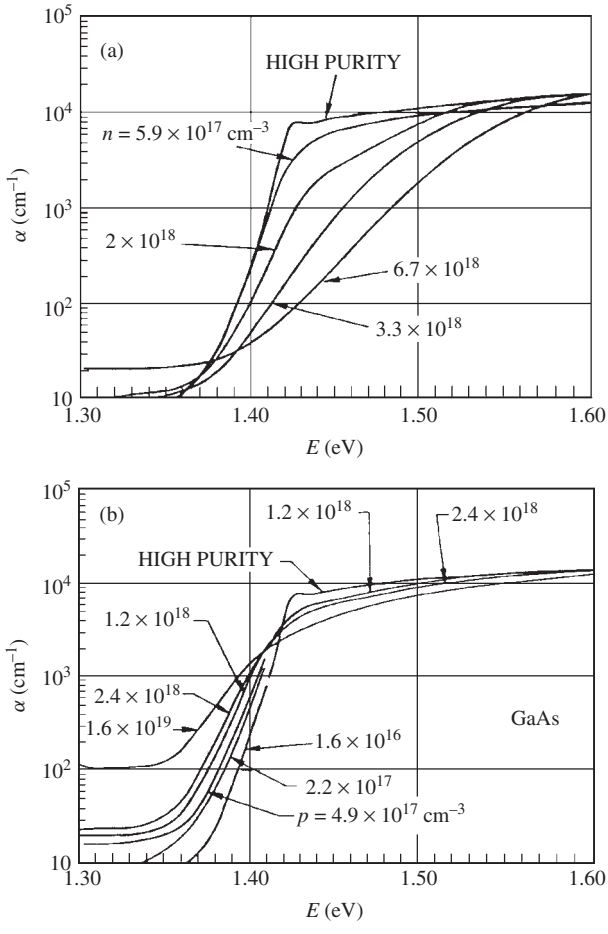

Figure 10.25 Absorption coefficient α for: (a) n-GaAs; (b) p-GaAs at 297 K. [From H. C. Casey, Jr., D. D. Sell, and K. W. Wecht, *J. Appl. Phys.* **46**, 250 (1975), reproduced by permission from the American Institute of Physics]

referred to as the Urbach tail [10.80], where $E_g(T)$ is the band-gap energy and $E_u(T)$ determines the width of the tail. The tail is generally attributed to disorder in the material that leads to a tail in the valence and conduction bands. At low temperature, dopant impurities as well as other structural imperfections introduce lattice disorder. At high temperature, the width of the tail is a direct measure of temperature-induced disorder and reflects the thermal occupancy of phonon states in the Brillouin zone via the electron–phonon interaction [10.81, 10.82]. We can, therefore, suspect that the Urbach parameter $E_u(T)$ has the same functional form as that of the critical-point linewidth broadening.

The Urbach parameter $E_u(T)$ can be written as [10.83]

$$E_u(T) = S_0 \left(\frac{1 + X}{2} + \frac{1}{e^{\theta/T} - 1} \right) \tag{10.133}$$

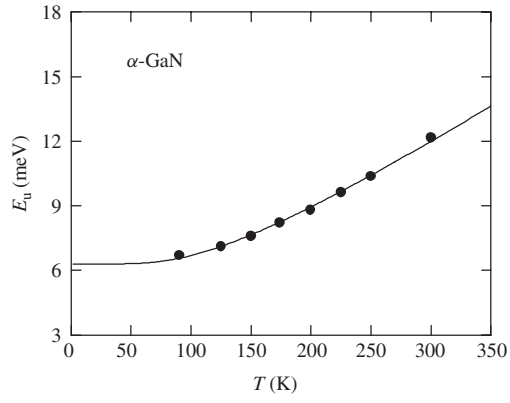

Figure 10.26 Urbach parameter E_u versus temperature T for undoped α-GaN grown on (0001) sapphire substrate. The experimental data are taken from Chichibu *et al.* [10.85]. The solid line represents the fit with Equation (10.133) with $S_0 = 12.6$ meV, $X = 0$ and $\theta = 350$ K

where X is a dimensionless parameter describing the contribution of 'frozen-in' structural disorder, to the width of the Urbach edge. In a well-ordered crystal, X is considered to be equal to zero.

The Urbach tail has been observed experimentally on some group-IV (Si [10.84]), III–V (α-GaN [10.85], GaAs [10.86], InP [10.87], InAs [10.88], InSb [10.89]) and II–VI semiconductors (α-ZnS [10.90], β-ZnS [10.90], w-CdS [10.91], CdTe [10.92]). In Figure 10.26, as an example, we show the Urbach parameter E_u–T data observed from undoped α-GaN grown on (0001) sapphire substrate [10.85]. The solid line indicates the calculated result of Equation (10.133) with $S_0 = 12.6$ meV, $X = 0$ and $\theta = 350$ K. It is seen that the calculated curve shows good agreement with the experimental data. The $\theta = 350$ K determined here is much smaller than $\theta_D = 821$ K, the Debye characteristic temperature (see Section 2.3). This fact suggests that the dominant scattering process in optical absorption of α-GaN is due to electron–acoustic phonon or exciton–acoustic phonon interaction.

10.4 THE INTERBAND TRANSITION REGION

10.4.1 Model dielectric function

Let us present a calculation model for the complex dielectric function, namely, the model dielectric function (MDF), which covers the optical response of semiconductors over a wide range of photon energies. The model is based on the Kramers–Kronig transformation and is strongly connected with the electronic energy-band structure of the medium [10.2]. The model predicts distinct structures at energies of the critical points in the Brillouin zone.

In the MDF, $\varepsilon_2(E)$ can be simply given from Equation (10.95) by

$$\varepsilon_2(E) = \sum_{s=1}^{M} \frac{4e^2\hbar^2}{\pi(\mu^s)^2 E^2} |P_{cv}^s(\boldsymbol{k})|^2 J_{cv}^s(E) \tag{10.134}$$

where $J_{cv}^{s}(E)$ is the joint density-of-states function of the sth interband critical point. As can be understood from Equation (10.134), the joint density-of-states function mainly determines the interband contribution to $\varepsilon_2(E)$ and thus to the optical constants of solids. Analytical behavior of $J_{cv}^{s}(E)$ at various types of critical point is well defined (Table 10.7). The Kramers–Kronig relations ensure that $\varepsilon_1(E)$ can be calculated at each photon energy if $\varepsilon_2(E)$ is known explicitly over the entire photon-energy range, and vice versa. In the following, we summarize the MDF for the critical points of each energy gap [10.56]. Combining all these contributions, we can obtain the spectral dependence of $\varepsilon(E)$ of the material.

(a) Fundamental absorption edge

1. Direct absorption edge. The contributions of the E_0 and $E_0 + \Delta_0$ transitions to $\varepsilon(E)$ have already been discussed in Section 10.3.3. These results are

$$\varepsilon(E) = AE_0^{-3/2}\left[f(\chi_0) + \frac{1}{2}\left(\frac{E_0}{E_0+\Delta_0}\right)^{3/2} f(\chi_{so})\right] \tag{10.135}$$

for the free electron–hole pair transitions (Equation (10.99))

$$\varepsilon(E) = \sum_{n=1}^{\infty} \frac{1}{n^3} \frac{F^{D}}{[E_0 - (G^{3D}/n^2)]^2 - E^2 - i2E\Gamma} \tag{10.136}$$

for the discrete-exciton transitions (Equation (10.117)) and

$$\varepsilon(E) = \frac{F^{C}E_{ex}^{C1}}{G^{3D}(E+i\Gamma)^2} \ln \frac{E_0^2}{E_0^2 - (E+i\Gamma)^2} \tag{10.137}$$

for the continuum-exciton transitions (Equation (10.121)).

2. Indirect absorption edge. The contribution of the indirect transitions to $\varepsilon(E)$ has already been presented in Section 10.3.3. The one-electron contribution of the indirect transitions to $\varepsilon(E)$ is written as (Equation (10.113))

$$\varepsilon(E) = \frac{2D}{\pi}(2n_q + 1)\left[-\frac{(E_g^{ID})^2}{(E+i\Gamma)^2}\ln\left(\frac{E_c}{E_g^{ID}}\right) + \frac{1}{2}\left(1 + \frac{E_g^{ID}}{E+i\Gamma}\right)^2 \ln\frac{E+i\Gamma+E_c}{E+i\Gamma+E_g^{ID}} + \frac{1}{2}\left(1 - \frac{E_g^{ID}}{E+i\Gamma}\right)^2 \ln\frac{E+i\Gamma-E_c}{E+i\Gamma-E_g^{ID}}\right] \tag{10.138}$$

The contribution of the indirect-exciton transitions to $\varepsilon(E)$ has also been presented in Section 10.3.3(c).

(b) E_1 and $E_1 + \Delta_1$ transitions

The E_1 and $E_1 + \Delta_1$ transitions in the diamond-type and zinc-blende-type semiconductors occur along the $\langle 111 \rangle$ direction or at the L point in the Brillouin zone. These transitions

are of the three-dimensional M_1 type. Since the M_1 critical-point longitudinal effective mass m_l is much larger than its transverse counterparts, the m_t values, one can treat these critical points as two-dimensional minima, two-dimensional M_0 (Figure 10.18). The contribution to $\varepsilon(E)$ of this type of two-dimensional minima can be written as

$$\varepsilon(E) = -B_1 \chi_{1d}^{-2} \ln(1 - \chi_{1d}^{-2}) - B_{1sd} \chi_{1sd}^{-2} \ln(1 - \chi_{1sd}^{-2}) \tag{10.139}$$

with

$$\chi_{1d} = \frac{E + i\Gamma}{E_1} \tag{10.140a}$$

$$\chi_{1sd} = \frac{E + i\Gamma}{E_1 + \Delta_1} \tag{10.140b}$$

In the case of the three-dimensional M_1 critical-point excitons (i.e., saddle-point or hyperbolic excitons), the effective mass approximation equation is much more difficult to solve. However, in the limit $m_l^{-1} \to 0$ the equation predicts a series of two-dimensional Wannier-type excitons [10.93]

$$E_{x1}^{2D} = E_1 - \frac{4G_1^{2D}}{(2n-1)^2} \tag{10.141a}$$

$$E_{x\Delta}^{2D} = E_1 + \Delta_1 - \frac{4G_{1\Delta}^{2D}}{(2n-1)^2} \tag{10.141b}$$

where G_1^{2D} ($G_{1\Delta}^{2D}$) is the two-dimensional exciton Rydberg energy. The contribution of the two-dimensional excitons to $\varepsilon(E)$ is written as

$$\varepsilon(E) = \sum_{n=1}^{\infty} \left\{ \frac{B_{1x}}{(2n-1)^3} \left[\frac{1}{(E_1 - [4G_1^{2D}/(2n-1)^2])^2 - E^2 - i2E\Gamma} \right] + \frac{B_{2x}}{(2n-1)^3} \left[\frac{1}{(E_1 + \Delta_1 - [4G_{1\Delta}^{2D}/(2n-1)^2])^2 - E^2 - i2E\Gamma} \right] \right\} \tag{10.142}$$

where B_{1x} (B_{2x}) is the exciton strength parameter proportional to the envelope function of the two-dimensional excitons. The envelope function can now be given by

$$|\phi_n^{2D}(0)|^2 = \frac{16V_0}{\pi (a_B^{2D})^3 (2n-1)^3} \tag{10.143}$$

where a_B^{2D} is the two-dimensional exciton Bohr radius and V_0 is the volume of the unit cell. The two-dimensional effective mass approximation also gives the continuum part of the exciton states [10.93]. One can, however, consider that the contribution to $\varepsilon(E)$ of this part may be similar to that of the one-electron approximation (Equation (10.139)).

(c) E_0', E_2 and E_1' transitions

The more pronounced structure found in the diamond-type and zinc-blende-type semiconductors in the region of higher energy than E_1 and $E_1 + \Delta_1$ is labeled E_2 or E_0'.

The nature of the E_2 (E_0') transitions is more complicated. They do not correspond to a single, well-defined critical point. If the E_0' transitions occur at Γ, then the critical point should be of three-dimensional M_0 (three-dimensional M_1) type. However, the fit shows that neither the three-dimensional M_0 nor the three-dimensional M_1 model represents the peculiar line shapes of ε_1 and ε_2 in the E_0' (E_2) spectral region. The best fit is obtained with a damped harmonic oscillator (DHO) model.

The DHO model now provides

$$\varepsilon(E) = \frac{C}{(1 - \chi_2^2) - i\chi_2\gamma} \tag{10.144}$$

with

$$\chi_2 = \frac{E}{E_2}\left(\text{or } \frac{E}{E_0'}\right) \tag{10.145}$$

where C is the dimensionless strength parameter and γ is the dimensionless broadening parameter. Note that in the limit $\gamma \to 0$ the ε_1 spectrum of the DHO is equivalent to the classical Drude–Lorentz formula, namely

$$\varepsilon_1(E) = \frac{C}{1 - \chi_2^2} \tag{10.146}$$

The DHO is regarded as of two-dimensional M_1 type to a good approximation.

A many-particle effect at the E_2-structure region of the semiconductor has been treated with its detailed energy-band structure [10.94, 10.95]. Results have shown that the absorption at the E_2 edge is markedly weakened, with no drastic change in its shape, by introducing the excitonic interaction. This fact supports the hypothesis that the DHO model is a good representation for the E_2 transitions both with and without the presence of the excitonic interaction.

The E_2 structures in some III–V and II–VI semiconductors are well fitted by the DHO model (Equation (10.144)). However, the structures in the group-IV semiconductors (Si, Ge and α-Sn) could not be successfully fitted by the DHO alone. It is found that the best result can be obtained with a mixture of the DHO and a two-dimensional maximum (M_2) [10.96, 10.97].

The contribution of the two-dimensional maximum to $\varepsilon(E)$ can be given by

$$\varepsilon(E) = -F\chi_{2m}^{-2} \ln \frac{1 - \chi_{cl}^2}{1 - \chi_{2m}^2} \tag{10.147}$$

with

$$\chi_{2m} = \frac{E + i\Gamma}{E_2} \tag{10.148}$$

$$\chi_{cl} = \frac{E + i\Gamma}{E_{cl}} \tag{10.149}$$

where F and Γ represent the strength and broadening parameters of the two-dimensional M_2 (E_2) transitions, respectively, and E_{cl} is a low-energy cutoff assumed to be $E_{cl} \sim E_1$.

(d) Plasma and *d*-band effects

The fundamental optical spectra of many semiconductors are dominated by strong interband transitions observed in the range between the fundamental absorption edge and about 10 eV. Further weak structure is observed around 10–20 eV due to the onset of the real transitions from atomic *d*-band levels into the conduction band. Between these two regions the optical spectra are characterized by a rapid, smooth decrease in the reflectivity or absorption which is similar to the behavior seen in certain metals in the ultraviolet region [10.2]. In this so-called plasma region the valence electrons can behave like free particles and take part in collective oscillations. The energy-loss curve $-\mathrm{Im}\varepsilon^{-1}$ for ZnSe illustrates this behavior well, as demonstrated in Figure 10.27(b). Because Si has no *d* electrons, we cannot observe *d*-band transitions in the optical spectra of this material (Figure 10.27(a)).

Optical properties in the plasma and *d*-band region of semiconductors have been extensively discussed by Philipp and Ehrenreich [10.4], starting from the frequency-dependent dielectric function obtained in the random-phase approximation. The simplest system is represented when a single group of the valence bands $|v\rangle$ is well separated from the core states. Then, at frequencies sufficiently high so that the oscillator strengths of transitions from $|v\rangle$ to higher bands is exhausted, $\varepsilon(E)$ can be described by the Drude model modified by a damping term with the relaxation time τ_{pv}

$$\varepsilon(\omega) = 1 - \frac{\omega_{\mathrm{pv}}^2}{(\omega + i\tau_{\mathrm{pv}}^{-1})^2} \tag{10.150}$$

where the valence-electron plasma frequency ω_{pv} is given by (N_{v} = the density of the valence electrons)

$$\omega_{\mathrm{pv}} = \sqrt{\frac{N_{\mathrm{v}} e^2}{m_{\mathrm{e}} \varepsilon_\infty \varepsilon_0}} \tag{10.151}$$

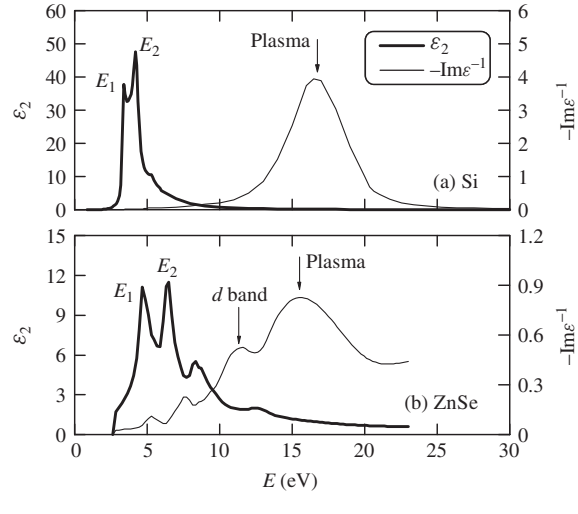

Figure 10.27 Spectral dependence of $\varepsilon_2(E)$ and energy-loss function $-\mathrm{Im}\varepsilon(E)^{-1}$ for: (a) Si; (b) ZnSe. The experimental data plotted are taken from Adachi [10.5]

This situation is met with Si where no d-bands exist and the valence band lies approximately 100 eV above the highest $2p$ core states ($L_{2,3}$ shell). The optical constants of Si above ~6 eV can thus be described well by Equation (10.150) with a value of four electrons per atom for N_v.

When d-bands are present, as in Ge and ZnSe, Equation (10.150) is modified by the oscillator strength coupling between the valence and d-band electrons and can now be written as

$$\varepsilon(\omega) = (1 + \delta\varepsilon_0)\left[1 - \frac{\Omega_{pv}^2}{(\omega + i\tau_{pv}^{-1})^2}\right] \tag{10.152}$$

where the contribution of the d-band electrons to the static dielectric constant is described by $\delta\varepsilon_0$ and Ω_{pv} is an effective plasma frequency different from ω_{pv} due to the influence of the d-band electrons. The relaxation time τ_{pv} in Equation (10.150) or (10.152) lies in the range $1.4-1.8 \times 10^{-16}$ s for diamond-type and zinc-blende-type semiconductors [10.98]. This scattering time is several orders of magnitude smaller than that for lattice or impurity scattering. It is thus considered that electron–electron scattering is the dominant scattering mechanism in the plasma region. If the d-band and valence-electron plasma peaks are well separated as in β-ZnS, we can take account of these contributions independently. In this case, the DHO (Equation (10.144)) is a good representation for the contribution of the d-band electrons to $\varepsilon(E)$ [10.99].

10.4.2 Fundamental optical spectra

Determination of the optical constants above the first absorption edge becomes increasingly difficult, since ε_1 and ε_2 or n and k can no longer be measured independently. The majority of data on the optical constants above the fundamental absorption edge has been derived from normal-incidence reflectivity measurements over a wide spectral range, and the subsequent calculation of the phase shift by means of the Kramers–Kronig relations. Spectroscopic ellipsometry has also been used as an advantageous technique to obtain the fundamental optical spectra of solids. This technique is unquestionably more powerful for a number of reasons. For example, both the real and imaginary parts of the complex dielectric function $\varepsilon = \varepsilon_1 + i\varepsilon_2$ or complex refractive index $n^* = n + ik$ can be obtained directly on a wavelength-by-wavelength basis without having to resort to multiple measurement or Kramers–Kronig analysis. In the following, we present the optical spectra at and above the first absorption edges of Si, GaAs and w-CdS.

(a) Si

We show in Figures 10.28(a) and 10.28(b) the $\varepsilon(E) = \varepsilon_1(E) + i\varepsilon_2(E)$ and $n^*(E) = n(E) + ik(E)$ spectra for Si at $T = 300$ K, respectively. The solid lines represent the MDF fits to the experimental data (open circles). The fitted MDF parameters are listed in Table 10.8. The vertical arrows in Figure 10.28(a) indicate the positions of the E_0', E_1 and E_2 critical points. The corresponding $\alpha(E)$ and $R(E)$ spectra are shown in Figure 10.29. Here, we have made the assumption $G_1^{2D} = 0$ eV, since the detailed value is not yet well known for Si. It should be noted that the experimental ε_1 values are usually somewhat

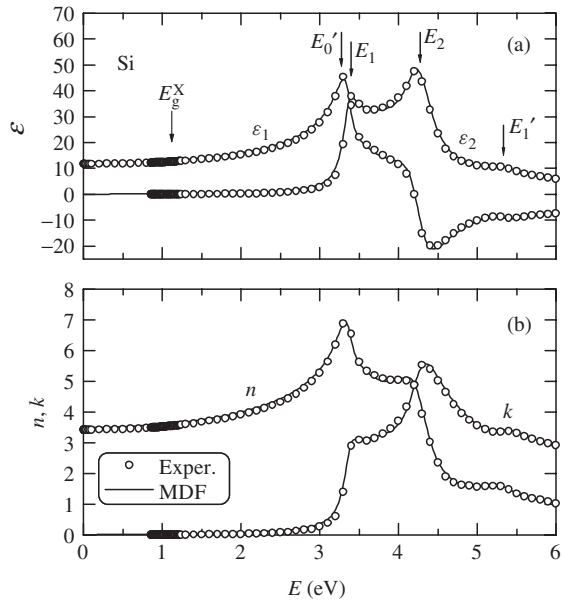

Figure 10.28 (a) Complex dielectric function $\varepsilon(E) = \varepsilon_2(E) + i\varepsilon_2(E)$; (b) complex refractive index $n^*(E) = n(E) + ik(E)$ for Si at 300 K. The experimental data are taken from the tabulation by Adachi [10.5]. The solid lines represent the MDF-calculated results. The fitted MDF parameters are listed in Table 10.8

Table 10.8 MDF critical-point parameter used in the calculation of $\varepsilon(E)$ for Si

Parameter	Value	Parameter	Value
E_1 (eV)	3.38	E_0' (eV)	3.36
B_1	5.22	C	0.30
B_{1x} (eV^2)	8.79	γ	0.12
Γ (eV)	0.08	E_1' (eV)	5.3
E_2 (eV)	4.27	C	0.3
C	2.96	γ	0.1
γ	0.10	$\varepsilon_{1\infty}$	0.20
F	4.35		
Γ (eV)	0.10		

larger than those obtained from the MDF calculation. To improve the fit, therefore, we include in the calculation an additional term $\varepsilon_{1\infty}$ in ε_1. This term is assumed to be nondispersive and may arise from other higher-lying interband transitions.

The fundamental absorption edge of Si corresponds to indirect transitions from the highest valence band at the Γ point to the lowest conduction band near X, E_g^X. The lowest direct transitions in Si occur at or near the Γ point, E_0'. Because of the very weak nature of the indirect absorption edge, its related structure cannot be clearly found in the

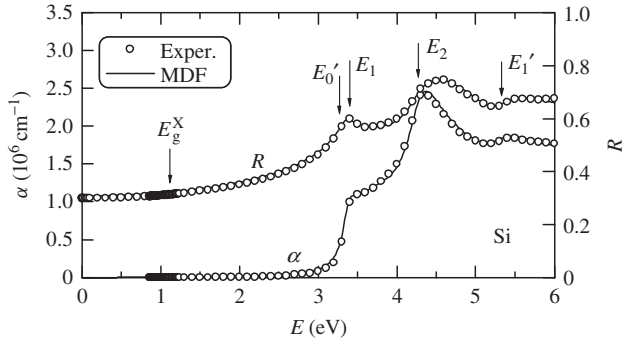

Figure 10.29 Optical absorption $\alpha(E)$ and normal-incidence reflectivity $R(E)$ for Si at 300 K. The experimental data are taken from the tabulation by Adachi [10.5]. The solid lines represent the MDF-calculated results

fundamental optical spectra of Figures 10.28 and 10.29. Note that by using the MDF, the causality, linearity, reality, Kramers–Kronig requirements and compulsory properties of $\varepsilon(E)$ can be satisfied automatically.

(b) GaAs

The lowest direct transitions in GaAs occur at ~1.4 (E_0) and ~1.7 eV ($E_0 + \Delta_0$). The indirect band-gap energies are at ~1.7 (E_g^L) and ~1.9 eV (E_g^X), respectively. The two-dimensional one-electron and excitonic transitions occur at ~2.9 (E_1) and ~3.1 eV ($E_1 + \Delta_1$). The E_0' and E_2 transitions are observed at ~4.5 and ~4.9 eV, respectively. Figures 10.30(a) and 10.30(b) show the $\varepsilon(E) = \varepsilon_1(E) + i\varepsilon_2(E)$ and $n^*(E) = n(E) + ik(E)$ spectra for GaAs at $T = 300$ K, respectively. The positions of the various critical points, such as E_0 and E_1, are suggested in Figure 10.30(a) by the vertical arrows. As for Si, we have made the assumption $G_1^{2D} = G_{1\Delta}^{2D} = 0$ eV for GaAs. The fitted MDF parameters for GaAs are listed in Table 10.9. It is understood from Figure 10.30 that the MDF explains the peculiar $\varepsilon(E)$ and $n^*(E)$ spectra observed in GaAs very well.

Figure 10.31 shows the experimental $\alpha(E)$ and $R(E)$ spectra for GaAs, together with those for the MDF results. The strongest peak in α occurs at ~5 eV. This peak corresponds to the E_2 transitions. In $R(E)$, the critical-point structures due to E_0, E_1, $E_1 + \Delta_1$, E_0' and E_2 can be clearly seen. An excellent agreement can be achieved between the experimental and MDF-calculated spectra over the entire range of photon energies.

(c) *w*-CdS

CdS usually crystallizes in the wurtzite lattice. The material is thus optically anisotropic (uniaxial). In the uniaxial media, two different solutions of the wave equation exist, which describe the ordinary ($\boldsymbol{E} \perp c$) and extraordinary rays ($\boldsymbol{E} \parallel c$). We show in Figures 10.32(a) and 10.32(b) the $\varepsilon(E) = \varepsilon_1(E) + i\varepsilon_2(E)$ and $n^*(E) = n(E) + ik(E)$ spectra for w-CdS obtained at $T = 300$ K, respectively. Figures 10.33(a) and 10.33(b) also show the experimental $\alpha(E)$ and $R(E)$ spectra for w-CdS at $T = 300$ K, respectively.

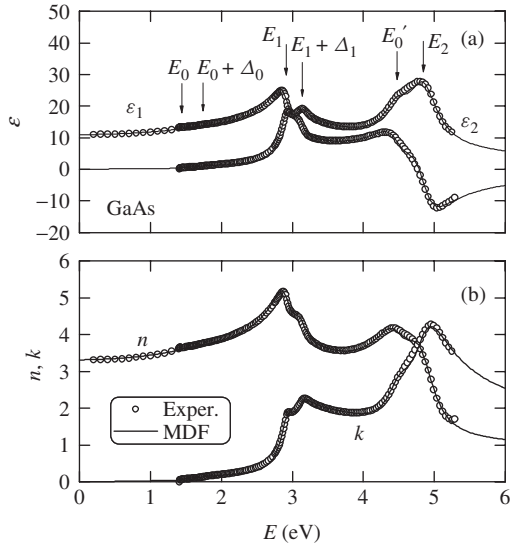

Figure 10.30 (a) Complex dielectric function $\varepsilon(E) = \varepsilon_2(E) + i\varepsilon_2(E)$; (b) complex refractive index $n^*(E) = n(E) + ik(E)$ for GaAs at 300 K. The experimental data are taken from the tabulation by Adachi [10.5]. The solid lines represent the MDF-calculated results. The fitted MDF parameters are listed in Table 10.9

Table 10.9 MDF critical-point parameter used in the calculation of $\varepsilon(E)$ for GaAs

Parameter	Value	Parameter	Value
E_0 (eV)	1.44	E_0' (eV)	4.48
$E_0 + \Delta_0$ (eV)	1.74	C	0.90
A (eV)	2.80	γ	0.10
Γ (eV)	0.025	E_2 (eV)	4.85
E_1 (eV)	2.91	C	1.77
$E_1 + \Delta_1$ (eV)	3.14	γ (eV)	0.10
B_1	4.00	$\varepsilon_{1\infty}$	0.90
B_2	2.00		
B_{1x} (eV^2)	6.40		
B_{2x} (eV^2)	3.45		
Γ (eV)	0.12		

The fundamental absorption edge of w-CdS corresponds to direct transitions at the Γ point in the Brillouin zone. The combined effect of the spin–orbit and crystal-field perturbations in the wurtzite lattice splits the Γ_{15} valence band into Γ_9, Γ_7 and Γ_7 valence bands. The absorption edge of w-CdS thus exhibits three excitonic structures which are particularly sharp at low temperatures. The structures of Γ_7 symmetry (E_{0B} and E_{0C}) can be observed for both $\boldsymbol{E} \perp c$ and $\boldsymbol{E} \parallel c$, while that of Γ_9 symmetry (E_{0A}) can be observed only for $\boldsymbol{E} \perp c$.

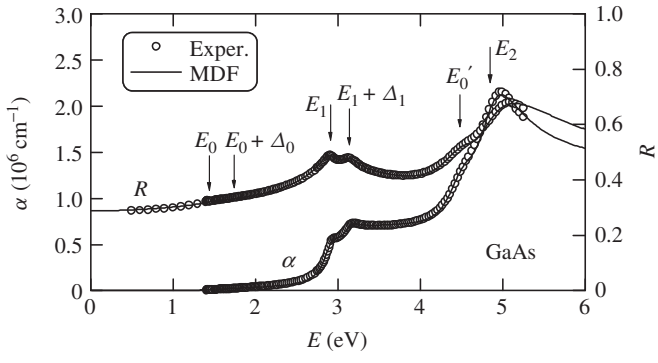

Figure 10.31 Optical absorption $\alpha(E)$ and normal-incidence reflectivity $R(E)$ for GaAs at 300 K. The experimental data are taken from the tabulation by Adachi [10.5]. The solid lines represent the MDF-calculated results

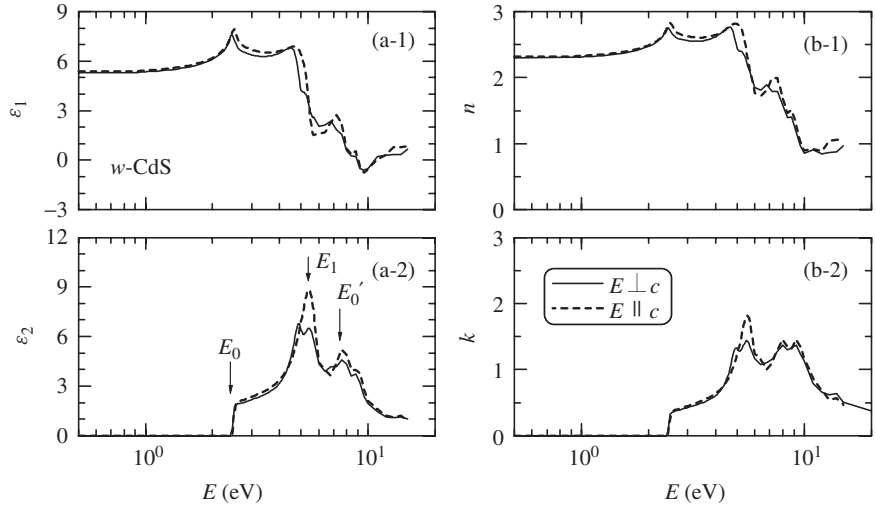

Figure 10.32 (a) Complex dielectric function $\varepsilon(E) = \varepsilon_2(E) + i\varepsilon_2(E)$; (b) complex refractive index $n^*(E) = n(E) + ik(E)$ for w-CdS at 300 K. The experimental data are taken from the tabulation by Adachi [10.5]

The E_{1A} and E_{1B} structures in w-CdS (~4.8–5.5 eV) correspond to the E_1 and $E_1 + \Delta_1$ transitions in the zinc-blende-type semiconductors, except for the existence of a strong polarization effect related to the optical anisotropy of wurtzite. For $\boldsymbol{E} \parallel c$, only the E_{1B} peak is seen, while the E_{1A} and E_{1B} peaks are seen for $\boldsymbol{E} \perp c$. The E_{1A} peak may be related to transitions along the $\Gamma \rightarrow$ A direction of the Brillouin zone. The E_{1B} structure may originate from transitions along the U direction in the Brillouin zone. Note that in w-CdSe the E_{1A} peak splits into two peaks by the spin–orbit interaction [10.100]. The E_0' structure may originate from transitions at or near the Γ point. Reflectivity measurements revealed additional weak peaks, F_1, E_2, E_1', etc., at energies higher than 7 eV [10.101].

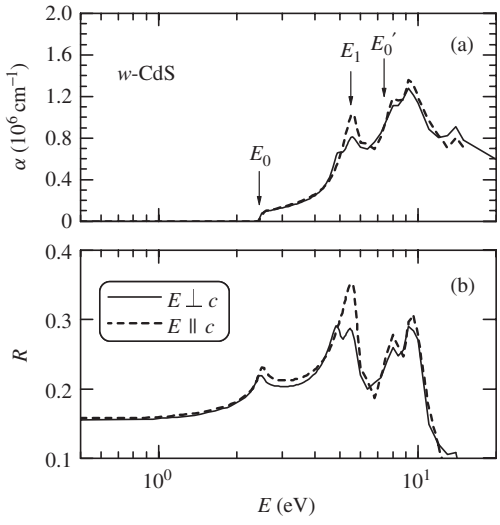

Figure 10.33 (a) Optical absorption $\alpha(E)$; (b) normal-incidence reflectivity $R(E)$ for w-CdS at 300 K. The experimental data are taken from the tabulation by Adachi [10.5]

10.4.3 External perturbation and doping effects

(a) Temperature effect

The effect of temperature leads not only to the shift of the critical-point energies, but also on the broadening of the critical-point structure. We show in Figure 10.34 the temperature dependence of the dielectric function $\varepsilon(E)$ of GaAs measured from $T = 22$ to 753 K using spectroscopic ellipsometry in the 1.3–5.5 eV photon-energy range by Lautenschlager *et al.* [10.102].

The main structures seen in Figure 10.34 are due to the E_1, $E_1 + \Delta_1$, E_0' and E_2 transitions which are clearly observed from 22 up to 753 K. Other weak transitions, such as E_0, $E_0 + \Delta_0$ and some others in the 4.2–5.5 eV region, are observed only at lower temperatures and are difficult to distinguish in Figure 10.34.

It has been found [10.103] that the sharp peaks appearing at the $E_1/(E_1 + \Delta_1)$ edge regions cannot be explained only by the one-electron approximation, Equation (10.139). The two-dimensional-exciton term of Equation (10.142) improves the MDF fit very well. We have already mentioned the temperature dependence of the $E_0/(E_0 + \Delta_0)$ structures of GaAs in Section 10.3.3.

(b) Pressure effect

The dependence on pressure of the complex dielectric functions of Ge and GaAs has been studied theoretically by Alouani *et al.* [10.104] based on the band-structure calculation. They calculated the band structures and optical matrix elements from the relativistic self-consistent linear muffin-tin orbital scheme. All critical-point peaks in $\varepsilon_2(E)$ moved toward higher energies as the pressure was increased. Since their origins in $\boldsymbol{k}$ space

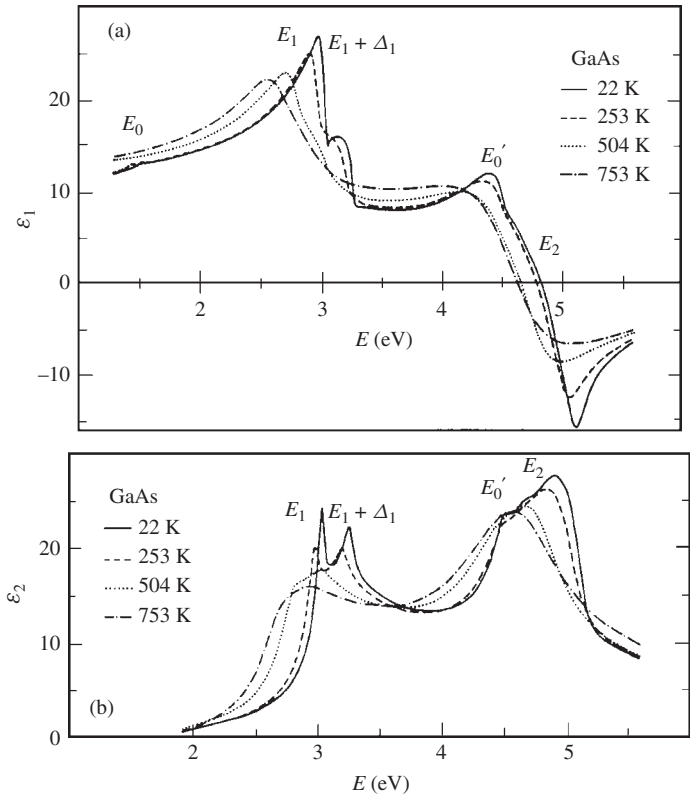

Figure 10.34 (a) Real; (b) imaginary parts of the complex dielectric function of GaAs measured at $T = 22 - 753$ K. [From P. Lautenschlager, M. Garriga, S. Logothetidis, and M. Cardona, *Phys. Rev. B* **35**, 9174 (1987), reproduced by permission from the American Physical Society]

remain unchanged under hydrostatic pressure, the shifts of the peaks to higher energies are considered to be due to the increase of the critical-point energies. To our knowledge, however, no experimental data has been reported on the pressure dependence of the optical constants in the interband transition regions of semiconductors, except at the first absorption edge.

(c) Doping effect

It is well known that heavy doping with impurities influences considerably the physical properties of semiconductors, in particular, transport and optical properties. At moderately low doping levels, localized impurity states develop close to the band edges [10.105]. With increasing dopant concentration the localized states overlap, producing an impurity band. This impurity band is separated from the host conduction or valence band by the so-called Mott gap. At still higher dopant concentrations, the impurity and host bands become mixed to build a new continuum, so that there is no longer a clear distinction between band and impurity states. In this way the degenerate semiconductor resembles a metal [10.105].

The effects of doping on the fundamental absorption edge have been discussed in Section 10.3.3. The main effects of doping on this edge are the formation of band tail because of the random potential of the doped impurities, the Burstein–Moss shift due to the filling of the conduction (valence) band by electrons (holes) and the shrinkage of the band-gap by many-body effects where correlation as well as exchange plays an important role.

The higher edges, above the first absorption one, have been less studied. Only optical techniques, such as reflectivity, electroreflectance, photoluminescence, spectroscopic ellipsometry and resonant Raman scattering, have been used [10.105]. It should be noted that at higher edges the exchange term plays only a small role due to the fact that carriers are located in a small region of $\boldsymbol{k}$ space, different from the region where the transitions occur. The Mott transition is also irrelevant to this problem [10.105].

Spectroscopic ellipsometry has been successfully used to study the effects of doping for Si [10.106, 10.107], Ge [10.105] and GaAs [10.108]. All these studies revealed that the $\varepsilon(E)$ spectrum of heavily doped sample is very similar to that of the undoped material, except that the E_1 and E_2 structures are broadened and shifted to lower energies. The effects of heavy doping at lower photon energies can be described by the Drude model of Equation (10.150) with lifetimes determined by scattering from lattice vibrations [10.106].

When comparing the results obtained for Si and Ge [10.105–10.107] with those for GaAs [10.108], there appear some common features, but also some noticeable differences. The common features concern the qualitatively similar dependence of ΔE_{i} (critical-point energy shift) and $\Delta \Gamma_{\mathrm{i}}$ (Lorentz broadening shift) on doping concentration and the possibility of expressing both effects with the same semiempirical relations, namely, $\Delta E_{\mathrm{i}} \sim p^{\alpha}(n^{\alpha})$ and $\Delta \Gamma_{\mathrm{i}} \sim p^{\alpha}(n^{\alpha})$ [10.108]. The most significant difference is that in GaAs the experimental values of both ΔE_{i} and $\Delta \Gamma_{\mathrm{i}}$ differ considerably for n-type and p-type samples. The ΔE_{i} and $\Delta \Gamma_{\mathrm{i}}$ for n-type GaAs at $n = 1 \times 10^{19}$ cm^{-3} is found to be about 3–4 times larger than those for p-type GaAs ($p = 1 \times 10^{19}$ cm^{-3}). These results have been compared with second-order perturbation calculations of the effects of substitutional impurities on the energy-band structure of GaAs [10.108].

10.5 FREE-CARRIER ABSORPTION AND RELATED PHENOMENA

10.5.1 Free-carrier absorption

Optical absorption can be divided into three separate processes of interest, which are schematically shown in Figure 10.35. The direct or indirect transitions from the valence to the conduction band give rise to the interband absorption contribution α_{VC}. A normal free-carrier absorption α_{FC} is dependent on photon energy approximately as

$$\alpha_{\mathrm{FC}}(E) \propto E^{m} \tag{10.153}$$

where m is dependent on various intraband scattering processes, that is, $m \sim -2.5$ limited by polar optical phonons (α_{oph}), $m \sim -1.5$ limited by acoustic phonons (α_{aph}) and $m \sim -3.5$ limited by ionized-impurity scattering (α_{i}) [10.2]. The final and initial states of the electrons in these transitions lie within the same conduction band. The resulting free-carrier

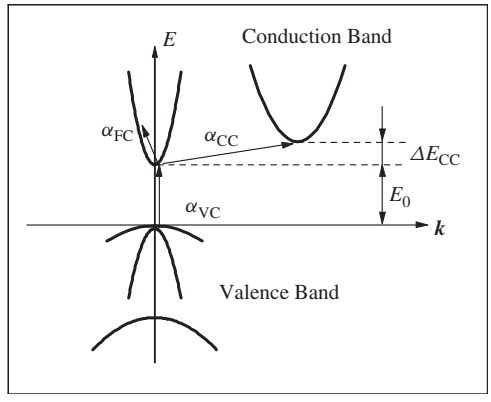

Figure 10.35 Band diagram of the optical absorption in a semiconductor: α_{VC}, direct interband transition from the valence to the conduction band; α_{CC}, indirect interconduction-band transition; α_{FC}, free-carrier intraband transition

absorption is therefore called 'intraband.' The final process depicted in Figure 10.35 is an interconduction-band absorption α_{CC} (see Section 10.5.2). The α_{VC} (α_{CC}) takes place when $E \geqslant E_0$ ($E \geqslant \Delta E_{CC}$). The α_{FC} becomes significant at longer wavelengths.

A free-carrier absorption process in Equation (10.153) is the annihilation of a photon with the excitation of a carrier from a filled state below the Fermi energy E_F to an empty state above it. The energy and momentum have to be conserved in this process, because of absorption or emission of polar optical phonons (α_{oph}), acoustic phonons (α_{aph}) or via scattering with ionized impurities (α_i). A review of theoretical studies of the optical absorption in the free-carrier absorption region has been given by Haga and Kimura [10.109] and Fan [10.110].

A free-carrier effect on the optical properties of simple metals can be described in terms of the classical Drude theory [10.6]. We shall consider this theory since free carriers introduced into semiconductors by doping behave in many ways like those in the simple metals. The main difference between the two is that the carrier concentration in a semiconductor can be changed by doping. Since the doping concentration is typically less than 10^{20} cm^{-3}, the plasma frequencies of carriers in semiconductors are usually in the infrared region (Equation (10.36)), whereas they are in the visible or ultraviolet for metals.

The Drude model starts with an equation of motion for an electron of charge e and mass m_e

$$m_e\left(\frac{d^2x}{dt^2} + \Gamma\frac{dx}{dt} + \omega_0^2 x\right) = eE_f \exp(i\omega t) \tag{10.154}$$

with the damping constant Γ, the restoring force $m_e\omega_0^2 x$ and the field of an electromagnetic wave $E_f \exp(i\omega t)$. This leads to the following dielectric constant [10.2]

$$\varepsilon(\omega) = 1 + \left(\frac{Ne^2}{m_e\varepsilon_0}\right)\left(\frac{1}{\omega_0^2 - \omega^2 - i\Gamma\omega}\right) \tag{10.155}$$

where N is the number of free electrons per unit volume. Since there is no restoring force for the free electrons, we rightly put $\omega_0 \to 0$. Then, Equation (10.155) can be written as

$$\varepsilon(\omega) = \varepsilon_\infty \left(1 - \frac{\omega_p^2}{\omega(\omega + i\Gamma)}\right) \tag{10.156}$$

where we have used the relation between the plasma frequency ω_p, which was screened by the dielectric constant ε_∞, and carrier concentration n (N) of Equation (10.36). From Equation (10.156), we obtain

$$\varepsilon_1(\omega) = \varepsilon_\infty \left(1 - \frac{\omega_p^2}{\omega^2 + \Gamma^2}\right) \tag{10.157a}$$

$$\varepsilon_2(\omega) = \frac{\varepsilon_\infty \omega_p^2 \Gamma}{\omega(\omega^2 + \Gamma^2)} \tag{10.157b}$$

The imaginary part of the dielectric function $\varepsilon_2(E)$ is proportional to Γ; hence, the absorption coefficient is too. The reason for this is well known in metal optics [10.6].

From Equation (10.157b), we obtain

$$\alpha(\omega) = \frac{4\pi}{\lambda} k(\omega) = \frac{\omega}{nc} \varepsilon_2(\omega) = \frac{\varepsilon_\infty \omega_p^2 \Gamma}{nc(\omega^2 + \Gamma^2)} \tag{10.158}$$

where n is the refractive index and c is the speed of light. In the low-frequency limit, this equation becomes

$$\alpha(\omega \to 0) = \frac{\varepsilon_\infty \omega_p^2}{nc\Gamma} = \frac{4\pi N e^2}{ncm_e\Gamma} \tag{10.159}$$

On the other hand, the low-field conductivity for free carriers or for a simple band structure can be written as

$$\sigma = Ne\mu = \frac{Ne^2\tau}{m_e} \tag{10.160}$$

where μ is the low-field mobility and τ is a phenomenological scattering time introduced to account for the scattering of the carrier by phonons and impurities. Comparing α in Equation (10.159) with σ in Equation (10.160), we obtain

$$\alpha = \frac{4\pi\sigma}{nc} \tag{10.161}$$

We can thus equate Γ to τ^{-1} and recognize a distant resemblance between the free-carrier absorption and carrier transport properties. In fact, temperature dependence of low-field mobility, which is limited by each scattering mechanism, shows nearly the same temperature dependence as expected in the free-carrier absorption mechanisms. Quantum-mechanical investigations [10.111] showed that Equation (10.161) is valid only for photon energies which are small compared with the carrier energies ($\hbar\omega < kT$).

Figure 10.36 shows a typical example for the free-carrier absorption in *n*-InP measured by Ballman *et al*. [10.112]. The experimental data indicate that an absorption minimum exists at about 1.6 μm, in agreement with the results reported by others [10.113, 10.114]. At wavelengths $\lambda > 1.6$ μm, free-carrier absorption dominates in the spectra. The dashed line in Figure 10.36 gives a slope that is limited by the ionized impurity scattering ($m \sim 3.5$). The power index m for a heavily doped sample (c) just corresponds to 3.5. It has also been found [10.115] that for *n*-InP m increases with increasing n from about 2.0 ($n \sim 1 \times 10^{16}$ cm^{-3}) to about 3.5 ($n \sim 1 \times 10^{18}$ cm^{-3}). For wavelengths $\lambda \sim 1.3$ μm, the absorption coefficients are still proportional to the free-carrier concentration. This fact may suggest the dominance of interconduction-band absorption in that spectral region (see Section 10.5.2, below).

The infrared absorption spectra for *p*-InP are shown in Figure 10.37. They have been measured by Casey and Carter [10.116] for λ from 1.0 to 3.4 μm for hole concentrations from $p = 3.1 \times 10^{17}$ to 6.6×10^{18} cm^{-3} at $T = 297$ K. The spectrum taken for lightly doped *p*-InP ($p = 6.0 \times 10^{16}$ cm^{-3}) by Ballman *et al*. [10.112] is also shown by the

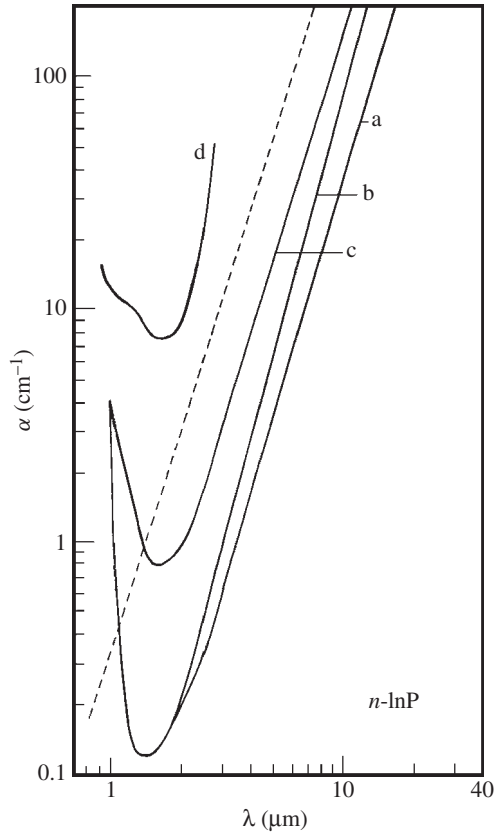

Figure 10.36 Free-carrier absorption in *n*-InP. The electron concentrations are; (a) 3.3×10^{16} cm^{-3}; (b) 4.0×10^{17} cm^{-3}; (c) 8.8×10^{17} cm^{-3}; (d) 5.0×10^{18} cm^{-3}. The dashed line gives a slope that is limited by ionized-impurity scattering. [From A. A. Ballman, A. M. Glass, R. E. Nahory, and H. Brown, *J. Cryst. Growth* **62**, 198 (1983), reproduced by permission from Elsevier]

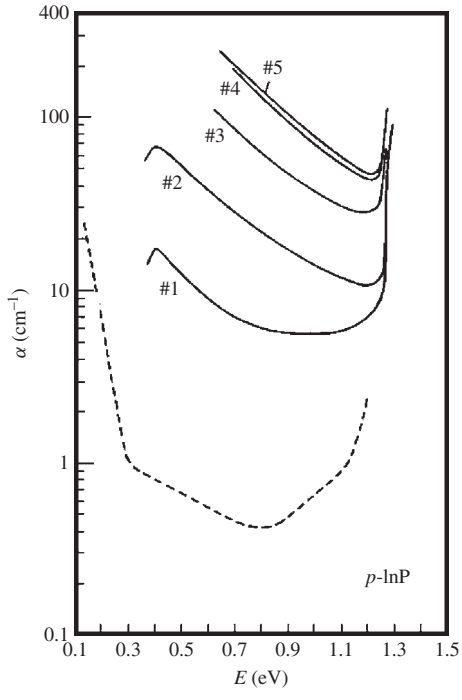

Figure 10.37 Infrared absorption spectra for p-InP at 297 K. The hole concentrations are: (a) 3.1×10^{17} cm^{-3}; (b) 8.6×10^{17} cm^{-3}; (c) 1.9×10^{18} cm^{-3}; (d) 5.3×10^{18} cm^{-3}; (e) 6.6×10^{18} cm^{-3}. [From H. C. Casey, Jr. and P. L. Carter, *Appl. Phys. Lett.* **44**, 82 (1984), reproduced by permission from the American Institute of Physics.] The spectrum taken for lightly doped p-InP ($p = 6.0 \times 10^{16}$ cm^{-3}) by Ballman *et al.* [10.112] is also plotted as the dashed line

dashed line. Similar to the case for n-type semiconductors, the absorption coefficient increases as the hole concentration increases. The concentration variation of α can be written as $\alpha = 14(p/10^{18}\ \text{cm}^{-3})\ \text{cm}^{-1}$ at $\lambda = 1.3\ \mu$m and $20(p/10^{18}\ \text{cm}^{-3})\ \text{cm}^{-1}$ at $\lambda = 1.5\ \mu$m [10.116]. Peaks observed at about 0.4 eV are due to intervalence-band absorption (see Section 10.5.2).

10.5.2 Interconduction-band and intervalence-band absorption

(a) Interconduction-band absorption

The interconduction-band absorption mechanism is schematically shown in Figure 10.35. A promising theoretical interpretation of the interconduction-band absorption was given by Haga and Kimura [10.109]. Briefly, as a photon is absorbed by the crystal, an electron at the bottom of the lowest conduction-band minimum makes a transition to an intermediate state in a higher band at the same point in $\boldsymbol{k}$ space. Then, interacting with an imperfection or with phonons, the electron is scattered to a lower-lying conduction-band minimum (Figure 10.35). The transition mechanism can, thus, be expressed by a second-order perturbation process, as for the indirect optical transition mechanism.

Actually, an optical transition between the lowest conduction band and a higher valley not at the same point in $\boldsymbol{k}$ space is very complicated because of the large number of virtual intermediate sates the transition involves. Haga and Kimura [10.109] introduced a simplification into the theory by separating the transition into I-type and D-type processes, depending on which type of intermediate is most important.

In the I-type process, the intermediate states are in other bands below and above either the initial state or the final state, depending upon whether the electromagnetic interaction is considered before or after the scattering interaction that supplies the necessary change in wavenumber. The E dependence of this absorption results from a density-of-states argument, yielding a fairly well-defined threshold for the onset of absorption and a more slowly varying dependence of the transition probability on E [10.109, 10.114]. The interconduction-band absorption seen in Figure 10.36 for n-InP is a typical example of the I-type process. This type of process has also been observed in n-GaAs [10.117].

In the D-type process the intermediate state is almost identical to the initial state, and partially because of the energy denominators of $\pm E$ in these states the absorption incorporates a E^{-3} dependence. The D-type absorption yields a narrow and peaked band [10.109, 10.114].

Figure 10.38 shows the infrared absorption spectrum of n-GaP measured in the wavelength range 1–10 μm by Wiley and DiDomenico [10.118]. The sample measured was Te-doped with $n \sim 3 \times 10^{17}$ cm^{-3}. The absorption peaking at $\lambda \sim 3$ μm is typical of the D-type interconduction-band absorption. The background is due to the normal free-carrier absorption. The D-type absorption has been observed not only in n-GaP, but also in n-Si [10.119], n-AlSb [10.120] and n-GaSb [10.121].

(b) Intervalence-band absorption

The interband free-carrier absorption occurs not only in the n-type semiconductors but also in p-type ones. In p-type semiconductors, the intervalence-band absorption originates from direct transitions between different branches of the valence band at $\boldsymbol{k} = 0$. The absorption bands peaking at $E \sim 0.4$ eV in Figure 10.37 are due to the intervalence-band absorption.

We show schematically in Figure 10.39 possible types of the intervalence-band transitions in the zinc-blende-type semiconductors. We can expect from Figure 10.39 three types of intervalence-band absorption: SO → HH; SO → LH; and LH → HH. The zinc-blende-type semiconductor has a T_d point-group symmetry. The heavy-hole (HH) and LH (light-hole) bands have Γ_8 symmetry, while the spin–orbit (SO) split-off band has Γ_7 symmetry. The selection rules for the optical transitions between different branches of the valence band can, then, be given by the direct products

$$\text{SO} \rightarrow \text{HH}: \quad \Gamma_7 \times \Gamma_8 = \Gamma_3 + \Gamma_4 + \Gamma_5 \tag{10.162a}$$

$$\text{SO} \rightarrow \text{LH}: \quad \Gamma_7 \times \Gamma_8 = \Gamma_3 + \Gamma_4 + \Gamma_5 \tag{10.162b}$$

$$\text{LH} \rightarrow \text{HH}: \quad \Gamma_8 \times \Gamma_8 = \Gamma_1 + \Gamma_2 + \Gamma_3 + 2\Gamma_4 + 2\Gamma_5 \tag{10.162c}$$

The polarization vector $\boldsymbol{E} \perp (x, y, z)$ of the point group T_d belongs to Γ_5 symmetry. All these products contain the representation of Γ_5 symmetry, indicating that the dipole transitions are possible.

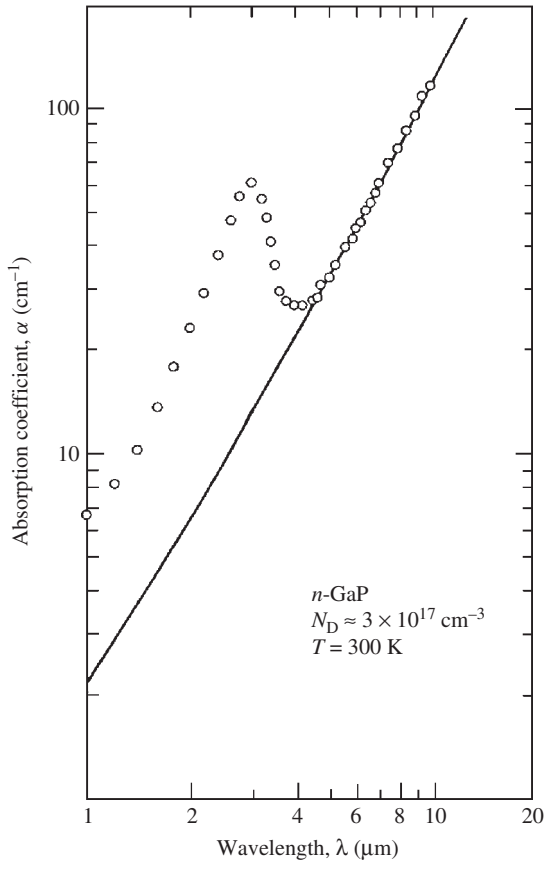

Figure 10.38 Infrared absorption spectrum of *n*-GaP measured in the wavelength range 1–10 μm. The sample used was Te doped, with $n \sim 3 \times 10^{17}$ cm^{-3}. The absorption peaking at $\lambda \sim 3$ μm is typical of the *D*-type interconduction-band absorption. [From J. D. Wiley and M. DiDomenico, Jr., *Phys. Rev. B* **1**, 1655 (1970), reproduced by permission from the American Physical Society]

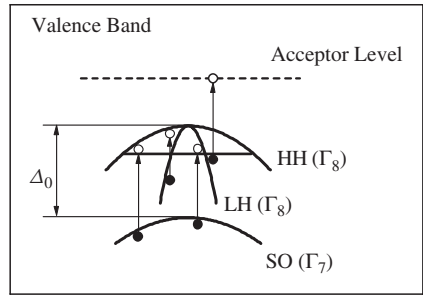

Figure 10.39 Schematic representation of the intervalence-band absorption in a *p*-type, zinc-blende semiconductor

As mentioned in Section 10.3.3, the joint density-of-states function $J_{\alpha\beta}(E)$ measures the product density of full and empty states of equal energy difference. This quantity mainly determines the interband contribution to $\varepsilon_2(E)$ and, thus, to the optical constants of semiconductors. According to the different combinations of the signs of hole masses, we obtain [10.122]

$$J_{\mathrm{HH-SO}}(E) = \begin{cases} V_0\sqrt{E-\Delta_0} & (E > \Delta_0) \\ 0 & (E < \Delta_0) \end{cases} \tag{10.163a}$$

$$J_{\mathrm{LH-SO}}(E) = \begin{cases} 0 & (E > \Delta_0) \\ V_1\sqrt{\Delta_0 - E} & (E < \Delta_0) \end{cases} \tag{10.163b}$$

$$J_{\mathrm{HH-LH}}(E) = V_2\sqrt{E} \tag{10.163c}$$

The SO $\rightarrow$ LH transitions are generally not so important because of a low density of states in the LH band and a very low hole occupancy of final states for transitions at the band-gap energy Δ_0. The larger density of states and hole occupancy in the HH band may produce much greater absorption for the SO $\rightarrow$ HH transitions than for the SO $\rightarrow$ LH transitions.

Intervalence-band absorption has been observed experimentally in various p-type semiconductors, such as Ge [10.123], AlSb [10.124], GaAs [10.124–10.126], GaSb [10.121], InP [10.116, 10.126], InAs [10.127] and InSb [10.128]. Figure 10.40

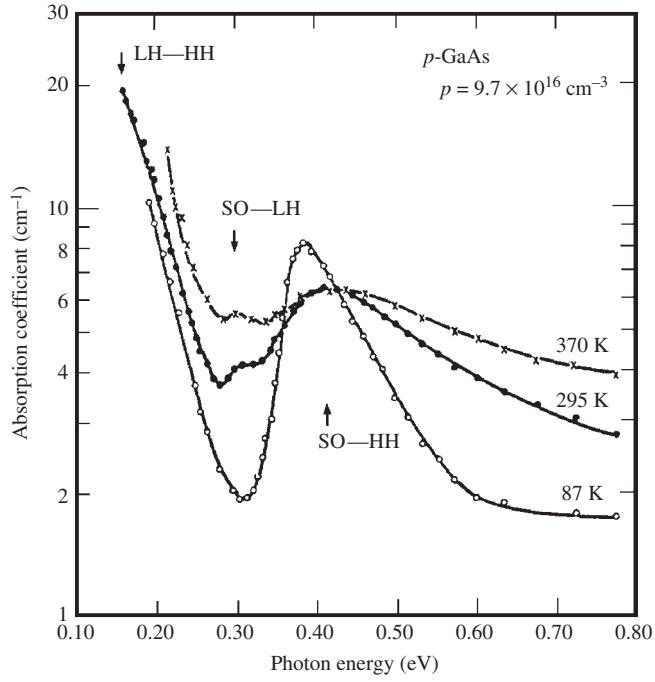

Figure 10.40 Optical absorption spectra of p-GaAs ($p \sim 9.7 \times 10^{16}$ cm^{-3}) as a function of temperature from 87 to 370 K. [From R. Braunstein, *J. Phys. Chem. Solids* **8**, 280 (1959), reproduced by permission from Elsevier]

shows, as an example, the intervalence-band absorption observed in p-GaAs ($p \sim 9.7 \times 10^{16}$ cm^{-3}) by Braunstein [10.125]. At $T = 295$ K, there is a band at 0.42 eV, a partially resolved band at 0.31 eV and the onset of a band at 0.25 eV. As the temperature is decreased, the bands sharpen and become slightly displaced from the room-temperature positions. The band at 0.42 eV is attributed to transitions between the SO and HH bands; the peak at 0.31 eV is attributed to transitions between the SO and LH bands. The onset of the absorption band at 0.25 eV is also attributed to transitions between the LH and HH bands.

10.5.3 Free-carrier-induced change in refractive index

From Equation (10.157a) and in the limit $\Gamma \to 0$ cm^{-1}, we obtain the free-carrier-induced change in the refractive index Δn_{f}

$$\Delta n_{\mathrm{f}} = \frac{\partial n}{\partial N}\Delta N = -\frac{e^2\lambda^2 \Delta N}{8\pi^2 n \varepsilon_0 c^2 m_{\mathrm{e}}} \tag{10.164}$$

where we have used $n^2 \sim \varepsilon_1$ and $2n\Delta n \sim \Delta\varepsilon_1$. The above equation suggests that the change in refractive index Δn_{f} is directly proportional to λ^2, ΔN and n^{-1}.

When both electrons and holes are present in a substance, as is usual for injection lasers, the change Δn_{f} can be written, from Equation (10.164), as

$$\Delta n_{\mathrm{f}} = \frac{\partial n}{\partial N}\Delta N = -\frac{e^2\lambda^2}{8\pi^2 n \varepsilon_0 c^2}\left(\frac{\Delta N}{m_{\mathrm{e}}} + \frac{\Delta P}{m_{\mathrm{h}}}\right) \tag{10.165}$$

where ΔP is the change in the hole concentration.

REFERENCES

[10.1] J. F. Nye, *Physical Properties of Crystals* (Clarendon, Oxford, 1972).
[10.2] See, for example, G. Harbeke, in *Optical Properties of Solids*, edited by F. Abelès (North-Holland, Amsterdam, 1972), p. 21.
[10.3] P. Nozieres and D. Pines, *Phys. Rev.* **113**, 1254 (1959).
[10.4] H. R. Philipp and H. Ehrenreich, *Phys. Rev.* **129**, 1550 (1963).
[10.5] S. Adachi, *Optical Constants of Crystalline and Amorphous Semiconductors: Numerical Data and Graphical Information* (Kluwer Academic, Boston, 1999).
[10.6] See, for example, F. Wooten, *Optical Properties of Solids* (Academic, New York, 1972).
[10.7] L. Marton, *Rev. Mod. Phys.* **28**, 172 (1956).
[10.8] G. A. Samara, *Phys. Rev. B* **27**, 3494 (1983).
[10.9] Y. P. Varshni, *Physica* **34**, 149 (1967).
[10.10] A. R. Goñi, K. Syassen, K. Strössner, and M. Cardona, *Semicond. Sci. Technol.* **4**, 246 (1989).
[10.11] A. R. Goñi, K. Syassen, and M. Cardona, *Phys. Rev. B* **41**, 10104 (1990).
[10.12] G. Theodorou and G. Tsegas, *Phys. Status Solidi B* **211**, 197 (1999).
[10.13] J.-M. Wagner and F. Bechstedt, *Phys. Rev. B* **62**, 4526 (2000).
[10.14] B. H. Bairamov, I. P. Ipatova, V. A. Milorava, V. V. Toporov, K. Naukkarinen, T. Tuomi, G. Irmer, and J. Monecke, *Phys. Rev. B* **38**, 5722 (1988).

[10.15] S. Adachi, *GaAs and Related Materials: Bulk Semiconducting and Superlattice Properties* (World Scientific, Singapore, 1994).
[10.16] R. T. Holm, J. W. Gibson, and E. D. Palik, *J. Appl. Phys.* **48**, 212 (1977).
[10.17] A. Mooradian and G. B. Wright, *Phys. Rev. Lett.* **16**, 999 (1966).
[10.18] J. D. Axe and R. Hammer, *Phys. Rev.* **162**, 700 (1967).
[10.19] C. G. Olson and D. W. Lynch, *Phys. Rev.* **177**, 1231 (1969).
[10.20] H. R. Chandrasekhar and A. K. Ramdas, *Phys. Rev. B* **21**, 1511 (1980).
[10.21] A. A. Kukharskii, *Solid State Commun.* **13**, 1761 (1973).
[10.22] C. C. Wang, M. Cardona, and A. G. Fischer, *RCA Rev.* **25**, 159 (1964).
[10.23] M. Balkanski, in *Optical Properties of Solids*, edited by F. Abelès (North-Holland, Amsterdam, 1972), p. 529.
[10.24] G. Mirjalili, T. J. Parker, S. F. Shayesteh, M. M. Bülbül, S. R. P. Smith, T. S. Cheng, and C. T. Foxon, *Phys. Rev. B* **57**, 4656 (1998).
[10.25] R. J. Collins and H. Y. Fan, *Phys. Rev.* **93**, 674 (1954).
[10.26] M. M. Pradhan, R. K. Garg, and M. Arora, *Infrared Phys.* **27**, 25 (1987).
[10.27] Z. Jichang, W. Jiangen, M. Bilan, Z. Jingbing, and Q. Fenyuan, *Infrared Phys.* **33**, 381 (1992).
[10.28] R. J. Elliott, *Phys. Rev.* **108**, 1384 (1957).
[10.29] R. S. Knox, *Theory of Excitons* (Academic, New York, 1963).
[10.30] D. C. Reynolds and T. C. Collins, *Excitons: Their Properties and Uses* (Academic, New York, 1981).
[10.31] M. D. Sturge, *Phys. Rev.* **127**, 768 (1962).
[10.32] A. R. Goñi, A. Cantarero, K. Syassen, and M. Cardona, *Phys. Rev. B* **41**, 10111 (1990).
[10.33] A. Mang, K. Reimann, and St. Rübenacke, *Solid State Commun.* **94**, 251 (1995).
[10.34] A. Mang, K. Reimann, St. Rübenacke, and M. Steube, *Phys. Rev. B* **53**, 16283 (1996).
[10.35] K. Reimann and M. Steube, in *Proc. 25th Int. Conf. Phys. Semicond.*, edited by N. Miura and T. Ando (Springer, Berlin, 2001), p. 1533.
[10.36] See, K. Reimann, M. Haselhoff, St. Rübenacke, and M. Steube, *Phys. Status Solidi B* **198**, 71 (1996).
[10.37] D. W. Langer, R. N. Euwema, K. Era, and T. Koda, *Phys. Rev. B* **2**, 4005 (1970).
[10.38] M. Julier, J. Campo, B. Gil, J. P. Lascaray, and S. Nakamura, *Phys. Rev. B* **57**, R6791 (1998).
[10.39] P. P. Paskov, T. Paskova, P. O. Holtz, and B. Monemar, *Phys. Rev. B* **64**, 115201 (2001).
[10.40] B. Gil, *Phys. Rev. B* **64**, 201310 (2001); B. Gil, A. Lusson, V. Sallet, S.-A. Said-Hassani, R. Triboulet, and P. Bigenwald, *Jpn. J. Appl. Phys.* **40**, L1089 (2001).
[10.41] D. T. F. Marple, *J. Appl. Phys.* **35**, 539 (1964).
[10.42] S. H. Wemple and M. DiDomenico, Jr., *Phys. Rev. B* **3**, 1338 (1971).
[10.43] M. A. Afromowitz, *Solid State Commun.* **15**, 59 (1974).
[10.44] A. N. Pikhtin and A. D. Yas'kov, *Sov. Phys. Semicond.* **12**, 622 (1978).
[10.45] S. Adachi, *J. Appl. Phys.* **53**, 5863 (1982).
[10.46] L. I. Korovin, *Sov. Phys. Solid State* **1**, 1202 (1960).
[10.47] M. Cardona, in *Solid State Physics, Nuclear Physics and Particle Physics*, edited by I. Saavedra (Benjamin, New York, 1968), p. 737.
[10.48] P. Y. Yu and M. Cardona, *J. Phys. Chem. Solids* **34**, 29 (1973).
[10.49] S. Adachi, *J. Appl. Phys.* **58**, R1 (1985).
[10.50] S. Adachi, *J. Appl. Phys.* **61**, 4869 (1987).
[10.51] T. S. Moss, *Optical Properties of Semiconductors* (Butterworth, London, 1959).
[10.52] M. Toda, *IEEE J. Quantum Electron.* **QE-23**, 483 (1987).
[10.53] D. R. Penn, *Phys. Rev.* **128**, 2093 (1962).
[10.54] P. Y. Yu and M. Cardona, *Phys. Rev. B* **2**, 3193 (1970).
[10.55] See, for example, R. Dalven, in *Solid State Physics*, edited by H. Ehrenreich, F. Seitz, and D. Turnbull, (Academic, New York, 1973), vol. 28, p. 179.

[10.56] S. Adachi, *Optical Properties of Crystalline and Amorphous Semiconductors: Materials and Fundamental Principles* (Kluwer Academic, Boston, 1999).
[10.57] E. Gini and H. Melchior, *J. Appl. Phys.* **79**, 4335 (1996).
[10.58] G. E. Jellison, Jr. and H. H. Burke, *J. Appl. Phys.* **60**, 841 (1986).
[10.59] M. Bertolotti, V. Bogdanov, A. Ferrari, A. Jascow, N. Nazorova, A. Pikhtin, and L. Schirone, *J. Opt. Soc. Am. B* **7**, 918 (1990).
[10.60] J. A. McCaulley, V. M. Donnelly, M. Vernon, and I. Taha, *Phys. Rev. B* **49**, 7408 (1994).
[10.61] G. Ghosh, *Appl. Phys. Lett.* **66**, 3570 (1995).
[10.62] S. R. Kisting, P. W. Bohn, E. Andideh, I. Adesida, B. T. Cunningham, G. E. Stillman, and T. D. Harris, *Appl. Phys. Lett.* **57**, 1328 (1990).
[10.63] H. H. Li, *J. Phys. Chem. Ref. Data* **13**, 103 (1984).
[10.64] K. Strössner, S. Ves, and M. Cardona, *Phys. Rev. B* **32**, 6614 (1985).
[10.65] M. Lindner, G. F. Schötz, P. Link, H. P. Wagner, W. Kuhn, and W. Gebhardt, *J. Phys. Condens. Matter* **4**, 6401 (1992).
[10.66] E. Griebl, G. F. Schötz, C. Birzer, W. Kerner, T. Reisinger, B. Hahn, and W. Gebhardt, *Acta Phys. Polonica A* **88**, 995 (1995).
[10.67] Z.-H. Zhou, B. Choi, M. I. Flik, S. Fan, and R. Reif, *J. Appl. Phys.* **76**, 2448 (1994).
[10.68] V. B. Bogdanov, A. N. Pikhtin, V. F. Tsvetkov, and A. D. Yaskov, *Opt. Spectrosc.* **52**, 644 (1982).
[10.69] D. D. Sell, H. C. Casey, Jr., and K. W. Wecht, *J. Appl. Phys.* **45**, 2650 (1974).
[10.70] P. P. Paskov, *IEEE J. Quantum Electron.* **30**, 2771 (1994).
[10.71] P. Martin, E. M. Skouri, L. Chusseau, and C. Alibert, *Appl. Phys. Lett.* **67**, 881 (1995).
[10.72] L. Chusseau, P. Martin, C. Brasseur, C. Alibert, P. Hervé, P. Arguel, F. Lozes-Dupuy, and E. V. K. Rao, *Appl. Phys. Lett.* **69**, 3054 (1996).
[10.73] P. P. Paskov, *J. Appl. Phys.* **81**, 1890 (1997).
[10.74] F. Bassani and G. P. Parravicini, *Electronic States and Optical Transitions in Solids* (Pergamon, Oxford, 1975).
[10.75] M. R. Lorenz, R. Chicotka, G. D. Pettit, and P. J. Dean, *Solid State Commun.* **8**, 693 (1970).
[10.76] A. R. Goñi, K. Strössner, K. Syassen, and M. Cardona, *Phys. Rev. B* **36**, 1581 (1987).
[10.77] K. Strössner, S. Ves, C. K. Kim, and M. Cardona, *Phys. Rev. B* **33**, 4044 (1986).
[10.78] H. C. Casey, Jr., D. D. Sell, and K. W. Wecht, *J. Appl. Phys.* **46**, 250 (1975).
[10.79] G. B. Lush, M. R. Melloch, M. S. Lundstrom, H. F. MacMillan, and S. Asher, *J. Appl. Phys.* **74**, 4694 (1993).
[10.80] F. Urbach, *Phys. Rev.* **92**, 1324 (1953).
[10.81] J. D. Dow and D. Redfield, *Phys. Rev. B* **5**, 594 (1972).
[10.82] C. W. Greeff and H. R. Glyde, *Phys. Rev. B* **51**, 1778 (1995).
[10.83] S. R. Johnson and T. Tiedje, *J. Appl. Phys.* **78**, 5609 (1995).
[10.84] C. H. Grein and S. John, *Phys. Rev. B* **39**, 1140 (1989).
[10.85] S. Chichibu, T. Mizutani, T. Shioda, H. Nakanishi, T. Deguchi, T. Azuhata, T. Sota, and S. Nakamura, *Appl. Phys. Lett.* **70**, 3440 (1997).
[10.86] A. Iribarren, R. Castro-Rodríguez, V. Sosa, and J. L. Peña, *Phys. Rev. B* **58**, 1907 (1998).
[10.87] M. Beaudoin, A. J. G. DeVries, S. R. Johnson, H. Laman, and T. Tiedje, *Appl. Phys. Lett.* **70**, 3540 (1997).
[10.88] J. R. Dixon and J. M. Ellis, *Phys. Rev.* **123**, 1560 (1961).
[10.89] S. W. Kurnick and J. M. Powell, *Phys. Rev.* **116**, 597 (1959).
[10.90] Y. Brada, B. G. Yacobi, and A. Peled, *Solid State Commun.* **17**, 1975 (1975).
[10.91] A. E. Rakhshani, *J. Phys.: Condens. Matter* **12**, 4391 (2000).
[10.92] J. T. Mullins, J. Carles, and A. W. Brinkman, *J. Appl. Phys.* **81**, 6374 (1997).
[10.93] B. Velický and J. Sak, *Phys. Status Solidi* **16**, 147 (1966).
[10.94] W. Hanke and L. J. Sham, *Phys. Rev. B* **21**, 4656 (1980).
[10.95] M. del Castillo-Mussot and L. J. Sham, *Phys. Rev. B* **31**, 2092 (1985).

[10.96] S. Adachi, *Phys. Rev. B* **38**, 12966 (1988).
[10.97] S. Adachi, *J. Appl. Phys.* **66**, 813 (1989).
[10.98] D. L. Greenaway and G. Harbeke, *Optical Properties and Band Structure of Semiconductors* (Pergamon, Oxford, 1968).
[10.99] T. Tsuchiya, S. Ozaki, and S. Adachi, *J. Phys.: Condens. Matter* **15**, 3717 (2003).
[10.100] S. Logothetidis, M. Cardona, P. Lautenschlager, and M. Garriga, *Phys. Rev. B* **34**, 2458 (1986).
[10.101] M. Cardona and G. Harbeke, *Phys. Rev.* **137**, A1467 (1964).
[10.102] P. Lautenschlager, M. Garriga, S. Logothetidis, and M. Cardona, *Phys. Rev. B* **35**, 9174 (1987).
[10.103] S. Adachi, *Phys. Rev. B* **41**, 1003 (1990).
[10.104] M. Alouani, L. Brey, and N. E. Christensen, *Phys. Rev. B* **37**, 1167 (1988).
[10.105] See, L. Viña and M. Cardona, *Phys. Rev. B* **34**, 2586 (1986), and references cited therein.
[10.106] D. E. Aspnes, A. A. Studna, and E. Kinsbron, *Phys. Rev. B* **29**, 768 (1984).
[10.107] L. Viña and M. Cardona, *Phys. Rev. B* **29**, 6739 (1984).
[10.108] F. Lukeš, S. Gopalan, and M. Cardona, *Phys. Rev. B* **47**, 7071 (1993).
[10.109] E. Haga and H. Kimura, *J. Phys. Soc. Jpn* **18**, 777 (1963); **19**, 471 (1964); **19**, 658 (1964); **19**, 1596 (1964).
[10.110] H. Y. Fan, in *Semiconductors and Semimetals*, edited by R. K. Willardson and A. C. Beer (Academic, New York, 1967), Vol. 3, p. 405.
[10.111] W. P. Dumke, *Phys. Rev.* **124**, 1813 (1961).
[10.112] A. A. Ballman, A. M. Glass, R. E. Nahory, and H. Brown, *J. Cryst. Growth* **62**, 198 (1983).
[10.113] M. R. Lorenz, W. Reuter, W. P. Dumke, R. J. Chicotka, G. D. Pettit, and J. M. Woodall, *Appl. Phys. Lett.* **13**, 421 (1968).
[10.114] W. P. Dumke, M. R. Lorenz, and G. D. Pettit, *Phys. Rev. B* **1**, 4668 (1970).
[10.115] M. Yamaguchi, A. Yamamoto, S. Shinoyama, and H. Sugiura, *J. Appl. Phys.* **53**, 633 (1982).
[10.116] H. C. Casey, Jr. and P. L. Carter, *Appl. Phys. Lett.* **44**, 82 (1984).
[10.117] A. S. Jordan, *J. Appl. Phys.* **51**, 2218 (1980).
[10.118] J. D. Wiley and M. DiDomenico, Jr., *Phys. Rev. B* **1**, 1655 (1970).
[10.119] W. Spitzer and H. Y. Fan, *Phys. Rev.* **108**, 268 (1957).
[10.120] W. J. Turner and W. E. Reese, *Phys. Rev.* **117**, 1003 (1960).
[10.121] W. M. Becker, A. K. Ramdas, and H. Y. Fan, *J. Appl. Phys.* **32**, 2094 (1961).
[10.122] S. Adachi, *J. Appl. Phys.* **53**, 8775 (1982).
[10.123] H. B. Briggs and R. C. Fletcher, *Phys. Rev.* **91**, 1342 (1953).
[10.124] R. Braunstein and E. O. Kane, *J. Phys. Chem. Solids* **23**, 1423 (1962).
[10.125] R. Braunstein, *J. Phys. Chem. Solids* **8**, 280 (1959).
[10.126] C. H. Henry, R. A. Logan, F. R. Merritt, and J. P. Luongo, *IEEE J. Quantum Electron.* **QE-19**, 947 (1983).
[10.127] F. Matossi and F. Stern, *Phys. Rev.* **111**, 472 (1958).
[10.128] G. W. Gobeli and H. Y. Fan, *Phys. Rev.* **119**, 613 (1960).

11 Elasto-optic, Electro-optic and Nonlinear Optical Properties

11.1 Elasto-optic effect 283
11.1.1 Theoretical expression 283
11.1.2 Experimental value 285
11.2 Linear electro-optic constant 291
11.2.1 Theoretical expression 291
11.2.2 Experimental value 294
11.3 Quadratic electro-optic constant 295
11.3.1 Theoretical expression 295
11.3.2 Experimental value 298
11.4 Franz–Keldysh effect 300
11.4.1 Theoretical expression 300
11.4.2 Experimental value 301
11.5 Nonlinear optical constant 302
11.5.1 Second-order nonlinear optical susceptibility 302
11.5.2 Third-order nonlinear optical susceptibility 308
11.5.3 Two-photon absorption 309
References 311

11.1 ELASTO-OPTIC EFFECT

11.1.1 Theoretical expression

Knowledge of the elasto-optic or photoelastic behavior plays an important role not only in the design of elasto-optic devices, such as light modulators, deflectors and switches [11.1, 11.2], but also in the analysis of strain problems in semiconductor heteroepitaxy [11.3–11.5]. The distribution of stress in heteroepitaxial layers is a subject of perennial interest since internal stress arises normally in thin epitaxial films during their preparation by heteroepitaxial growth.

It is noted that the photoelasticity is dependent on wavelength. There are several theoretical works dealing with the spectral dependence of photoelasticity [11.6–11.11]. The application of an external uniaxial stress to a solid produces a change in its crystal symmetry that results in significant changes in its electronic and optical properties. Optically isotropic semiconductors, such as Si and GaAs, then become birefringent under the action of this stress.

Properties of Group-IV, III–V and II–VI Semiconductors Sadao Adachi

© 2005 John Wiley & Sons, Ltd

ISBN: 0-470-09032-4

The uniaxial stress effect can be expressed as

$$\alpha_{\mathrm{pe}} = \frac{\Delta\varepsilon_{ij}}{X} = -\sum_{mn} \varepsilon_{ii}\,\varepsilon_{jj}\,p_{ijkl}\,S_{klmn} \tag{11.1}$$

where α_{pe} is the linear photoelastic coefficient, ε_{ii} (ε_{jj}) is the component of the dielectric tensor in the absence of the stress, p_{ijkl} is the component of the photoelastic tensor and S_{klmn} is the component of the elastic compliance tensor; $\Delta\varepsilon_{ij}$ is the change in the dielectric constant parallel ($\|$) and perpendicular ($\perp$) to the direction of the stress X:

$$\Delta\varepsilon_{ij} = \varepsilon(\|) - \varepsilon(\perp) = \alpha_{\mathrm{pe}} X \tag{11.2}$$

The photoelastic tensor is, in general, a *complex* fourth-rank tensor. We summarize in Table 11.1 the form of the photoelastic tensor $[p]$ for the cubic, hexagonal and rhombohedral systems, where m and n in p_{mn} represent ij and kl, respectively, according to the rules $xx \to 1$, $yy \to 2$, $zz \to 3$, $yz \to 4$, $zx \to 5$ and $xy \to 6$ [11.12].

The photoelastic component p_{ijkl} can be defined by means of the inverse dielectric constant as

$$\Delta\left(\frac{1}{\varepsilon}\right)_{ij} = -\frac{\Delta\varepsilon_{ij}}{\varepsilon_{ii}\,\varepsilon_{jj}} = \sum_{kl} p_{ijkl}\,e_{kl} \tag{11.3}$$

Table 11.1 Form of the photoelastic tensor for semiconductors of certain symmetry classes

Symmetry class	Material	Tensor form
Cubic	Si, 3C-SiC, GaAs, MgO, ZnSe, etc.	$\begin{bmatrix} p_{11} & p_{12} & p_{12} & 0 & 0 & 0 \\ p_{12} & p_{11} & p_{12} & 0 & 0 & 0 \\ p_{12} & p_{12} & p_{11} & 0 & 0 & 0 \\ 0 & 0 & 0 & p_{44} & 0 & 0 \\ 0 & 0 & 0 & 0 & p_{44} & 0 \\ 0 & 0 & 0 & 0 & 0 & p_{44} \end{bmatrix}$
Hexagonal	4H-SiC, h-BN, α-GaN, w-CdS, etc.	$\begin{bmatrix} p_{11} & p_{12} & p_{13} & 0 & 0 & 0 \\ p_{12} & p_{11} & p_{13} & 0 & 0 & 0 \\ p_{31} & p_{31} & p_{33} & 0 & 0 & 0 \\ 0 & 0 & 0 & p_{44} & 0 & 0 \\ 0 & 0 & 0 & 0 & p_{44} & 0 \\ 0 & 0 & 0 & 0 & 0 & p_{66} \end{bmatrix}$ $p_{66} = 1/2(p_{11} - p_{12})$
Rhombohedral	15R-SiC	$\begin{bmatrix} p_{11} & p_{12} & p_{13} & p_{14} & 0 & 0 \\ p_{12} & p_{11} & p_{13} & -p_{14} & 0 & 0 \\ p_{31} & p_{31} & p_{33} & 0 & 0 & 0 \\ p_{41} & -p_{41} & 0 & p_{44} & 0 & 0 \\ 0 & 0 & 0 & 0 & p_{44} & p_{41} \\ 0 & 0 & 0 & 0 & p_{14} & p_{66} \end{bmatrix}$ $p_{66} = 1/2(p_{11} - p_{12})$

where e_{kl} is the strain component that is connected with the stress through Equation (4.22). The first-order change in the dielectric constant $\Delta\varepsilon$ is given by

$$\Delta\varepsilon = \sum_i \left(\frac{\partial\varepsilon}{\partial M_i}\Delta M_i + \frac{\partial\varepsilon}{\partial E_{gi}}\Delta E_{gi} \right) \tag{11.4}$$

where M_i and E_{gi} are, respectively, the strength parameter and critical-point energy of the ith transition (E_0, $E_0 + \Delta_0$, E_1, $E_1 + \Delta_1$, E_0', etc.). Introducing the one-electron term in Equation (10.78) ($\varepsilon_1(E) \sim n(E)^2$) into Equation (11.4), we obtain the expression for the photoelastic coefficient α_{pe} in the transparent region of cubic semiconductors as [11.10]

$$\alpha_{pe} = C^* \left\{ -g(\chi_0^*) + \frac{4E_0}{\Delta_0} \left[f(\chi_0^*) - \left(\frac{E_0}{E_0 + \Delta_0} \right)^{3/2} f(\chi_{so}^*) \right] \right\} + D^* \tag{11.5}$$

with

$$C^* = \begin{cases} \dfrac{3}{4} A^* b (S_{11} - S_{12}) E_0^{-1} & \text{for } \boldsymbol{X} = [100] \\ \dfrac{\sqrt{3}}{8} A^* d S_{44} E_0^{-1} & \text{for } \boldsymbol{X} = [111] \end{cases} \tag{11.6}$$

$$g(\chi_0^*) = \chi_0^{*-2} \left[2 - (1 + \chi_0^*)^{-1/2} - (1 - \chi_0^*)^{-1/2} \right] \tag{11.7}$$

where b and d are the shear deformation potentials of the valence bands (Section 8.1) and $f(\chi)$ and χ_0^* (χ_{so}^*) are defined by Equations (10.79) and (10.80), respectively. In Equation (11.5), the first term corresponds to the contributions from the E_0 and $E_0 + \Delta_0$ transitions and the second term D^* corresponds to those from other, far-off critical points in the band structure (E_1, $E_1 + \Delta_1$, E_0', etc.). Like B^* in Equation (10.78), the term D^* in Equation (11.5) is assumed to be nondispersive. The first and second terms in the curly bracket of Equation (11.5) come from the change in E_g and M with the applied stress, respectively. It is noted that $g(\chi_0^*)$ shows a very sharp dispersion near the band edge, $\chi_0^* \sim 1.0$, compared with $f(\chi_0^*)$. The parameters C^* and D^* are treated as adjustable parameters to fit experimental data. The photoelastic constants for hexagonal semiconductors can also be expressed in essentially the same form as Equation (11.5) [11.13].

11.1.2 Experimental value

The photoelastic coefficient α_{pe} or photoelastic constant p_{ij} can be determined from a stress-induced birefringence (piezobirefringence) measurement. Piezobirefringence data have been reported for a variety of semiconductors. These data are accurate especially in the region below or near the fundamental absorption edge. This is because the measurement employs transmission of light through the sample and is consequently limited to a frequency range where the material is transparent.

Table 11.2 summarizes the p_{ij} values in the long-wavelength limit ($E \to 0$ eV) for some cubic group-IV, III–V and II–VI semiconductors. The same values, but for hexagonal semiconductors, are listed in Table 11.3. Figure 11.1 also plots the $p_{11} - p_{12}$ and p_{44} values in the long-wavelength limit versus lowest direct band-gap energy E_0 for

Table 11.2 Photoelastic constant p_{ij} in the long-wavelength limit ($E \to 0$ eV) for some cubic group-IV, III–V and II–VI semiconductors

System	Material	$p_{11} - p_{12}$	p_{44}	System	Material	$p_{11} - p_{12}$	p_{44}
IV	Diamond	−0.31	−0.17	II–VI	MgO	−0.257	−0.096
	Si	−0.111	−0.051		β-ZnS	−0.08	−0.08
	Ge	−0.028	−0.073		ZnSe	−0.08	−0.08
	3C-SiC	−0.160[a]	−0.125[a]		ZnTe	−0.04	−0.03
					CdTe	−0.135	−0.057
III–V	c-BN	−0.174[a]	−0.136[a]				
	c-AlN	0.011[a]	0.009[a]				
	AlSb	−0.100	−0.067				
	β-GaN	0.018[a]	0.014[a]				
	GaP	−0.112	−0.091				
	GaAs	−0.060	−0.065				
	GaSb	−0.033	−0.062				
	InP	−0.03	−0.07				
	InAs	0.006	0.044				
	InSb	0.04	0.01				

[a] Estimated

Table 11.3 Photoelastic constant p_{ij} in the long-wavelength limit ($E \to 0$ eV) for some hexagonal semiconductors

System	Material	p_{11}	p_{12}	p_{13}	p_{31}	p_{33}	p_{44}	p_{66}
III–V	w-AlN	0.020[a]	0.005[a]	0.004[a]		0.022[a]	0.007[a]	0.007[a]
	α-GaN	0.031[a]	0.008[a]	0.006[a]		0.033[a]	0.010[a]	0.012[a]
II–VI	ZnO	|0.222|	|0.099|	−0.111	|0.088|	−0.235	−0.0585	
	α-ZnS	−0.115	0.017	0.025	0.0271	−0.13	−0.0627	−0.066
	w-CdS				−0.03		−0.08	−0.04

[a] Estimated

some cubic semiconductors. The solid lines in Figure 11.1 show the least-squares fit with: (a) $p_{11} - p_{12} = -0.046 - 0.071 \ln E_0$; and (b) $p_{44} = -0.042 - 0.034 \ln E_0$ (E_0 in eV), respectively. Both $p_{11} - p_{12}$ and p_{44} are found to decrease with increasing E_0 from positive values, passing through zero at $E_0 \sim 0.3 - 0.5$ eV, to negative values.

Materials whose lowest gap is direct, or with a direct band gap only slightly above the indirect one (e.g., Ge), have a strong dispersion of the photoelastic coefficients in the spectral region near this gap [11.6, 11.13]. In contrast, materials whose lowest gap is indirect and far removed from a direct band gap, such as Si and GaP, have very weak photoelastic dispersion near the indirect band-gap region [11.6, 11.14, 11.15]. Strong resonant enhancement in the photoelastic coefficients near the direct band gap was first observed in ZnO and CdS by Tell *et al.* [11.16].

The experimental dispersion of α_{pe} with stress $\boldsymbol{X} \| [100]$ and $\boldsymbol{X} \| [111]$ for GaP, GaAs, InP and InAs are shown in Figures 11.2 and 11.3. The experimental data are taken for

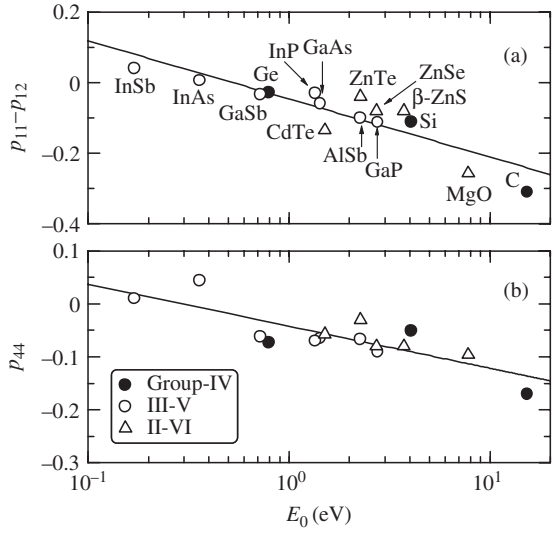

Figure 11.1 Photoelastic constants: (a) $p_{11} - p_{12}$; (b) p_{44} in the long-wavelength limit ($E \to 0$ eV) versus E_0 for some cubic group-IV, III–V and II–VI semiconductors. The solid lines represent the least-squares fit with (a) $p_{11} - p_{12} = -0.046 - 0.071 \ln E_0$ and (b) $p_{44} = -0.042 - 0.034 \ln E_0$ (E_0 in eV), respectively

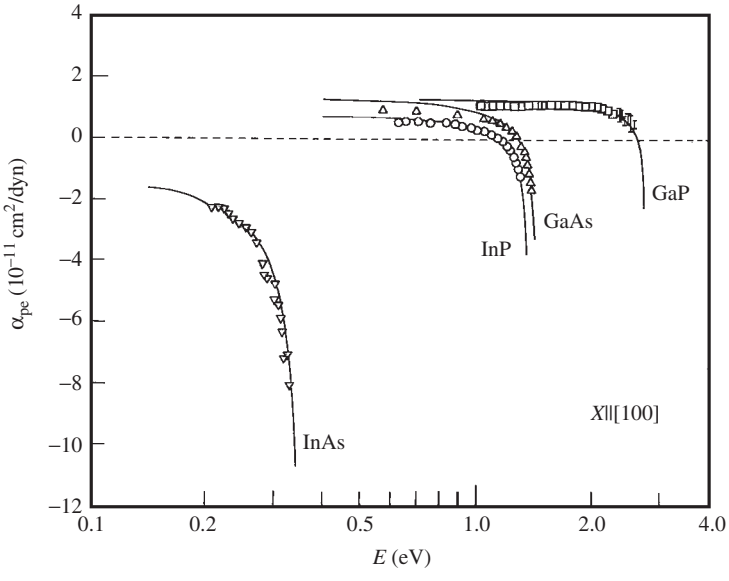

Figure 11.2 Dispersion of the photoelastic coefficient α_{pe} with $\boldsymbol{X} \| [001]$ for GaP, GaAs, InP and InAs. The solid lines represent the calculated results of Equation (11.5). The fitted C^* and D^* values are summarized in Table 11.4

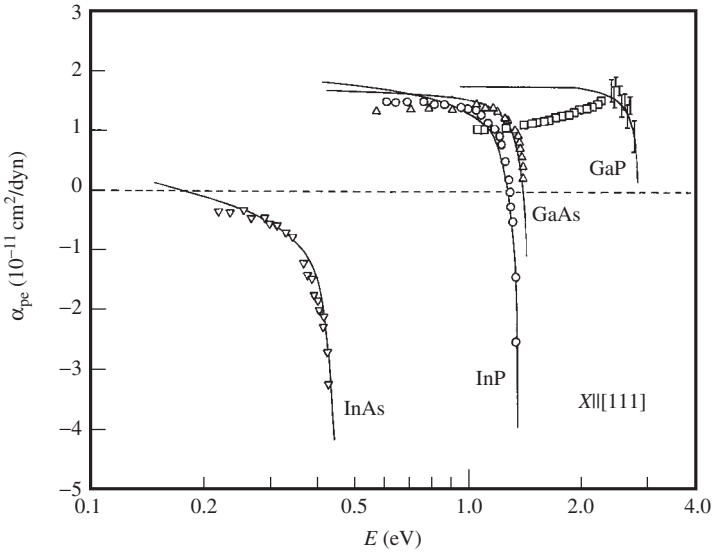

Figure 11.3 Dispersion of the photoelastic coefficient α_{pe} with $\boldsymbol{X}\|[111]$ for GaP, GaAs, InP and InAs. The solid lines represent the calculated results of Equation (11.5). The fitted C^* and D^* values are summarized in Table 11.4

Table 11.4 Dispersion parameters, C^* and D^*, used for the calculation of photoelastic coefficient α_{pe} in Equation (11.5) for GaP, GaAs, InP and InAs

Material	C^* (10^{-11} cm^2/dyn)		D^* (10^{-11} cm^2/dyn)	
	$\boldsymbol{X}\|[100]$	$\boldsymbol{X}\|[111]$	$\boldsymbol{X}\|[100]$	$\boldsymbol{X}\|[111]$
GaP	−0.18	−0.06	1.73	1.92
GaAs	−0.46	−0.21	2.22	2.12
InP	−0.29	−0.36	1.39	2.60
InAs	−2.58	−1.48	2.19	2.32

GaP and InP from [11.15], for GaAs from [11.6] and for InAs from [11.17]. The solid lines represent the calculated results of Equation (11.5). The fitted C^* and D^* values are listed in Table 11.4.

It is evident from Figures 11.2 and 11.3 that the theoretical and experimental α_{pe} values agree quite well at photon energies close to E_0. In the present model, the photoelastic coefficient α_{pe} is expressed as a sum of the dispersive contribution arising from the lowest direct band-gap transitions ($E_0/(E_0 + \Delta_0)$) and nondispersive background contribution (D^*) arising from the higher-gap transitions. These contributions are opposite in sign to each other (see Table 11.4). We can, therefore, expect that $\alpha_{pe} = 0$ at which the lowest direct band-gap contribution is exactly cancelled by the higher-gap contribution. Note that the parameter C^* is a strong function of E_0, i.e., $C^* \propto A^* E_0^{-1} \propto E_0^{-5/2}$, see Equation (11.6). This promises that a smaller E_0-gap material has a larger E_0-gap contribution, $|C^*|$. The fact can be confirmed in Table 11.4. If a material has a smaller $-C^*$

value (e.g., GaP, GaAs and InP), then the sign of the photoelastic coefficient is positive for long wavelengths and negative when $E \rightarrow E_0$. On the other hand, material having a larger $-C^*$ value (e.g., InAs and InSb) does not exhibit such a reversal in sign of α_{pe} [11.17].

Note that from Equation (11.1) we obtain

$$\alpha_{pe}(E) = \begin{cases} -\varepsilon_1(E)^2(p_{11} - p_{12})(S_{11} - S_{12}) & \text{for } \boldsymbol{X} = [100] \\ -\varepsilon_1(E)^2 p_{44} S_{44} & \text{for } \boldsymbol{X} = [111] \end{cases} \tag{11.8}$$

By introducing numerical $\varepsilon_1(E)$ and S_{ij} values into Equation (11.8), it is possible to obtain the spectral dependence of $p_{11} - p_{12}$ and p_{44}.

Macroscopically, the Brillouin scattering cross-section is given by the square of the photoelastic constants [11.18, 11.19]. By performing Brillouin scattering measurements, the spectral dependence of p_{ij} has been successfully determined on such semiconductors as GaP [11.20], GaAs [11.21], ZnO [11.8], β-ZnS [11.22], ZnSe [11.23], ZnTe [11.24], w-CdS [11.25] and w-CdSe [11.26].

The linear photoelastic coefficient α_{pe} can be obtained through the relation of Equation (11.2). Increasing the stress $\boldsymbol{X}$, however, usually increases the birefringence in the manner

$$\Delta\varepsilon_{ij} = \varepsilon(\|) - \varepsilon(\perp) = \alpha_{pe}\boldsymbol{X} + \beta_{pe}\boldsymbol{X}^2 + \cdots\cdots \tag{11.9}$$

where β_{pe} is the so-called quadratic photoelastic coefficient. The quadratic coefficient β_{pe} has been determined in several semiconductors, such as Ge [11.6], GaAs [11.6], GaSb [11.17] and InAs [11.17].

The determination of the figure of merit M_2 is the first step for use of materials as in elasto-optic devices. It can be defined by

$$M_2 = \frac{n^6 p_{ij}^2}{g v_s^2} \tag{11.10}$$

where n is the refractive index, p_{ij} is the photoelastic constant for the definite crystallographic orientation, g is the crystal density and v_s is the acoustic wave velocity. A pulse technique has been demonstrated by Dixon and Cohen [11.27] for measuring M_2 in optically transparent media with respect to a fused silica taken as a reference. This method has been successfully applied to some important III–V semiconductors, GaAs and InP [11.28, 11.29], and M_2 values as high as 1200 times those of silica have been obtained at near-resonance conditions, i.e., $E \rightarrow E_0$ [11.29].

In the visible–ultraviolet region, above the fundamental absorption edge, the elasto-optic response in semiconductors can be determined quantitatively from stress-induced optical measurements, such as piezoelectroreflectance [11.30], piezoreflectance [11.31] and stress-induced Raman scattering [11.15, 11.32]. However, absolute values for the elasto-optic tensor are not accurately known. More recently, Etchegoin *et al.* [11.33] performed ellipsometric measurements of the linear optical response function of Ge under uniaxial stress. These measurements allowed the experimental values to be directly obtained of the complex component of the linear piezo-optical coefficients, P_{11}, P_{12} and P_{44}, in the visible–ultraviolet region. The frequency-dependent components were obtained in absolute units with no additional assumptions. This is the principal advantage of

'piezoellipsometry' with respect to other stress-induced optical measurements. Here, the linear piezo-optical coefficient P_{ijkl} is defined by

$$\Delta\varepsilon_{ij}(E) = P_{ijkl}(E)X_{kl} \tag{11.11}$$

where m and n in P_{mn} represent ij and kl, respectively, according to the rules $xx \rightarrow 1$, $yy \rightarrow 2$, $zz \rightarrow 3$, $yz \rightarrow 4$, $zx \rightarrow 5$ and $xy \rightarrow 6$ [11.12].

Piezoellipsometry has also been used to determine the piezo-optical properties above the direct band-gap energy E_0 for Si [11.34], GaAs [11.35], InP [11.36], ZnSe [11.37] and ZnTe [11.37]. Figure 11.4 shows, as an example, the spectral dependence of the

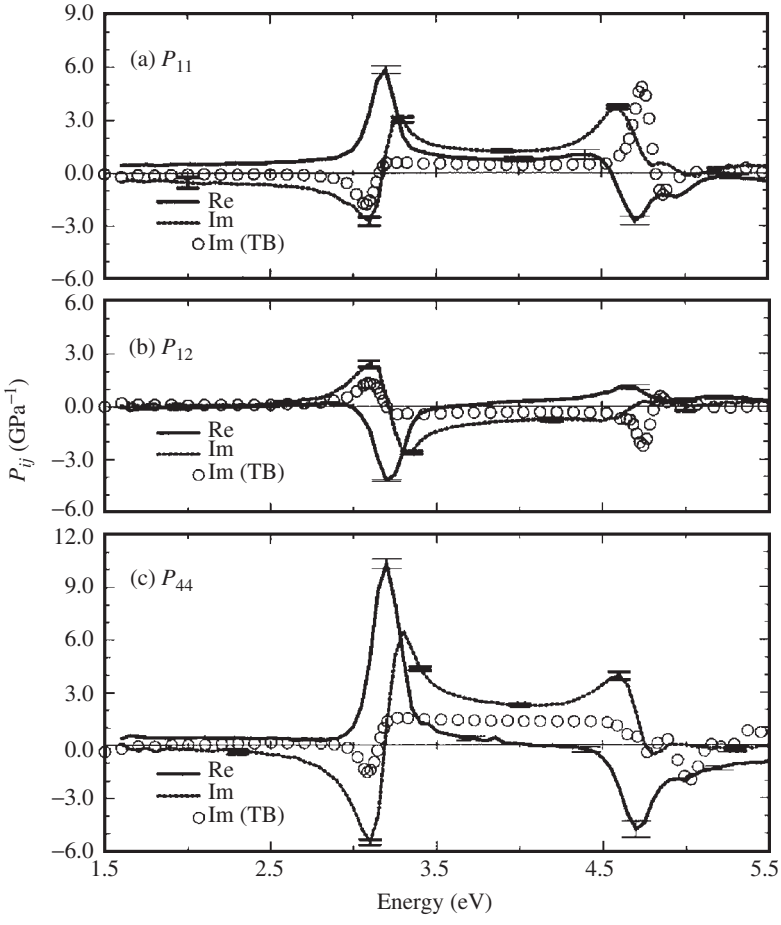

Figure 11.4 Spectral dependence of the piezo-optical coefficients: (a) P_{11}; (b) P_{12}; (c) P_{44}, as determined at 300 K in the 1.5–5.5 eV range for InP. The real and imaginary parts of each component are plotted by the solid and dotted lines, respectively, together with the imaginary parts of the piezo-optical coefficients obtained from semi-empirical tight-binding (TB) calculation. [From D. Rönnow, P. Santos, M. Cardona, E. Anastassakis, and M. Kuball, *Phys. Rev. B* **57**, 4432 (1998), reproduced by permission from the American Physical Society]

piezo-optical coefficients, P_{11}, P_{12} and P_{44}, measured at $T = 300$ K in the 1.5–5.5 eV range for InP [11.36]. The real and imaginary parts of each component are plotted in Figure 11.4, together with the imaginary parts of the piezo-optical coefficients obtained from semi-empirical tight-binding (TB) calculation. The structures seen at ~3.2 and 4.7 eV correspond to the E_1 and E_0' (E_2) critical points, respectively. The piezo-optical coefficients P_{11} and P_{12} were determined from $\boldsymbol{X} \| [001]$, while P_{44} was obtained from the difference between $\varepsilon^{\|}$ and $\varepsilon^{\perp}$ measured with $\boldsymbol{X} \| [111]$. Data up to 0.4 GPa were analyzed; at higher pressures, nonlinearities occurred, especially close to the critical points. By performing numerical analysis of these data, the deformation potentials at the E_1 and $E_1 + \Delta_1$ edges were determined and compared with the results of band-structure calculation.

11.2 LINEAR ELECTRO-OPTIC CONSTANT

11.2.1 Theoretical expression

It is of considerable interest to investigate the electro-optic effect in semiconductors. The effect affords a convenient and widely used means of controlling the intensity and phase of optical radiation in crystals. This property has been extensively explored and used for a wide variety of optoelectronic devices [11.38]. Accurate values of the electro-optic constant as a function of wavelength are especially important in the design and analysis of such optoelectronic devices. It is also of scientific interest to obtain analytical expression for the electro-optic effects in semiconductors.

There have been several theoretical works dealing with the spectral dependence of the electro-optic effects [11.39–11.45]. DiDomenico and Wemple [11.39] proposed a microscopic tensor theory of the electro-optic and nonlinear optical effects in ferroelectrics in terms of energy-band diagrams. Garrett [11.40] presented a one-dimensional anharmonic oscillator model to explain a number of nonlinear optical phenomena. Garrett's model has been extended by Sugie and Tada [11.41] to a three-dimensional oscillator model so that it is applicable to materials with arbitrary crystal structures. The electro-optic effects in the region close to the E_0 edge have also been discussed by Adachi and Oe [11.42, 11.43] and Adachi [11.44] in terms of electric-field-induced modulation of electronic energy-band structure. Hernandez-Cabrera *et al.* [11.45] have analyzed the linear electro-optic effect theoretically by means of a microscopic simple model (tight-binding scheme) without any fitting parameters.

In a lossless media, the electronic energy density can be written, using Equation (10.5), as

$$W = \frac{1}{2}\boldsymbol{E} \cdot \boldsymbol{D} = \frac{1}{2\varepsilon_0}\left(\frac{D_x^2}{\varepsilon_x} + \frac{D_y^2}{\varepsilon_y} + \frac{D_z^2}{\varepsilon_z}\right) = \frac{1}{2\varepsilon_0}\left(\frac{D_x^2}{n_x^2} + \frac{D_y^2}{n_y^2} + \frac{D_z^2}{n_z^2}\right) \tag{11.12}$$

where the directions x, y and z are the principal dielectric axes. By substituting in Equation (11.12) $Wx^2 = \varepsilon_0 E_x^2/2, \ldots,$ and $Wx^2 = D_x^2/2\varepsilon_0, \ldots,$ the following index ellipsoids are obtained

$$\begin{cases} n_x^2 x^2 + n_y^2 y^2 + n_z^2 z^2 = 1 \\ \dfrac{x^2}{n_x^2} + \dfrac{y^2}{n_y^2} + \dfrac{z^2}{n_z^2} = 1 \end{cases} \tag{11.13}$$

Let us take the equation of the index ellipsoid in the presence of an electric field as

$$\left(\frac{1}{n^2}\right)_1 x^2 + \left(\frac{1}{n^2}\right)_2 y^2 + \left(\frac{1}{n^2}\right)_3 z^2 + 2\left(\frac{1}{n^2}\right)_4 yz + 2\left(\frac{1}{n^2}\right)_5 zx + 2\left(\frac{1}{n^2}\right)_6 xy = 1 \tag{11.14}$$

where we used the convention $xx \rightarrow 1$, $yy \rightarrow 2$, $zz \rightarrow 3$, $yz \rightarrow 4$, $zx \rightarrow 5$ and $xy \rightarrow 6$. The linear electro-optic or Pockels effect refers to a change in the coefficients

$$\left(\frac{1}{n^2}\right)_i \quad i = 1, \ldots, 6$$

to an applied electric field. The linear electro-optic effect can, then, be defined by

$$\Delta\left(\frac{1}{n^2}\right)_{ij} = \Delta\left(\frac{1}{\varepsilon}\right)_{ij} = r_{ijk} E_k \tag{11.15}$$

where r_{ijk} is the linear electro-optic constant, E_k is the applied electric field and the indices i, j and k refer to the rectangular coordinate axes, x, y and z.

Table 11.5 summarizes the form of the linear electro-optic tensor $[r]$ for the cubic, hexagonal and rhombohedral systems, where m and n in r_{mn} represent ij and n, respectively, according to the rules $xx \rightarrow 1$, $yy \rightarrow 2$, $zz \rightarrow 3$, $yz \rightarrow 4$, $zx \rightarrow 5$, $xy \rightarrow 6$ (m) and $x \rightarrow 1$, $y \rightarrow 2$, $z \rightarrow 3$ (n) [11.12].

In order to describe the linear electro-optic effect rigorously, we must take into account a possible piezoelectrically induced elasto-optic contribution to the impermeability change. The electro-optic constant in this case can be written as

$$r_{ijk}^{\mathrm{T}} = r_{ijk}^{\mathrm{S}} + r_{ijk}^{\mathrm{P}} \tag{11.16}$$

where r_{ijk}^{T} is the free value determined at constant stress (e.g., by making a measurement at low frequencies well below the acoustic resonance of the sample), r_{ijk}^{S} is the clamped value determined at constant strain (e.g., at high frequencies well above the acoustic resonance of the sample) and r_{ijk}^{P} is the elasto-optic contribution to the impermeability change.

The electro-optic tensor $[r]$ is, in general, a *complex* third-rank tensor. Since the imaginary part of the dielectric constant may be taken as zero in the region near or below the fundamental absorption edge, the tensor component r_{ijk} in this region can be regarded as a *real* physical constant to a good approximation. Then, from Equation (11.15), we can write

$$r_{ijk} = \Delta\left(\frac{1}{\varepsilon}\right)_{ij} \frac{1}{E_k} = -\frac{\Delta\varepsilon_{ij}}{\varepsilon_{ii}\varepsilon_{jj}E_k} \tag{11.17}$$

The elasto-optic contribution r_{ijk}^{P} is now written, for the zinc-blende family, as

$$r_{ijk}^{\mathrm{P}} = \sum_{mn} p_{ijmn} S_{mnuv} e_{kmn} = \sum_{mn} p_{ijmn} d_{kmn} \tag{11.18}$$

where p_{ijmn} is the photoelastic constant, S_{mnuv} is the elastic compliance constant (Section 3.1) and e_{kmn} (d_{kmn}) is the piezoelectric stress (strain) constant (Section 5.1). Since p_{ijmn} is a wavelength-dependent quantity, r_{ijk}^{P} is spectrally dependent.

Table 11.5 Form of the linear electro-optic tensor for semiconductors of certain symmetry classes

Symmetry class	Material	Tensor form
Cubic (Class O_h)	Si, Ge, MgO, etc.	$\begin{bmatrix} 0 & 0 & 0 \\ 0 & 0 & 0 \\ 0 & 0 & 0 \\ 0 & 0 & 0 \\ 0 & 0 & 0 \\ 0 & 0 & 0 \end{bmatrix}$ Showing no linear electro-optic effect
Cubic (Class T_d)	3C-SiC, GaAs, ZnSe, etc.	$\begin{bmatrix} 0 & 0 & 0 \\ 0 & 0 & 0 \\ 0 & 0 & 0 \\ r_{41} & 0 & 0 \\ 0 & r_{41} & 0 \\ 0 & 0 & r_{41} \end{bmatrix}$
Hexagonal (Class C_{6v})	2H-SiC, α-GaN, w-CdS, etc.	$\begin{bmatrix} 0 & 0 & r_{13} \\ 0 & 0 & r_{13} \\ 0 & 0 & r_{33} \\ 0 & r_{42} & 0 \\ r_{42} & 0 & 0 \\ 0 & 0 & 0 \end{bmatrix}$
Hexagonal (Class D_{6h})	h-BN	$\begin{bmatrix} 0 & 0 & 0 \\ 0 & 0 & 0 \\ 0 & 0 & 0 \\ 0 & 0 & 0 \\ 0 & 0 & 0 \\ 0 & 0 & 0 \end{bmatrix}$ Showing no linear electro-optic effect
Rhombohedral (Class C_{3v})	15R-SiC	$\begin{bmatrix} 0 & -r_{22} & r_{13} \\ 0 & r_{22} & r_{13} \\ 0 & 0 & r_{33} \\ 0 & r_{42} & 0 \\ r_{42} & 0 & 0 \\ -r_{22} & 0 & 0 \end{bmatrix}$

Let us consider in the transparent region ($\varepsilon \sim \varepsilon_1$) of a zinc-blende-type semiconductor. The quantity $\Delta\varepsilon_1$ required to calculate r_{ijk}^{S} can be obtained by taking account of the changes in the lowest direct band-gap parameters [11.42]

$$\Delta\varepsilon_1 = \frac{\partial\varepsilon_1}{\partial E_0}\Delta E_0 + \frac{\partial\varepsilon_1}{\partial M}\Delta M + \frac{\partial^2\varepsilon_1}{\partial E_0^2}(\Delta E_0)^2 + \frac{\partial^2\varepsilon_1}{\partial M^2}(\Delta M)^2 + \frac{\partial^2\varepsilon_1}{\partial E_0 \partial M}(\Delta E_0 \Delta M) + \cdots\cdots \tag{11.19}$$

where ΔE_0 and ΔM are, respectively, changes in E_0 and M (critical-point energy and strength parameter) with the electric field E. The specific physical process considered here is the linear electro-optic effect. We can thus neglect the higher-order derivative terms in Equation (11.19). Then, Equation (11.19) can be reduced to

$$\Delta\varepsilon_1 = \frac{\partial\varepsilon_1}{\partial E_0}\Delta E_0 + \frac{\partial\varepsilon_1}{\partial M}\Delta M \tag{11.20}$$

The critical-point parameter changes ΔE_0 and ΔM are now written in terms of the first-order Stark-like effect as

$$\begin{aligned} \Delta E_0 &= a_1 E \\ \Delta M &= b_1 E \end{aligned} \tag{11.21}$$

Introducing the one-electron term in Equation (10.78) ($\varepsilon_1(E) \sim n(E)^2$) and Equation (11.21) into Equation (11.20), we obtain the expression for the linear electro-optic constant in the transparent region of a zinc-blende-type semiconductor as [11.42]

$$r_{41}^{\mathrm{S}}(E) = -\left(\frac{1}{\varepsilon_1^2}\right)\left[A^*\left(\frac{1}{2}\right)E_0^{-1}a_1 g(\chi_0^*) + b_1 f(\chi_0^*) + F'\right] \tag{11.22}$$

where F' represents the strength of the higher-gap contribution (nondispersive) and $f(\chi_0^*)$ and $g(\chi_0^*)$ are defined by Equations (10.79) and (11.7), respectively. In obtaining Equation (11.22), we considered only the E_0-gap contribution. This is based on the fact that most zinc-blende semiconductors have small Δ_0 gaps compared with their E_0 values. The $E_0 + \Delta_0$-gap contribution can, therefore, be successfully included into that of the E_0 gap. For some semiconductors, such as GaSb, InAs, InSb, ZnTe and CdTe, the $E_0 + \Delta_0$-gap energies are much larger than their E_0-gap ones, and, therefore, their $E_0 + \Delta_0$-gap contribution can be rightly included into the higher-gap contribution, namely F'.

It is noted that $g(\chi_0^*)$ shows a very sharp dispersion near E_0 compared with $f(\chi_0^*)$. Thus, the second term in the square bracket of Equation (11.22) can be included into the nondispersive term F'. The linear electro-optic constant r_{41}^{S} in the zinc-blende-type semiconductors can be finally written as [11.42]

$$r_{41}^{\mathrm{S}}(E) = -\left(\frac{1}{\varepsilon_1^2}\right)[E^* g(\chi_0^*) + F^*] \tag{11.23}$$

with

$$E^* = \tfrac{1}{2}A^* E_0^{-1} a_1 \tag{11.24}$$

The parameters E^* and F^* can be treated as adjustable parameters to fit the experimental data.

11.2.2 Experimental value

The linear electro-optic constants have been measured for a variety of semiconductors. We list in Table 11.6 the electro-optic constant r_{41}^{S} in the long-wavelength limit ($E \to 0$ eV) determined experimentally for some cubic semiconductors. The electro-optic constants r_{ijk}^{S} for hexagonal semiconductors are also listed in Table 11.7.

Table 11.6 Clamped value of the linear electro-optic constant r_{41}^{S} in the long-wavelength limit ($E \rightarrow 0$ eV) for some cubic group-IV, III–V and II–VI semiconductors

System	Material	r_{41}^{S} (pm/V)	System	Material	r_{41}^{S} (pm/V)
IV	Diamon	a	II–VI	β-ZnS	1.4 ($\lvert r_{41}^{S} \rvert$)
	Si	a		ZnSe	-2.2^{b}
	Ge	a		ZnTe	3.9 ($\lvert r_{41}^{T} \rvert$)^{b}
	α-Sn	a		CdTe	4.1 ($\lvert r_{41}^{S} \rvert$)
	3C-SiC	-2.7			
III–V	GaP	-1.10 ($\lambda = 1.153$ μm)			
	GaAs	-1.80 ($\lambda = 10.6$ μm)			
	InP	-1.68 ($\lambda = 1.50$ μm)			

[a] Principally showing no linear electro-optic effect
[b] Free value

Table 11.7 Clamped value of the linear electro-optic constant r_{ij}^{S} in the long-wavelength limit ($E \rightarrow 0$ eV) for some hexagonal semiconductors (in pm/V)

System	Material	r_{13}	r_{33}	r_{42}	Comment
III–V	α-GaN	0.57	1.91		$\lambda = 0.633$ μm
II–VI	ZnO	0.96	1.9		$\lambda = 3.39$ μm
	α-ZnS	0.92	1.7		$\lambda = 0.633, 3.39$ μm
	w-CdS	2.45[a]	2.75[a]		$\lambda = 10.6$ μm
	w-CdSe	1.8	4.3		$\lambda = 3.39$ μm

[a] Free value

In Figure 11.5, we plot the experimental r_{41}^{S} values for GaP [11.46], GaAs [11.47] and InP [11.48] as a function of wavelength. The solid lines represent the calculated results of Equation (11.23). The fitted strength parameters E^{*} and F^{*} are listed in Table 11.8. The InAs values are estimated from those of GaP, GaAs and InP (Bs) by the relation [11.49]

$$B_{\mathrm{InAs}} = B_{\mathrm{GaP}} + B_{\mathrm{GaAs}} - B_{\mathrm{InP}} \tag{11.25}$$

It has been shown that r_{41}^{P} is much smaller than r_{41}^{S} in many cubic semiconductors, hence $r_{41}^{T} \simeq r_{41}^{S}$ [11.42]. It is also concluded that the E_0 gap can strongly contribute to the dispersion of r_{41}^{T}, especially for photon energies close to the E_0 gap, but not to its absolute value.

11.3 QUADRATIC ELECTRO-OPTIC CONSTANT

11.3.1 Theoretical expression

The effect linearly proportional to E is the linear electro-optic or Pockels effect and that proportional to E^2 is the so-called quadratic electro-optic or Kerr effect. As discussed in

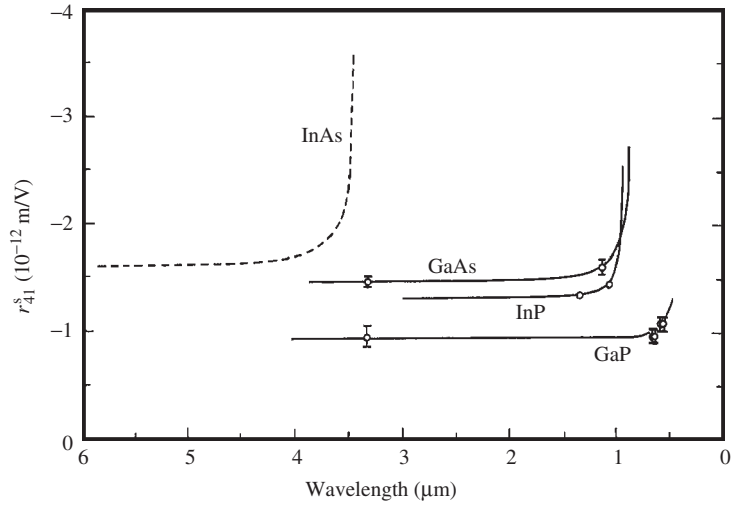

Figure 11.5 Dispersion of the linear electro-optic constant r_{41}^S determined experimentally for GaP, GaAs and InP. The solid lines represent the calculated results of Equation (11.23). The fitted E^* and F^* values are listed in Table 11.8. The dashed line shows the estimated dispersion for InAs

Table 11.8 Dispersion parameters, E^* and F^*, used for the calculation of linear electro-optic constant r_{41}^S in Equation (11.23) for GaP, GaAs, InP and InAs

Material	E^* (pm/V)	F^* (pm/V)
GaP	−83	17
GaAs	−71	123
InP	−42	91
InAs	−30[a]	197[a]

[a] Estimated

Section 11.2, the linear electro-optic effect has been intensively investigated for various semiconductors. However, a few studies have been done on the quadratic effects for semiconductors.

There have been a very little theoretical work on the quadratic electro-optic effects for semiconductors [11.43]. To explain the quadratic effect, we must expand the change in the dielectric impermeability of Equation (11.15) to higher order

$$\Delta\left(\frac{1}{\varepsilon}\right)_{ij} = r_{ijk}E_k + R_{ijkl}E_kE_l + \cdots\cdots \tag{11.26}$$

where R_{ijkl} is the quadratic electro-optic constant. In semiconductors with a center of symmetry, such as Si and Ge, only the second-order term and higher even-order terms can exist, and so one might expect that the effects are very small in moderate electric fields. If a center of symmetry is lacking, as in the zinc-blende-type semiconductors, not

only even-order, but also odd-order effects can exist. The effect given by the second-order term and higher even-order terms, which can occur in all substances, is known as the Kerr effect.

The quadratic electro-optic tensor is, in general, a *complex* fourth-rank tensor. We summarize in Table 11.9 the form of the quadratic electro-optic tensor $[R]$ for the cubic, hexagonal and rhombohedral systems, where m and n in R_{mn} represent ij and kl, respectively, according to the rules $xx \rightarrow 1$, $yy \rightarrow 2$, $zz \rightarrow 3$, $yz \rightarrow 4$, $zx \rightarrow 5$ and $xy \rightarrow 6$. Since the imaginary part of the dielectric constant may be taken as zero in a transparent region of semiconductors, the quadratic electro-optic constant is regarded as a *real* physical constant to a good approximation.

If we neglect higher-order terms than the second in the electric field, the Kerr coefficient R_{ijkl} in a zinc-blende family can be written as

$$R_{ijkl} = \Delta\left(\frac{1}{\varepsilon}\right)_{ij} \frac{1}{E_k E_l} = -\frac{\Delta\varepsilon_{ij}}{\varepsilon_{ii}\varepsilon_{jj} E_k E_l} = -\frac{\Delta\varepsilon_1}{\varepsilon_1^2 E^2} \tag{11.27}$$

As in Equation (11.21), the band parameter changes are written in terms of the first-order and second-order Stark-like effects as

$$\begin{aligned} \Delta E_0 &= a_1 E + a_2 E^2 \\ \Delta M &= b_1 E + b_2 E^2 \end{aligned} \tag{11.28}$$

Table 11.9 Form of the quadratic electro-optic tensor for semiconductors of certain symmetry classes

Symmetry class	Material	Tensor form
Cubic	Si, 3C-SiC, GaAs, MgO, ZnSe, etc.	$\begin{bmatrix} R_{11} & R_{12} & R_{12} & 0 & 0 & 0 \\ R_{12} & R_{11} & R_{12} & 0 & 0 & 0 \\ R_{12} & R_{12} & R_{11} & 0 & 0 & 0 \\ 0 & 0 & 0 & R_{44} & 0 & 0 \\ 0 & 0 & 0 & 0 & R_{44} & 0 \\ 0 & 0 & 0 & 0 & 0 & R_{44} \end{bmatrix}$
Hexagonal	4H-SiC, h-BN, α-GaN, w-CdS, etc.	$\begin{bmatrix} R_{11} & R_{12} & R_{13} & 0 & 0 & 0 \\ R_{12} & R_{11} & R_{13} & 0 & 0 & 0 \\ R_{31} & R_{31} & R_{33} & 0 & 0 & 0 \\ 0 & 0 & 0 & R_{44} & 0 & 0 \\ 0 & 0 & 0 & 0 & R_{44} & 0 \\ 0 & 0 & 0 & 0 & 0 & R_{66} \end{bmatrix}$ $R_{66} = 1/2(R_{11} - R_{12})$
Rhombohedral	15R-SiC	$\begin{bmatrix} R_{11} & R_{12} & R_{13} & R_{14} & 0 & 0 \\ R_{12} & R_{11} & R_{13} & -R_{14} & 0 & 0 \\ R_{31} & R_{31} & R_{33} & 0 & 0 & 0 \\ R_{41} & -R_{41} & 0 & R_{44} & 0 & 0 \\ 0 & 0 & 0 & 0 & R_{44} & 2R_{41} \\ 0 & 0 & 0 & 0 & R_{14} & R_{66} \end{bmatrix}$ $R_{66} = 1/2(R_{11} - R_{12})$

The specific physical process considered here is the quadratic electro-optic effect. The change $\Delta\varepsilon_1$ in Equation (11.27) can, thus, be written as

$$\Delta\varepsilon_1 = \frac{\partial\varepsilon_1}{\partial E_0}(\Delta E_0)_\mathrm{s} + \frac{\partial\varepsilon_1}{\partial M}(\Delta M)_\mathrm{s} + \frac{\partial^2\varepsilon_1}{\partial E_0 \partial M}(\Delta E_0)_\mathrm{f}(\Delta M)_\mathrm{f} + \frac{\partial^2\varepsilon_1}{\partial E_0^2}(\Delta E_0)_\mathrm{f}^2 + \frac{\partial^2\varepsilon_1}{\partial M^2}(\Delta M)_\mathrm{f}^2 \tag{11.29}$$

where the subscripts f and s, respectively, indicate the contributions from the first-order and second-order Stark effects to the quadratic electro-optic constant.

Introducing the one-electron term in Equation (10.78) ($\varepsilon_1(E) \sim n(E)^2$) and Equation (11.28) into Equation (11.29), we finally obtain the expression for the quadratic electro-optic constant in the transparent region of zinc-blende-type semiconductors as [11.43]

$$R_{ijkl}(E) = -\left(\frac{1}{\varepsilon_1^2}\right)[G^* h(\chi_0^*) + H^*] \tag{11.30}$$

with

$$G^* = -\tfrac{1}{4} A^* E_0^{-2} a_1^2 \tag{11.31}$$

$$h(\chi_0^*) = \chi_0^{*-2}\left[2 - (1+\chi_0^*)^{-3/2} - (1-\chi_0^*)^{-3/2}\right] \tag{11.32}$$

where H^* represents the strength of the nondispersive term arising both from the E_0-gap and higher-gap contributions and χ_0^* is defined by Equation (10.80). The parameters G^* and H^* can be treated as adjustable parameters to fit the experimental data.

As in Equation (11.16), the quadratic electro-optic constant R_{ijkl} can be given by a sum of the two terms

$$R_{ijkl}^\mathrm{T} = R_{ijkl}^\mathrm{S} + R_{ijkl}^\mathrm{P} \tag{11.33}$$

where R_{ijkl}^P is the product of the photoelastic tensor p_{ijkl} and quadratic electrostrictive tensor Q_{mnkl}

$$R_{ijkl}^\mathrm{P} = \sum p_{ijkl} Q_{mnkl} \tag{11.34}$$

It is usually assumed that $R_{ijkl}^\mathrm{T} \simeq R_{ijkl}^\mathrm{S}$ since the detailed values of Q_{mnkl} are not well known at present.

11.3.2 Experimental value

The quadratic electro-optic effect has been experimentally studied for several semiconductors [11.50–11.52]. Reinhart *et al.* [11.50] have observed a small quadratic electro-optic effect in GaP. The quadratic electro-optic constant R_{ijkl} of GaAs has been determined by Faist and Reinhart [11.51] at $\lambda = 1.09$ and 1.15 μm and by Berseth *et al.* [11.52] at $\lambda = 1.32$ and 1.52 μm. These authors used $Al_xGa_{1-x}As$/GaAs double-heterostructure waveguides. We list in Table 11.10 the values of R_{11} and R_{12} obtained by them. These experimental results are plotted in Figure 11.6. A theoretical curve [11.53] using the

Table 11.10 Quadratic electro-optic constant R_{ij} for GaAs (in 10^{-21} m^2/V^2)

Wavelength (μm)	Energy (eV)	R_{11}	R_{12}
1.09	1.138	-29 ± 7	-24 ± 6
1.15	1.078	-20 ± 5	-18 ± 5
1.32	0.939	-9.3 ± 2.8	-5.1 ± 1.9
1.52	0.915	-3.2 ± 2.3	-5.1 ± 2.6

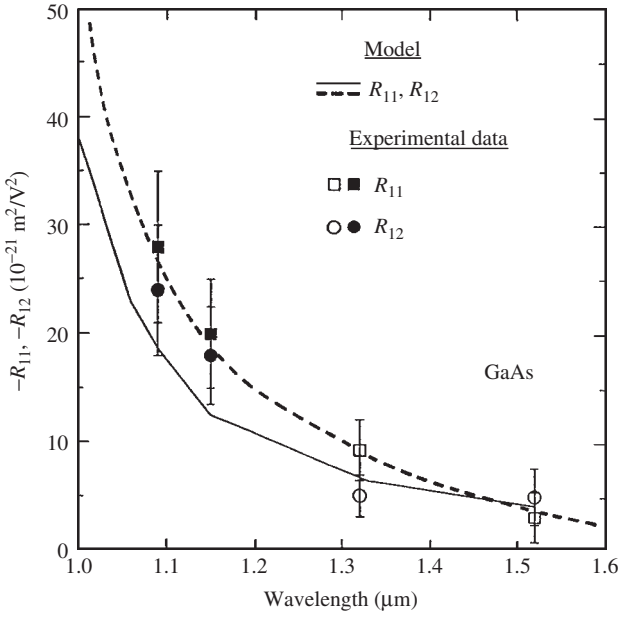

Figure 11.6 Quadratic electro-optic constants, R_{11} and R_{12}, as a function of wavelength for GaAs. The experimental data are taken from Faist and Reinhart (solid symbols) [11.51] and from Berseth *et al*. (open symbols) [11.52]. The solid line represents the calculated result of Alping and Coldren [11.53] based on the Kramers–Kronig transformation of the Franz–Keldysh effect. The dashed line shows the calculated result of Equation (11.30)

Kramers–Kronig calculation of the Franz–Keldysh effect is shown in Figure 11.6 by the solid line. As this calculation model does not accurately represent the energy-band structure, it does not account for the difference between the transverse electric (TE) and transverse magnetic (TM) modes. The quadratic electro-optic constant R_{11}, corresponding to the TM polarization, is believed to be larger than $|R_{12}|$ (TE polarization) because the electroabsorption is slightly larger in heterostructures for the TM polarization [11.52].

The dashed line in Figure 11.6 shows the calculated dispersion curve of Equation (11.30). It is clear that this curve well explains the experimental data. The strength parameters determined here are as follows: $G^* = -4.0 \times 10^{-19}$ m^2/V^2 and $H^* = -2.0 \times 10^{-18}$ m^2/V^2. It is also easily understood that the quadratic electro-optic constant shows very strong dispersion compared with the linear electro-optic

constants (Figure 11.5). Bach *et al.* [11.54] observed the quadratic electro-optic effect in $In_{1-x}Ga_xAs_yP_{1-y}$/InP double-heterostructure waveguides. They also found that the values of the quadratic constant $R_{11}-R_{12}$ vary greatly with photon energy.

11.4 FRANZ–KELDYSH EFFECT

11.4.1 Theoretical expression

The Franz–Keldysh effect is an electric-field-induced change in the complex dielectric constant of a semiconductor, occurring at photon energies close to the intrinsic absorption edge. This effect has two parts, electroabsorption and electrorefraction, which are respectively changes of the absorption coefficient and refractive index due to an applied electric field.

The Franz–Keldysh electroabsorption coefficient is calculated from the expressions derived by Tharmalingam [11.55] and Callaway [11.56]. A detailed theoretical treatment on the basis of a one-electron band structure has been given by Aspnes [11.57]. For a simple conduction-band minimum and valence-band maximum (three-dimensional M_0 critical point) in the weak-field approximation at a photon energy $\hbar\omega$ and a electric field E, the absorption coefficient α (cm^{-1}) can be given by [11.55–11.57]

$$\alpha(\omega, E) = \sum_j A_j E^{1/3} \left[\left| \left(\frac{\mathrm{d}Ai(z)}{\mathrm{d}z} \right)_{\beta_j} \right|^2 - \beta_j |Ai(\beta_j)|^2 \right] \tag{11.35}$$

with

$$A_j = 7.65 \times 10^5 \frac{(2\mu_j)^{4/3}}{n\hbar\omega} \tag{11.36a}$$

$$\beta_j = 1.1 \times 10^5 \frac{(E_0 - \hbar\omega)(2\mu_j)^{1/3}}{E^{2/3}} \tag{11.36b}$$

where the sum in Equation (11.35) is over the light-hole and heavy-hole valence bands, $Ai(x)$ denotes the Airy function, μ_j is the combined density-of-states mass and n is the refractive index. As $E \to 0$ V/cm, Equation (11.35) goes over into the familiar expression for the absorption due to direct allowed transitions

$$\alpha(\omega, 0) = \sum_j \frac{A_j}{\pi} 3.3 \times 10^2 (2\mu_j)^{1/6} \sqrt{\hbar\omega - E_0} \tag{11.37}$$

that is, $\alpha(\omega, 0) \propto (\hbar\omega - E_0)^{1/2}$. The field-induced change in α is then given by $\Delta\alpha(\omega, E) = \alpha(\omega, E) - \alpha(\omega, 0)$.

Although the theoretical expressions due to Tharmalingam [11.55] and Callaway [11.56] have been widely used in the past, it is now clear as a result of later work [11.58, 11.59] that an expression due to Rees [11.60], which, rather than providing absolute values, relates the absorption coefficient at two different fields, provides a better means of fitting the results. The expression due to Rees is now given by

$$\alpha(\omega, E) = C \int_{-\infty}^{\infty} \alpha(\omega - \omega_2, 0) Ai(-C\omega_2) \mathrm{d}\omega_2 \tag{11.38}$$

with

$$C = \left(\frac{32\pi^2\mu}{h^2e^2E^2}\right)^{1/3} \tag{11.39}$$

where C depends only weakly on the material parameter via μ.

The contribution of the electroabsorption change to the real part of the refractive index n can be calculated from the Kramers–Kronig relationship (electrorefraction)

$$\Delta n(\omega, E) = \frac{c\hbar}{\pi}\int_0^\infty \frac{\Delta\alpha(\omega, E)}{(\hbar\omega')^2 - (\hbar\omega)^2}\mathrm{d}(\hbar\omega') \tag{11.40}$$

where c is the velocity of light in vacuum.

11.4.2 Experimental value

Franz–Keldysh electroabsorption has been observed experimentally in many semiconductors, such as Si [11.61], Ge [11.62], SiC [11.63], GaP [11.64], GaAs [11.59], InP [11.58], InAs [11.65] and ZnSe [11.66]. We show in Figure 11.7, as an example, the experimental data by Wight *et al*. for GaAs [11.59]. The experimental absorption coefficient is plotted

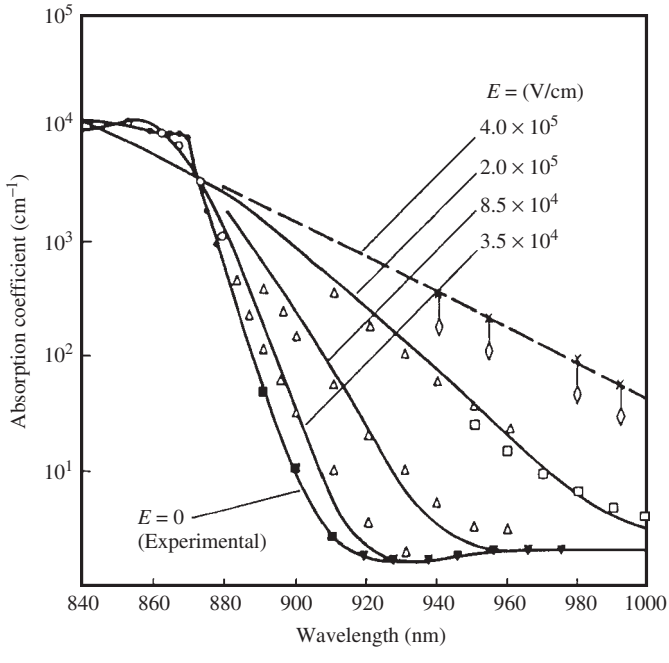

Figure 11.7 Absorption edge of high-purity GaAs as a function of electric field E measured at 300 K. The solid lines represent the theoretical curves based on Rees's electroabsorption (Franz–Keldysh) expression. [From D. R. Wight, A. M. Keir, G. J. Pryce, J. C. H. Birbeck, J. M. Heaton, R. J. Norcross, and P. J. Wright, *IEE Proc.-J* **135**, 39 (1988), reproduced by permission from the Institute of Electrical Engineers]

for electric fields in the range $E = 3.5 \times 10^4$–4.0×10^5 V/cm. Since the applied electric field is generally obtained by making measurements within a depletion region, one experimental difficulty is that of ensuring a uniform field. As a result, the absorption coefficient is often given as a function of voltage so that the results remain device specific. There are exceptions, however, where the use of thick high-quality, low-doped (up to 10^{15} cm^{-3}) epitaxial layers has ensured a highly uniform field and low built-in field at zero applied bias [11.67]. The epitaxial layer used for the measurements by Wight *et al.* (Figure 11.7) was high resistivity and had a net electron concentration of $\sim 1 \times 10^{15}$ cm^{-3}. The solid lines in Figure 11.7 represent the calculated results of Equation (11.38). The experimental variation of the electroabsorption with wavelength is found to be in good agreement with the calculated curves.

Direct measurements of the electrorefractive effect in GaAs have been performed by Van Eck *et al.* [11.58] using a Mach–Zehnder interferometer. Average values of $\Delta n = 2 \times 10^{-5}$–$6 \times 10^{-5}$ were found for fields in the range 2.6×10^4–5.2×10^4 V/cm at photon energies 20–40 meV below the E_0 edge.

11.5 NONLINEAR OPTICAL CONSTANT

11.5.1 Second-order nonlinear optical susceptibility

Historically, in 1961 Franken *et al.* discovered a second-harmonic generation in quartz [11.68]. This was the onset of a new field, nonlinear optics, which has reached a high level of maturity and has set the foundation of optics to various areas. Its formation in terms of dielectric susceptibilities, however, provides the natural framework to formulate the classical Pockels (Section 11.2) and Kerr effects (Section 11.3) as nonlinear optical phenomena. Let us consider first the second-order nonlinear optical susceptibility for various semiconductors.

The interaction between electromagnetic waves propagating inside a semiconductor can be described by the following nonlinear polarization vector

$$\left(\frac{1}{\varepsilon_0}\right) P_i = \chi_{ij}^{(1)} E_j + \chi_{ijk}^{(2)} E_j E_k + \chi_{ijkl}^{(3)} E_j E_k E_l + \cdots \cdots \tag{11.41}$$

where $\chi^{(i)}$ $(i \geqslant 2)$ is the ith-order nonlinear susceptibility tensor of the crystal. The first term on the right-hand side of Equation (11.41) represents the linear optics. The second-order nonlinear susceptibility tensor gives rise to the phenomena of second-harmonic generation, dc rectification, linear electro-optic or Pockels effect, parametric generation, etc. (see Table 11.12).

We show in Table 11.11 the independent non-vanishing tensor elements of the second-order nonlinear optical susceptibility $\chi_{ijk}^{(2)}$ for semiconductors of certain symmetry classes [11.69]. Among crystals without inversion symmetry, those with the zinc-blende structure, such as 3C-SiC, GaAs and ZnSe, have the simplest form of $\chi_{ijk}^{(2)}$. They belong to the class of T_d $(\bar{4}3m)$ cubic point group. Although there are many symmetry operations associated with T_d, only the 180° rotations about the three four-fold axes and mirror reflections about the diagonal planes are needed to reduce the independent elements in $\chi_{ijk}^{(2)}$. The 180° rotations make $\chi_{iii}^{(2)} = -\chi_{iii}^{(2)} = 0$, $\chi_{iij}^{(2)} = -\chi_{iij}^{(2)} = 0$ and $\chi_{ijj}^{(2)} = -\chi_{ijj}^{(2)} = 0$, where

Table 11.11 Independent non-vanishing element of $\chi^{(2)}_{ijk}(-\omega;\omega_1,\omega_2)$ for semiconductors of certain symmetry classes

Symmetry class	Material	Non-vanishing element
Cubic (Class O_h)	Si, Ge, MgO, etc.	Showing no second-order optical nonlinearity (all 27 elements are zero)
Cubic (Class T_d)	3C-SiC, GaAs, ZnSe, etc.	$xyz = xzy = yxz = yzx = zxy = zyx$
Hexagonal (Class C_{6v})	2H-SiC, α-GaN, w-CdS, etc.	$xzx = yzy$, $xxz = yyz$, $zxx = zyy$, zzz
Hexagonal (Class D_{6h})	h-BN	Showing no second-order optical nonlinearity (all 27 elements are zero)
Rhombohedral (Class C_{3v})	15R-SiC	$xzx = yzy$, $xxz = yyz$, $zxx = zyy$, zzz $yyy = -yxx = -xxy = -xyx$ (mirror plane perpendicular to $\boldsymbol{x}$)

Source: Y. R. Shen, *The Principles of Nonlinear Optics* (Wiley-Interscience, New York, 1984)

i, j and k refer to the three principal axes (x, y and z) of the crystals. The mirror reflections lead to the invariance of $\chi^{(2)}_{ijk}$ ($i \neq j \neq k$) under permutation of the Cartesian indices. Consequently, $\chi^{(2)}_{ijk}$ ($i \neq j \neq k$) is the only independent element in $\chi^{(2)}_{ijk}$ for the zinc-blende crystals (Table 11.11).

One should write for the polarization at frequency ω in the presence of a static electric field E as

$$\begin{aligned} P_i(\omega, E) &= P_i(\omega, 0) + \varepsilon_0 \delta\chi_{ij}(\omega) E_j(E) \\ &= P_i(\omega, 0) + \varepsilon_0 \Big\{ 2\chi^{(2)}_{ijk}(-\omega; 0, \omega) E_k(0) \\ &\quad + 3\chi^{(3)}_{ijkl}(-\omega; 0, 0, \omega) E_k(0) E_l(0) + \cdots\cdots \Big\} E_j(E) \\ &= P_i(\omega, 0) - \varepsilon_0 \varepsilon_{ii}(\omega) \varepsilon_{jj}(\omega) \{ r_{ijk} E_k(0) + R_{ijkl} E_k(0) E_l(0) + \cdots\cdots \} E_j(E) \end{aligned} \tag{11.42}$$

From Equation (11.42), we obtain

$$r_{ijk} = -\frac{2\chi^{(2)}_{ijk}(-\omega; 0, \omega)}{\varepsilon_{ii}(\omega)\varepsilon_{jj}(\omega)} \tag{11.43}$$

$$R_{ijkl} = -\frac{3\chi^{(3)}_{ijkl}(-\omega; 0, 0, \omega)}{\varepsilon_{ii}(\omega)\varepsilon_{jj}(\omega)} \tag{11.44}$$

where r_{ijk} and R_{ijkl} are, respectively, the linear and quadratic electro-optic constants. It is understood from Equations (11.43) and (11.44) that the Pockels and Kerr electro-optic effects correspond to the second-order and third-order nonlinear optical processes,

Table 11.12 Susceptibilities and nonlinear optical processes in semiconductors

Susceptibility	Nonlinear optical process
$\chi^{(2)}_{ijk}(-2\omega;\omega,\omega)$	Second-harmonic generation
$\chi^{(2)}_{ijk}(-\omega_1 \mp \omega_2;\omega_1,\pm\omega_2)$	Parametric process
$\chi^{(2)}_{ijk}(-\omega;0,\omega)$	Pockels electro-optic effect
$\chi^{(2)}_{ijk}(0;\omega,-\omega)$	Optical rectification
$\chi^{(3)}_{ijkl}(-3\omega;\omega,\omega,\omega)$	Third-harmonic generation
$\chi^{(3)}_{ijkl}(-\omega_1 \mp \omega_2 \mp \omega_3;\omega_1,\pm\omega_2,\pm\omega_3)$	Frequency mixing
$\chi^{(3)}_{ijkl}(-\omega;\omega,\omega,-\omega)$	Optical Kerr effect
$\chi^{(3)}_{ijkl}(-\omega;0,0,-\omega)$	Kerr electro-optic effect
$\chi^{(3)}_{ijkl}(-2\omega;0,\omega,\omega)$	Electric-field-induce second-harmonic generation

respectively. Table 11.12 summarizes various nonlinear optical processes and their related dielectric susceptibility expressions [11.38].

It is useful to introduce the d matrix for the description of the second-order nonlinear part of the polarization vector as

$$\begin{bmatrix} P_1 \\ P_2 \\ P_3 \end{bmatrix} = \begin{bmatrix} d_{11} & d_{12} & d_{13} & d_{14} & d_{15} & d_{16} \\ d_{21} & d_{22} & d_{23} & d_{24} & d_{25} & d_{26} \\ d_{31} & d_{32} & d_{33} & d_{34} & d_{35} & d_{36} \end{bmatrix} \begin{bmatrix} E_1^2 \\ E_2^2 \\ E_3^2 \\ 2E_2E_3 \\ 2E_3E_1 \\ 2E_1E_2 \end{bmatrix} \tag{11.45}$$

where m and n in d_{mn} of Equation (11.45) represent m and ij, respectively, according to the rules $x \to 1$, $y \to 2$, $z \to 3$ (m) and $xx \to 1$, $yy \to 2$, $zz \to 3$, $yz \to 4$, $zx \to 5$, $xy \to 6$ (n). Table 11.13 lists the tensor form of the d matrix for crystals of certain symmetry classes. For a cubic T_d class, the only non-vanishing components are $d_{14} = d_{25} = d_{36} = 1/2\chi^{(2)}_{14}(-2\omega;\omega,\omega)$, but for a crystal with lower symmetric properties, the number of the non-vanishing components increases.

The nonlinear optical constants have been measured for a variety of semiconductors. We list in Table 11.14 the nonlinear optical constant $\chi^{(2)}_{123}(-2\omega;\omega,\omega)$ in the long-wavelength limit ($E \to 0$ eV) for some cubic semiconductors. The nonlinear optical constants $\chi^{(2)}_{ijk}(-2\omega;\omega,\omega)$ for hexagonal semiconductors are listed in Table 11.15. Note that 1 m/V $= 3 \times 10^4/4\pi$ esu (1 esu $= 4\pi/(3 \times 10^4)$ m/V).

The nonlinear optical constants $\chi^{(2)}_{123}(-2\omega;\omega,\omega)$ plotted as a function of the lowest direct band-gap energy E_0 for some cubic III–V and II–VI semiconductors are shown in Figure 11.8. The solid line represents the least-squares fit with the relation (E_0 in eV; χ in pm/V)

$$\chi^{(2)}_{123}(-2\omega;\omega,\omega) = \left(\frac{185}{E_0}\right)^{1.13} \tag{11.46}$$

Table 11.13 Form of the second-order nonlinear optical susceptibility tensor d_{ij} for semiconductors of certain symmetry classes

Symmetry class	Material	Tensor form
Cubic (Class O_h)	Si, Ge, MgO, etc.	$\begin{bmatrix} 0 & 0 & 0 & 0 & 0 & 0 \\ 0 & 0 & 0 & 0 & 0 & 0 \\ 0 & 0 & 0 & 0 & 0 & 0 \end{bmatrix}$ Showing no second-order optical nonlinearity
Cubic (Class T_d)	3C-SiC, GaAs, ZnSe, etc.	$\begin{bmatrix} 0 & 0 & 0 & d_{14} & 0 & 0 \\ 0 & 0 & 0 & 0 & d_{14} & 0 \\ 0 & 0 & 0 & 0 & 0 & d_{14} \end{bmatrix}$
Hexagonal (Class C_{6v})	2H-SiC, α-GaN, w-CdS, etc.	$\begin{bmatrix} 0 & 0 & 0 & 0 & d_{15} & 0 \\ 0 & 0 & 0 & d_{15} & 0 & 0 \\ d_{31} & d_{31} & d_{33} & 0 & 0 & 0 \end{bmatrix}$
Hexagonal (Class D_{6h})	h-BN	$\begin{bmatrix} 0 & 0 & 0 & 0 & 0 & 0 \\ 0 & 0 & 0 & 0 & 0 & 0 \\ 0 & 0 & 0 & 0 & 0 & 0 \end{bmatrix}$ Showing no second-order optical nonlinearity
Rhombohedral (Class C_{3v})	5R-SiC	$\begin{bmatrix} 0 & 0 & 0 & 0 & d_{15} & -d_{22} \\ -d_{22} & d_{22} & 0 & d_{15} & 0 & 0 \\ d_{31} & d_{31} & d_{33} & 0 & 0 & 0 \end{bmatrix}$

It is evident from Figure 11.8 that a smaller E_0-gap material has a larger value of $\chi^{(2)}_{123}(-2\omega;\omega,\omega)$.

Various theoretical calculations have been established to describe the dispersion of the nonlinear optical coefficients of crystals [11.70]. Most of them are founded on the calculation of the relevant matrix elements on the basis of the known electronic energy-band structure. The simplest way to estimate the frequency dependence of the nonlinear optical susceptibilities is the use of Miller's parameter [11.71]. If the linear electro-optic constant is defined in terms of polarization rather than electric field, the resulting coefficient

$$f_{ijk} = \frac{r_{ijk}}{\varepsilon_0(\varepsilon_k - 1)} \tag{11.47}$$

varies over a much narrower range, for a variety of crystals, than r_{ijk}. The Miller delta is a similar coefficient defined by

$$\Delta_{ijk} = \frac{\chi^{(2)}_{ijk}(-\omega_3;\omega_1,\omega_2)}{2(\varepsilon_i(\omega_3)-1)(\varepsilon_j(\omega_1)-1)(\varepsilon_k(\omega_2)-1)} = \frac{d_{ijk}(-\omega_3;\omega_1,\omega_2)}{(\varepsilon_i(\omega_3)-1)(\varepsilon_j(\omega_1)-1)(\varepsilon_k(\omega_2)-1)} \tag{11.48}$$

Theoretically, the Miller delta is considered to be independent of frequency if the system has a single anharmonic oscillator or a single resonance frequency, which may

Table 11.14 Second-order $\chi^{(2)}_{123}(-2\omega;\omega,\omega)$ and third-order nonlinear optical susceptibilities $\chi^{(3)}_{ijkl}(-3\omega;\omega,\omega,\omega)$ in the long-wavelength limit ($E \to 0$ eV) for some cubic group-IV, III–V and II–VI semiconductors

System	Material	$\chi^{(2)}_{123}$ (10^{-8} esu)	$\chi^{(3)}_{1111}$ (10^{-11} esu)	$\chi^{(3)}_{1212}$ (10^{-11} esu)
IV	Diamond	*a*	0.0184	0.00688
	Si	*a*	2.4	1.2
	Ge	*a*	10	5.2
	α-Sn	*a*		
	3C-SiC	14.5[b]	0.029[b]	0.014[b]
III–V	*c*-BN	0.24–0.81[b]		
	AlP	9.6[b]	1.39[b]	0.92[b]
	AlAs	15.3	0.97[b]	0.73[b]
	AlSb	23.4	7.52[b]	5.54[b]
	β-GaN	2.4–2.8[b]		
	GaP	33	2.10[b]	1.34[b]
	GaAs	89	8.9	1.6
	GaSb	250	3.4–187.2[b]	5.1–42.7[b]
	InP	68.5	0.23–9.84[b]	0.6–5.69[b]
	InAs	200	6.2–10 179[b]	3.0–966[b]
	InSb	524	8×10^3, 10^9, 10^{11}	0.79–1.47 $\times 10^4$[b]
II–VI	MgO		0.00294	0.00142
	β-ZnS	14.6	0.20[b]	0.15[b]
	ZnSe	37.4	1.2	1.2
	ZnTe	44	2.87[b]	1.53[b]
	c-CdS	7.4[b]	1.00[b]	0.57[b]
	c-CdSe	23.7[b]	2.95[b]	1.52[b]
	CdTe	28.2	5.41[b]	4.02[b]

[a] Principally showing no second-order nonlinear optical effect
[b] Calculated or estimated

Table 11.15 Second-order nonlinear optical susceptibility d_{ij} in the long-wavelength limit ($E \to 0$ eV) for some hexagonal and rhombohedral semiconductors (in pm/V)

System	Material	d_{15}	d_{31}	d_{33}	Comment
IV	6H-SiC		−2	12	$\lambda = 1.064$ μm
	15R-SiC		−3.1	5.2	Calc.
III–V	*w*-AlN	$\leqslant\lvert 0.26\rvert$		−6.3	$\lambda = 1.064$ μm
	α-GaN	8.0	8.2	−16.5	$\lambda = 1.064$ μm
	InN	2.8		3.1	Calc.
II–VI	ZnO	3.0	0.68	−7.16	$\lambda = 1.064$ μm
	α-ZnS	21	−19	37	
	w-CdS	29	−26	44	
	w-CdSe	31	−18	36	

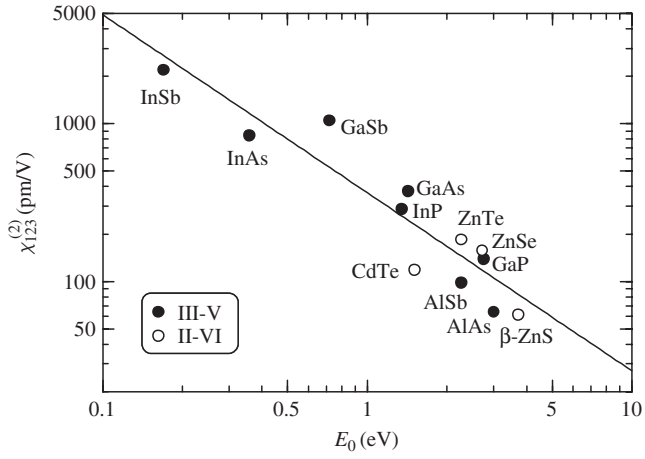

Figure 11.8 Experimental $\chi^{(2)}_{123}$ versus E_0 for some cubic III–V and II–VI semiconductors. The solid line represents the least-squares fit with $\chi^{(2)}_{123} = (185/E_0)^{1.13}$ (E_0 in eV; $\chi^{(2)}_{123}$ in pm/V)

not be a good approximation in actual materials. In fact, it has been shown experimentally [11.72] that the Miller delta is barely constant over the wavelength range measured for some dielectrics and semiconductors.

Wagner *et al.* [11.73] determined the absolute values of the second-harmonic-generation coefficient $|d_{14}|$ for β-ZnS, ZnSe and ZnTe in the fundamental radiation wavelength range from 520 to 1321 nm using various pulsed laser sources. They observed a strong dispersion in $|d_{14}|$ above the E_0-gap, showing a maximum at a second-harmonic frequency close to the E_1-gap. We reproduce in Figure 11.9 their results for ZnSe [11.73].

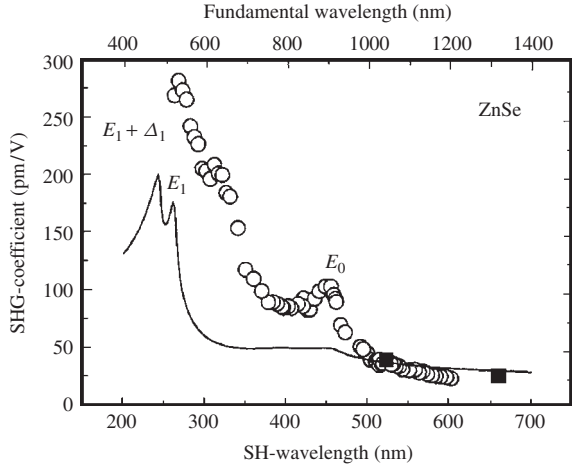

Figure 11.9 Experimental dispersion of the second-harmonic-generation (SHG) coefficient $|d_{14}|$ in ZnSe as a function of fundamental radiation wavelength. The solid line gives the theoretical dispersion curve. [From H. P. Wagner, M. Kühnelt, W. Langbein, and J. M. Hvam, *Phys. Rev. B* **58**, 10494 (1998), reproduced by permission from the American Physical Society]

11.5.2 Third-order nonlinear optical susceptibility

The effects arising from the third-order nonlinear optical susceptibility are third-harmonic generation, quadratic electro-optic or Kerr effect, two-photon absorption, stimulated light scattering, etc. (see Table 11.12). Although there has been an upsurge of interest in the enhancement of the higher-order nonlinear optical processes in low-dimensional semiconductor materials in recent years [11.74], the fundamental process in the bulk semiconductor itself cannot be completely understood. It should be noted that the third-order nonlinear optical effect can be observed in almost all media. Table 11.16 lists the independent non-vanishing tensor elements of the third-order nonlinear optical susceptibility $\chi^{(3)}_{ijkl}$ for the more commonly encountered classes of media [11.69].

If the dispersion of $\chi^{(m)}$ can be neglected, then the permutation symmetry

$$\begin{aligned}\chi^{(m)*}(\omega = \omega_1 + \omega_2 + \cdots + \omega_m) &= \chi^{(m)}(\omega_1 = -\omega_2 - \cdots - \omega_m + \omega) \\ &= \cdots\cdots \\ &= \chi^{(m)}(\omega_m = \omega - \omega_1 - \cdots - \omega_{m-1}) \end{aligned} \quad (11.49)$$

becomes independent of ω. Consequently, a symmetry relation now exists between different elements of the same $\chi^{(m)}$ tensor, that is, $\chi^{(m)}$ remains unchanged when the Cartesian indices are permutated. This is known as the Kleinman conjecture, with which the number of independent elements of $\chi^{(m)}$ can be greatly reduced. The Kleinman conjecture promises that, for cubic semiconductors, there are only two nonzero independent elements in $\chi^{(3)}$, namely, $\chi^{(3)}_{1111}$ and $\chi^{(3)}_{1122} = \chi^{(3)}_{1212} = \chi^{(3)}_{1221}$. It should be noted, however, that since

Table 11.16 Independent non-vanishing element of $\chi^{(3)}_{ijkl}(-\omega; \omega_1, \omega_2, \omega_3)$ for semiconductors of cubic and hexagonal symmetry classes

Symmetry class	Material	Non-vanishing element
Cubic (Classes O_h and T_d)	Si, Ge, 3C-SiC, GaAs, MgO, ZnSe, etc.	$xxxx = yyyy = zzzz$ $yyzz = zzyy = zzxx = xxzz = xxyy = yyxx$ $yzyz = zyzy = zxzx = xzxz = yxyx = xyxy$ $yzzy = zyyz = zxxz = xzzx = xyyx = yxxy$
Hexagonal (Classes C_{6v} and D_{6h})	2H-SiC, α-GaN, w-CdS, h-BN, etc.	$xxxx = yyyy = xxyy + xyyx + xyxy$ $zzzz$ $xxyy = yyxx$ $xyyx = yxxy$ $xyxy = yxyx$ $yyzz = xxzz$ $zzyy = zzxx$ $zyyz = zxxz$ $yzzy = xzzx$ $yzyz = xzxz$ $zyzy = zxzx$

Source: Y. R. Shen, *The Principles of Nonlinear Optics* (Wiley-Interscience, New York, 1984)

all media are dispersive, the Kleinman conjecture is a good approximation only when all frequencies involved are far from resonances such that the dispersion of $\chi^{(m)}$ is relatively unimportant.

For the third-harmonic generation coefficient $\chi^{(3)}_{ijkl}(-3\omega;\omega,\omega,\omega)$, there is only a single frequency ω present, and so $\chi^{(3)}$ will be symmetric in the last three indices. The number of independent tensor elements in such case can be reduced from 4 to 2 for the cubic class ($\chi^{(3)}_{1111}$ and $\chi^{(3)}_{1212}$) and from 11 to 4 for the hexagonal class ($\chi^{(3)}_{1111}$, $\chi^{(3)}_{3333}$, $\chi^{(3)}_{1133}$ and $\chi^{(3)}_{3311}$).

The nonlinear optical constants have been experimentally determined for several semiconductors. Table 11.14 summarizes the values of $\chi^{(3)}_{ijkl}(-3\omega;\omega,\omega,\omega)$ in the long-wavelength limit ($E \to 0$ eV) for some cubic semiconductors. These values are listed in esu, where 1 esu $= 4\pi/(9\times10^8)$ m^2/V^2 (1 m^2/V^2 $= 9\times10^8/4\pi$ esu).

11.5.3 Two-photon absorption

In a two-photon absorption process, two photons are simultaneously absorbed to excite a material system. Being a higher-order process, its absorption coefficient is many orders of magnitude smaller than that of a one-photon absorption. Using third-order optical susceptibility tensor $\chi^{(3)}$, the two-photon absorption coefficient β is described by

$$\beta = \frac{24(2\pi)^2\omega}{c^2n^2(\omega)}\,\mathrm{Im}\chi^{(3)}_{ijkl}(-\omega;\omega,\omega,-\omega) \tag{11.50}$$

where $n(\omega)$ is the refractive index of the light at frequency ω and the spatial indices i, j, k, l are determined by the sample symmetry and the incident light polarization, in such a way that for a laser beam plane-polarized along the z axis of the sample, the relevant quantity is Im $\chi^{(3)}_{zzzz}$.

The two-photon absorption is conceptually very simple and can be given by phenomenologically

$$\frac{\mathrm{d}I}{\mathrm{d}z} = -(\alpha + \beta I)I \tag{11.51}$$

where α is the linear absorption coefficient and the two-photon absorption coefficient β can be calculated by second-order perturbation theory in terms of transition probability W_2 as

$$\beta = \frac{4W_2h\nu}{I^2} \tag{11.52}$$

with

$$W_2 = \frac{1}{(2\pi)^2h}\int\left|\frac{\sum_i\langle\Psi_\mathrm{c}|H_\mathrm{eR}|\Psi_i\rangle\langle\Psi_i|H_\mathrm{eR}|\Psi_\mathrm{v}\rangle}{E_i - E_\mathrm{v} - h\nu}\right|^2\delta(E_\mathrm{c}(\boldsymbol{k}) - E_\mathrm{v}(\boldsymbol{k}) - 2h\nu)\,\mathrm{d}^3k \tag{11.53}$$

where Ψ is the electron wavefunction, H_eR is the electron–radiation interaction Hamiltonian and the indices c, v and i refer to the conduction band, valence band and intermediate

state in the two-photon absorption process, respectively. Because of the summation over all the intermediate states, it is very difficult to calculate Equation (11.53) exactly. Practically, these summations are taken over a limited number of intermediate states, which are deemed to be dominant.

The scaling and nonlinear optical phenomena in semiconductors have been discussed by Sheik-Bahae *et al.* [11.75]. A simple two-parabolic band model has been used to calculate various nonlinear optical responses, such as the two-photon absorption coefficient, ac Stark effect and Raman scattering cross-section. The two-photon absorption coefficient $\beta(\omega)$ reported by these authors can be expressed as

$$\beta(\omega) = \frac{K\sqrt{E_p}}{n_0^2 E_g^3} F\left(\frac{\hbar\omega}{E_g}\right) \tag{11.54}$$

where E_p is related to the Kane momentum parameter ($\sim$21 eV for most direct band-gap semiconductors) and K is a material-independent constant equal to 1940 when E_p and E_g are in eV and β is in cm/GW. The function $F(x)$ is dependent on the assumed band-structure model and is a function only of the ratio of the photon energy to the band-gap energy of the material, $x = \hbar\omega/E_g$. Sheik-Bahae *et al.* also obtained the nonlinear index of refraction $n_2(\omega)$ from the nonlinear absorption using a Kramers–Kronig transformation as

$$n_2(\omega) = \frac{K'\sqrt{E_p}}{n_0 E_g^4} G\left(\frac{\hbar\omega}{E_g}\right) \tag{11.55}$$

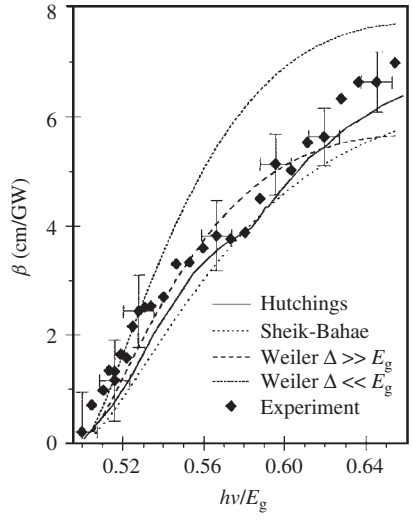

Figure 11.10 Two-photon absorption coefficient β in ZnSe at room temperature. Symbols represent the measured values. Horizontal error bars account for the spread in the value of the ZnSe energy gap. Lines show the predictions of different theoretical models. [From M. Dabbicco and M. Brambilla, *Solid State Commun.* **114**, 515 (2000), reproduced by permission from Elsevier]

where $K' = 9.4 \times 10^{-9}$ when E_p and E_g are in eV, n_2 is in esu, and the function G is again dependent only on the ratio of the photon energy to the band-gap energy of the material.

The two-photon absorption coefficient has been discussed both experimentally and theoretically for some group-IV (Si [11.76]), III–V (α-GaN [11.77], GaP [11.78], GaAs [11.76] and InSb [11.79]) and II–VI semiconductors (ZnO [11.80, 11.81], α-ZnS [11.82], β-ZnS [11.83], ZnSe [11.84], ZnTe [11.85], w-CdS [11.83], w-CdSe [11.86] and CdTe [11.87]). We show in Figure 11.10, as an example, the two-photon absorption spectrum measured for ZnSe at room temperature [11.84]. The Ti: sapphire laser used in this study was tunable over the 700–980 nm (1.77–1.27 eV) spectral range, which scaled to the ZnSe E_0-gap energy ~2.7 eV at room temperature. The theoretical plots shown in Figure 11.10 are predicted by several models [11.75, 11.88, 11.89], including the two-parabolic band model of Equation (11.54) by Sheik-Bahae *et al*. [11.75]. The experimental data revealed an inflection point at $h\nu/E_g \sim 0.58$, which may be originating from the spin–orbit split-off valence band. It has been concluded that general scaling laws for the calculation of the two-photon absorption coefficient provide a good estimate of the strength of the absorption, but fail to account for details of the spectrum.

REFERENCES

[11.1] R. W. Dixon, *J. Appl. Phys.* **38**, 5149 (1967).
[11.2] See, for example, *Guided-Wave Acousto-Optics*, edited by C. S. Tsai (Springer, Berlin, 1990).
[11.3] F. K. Reinhart and R. A. Logan, *J. Appl. Phys.* **44**, 3171 (1973).
[11.4] J. P. van der Ziel and A. C. Gossard, *J. Appl. Phys.* **48**, 3018 (1977).
[11.5] H. Booyens and J. H. Basson, *J. Appl. Phys.* **51**, 4368 (1980).
[11.6] C. H. Higginbotham, M. Cardona, and F. H. Pollak, *Phys. Rev.* **184**, 821 (1969).
[11.7] S. H. Wemple and M. DiDomenico, Jr., *Phys. Rev. B* **1**, 193 (1970).
[11.8] R. Berkowicz and T. Skettrup, *Phys. Rev. B* **11**, 2316 (1975).
[11.9] M. Sugie and K. Tada, *Jpn. J. Appl. Phys.* **15**, 257 (1976).
[11.10] S. Adachi and K. Oe, *J. Appl. Phys.* **54**, 6620 (1983).
[11.11] S. A. Geidur and A. D. Yaskov, *Opt. Spectrosc.* (USSR) **57**, 45 (1984).
[11.12] J. F. Nye, *Physical Properties of Crystals* (Clarendon, Oxford, 1972).
[11.13] P. Y. Yu and M. Cardona, *J. Phys. Chem. Solids* **34**, 29 (1973).
[11.14] L. N. Glurdzhidze, A. P. Izergin, Z. N. Kopylova, and A. D. Remenyuk, *Sov. Phys. Semicond.* **7**, 305 (1973).
[11.15] F. Canal, M. H. Grimsditch, and M. Cardona, *Solid State Commun.* **29**, 523 (1979).
[11.16] B. Tell, J. M. Worlock, and R. J. Martin, *Appl. Phys. Lett.* **6**, 123 (1965).
[11.17] P. Y. Yu, M. Cardona, and F. H. Pollak, *Phys. Rev. B* **3**, 340 (1971).
[11.18] G. B. Benedek and K. Fritch, *Phys. Rev.* **149**, 647 (1966).
[11.19] C. Hamaguchi, *J. Phys. Soc. Jpn* **35**, 832 (1973).
[11.20] S. Adachi and C. Hamaguchi, *Physica* **97B**, 187 (1979).
[11.21] D. K. Garrod and R. Bray, *Phys. Rev. B* **6**, 1314 (1972).
[11.22] Y. Itoh, M. Fujii, C. Hamaguchi, and Y. Inuishi, *J. Phys. Soc. Jpn* **48**, 1972 (1980).
[11.23] S. Adachi and C. Hamaguchi, *Phys. Rev. B* **19**, 938 (1979).
[11.24] S. Adachi and C. Hamaguchi, *J. Phys. Soc. Jpn* **43**, 1637 (1977).
[11.25] K. Ando and C. Hamaguchi, *Phys. Rev. B* **11**, 3876 (1975).
[11.26] K. Yamamoto, K. Misawa, H. Shimizu, and K. Abe, *J. Phys. Chem. Solids* **37**, 181 (1976).
[11.27] R. W. Dixon and M. G. Cohen, *Appl. Phys. Lett.* **8**, 205 (1966).

[11.28] N. Suzuki and K. Tada, *Jpn. J. Appl. Phys.* **23**, 1011 (1984).
[11.29] P. Renosi and J. Sapriel, *Appl. Phys. Lett.* **64**, 2794 (1994).
[11.30] F. H. Pollak and M. Cardona, *Phys. Rev.* **172**, 816 (1968).
[11.31] M. Chandrasekhar and F. H. Pollak, *Phys. Rev. B* **15**, 2127 (1977).
[11.32] M. Chandrasekhar, M. H. Grimsditch, and M. Cardona, *Phys. Rev. B* **18**, 4301 (1978).
[11.33] P. Etchegoin, J. Kircher, M. Cardona, and C. Grein, *Phys. Rev. B* **45**, 11721 (1992).
[11.34] P. Etchegoin, J. Kircher, and M. Cardona, *Phys. Rev. B* **47**, 10292 (1993).
[11.35] P. Etchegoin, J. Kircher, M. Cardona, C. Grein, and E. Bustarret, *Phys. Rev. B* **46**, 15139 (1992).
[11.36] D. Rönnow, P. Santos, M. Cardona, E. Anastassakis, and M. Kuball, *Phys. Rev. B* **57**, 4432 (1998).
[11.37] D. Rönnow, M. Cardona, and L. F. Lastras-Martínez, *Phys. Rev. B* **59**, 5581 (1999).
[11.38] See, for example, F. Agulló-López, J. M. Cabrera, and F. Agulló-Rueda, *Electrooptics: Phenomena, Materials and Applications* (Academic, London, 1994).
[11.39] M. DiDomenico, Jr. and S. H. Wemple, *J. Appl. Phys.* **40**, 720 (1969).
[11.40] C. G. B. Garrett, *IEEE J. Quantum Electron.* **QE-4**, 70 (1968).
[11.41] M. Sugie and K. Tada, *Jpn. J. Appl. Phys.* **12**, 215 (1973).
[11.42] S. Adachi and K. Oe, *J. Appl. Phys.* **56**, 74 (1984).
[11.43] S. Adachi and K. Oe, *J. Appl. Phys.* **56**, 1499 (1984).
[11.44] S. Adachi, *J. Appl. Phys.* **72**, 3702 (1992).
[11.45] A. Hernandez-Cabrera, C. Tejedor, and F. Meseguer, *J. Appl. Phys.* **58**, 4666 (1985).
[11.46] D. F. Nelson and E. H. Turner, *J. Appl. Phys.* **39**, 3337 (1968).
[11.47] M. Sugie and K. Tada, *Jpn. J. Appl. Phys.* **15**, 421 (1976).
[11.48] K. Tada and N. Suzuki, *Jpn. J. Appl. Phys.* **19**, 2295 (1980).
[11.49] S. Adachi, *Physical Properties of III–V Semiconductor Compounds: InP, InAs, GaAs, GaP, InGaAs, and InGaAsP* (Wiley-Interscience, New York, 1992).
[11.50] F. K. Reinhart, D. F. Nelson, and J. McKenna, *Phys. Rev.* **177**, 1208 (1969).
[11.51] J. Faist and F.-K. Reinhart, *J. Appl. Phys.* **67**, 7006 (1990).
[11.52] C.-A. Berseth, C. Wuethrich, and F.-K. Reinhart, *J. Appl. Phys.* **71**, 2821 (1992).
[11.53] A. Alping and L. A. Coldren, *J. Appl. Phys.* **61**, 2430 (1987).
[11.54] H. G. Bach, J. Krauser, H. P. Nolting, R. A. Logan, and F.-K. Reinhart, *Appl. Phys. Lett.* **42**, 692 (1983).
[11.55] K. Tharmalingam, *Phys. Rev.* **130**, 2204 (1963).
[11.56] J. Callaway, *Phys. Rev.* **130**, 549 (1963); **134**, A998 (1964).
[11.57] D. E. Aspnes, *Phys. Rev.* **153**, 972 (1967).
[11.58] T. E. Van Eck, L. M. Walpita, W. S. C. Chang, and H. H. Wieder, *Appl. Phys. Lett.* **48**, 451 (1986).
[11.59] D. R. Wight, A. M. Keir, G. J. Pryce, J. C. H. Birbeck, J. M. Heaton, R. J. Norcross, and P. J. Wright, *IEE Proc.-J* **135**, 39 (1988).
[11.60] H. D. Rees, *J. Phys. Chem. Solids* **29**, 143 (1968).
[11.61] M. Chester and P. H. Wendland, *Phys. Rev. Lett.* **13**, 193 (1964).
[11.62] B. O. Seraphin, R. B. Hess, and N. Bottka, *J. Appl. Phys.* **36**, 2242 (1965).
[11.63] R. G. Verenchikova and A. O. Konstantinov, *Sov. Phys. Semicond.* **18**, 242 (1984).
[11.64] O. Gasakov, D. N. Nasledov, and S. V. Slobodchikov, *Phys. Status Solidi* **35**, 139 (1969).
[11.65] M. P. Mikhaĭlova, D. N. Nasledov, and S. V. Slobodchikov, *Sov. Phys. Solid State* **7**, 1031 (1965).
[11.66] K. Hirabayashi and K. Ono, *Jpn. J. Appl. Phys.* **29**, L1672 (1990).
[11.67] D. J. Robbins, in *Properties of Gallium Arsenide*, 2nd Edition, EMIS Datareviews Series No. 2 (INSPEC, London, 1991), p. 167.
[11.68] P. A. Franken, A. E. Hill, C. W. Peters, and G. Weinreich, *Phys. Rev. Lett.* **7**, 118 (1961).
[11.69] Y. R. Shen, *The Principles of Nonlinear Optics* (Wiley-Interscience, New York, 1984).

[11.70] See, for example, S. Scandolo and F. Bassani, *Phys. Rev. B* **51**, 6928 (1995), and references therein.
[11.71] R. C. Miller, *Appl. Phys. Lett.* **5**, 17 (1964).
[11.72] I. Shoji, T. Kondo, A. Kitamoto, M. Shirane, and R. Ito, *J. Opt. Soc. Am. B* **14**, 2268 (1997).
[11.73] H. P. Wagner, M. Kühnelt, W. Langbein, and J. M. Hvam, *Phys. Rev. B* **58**, 10494 (1998).
[11.74] See, for example, *Semiconductors and Semimetals*, edited by R. K. Willardson and E. R. Weber (Academic, San Diego, 1999), Vols. 58 and 59 (Volume Editors, E. Garmire and A. Kost).
[11.75] M. Sheik-Bahae, D. C. Hutchings, D. J. Hagan, and E. W. Van Stryland, *IEEE J. Quantum Electron.* **27**, 1296 (1991).
[11.76] M. Murayama and T. Nakayama, *Phys. Rev. B* **52**, 4986 (1995).
[11.77] C.-K. Sun, J.-C. Liang, J.-C. Wang, F.-J. Kao, S. Keller, M. P. Mack, U. Mishra, and S. P. DenBaars, *Appl. Phys. Lett.* **76**, 439 (2000).
[11.78] C. B. de Araujo and H. Lotem, *Phys. Rev. B* **18**, 30 (1978).
[11.79] A. Miller, A. Johnston, J. Dempsey, J. Smith, C. R. Pidgeon, and G. D. Holah, *J. Phys. C: Solid State Phys.* **12**, 4839 (1979).
[11.80] G. Kobbe and C. Klingshirn, *Z. Phys. B* **37**, 9 (1980).
[11.81] X. J. Zhang, W. Ji, and S. H. Tang, *J. Opt. Soc. Am. B* **14**, 1951 (1997).
[11.82] Y. Bae, J. J. Song, and Y. B. Kim, *J. Appl. Phys.* **53**, 615 (1982).
[11.83] T. D. Krauss and F. W. Wise, *Appl. Phys. Lett.* **65**, 1739 (1994).
[11.84] M. Dabbicco and M. Brambilla, *Solid State Commun.* **114**, 515 (2000).
[11.85] I. M. Catalano and A. Cingolani, *Phys. Rev. B* **19**, 1049 (1979).
[11.86] I. B. Zotova and Y. J. Ding, *Appl. Opt.* **40**, 6654 (2001).
[11.87] A. A. Said, M. Sheik-Bahae, D. J. Hagan, T. H. Wei, J. Wang, J. Young, and E. W. Van Stryland, *J. Opt. Soc. Am. B* **9**, 405 (1992).
[11.88] M. H. Weiler, *Solid State Commun.* **39**, 937 (1981).
[11.89] D. C. Hutchings and E. W. Van Stryland, *J. Opt. Soc. Am. B* **11**, 2065 (1992).

12 Carrier Transport Properties

12.1 Low-field mobility: electrons 315
12.1.1 Electron scattering mechanism 315
12.1.2 Three-valley model 320
12.1.3 Room-temperature value 321
12.1.4 External perturbation and doping effects 324
12.1.5 Hall factor 328
12.2 Low-field mobility: holes 331
12.2.1 Hole scattering mechanism 331
12.2.2 Room-temperature value 333
12.2.3 External perturbation and doping effects 333
12.3 High-field transport: electrons 339
12.3.1 Electron drift velocity–field characteristic 339
12.3.2 Electron saturation drift velocity 347
12.4 High-field transport: holes 349
12.4.1 Hole drift velocity–field characteristic 349
12.4.2 Hole saturation drift velocity 352
12.5 Minority-carrier transport: electrons in p-type materials 353
12.5.1 Minority-electron mobility 353
12.5.2 Minority-electron drift velocity 356
12.5.3 Minority-electron lifetime and diffusion length 356
12.6 Minority-carrier transport: holes in n-type materials 359
12.6.1 Minority-hole mobility 359
12.6.2 Minority-hole lifetime and diffusion length 360
12.7 Impact ionization coefficient 362
12.7.1 Theoretical consideration 362
12.7.2 Experimental value 365
References 369

12.1 LOW-FIELD MOBILITY: ELECTRONS

12.1.1 Electron scattering mechanism

Hall mobility is a popular parameter used to characterize the microscopic quality of semiconductors. An accurate comparison between experimental carrier mobility and theoretical calculation is of great importance for the determination of a variety of fundamental material parameters and carrier scattering mechanisms. There are various carrier scattering

Properties of Group-IV, III–V and II–VI Semiconductors Sadao Adachi

© 2005 John Wiley & Sons, Ltd

ISBN: 0-470-09032-4

Table 12.1 Various possible electron scattering mechanisms in semiconductors

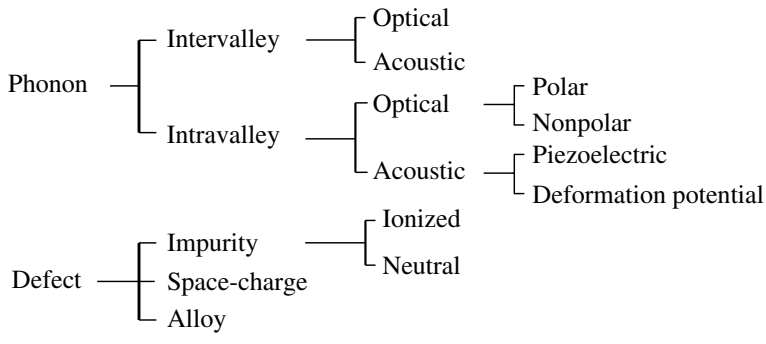

mechanisms in semiconductors; Table 12.1 shows an outline of the possible mechanisms. The effect of the individual scattering mechanisms on the total calculated electron mobility can be visualized by Matthiessen's rule

$$\frac{1}{\mu^{\mathrm{e}}_{\mathrm{TOT}}} = \sum_i \frac{1}{\mu^{\mathrm{e}}_i} \tag{12.1}$$

Thus, the total mobility $\mu^{\mathrm{e}}_{\mathrm{TOT}}$ can be calculated from the scattering-limited mobilities μ^{e}_i of each scattering mechanism. In the following, we present specific expressions for μ^{e}_i associated with various scattering mechanisms in cubic semiconductors [12.1–12.5]. Table 12.2 summarizes the mass and temperature dependences of μ^{e}_i obtained from these expressions.

Table 12.2 Temperature and mass dependences of the electron mobility for different scattering mechanisms in semiconductors

Scattering process	Temperature dependence	Mass dependence
Intervalley		−5/2
Polar optical		−3/2
Nonpolar optical	−3/2 ($kT \gg \hbar\omega_{\mathrm{o}}$)	−5/2
Piezoelectric	−1/2	−3/2
Deformation potential	−3/2	−5/2
Ionized impurity	3/2	−1/2
Neutral impurity	0	0
Space-charge	−1/2	−1/2
Alloy	−1/2	−5/2

(a) Intervalley scattering

In materials in which the conduction-band minimum is at the Γ point, the electrons, after being scattered by the lattice, usually remain in the same valley. This kind of lattice scattering is called intravalley scattering. In materials with the lowest conduction-band minima in the ⟨100⟩ (X) or ⟨111⟩ (L) directions, the electrons may be scattered by the phonons from one valley to another valley having its energy minimum at the nearly same level. In such transitions, the wavevector of the electrons changes significantly, so that only phonons with large wavevectors may cause such scattering and the corresponding phonons are often referred to as intervalley phonons. It should be noted that the intervalley phonons may be of either kind, optical or acoustic.

The intervalley scattering is important at low fields in materials with the lowest conduction-band minimum at the X or L point. The intervalley scattering-limited mobility from a $\boldsymbol{k}$ state in the i valley to a state in the j valley can be given by [12.6]

$$\mu_{\text{iv}}^{\text{e}} = \frac{8\sqrt{\pi}}{3(m_j^*)^{5/2}} \frac{e\hbar^2 g\sqrt{k\Xi}}{\sqrt{3}ND_{ij}^2} \left(\frac{\sqrt{\dfrac{T}{\Xi} + \dfrac{2}{3} + \dfrac{\Delta E_{ij}}{kT}}}{e^{\Xi/T} - 1} + \frac{\sqrt{\dfrac{T}{\Xi} - \dfrac{2}{3} + \dfrac{\Delta E_{ij}}{kT}}}{1 - e^{\Xi/T}} \right)^{-1}$$

$$\text{for } \frac{T}{\Xi} \geqslant \frac{2}{3} + \frac{\Delta E_{ij}}{kT} \tag{12.2}$$

where g is the crystal density, Ξ is the intervalley (optical or acoustic) phonon temperature, N is the number of equivalent minima ($N = 1$ for the Γ minimum, $N = 3$ for the X minima and $N = 4$ for the L minima), ΔE_{ij} is the intervalley energy separation, m_j^* is the electron effective mass in a single j minimum and D_{ij} is the intervalley deformation potential. The last term on the right-hand side is 0 for $T/\Xi < (2/3 + \Delta E_{ij}/kT)$. Note that Equation (12.2) corresponds to the case $i \neq j$ (i.e., nonequivalent intervalley scattering). In the case of equivalent intervalley scattering ($i = j$), the equation is applicable when N is changed to $(N - 1)$ and $\Delta E_{ij} = 0$. It should also be noted that the intervalley scattering is usually treated, formally, in the same way as intravalley scattering by nonpolar optical phonons with a deformation potential interaction (see Equation (12.6)).

(b) Polar optical scattering

Polar optical scattering occurs through the polarization produced by the optical vibrations due to the ionic charges associated with the atoms forming the material. The displacement of the neighboring atoms of opposite ionic charges results in dipole moments, the potential associated with which scatters the electrons. The polar optical phonon scattering is often the most important scattering mechanism, particularly in ionic semiconductors at liquid nitrogen or higher temperatures.

The polar optical phonon scattering-limited mobility can be given by

$$\mu_{\text{po}}^{\text{e}} = \frac{2^{9/2}\sqrt{\pi}\hbar^2 (kT)^{1/2} (e^{T_{\text{po}}/T} - 1)\chi(T_{\text{po}}/T)}{3ekT_{\text{po}}(m_{\text{c}}^{\alpha})^{3/2}\varepsilon_0^{-1}(\varepsilon_\infty^{-1} - \varepsilon_{\text{s}}^{-1})} \tag{12.3}$$

where m_c^α is the conductivity effective mass ($\alpha = \Gamma$, X or L), ε_∞ and ε_s are, respectively, the high-frequency and static dielectric constants, T_{po} is the polar optical phonon temperature ($kT_{po} = \hbar\omega_{LO}$) and $\chi(T_{po}/T)$ is a slowly varying function of T.

(c) Nonpolar optical scattering

The deformation of the crystal due to nonpolar optical phonons can produce a perturbing potential proportional to the optical lattice strain. The strength of this interaction is known to be very weak for electrons at the Γ-conduction-band and X-conduction-band minima. It is, however, strong for minima along the ⟨111⟩ (L) directions. Since in most III–V and II–VI semiconductors the lowest conduction-band minimum is at the Γ point, this type of scattering is of less importance.

The nonpolar optical phonon scattering-limited mobility can be written, in approximate forms, as

$$\mu_{npo}^{e} = \frac{2\sqrt{2\pi}\, g\hbar^4 e\omega_o^2}{3D_o^2 (m_c^\alpha)^{5/2}(kT)^{3/2}}, \qquad kT \gg \hbar\omega_o \tag{12.4a}$$

$$\mu_{npo}^{e} = \frac{\sqrt{2\hbar\omega_o}\,\pi g\hbar^4 e}{D_o^2 (m_c^\alpha)^{5/2} n_o}, \qquad kT \ll \hbar\omega_o \tag{12.4b}$$

where ω_o is the nonpolar optical phonon frequency, $n_o = 1/[\exp(\hbar\omega_o/kT) - 1]$ and D_o is the nonpolar optical phonon deformation potential given in energy per unit strain.

(d) Piezoelectric scattering

The piezoelectric scattering is caused by acoustic phonons through the piezoelectric effect. The piezoelectric effect can be observed in crystals lacking a center of symmetry, which includes all compound semiconductors (but not diamond, Si and Ge). The piezoelectric scattering is, thus, important in all compound semiconductors. It may also be stronger in materials with the wurtzite structure than in materials with the sphalerite (zinc-blende) structure due to the lower symmetry of the former structure.

The piezoelectric scattering-limited mobility can be given by

$$\mu_{pz}^{e} = \frac{16\sqrt{2\pi}\,\varepsilon_0\varepsilon_s\hbar^2}{3\sqrt{kT}\, eK^2 (m_c^\alpha)^{3/2}} \tag{12.5}$$

where K is the electromechanical coupling constant. Note that $\mu_{pz}^{e} \propto T^{-1/2}$, so this mechanism tends to dominate at low temperatures.

(e) Deformation potential scattering

The scattering of the carriers through the deformation potential is called deformation potential scattering. Due to the changes in the spacing of the lattice atoms, the conduction-band and valence-band edges may vary from point to point. The potential so produced

due to the deformation of the crystal is called the deformation potential, the magnitude of which is evidently proportional to the strain produced by the lattice vibrations.

The deformation potential scattering-limited mobility is given by

$$\mu_{\mathrm{dp}}^{\mathrm{e}} = \frac{2\sqrt{2\pi}\hbar^4 C_{\mathrm{l}} e}{3E_1^2 (m_{\mathrm{c}}^{\alpha})^{5/2} (kT)^{3/2}} \tag{12.6}$$

where E_1 is the acoustic deformation potential and C_{l} is the longitudinal elastic constant defined by

$$C_{\mathrm{l}} = \tfrac{1}{5}(3C_{11} + 2C_{12} + 4C_{44}) \tag{12.7}$$

(f) Ionized impurity scattering

Ionized impurities can scatter electrons through their screened Coulomb potential

$$\Delta V = \frac{Ze^2}{4\pi\varepsilon_{\mathrm{s}} r} e^{-r/\lambda_{\mathrm{D}}} \tag{12.8}$$

where Ze is the ionic charge (e = elementary charge) and λ_{D} is the Debye length. The corresponding ionized impurity scattering-limited mobility can be given by

$$\mu_{\mathrm{ii}}^{\mathrm{e}} = \frac{128\sqrt{2\pi}\varepsilon_0^2 \varepsilon_{\mathrm{s}}^2 (kT)^{3/2}}{N_{\mathrm{I}} Z^2 e^3 (m_{\mathrm{c}}^{\alpha})^{1/2} \left[\ln(1+y) - y/(1+y)\right]} \tag{12.9}$$

with

$$y = \frac{24\varepsilon_0 \varepsilon_{\mathrm{s}} m_{\mathrm{c}}^{\alpha} (kT)^{3/2}}{\hbar^2 e^2 n} \tag{12.10}$$

where N_{I} and n are the ionized impurity and free-electron concentrations, respectively.

(g) Neutral impurity scattering

When an electron passes close to a neutral atom, momentum can be transferred through a collision with a bound electron on the atom. The mobility in this case can be written as

$$\mu_{\mathrm{ni}}^{\mathrm{e}} = \frac{e^3 m_{\mathrm{c}}^{\alpha}}{80\pi N_0 \hbar^3 \varepsilon_0 \varepsilon_{\mathrm{s}}} \tag{12.11}$$

where N_0 is the concentration of the neutral impurity.

(h) Space-charge scattering

Weisberg [12.7] has discussed the mobility due to space-charge scattering which is given by

$$\mu_{\mathrm{sc}}^{\mathrm{e}} = \frac{2^{3/2} e}{3\sqrt{\pi k T m_{\mathrm{c}}^{\alpha}} N \sigma_{\mathrm{sc}}} \tag{12.12}$$

where N is the impurity or defect concentration and σ_{sc} is the space-charge scattering cross-section.

(i) Alloy scattering

In alloy semiconductors, the electrons see potential fluctuations as a result of the composition disorder. This kind of scattering, so-called alloy scattering is important in some of the III–V ternaries and quaternaries. The alloy scattering-limited mobility in ternary alloy can be given by

$$\mu_{al}^{e} = \frac{\sqrt{2\pi} e\hbar^4 N_{al}}{3(m_c^{\alpha})^{5/2}(kT)^{1/2} x(1-x)(\Delta U)^2} \tag{12.13}$$

where N_{al} is the density of alloy sites, x and $(1-x)$ are the mole fractions of the binary end compounds and ΔU_e is the alloy scattering potential.

(j) Carrier–carrier scattering

In a process where an electron is scattered by another electron, the total momentum of carrier gas is unchanged. Hence, carrier–carrier scattering alone has no significant influence on the mobility. However, since it is always combined with other scattering processes, it is sometimes quite important. For example, the dominating ionized impurity scattering-limited mobility μ_{ii}^{e} in a nondegenerate semiconductor can be reduced to a value by a factor of about 0.6. The changes for scattering by phonons are less pronounced. Evidently the importance of the carrier–carrier scattering is only at high carrier concentrations, say, $n > 10^{18}$ cm^{-3}.

12.1.2 Three-valley model

A three-valley model of the conduction band is used to account for the Γ, L and X valleys of semiconductors. Considering the Γ minimum as the energy reference, the electron concentration in the Γ minimum and those in the L and X minima relative to the Γ minimum are given by

$$n_{\Gamma} = 2\left(\frac{2\pi m_e^{\Gamma} kT}{h^2}\right)^{3/2} \exp\left(-\frac{E_F}{kT}\right) \tag{12.14a}$$

$$\frac{n_L}{n_{\Gamma}} = \left(\frac{m_e^{L}}{m_e^{\Gamma}}\right)^{3/2} \exp\left(-\frac{\Delta E_{\Gamma L}}{kT}\right) \tag{12.14b}$$

$$\frac{n_X}{n_{\Gamma}} = \left(\frac{m_e^{X}}{m_e^{\Gamma}}\right)^{3/2} \exp\left(-\frac{\Delta E_{\Gamma X}}{kT}\right) \tag{12.14c}$$

where $\Delta E_{\Gamma L}$ and $\Delta E_{\Gamma X}$ are the energy separations between the Γ–L and Γ–X minima, respectively (see Section 6.5). The total carrier density is given by

$$n = n_\Gamma + n_L + n_X \tag{12.15}$$

and the conductivity can be written as

$$\sigma = e \sum_\alpha n_\alpha \mu_\alpha \tag{12.16}$$

where μ_α is the mobility in the αth valley.

The electron Hall mobility μ_H and electron Hall concentration n_H are now given by

$$\mu_H = \mu_\Gamma \frac{1 + (n_L/n_\Gamma)(\mu_L/\mu_\Gamma)^2 + (n_X/n_\Gamma)(\mu_X/\mu_\Gamma)^2}{1 + (n_L/n_\Gamma)(\mu_L/\mu_\Gamma) + (n_X/n_\Gamma)(\mu_X/\mu_\Gamma)} \tag{12.17}$$

$$n_H = n_\Gamma \frac{[1 + (n_L/n_\Gamma)(\mu_L/\mu_\Gamma) + (n_X/n_\Gamma)(\mu_X/\mu_\Gamma)]^2}{1 + (n_L/n_\Gamma)(\mu_L/\mu_\Gamma)^2 + (n_X/n_\Gamma)(\mu_X/\mu_\Gamma)^2} \tag{12.18}$$

In a single-valley model, the Hall factor is usually assumed to be unity. This assumption is very poor when many bands are involved. The Hall factor γ in the three-valley model will be presented in Section 12.1.5.

12.1.3 Room-temperature value

The low-field electron Hall mobility μ_e has been measured for a variety of semiconductors. We list in Table 12.3 the room-temperature (μ_{300K}) and peak mobility values (μ_{peak}) for some cubic, hexagonal and rhombohedral semiconductors, together with their lowest conduction-valley conductivity masses m_c^α. The corresponding μ_{300K} and μ_{peak} versus m_c^α plots are shown in Figures 12.1(a) and 12.1(b), respectively. As expected from Table 12.2, a smaller m_c^α material may have a larger μ_{300K} or μ_{peak} value. This tendency can be clearly recognized in Figure 12.1. The solid lines in Figures 12.1(a) and 12.1(b) represent the least-squares fit with the relation (m_c^α in m_0; μ in $cm^2/V\ s$)

$$\mu_{300K} = \left(\frac{32.1}{m_c^\alpha}\right)^{1.26} \tag{12.19a}$$

$$\mu_{peak} = \left(\frac{39.0}{m_c^\alpha}\right)^{1.60} \tag{12.19b}$$

Figure 12.2 plots the 300 K mobility μ_{300K} versus lowest direct band-gap energy E_0 for some direct band-gap semiconductors. The solid line shows the least-squares fit with (E_0 in eV; μ_{300K} in $cm^2/V\ s$)

$$\ln \mu_{300K} = 10.3 - 1.41 E_0 \tag{12.20}$$

Table 12.3 300 K (μ_{300K}) and peak Hall mobilities (μ_{peak}) for electrons in some cubic, hexagonal and rhombohedral semiconductors. The conductivity electron mass m_c^α in the lowest conduction band is also presented in the third column

System	Material	m_c^α/m_0	μ_{300K} (cm^2/V s)	μ_{peak} (cm^2/V s)
IV	Diamond	0.48	2800	9000 ($T \sim 80$ K)
	Si	0.259	1750[a]	500000 ($T \sim 8$ K)[a]
	Ge	0.119	2300	530000 ($T \sim 11$ K)
	α-Sn	0.029[b]		80800 ($T = 4.2$ K)
	3C-SiC	0.32	980	3000 ($T \sim 66$ K)
	6H-SiC		375	10940 ($T = 50$ K)
	15R-SiC		500	1700 ($T \sim 90$ K)
III–V	c-BN	0.31		4 ($T = 900$ K)
	BP	0.28	190	190 ($T = 300$ K)
	AlP	0.31	80	80 ($T = 300$ K)
	AlAs	0.26	294	294 ($T = 300$ K)
	AlSb	0.29	200	700 ($T = 77$ K)
	α-GaN	0.21	1245	7400 ($T \sim 60$ K)
	β-GaN	0.15	760	11000 ($T \sim 50$ K)
	GaP	0.37	189	3100 ($T \sim 70$ K)
	GaAs	0.067	9340	400000 ($T = 28 - 40$ K)
	GaSb	0.039	12040	12700 ($T = 77$ K)
	InN	0.12	3100	5000 ($T \sim 150$ K)
	InP	0.07927	6460	400000 ($T \sim 45$ K)
	InAs	0.024	30000	170000 ($T = 77$ K)
	InSb	0.013	77000	1100000 ($T \sim 50$ K)
II–VI	ZnO	0.234	226	2400 ($T = 40$ K)
	α-ZnS	0.28	140	300 ($T = 185$ K)
	β-ZnS	0.2	107	
	ZnSe	0.137	1500	13600 ($T = 55.6$ K)
	ZnTe	0.117	600	
	c-CdS	0.14	70–85	
	w-CdS	0.151	390	70000 ($T = 1.8$ K)
	w-CdSe	0.125	900	20000 ($T \sim 23$ K)
	CdTe	0.09	1050	100000 ($T \sim 30$ K)
	β-HgS	0.012[b]	230	580 ($T \sim 4.2$ K)
	HgSe	0.019[b]	22000	170000 ($T \sim 20 - 30$ K)
	HgTe	0.030[b]	26500	1400000 ($T = 4.2$ K)

[a] Drift (conductivity) mobility
[b] Showing negative band-gap (semimetalic) nature

Similarly, we plot in Figure 12.3 the 300 K mobility, μ_{300K}, versus inverse Γ-valley electron conductivity mass, $1/m_e^\Gamma$, for those semiconductors. The solid line in Figure 12.3 represents the least-squares fit with (m_e^Γ in m_0; μ_{300K} in cm^2/V s)

$$\mu_{300K} = \left(\frac{3.0}{m_e^\Gamma}\right)^{2.11} \tag{12.21}$$

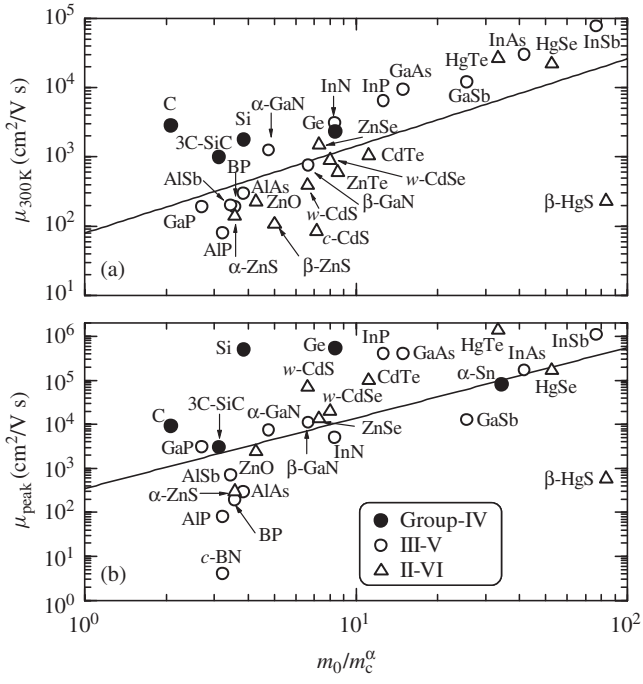

Figure 12.1 (a) Electron Hall mobility at 300 K, μ_{300K}, (b) electron Hall peak mobility, μ_{peak}, versus inverse electron conductivity mass, m_0/m_c^α, at the lowest conduction band for some group-IV, III–V and II–VI semiconductors

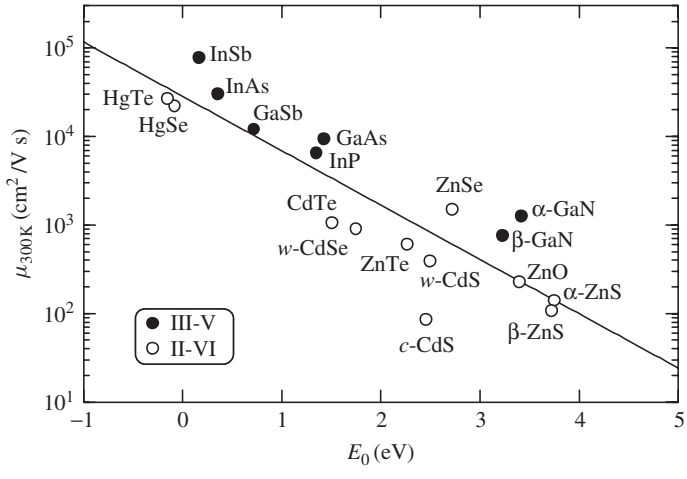

Figure 12.2 Electron Hall mobility at 300 K, μ_{300K}, versus E_0 for some III–V and II–VI semiconductors. The solid line represents the least-squares fit with $\ln \mu_{300K} = 10.3 - 1.41E_0$ (E_0 in eV; μ_{300K} in cm^2/V s)

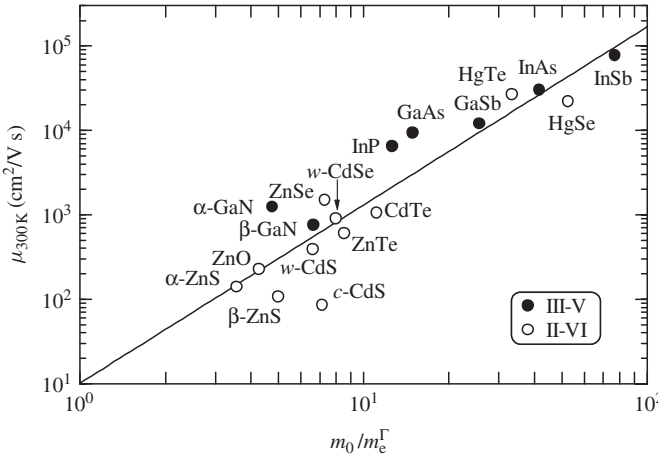

Figure 12.3 Electron Hall mobility at 300 K, μ_{300K}, versus inverse Γ-valley electron conductivity mass m_0/m_e^Γ for some III–V and II–VI semiconductors. The solid line represents the least-squares fit with $\mu_{300K} = (3.0/m_e^\Gamma)^{2.11}$ (m_e^Γ in m_0; μ_{300K} in cm^2/V s)

It is evident from Figures 12.2 and 12.3 that the Γ-valley electron mobility increases with decreasing E_0 or m_e^Γ. We have already shown that the E_0 energy increases proportionally with increasing m_e^Γ (Section 7.1.2).

12.1.4 External perturbation and doping effects

(a) Temperature effect

Figure 12.4 shows the electron Hall mobility μ_e versus temperature for relatively pure n-type GaP, GaAs, InP and InAs. The data are taken for GaP from [12.8], for GaAs from [12.9, 12.10], for InP from [12.11] and for InAs from [12.12]. Low-field transport properties of III–V semiconductors have been studied in some detail. However, there are still discrepancies in various values of the acoustic deformation potential E_1. The existence of ionized impurity scattering and carrier compensation problems makes analysis very difficult.

The μ_e data for GaAs and InP in Figure 12.4 increase as the temperature increases, showing a peak value at $T \sim 50$ K, and then drastically decrease with further increase of T. For $T \leqslant 10$ K, the mobility values approximately follow the relation $\mu_e \propto T^{3/2}$, i.e., ionized impurity scattering (see Table 12.2).

As clearly seen in Figure 12.4, the indirect band-gap material GaP has relatively a lower mobility value than GaAs, InP and InAs. This is because of a relatively larger conductivity mass in the satellite valley than in the central valley (Γ) for many semiconductors. The intervalley scattering also lowers the electron mobility in the indirect band-gap materials. Toyama *et al.* [12.13] determined the intervalley deformation potential constant D_{ij} of GaP to be 7 eV/Å from Hall measurements. Rode [12.3] obtained a value of $D_{ij} = 12$ eV/Å by fitting the Hall data of Casey *et al.* [12.14]. Fletcher and Butcher [12.15] analyzed the μ_e data of Taylor *et al.* [12.16] and obtained $D_{ij} = 10$ eV/Å.

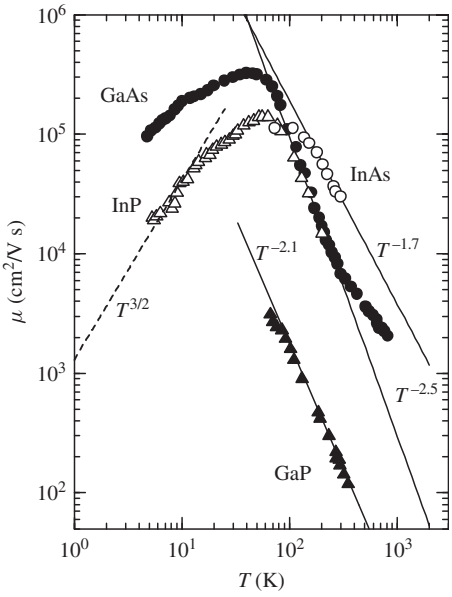

Figure 12.4 Electron Hall mobility μ versus temperature T for relatively pure n-type GaP, GaAs, InP and InAs. The experimental data are gathered from various sources (see text)

Wiley and DiDomenico [12.17] also reported values of $D_{ij} = 8$ eV/Å and $E_1 \sim 10$ eV by analyzing their measured free-carrier absorption data of n-GaP.

The mobility data obtained from different experiments above 100 K in many semiconductors are essentially identical and may therefore be taken to represent the lattice scattering-limited mobility. Stillman *et al.* [12.9] showed that the temperature dependence of μ_e for GaAs can be explained by contributions of three scattering mechanisms: polar phonon scattering, acoustic phonon (deformation potential) scattering and ionized impurity scattering. We reproduce in Figure 12.5 their temperature variations of the electron Hall mobility for three different samples [12.9]. At low temperatures below about 50 K, the dominant scattering mechanism is ionized impurity scattering ($\mu_e \propto T^{3/2}$, see also Figure 12.4). Above 70 K, the mobility is almost entirely limited to polar optical scattering. Lesser scattering processes, such as piezoelectric and carrier-carrier scattering, were omitted in these analyses.

As seen in Figure 12.4, the lattice scattering-limited mobilities in III–V semiconductors can be approximated by $\mu_e \propto T^{-m}$ with $m \sim 1.7$–2.5. Similarly, we obtain $m \sim 1.7$–2.3 for diamond [12.18], ~2.2–2.4 for Si [12.19–12.21] and ~1.6–2.5 for Ge [12.22–12.24].

(b) Pressure effect

The pressure dependence of the electron Hall mobility μ_e has been studied for various semiconductors, such as Si [12.25], Ge [12.26], GaAs [12.27], GaSb [12.28], InP [12.27], InAs [12.29, 12.30] and InSb [12.31]. All these data showed that μ_e decreases with

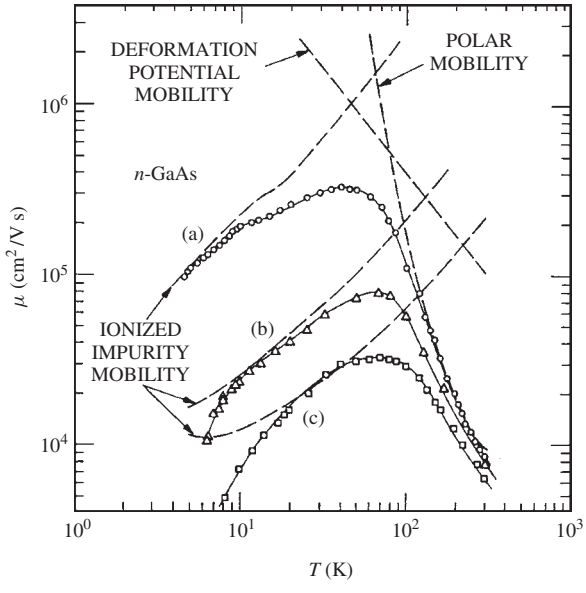

Figure 12.5 Temperature variation of the electron Hall mobility μ measured at 5 kG for three different n-GaAs samples. In the temperature range from 300 to 77 K, the mobility for sample (a) is dominated by polar optical scattering. Samples (b) and (c) show increased effects of ionized-impurity scattering. [From G. E. Stillman, C. M. Wolfe, and J. O. Dimmock, *J. Phys. Chem. Solids* **31**, 1199 (1970), reproduced by permission from Elsevier]

increasing pressure. This can be easily understood by distinguishing each scattering mechanism in the manner

$$\frac{\mathrm{d}\ln\mu_i^{\mathrm{e}}}{\mathrm{d}p} = \frac{1}{\mu_i^{\mathrm{e}}}\frac{\mathrm{d}\mu_i^{\mathrm{e}}}{\mathrm{d}p} \propto s\frac{\mathrm{d}m_{\mathrm{c}}^{\alpha}}{\mathrm{d}p} \tag{12.22}$$

where $s = -5/2$ for $\mu_{\mathrm{iv}}^{\mathrm{e}}$, $-3/2$ for $\mu_{\mathrm{po}}^{\mathrm{e}}$, $-1/2$ for $\mu_{\mathrm{ii}}^{\mathrm{e}}$, etc. ($s \leqslant 0$, see Table 12.2) and $\mathrm{d}m_{\mathrm{c}}^{\alpha}/\mathrm{d}p$ is usually positive. Thus, we find that $\mathrm{d}\ln\mu_i^{\mathrm{e}}/\mathrm{d}p$ is negative, i.e., μ_i^{e} usually decreases with increasing pressure p. The experimental $\mathrm{d}\ln\mu_i^{\mathrm{e}}/\mathrm{d}p$, values reported are of the order of 10^{-6} bar [12.25, 12.30].

(c) Doping effect

An analytical expression relating carrier mobility μ and carrier concentration n represents an important tool for designing and analyzing semiconductor devices. Models by Arora *et al.* [12.21], Klaassen [12.32], Caughey and Thomas [12.33], Mohammad *et al.* [12.34] and Sotoodeh *et al.* [12.35] are examples of empirical mobility.

The low-field model used by Sotoodeh *et al.* [12.35] is expressed by

$$\mu(T,n) = \mu_{\min} + \frac{\mu_{\max} \times \left(\dfrac{300}{T}\right)^{\theta_1} - \mu_{\min}}{1 + \left(\dfrac{n}{n_{\mathrm{ref}} \times (T/300)^{\theta_2}}\right)^{\alpha}} \tag{12.23}$$

where μ_{max} and n_{ref} values are at $T = 300$ K. All the fitting parameters in Equation (12.23) are non-negative. This equation promises that at very low doping concentration $\mu(T)$ saturates at $\mu_{max}(T)$ and at high doping concentration at $\mu_{min}(T)$. $n_{ref}(T) = n_{ref} \times (T/300)^{\theta_2}$ is the doping concentration at which mobility reduces to almost half of its maximum value at low doping. At $T = 300$ K, Equation (12.23) agrees exactly with the empirical expression proposed by Caughey and Thomas [12.33]

$$\mu(n) = \mu_{min} + \frac{\mu_{max} - \mu_{min}}{1 + (n/n_{ref})^{\alpha}} \tag{12.24}$$

Data on μ versus electron concentration n are available for many semiconductors. We summarize in Table 12.4 the fitted parameters, μ_{min}, μ_{max}, n_{ref} and α, in Equation (12.24) obtained from analyzing the 300 K data for various group-IV, III–V and II–VI semiconductors. Figures 12.6–12.8 show the fitted results using Equation (12.24) for Si, α-GaN and ZnSe, respectively. The experimental data plotted in Figure 12.6 are taken from Baccarani and Ostoja [12.36] and Masetti *et al.* [12.37], and those in Figure 12.7 are obtained from Mohammad *et al.* [12.38].

Table 12.4 Empirical expression for the carrier mobility μ in n-type semiconductors as a function of free-electron concentration n at 300 K

$$\mu = \mu_{min} + \frac{\mu_{max} - \mu_{min}}{1 + (n/n_{ref})^{\alpha}}$$

System	Material	μ_{min} (cm^2/V s)	μ_{max} (cm^2/V s)	n_{ref} (cm^{-3})	α
IV	Si	100	1480	1.0×10^{17}	0.80
	Ge	0	4500	1.0×10^{17}	0.45
	3C-SiC	50	1550	1.5×10^{17}	1.00
	4H-SiC	0	1400	1.0×10^{17}	0.50
	6H-SiC	0	650	1.0×10^{18}	0.60
III–V	AlAs	10	400	5.46×10^{17}	1.00
	α-GaN	85	5300	1.0×10^{15}	0.45
	β-GaN	65	1350	1.0×10^{18}	0.80
	GaP	10	152	4.4×10^{18}	0.80
	GaAs	500	9400	6.0×10^{16}	0.394
	GaSb	0	9500	1.0×10^{17}	0.60
	InN	100	5400	1.0×10^{17}	0.80
	InP	0	5000	4.0×10^{17}	0.45
	InAs	1000	34000	1.1×10^{18}	0.32
	InSb	0	92000	3.0×10^{17}	0.68
II–VI	ZnO ($\boldsymbol{j} \perp c$)	30	280	5.0×10^{17}	0.50
	ZnO ($\boldsymbol{j} \parallel c$)	30	250	5.0×10^{17}	0.50
	α-ZnS	80	800	5.0×10^{17}	0.60
	β-ZnS	85	800	3.0×10^{14}	0.50
	ZnSe	30	1730	7.0×10^{16}	0.55
	ZnTe	0	1000	7.0×10^{18}	1.5

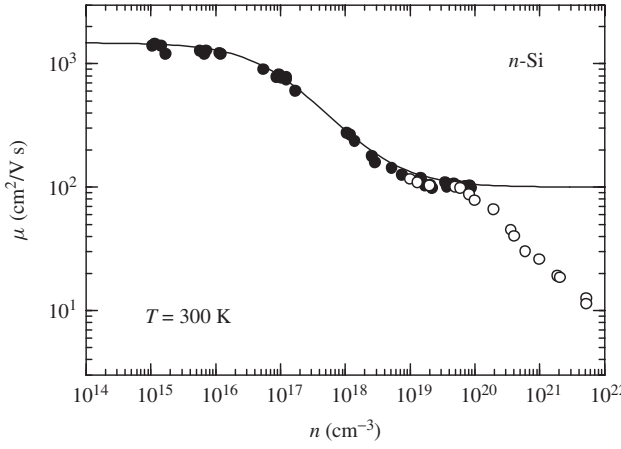

Figure 12.6 Electron Hall mobility μ versus electron concentration n in n-Si at 300 K. The experimental data are taken from Baccarani and Ostoja (●) [12.36] and Masetti *et al.* (○) [12.37]. The solid line represents the calculated result with $\mu = 100 + 1380/[1 + (n/10^{17})^{0.80}]$, where n is in cm^{-3} and μ is in $\text{cm}^2/\text{V s}$. [From S. Adachi, *Handbook on Physical Properties of Semiconductors Volume 1: Group-IV Semiconductors* (Kluwer Academic, Boston, 2004), reproduced by permission from Kluwer Academic Publishers]

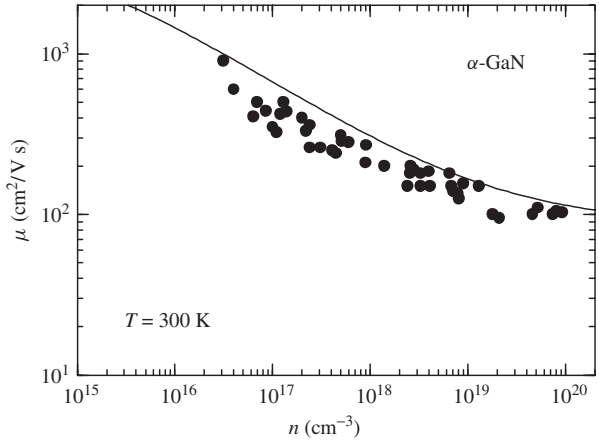

Figure 12.7 Electron Hall mobility μ versus electron concentration n for n-type α-GaN at 300 K. The experimental data are taken from Mohammad *et al.* [12.38]. The solid line represents the calculated result with $\mu = 85 + 5215/[1 + (n/10^{15})^{0.45}]$, where n is in cm^{-3} and μ is in $\text{cm}^2/\text{V s}$. [From S. Adachi, *Handbook on Physical Properties of Semiconductors Volume 2: III–V Compound Semiconductors* (Kluwer Academic, Boston, 2004), reproduced by permission from Kluwer Academic Publishers]

12.1.5 Hall factor

The Hall effect is the principal mean of characterizing the microscopic quality of semiconductors. The carrier concentration n can be determined from Hall coefficient R_H by

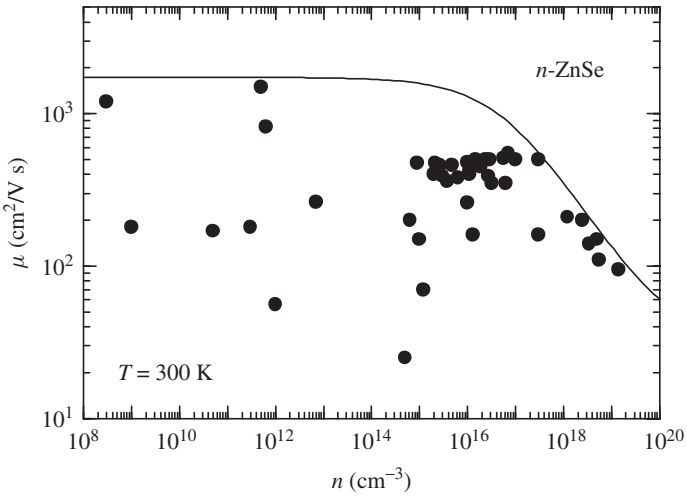

Figure 12.8 Electron Hall mobility μ versus electron concentration n in n-ZnSe at 300 K. The experimental data are gathered from various sources. The solid line represents the calculated result with $\mu = 30 + 1700/[1 + (n/7 \times 10^{16})^{0.55}]$, where n is in cm^{-3} and μ is in $\text{cm}^2/\text{V s}$. [From S. Adachi, *Handbook on Physical Properties of Semiconductors Volume 3: II–VI Compound Semiconductors* (Kluwer Academic, Boston, 2004), reproduced by permission from Kluwer Academic Publishers]

the relation

$$n = \frac{\gamma}{eR_{\text{H}}} \tag{12.25}$$

where e is the elementary charge and γ is a dimensionless parameter of order one called the Hall factor or the Hall scattering factor. The Hall factor γ is dependent on both the band structure and scattering mechanisms of the semiconductor, as well as on the magnetic field.

The carrier concentration n can be used to determine the mobility from the definition

$$\mu_{\text{c}} \equiv \frac{\sigma}{ne} = \frac{\sigma R_{\text{H}}}{\gamma} \tag{12.26}$$

where σ is the conductivity. Since the γ value is not known precisely, it is often set equal to one for convenience. Unfortunately, this assumption is exactly valid only for degenerate semiconductors or when the magnetic field is high enough that the magnetic motion dominates the scattering. This occurs when $\omega_{\text{c}}\tau \gg 1$, where $\omega_{\text{c}} = eH/m^*$ is the cyclotron frequency and $\tau = \sigma m^*/ne^2$ is the carrier scattering time (H = magnetic field strength; m^* = effective carrier mass). It should be noted that the condition $\omega_{\text{c}}\tau \gg 1$ is unattainable for many practical situations. Because of this, a distinction is made between two mobility definitions, μ_{c} and μ_{H}. The conductivity or drift mobility μ_{c} is defined by Equation (12.26), while the Hall mobility is defined as

$$\mu_{\text{H}} \equiv \sigma R_{\text{H}} \tag{12.27}$$

Thus, the Hall factor is given by the ratio

$$\gamma = \frac{\mu_H}{\mu_c} = \frac{\sigma R_H}{(\sigma R_H/\gamma)} \tag{12.28}$$

The Hall mobility is the easiest to measure and is, therefore, widely determined experimentally. On the other hand, the conductivity mobility is the easiest to calculate since it contains only one component of the magnetoconductivity tensor in the direction of the current, in contrast to the Hall mobility that contains both diagonal and non-diagonal components of the magnetoconductivity tensor.

The temperature dependence of the Hall factor has been measured for many semiconductors. We show in Figure 12.9, as an example, the Hall factor γ measured for electrons and holes in high-purity n-type and p-type Ge [12.22]. The Hall factor γ for electrons is nearly constant at $\sim$1.0. The factor γ for holes shows significant temperature dependence. The electron mobility for $50 \leqslant T \leqslant 300$ K was found to obey $\propto T^{-1.66}$ [12.22], i.e., in reasonable agreement with the lattice scattering-limited mobility $\mu \propto T^{-3/2}$. In the region $T > 100$ K where γ for holes gradually increased with increasing T, the hole mobility showed the temperature dependence of $\propto T^{-2.33}$, suggesting a complex scattering mechanism of holes in p-Ge.

The Hall factor γ as a function of magnetic field B measured for 6H-SiC at 300 K is shown in Figure 12.10 [12.39]. The magnetic field B was applied to the direction parallel to the c axis of the sample. In Figure 12.10, γ is less than unity; however, it approaches unity as B increases. The solid line represents the theoretical analysis based on the anisotropic electron transport with an energy-independent scattering time developed for the Hall coefficient in n-type Ge. The analysis suggested that the electron mass in 6H-SiC along the c direction is 5.2 times larger than that in the transverse direction [12.39]. It is thus concluded that the Hall measurement can be utilized as a simple, but effective method for determining the mass anisotropy parameter in SiC.

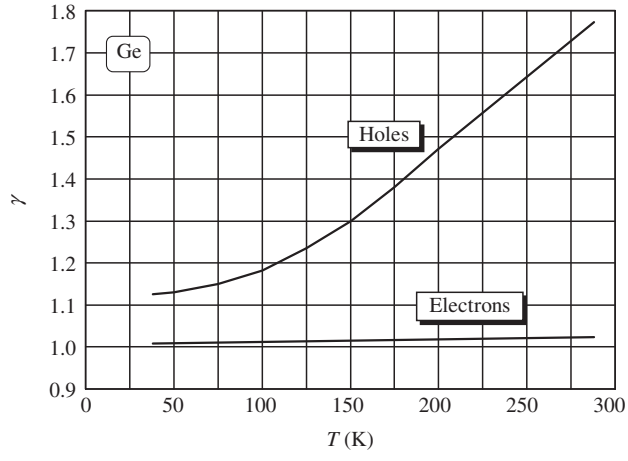

Figure 12.9 Hall factor γ for electrons and holes in n-Ge and p-Ge as a function of temperature T. [From F. J. Morin, *Phys. Rev.* **93**, 62 (1954), reproduced by permission from the American Physical Society]

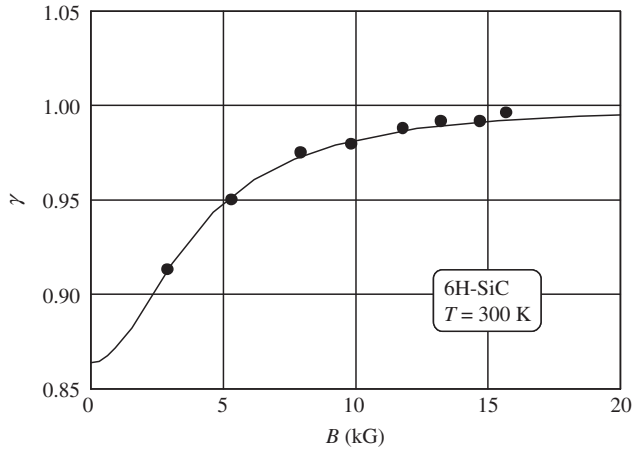

Figure 12.10 Hall factor γ as a function of magnetic field B measured for electrons in 6H-SiC at 300 K for ($\boldsymbol{j} \perp c$, $\boldsymbol{B} \| c$). The solid line represents the theoretical fit. [From G. D. Chen, J. Y. Lin, and H. X. Jiang, *Appl. Phys. Lett.* **68**, 1341 (1996), reproduced by permission from the American Institute of Physics]

The Hall mobility in the three-valley model has been given in Section 12.1.2. The conductivity mobility μ_c and Hall factor γ in that model can be, respectively, written as

$$\mu_c = \mu_\Gamma \frac{1 + (n_L/n_\Gamma)(\mu_L/\mu_\Gamma) + (n_X/n_\Gamma)(\mu_X/\mu_\Gamma)}{1 + (n_L/n_\Gamma) + (n_X/n_\Gamma)} \tag{12.29}$$

$$\gamma = \frac{[1 + (n_L/n_\Gamma) + (n_X/n_\Gamma)][1 + (n_L/n_\Gamma)(\mu_L/\mu_\Gamma)^2 + (n_X/n_\Gamma)(\mu_X/\mu_\Gamma)^2]}{[1 + (n_L/n_\Gamma)(\mu_L/\mu_\Gamma) + (n_X/n_\Gamma)(\mu_X/\mu_\Gamma)]^2} \tag{12.30}$$

12.2 LOW-FIELD MOBILITY: HOLES

12.2.1 Hole scattering mechanism

The valence band of $A^N B^{8-N}$ semiconductors consists of the three atomic p-like bands, the light-hole (LH), heavy-hole (HH) and spin–orbit split-off (SO) bands. Hole transport at the top of the valence band is, then, complicated by the following essential facts: (1) the degeneracy of the valence band, the influence of the light holes and interband scattering between the LH and HH bands; (2) the p-type symmetry of hole wavefunctions; and (3) the warping of the HH band. A dominant role of polar optical scattering can also hardly be expected on physical grounds because large values of the HH mass favor acoustic and nonpolar optical deformation potential scattering.

The correct way of handling the degeneracy of valence bands is by solving a set of coupled Boltzmann equations; the simplest model results from assuming that the HH and LH bands are decoupled. The mobilities of the two bands are, then, simply additive and it is easy to show that [12.40]

$$\mu_{\text{eff}} = \frac{p_1\mu_1 + p_2\mu_2}{p_1 + p_2} \tag{12.31}$$

where μ_{eff} is the effective or measured mobility and p_1 and p_2 are the average densities of holes in the HH and LH bands (the total hole concentration is thus $p = p_1 + p_2$). If the bands are assumed to be approximately spherical, then $p_1/p_2 = (m_1/m_2)^{3/2} = (m_{\text{HH}}/m_{\text{LH}})^{3/2} \equiv d^{3/2}$, where m_{HH} and m_{LH} are, respectively, the HH and LH masses. Equation (12.31) can then be written as

$$\mu_{\text{eff}} = \frac{(\mu_2/\mu_1) + d^{3/2}}{1 + d^{3/2}} \tag{12.32}$$

When μ_1 and μ_2 are calculated using the standard expressions for the mobilities, the ratio μ_2/μ_1 can be reduced to a simple power of d, depending on the mass dependence of the scattering mechanism under consideration. This approach yields

$$\mu_{\text{ii}}^{\text{h}} = 1.5\left(\frac{d^{1/2} + d^{3/2}}{1 + d^{3/2}}\right)\mu_{\text{ii}}^{\text{e}} \tag{12.33a}$$

$$\mu_{\text{po}}^{\text{h}} = 2K\mu_{\text{po}}^{\text{e}} \tag{12.33b}$$

$$\mu_{\text{sc}}^{\text{h}} = \left(\frac{d^{5/2} + d^{3}}{(1 + d^{3/2})^2}\right)\mu_{\text{sc}}^{\text{e}} \tag{12.33c}$$

$$\mu_{\text{al}}^{\text{h}} = \left(\frac{d^{5/2} + d^{3}}{(1 + d^{3/2})^2}\right)\mu_{\text{al}}^{\text{e}} \tag{12.33d}$$

and

$$\mu_{\text{ac,npo}}^{\text{h}} = 3.17 \times 10^{-4}\frac{d^{5/2}(1 + d^{1/2})}{(1 + d^{3/2})^2}\frac{g v^{-2}}{(m_{\text{HH}}/m_0)^{5/2}}\frac{S(\theta, \eta, T)T^{-3/2}}{E_{\text{ac,h}}^2} \tag{12.33e}$$

where $\mu_{\text{ii}}^{\text{e}}$, $\mu_{\text{po}}^{\text{e}}$, $\mu_{\text{sc}}^{\text{e}}$ and $\mu_{\text{al}}^{\text{e}}$ are obtained from the equations for electrons, but substituting the HH effective mass m_{HH}. The factor 1.5 in Equation (12.33a) and the factor 2 in Equation (12.33b) take into account the p-like symmetry of the hole wavefunctions and K is a correction factor to take into account the contribution from the light holes, shown graphically by Wiley [12.40]; $\mu_{\text{ac,npo}}^{\text{h}}$ is the hole mobility combined with acoustic scattering-limited and nonpolar optical scattering-limited mobilities. g is the crystal density and $\overline{v}$ is an average sound velocity defined by

$$\overline{v} = \sqrt{\frac{C_{\text{l}} + 2C_{\text{t}}}{3g}} \tag{12.34}$$

with

$$C_{\text{l}} = \tfrac{1}{5}(3C_{11} + 2C_{12} + 4C_{44}) \tag{12.35a}$$

$$C_{\text{t}} = \tfrac{1}{5}(C_{11} - C_{12} + 3C_{44}) \tag{12.35b}$$

where C_{ij} are the elastic stiffness constants. $E_{\text{ac,h}}$ is the hole deformation potential defined by

$$E_{\text{ac,h}} = \sqrt{\frac{\beta + 2}{6\beta}}\Xi_{\text{eff}} \tag{12.36}$$

with $\beta = C_l/C_t$. Ξ_{eff} in Equation (12.36) is now given by

$$\Xi_{eff} = \sqrt{a^2 + \frac{C_l}{C_t}\left(b^2 + \frac{1}{2}d^2\right)} \tag{12.37}$$

where a, b and d are the valence-band deformation potentials.

In Equation (12.33e), S is a strongly temperature-dependent function [12.40, 12.41], θ is the characteristic temperature of the optical phonons and $\eta = (E_{npo}/E_{ac,h})^2$, where E_{npo} is the phenomenological optical deformation potential which can be related to the optical phonon deformation potential d_0 by the expression

$$E_{npo} = \frac{M_1 + M_2}{2\sqrt{M_1 M_2}}\sqrt{\frac{C_l(\beta + 2)}{2g\omega_0^2 a_0^2 \beta}}d_0 \tag{12.38}$$

M_1 and M_2 are the masses of the atoms in a unit cell, ω_0 is the angular frequency of zone-center longitudinal optical phonons and a_0 is the lattice constant. Note that the expression given by Equation (12.33e) differs from one given earlier by Wiley and DiDomenico [12.41] by a factor $(1 + d^{-3/2})^{-1}$, which was shown by Costato *et al.* [12.42] to take interband scattering into account explicitly. Wiley [12.40] has shown that the values of $E_{ac,h}$ do not vary from material to material: 3.5 eV (GaAs, AlAs and GaP), 3.6 eV (InP) and 3.2 eV (InAs).

12.2.2 Room-temperature value

We summarize in Table 12.5 the 300 K (μ_{300K}) and peak Hall mobilities (μ_{peak}) for holes in some cubic and hexagonal semiconductors. Figure 12.11 also plots the μ_{300K} and μ_{peak} values versus lowest direct band-gap energy E_0 for these semiconductors. In contrast to the electrons in Section 12.1.3, there appears to be no clear relationship between μ_{300K} (μ_{peak}) and E_0. This can be understood from the fact that the hole (HH) effective mass differ not so largely by material to material.

12.2.3 External perturbation and doping effects

(a) Temperature effect

Figure 12.12 shows the temperature dependence of the hole Hall mobility μ_h for p-type GaP, GaAs, InP and InAs. The experimental data are taken for GaP from [12.43], for GaAs from [12.44, 12.45], for InP from [12.46] and for InAs from [12.47]. The samples used in these studies had relatively high purity, except InAs. Because of its small band-gap, $E_0 = 0.36$ eV at 300 K, InAs becomes intrinsic at high temperatures. We must, therefore, resort to rather heavy doping with acceptor dopants in order to obtain p-type InAs samples. The data shown in Figure 12.12 were taken for a sample with $p \sim 2 \times 10^{17}$ cm^{-3} at $T \sim 150$ K.

For InP, the empirical law $\mu \propto T^{-2}$ is found to hold at $T > 100$ K; μ decreases strongly at $T < 40$ K because of the onset of impurity conduction. The hole mobility in

Table 12.5 300 K (μ_{300K}) and peak Hall mobilities (μ_{peak}) for holes in some cubic and hexagonal semiconductors

System	Material	μ_{300K} (cm^2/V s)	μ_{peak} (cm^2/V s)
IV	Diamond	1500	6000 ($T \sim 110$ K)
	Si	450[a]	350000 ($T = 6$ K)[a]
	Ge	2400	550000 ($T \sim 8$ K)
	α-Sn		25800 ($T = 25$ K)
	3C-SiC	~60	~80 ($T \sim 210$ K)
	6H-SiC	100	240 ($T \sim 150$ K)
III–V	BP	500	500 ($T = 300$ K)
	w-AlN	14	
	AlP	450	
	AlAs	105	105 ($T = 300$ K)
	AlSb	420	5000 ($T \sim 50$ K)
	α-GaN	370	500 ($T \sim 250$ K)
	β-GaN	350	1250 ($T \sim 120$ K)
	GaP	140	2050 ($T \sim 55$ K)
	GaAs	450	28000 ($T \sim 22$ K)
	GaSb	1624	13300 ($T \sim 25$ K)
	InP	180	3000 ($T \sim 60$ K)
	InAs	450	1200 ($T \sim 70$ K)
	InSb	1100	29000 ($T \sim 20 - 30$ K)
II–VI	β-ZnS	72	
	ZnSe	355	596 ($T = 77$ K)
	ZnTe	100	6500 ($T = 35$ K)
	w-CdS	48	
	w-CdSe	50	
	CdTe	104	1200 ($T = 170$ K)
	HgTe	320	45000 ($T \sim 10$ K)

[a] Drift (conductivity) mobility

GaAs rises as the temperature is lowered, obeying the law $\mu \propto T^{-2}$ in the range $80 < T < 200$ K, and tends to reach a maximum $\mu \sim 3 \times 10^4$ cm^2/V s at 20 K. The mobility in GaP also rises as the temperature is lowered, reaches a maximum $\mu \sim 2 \times 10^3$ cm^2/V s and decreases dramatically with further decrease of T. The temperature dependence of μ for InAs shows a T^{-2} power law for $T > 250$ K. Below 200 K, the ionized impurity scattering dominates other scattering mechanisms.

Figure 12.13(a) shows the total and partial conductivity mobilities μ_c and experimental results in the phonon-limited regime of p-Si as a function of temperature [12.48]. The corresponding Hall mobility results are shown in Figure 12.13(b). The experimental data in Figure 12.13(a) are taken from [12.49, 12.50] and those in Figure 12.13(b) are from [12.49]. The conductivity and Hall mobilities were calculated without the relaxation-time approximation form solutions of the full Boltzmann equation, with accurate HH, LH and SO wavefunctions and valence-band dispersions. Only the optical phonon deformation potential d_0 was adjusted to yield agreement with transport data at room temperature.

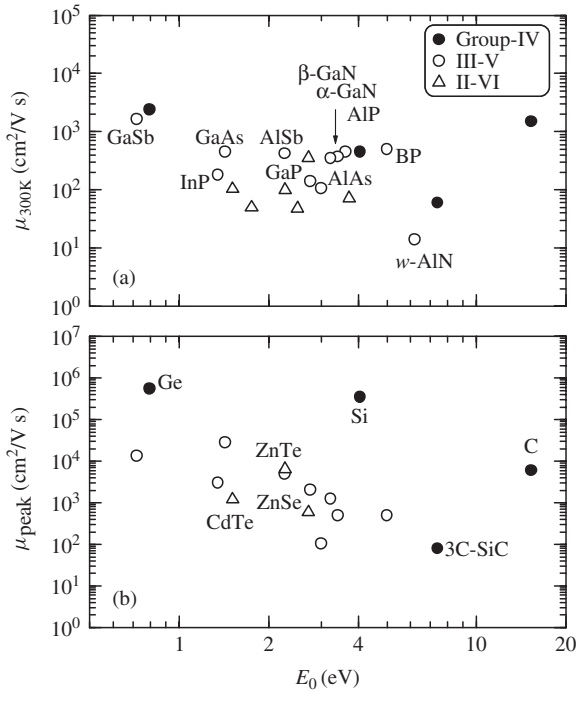

Figure 12.11 (a) Hole Hall mobility at 300 K, μ_{300K}; (b) hole Hall peak mobility, μ_{peak}, versus E_0 for some group-IV, III–V and II–VI semiconductors

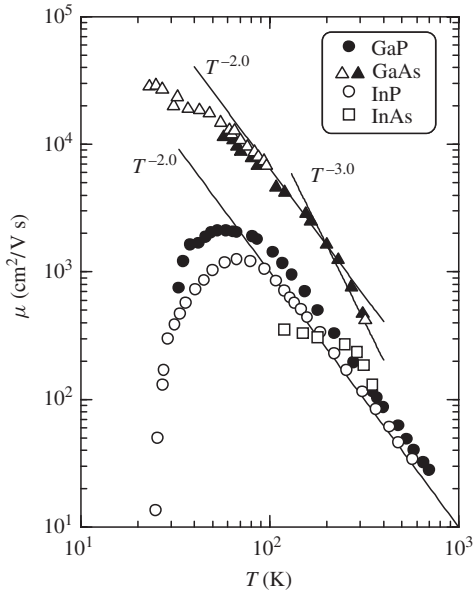

Figure 12.12 Hole Hall mobility μ versus temperature T for p-type GaP, GaAs, InP and InAs. The experimental data are gathered from various sources (see text)

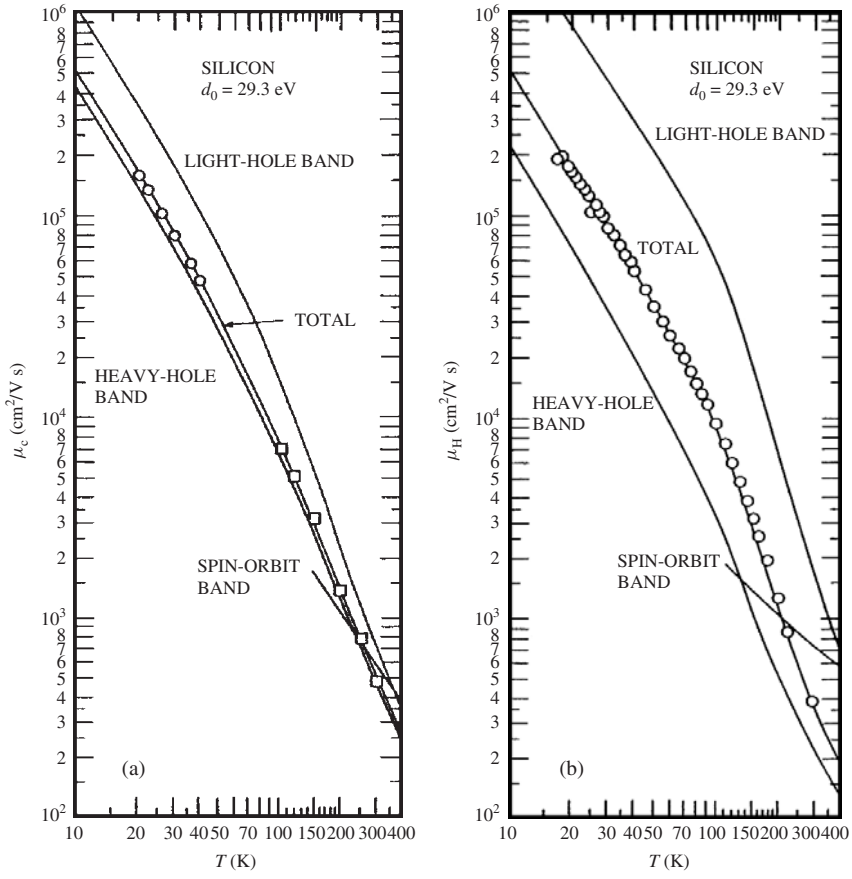

Figure 12.13 (a) Total and partial conductivity mobilities μ_c and experimental results in the phonon-limited regime of p-Si as a function of temperature. Calculated curves: solid lines. Circles: sample 1202-H of Mitchel and Hemenger [12.49], $N_A = 6.57 \times 10^{11}$ cm^{-3}, $N_D = 3.96 \times 10^{11}$ cm^{-3}. Squares: Ludwig and Watters [12.50], minority-carrier drift mobility on n-type samples with resistivities between 19–180 Ω cm; (b) total and partial Hall mobilities μ_H and experimental results in the phonon-limited regime of p-Si as a function of temperature. Calculated curves: solid lines. Circles: sample 1202-H of Mitchel and Hemenger [12.49], $N_A = 6.57 \times 10^{11}$ cm^{-3}, $N_D = 3.96 \times 10^{11}$ cm^{-3}. [From F. Szmulowicz, *Appl. Phys. Lett.* **43**, 485 (1983), reproduced by permission from the American Institute of Physics]

As seen in Figure 12.13, the theoretical mobilities agree quite well with the experimental data over the entire temperature range. The average slope in the 100–300 K region is found to be about 2.4 in Figure 12.13(a) and 2.9 in Figure 12.13(b).

The Hall factor $\gamma = \mu_H/\mu_c$ as a function of temperature T for p-Si obtained from Figure 12.13 is plotted in Figure 12.14 [12.48]. The low-temperature region is found to agree with the data of Mitchel and Hemenger [12.49] (△). The single point of Reid and Willardson [12.51] at 77 K (□) makes it plausible that the γ factor continues to rise to 80 K. From the data of Long [12.52] (▽) and Morin and Maita [12.53] (◇), it is apparent that the γ factor should decrease and level out as predicted. The optical deformation

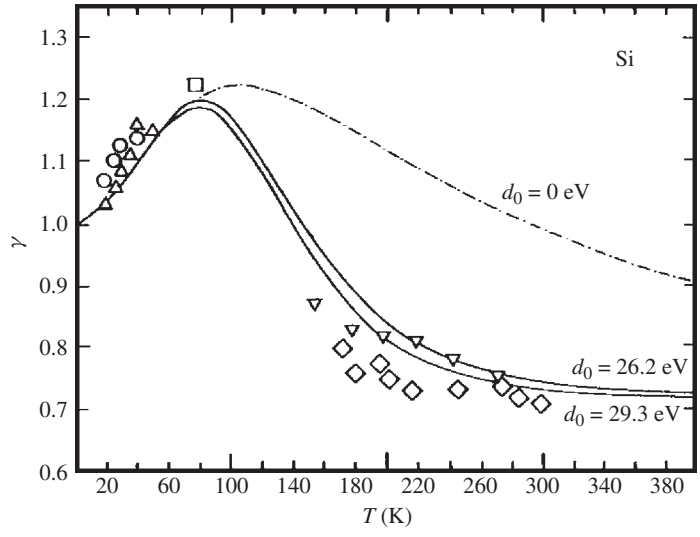

Figure 12.14 Theoretical and experimental Hall factor γ as a function of temperature for p-Si. Circles: sample 1202-H of Mitchel and Hemenger [12.49], $N_A = 6.57 \times 10^{11}$ cm^{-3}, $N_D = 3.96 \times 10^{11}$ cm^{-3}. Triangles: sample 1300-V of Mitchel and Hemenger [12.49], $N_A = 9.14 \times 10^{11}$ cm^{-3}, $N_D = 3.33 \times 10^{11}$ cm^{-3}. Square: sample 8A of Reid and Willardson [12.51], $N_A - N_D = 4 \times 10^{12}$ cm^{-3}. Inverted triangles: Long [12.52], $N_A - N_D = 3.5 \times 10^{14}$ cm^{-3}. Diamonds: sample 127 of Morin and Maita [12.53], $N_A = 7 \times 10^{14}$ cm^{-3}, $N_D = 2.2 \times 10^{14}$ cm^{-3}. The $d_0 = 0$ eV curve represents the calculated pure acoustic phonon result. [From F. Szmulowicz, *Appl. Phys. Lett.* **43**, 485 (1983), reproduced by permission from the American Institute of Physics]

potential d_0 determined from these fits is about 29 eV. This value is comparable to those reported in [12.54, 12.55] ($d_0 \sim 24.4$–33.6 eV), but is much smaller than the value of 41.5 eV reported in [12.56].

(b) Pressure effect

The pressure dependence of the hole Hall mobility μ_h has been studied for GaAs [12.57], InP [12.57] and InAs [12.30]. The hole Hall mobilities in GaAs and InP are observed to increase with pressure at a rate of 0.31%/kbar and 0.18%/kbar, respectively, while the mobility in InAs is decreased with pressure at ~0.4%/kbar.

(c) Doping effect

Data on μ versus hole concentration p are available for many semiconductors. We summarize in Table 12.6 the empirically fitted results using Equation (12.24) for the data of group-IV, III–V and II–VI semiconductors at $T = 300$ K. Figures 12.15–12.17 represent the fitted results of Equation (12.24) for Si, InSb and ZnTe, respectively. The experimental data in Figure 12.15 are taken from Masetti *et al*. [12.37] and Thurber *et al*. [12.58], in Figure 12.16 from Wiley [12.40] and those in Figure 12.17 are gathered from various sources.

Table 12.6 Empirical expression for the carrier mobility μ in p-type semiconductors as a function of free-hole concentration p at 300 K

$$\mu = \mu_{\min} + \frac{\mu_{\max} - \mu_{\min}}{1 + (p/p_{\text{ref}})^{\alpha}}$$

System	Material	$\mu_{\min}$ (cm^2/V s)	$\mu_{\max}$ (cm^2/V s)	p_{ref} (cm^{-3})	α
IV	Diamond	0	5100	1.0×10^{14}	0.66
	Si	40	540	2.0×10^{17}	0.53
	Ge	0	2900	1.0×10^{17}	0.45
	4H-SiC	15.9	124	1.76×10^{19}	0.34
	6H-SiC	13	108	2.0×10^{19}	0.40
III–V	AlAs	10	200	3.84×10^{17}	0.488
	AlSb	0	600	6.0×10^{17}	0.65
	α-GaN	0	410	1.0×10^{18}	0.75
	β-GaN	0	455	5.0×10^{17}	0.65
	GaP	10	147	1.0×10^{18}	0.85
	GaAs	20	491.5	1.48×10^{17}	0.38
	GaSb	0	2300	1.0×10^{17}	0.38
	InP	10	170	4.87×10^{18}	0.62
	InAs	20	530	1.1×10^{17}	0.46
	InSb	50	800	4.0×10^{18}	0.42
II–VI	β-ZnS	0	120	5.0×10^{18}	0.25
	ZnSe	0	550	1.0×10^{17}	0.38
	ZnTe	0	120	1.0×10^{18}	0.50

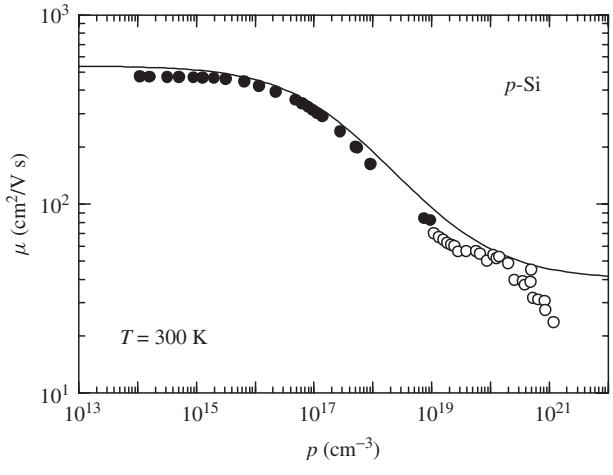

Figure 12.15 Hole Hall mobility μ versus hole concentration p in p-Si at 300 K. The experimental data are taken from Masetti *et al.* (○) [12.37] and Thurber *et al.* (●) [12.58]. The solid line represents the calculated result with $\mu = 40 + 500/[1 + (p/2 \times 10^{17})^{0.53}]$, where p is in cm^{-3} and μ is in cm^2/V s. [From S. Adachi, *Handbook on Physical Properties of Semiconductors Volume 1: Group-IV Semiconductors* (Kluwer Academic, Boston, 2004), reproduced by permission from Kluwer Academic Publishers]

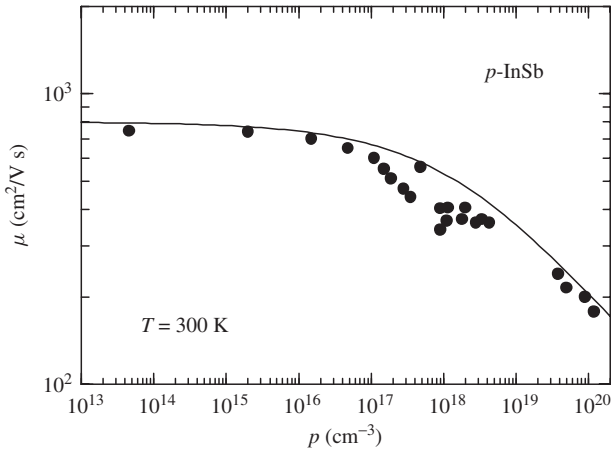

Figure 12.16 Hole Hall mobility μ versus hole concentration p in p-InSb at 300 K. The experimental data are taken from Wiley [12.40]. The solid line represents the calculated result with $\mu = 50 + 750/[1 + (p/4 \times 10^{18})^{0.42}]$, where p is in cm^{-3} and μ is in cm^2/V s. [From S. Adachi, *Handbook on Physical Properties of Semiconductors Volume 2: III–V Compound Semiconductors* (Kluwer Academic, Boston, 2004), reproduced by permission from Kluwer Academic Publishers]

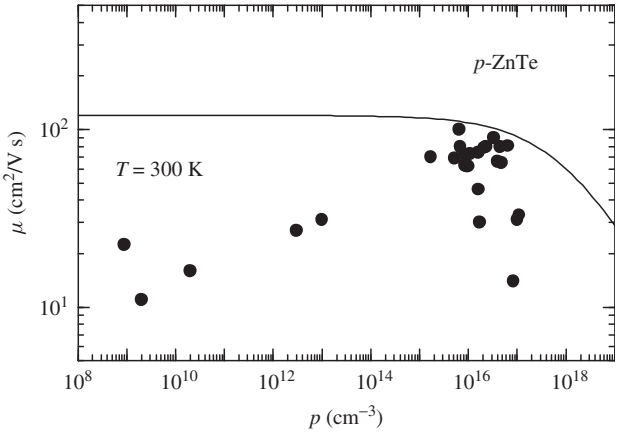

Figure 12.17 Hole Hall mobility μ versus hole concentration p in p-ZnTe at 300 K. The experimental data are gathered from various sources. The solid line represents the calculated result with $\mu = 120/[1 + (p/10^{18})^{0.50}]$, where p is in cm^{-3} and μ is in cm^2/V s. [From S. Adachi, *Handbook on Physical Properties of Semiconductors Volume 3: II–VI Compound Semiconductors* (Kluwer Academic, Boston, 2004), reproduced by permission from Kluwer Academic Publishers]

12.3 HIGH-FIELD TRANSPORT: ELECTRONS

12.3.1 Electron drift velocity–field characteristic

The carrier transport property in high electric fields is one of the most important parameters in electron device design. Performance of high-speed and microwave semiconductor

devices depends essentially on carrier velocity. It is thus very important to know the carrier drift velocity as a function of electric field in a bulk semiconductor. It is, however, very difficult to make a direct measurement of the drift velocity of electrons as a function of electric field in some semiconductors. This is because in high-conductivity material, the sample normally oscillates when the average field in the sample is above the threshold value. This type of microwave oscillation, known as the Gunn effect [12.59], is caused by the transfer of electrons from high-mobility valley to low-mobility valley in the conduction band of some III–V semiconductors. Principally, Gunn oscillation cannot be observed in an indirect band-gap semiconductor. In lower-conductivity samples, the electric field may become highly nonuniform within the sample, even if it does not oscillate.

Electron transport in a multivalley semiconductor depends in a detailed manner on the numbers of carriers in the individual valley portions of the conduction band. We show in Figure 12.18 an approximate band structure of GaAs. At low values of electric field the electrons are dominantly in the Γ valley. As the field increases and polar optical phonon scattering no longer effectively removes the excess carrier energy, a certain fraction of electrons, with the assistance of phonons, transfers to the subsidiary L valley, of which there are four equivalent valleys. The rate at which these electrons are transferred determines whether negative differential mobility will occur. At further increases in field the electrons can also transfer to the next higher valley, the X valley, of which there are three equivalent valleys. Transfer between any two valleys including equivalent valleys occurs.

We reproduce in Figure 12.19 the intervalley phonon scattering rate and impact ionization probability in GaAs as a function of electron energy [12.60]. The solid and dashed lines are obtained from a Monte Carlo simulation technique using the two sets of scattering parameters. In the low energy range, the scattering rate is very well known (LO phonon scattering) and proved by numerous experiments. We can see in Figure 12.19 that the average time between scattering is of the order of 10^{-12} s for energies below 0.036 eV ($\hbar\omega_{LO}$), 10^{-13} s for energies between 0.036 and 0.3 eV and 10^{-14} s above 0.3 eV ($\Delta E_{\Gamma L}$), when scattering to higher-band minima becomes possible via the intervalley deformation potential interaction.

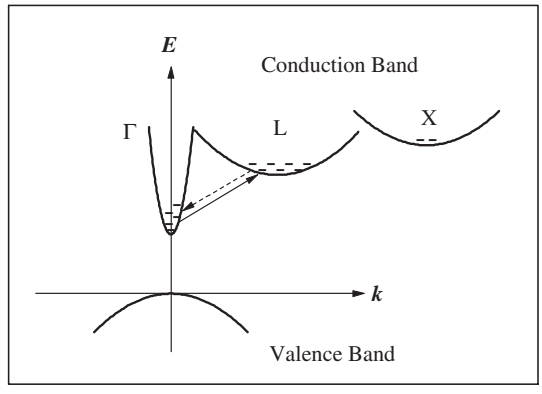

Figure 12.18 Approximate band structure of GaAs. At low values of electric fields the electrons are dominantly in the Γ valley. As the field increases, a certain fraction of electrons, with the assistance of phonons, transfers to the subsidiary L valley. At further increase in field the electrons can also transfer to the next higher valley X

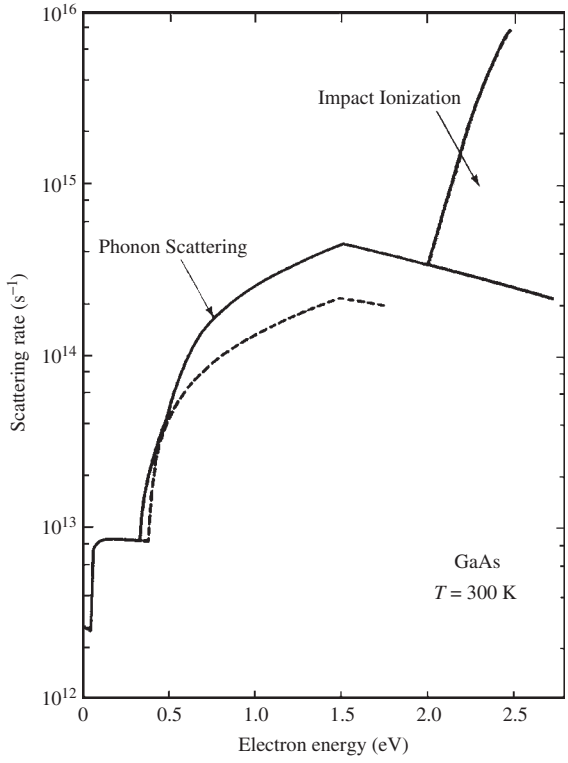

Figure 12.19 Phonon scattering rate and the impact ionization probability in GaAs as a function of electron energy. The solid and dashed lines are obtained from a Monte Carlo calculation using the two sets of scattering parameters. [From H. Shichijo and K. Hess, *Phys. Rev. B* **23**, 4197 (1981), reproduced by permission from the American Physical Society]

The optical phonon energy $\hbar\omega_{\mathrm{LO}}$ in many semiconductors is comparable or larger than thermal energy kT at room temperature and, as a result, the polar optical scattering must include the inelastic nature in any quantitative theory. When the scattering mechanism is elastic, e.g., impurity scattering, a relaxation time characterizing the rate at which momentum decay can be defined. From relaxation time, one can calculate the perturbation of an equilibrium electron distribution by a small electric field and, hence, electron mobility. When the scattering is inelastic, no relaxation time exists exactly, although in certain limits this approximation can be useful. The Boltzmann transport expression in which the average rates of energy loss and momentum loss through collisions are balanced by energy and momentum gain due to the electric field provides the following energy and momentum balance equations [12.1]

$$\left\langle \frac{\mathrm{d}\varepsilon}{\mathrm{d}t} \right\rangle_E + \sum_i \left\langle \frac{\mathrm{d}\varepsilon}{\mathrm{d}t} \right\rangle_i = 0 \tag{12.39a}$$

$$\left\langle \frac{\mathrm{d}p}{\mathrm{d}t} \right\rangle_E + \sum_i \left\langle \frac{\mathrm{d}p}{\mathrm{d}t} \right\rangle_i = 0 \tag{12.39b}$$

where the index i refers to the ith scattering mechanism and the subscript E refers to the electric field.

Let us consider a simple case in which energy loss of electrons comes from only polar optical scattering. This scattering is the most dominant mechanism near room temperature in many semiconductors. For a Maxwell–Boltzmann distribution at electron temperature T_e, the average rates of change of carrier energy and momentum due to polar optical interactions are readily found to be [12.1]

$$\left\langle \frac{d\varepsilon}{dt} \right\rangle_{po} = \sqrt{\frac{2k\theta_{po}}{\pi m_e^{\Gamma}}} e E_o \frac{e^{(\chi_0-\chi_e)-1}}{e^{\chi_0-1}} \sqrt{\chi_e} e^{\chi_e/2} K_0(\chi_e/2) \tag{12.40a}$$

$$\left\langle \frac{dp}{dt} \right\rangle_{po} = \frac{\sqrt{2m_e^{\Gamma}} e E_o N_q v_d}{3\sqrt{\pi k\theta_{po}}} \chi_e^{3/2} e^{\chi_e/2} \times [(e^{(\chi_0-\chi_e)}+1)K_1(\chi_e/2) + (e^{(\chi_0-\chi_e)}-1)K_0(\chi_e/2)] \tag{12.40b}$$

with

$$\theta_{po} = \frac{\hbar\omega_{LO}}{k} \tag{12.41}$$

$$E_o = \frac{m_e^{\Gamma} e \omega_{LO}}{\hbar} \left(\frac{1}{\varepsilon_\infty} - \frac{1}{\varepsilon_s} \right) \tag{12.42}$$

In Equations (12.40)–(12.42), θ_{po} and E_o are the Debye temperature and effective polarization field of the LO phonons, respectively, $\chi_e = \hbar\omega_{LO}/kT_e$, $\chi_0 = \hbar\omega_{LO}/kT_0$ with T_0 the lattice temperature, $N_q = 1/[\exp(\chi_0)-1]$, v_d is the electron drift velocity in the electric field E and K_0 and K_1 are modified Bessel functions of the second kind.

The equations for the changes in energy and momentum due to the applied electric field E are given by

$$\left\langle \frac{d\varepsilon}{dt} \right\rangle_E = e v_d E \tag{12.43a}$$

$$\left\langle \frac{dp}{dt} \right\rangle_E = eE \tag{12.43b}$$

Introducing Equations (12.40) and (12.43) into Equation (12.39), we obtain the electron mobility, μ_{po}, limited by the polar optical scattering as

$$\mu_{po}(T_0, E) = \left(\frac{m_e^{\Gamma} \chi_e E^2}{3k\theta_{po}} \frac{(e^{(\chi_0-\chi_e)}+1)K_1(\chi_e/2) + (e^{(\chi_0-\chi_e)}-1)K_0(\chi_e/2)}{(e^{(\chi_0-\chi_e)}-1)K_0(\chi_e/2)} \right)^{-1/2} \tag{12.44}$$

The electric field–electron temperature relation, E–T_e, can also be given by

$$\left(\frac{E}{E_o} \right)^2 = \frac{2}{3\pi} N_q^2 \chi_e^2 e^{\chi_e} (e^{(\chi_0-\chi_e)}-1)K_0(\chi_e/2) \times [(e^{(\chi_0-\chi_e)}+1)K_1(\chi_e/2) + (e^{(\chi_0-\chi_e)}-1)K_0(\chi_e/2)] \tag{12.45}$$

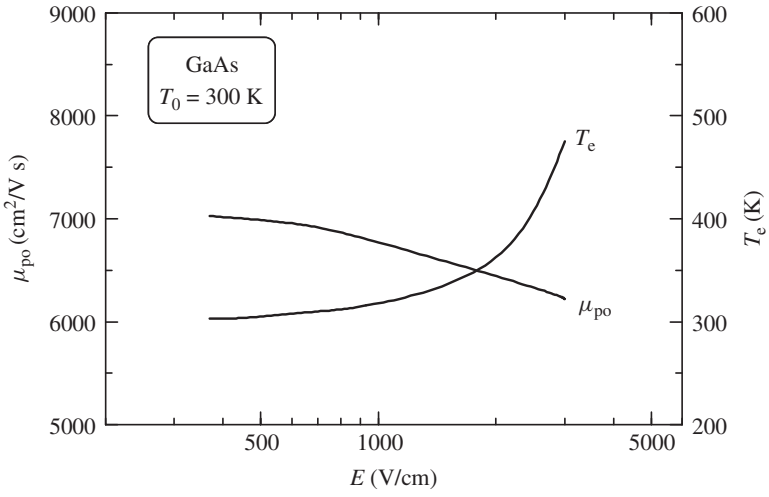

Figure 12.20 Polar optical scattering-limited mobility μ_{po} and electron temperature T_e as a function of electric field E for GaAs at the lattice temperature of $T_0 = 300$ K

Figure 12.20 shows the calculated results of the electron mobility μ_{po} at the lattice temperature of $T_0 = 300$ K as a function of electric field E for GaAs. The corresponding T_e values are also plotted. The calculated mobility μ_{po} decreases gradually with increasing E; in contrast the electron temperature T_e increases with increasing E. One can expect that experimental mobility, if one measured, would decrease dramatically at fields higher than $\sim 10^3$ V/cm because of the onset of nonequivalent intervalley scattering (Γ–L, Γ–X) at this field region. Note that this type of scattering processes is not taken into consideration in Figure 12.20.

In multivalley semiconductors at high electric fields, we must consider three sets of equations: a carrier balance equation, a momentum balance equation and an energy balance equation. Under uniform field condition these equations for two levels of transfer (e.g., Γ and L) represent particle, momentum and energy conservation [12.61]. For particle conservation, we obtain

$$\frac{d(a_1 n_1)}{dt} = -a_1 n_1 \Gamma_1 + a_2 n_2 \Gamma_2 \tag{12.46a}$$

$$\frac{d(a_2 n_2)}{dt} = a_1 n_1 \Gamma_1 - a_2 n_2 \Gamma_2 \tag{12.46b}$$

In Equation (14.46), there are n_1 electrons in each lower-energy valley and n_2 in each higher-energy valley. This equation indicates that there are $a_1 n_1$ electrons scattered out, distributed equally to the higher-energy valleys; and there are $a_2 n_2$ electrons scattered from the higher-energy valleys into the lower-energy valleys. The respective carrier scattering rates are designated Γ_1 and Γ_2, respectively. For uniform fields and steady state, a condition under which the velocity–field curve is generated, the following condition holds: $a_1 n_1 \Gamma_1 = a_2 n_2 \Gamma_2$.

For momentum conservation, the second set of equations describes the rate of change of momentum in the individual valleys under an applied field and scattering events. Under

uniform fields and for the low-energy carriers this equation is given by [12.61]

$$\frac{\mathrm{d}(n_1\boldsymbol{p}_1)}{\mathrm{d}t} = -n_1 e\boldsymbol{E} - n_1\boldsymbol{p}_1\Gamma_3 \tag{12.47}$$

where the momentum is designated $\boldsymbol{p}_1 = m_1\boldsymbol{v}_1$, Γ_3 is the momentum scattering rate for the low-energy carriers and $\boldsymbol{E}$ is the electric field vector. Under steady state conditions, $n_1 m_1 \boldsymbol{v}_1 = -(1/\Gamma_3)n_1 e\boldsymbol{E}$. Similar equations can be written for the high-energy valley carriers and also for holes.

For energy conservation, there are various forms in which the lower-energy valley and higher-energy valley energy equations can be described. If we cast the energy equations in terms of species 1 and species 2 electron temperatures T_1 and T_2, then [12.61]

$$\frac{\mathrm{d}(a_1 n_1 T_1)}{\mathrm{d}t} = \frac{m_1 v_1^2}{3k}[a_1 n_1(2\Gamma_3 - \Gamma_1) + a_1 n_2 \Gamma_2] - a_1 n_1 T_1 \Gamma_5 + a_2 n_2 T_2 \Gamma_6 \tag{12.48}$$

where Γ_5 denotes energy relaxation within species 1 valley plus energy exchange with species 2 valley and Γ_6 denotes return energy between species 2 and 1 valleys. The above analysis requires analytical calculations of the scattering rates. These are taken from scattering integrals.

There have been a fair number of publications on the theoretical and experimental electron velocity–electric field curves, v_e–E, of semiconductors. The v_e–E curve is known to be strongly dependent on both the material quality and temperature. This is because the carrier drift mechanism is largely influenced by scattering processes in the material. The v_e–E curve is also dependent on the direction of the electric field. We reproduce in Figure 12.21 the experimental electron velocity v_e as a function of electric field E obtained for high-purity n-type Si at temperatures between 8 and 300 K with the field applied along the ⟨100⟩ and ⟨111⟩ directions [12.62]. The v_e–E curves with the electric field applied along the ⟨100⟩, ⟨110⟩ and ⟨111⟩ directions at 8 K are also shown in Figure 12.22 [12.62]. The time-of-flight technique was used in these experiments.

The main features found in Figures 12.21 and 12.22 are: (i) the anisotropy effect increases with increasing temperature; (ii) the curves of the drift velocity along the ⟨100⟩ and ⟨111⟩ directions tend to join together at a value of the electric field increasing with temperature, even though such a joining has not been reached at all temperatures considered; (iii) at highest electric field a region of drift velocity nearly independent of the electric field is obtained; and (iv) a negative differential mobility region is found with electric field $\boldsymbol{E} \| \langle 100 \rangle$ for T below 40 K. It is known that the anisotropy of the electron drift velocity in Si is due to a repopulation of the 'hot' and 'cold' valleys at the minimum of the conduction band [12.1]. The negative differential mobility observed for $\boldsymbol{E} \| \langle 100 \rangle$ is a limiting case of such repopulation effect.

We compare in Figure 12.23 the v_e–E curves for Si (⟨111⟩), GaP, GaAs and InP at $T = 300$ K. These curves are obtained by calculating empirical equations in [12.19] for Si, in [12.63] for GaP and in [12.64] for GaAs and InP. The empirical equation used in [12.19] and [12.63] can be simply written as

$$v_e(E) = \frac{\mu E}{\left[1 + \left(\dfrac{\mu E}{v_s}\right)^{\beta}\right]^{1/\beta}} \tag{12.49}$$

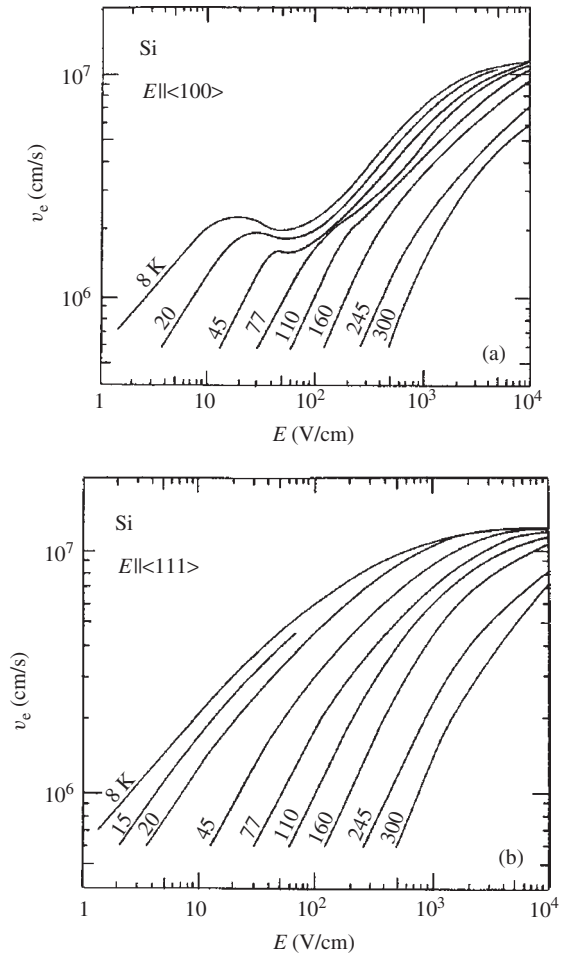

Figure 12.21 Electron drift velocity v_e as a function of electric field $\boldsymbol{E}$ applied parallel to: (a) ⟨100⟩; (b) ⟨111⟩ crystallographic directions in high-purity n-type Si at temperatures between 8 and 300 K. [From C. Canali, C. Jacoboni, F. Nava, G. Ottaviani, and A. Alberigi-Quaranta, *Phys. Rev. B* **12**, 2265 (1975), reproduced by permission from the American Physical Society]

while that proposed in [12.64] is given by

$$v_e(E) = \frac{\mu_0 E + (3v_m - 2\mu_0 E_M)\left(\dfrac{E}{E_M}\right)^2 + v_s\left(\dfrac{2v_m - \mu_0 E_M}{v_m - v_s}\right)\left(\dfrac{E}{E_M}\right)^3}{1 + \left(\dfrac{2v_m - \mu_0 E_M}{v_m - v_s}\right)\left(\dfrac{E}{E_M}\right)^3} \tag{12.50}$$

It is easily recognized from Figure 12.23 that InP is very promising for high-frequency transistors and high-speed logic applications. The extremely low electron velocities of Si and GaP are due to the large electron effective masses in the lowest conduction band (X) of these materials. The experimentally obtained saturation drift velocity in GaP is $\sim 1.25 \times$

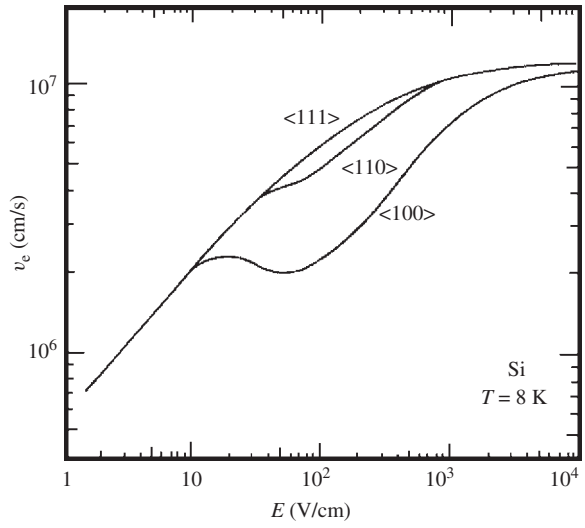

Figure 12.22 Electron drift velocity v_e as a function of electric field $\boldsymbol{E}$ applied parallel to the ⟨100⟩, ⟨110⟩ and ⟨111⟩ crystallographic directions in high-purity n-type Si at 8 K. [From C. Canali, C. Jacoboni, F. Nava, G. Ottaviani, and A. Alberigi-Quaranta, *Phys. Rev. B* **12**, 2265 (1975), reproduced by permission from the American Physical Society]

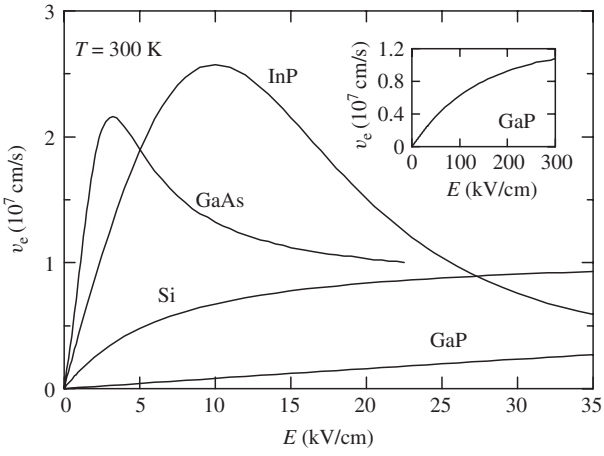

Figure 12.23 Electron drift velocity v_e versus electric field E for Si, GaP, GaAs and InP. The v_e–E curves are taken for Si from Jacoboni *et al.* [12.19], for GaP from Johnson and Eknoyan [12.63] and for GaAs and InP from Majumdart [12.64]

10^7 cm/s [12.63]. It has been found theoretically [12.65] that this value is sensitive only to the phonon coupling constant. For α-GaN [12.66], the observed electron velocity at $T =$ 300 K tended to saturate gradually with increasing E and reached a peak of 1.9×10^7 cm/s at $E \sim 225$ kV/cm. At fields higher than 250 kV/cm, an apparent slight decline in the electron velocity was observed.

12.3.2 Electron saturation drift velocity

(a) Temperature dependence

It is necessary to know the velocity–field curve in the higher-field regime in order to predict the frequency limitations of transit time-limited microwave devices, such as microwave transistors, IMPATTs (impact avalanche and transit time devices), transferred electron devices and optical devices, such as avalanche photodiodes and phototransistors. The electron velocity as a function of field in the higher-field regime has been measured for various semiconductors. We reproduce in Figure 12.24, as an example, the temperature-dependent electron velocity measured for GaAs [12.67]. The reason for the saturation of the velocity at high fields can be explained in thermal equilibrium terms. At low fields the electrons are in equilibrium with the lattice, and, on the average, they pick up as much energy per collision as they lose. As the electron velocity approaches the thermal velocity, the electrons, on the average, give more energy to the lattice than they receive per collision and the velocity saturates. We can understand from Figure 12.24 that the saturation velocity, obtained for an average electric field of about 100–200 kV/cm, gradually decreases with increasing temperature.

The temperature-dependent electron saturation velocity $v_{e,sat}(T)$ can be simply written as [12.68]

$$v_{e,sat}(T) = v_{e,sat}(0) - KT \tag{12.51}$$

where $v_{e,sat}(0)$ is the saturation velocity at the temperature $T = 0$ K. The $v_{e,sat}(0)$ and K values for InP ($In_{0.53}Ga_{0.47}As$) are, respectively, $v_{e,sat}(0) = 1.0 \times 10^7$ cm/s (7.7×10^6 cm/s) and $K = 7 \times 10^3$ cm/s K (5×10^3 cm/s K). Allam and Pribetich [12.69] also

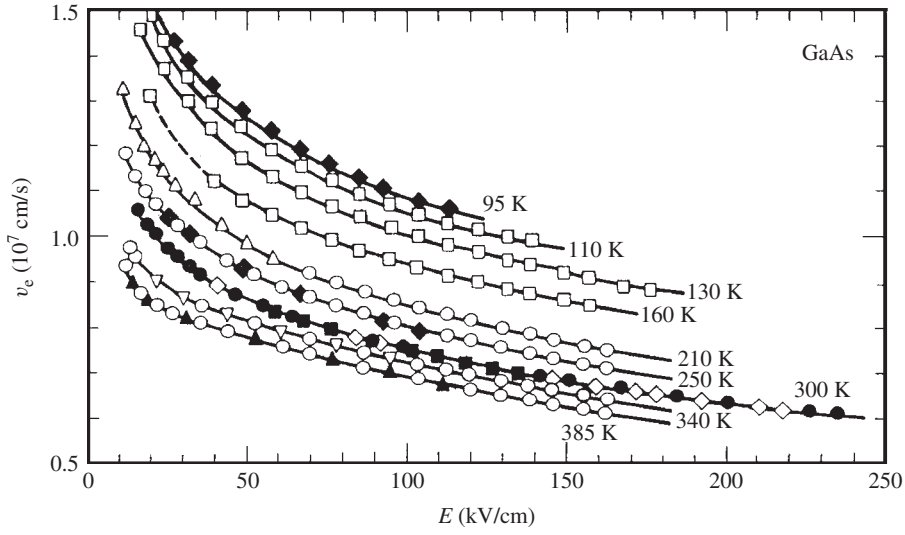

Figure 12.24 Temperature-dependent electron drift velocity v_e in GaAs measured for eight typical samples. [From T. H. Windhorn, T. J. Roth, L. M. Zinkiewicz, O. L. Gaddy, and G. E. Stillman, *Appl. Phys. Lett.* **40**, 513 (1982), reproduced by permission from the American Institute of Physics]

showed that the electron saturation velocity $v_{e,sat}(T)$ in GaAs can be expressed as

$$v_{e,sat}(T) = v_{e,sat}(T_0)\left(K_1 + \frac{K_2}{T}\right) \tag{12.52}$$

where $v_{s,sat}(T_0)$ is the saturation velocity at the ambient temperature $T_0 = 300$ K and K_1 and K_2 are constants. They obtained $v_{s,sat}(T_0) = 6.0 \times 10^6$ cm/s, $K_1 = 0.415$ and $K_2 = 175.4$ K at T between 300 and 500 K. The $v_{s,sat}(T_0)$ value is found to be nearly the same as that of $In_{0.53}Ga_{0.47}$ As, but is lower than that of InP ($\sim 8 \times 10^6$ cm/s).

More recently, Quay *et al.* [12.70] presented a model of the temperature-dependent saturation velocity $v_{e(h),sat}(T)$ for the electrons and holes. The expression derived by these authors can be written as

$$v_{e(h),sat}(T) = \frac{v_{e(h)s300}}{(1 - A) + A(T/300)} \tag{12.53}$$

The model is a two-parameter model, where the first parameter, $v_{e(h)s300}$, represents the saturation velocity at the lattice temperature $T_L = 300$ K and the second parameter A reflects the temperature dependence of the various material parameters involved in the saturation velocity phenomenon. We summarize in Table 12.7 the values of $v_{e(h)s300}$ and A obtained by Quay *et al.* [12.70]. Table 12.8 also lists the experimentally determined saturation velocity $v_{e,sat}$ in some hexagonal semiconductors [12.66, 12.71, 12.72].

(b) LO phonon scattering-limited electron saturation drift velocity

It is possible to estimate the electron saturation drift velocities in the Γ, L and X minima of semiconductors. If we assume that a single high-energy phonon (a long-wavelength LO phonon) dominates the energy relaxation, the expected saturation velocity $v_{e,sat}$ can be written as [12.65]

$$v^{\alpha}_{e,sat} = \sqrt{\frac{8\hbar\omega_{LO}}{3\pi m^{\alpha}_{c}}} \tag{12.54}$$

Table 12.7 $v_{e(h)s300}$ and A used for the calculation of the temperature-dependent saturation velocity in some group-IV and III–V semiconductors

$$v_{e(h),sat}(T) = \frac{v_{e(h)s300}}{(1 - A) + A(T/300)}$$

System	Material	Electrons		Holes	
		v_{es300} (10^7 cm/s)	A	v_{hs300} (10^7 cm/s)	A
IV	Si	1.02	0.74	0.72	0.37
	Ge	0.70	0.45	0.63	0.39
III–V	AlAs	0.85	0.45		
	GaAs	0.72	0.44	0.9	0.59
	InP	0.68	0.31		
	InAs	0.9	0.43		

Table 12.8 Electron saturation drift velocity $v_{e,sat}$ in some hexagonal semiconductors

System	Material	$v_{e,sat}$ (10^6 cm/s)	Comment
IV	4H-SiC	22[a]	$T = 300$ K, $\boldsymbol{E} \perp c$
	4H-SiC	8[b]	$T = 300$ K, $\boldsymbol{E} \parallel c$
	4H-SiC	7.5[b]	$T = 460$ K, $\boldsymbol{E} \parallel c$
	6H-SiC	19[a]	$T = 300$ K, $\boldsymbol{E} \perp c$
III–V	α-GaN	$\leqslant 19$[c]	$T = 300$ K, $\boldsymbol{E} \parallel c$

[a] I. A. Khan and J. A. Cooper, Jr., *IEEE Trans. Electron Dev.* **47**, 269 (2000)
[b] K. V. Vassilevski, K. Zekentes, A. V. Zorenko, and L. P. Romanov, *IEEE Electron Dev. Lett.* **21**, 485 (2000)
[c] M. Wraback, H. Shen, J. C. Carrano, T. Li, J. C. Campbell, M. J. Schurman, and I. T. Ferguson, *Appl. Phys. Lett.* **76**, 1155 (2000)

where m_c^α is the conductivity effective mass in the $\alpha = \Gamma$, L or X valley. If several scattering mechanisms are present, then the expression is far more complicated, as can be recognized from Equation (12.39).

We list in Table 12.9 the calculated $v_{e,sat}^\alpha$ values for some cubic group-IV, III–V and II–VI semiconductors. The calculated $v_{e,sat}^\Gamma$ value ($\sim 3 \times 10^7$ cm/s) for GaAs is considerably larger than the experimentally observed peak velocity $\sim 2 \times 10^7$ cm/s. However, the X-valley value $v_{e,sat}^X$ is comparable to the experimental saturation velocity $\sim 1 \times 10^7$ cm/s. We can, therefore, suppose that in GaAs the Γ-conduction electrons exhibit a peak velocity before reaching the phonon-limited saturation velocity ($v_{e,sat}^\Gamma$) due to the onset of the intervalley transfer processes, then the drift velocity is limited by the X-valley saturation velocity $v_{e,sat}^X$. Figure 12.25 plots the $v_{e,sat}^\alpha$ value in the lowest conduction valley $\alpha = \Gamma$, X or L versus $(m_c^\alpha)^{-1/2}$ for some cubic group-IV, III–V and II–VI semiconductors.

12.4 HIGH-FIELD TRANSPORT: HOLES

12.4.1 Hole drift velocity–field characteristic

High-field hole transport properties have been studied in many cases with a Monte Carlo technique. We reproduce in Figure 12.26 the total hole scattering rate in GaAs and $Al_{0.45}Ga_{0.55}As$ as a function of carrier energy [12.73]. In the valence band, the predominant scattering mechanisms are polar optical and deformation potential scatterings—when the effects of impurities can be ignored. In Figure 12.26, the total scattering rate includes both intraband and interband scattering and impact ionization, but not the effects of impurities. Impact ionization is treated as a scattering mechanism using the Keldysh formulation.

The hole drift velocity–electric field curve $v_h - E$ has been determined experimentally for several semiconductors, such as diamond [12.74], Si [12.75], Ge [12.76], GaAs [12.77], ZnSe [12.78], w-CdS [12.79] and CdTe [12.80]. We reproduce in Figure 12.27

Table 12.9 LO phonon scattering-limited electron saturation drift velocity $v_{e,sat}^{\alpha}$ in the $\alpha = \Gamma$, X and L valleys for some cubic group-IV, III–V and II–VI semiconductors

System	Material	$v_{e,sat}^{\alpha}$ (10^7 cm/s)		
		Γ	X	L
IV	Diamond		2.3	
	Si		1.9	
	Ge			2.2
	3C-SiC		2.37	
III–V	*c*-BN		2.6	
	BP		2.3	
	AlP		1.7	
	AlAs	2.2	1.7	2.3
	AlSb		1.5	
	β-GaN	3.0		
	GaP		1.4	
	GaAs	2.9	1.3	2.2
	GaSb	3.3	0.99	1.9
	InP	2.8	1.2	1.8
	InAs		4.3	
	InSb		5.2	
II–VI	*β*-MgS	1.9		
	β-MgSe	1.8		
	β-MgTe	1.8		
	β-ZnS	1.8		
	ZnSe	1.8		
	ZnTe	1.8		
	c-CdS	2.0		
	c-CdSe	1.8		
	CdTe	1.9		

the $v_h - E$ curves for high-purity Si measured at temperatures 6–300 K with the applied field $\boldsymbol{E}$ along the ⟨100⟩ and ⟨111⟩ directions using the time-of-flight technique [12.75]. The crystallographic direction dependence of the $v_h - E$ curve for high-purity Si along the ⟨100⟩, ⟨110⟩ and ⟨111⟩ directions at 6, 77 and 300 K are also shown in Figure 12.28 [12.75].

It is understood from Figures 12.27 and 12.28 that the ohmic region is reached for $T > 100$ K; for $T < 100$ K, it is not reached even at the lowest electric field. It is also evident that the hole drift velocity exhibits an anisotropic behavior with higher values for v_h in the ⟨100⟩ direction than in the ⟨111⟩ direction and with the lowest value in the ⟨110⟩ direction. This anisotropy is best evidenced by lowering the temperature T. At the highest fields $E \sim 10^4$, the anisotropy tends to saturate. An analysis using a single warped heavy-hole band model and a Monte Carlo technique suggests that the anisotropy of the hot hole transport can be explained as associated with warping of the valence band. The essentially same anisotropy has also been observed in diamond [12.74], Si [12.75] and Ge [12.76].

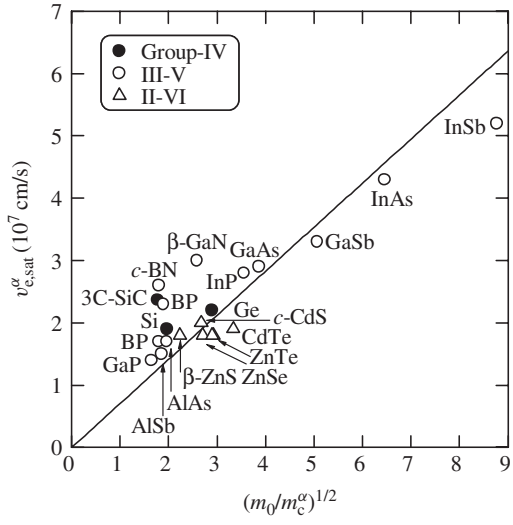

Figure 12.25 LO phonon scattering-limited electron saturation drift velocity $v^{\alpha}_{e,sat}$ in the lowest conduction valley $\alpha = \Gamma$, X or L versus $(m_0/m^{\alpha}_c)^{1/2}$ for some cubic group-IV, III–V and II–VI semiconductors

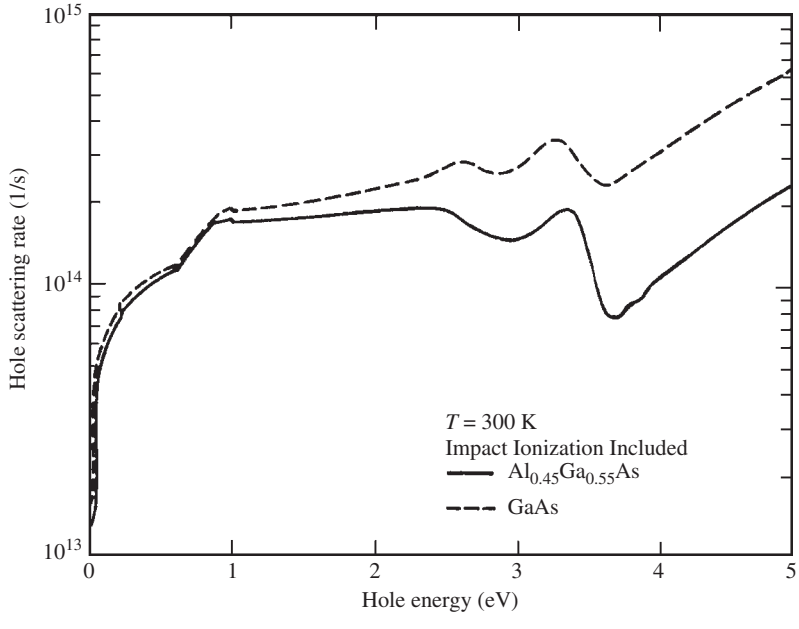

Figure 12.26 Total hole scattering rates for GaAs and $Al_{0.45}Ga_{0.55}As$ at 300 K as a function of energy obtained by a Monte Carlo technique. [From K. Brennan and K. Hess, *J. Appl. Phys.* **59**, 964 (1986), reproduced by permission from the American Institute of Physics]

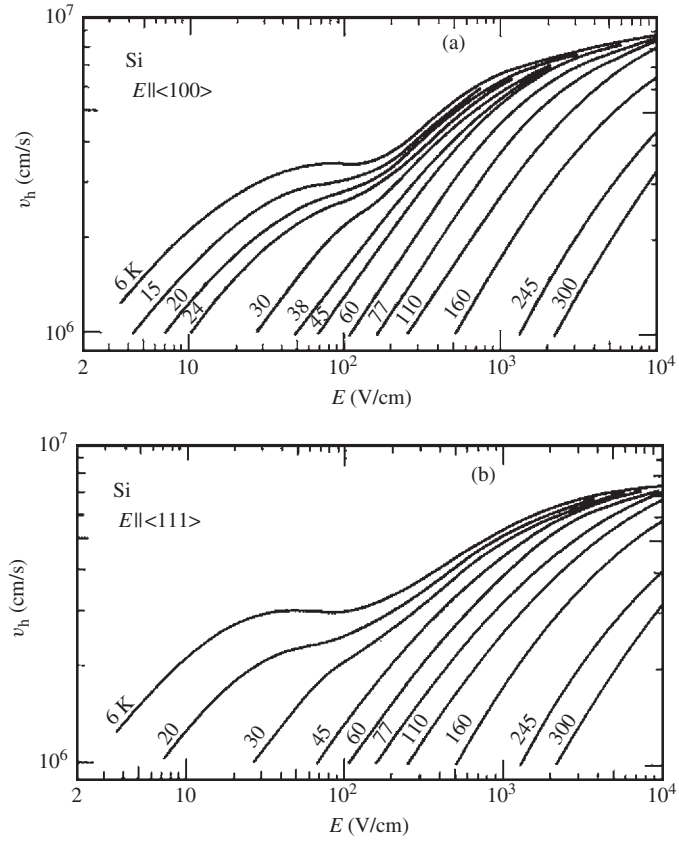

Figure 12.27 Hole drift velocity v_h as a function of electric field $\boldsymbol{E}$ applied parallel to: (a) ⟨100⟩; (b) ⟨111⟩ crystallographic directions in high-purity p-type Si at temperatures between 6 and 300 K. [From G. Ottaviani, L. Reggiani, C. Canali, F. Nava, and A. Alberigi-Quaranta, *Phys. Rev. B* **12**, 3318 (1975), reproduced by permission from the American Physical Society]

Figure 12.29 shows the steady-state hole drift velocity in GaAs at $T = 300$ K for electric field along the ⟨100⟩, ⟨110⟩ and ⟨111⟩ directions calculated with the Monte Carlo technique [12.81]. The dashed line represents the experimental data for fields along the ⟨100⟩ direction. It is seen in Figure 12.29 that there is no significant anisotropy in the calculated hole drift velocity through a large range of the electric fields. It is also found that the hole drift velocity saturates at fields of about 100 kV/cm. The hole peak velocity observed is about 7×10^6 cm/s, which is considerably lower than the electron peak velocity ($\sim 2 \times 10^7$ cm/s).

12.4.2 Hole saturation drift velocity

We list in Table 12.10 the experimental values of $v_{h,sat}$ at $T = 300$ K for some cubic group-IV and III–V semiconductors. The data are obtained from various sources. It is found that $v_{h,sat}$ is about 1×10^7 cm/s for many semiconductors.

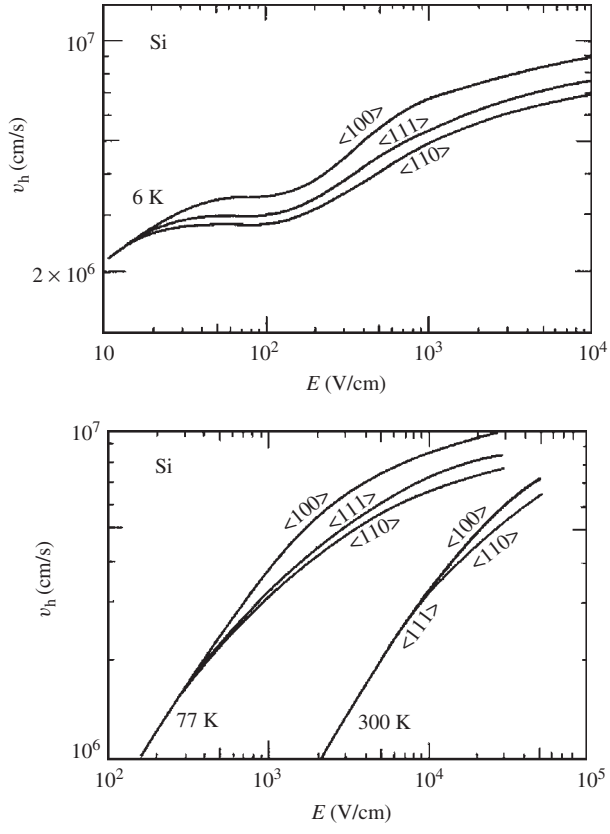

Figure 12.28 Hole drift velocity v_h as a function of electric field $\boldsymbol{E}$ applied parallel to the ⟨100⟩, ⟨110⟩ and ⟨111⟩ crystallographic directions in high-purity p-type Si at $T = 6$, 77 and 300 K. [From G. Ottaviani, L. Reggiani, C. Canali, F. Nava, and A. Alberigi-Quaranta, *Phys. Rev. B* **12**, 3318 (1975), reproduced by permission from the American Physical Society]

The temperature dependence of the hole saturation drift velocity $v_{h,sat}(T)$ obtained by Quay *et al*. [12.70] can be expressed as Equation (12.53). The values of v_{hs300} and A for Si, Ge and GaAs have been listed in Table 12.8.

12.5 MINORITY-CARRIER TRANSPORT: ELECTRONS IN *P*-TYPE MATERIALS

12.5.1 Minority-electron mobility

Majority-carrier transport in semiconductors has been the subject of intense theoretical and experimental work. However, minority-carrier transport has received much less attention. Short minority-carrier lifetimes and high Joule heating rates have usually hampered measurements of minority-carrier transport parameters. From a technological point of view, however, a better understanding of minority-carrier transport is of paramount

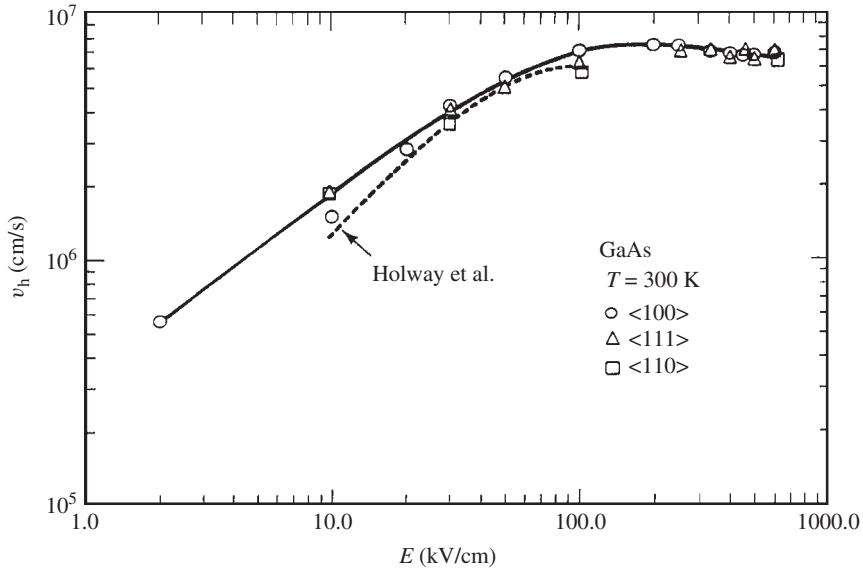

Figure 12.29 Steady-state hole drift velocity v_h in GaAs at 300 K as a function of applied electric field obtained from the Monte Carlo calculation. The dashed line represents the experimental data for fields along the ⟨100⟩ direction. [From K. Brennan and K. Hess, *Phys. Rev. B* **29**, 5581 (1984), reproduced by permission from the American Physical Society]

Table 12.10 Hole saturation drift velocity $v_{h,sat}$ in some cubic group-IV and III–V semiconductors at 300 K

System	Material	$v_{h,sat}$ (10^6 cm/s)	System	Material	$v_{h,sat}$ (10^6 cm/s)
IV	Diamond	11	III–V	GaAs	9
	Si	7.2		InP	7
	Ge	6.3			
	3C-SiC	10			

importance. Recent advances in analysis and design of heterojunction bipolar devices, for example, suggest that an accurate knowledge of transit minority-carrier behavior in the base region may lead to improved design. When this information is not available, the assumption is frequently made that its parameter value is equal to the majority-carrier value. This assumption is likely to be in considerable error, particularly for III–V direct band-gap semiconductors, because of the large differences between the conduction-band and valence-band densities of states and effective masses.

Measurements of the minority-electron mobility μ have been performed on several semiconductors, such as Si [12.82], Ge [12.83], α-GaN [12.84] and GaAs [12.85–12.87]. In high-purity p-Si, μ is independent of the acceptor concentration N_A and is essentially identical to that of the majority electrons, as shown in Figure 12.30. At high doping levels,

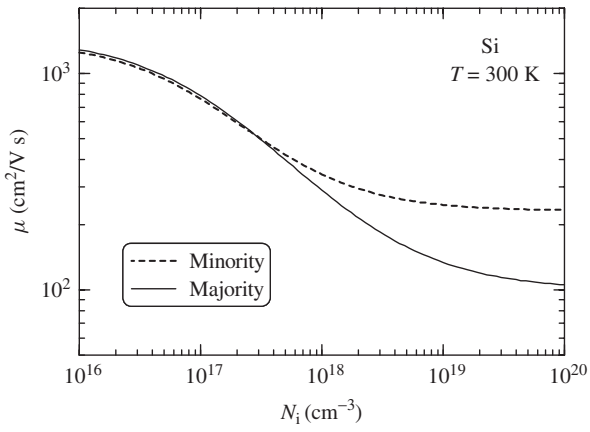

Figure 12.30 Minority-electron and majority-electron mobilities in Si as a function of impurity concentration N_i at 300 K. The dashed line represents the minority-electron mobility given by $\mu = 232 + 1180/[1 + (N_i/8 \times 10^{16})^{0.90}]$, while the solid line shows the majority-electron mobility given by $\mu = 100 + 1380/[1 + (N_i/10^{17})^{0.80}]$, where N_i is in cm^{-3} and μ is in cm^2/V s. [From S. Adachi, *Handbook on Physical Properties of Semiconductors Volume 1: Group-IV Semiconductors* (Kluwer Academic, Boston, 2004), reproduced by permission from Kluwer Academic Publishers]

the minority-electron mobility decreases less strongly than the majority-electron mobility and tends to saturate to a value about 2.5 times larger than the saturated majority value. The minority-electron mobility μ as a function of N_A obtained in p-Si at $T = 300$ K can be expressed as [12.88]

$$\mu = 232 + \frac{1180}{1 + \left(\dfrac{N_A}{8 \times 10^{16}}\right)^{0.90}} \tag{12.55}$$

where μ is in cm^2/V s and N_A is in cm^{-3}.

Figure 12.31 shows the dependence of minority-electron mobility μ as a function of acceptor doping concentration N_A in p-GaAs at $T = 300$ K. The experimental data are taken from Lowney and Bennett [12.85] and Kim *et al.* [12.86]. The solid line represents the theoretical result obtained from Monte Carlo technique [12.89]. For comparison, the majority-electron mobility versus donor concentration N_D data are shown by the dashed line. We can see from Figure 12.31 that the experimental mobility increases with acceptor concentrations above 10^{19} cm^{-3}, as expected from the theoretical calculation. This effect is explained by the reduction of plasmon scattering and carrier–carrier scattering (because of the Pauli exclusion principle) [12.85]. The minority-electron mobility in p-type α-GaN epilayer on (0001) sapphire substrate has also been measured using a diffusion time-of-flight technique by Guan *et al.* [12.84]. The mobility obtained by them is 0.12 cm^2/V s ($T = 300$ K), which is by about three orders of magnitude smaller than the majority-electron mobility owing to the higher concentration of Mg dopants in p-type α-GaN.

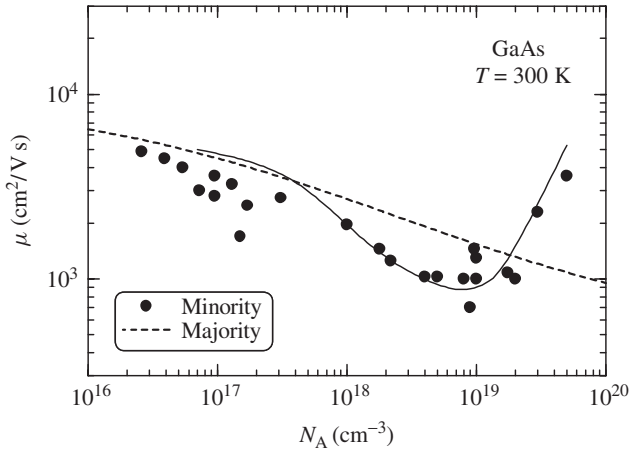

Figure 12.31 Dependence of the minority-electron mobility μ in p-GaAs as a function of acceptor doping concentration N_A. The experimental data are taken from Lowney and Bennett [12.85] and Kim *et al.* [12.86]. The solid line represents the theoretical result obtained from Monte Carlo technique by Furuta and Tomizawa [12.89]. The majority-electron mobility versus donor concentration N_D data are also shown by the dashed line

12.5.2 Minority-electron drift velocity

The minority-electron drift velocity–field characteristics have been determined for several p-type semiconductors, such as p-Si [12.90], p-Ge [12.91] and p-InSb [12.92]. We reproduce in Figure 12.32 the results obtained by Morohashi *et al.* [12.90] using the time-of-flight technique. For comparison, those on high-purity, high-resistivity n-Si are shown by the solid lines [12.93]. In the ohmic region, these data agree with each other; however, at low temperatures and/or high electric fields, they deviate slightly. The deviation is considered to be due to the ambipolar nature of minority carriers under an electric field [12.90]. In p-InSb, the ambipolar errors are found to be of the order of 10–15% [12.92]. The negative differential mobility has been observed in p-Ge only along the ⟨100⟩ direction at the temperatures as high as 200 K [12.91].

12.5.3 Minority-electron lifetime and diffusion length

The minority-carrier lifetime τ in semiconductors can be determined by different methods, such as photoconductivity, photoluminescence, electroluminescence decay and switching of the current in diodes. A considerable scatter of the lifetime can be generally found in a variety of semiconductors. This is probably due to the fact that some of the experiments measure diffusion length L

$$L = \sqrt{\frac{kT}{e}\tau\mu} \tag{12.56}$$

and assume mobility values μ. The electron diffusion length can now be computed at any doping level by introducing the available experimental data of μ and τ into Equation (12.56).

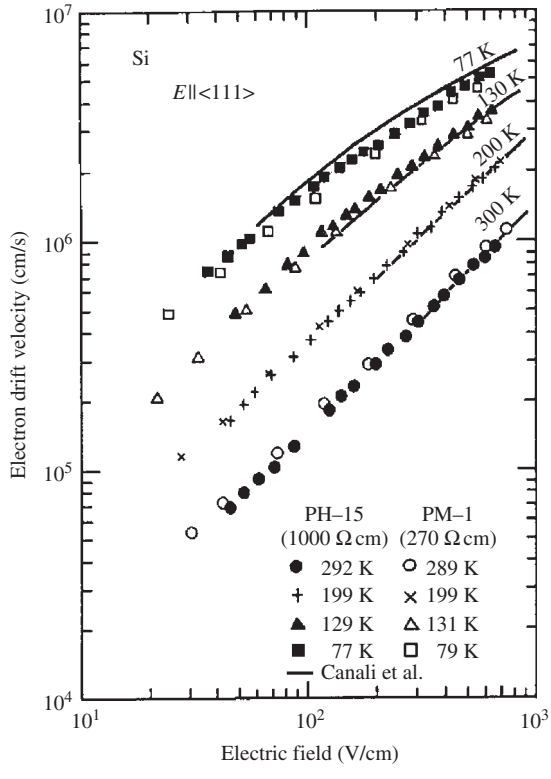

Figure 12.32 Minority-electron drift velocity as a function of electric field in p-Si measured using the time-of-flight technique at temperatures between 77 and 300 K. The solid lines represent those on high-purity, high-resistivity n-Si by Canali *et al*. [12.93]. [From M. Morohashi, N. Sawaki, and I. Akasaki, *Jpn. J. Appl. Phys.* **24**, 661 (1985), reproduced by permission from the Institute of Pure and Applied Physics]

It is known that the minority-carrier lifetime is dependent both on temperature T and doping density p or n. An empirical expression for the minority-electron lifetime τ in p-Si as a function of hole concentration p and temperature T obtained by Klaassen [12.32] can be written as

$$\tau^{-1} = (\tau_0^{-1} + C_{\text{SRH}} N_{\text{t}})(300/T)^{\alpha} + (C_{\text{Aug}} p^2)(T/300)^{\beta} \tag{12.57}$$

where $\tau_0 = 2.50$ ms is the intrinsic lifetime, $C_{\text{SRH}} = 3.00 \times 10^{-13}$ cm^3 s^{-1} is the Shockley–Read–Hall coefficient, N_{t} is the total impurity concentration, $C_{\text{Aug}} = 1.83 \times 10^{-31}$ cm^6 s^{-1} is the Auger coefficient, $\alpha = 1.77$ and $\beta = 1.18$.

We summarize in Table 12.11 the longest minority-electron lifetime τ and diffusion length L determined for some group-IV, III–V and II–VI semiconductors at $T = 300$ K. Figures 12.33 and 12.34 plot the minority-electron lifetime τ and diffusion length L versus hole concentration p for p-GaAs available in the literature. The solid lines in

Table 12.11 Longest minority-carrier lifetime τ and diffusion length L in some p-type and n-type semiconductors at 300 K

System	Material	Electrons (p-type)		Holes (n-type)	
		τ (μs)	L (μm)	τ (μs)	L (μm)
IV	Si	800	1000	1000	800
	Ge	$\geqslant$1000	$\geqslant$3000	$\geqslant$1000	$\geqslant$2000
	4H-SiC	0.08		0.7	0.2
	6H-SiC	11920[a]	1.8	8	0.68–1.46
III–V	α-GaN	10^{-4}	0.20	0.015	3.4
	GaP	$\sim$0.1	$\sim$7	$\sim$1	$\sim$20
	GaAs	$\sim 5 \times 10^{-3}$[b]	$\sim$10[b]	$\sim$3	$\sim$50
	InP		48		$>$20
	InAs	$\sim$3	$\sim$20	$\sim$0.03	$\sim$60
	InSb	10^{-4}[d]		$\sim$1[d]	32–38[d]
II–VI	ZnSe			0.07	1.20
	ZnTe		13		
	w-CdS			0.004	0.41–0.46
	w-CdSe				4.98
	CdTe		1.6		5.0

[a] Extremely long lifetime is considered to be due to the effect of traps
[b] Low injection level
[c] High injection level
[d] At $T \sim 80$ K

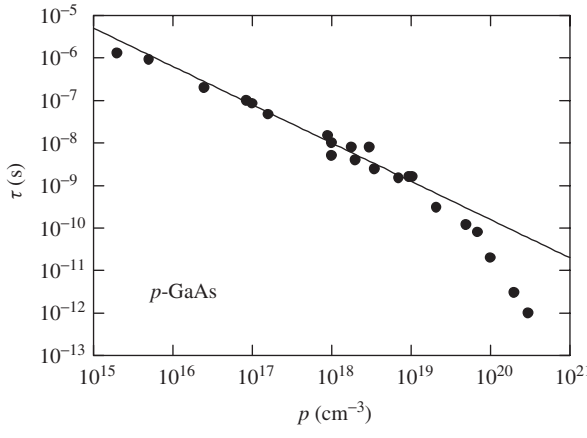

Figure 12.33 Minority-electron lifetime τ in p-GaAs at 300 K available in the literature. The solid line represents the fitted result with $\tau = (1.3 \times 10^9/p)^{0.90}$ (p in cm^{-3}; τ in s). [From S. Adachi, *Handbook on Physical Properties of Semiconductors Volume 2: III–V Compound Semiconductors* (Kluwer Academic, Boston, 2004), reproduced by permission from Kluwer Academic Publishers]

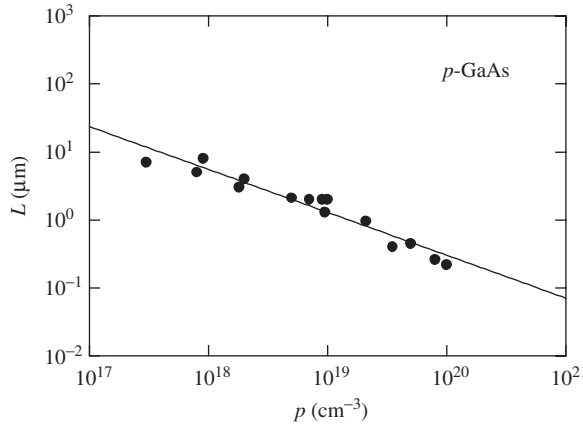

Figure 12.34 Minority-electron diffusion length L in p-GaAs at 300 K available in the literature. The solid line represents the fitted result with $L = (1.5 \times 10^{19}/p)^{0.63}$ (p in cm^{-3}; L in μm). [From S. Adachi, *Handbook on Physical Properties of Semiconductors Volume 2: III–V Compound Semiconductors* (Kluwer Academic, Boston, 2004), reproduced by permission from Kluwer Academic Publishers]

Figures 12.33 and 12.34, respectively, represent the fitted results with

$$\tau = \left(\frac{1.3 \times 10^9}{p}\right)^{0.90} \tag{12.58}$$

$$L = \left(\frac{1.5 \times 10^{19}}{p}\right)^{0.63} \tag{12.59}$$

where τ is in s, L is in μm and p is in cm^{-3}.

12.6 MINORITY-CARRIER TRANSPORT: HOLES IN *N*-TYPE MATERIALS

12.6.1 Minority-hole mobility

Measurements of the minority-hole mobility have been performed for several semiconductors, such as Si [12.94], Ge [12.83] and GaAs [12.95, 12.96]. The minority-hole mobility μ as a function of donor concentration N_D obtained in n-Si at $T = 300$ K by Swirhun *et al*. [12.97] can be expressed as

$$\mu = 130 + \frac{370}{1 + \left(\dfrac{N_D}{8 \times 10^{17}}\right)^{1.25}} \tag{12.60}$$

where μ is in cm^2/V s and N_D is in cm^{-3}. As shown in Figure 12.35, the minority-hole mobility in high-purity n-Si is independent of donor doping N_D. The minority-hole

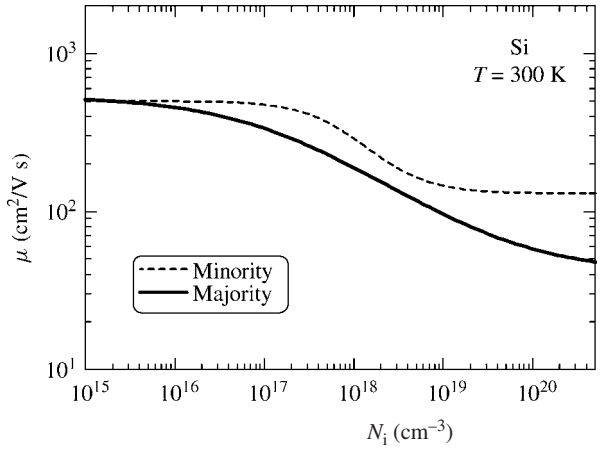

Figure 12.35 Minority-hole and majority-hole mobilities in Si as a function of impurity concentration N_i at 300 K. The dashed line represents the minority-hole mobility given by $\mu = 130 + 370/[1 + (N_i/8 \times 10^{17})^{1.25}]$, while the solid line shows the majority-hole mobility given by $\mu = 40 + 500/[1 + (N_i/2 \times 10^{17})^{0.53}]$, where N_i is in cm^{-3} and μ is in cm^2/V s. [From S. Adachi, *Handbook on Physical Properties of Semiconductors Volume 1: Group-IV Semiconductors* (Kluwer Academic, Boston, 2004), reproduced by permission from Kluwer Academic Publishers]

mobility in such high-purity n-Si is at around 500 cm^2/V s, which is essentially identical to the majority-hole mobility in p-Si. As the donor doping level increases, the minority-hole mobility starts to decrease just as the majority-hole mobility does. However, the onset of decay of μ in n-Si does not occur up to a donor doping level of $N_D \sim 1 \times 10^{17}$ cm^{-3}, while the drop of μ in p-Si is evident at an acceptor doping level of $N_A \sim 1 \times 10^{16}$ cm^{-3}.

We show in Figure 12.36 the experimental minority-hole mobility as a function of donor doping concentration N_D in n-GaAs at $T = 300$ K. The experimental data are taken from Casey *et al.* (●) [12.95], Lovejoy *et al.* (○) [12.96], Chuang *et al.* (▲) [12.98] and from Slater *et al.* (△) [12.99]. The solid line represents the experimental majority-hole mobilities. Lovejoy's and Slater's data show that the minority-hole mobility is always larger than the majority-hole data. Contrarily, the data of Casey *et al.* and Chuang *et al.* are much smaller than the majority-hole values. It should be noted that the theoretical prediction of Lowney and Bennett [12.85] by phase-shift analysis agrees reasonably with the experimental data of Casey *et al.*

The minority-hole mobilities in 6H-SiC and α-GaN can also be estimated to be in the range 8–30 cm^2/V s and ~5 cm^2/V s from minority-carrier lifetimes and diffusion lengths obtained by Anikin *et al.* [12.100] and Bandić *et al.* [12.101], respectively.

12.6.2 Minority-hole lifetime and diffusion length

The minority-hole lifetime is dependent both on temperature T and majority-electron concentration n. An empirical expression for the minority-hole lifetime τ in n-Si as a function of n and T obtained by Klaassen [12.32] can be represented by the same form

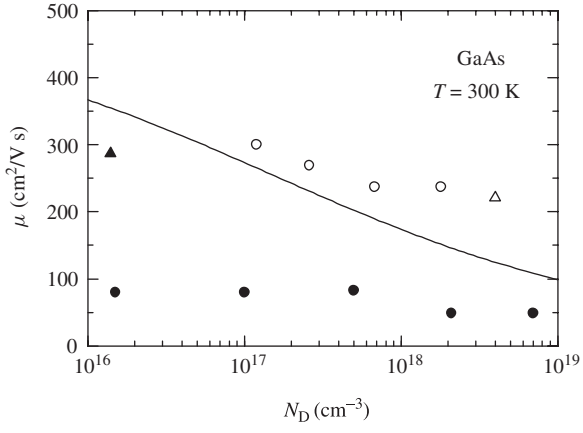

Figure 12.36 Minority-hole mobility μ as a function of donor doping concentration N_D in n-GaAs at 300 K. The experimental data are taken from Casey *et al.* (●) [12.95], Lovejoy *et al.* (○) [12.96], Chuang *et al.* (▲) [12.98] and from Slater *et al.* (△) [12.99]. The solid line represents the majority-hole mobility values. [From S. Adachi, *Handbook on Physical Properties of Semiconductors Volume 2: III–V Compound Semiconductors* (Kluwer Academic, Boston, 2004), reproduced by permission from Kluwer Academic Publishers]

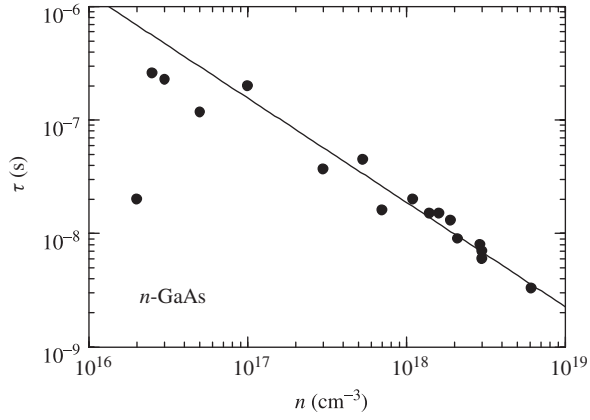

Figure 12.37 Minority-hole lifetime τ in n-GaAs at 300 K available in the literature. The solid line represents the fitted result with $\tau = (4.0 \times 10^9/n)^{0.92}$ (n in cm^{-3}; τ in s). [From S. Adachi, *Handbook on Physical Properties of Semiconductors Volume 2: III–V Compound Semiconductors* (Kluwer Academic, Boston, 2004), reproduced by permission from Kluwer Academic Publishers]

as in Equation (12.57). The fitting parameters determined are: $\tau_0 = 2.50$ ms, $C_{SRH} = 1.176 \times 10^{-12}$ cm^3 s^{-1}, $C_{Aug} = 2.78 \times 10^{-31}$ cm^6 s^{-1}, $\alpha = 0.57$ and $\beta = 0.72$.

We have already summarized in Table 12.11 the longest minority-hole lifetimes τ and diffusion lengths L for some group-IV, III–V and II–VI semiconductors at $T = 300$ K. Figures 12.37 and 12.38 plot the values of τ and L versus electron (donor) concentration n for n-GaAs available in the literature. The solid lines in Figures 12.37 and 12.38,

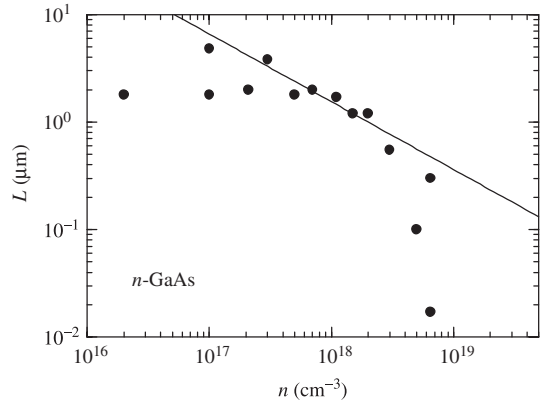

Figure 12.38 Minority-hole diffusion length L in n-GaAs at 300 K available in the literature. The solid line represents the fitted result with $L = (2.0 \times 10^{18}/n)^{0.63}$ (n in cm^{-3}; L in μm). [From S. Adachi, *Handbook on Physical Properties of Semiconductors Volume 2: III–V Compound Semiconductors* (Kluwer Academic, Boston, 2004), reproduced by permission from Kluwer Academic Publishers]

respectively, indicate the fitted results with

$$\tau = \left(\frac{4.0 \times 10^9}{n}\right)^{0.92} \tag{12.61}$$

$$L = \left(\frac{2.0 \times 10^{18}}{n}\right)^{0.63} \tag{12.62}$$

where τ is in s, L is in μm and n is in cm^{-3}.

12.7 IMPACT IONIZATION COEFFICIENT

12.7.1 Theoretical consideration

Impact ionization plays a crucial role in semiconductor devices, both as a basis for their operation and as a factor limiting their performance [12.102]. Avalanche photodiodes deliberately employ impact ionization to generate the carrier multiplication necessary for their operation [12.103, 12.104]. Impact ionization by hot carriers in an electric field is characterized by the ionization coefficients α for electrons and β for holes, which give the number of secondary carriers (electron–hole pairs) created by an initial hot carrier per centimeter of travel in an electric field E. By this definition, we obtain

$$\alpha = \frac{1}{n}\left(\frac{\mathrm{d}n}{\mathrm{d}x}\right) \text{ cm}^{-1}, \quad \beta = \frac{1}{p}\left(\frac{\mathrm{d}p}{\mathrm{d}x}\right) \text{ cm}^{-1} \tag{12.63}$$

where n and p are the electron and hole concentrations in cm^{-3}, respectively.

We show in Figure 12.39 examples of possible impact ionization processes for the electron-initiated and hole-initiated processes in a cubic semiconductor. The ionization

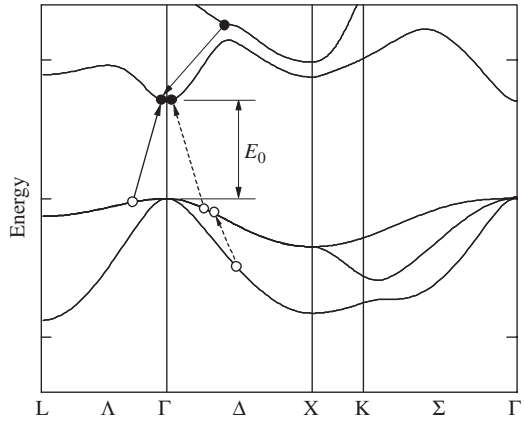

Figure 12.39 Examples of the impact ionization transitions in a cubic semiconductor. The ionization process initiated by a hot electron is shown by solid lines; it results in the transfer of an electron from the heavy-hole band to the conduction band. The ionization process initiated by a hot hole from the spin–orbit split-off band is shown by the dashed lines

threshold energy is the least energy of the initiating particle for which impact ionization can occur, consistent with conservation of energy and momentum. It is evident from Figure 12.39 that the threshold energy is at least as large as the band gap E_0. The electronic energy-band structure, thus, must allow the initiating particle to attain that energy.

Considering first the holes [12.105], one can see in Figure 12.39 that the conditions for the hole-initiated impact ionizations are rather similar for directions along the three symmetry axes ⟨001⟩ (Δ), ⟨110⟩ (Σ) and ⟨111⟩ (Λ)—a reflection of the nearly isotropic nature of the spin–orbit split-off (SO) band in many cubic semiconductors. Although a hot hole can always reach threshold in the direction of the electric field, holes must scatter at least one to enter the SO band. This scattering tends to randomize the distribution of hot carriers. Thus, we can expect that the orientation effect in the hole ionization coefficient will be small.

The electron threshold states, on the other hand, may show a considerable variation with orientation [12.105]. In the ⟨111⟩ direction (Λ), there is no threshold state for electron-initiated impact ionization. In the ⟨110⟩ direction (Σ), the threshold state occurs near the top of the conduction band. The threshold in the ⟨001⟩ direction (Δ) does not occur in the principal conduction band, but is separated from this conduction band by a small gap. Under a sufficiently high electric field, electrons can be expected to tunnel across this gap to threshold.

The threshold energies and their position in the Brillouin zone are determined by the following method, first proposed by Anderson and Crowell [12.106, 12.107]. Referring to Figure 12.40, the condition for the threshold is as follows

$$\nabla_k E_1(\boldsymbol{k}_1) = \nabla_k E_2(\boldsymbol{k}_2) = \nabla_k E_3(\boldsymbol{k}_3) \tag{12.64}$$

subject to conservation of energy

$$E_i(\boldsymbol{k}_i) = E_1(\boldsymbol{k}_1) + E_2(\boldsymbol{k}_2) - E_3(\boldsymbol{k}_3) \tag{12.65}$$

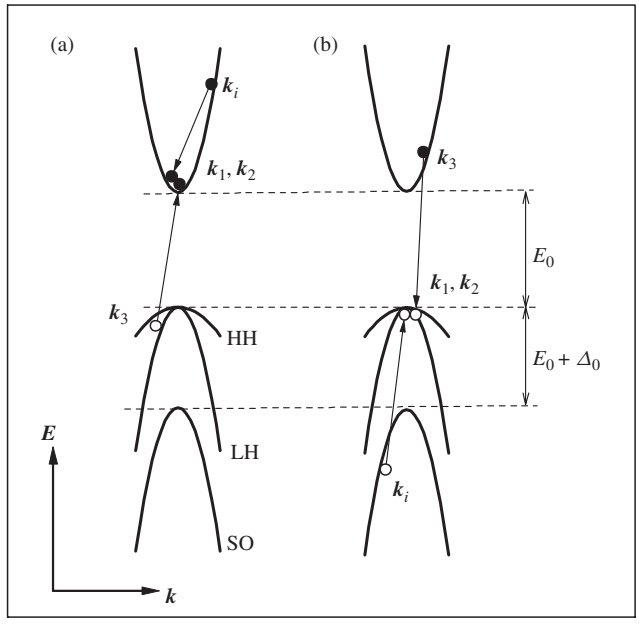

Figure 12.40 Impact-ionization transition in a schematic semiconductor band structure with features similar to those for III–V semiconductors: (a) electron-initiated transition; (b) hole-initiated transition

and conservation of crystal momentum

$$\boldsymbol{k}_i = \boldsymbol{k}_1 + \boldsymbol{k}_2 - \boldsymbol{k}_3 \tag{12.66}$$

In the case of nearly parabolic bands, these equations may be used to solve explicitly for the threshold energies $E_{i,\mathrm{e}}$ and $E_{i,\mathrm{h}}$, and particle wavevectors in closed form [12.107]

$$E_{i,\mathrm{e}} = E_0 \left(1 + \frac{m_\mathrm{e}}{m_\mathrm{HH} + m_\mathrm{e}}\right) \tag{12.67}$$

$$k_i = \sqrt{E_0 \left(\frac{2m_\mathrm{e}}{\hbar^2}\right) \left(1 + \frac{m_\mathrm{e}}{m_\mathrm{HH} + m_\mathrm{e}}\right)} \tag{12.68a}$$

$$k_1 = k_2 = k_i \left(\frac{m_\mathrm{e}}{2m_\mathrm{HH} + m_\mathrm{e}}\right) \tag{12.68b}$$

$$k_3 = k_i \left(\frac{m_\mathrm{HH}}{2m_\mathrm{HH} + m_\mathrm{e}}\right) \tag{12.68c}$$

for the electron-initiated ionization (Figure 12.40(a)) and

$$E_{i,\mathrm{h}} = E_0 \left(1 + \frac{m_\mathrm{SO}(1 - \Delta_0/E_0)}{2m_\mathrm{HH} - m_\mathrm{SO} + m_\mathrm{e}}\right) \tag{12.69}$$

$$k_i = \sqrt{(E_0 - \Delta_0)\left(\frac{2m_{SO}}{\hbar^2}\right)\left(\frac{2m_{HH} + m_e}{2m_{HH} - m_{SO} + m_e}\right)} \tag{12.70a}$$

$$k_1 = k_2 = k_i\left(\frac{m_{HH}}{2m_{HH} + m_e}\right) \tag{12.70b}$$

$$k_3 = k_i\left(\frac{m_e}{2m_{HH} + m_e}\right) \tag{12.70c}$$

for the hole-initiated ionization (Figure 12.40(b)). In Equations (12.67)–(12.70), m_e is the electron effective mass and m_{HH} and m_{SO} are, respectively, the heavy-hole (HH) and SO effective masses.

When $m_e = m_{HH} = m_{SO}$ and $\Delta_0 \to 0$ eV, both $E_{i,e}$ and $E_{i,h}$ are 3/2 the band-gap. Thus, the well-known 3/2 band-gap rule [12.108] is a direct result of the application of threshold criterion. The situation in real crystals is, however, considerably complicated.

12.7.2 Experimental value

(a) Electric-field dependence

According to Baraff's theory [12.109], the ionization coefficient α or β is represented, as a function of electric field E, as

$$\alpha(E) \text{ or } \beta(E) = A \exp -\left(\frac{B}{E}\right)^m \tag{12.71}$$

where $m = 1$ for low electric field in the avalanche region and $m = 2$ for higher electric field. We summarize in Table 12.12 the parameter values A and B for α and β with $m = 1$ determined experimentally for some group-IV [12.110–12.112], III–V [12.113, 12.114] and II–VI semiconductors [12.115] at 300 K.

Most of the early works erroneously assumed that the ionization rates α and β are equal. In 1974, Stillman *et al.* [12.116] showed that it is possible to achieve nearly pure electron and hole initiations in GaAs Schottky barrier avalanche photodiodes. Measurements of the multiplication characteristics of these devices indicated that α and β are not equal and that $\alpha > \beta$. Law and Lee [12.117] also used Schottky barrier devices to measure the ionization coefficients and found that $\alpha > \beta$ in lightly doped diodes and that $\beta > \alpha$ in heavily doped diodes. The use of Schottky barrier devices, however, still introduced difficulties in accurately modeling the electron injection into the high-field region because of the accompanying effects, such as barrier lowering, tunneling, etc. It is, thus, preferable to make ionization coefficient measurements on p–n junction devices where the injected carrier is more readily modeled. As in GaAs, α is usually larger than β in Si [12.118] and GaSb [12.119]; while $\beta > \alpha$ in Ge [12.118], 4H-SiC [12.120], 6H-SiC [12.120], InP [12.121] and InAs [12.122]; $\alpha \sim \beta$ in GaP [12.123]. The β/α ratios for Si and Ge are, respectively, 0.1–0.5 and 1.5–4 at $E = 3.3 \times 10^5$ V/cm [12.118]. We show in Figure 12.41, as an example, the electron (α) and hole ionization coefficients (β) as a function of reciprocal electric field ($1/E$) for Si at 300 K.

Table 12.12 Impact ionization parameters, A (10^6 cm^{-1}) and B (10^6 V/cm), used to calculate $\alpha(E)$ and $\beta(E)$ for some semiconductors at 300 K

$$\alpha(E) \text{ or } \beta(E) = A \exp - \left(\frac{B}{E}\right)$$

System	Material	α (electrons)		β (holes)		Comment
		A	B	A	B	
IV	Si[a]	0.74	1.16	0.725	2.2	
	Ge[b]	8.04	1.4	6.39	1.27	⟨100⟩ direction
	Ge[b]	2.72	1.1	1.72	0.937	⟨111⟩ direction
	4H-SiC[c]			3.25	17.9	
	6H-SiC[c]			2.6	15	
III–V	GaAs[d]	11	2.2	5.5	2.2	⟨100⟩ direction
	InP[e]	5.55	3.10	3.21	2.56	⟨100⟩ direction
	InP[e]	5.36	3.12	2.03	2.34	⟨110⟩ direction
II–VI	ZnSe[f]	42	4.23			$5.5 \times 10^5 < E < 7 \times 10^5$ V/cm

[a] V. A. Kuz'min, N. N. Kryukova, A. S. Kyuregyan, T. T. Mnatsakanov, and V. B. Shuman, *Sov. Phys. Semicond.* **9**, 481 (1975)
[b] T. Mikawa, S. Kagawa, T. Kaneda, Y. Toyama, and O. Mikami, *Appl. Phys. Lett.* **37**, 387 (1980)
[c] R. Raghunathan and B. J. Baliga, *Solid-State Electron.* **43**, 199 (1999)
[d] H. Ando and H. Kanbe, *Solid-State Electron.* **24**, 629 (1981)
[e] C. A. Armiento and S. H. Groves, *Appl. Phys. Lett.* **43**, 198 (1983)
[f] R. Mach and W. Ludwig, *Phys. Status Solidi A* **23**, 507 (1974)

(b) Temperature dependence

Temperature affects the electronic energy-band structure and can change in the impact ionization coefficients α and β. Temperature dependence of the ionization coefficients $\alpha(T)$ and $\beta(T)$ has been studied experimentally for semiconductors, such as Si [12.124–12.127], 4H-SiC [12.112], 6H-SiC [12.112, 12.128], GaAs [12.129, 12.130] and InP [12.121]. These data suggest that increasing T decreases α and β. Figure 12.42 shows, as an example, the ionization coefficients α and β for GaAs at 29° and 125°C. The experimental data are taken from Zheng *et al.* [12.130].

The data for Si obtained by Grant [12.125] can be expressed as

$$\alpha(E, T) \text{ or } \beta(E, T) = A \exp - \left(\frac{B + CT}{E}\right) \tag{12.72}$$

where $A = 6.2 \times 10^5$ cm^{-1} (2.0×10^6 cm^{-1}), $B = 1.05 \times 10^6$ V/cm (1.95×10^6 V/cm) and $C = 1.3 \times 10^3$ V/cm deg (1.1×10^3 V/cm deg) for α (β), respectively, with T in °C. Rang [12.126] reported an expression for the ionization coefficients α and β for Si given by

$$\alpha(E, T) \text{ or } \beta(E, T) = A_0[1 + A_1(T - 300)] \exp - \left(\frac{B_0[1 + B_1(T - 300)]}{E}\right) \tag{12.73}$$

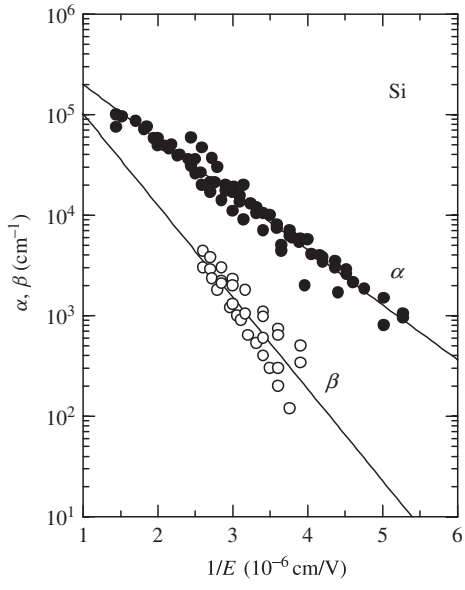

Figure 12.41 Electron (α) and hole ionization coefficients (β) as a function of reciprocal electric field ($1/E$) for Si at 300 K. The experimental data are taken from various sources. The solid lines represent the calculated results with $\alpha = 7.0 \times 10^5 \exp -(1.26 \times 10^6/E)$ cm^{-1} and $\beta = 8.3 \times 10^5 \exp -(2.10 \times 10^6/E)$ cm^{-1} (E in V/cm), respectively. [From S. Adachi, *Handbook on Physical Properties of Semiconductors Volume 1: Group-IV Semiconductors* (Kluwer Academic, Boston, 2004), reproduced by permission from Kluwer Academic Publishers]

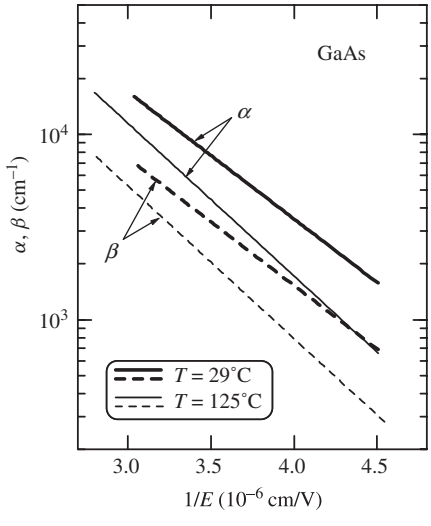

Figure 12.42 Ionization coefficients α and β for GaAs measured at 29° and 125°C. The experimental data are taken from Zheng *et al*. [12.130]. [From S. Adachi, *Handbook on Physical Properties of Semiconductors Volume 2: III–V Compound Semiconductors* (Kluwer Academic, Boston, 2004), reproduced by permission from Kluwer Academic Publishers]

where $A_0 = 1.286 \times 10^6$ cm^{-1} (1.438×10^6 cm^{-1}), $A_1 = 4.95 \times 10^{-4}$ K^{-1} (5.05×10^{-4} K^{-1}), $B_0 = 1.4 \times 10^6$ V/cm (2.02×10^6 V/cm) and $B_1 = 6.43 \times 10^{-4}$ K^{-1} (6.21×10^{-4} K^{-1}) for α (β), respectively, with T in K. The decreases in α and β with increasing T can be attributed to phonon scattering.

(c) Crystallographic direction dependence

Not only lattice temperature, but also crystallographic orientation affects the electronic energy-band structure and, thus, change in the impact ionization coefficients α and β. The dependence of the crystallographic orientation on the impact ionization coefficients has been studied experimentally on Si [12.127, 12.131], Ge [12.111], GaAs [12.105, 12.132, 12.133] and InP [12.114].

Figure 12.43 shows the impact ionization coefficients α and β measured in the three principal directions ⟨100⟩, ⟨110⟩ and ⟨111⟩ of Si at $T = 300$ K. The ionization coefficients α and β in Si are found to exhibit an anisotropic behavior with higher values in the ⟨100⟩ direction than in the ⟨110⟩ direction and with the lowest value in the ⟨111⟩ direction. In Ge, Mikawa *et al.* [12.111] found that the coefficients are larger in the ⟨111⟩ direction than in the ⟨100⟩ direction.

As mentioned in Section 12.7.1, the orientation effect in the hole ionization in a cubic semiconductor (GaAs) is small and hence the similarity in β. The difference in α can be explained by the ionization threshold energies varying in different crystallographic directions. Armiento and Groves [12.114] have found that, unlike the reports for GaAs,

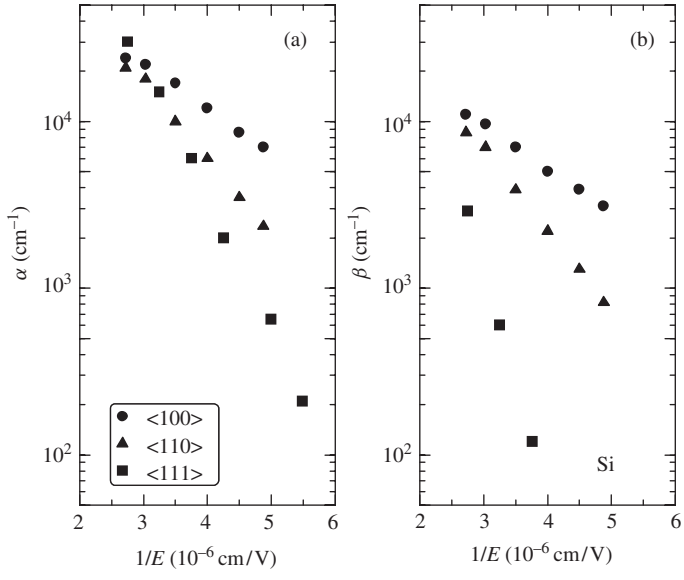

Figure 12.43 Impact ionization coefficient for: (a) electrons; (b) holes in the ⟨100⟩, ⟨110⟩ and ⟨111⟩ directions for Si. The experimental data are taken from Lee *et al.* [12.127] and Lee [12.131]. [From S. Adachi, *Handbook on Physical Properties of Semiconductors Volume 1: Group-IV Semiconductors* (Kluwer Academic, Boston, 2004), reproduced by permission from Kluwer Academic Publishers]

no significant orientation dependence of the impact ionization coefficients exists in InP. Momentum randomizing collisions with phonons, which result in intervalley transfer of energetic electrons, are believed to be the reason for the lack of anisotropy in the electron impact ionization coefficient of InP.

REFERENCES

[12.1] E. M. Conwell, *High Field Transport in Semiconductors* (Academic, New York, 1967).
[12.2] K. Seeger, *Semiconductor Physics* (Springer, Vienna, 1973).
[12.3] D. L. Rode, in *Semiconductors and Semimetals*, edited by R. K. Willardson and A. C. Beer (Academic, New York, 1975), Vol. 10, p. 1.
[12.4] B. R. Nag, *Electron Transport in Compound Semiconductors* (Springer, Berlin, 1980).
[12.5] D. C. Look, *Electrical Characterization of GaAs Materials and Devices* (Wiley, Chichester, 1989).
[12.6] P. K. Bhattacharya, U. Das, and M. J. Ludowise, *Phys. Rev. B* **29**, 6623 (1984).
[12.7] L. R. Weisberg, *J. Appl. Phys.* **33**, 1817 (1962).
[12.8] M. G. Graford, W. O. Groves, A. H. Herzog, and D. E. Hill, *J. Appl. Phys.* **42**, 2751 (1971).
[12.9] G. E. Stillman, C. M. Wolfe, and J. O. Dimmock, *J. Phys. Chem. Solids* **31**, 1199 (1970).
[12.10] P. Blood, *Phys. Rev. B* **6**, 2257 (1972).
[12.11] D. A. Anderson and N. Apsley, *Semicond. Sci. Technol.* **1**, 187 (1986).
[12.12] G. R. Cronin and S. R. Borrello, *J. Electrochem. Soc.* **114**, 1078 (1967).
[12.13] M. Toyama, M. Naito, and A. Kasami, *Jpn. J. Appl. Phys.* **8**, 358 (1969).
[12.14] H. C. Casey, Jr., F. Ermanis, L. C. Luther, and L. R. Dawson, *J. Appl. Phys.* **42**, 2130 (1971).
[12.15] K. Fletcher and P. N. Butcher, *J. Phys. C: Solid State Phys.* **6**, 976 (1973).
[12.16] R. C. Taylor, J. F. Woods, and M. R. Lorenz, *J. Appl. Phys.* **39**, 5404 (1968).
[12.17] J. D. Wiley and M. DiDomenico, Jr., *Phys. Rev. B* **1**, 1655 (1970).
[12.18] Obtained from data by F. Nava, C. Canali, C. Jacoboni, L. Reggiani, and S. F. Kozlov, *Solid State Commun.* **33**, 475 (1980).
[12.19] C. Jacoboni, C. Canali, G. Ottaviani, and A. A. Quaranta, *Solid-State Electron.* **20**, 77 (1977).
[12.20] J. M. Dorkel and Ph. Leturcq, *Solid-State Electron.* **24**, 821 (1981).
[12.21] N. D. Arora, J. R. Hauser, and D. J. Roulston, *IEEE Trans. Electron Dev.* **ED-29**, 292 (1982).
[12.22] F. J. Morin, *Phys. Rev.* **93**, 62 (1954).
[12.23] P. P. Debye and E. M. Conwell, *Phys. Rev.* **93**, 693 (1954).
[12.24] O. A. Golikova and A. V. Petrov, *Sov. Phys. Solid State* **6**, 2443 (1965).
[12.25] D. Lancefield, PhD Thesis, University of Surry, UK (1985).
[12.26] M. I. Nathan, W. Paul, and H. Brooks, *Phys. Rev.* **124**, 391 (1961).
[12.27] D. Lancefield, A. R. Adams, and M. A. Fisher, *J. Appl. Phys.* **62**, 2342 (1987).
[12.28] K. Hoo and W. M. Becker, *Phys. Rev. B* **14**, 5372 (1976).
[12.29] G. D. Pitt and M. K. R. Vyas, *J. Phys. C: Solid State Phys.* **6**, 274 (1973).
[12.30] N. N. Sirota, V. B. Shipilo, and F. A. Shipilo, *Sov. Phys. Semicond.* **9**, 1047 (1976).
[12.31] E. Litwin-Staszewska, W. Szymańska, and R. Piotrzkowski, *Phys. Status Solidi B* **106**, 551 (1981).
[12.32] D. B. M. Klaassen, *Solid-State Electron.* **35**, 953 (1992); **35**, 961 (1992).
[12.33] D. M. Caughey and R. E. Thomas, *Proc. IEEE* **55**, 2192 (1967).
[12.34] S. N. Mohammad, A. V. Bemis, R. L. Carter, and R. B. Renbeck, *Solid-State Electron.* **36**, 1677 (1993).

[12.35] M. Sotoodeh, A. H. Khalid, and A. A. Rezazadeh, *J. Appl. Phys.* **87**, 2890 (2000).
[12.36] G. Baccarani and P. Ostoja, *Solid-State Electron.* **18**, 579 (1975).
[12.37] G. Masetti, M. Severi, and S. Solmi, *IEEE Trans. Electron Dev.* **ED-30**, 764 (1983).
[12.38] S. N. Mohammad, A. A. Salvador, and H. Morkoç, *Proc. IEEE* **83**, 1306 (1995).
[12.39] G. D. Chen, J. Y. Lin, and H. X. Jiang, *Appl. Phys. Lett.* **68**, 1341 (1996).
[12.40] J. D. Wiley, in *Semiconductors and Semimetals*, edited by R. K. Willardson and A. C. Beer (Academic, New York, 1975), Vol. 10, p. 91.
[12.41] J. D. Wiley and M. DiDomenico, Jr., *Phys. Rev. B* **2**, 427 (1970).
[12.42] M. Costato, G. Gagliani, C. Jacoboni, and L. Reggiani, *J. Phys. Chem. Solids* **35**, 1605 (1974).
[12.43] H. C. Casey, Jr., F. Ermanis, and K. B. Wolfstirn, *J. Appl. Phys.* **41**, 2945 (1969).
[12.44] K.-H. Zschauer, in *Proc. 4th Inter. Symp. GaAs and Related Compounds*, Boulder, 1972 (Institute of Physics, London, 1973), p. 3.
[12.45] A. L. Mears and R. A. Stradling, *J. Phys. C: Solid State Phys.* **4**, L22 (1971).
[12.46] D. N. Nasledov, Y. G. Popov, N. V. Siukaev, and S. P. Starosel'tseva, *Sov. Phys. Semicond.* **3**, 387 (1969).
[12.47] O. G. Folberth, O. Madelung, and H. Weiss, *Z. Naturf.* **9a**, 954 (1954).
[12.48] F. Szmulowicz, *Appl. Phys. Lett.* **43**, 485 (1983).
[12.49] W. C. Mitchel and P. M. Hemenger, *J. Appl. Phys.* **53**, 6880 (1982).
[12.50] G. W. Ludwig and R. L. Watters, *Phys. Rev.* **101**, 1699 (1956).
[12.51] F. J. Reid and R. K. Willardson (unpublished); see, A. C. Beer, in *Solid State Phys.*, edited by F. Seitz and D. Turnbull (Academic, New York, 1963), Vol. 4 (Suppl.), p. 209.
[12.52] D. Long, *Phys. Rev.* **107**, 672 (1957).
[12.53] F. J. Morin and J. P. Maita, *Phys. Rev.* **96**, 28 (1954).
[12.54] F. Cerdeira and M. Cardona, *Phys. Rev. B* **5**, 1440 (1972).
[12.55] C. Jacoboni, G. Gagliani, L. Reggiani, and O. Turci, *Solid-State Electron.* **21**, 315 (1978).
[12.56] M. V. Fischetti and S. E. Laux, *J. Appl. Phys.* **80**, 2234 (1996).
[12.57] A. R. Adams and L. G. Shantharama, *Physica B* **139&140**, 419 (1986).
[12.58] W. R. Thurber, R. L. Mattis, Y. M. Liu and J. J. Filliben, *J. Electrochem. Soc.* **127**, 2291 (1980).
[12.59] J. B. Gunn, *Solid State Commun.* **1**, 88 (1963).
[12.60] H. Shichijo and K. Hess, *Phys. Rev. B* **23**, 4197 (1981).
[12.61] H. L. Grubin, in *Properties of Aluminium Gallium Arsenide*, EMIS Datareviews Series No. 7, edited by S. Adachi (INSPEC, London, 1993), p. 197.
[12.62] C. Canali, C. Jacoboni, F. Nava, G. Ottaviani, and A. Alberigi-Quaranta, *Phys. Rev. B* **12**, 2265 (1975).
[12.63] R. H. Johnson and O. Eknoyan, *J. Appl. Phys.* **58**, 1402 (1985).
[12.64] A. Majumdart, *Solid-State Electron.* **39**, 1251 (1996).
[12.65] D. K. Ferry, *Phys. Rev. B* **12**, 2361 (1975).
[12.66] M. Wraback, H. Shen, J. C. Carrano, T. Li, J. C. Campbell, M. J. Schurman, and I. T. Ferguson, *Appl. Phys. Lett.* **76**, 1155 (2000).
[12.67] T. H. Windhorn, T. J. Roth, L. M. Zinkiewicz, O. L. Gaddy, and G. E. Stillman, *Appl. Phys. Lett.* **40**, 513 (1982).
[12.68] S. Adachi, *Physical Properties of III–V Semiconductor Compounds: InP, InAs, GaAs, GaP, InGaAs, and InGaAsP* (Wiley-Interscience, New York, 1992).
[12.69] R. Allam and J. Pribetich, *Electron. Lett.* **26**, 688 (1990).
[12.70] R. Quay, C. Moglestue, V. Palankovski, and S. Selberherr, *Mater. Sci. Semicond. Proc.* **3**, 149 (2000).
[12.71] I. A. Khan and J. A. Cooper, Jr., *IEEE Trans. Electron Dev.* **47**, 269 (2000).
[12.72] K. V. Vassilevski, K. Zekentes, A. V. Zorenko, and L. P. Romanov, *IEEE Electron Dev. Lett.* **21**, 485 (2000).
[12.73] K. Brennan and K. Hess, *J. Appl. Phys.* **59**, 964 (1986).

[12.74] L. Reggiani, S. Bosi, C. Canali, F. Nava, and S. F. Kozlov, *Phys. Rev. B* **23**, 3050 (1981).
[12.75] G. Ottaviani, L. Reggiani, C. Canali, F. Nava, and A. Alberigi-Quaranta, *Phys. Rev. B* **12**, 3318 (1975).
[12.76] L. Reggiani, C. Canali, F. Nava, and G. Ottaviani, *Phys. Rev. B* **16**, 2781 (1977).
[12.77] L. S. Holway, S. R. Steele, and M. G. Alderstein, in *Proc. 7th Biennial Cornell Electrical Engineering Conference* (Cornell University Press, New York, 1979), p. 199.
[12.78] J. L. Heaton III, G. H. Hammond, and R. B. Goldner, *Appl. Phys. Lett.* **20**, 333 (1972).
[12.79] P. G. Le Comber, W. E. Spear, and A. Weinmann, *Brit. J. Appl. Phys.* **17**, 467 (1966).
[12.80] C. Canali, G. Ottaviani, M. Martini, and K. Zanio, *Appl. Phys. Lett.* **19**, 51 (1971).
[12.81] K. Brennan and K. Hess, *Phys. Rev. B* **29**, 5581 (1984).
[12.82] See, J. A. del Alamo, in *Properties of Silicon*, EMIS Datareviews Series No. 4 (INSPEC, London, 1988), p. 145.
[12.83] T. P. McLean and E. G. S. Paige, *J. Phys. Chem. Solids* **18**, 139 (1961).
[12.84] Z. P. Guan, J. Z. Li, G. Y. Zhang, S. X. Jin, and X. M. Ding, *Semicond. Sci. Technol.* **15**, 51 (2000).
[12.85] J. R. Lowney and H. S. Bennett, *J. Appl. Phys.* **69**, 7102 (1991).
[12.86] D. M. Kim, S. Lee, M. I. Nathan, A. Gopinath, F. Williamson, K. Beyzavi, and A. Ghiasi, *Appl. Phys. Lett.* **62**, 861 (1993).
[12.87] K. Beyzavi, K. Lee, D. M. Kim, M. I. Nathan, K. Wrenner, and S. L. Wright, *Appl. Phys. Lett.* **58**, 1268 (1991).
[12.88] S. E. Swirhun, Y.-H. Kwart, and R. M. Swanson, in *Proc. Int. Electron Dev. Meeting*, Los Angeles, CA, USA, Dec. 1986 (IEEE, USA, 1986), p. 24.
[12.89] T. Furuta and M. Tomizawa, *Appl. Phys. Lett.* **56**, 824 (1990).
[12.90] M. Morohashi, N. Sawaki, and I. Akasaki, *Jpn. J. Appl. Phys.* **24**, 661 (1985).
[12.91] A. Neukermans and G. S. Kino, *Phys. Rev. B* **7**, 2693 (1973).
[12.92] A. Neukermans and G. S. Kino, *Phys. Rev. B* **7**, 2703 (1973).
[12.93] C. Canali, G. Ottaviani, and A. A. Quaranta, *J. Phys. Chem. Solids* **32**, 1707 (1971).
[12.94] See, J. A. del Alamo, in *Properties of Silicon*, EMIS Datareviews Series No. 4 (INSPEC, London, 1988), p. 162.
[12.95] H. C. Casey, Jr., B. I. Miller, and E. Pinkas, *J. Appl. Phys.* **44**, 1281 (1973).
[12.96] M. L. Lovejoy, M. R. Melloch, M. S. Lundstrom, and R. K. Ahrenkiel, *Appl. Phys. Lett.* **61**, 2683 (1992).
[12.97] S. E. Swirhun, J. A. del Alamo, and R. M. Swanson, *IEEE Electron Dev. Lett.* **EDL-7**, 168 (1986).
[12.98] H. L. Chuang, M. E. Klausmeier-Brown, M. R. Melloch, and M. S. Lundstrom, *J. Appl. Phys.* **66**, 273 (1989).
[12.99] D. B. Slater, Jr., P. M. Enquist, F. E. Najjar, M. Y. Chen, J. A. Hutchby, A. S. Morris, and R. J. Trew, *IEEE Electron Dev. Lett.* **12**, 54 (1991).
[12.100] M. M. Anikin, A. S. Zubrilov, A. A. Lebedev, A. P. Strel'chuk, and A. E. Cherenkov, *Sov. Phys. Semicond.* **25**, 289 (1991).
[12.101] Z. Z. Bandić, P. M. Bridger, E. C. Piquette, and T. C. McGill, *Appl. Phys. Lett.* **72**, 3166 (1998).
[12.102] S. M. Sze, *Physics of Semiconducting Devices* (Wiley-Interscience, New York, 1981).
[12.103] G. E. Stillman, V. M. Robbins, and N. Tabatabaie, *IEEE Trans. Electron Dev.* **ED-31**, 1643 (1984).
[12.104] F. Capasso, in *Semiconductors and Semimetals*, edited by R. K. Willardson and A. C. Beer (Academic, New York, 1985), Vol. 22 (Volume Editor: W. T. Tsang), Part D, p. 1.
[12.105] T. P. Pearsall, F. Cappaso, R. E. Nahory, M. A. Pollack, and J. R. Chelikowsky, *Solid-State Electron.* **21**, 297 (1978).
[12.106] C. L. Anderson and C. R. Crowell, *Phys. Rev. B* **5**, 2267 (1972).
[12.107] T. P. Pearsall, *Appl. Phys. Lett.* **35**, 168 (1979).

[12.108] P. A. Wolff, *Phys. Rev.* **95**, 1415 (1954).
[12.109] G. A. Baraff, *Phys. Rev.* **128**, 2507 (1962).
[12.110] V. A. Kuz'min, N. N. Kryukova, A. S. Kyuregyan, T. T. Mnatsakanov, and V. B. Shuman, *Sov. Phys. Semicond.* **9**, 481 (1975).
[12.111] T. Mikawa, S. Kagawa, T. Kaneda, Y. Toyama, and O. Mikami, *Appl. Phys. Lett.* **37**, 387 (1980).
[12.112] R. Raghunathan and B. J. Baliga, *Solid-State Electron.* **43**, 199 (1999).
[12.113] H. Ando and H. Kanbe, *Solid-State Electron.* **24**, 629 (1981).
[12.114] C. A. Armiento and S. H. Groves, *Appl. Phys. Lett.* **43**, 198 (1983).
[12.115] R. Mach and W. Ludwig, *Phys. Status Solidi A* **23**, 507 (1974).
[12.116] G. E. Stillman, C. M. Wolfe, J. A. Rossi, and A. G. Foyt, *Appl. Phys. Lett.* **24**, 471 (1974).
[12.117] H. D. Law and C. A. Lee, *Solid-State Electron.* **21**, 331 (1978).
[12.118] See, J. Lee, A. L. Gutierrez-Aitken, S. H. Li, and P. K. Bhattacharya, *Appl. Phys. Lett.* **66**, 204 (1995).
[12.119] O. Hildebrand, W. Kuebart, and M. H. Pilkuhn, *Appl. Phys. Lett.* **37**, 801 (1980).
[12.120] T. P. Chow, V. Khemka, J. Fedison, N. Ramungul, K. Matocha, Y. Tang, and R. J. Gutmann, *Solid-State Electron.* **44**, 277 (2000).
[12.121] T. Taguchi, T. Torikai, Y. Sugimoto, K. Makita, and H. Ishihara, *J. Appl. Phys.* **59**, 476 (1986).
[12.122] M. P. Mikhaĭlova, A. A. Rogachev, and I. N. Yassievich, *Sov. Phys. Semicond.* **10**, 866 (1976).
[12.123] B. K. Ridley, *Semicond. Sci. Technol.* **2**, 116 (1987).
[12.124] D. R. Decker and C. N. Dunn, *J. Electron. Mater.* **4**, 527 (1975).
[12.125] W. N. Grant, *Solid-State Electron.* **16**, 1189 (1973).
[12.126] T. Rang, *Radioelectron. Commun. Syst.* **28**, 91 (1985).
[12.127] C. A. Lee, R. A. Logan, R. L. Batdorf, J. J. Kleimack, and W. Wiegmann, *Phys. Rev.* **134**, A761 (1964).
[12.128] A. O. Konstantinov, in *Proc. ICACSC90*, edited by G. L. Harris, M. G. Spencer, and C.-Y. W. Yang, Washington DC, 1990, p. 231.
[12.129] V. J. Chang and S. M Sze, *J. Appl. Phys.* **40**, 5392 (1969).
[12.130] X. G. Zheng, P. Yuan, X. Sun, G. S. Kinsey, A. L. Holmes, B. G. Streetman, and J. C. Campbell, *IEEE J. Quantum Electron.* **36**, 1168 (2000).
[12.131] C. A. Lee, *RADC Tech. Rep.* RADC-TR-93-182 (1983).
[12.132] T. P. Pearsall, R. E. Nahory, and J. R. Chelikowsky, *Phys. Rev. Lett.* **39**, 295 (1977).
[12.133] See, S. M. Cho and H. H. Lee, *J. Appl. Phys.* **71**, 1298 (1992).

Index

Plain type locators refer to text treatments: page references in **bold** or *italic* type indicate reference to a table or figure only. Semiconductors identified chemically are listed as their formulae while Greek letters and numerals are alphabetized as though spelled out.

absorption coefficients
  free electron-hole pair transitions *248*
  Si, wavenumber and *229*
  spectral dependence in InP *225*
  Urbach tails 256–8
acoustic deformation potential. *See* intravalley deformation potentials.
acoustic phonons
  deformation potential scattering 318–19
  dispersion relations 79
  optical and 75–6
  piezoelectric scattering 318
air, refractive index effects 241
Al/GaAs
  hole scattering rates *351*
  interband transitions 239
Al/GaN electron affinity 196
AlAs
  Fröhlich coupling constant 99
  low-temperature absorption spectrum 253–4
  phonon frequencies 80–1
alloy scattering 320
AlP, piezoelectric stress constant 97–8
AlSb, absorption spectra and pressure 255, *256*
anion atomic number *119*, *133*
atomic mass
  Debye temperature and 29
  optical phonon frequency and 82, **83**, *84*
atomic weights **6**
Au/semiconductor contact case study 202–4
avalanche photodiodes 347, 362, 365
band-gap energies
  See also energy-band structure.
  breakdown field and *206*
  exciton binding energies and 233–5
  Schottky barrier height and 199, *203*, **204**
band-gap narrowing on doping 128–30
Baraff's theory 365
barriers. *See* Schottky barriers.
β-Sn. *See* phase transitions.
birefringence
  piezobirefringence 285
Bir–Pikus deformation potentials 114–15, 173
BIS (bremsstrahlung isochromat spectroscopy) 112, *113*
Bloch functions 103, 230
Bohr radius and band-gap energies *235*
Boltzmann equations 331
Born ratio **57**, **58**
Bose–Einstein occupation factor 121, 249
BP
  covalency and reststrahlen effect 226
  Knoop microhardness 67
breakdown voltage and Schottky barrier height 206–7
bremsstrahlung isochromat spectroscopy 112, *113*
Brillouin scattering measurements 289
Brillouin zones 73–5
  See also zone center.
  energy-band structure and 104
  energy-band transitions in CdSe 111
  face-centered cubic structures 74
  free electron-hole pair transitions 245

Properties of Group-IV, III–V and II–VI Semiconductors Sadao Adachi

© 2005 John Wiley & Sons, Ltd

ISBN: 0-470-09032-4

Brillouin zones (*continued*)
hexagonal semiconductors 74–5
higher-lying direct band gaps 130
impact-ionization thresholds and 363
lowest indirect band gaps 137
rhombohedral semiconductors 75
bulk modulus 56–61, **62**
hexagonal semiconductors 61–2, **63**
Knoop microhardness and 63–7
Burstein–Moss effects 127, 256

camel's back structures 158–9
carrier transport properties 315–69
See also electrons; holes.
carrier carrier scattering 320, 355
cation atomic number 196, *197*
Cauchy ratio **57**, **58**
CdS
crystal structure of w- or β-CdS 6, *8*
linear pressure coefficient for w-CdS 206
optical spectrum above the first absorption edge 265–7
third-order elastic constant of w-CdS **53**
CdSe
energy-band structure of w-CdSe *109*, 111
linear pressure coefficient for w-CdSe 206
CdTe
band-gap temperature effects *135*
cleavage energies 18
Debye temperature versus temperature *29*
specific heat versus temperature *27*
Clausius–Clapeyron equation 24
cleavage energy calculation 18–20
cleavage planes 15–8
experimental surface energies and **20**
coefficient of expansion 30–3
See also linear thermal expansion coefficient; volume thermal expansion coefficient.
cold-cathode devices 195
complex dielectric constant 300
complex dielectric function 213
w-CdS *267*
GaAs *216*, *266*
indirect optical transitions 249
Si *264*
temperature effects in GaAs *269*
complex dielectric permitivity 222–3
complex refractive index 213
w-CdS *267*
GaAs *266*
Si *264*
compliance. *See* elastic compliance.
conduction energy bands
conduction-valley energy separations 142
interconduction-band absorption 274–5
conduction-band deformation potentials
L-point hydrostatic and shear 183–4, **185**
wurtzite crystal structure **176**
X-point hydrostatic and interband 189
X-point hydrostatic and shear 188, **189**
conduction-band degeneracy 158
conduction-band electrons
density of states 113
effective mass 112
three-valley model 320–1
conduction-band energies
See also electron affinity.
conduction-band Hamiltonian 114
deformation potentials and 173
conduction-band mass nonparabolicity 157
conduction-band structure and reststrahlen spectra 225–6
conduction-band symmetry
wurtzite crystal structure 111
zinc-blende crystal structure 190
conduction-valley energy separations 141–2
conductivity effective mass 148
conductivity electron mass **161, 322**, *323*, *324*
constant energy surfaces
cubic semiconductors 147, *148*
deformation potentials and 174
hexagonal semiconductors 148
hole effective masses 162, *163*
continuum exciton states 232, 251–2
covalency
crystal structure and 4
elastic stiffness and 46, *47*
ionicity and 1
reststrahlen effect and 226
critical-point energies
energy-band structure of CdSe **110**
energy-band structure of InP **107**
ZnO 122–3
critical points
interband optical constants and 244–5
model dielectric function and 258
phonon dispersion and 79
crystal densities 14
cubic semiconductors **7**
hexagonal and rhombohedral semiconductors **8**
sound velocity and 68, **69**

crystal-field splitting energies 108, 115, 117–18, **119**
crystal structure 4–10
See also diamond; wurtzite; zinc-blende.
cleavage planes and **17**, 18
diamond crystal structure 4, *8*
easily or normally grown structures **10**, **11**
hexagonal and rhombohedral structures 7–9
high-pressure transitions 14–15, **16**
lattice constants and 12
rocksalt structure *8*, 9–10
space groups 10, **11**
crystal symmetry
See also symmetry classes
effect on dielectric and optical properties **212**
electron state classification and 73
crystallographic direction and impact ionization 368–9
crystallographic planes
Poisson's ratio 53, **56**
sound propagation and **70**, **71**
cubic semiconductors
cleavage energies, calculated **19**
crystal densities **7**
diamond crystal structure 4
face-centered cubic structures 9–10
face-centered cubic structures 74
lattice constants and molecular weights **7**
phonon dispersion curves 75–7
thermal conductivity and Phillips ionicity 35, *36*
thermal expansion coefficients **31**
zinc-blende crystal structure 6
cyclotron resonance techniques
electron effective mass and 148, 151, 157
polaron mass and 168–9

d-band effects and model dielectric function 262–3
D-type transition processes 275
DP *See* deformation potentials.
damped harmonic oscillator model 261, 263
Debye function 28
Debye temperature 28–30
E_0-gap energies and 120, *122*
low-temperature limit **30**
Marcus–Kennedy formula 29
tabulated **25**
Varshi β parameter and *135*
Debye's T^3 Law 27, 28
Debye–Waller factor 35
deformation potential scattering 318–19
deformation potentials
Γ-point intravalley deformation potential 173–183
high-symmetry-point intravalley deformation potential 183–9
intervalley deformation potentials 189–192
density of states. *See* electron density of states; phonon density of states; joint density of states.
deposition and phase diagrams 23
DHO (damped harmonic oscillator) model 261, 263
diamond, synthetic, specific heat versus temperature *27*
diamond crystal structure 4, *8*
See also cubic semiconductors.
cleavage planes 17
energy-band structure 104–6
molecular density 13
dielectric functions.
See also complex dielectric function; high-frequency dielectric constant.
effective dielectric constant 215
static dielectric constant 217–20, 227–8, 235
dielectric permitivity 211–12
plasma contribution 224
single harmonic oscillator model 222–3
dielectric susceptibilities 212
nonlinear optics and 302, 304
diffusivity. *See* thermal diffusivity.
direct band-gap energies
dielectric constants and *220*
hexagonal semiconductors 115, **117**
linear electro-optic constant and 293
photoelastic coefficient dispersion and 286
direct–indirect-gap transition pressure 142–3
discrete excitonic transitions 251–2
dispersion models of refractive indexes 236–44
doped semiconductors
E_0-gap energies 126–30
electron effective mass, Γ valley 155–8
Hall hole mobility 337–9
hole effective masses 170–1
interband transition region 269–70
Knoop microhardness 68
lattice constant of Te doped GaAs 13
low-field electron mobility 326–8

doped semiconductors (*continued*)
majority- and minority-hole mobilities 359–60
minority-electron mobility *356*
optical absorption 255–6
refractive index 243–4
thermal conductivity 38
double-heterojunction lasers 240
Drude model 262, 270, 271–2
Drude–Lorentz formula 261
Dulong and Petit's Law 27, 28
E_0-gap energies 114–30
cubic semiconductors 115, **116**
doping effects 126–30
electron affinity and *198*
electron deformation potential and 179–80
electron effective mass and *149*, **150**, *152*
lattice constants and 115, *117*, *118*
molecular weights and *118*
temperature and pressure coefficients 120–5, 127

E_1-gap energies 130–7
hydrostatic and interband deformation potentials 186–8
lattice constant and *130*
effective dielectric constant 215
effective lattice constants. *See* lattice constants.
effective masses. *See* electron effective mass; hole effective mass.
elastic compliance 41–4
See also elastic stiffness constant.
cubic semiconductors **45**
hexagonal semiconductors **46**
elastic constants 41–51
lattice constants and 29
third-order elastic constants 51–3, 60
elastic properties 41–71
bulk modulus and related properties 56–61, **62**
elastic constants 41–51
microhardness 62–8
Poisson's ratio 54–6
sound velocity 68–71
third-order elastic constants 51–3, 60
Young's modulus and related properties 53–62
elastic stiffness constant 41–4
covalency and 46, *47*
cubic semiconductors **45**, 48–9, **52**
hexagonal semiconductors **46, 52**
lattice constant and 46–7, *48*, 49
Phillips ionicity and 46, *47*
piezoelectric constants and 98
pressure effects 50–1
sound velocity and 68
temperature effects 48–50
elasto-optic effect 283–91
experimental values 285–91
theoretical expression 283
elasto-optic devices 283, 289
electroabsorption coefficients *See* Franz–Keldysh effect.
electromechanical coupling constant 99, **100**
electron affinity 195–8
negative electron affinity 195
numerical values **196**
electron concentration and mobility 327–8
electron conductivity mass **161**, 322–4
electron conductivity mobility 329–30
electron density of states 111–13
conductivity masses and **161**
doping effects 127
electron effective mass and 148
hole effective masses **164**, **168,** 171
electron diffusion length 356–9
electron drift mobility 329–30
electron drift velocity 339–46
electron saturation drift velocity 347–9, *351*
electron effective mass, Γ valley 147–58
See also hole effective mass.
conduction-band electrons 112
doping effects 155–8
E_0-gap energies and *149*, **150**, *152*
optical effective mass 156
polaron effect 151–2
pressure effects 153–5
temperature effects 152–3
electron effective mass, satellite valley 158–9
electron mobility 316
See also low-field electron mobility.
electron drift mobility 329–30
electron saturation drift velocity 347–9, *351*
electron scattering mechanisms 315–20
alloy scattering 320
carrier–carrier scattering 320
deformation potential scattering 318–19
GaAs at different temperatures 325, *326*
intervalley electron scattering 317
ionized impurity scattering 319
neutral impurity scattering 319

nonpolar optical phonon scattering 318
piezoelectric scattering 318
polar optical scattering 317–18, 341–2, *343*
space-charge scattering 319–20
tabulated **316**
electron temperature and electric field 343–4
electron transport devices 207
electronic energy density formula 291
electronic work function
electron affinity and 199
Schottky barrier height and *200*, *201*, **202**
electron-initiated impact ionizations 362–7
impact ionization parameters 365
electron–phonon interactions 99, 122–124
Urbach tails and 257
electrorefractive effect 302
elements
atomic weights **6**
isotopic abundances 3–4
ellipsometry
piezoellipsometry 289
spectroscopic ellipsometry 270
energy-gap values and Phillips ionicity 2
energy-band structure
See also band-gap energies; conduction energy bands; E_0-gap region; E_1-gap region; valence energy bands.
conduction-band effective Hamiltonian 114
conduction-valley energy separations 141–2
diamond crystal structure *104*
direct–indirect-gap transition pressure 142–3
E_0-gap region 114–30
E_1-gap energies 130–7
effective masses 147–71
electron density of states 111–13
energy-band gaps 103–143
GaAs *340*
heavily doped semiconductors *128*
higher-lying direct band gaps 130–7
impact ionization and 363
lowest indirect gaps 137–42
optical absorption band diagram *271*
stress effects *174*, 177
valence band effective Hamiltonian 114
wurtzite crystal structure 108–11
zinc-blende crystal structure 106–8
entropy and negative thermal expansion 32
envelope functions 232
exciton binding energies 233–5
exciton states 230–6
indirect band-gap effects 232–3
excitonic transitions 251–3
excitonic-gap energies in ZnO 122–3
external perturbation effects. *See* pressure effects; temperature effects.

face-centered cubic crystal structure 4, 9–10, 74
Faraday rotation 156
Fermi energy levels
doped semiconductors 128–30
GaAs 156–7, 202
FET (field-effect transistor) devices 203
figure of merit determinations 34, 99
breakdown voltage and 206–7
elasto-optic devices 289
first-neighbor distance. *See* near-neighbor distance.
Franz–Keldysh effect 300–2
experimental value 301
Kramers–Kronig transformation 298–9
theoretical expression 300
free-carrier absorption 270–4
free-electron numbers and effective dielectric constant 215–16
See also electron concentration.
free electron-hole pair transitions 245–50
free-carrier induced refractive index changes 278
free-exciton binding energies 230
Fröhlich coupling constant 99–101, 151
fundamental absorption edge 230–58
free-exciton parameters at **234**
optical absorption 244–56
Urbach tails 256–8

GaAs
absorption coefficient *257*
absorption edge as a function of electric field *301*
band-gap narrowing on doping 127, *129*
cleavage planes and energies 17–18
complex dielectric function and temperature *269*
conduction-band mass anisotropy 154, 157
direct–indirect-gap transition pressure 142–3
E_0-gap energies and temperature 120
E_1-gap stress dependency *187*
effective mass 152, *153, 155*

GaAs (*continued*)
electron density of states 112–13
electron diffusion length *359*
electron drift velocity *346, 347*
electrorefractive effect 302
energy-band structure *340*
exciton binding energies and pressure 234–5
excitonic absorption 254–5
Fermi levels 128–30
figures of merit 289
Fröhlich coupling constant 99
Gunn effect 189–90
Hall mobilities and temperature 324, *325*, 333–4, *335*
hole drift velocity *354*
hole scattering rates *351*
impact ionization temperature effects *367*
lattice constant with Te doping 13
lattice parameter pressure dependence *61*
linear electro-optic constant dispersion 296
minority-electron lifetime and hole concentration *358*
minority-hole diffusion length in *n*-GaAs *362*
minority-hole lifetime and mobility in *n*-GaAs *361*
optical absorption 256, *277*
optical spectrum above the first absorption edge 265–6
phonon density of states 79–80
phonon dispersion curve 76–7
phonon frequencies 80–1, *86*
phonon scattering rate and electron energy *341*
photoelastic coefficient dispersion and *287*, *288*
piezoelectric stress constant 97
polar optical scattering and electric field *343*
quadratic electro-optic constant 298–9
Schottky barrier height *201*, 204, 205–6
specific heat versus temperature *27*
spectral characteristics *216*
static dielectric constant *221*
thermal conductivity 38–39
zinc-blende crystal structure 6, *8*
Γ-point. *See* Brillouin zone; zone center.
GaN
Hall mobility and electron concentration in α-GaN *328*
Schottky barrier height and metal work function *200*
spectral variations 226–8
Urbach parameter for α-GaN *258*
GaP
electron drift velocity and electric field *346*
electro-optic constants 296, 298
Hall mobilities and temperature 324, *325*, 333–4, *335*
indirect band-gap energies and temperature *139*
infrared absorption spectrum of *n*-GaP *276*
linear thermal expansion coefficient versus temperature **34**
photoelastic coefficient dispersion and *287*, *288*
refractive-index dispersion and pressure *244*
GaSb
conduction-band symmetry anomaly 190
phase diagram for Ge, Si and 23, *24*
thermal conductivity versus temperature *36*, 37
Gaussian-broadened density of states 112, *113*
Ge
Debye temperature versus temperature *29*
dielectric constant pressure coefficients 222
electron density of states 112, *113*
Hall scattering factor in *n*- and *p*-Ge *330*
phase diagram for GaSb, Si and 23, *24*
gold 202–4
Grüneisen parameters
mode Grüneisen parameter 86–8, 90
thermal Grüneisen parameter 24, 32
Grüneisen's Rule 30, 32, 88
Gunn effect 189–90, 340

Hall hole mobility 333–7
p-Si 334, *336*
hole concentration and 337–9
pressure effects 337
Hall mobility 315–31
conductivity electron mass and **322**, *323*, *324*
lowest direct band-gap energy and *323*
temperature effects 324–5
three-valley model 321

Hall scattering factor 328–31
p-Si 336–7
hardness 62–8
Harrison ionicity 2–3
heat capacity. *See* specific heat.
heteroepitaxial growth 283
heterojunction bipolar devices 354
heteropolar crystals
See also ionicity.
infrared activity 222
hexagonal and rhombohedral semiconductors **8**
higher-lying direct band-gap energies **137**
hexagonal semiconductors
See also wurtzite.
Brillouin zones 74
cleavage energies, calculated **19**
electromechanical coupling constant **100**
hexagonal close-packed crystal structure 6, *8*
phonon dispersion curves 77–9
thermal expansion coefficients **32**
HgS, rhombohedral structure 9
HgTe
cleavage energies 18
thermal expansion coefficient versus temperature *33*
high-symmetry-point intravalley deformation potential 183–9
higher-lying direct band-gap energies 130–7
hexagonal and rhombohedral semiconductors **137**
temperature and pressure coefficients **136**
high-field electron transport 339–49
electron drift velocity 339–46
electron saturation drift velocity 347–8
high-field hole transport 349–53
hole drift velocity 349
high-frequency dielectric constant 217–20
pressure coefficient of refractive index and 243
temperature effects 227–8
hole conductivity mobility 334, *336*
hole drift velocity and electric field and *352*, *353*
hole effective masses 159–71
doping effect 170–1
functional expressions and numerical values 164–5
hexagonal and rhombohedral semiconductors 167
polaron effect 168–9
pressure effects 170
temperature effects 170
hole mobility, low field 331–9
hole saturation drift velocity 352–3, **354**
hole scattering mechanisms 331–3, 349
hole-initiated impact ionizations 362–7
homopolar semiconductor spectra 228
Hooke's law 41
hydrostatic deformation potentials **181**, 183–4, **185**, **188**
hydrostatic pressure. *See* pressure effects.

I-type transition processes 275
ideal Schottky–Mott contacts 198–9, 201–2
impact ionization coefficients 362–9
electric field and *367*
electric field dependence 365–6
experimental values 365–8
temperature effects 366–8
theoretical considerations 362–5
impact ionization parameters **366**, *367*
impact ionization potential, in GaAs *341*
impact ionization transitions *363*, *364*
impurities. *See* doped semiconductors.
In/GaAs, In/GaAs/P, In/GaAs/Sb interband transitions 239
InAs
Hall hole mobility and temperature 333–4, *335*
Hall mobility temperature effects 324, *325*
linear electro-optic constant dispersion 296
photoelastic coefficient dispersion and *287*, *288*
indirect band gaps
exciton states 232–3
Hall mobility and 324
lowest indirect band gaps 137–42
pressure effects 184
temperature and pressure coefficients **140**
indirect excitonic transitions 252–3
indirect transitions
energy-band structure of InP 106–7
energy-band structure of Si 105
indirect optical transitions 248, *249*
infrared absorption spectrum
n-GaP *276*
p-InP *274*
heteropolar crystals 222
injection lasers and refractive indices 219, 240, 278

InN
E_0-gap energies and 115, *118*
zone-center effective mass 151
InP
Debye temperature versus temperature *29*
doping and Knoop microhardness 68
electron drift velocity and electric field *346*
electron-initiated impact ionization coefficient 369
energy-band structure 106–8
figures of merit 289
free-carrier absorption in *n*-InP *273*
Hall mobilities and temperature 324, *325*, 333–4, *335*
infrared absorption spectrum of *p*-InP *274*
linear electro-optic constant dispersion 296
photoelastic coefficient dispersion and *287*, *288*
piezo-electric stress constant 97–8
piezooptical coefficients 290–1
potential applications 345
Schottky diodes based on 205
spectral absorption and reflectivity *225*
spin–orbit splitting anomaly 133
temperature coefficient of refractive index 242
InP/As/Sb interband transitions 239
InSb, Hall hole mobility and hole concentration *339*
interband deformation potentials, E_1-gap energies **188**
interband magnetooptical measurements 148
interband transitions 258–70
See also energy-band structure.
doping effect 269–70
energy-band structure of CdSe *109*
energy-band structure of Si 104–5
fundamental optical spectra 263–8
model dielectric function 258–63
simplified interband transition model 238–9
temperature and pressure effects 268–9
interconduction-band absorption 274–5
internal strain parameter 182
intervalence-band absorption 275–8, *277*
intervalley deformation potentials 189–92
intervalley electron scattering 317
scattering times 190, 191
intraband transitions 271
intravalley deformation potentials, Γ point 173–83
cubic semiconductor conduction bands **175**
cubic semiconductor valence bands **178**
hydrostatic deformation potentials **181**
optical phonon deformation potential 181–3
intravalley deformation potentials, L point 183–8
valence-band deformation potentials 186, **187**
intravalley deformation potentials, X point 188–9
ionicity 1–3
lattice instability and 35
phonon dispersion and 77
values **3**, *4*
ionization coefficients, impact ionization 362–9
ionized impurity scattering 319, 334
isothermal compressibility 27, 32
isotopic abundances 3–4, **5**
isotropy factor **57**, **58, 59**

joint density-of-states function
critical points and 245, **246**, *247*, 259
intervalence-band absorption and 277

$k \cdot p$ perturbation method
effective mass and pressure 154
effective mass and temperature 152
hole effective masses 162, 171
k space *See* reciprocal space.
Kane momentum parameter 310
Kerr effect 295, 297, 302, 303–4
Ketteler–Helmholtz formula 237
Kleinman conjecture 308–9
Knoop microhardness 63–8
bulk modulus and 63–7
inverse unit-cell volume and 63–4, *65*
transition pressures and 67–8
Kramers–Kronig relations 213, 301
Kramers–Kronig transformations
excitonic transitions 251, 252
Franz–Keldysh effect 298–9
free electron-hole pair transitions 246, 250
model dielectric function and 258
nonlinear refractive index 310
Kronecker delta 212

L-point intravalley deformation potentials 183–8
Langreth's formula 151

lasers and refractive indices 219, 240, 278
lattice absorption. *See* absorption coefficient.
lattice constants
  crystal structure and **11**, 12–13
  cubic semiconductors **7**
  Debye temperature and 28–9
  E_0-gap energies and 115, *117*, *118*
  E_1-gap energies *130*
  elastic constants and 46–7, *48*, 49
  electron affinity and 196, *197*
  external dependencies 13
  hexagonal and rhombohedral semiconductors **8**
  melting points and *26*
  molecular weights and 115–17
  optical phonon deformation potential and *183*
  shear deformation potential and *180*
  transition pressures and *15*
lattice dynamic properties 73–92
  mode Grüneisen parameter 87–8
  phonon deformation potential 88–92
  phonon dispersion relation 73–80
  phonon frequencies 80–7
lattice imperfections and Urbach tails 257–8
lattice parameter pressure dependence *61*
lattice thermal conductivity 34–5, **37**
lattice vibrations
  Debye temperature and 28
  reststrahlen region and 216
lead salts 242
linear compressibility **57**, **58**
  hexagonal and rhombohedral semiconductors 61–2, **63**
linear electro-optic constant 291–5
  experimental value 294, **295**
  symmetry and **293**
  theoretical expression 291
linear thermal expansion coefficients
  energy-gap calculations and 123
  specific heat and 27, 30
  temperature variation of, for GaP **34**
LO phonon scattering 348, **350**, *351*
Lorentzian line shape 224
low-field electron mobility 315–31
  See also Hall mobility.
  doping effects 326–8
  electron scattering mechanisms 315–20
  Hall scattering factor 328–31
  pressure effects 325–6
  room-temperature values 321–4
  temperature effects 324–5
  three-valley model 320–1
low-field hole mobility 331–9
  hole scattering mechanisms 331–3
  room-temperature values 333, **334**, *335*
Luttinger parameters
  wurtzite structures 160–1, **163**,
  zinc-blende structures 114–15, 160, **165**, *166*
  hexagonal and rhombohedral semiconductors **169**
Lyddane–Sachs–Teller relationship 218, 223

Mach–Zehnder interferometry 302
magnetic field and Hall scattering *331*
magnetophonon resonance techniques
  effective mass doping effects and 156
  electron effective mass and 148, 152
majority-electron mobilities 353, *355*
Marcus–Kennedy formula 29
Matthiessen's rule 316
MDF. *See* model dielectric function.
melting points 23–6
  lattice constants and *26*
  tabulated **25**
metals and Schottky barriers 199, 205
MgO
  Knoop microhardness 67
  rocksalt crystal structure *8*, 9–10
microhardness 62–8
Miller's parameter 305–7
minority-carrier transport
  electrons in p-type materials 353–9
  holes in n-type materials 359–62
minority-electron drift velocity 356–7
minority-electron lifetime 356–8
minority-electron mobility 353–6
minority-hole diffusion length 360–2
minority-hole lifetime 360–2
minority-hole mobility 359–60
model dielectric function 258–63
  E_1 and $E_1 + \Delta_1$ transitions 259–60
  critical-point parameters for GaAs **266**
  critical-point parameters for Si **264**
  fundamental absorption edge 259
  higher-energy transitions 260–1
  plasma and d-band effects 262–3
molecular density 13
molecular weights 4
  cubic semiconductors **7**
  E_0-gap energies and *118*

molecular weights (*continued*)
E_1-gap energies and *132*
hexagonal and rhombohedral semiconductors **8**
lattice constants and *12*
momentum space. *See* reciprocal space.
Monte Carlo simulation 340–1, 349–51, 354–6
Moss's rule 240–1
Mott gap 269–70
Murnaghan equation 59, *61*

near-neighbor distance 12–13
bulk modulus and 57–8
negative electron affinity 195
negative thermal expansion 32
neutral impurity scattering 319
neutron scattering measurements
phonon density of states 79
phonon dispersion and 76
phonon frequencies 80
no barrier electron emission 195
nonlinear optical constants 302–11
experimental value 304, **306**
form and symmetry class **305**
second-harmonic-generation coefficient 307
second-order susceptibilities 302–7, **306**
third-order susceptibilities 308–9
two-photon absorption 309–11
nonpolar optical phonon scattering 318
normal-incidence reflectivity 214
GaAs *267*
Si *265*
spectral dependence in InP *225*
w-CdS *268*

optical absorption
band diagram *271*
w-CdS *268*
doping effect 255–6
excitonic transitions 251–3
experimental work 253–6
free electron-hole pair transitions 245–50
at the fundamental absorption edge 244–56
GaAs *267*
multiphonon absorption spectra 228–30
Si *265*
optical dielectric constant 215
optical dispersion relations 79, 211–17
indirect band gaps and 137–8
optical dispersion relation 213–14
optical spectra 216–17
optical sum rule 214–16
optical phonon deformation potential
Γ-valance-band states 181–3
L-conduction-band states 185, **186**
optical phonon frequencies 82, **83**, *84*
cubic semiconductors **81**
frequency difference 82, **83**, *84*
hexagonal semiconductors **82**
mode Grüneisen parameter **87**, **88**
pressure effects 86–7
strain effects 89
stress effects 90
temperature effects 85
optical phonon scattering 317–18, 341–2, *343*
LO phonon scattering 348, **350**, *351*
valence-band deformation potentials and 176
optical properties 211–78
free-carrier absorption 270–4
fundamental absorption edge 230–58
interband transition region 258–70
interconduction-band absorption 274–5
intervalence-band absorption 275–78
optical dispersion relations 211–17
reststrahlen region 217–30
optical spectra 216–17
interband transitions and 105, 263–8
optical sum rule 214–16
optoelectronic devices 291
orbital configuration and crystal structure 4, 6

Pauling ionicity 2, **3**
PDP. *See* phonon deformation potential.
Penn model, refractive index 241–2
performance and microhardness 63
phase diagrams 23, *24*
phase space. *See* reciprocal space.
phase transitions 14–15, **16**
See also transition pressure.
direct–indirect-gap transition pressure and 143
Phillips ionicity 2, **3**
elastic stiffness and 46, *47*
energy-gap pressure effects and *127*
Fröhlich coupling constant and **100**, 101
isotropy factor and **59**
optical phonon frequency and 82, **83**, *84*

piezoelectric stress constant and 95–7
shear deformation potential and *179*
thermal conductivity and 35, *36*
phonon deformation potential
cubic semiconductors 88–91
hexagonal semiconductors 910–12
phonon density of states 79–80
phonon dispersion relation 73–80
dispersion curves 75–9
phonon frequencies 80–7
reststrahlen spectra 224
phonon scattering
electron energy and, in GaAs *341*
electron saturation drift velocity and 348, **350**
LO phonon scattering 348, **350**, *351*
phonons
See also acoustic phonons; optical phonons.
acoustoelectric amplification 99
optical and acoustic 75–6
thermal conductivity and 33–4
photoelastic coefficient 285
dispersion factors **288**
wavelength and 289
photoelastic constants **286**, **287**
See also elasto-optical effect.
photoluminescence excitation spectroscopy 129
photon energy and effective dielectric constant 215–16
photoreflectance measurements 122
piezo(electro)reflectance 289
piezobirefringence 285
piezoelectric scattering 318
piezoelectric strain constant 98–9
cubic semiconductors **97**
hexagonal semiconductors **98**
tensor form **96**
piezoelectric stress constant 95–8
cubic semiconductors **97**
hexagonal semiconductors **98**
relationship to coupling constant 99
relationship to strain constant 98
tensor form **96**
piezoellipsometry 290
piezo-optical coefficients 290–1
Pikhtin–Yas'kov formula 238
plasma effects, model dielectric function 262–3
plasmon scattering 355
Pockels effect 292, 295, 302, 303–4
point groups 10, **11**, 74
Poisson's ratio
cubic lattices 54–6
hexagonal semiconductors 60, **61**, **62**
polar optical phonon scattering 317–18, 341–2, *343*
polarization
dielectric permitivity and 211
nonlinear polarization vector 302–3
sound propagation and **69**
polaron effect 151–2, 168–9
polytypes, SiC crystals 7–9
power-dissipating devices 34
pressure coefficients **26**
E_0-gap energies 180
Ge dielectric constants 222
Schottky barrier height and 206
pressure effects
See also stress effects.
dielectric constants 220–2, 227–8, 235
direct–indirect-gap transition pressure 142–3
E_0-gap energies 124–5
elastic stiffness 50–1
electron effective mass, Γ valley 153–5
exciton binding energies 234–5
Hall hole mobility 337
hole effective masses 170
hydrostatic deformation potentials **181**, 183–4, **185**, **188**
indirect band gaps and 139–41
low-field electron mobility 325–6
optical absorption spectra 254–5
phase transitions and 14–15, **16**
phonon frequencies and 86–87
refractive index 242–4
Schottky barrier height 205–6
propagation direction, sound 69, **70**, **71**

quadratic electro-optic constant 295–300
experimental value 298
symmetry class and **297**
theoretical expression 295
quadratic photoelastic coefficient 289

Raman spectroscopy 80, 289
reciprocal lattice 74, 104
reciprocal space 73
See also Brillouin zones.
energy-band structure and 104
reduced atomic mass
optical phonon frequency and 82, **83**

reduced atomic mass (*continued*)
phonon deformation potential and 89
reduced exciton mass 235
refractive indices
complex refractive index 213
doping effect 243–4
E_0-gap energies and *240*
Franz–Keldysh effect and 301
free-carrier induced changes 278
injection lasers and 219, 240, 278
near the fundamental absorption edge 236–44
pressure effects 242–4
temperature effects 241–2
relaxation times, impurity scattering 341
reststrahlen spectra 217–30
hexagonal semiconductors 226–7
introduced 216
multiphonon optical absorption spectra 228–30
rocksalt crystal structure 222
zinc-blende crystal structure 222
rhombohedral semiconductors
See also hexagonal and rhombohedral semiconductors.
α-HgS 9
Brillouin zones 75
rocksalt crystal structure *8*, 9–10
molecular density and near-neighbor distance 13
reststrahlen spectra 222
Rydberg energy 231, 260

satellite valley electron effective mass 158–9
scaling parameter, thermal conductivity 35
Schottky barrier devices 203, 365
Schottky barriers 198–207
Au/semiconductor case study 202–4
barrier height and metal work function *200*, *201*, **202**
breakdown voltage 206–7
electroreflectance 187
ideal Schottky–Mott contacts 198–9, 201–2
surface reconstruction 204–5
Schrödinger equations 103, 230
second-harmonic generation coefficient *307*
Sellmeier equation 237
shear modulus **57**, **58**, 67
hexagonal semiconductors 61–2
SHG. *See* second-harmonic generation coefficient.
Shubnikov–de Haas effect 148, 156
Si
absorption coefficient and wavenumber *229*
band-gap narrowing on doping 127, *128*, *129*
cleavage energies 18
diamond crystal structure 4, *8*
electron drift velocity and electric field for *n*-type Si *345*, *346*
energy-band structure *104*
Hall hole mobility for *p*-Si 334, *336, 338*
Hall mobility and electron concentration in *n*-Si *328*
hole drift velocity for *p*-Si *353*
impact ionization coefficient anisotropy *368*
lattice parameter pressure dependence *61*
majority- and minority-hole mobilities *360*
metal (silicide) contacts 205–6
minority-electron drift velocity in *p*-Si *357*
minority-electron mobility in *p*-Si 355
optical spectrum above the first absorption edge 263–5
phase diagram for Ge, GaSb and 23, *24*
phonon dispersion curve 77
plasma effects *262*
SiC
crystal polytypes 7–9
Hall factor and magnetic field *331*
Schottky barrier height and metal work function *200*
simplified interband transition model 238–9
single oscillator models
dielectric permitivity 222–3, 224
refractive index 237–8
β-Sn. *See* phase transitions.
sound velocity 68–71
space groups 10, **11**, 74
space-charge scattering 319–20
specific heats 26–7
linear expansion coefficient and 30
tabulated **25**
spectral characteristics, GaAs *216*
spectral variation, complex dielectric permitivity *223*
spectroscopic ellipsometry 270
sphalerite. *See* zinc-blende.
spin-exchange interaction constant 236
spin–orbit interactions
diamond crystal structure 105–6
E_0-gap region 114–15

wurtzite crystal structure 108–9
zinc-blende crystal structure *107*
spin–orbit split-off energies
anion atomic number and *119*
anion atomic number and *133*
E_0-gap energies and 117–18, **119**
E_1-gap energies and 132–3, *134*
two-photon absorption 311
Stark-like effects 294, 297, 298
static dielectric constant 217–20
temperature and pressure effects 227–8, 235
stress effects
See also piezoelectric effects.
E_1-gap energies *187*
elasto-optic effect 284
epitaxial films 283
phonon deformation potential 88–92
zinc-blende energy-band structure *174*, 177
stress-induced birefringence 285
structural properties 1–20
cleavage properties 15–20
crystal structure 4–10
ionicity 1–3
isotopic abundances 3–4, **5**
lattice constants 12–13
molecular and crystal densities 13–14
molecular weights 4, **7**
phase transitions 14–15, **16**
space groups 10, **11**
surface energies
cleavage energies and 18–20, **19**
experimentally determined 20, **20**
surface polarity and cleavage energy 18
surface reconstruction and Schottky barrier height 204–5
symmetries
See also crystal structure.
effect on dielectric and optical properties **212**
piezoelectric effects and 95, **96,** 318
space groups and point groups 10, **11**
wurtzite conduction and valence bands 111
symmetry classes
See also space groups.
elastic constant and **42**, **43**
linear electro-optic tensor form **293**
photoelastic tensor form **284**
quadratic electro-optic tensor form **297**
second-order nonlinear optical susceptibility tensor **305**
thermal conductivity and **34**
thermal expansion coefficient and 30–1
third-order nonlinear optical susceptibility tensor **308**

temperature coefficient of refractive index 242
temperature effects
dielectric constants 219–20, 227–8
E_0-gap energies and 120–4
E_1-gap energies and 133–4, *135*
elastic stiffness 48–50
electron affinity 198
electron effective mass, Γ valley 152–3
electron saturation drift velocity 347–8
Hall hole mobility 335–7
Hall scattering factor 330
hole effective masses 170
hole saturation drift velocity 353
impact ionization coefficients 366–8
indirect band gaps and 138–9
low-field electron mobility 324–5
optical absorption spectra 253–4
phonon frequencies and 84–6
refractive index 241–2
Schottky barrier height 205
thermal expansion coefficients 32
thermal conductivity 33–9
symmetry classes and **34**
temperature variation *36*, **37**
thermal expansion coefficient and **31**
thermal deformation and symmetry 30–1
thermal diffusivity 39
thermal expansion coefficients 30–3
See also linear thermal expansion coefficient.
volume thermal expansion coefficient 88
thermal properties 23–39
Debye temperature 28–30
melting points 23–6
specific heats 26–7
thermal conductivity 33–8
thermal diffusivity 39
thermal expansion coefficients 30–3
thermal resistivity. *See* thermal conductivity.
thermoelectronic devices 34
third-order elastic constants 51–3, 60
third-order nonlinear optical susceptibility tensor **308**
Thomas–Reich–Kuhn sum rule 214
three-valley model, electron mobility 320–1
transit time devices 347

transition pressures **14**, *15*
direct–indirect-gap transition pressure 143
Knoop microhardness and 67–8
two-particle wave equations 230
two-photon absorption 309–11

ultrasound
amplification 99
measurements 42–3, 50
unit-cell volume and Knoop microhardness 63–4, *65*
Urbach tails 256–8

valence energy bands
anisotropy 162
components 331
conduction band transitions 105
conduction-valley energy separations 142
degeneracy 331
electron density of states 113
intervalence-band absorption 275–8
splitting *110*
symmetry 111
valence-band deformation potentials 175–9
hexagonal semiconductors **180**
L-valence-band states 186, **187**
notations **177**
valence-band Hamiltonian 114
deformation potentials and 176
Varshni equations for temperature dependence
E_0 band-gap energy 120, 121, *122*, 220
elastic stiffness 50
electron effective mass 152–3
higher-lying direct band gaps 133, *135*
indirect band gaps and 138–9
optical phonon frequency 85–6
Vickers indentation method 63
Voigt averaged sheer modulus 67
volume thermal expansion coefficient 88

Wiedemann–Franz–Lorenz law 38
Wigner–Seitz unit cell 104
wurtzite crystal structure 6, *8*
See also hexagonal semiconductors.
conduction-band and valence-band symmetries 162–3
E_0-gap region 114–15
electron effective mass and E_0-gap region **151**
energy-band structure 108–11
molecular density 13
near-neighbor distance 13
phonon dispersion compared with zinc-blende 77–8
SiC 9
valence-band splitting *110*

X-point intravalley deformation potentials 188–9
XPS (X-ray photoelectron spectroscopy) 112, *113*, 128, 196
X-ray crystal density 14

Young's modulus 53–62
hexagonal semiconductors 60, **61**, **62**

zinc-blende crystal structure 6, *8*
See also cubic semiconductors.
cleavage planes in *17*, 18
conduction-band Hamiltonian 158
conduction-band symmetry 190
E_0-gap region 114
elasto-optic contribution 292
electromechanical coupling constant **100**
energy-band stress effects *174*
energy-band structure 106–8
intervalence-band absorption 275, *276*
linear electro-optic constant 294
molecular density 13
near-neighbor distance 12
nonlinear susceptibility **303**
phonon deformation potential 89
phonon dispersion compared with wurtzite 77–8
piezoelectric effects 95
quadratic electro-optic constant 296, 298
reststrahlen spectra 222
valence-band splitting *110*
valence-band Hamiltonian 160
ZnO
E_0-gap energies and temperature 122, *123*, *124*
electron affinity 196
linear pressure coefficient 206
phonon dispersion curve 77, *78*
Schottky barrier height and metal work function *201*
spin-exchange interaction constant 236
thermal expansion coefficient versus temperature 32, *33*
ZnS thermal conductivity **32**, 34

ZnSe
electron density of states 112–13
Hall mobility and electron concentration in *n*-ZnSe *329*
plasma and *d*-band spectral effects 262–3
second-harmonic-generation coefficient *307*
two-photon absorption coefficient 310–11
ZnTe
Hall hole mobility and hole concentration in *p*-ZnTe *339*
lattice parameter pressure dependence *61*
refractive-index dispersion *239*
Schottky barrier height and metal work function *203*
thermal expansion coefficient versus temperature *33*
zone-center effective mass
cubic semiconductors **150**
wurtzite crystal structure **151**
zone-center Γ point 74–5
Γ-valley electron effective mass 147–58
intravalley deformation potential 173–83